

Universidade do Minho
Escola de Engenharia

José Luís Ferreira da Silva Ramos

Damage Identification on Masonry Structures Based on Vibration Signatures

Identificação de Dano em Estruturas de Alvenaria Baseada na Medição de Vibrações

Tese de Doutoramento
Engenharia Civil / Estruturas

Trabalho efectuado sob a orientação do
Professor Doutor Paulo José Brandão Barbosa Lourenço
Universidade do Minho
Doutor Alfredo Peres de Noronha Campos Costa
Investigador Principal do LNEC

Setembro de 2007

DECLARAÇÃO

José Luís Ferreira da Silva Ramos

Endereço electrónico: lramos@civil.uminho.pt Telefone: 253 510 200

Número do Bilhete de Identidade: 10837303

Título dissertação □/tese □

Damage Identification on Masonry Structures Based on Vibration Signatures

Identificação de Dano em Estruturas de Alvenaria Baseada na Medição de Vibrações

Orientador:

Professor Doutor Paulo José Brandão Barbosa Lourenço

Universidade do Minho

Doutor Alfredo Peres de Noronha Campos Costa

Investigador Principal do LNEC

Ano de conclusão: 2007

Designação do Doutoramento:

Doutoramento em Engenharia Civil – Estruturas

É AUTORIZADA A REPRODUÇÃO INTEGRAL DESTA TESE/TRABALHO APENAS PARA EFEITOS DE INVESTIGAÇÃO, MEDIANTE DECLARAÇÃO ESCRITA DO INTERESSADO, QUE A TAL SE COMPROMETE

Universidade do Minho, ___/___/_____

Assinatura: _____

…to Inês and André

Acknowledgements

This thesis would not be completed without the help of all that, directly or indirectly, were involved in my work and successfully contributed to its conclusion. Among the different support, I would like to express my gratitude to:

- Professor Paulo Lourenço, my supervisor and mentor, for his full support and encouragement, the interesting discussions, patience and careful reading;
- Doctor Alfredo Campos-Costa, my co-supervisor, for the permanent and interesting discussions, and the tremendous help and support in the beginning of the works;
- Professor Guido de Roeck for his kindness and for accepting me in his workgroup in the Katholiek Universiteit Leuven, during a period of six months in 2006. The fruitful discussions and the software MACEC successfully contributed to my work;
- The closer colleagues in University of Minho, for their support and interest in my work, especially Daniel, Graça, Isabel, Sena, Jorge, Tiago, Eduardo, and Vítor. Special thanks to Salvador, Lukasz and Rolando for the collaboration in the laboratory tests;
- The colleagues in Katholiek Universiteit Leuven, Özer, Mattias, David, Stijn and Edwin, for the nice welcome and for the exchange of cultural and scientific knowledge;
- Matos, Marco, and Gonçalves for their tremendous help and support in the laboratory works;
- João Roque for his help in the experimental tests and numerical analysis of the Jerónimos Church;
- Filippo Casarin for his continuous encouragement and interest in my work;
- Leandro Marques for the close collaboration in the experimental and numerical works of the Mogadouro Clock Tower;
- Anabela Martins for helping download the data from the dynamic monitoring system of Jerónimos Church;
- The City Council of Mogadouro and Arq. Alexandra Machado, for their unconditional support in the experimental tests in the Mogadouro Clock Tower;

- The Portuguese Science Foundation (FCT) for the grant awarded during 2006, Contract SFRH/BD/24688/2005;
- The Project ECOLEADER-LIS, Enhancing Seismic Resistance and Durability of Natural Stone Masonry, for the opportunity to study one mock-up building in the National Laboratory of Civil Engineering.

And finally, I would like to make a special acknowledgment to my family:

- My parents and fathers-in-law for they support and continuously interest for my work, and for all the assistance to Marília during my scholarship in Leuven;
- My brother Tó Manuel for his support and patience during all the work;
- My brother Paulo and my brother-in-law Francisco for their support and help in the Mogadouro Clock Tower tests;
- And last, but not the least, my wife, Marília, and my children, Inês and André, for their love and their forgiveness for all the time that I was absent.

Abstract

Preservation of architectural heritage is considered a fundamental issue in the cultural life of modern societies. In addition to their historical interest, monuments significantly contribute to the economy of cities and countries by providing key attractions. In this context, structural damage identification at an early stage plays an important role for heritage preservation.

Damage on masonry structures mainly relates to cracks, foundation settlements, material degradation and displacements. When cracks occur, generally they are localized, splitting the structures in macroblocks. Dynamic based methods to assess the damage are an attractive tool to this type of structures because they are non-destructive methods and are able to capture the global structural behavior.

Motivated by the above reasons, this thesis aims at exploring damage in masonry structures at an early stage by vibration measurements. For this purpose, and after a state of the art review, one arch and one wall model were constructed in the laboratory. These replicates of historical constructions were built as reference, undamaged, state. Afterwards, progressive damage was induced and sequential modal identification analysis was performed at each damage stage, aiming at finding adequate correspondence between dynamic behavior and internal crack growth. Comparisons between different techniques based on vibrations measurements were made to evaluate which method is more adequate to identify damage in masonry constructions. The dynamic based methods allowed detecting and locating the damage in the specimens. The different methods were also classified with respect to the damage identification level and a methodology based on the combination of different methods is proposed for damage identification in masonry structures.

In order to further apply the conclusions resulting from the analyses in the laboratory tests to real case studies, two monuments in Portugal were also studied: the Clock Tower of Mogadouro and the Church of Jerónimos Monastery, in Lisbon. Vibration sensors, temperature sensors, relative air humidity sensors and wind sensors were installed in the two monuments. Dynamic based analysis was used to estimate the modal parameters, followed by statistical analysis to evaluate the environmental and loading effects on the dynamic response. The aim is to use the dynamic based methods as a part of a health monitoring approach to preserve the historical constructions. A relevant conclusion is that environmental effects are very significant and, if not properly tackled, mask any dynamic damage analysis.

Resumo

A preservação do património arquitectónico é actualmente um aspecto fundamental das sociedades modernas. Para além do interesse histórico, ao criarem pontos de atracção os monumentos contribuem significativamente para a economia das cidades e dos países. Neste âmbito, a identificação de dano estrutural numa fase inicial torna-se muito importante para a preservação do património.

O dano em estruturas de alvenaria caracteriza-se, essencialmente, pela ocorrência de fendas, assentamento das fundações, degradação dos materiais e deformações excessivas. Quando ocorrem fendas, normalmente elas são localizadas e dividem as estruturas em macroblocos. Por serem métodos não-destrutivos e capazes de identificar o comportamento estrutural global, os métodos de identificação de dano baseados na análise dinâmica são muito atractivos para este tipo de estruturas.

Em função destas considerações, a presente tese tem como objectivo a identificação de dano em estruturas de alvenaria ainda num estado muito inicial. Para esse fim e após uma revisão do estado da arte, foram estudados em laboratório dois modelos à escala reduzida, nomeadamente um arco e uma parede. Em ambos os modelos foram aplicados cenários de dano progressivo. Para o estado inicial e para cada cenário de dano foram realizadas identificações dinâmicas para estudar a relação entre a progressão do dano e a variação da resposta dinâmica. Vários métodos de identificação de dano foram utilizados com o intuito de avaliar qual ou quais métodos são mais adequados para a identificação de dano em estruturas de alvenaria. A partir dos métodos dinâmicos foi possível identificar o dano nos modelos. Os diferentes métodos foram ainda classificados de acordo com o nível de identificação e uma metodologia de análise baseada na combinação de alguns métodos foi proposta para identificar o dano em estruturas de alvenaria.

Tendo em vista aplicar em casos reais o conhecimento adquirido nos testes laboratoriais, dois monumentos em Portugal foram estudados: a Torre do Relógio em Mogadouro e a Igreja do Mosteiro dos Jerónimos em Lisboa. Foram instalados nos monumentos sensores de vibração, temperatura, humidade, deformação e vento. As propriedades modais das estruturas foram medidas experimentalmente e os efeitos dos parâmetros ambientais foram avaliados por intermédio de uma análise estatística. O objectivo final é possibilitar a utilização de métodos baseados na medição de vibrações como parte do plano de monitorização e manutenção dos monumentos. Uma conclusão relevante é que os parâmetros ambientais têm um efeito significativo na resposta dinâmica da estruturas, sendo necessário avaliá-los convenientemente para ser possível a identificação de dano.

Glossary

List of Symbols

α, β	Penalty factors
α^m	Normalized scale factors
χ	Mother wavelet
Δt	Sampling period
Δf	Frequency resolution
ΔL	Distance between points
Φ	Eigenvectors matrix
Φ_m	Mass-normalized eigenvectors matrix
ϕ	Mass-scaled mode shapes
Γ_m	Mass-normalized mode shape matrix
γ^2	Coherence function
φ	Real eigenvectors or real mode shapes
φ_{exp}	Measured modal displacement
κ	Calculated modal curvatures
λ_i^2	Real eigenvalues or real eigen frequencies
Λ	Eigenvalues matrix
ε	Strain deformation
π	Objective function
π	Pi constant
$\nabla\pi(\theta)$	Gradient of the objective function
ϑ, ϑ_n	Phase angle
$\nabla^2\pi(\theta)$	Hessian of the objective function
Ω_{m}	Diagonal modal stiffness matrix
ω_D	Damped frequency
ω	Eigen frequency or resonant frequency
ω_n	Natural frequency
θ	Updating parameters
$\hat{\sigma}_x, \hat{\sigma}_y$	Estimated standard deviation
τ	Impulse instant

ξ	Damping coefficient
Ψ	Complex modes shape matrix
ψ	Calculated modal rotations

$\boldsymbol{A}$	Discrete-time state matrix
a	Wavelet dilated
a_0, a_i	Coefficients
$\boldsymbol{A}^{AR}$	Parameter matrix from auto-regressive part
$\boldsymbol{A}_c$	Continuous-time state matrix
a_n, b_n	Spectral Fourier coefficients
A_q, B_q	Operator polynomials
$\boldsymbol{B}$	Discrete-time input matrix
b	Wavelet translated
$\boldsymbol{B}_2$	Matrix with the location inputs
$\boldsymbol{B}_c$	Continuous-time input matrix
C	Constant
c	Damping constant
$\boldsymbol{C}$	Discrete-time output matrix
$\boldsymbol{C}_2$	Viscous damping matrix
$\boldsymbol{C}_a$	Location matrices for accelerations
$\boldsymbol{C}_c$	Continuous-time output matrix
$\boldsymbol{C}_d$	Location matrices for displacements
ci	Confidence intervals
$\boldsymbol{C}^{MA}$	Parameter matrices from moving average part
$\boldsymbol{C}_v$	Location matrices for velocities
$\boldsymbol{D}$	Discrete-time direct transmission matrix
d	Number of estimated parameters
$\boldsymbol{D}_c$	Continuous-time direct transmission matrix
E_χ	Entropy energy
EI	Bending stiffness
e_k	Residuals
$\boldsymbol{e}_k$	Stochastic white noise vector process
$\boldsymbol{F}$	Flexibility matrix
$f_{\max}$	Maximum frequency of interest
f_{Nyq}	Nyquits frequency
F_r	Rotational flexibility
f_S	Sampling frequency
f_t	Tensile strength
g	Gravity acceleration
$\boldsymbol{G}(\theta)$	Hessian matrix
GJ	Torsion stiffness
$\boldsymbol{H}$	Frequency response function matrix
$\boldsymbol{h}$	Hankle matrix
$H(\omega)$	Frequency response function
$\boldsymbol{I}$	Identity matrix
$\boldsymbol{J}(\theta)$	Jacobian matrix
$\boldsymbol{K}$	Stiffness matrix
k_e	System stiffness
k^l	Loading stiffness

k^m	Modal stiffness
K_r	Rotational stiffness
k^u	Unloading stiffness
L	Length of a structural element
$\boldsymbol{L}$,$\boldsymbol{Q}$	Factors from a LQ factorization
$\boldsymbol{M}$	Mass matrix
m	System mass
M^m	Bending Moment
m^m	Modal mass
N	Number of samples
na	Autoregressive order
nb	Exogeneous order
nk	Number of delays
$P(\omega)$	Fourier transforms of the excitation $p(t)$
$\boldsymbol{p}(t)$	Generalized excitation vector
$p(t)$	Time-dependent excitation of a system
q	Shift operator
$\ddot{q}$ (t)	Time-dependent acceleration of a system
$\dot{q}$ (t)	Time-dependent velocity of a system
$Q(\omega)$	Fourier transforms of the response $q(t)$
$\boldsymbol{q}(t)$	Generalized response vector
$q(t)$	Time-dependent displacement of a system
$\boldsymbol{q}_m(t)$	Modal displacements
$r(\theta)$	Residuals
r_{xy}	Correlation coefficient
$r_{xy}{}^2$	Coefficient of determination
$\hat{R}_{xy}$	Estimated covariance
$\boldsymbol{S}_{(i,i)}$, $\boldsymbol{S}_{(j,j)}$	Auto Power Density Function
$\boldsymbol{S}_{(i,j)}$	Cross Power Density Function
S_f	Significant indicator
T	Period
t_k	Time instant
T^m	Torsion moment
T_n	Natural period
T_S	Complete measured time
$\boldsymbol{U}_{(\omega)}$	Fourier spectrums of the excitation
$\boldsymbol{u}(t)$	Input vector
$u(t)$	System dynamic response
$\boldsymbol{u}^{env}{}_k$	Environmental effects
v	Calculated modal displacement
V	Loss function
$\boldsymbol{v}_k$	Measurement noise
W	Weight constant
$w(t)$	Window time function
$\boldsymbol{w}_k$	Process noise
$X(\omega)$	Fourier transform of x(t)
$\boldsymbol{x}(t)$	State vector
$x(t)$	Time signal or periodic signal
x_k	Discrete-time space state vector

$\boldsymbol{Y}_{(\omega)}$	Fourier spectrums of the response
$\boldsymbol{y}(t)$	Response vector
$\boldsymbol{Y}_f$	Future information of the hankle matrix
$\boldsymbol{Y}_p^{ref}$	Past information of the hankle matrix
Z	Normalized damage index

List of Abbreviations

ADC	Analogue to Digital Converter
ARMA	Auto-Regressive Moving Average
ARMAV	Auto-Regressive Moving Average Vector models
ARX	AutoRegressive output with an eXogeneous input part model
CFM	Changes in Flexibility Matrix method
CLM	Coupled Local Minimisers
COMAC	Co-ordinate Modal Assurance Criterion
CWT	Continuous Wavelet Transform
DAQ	Data AcQuisition system
DFT	Discrete Fourier transform
DIM	Damage Index Method
DS	Damage Scenario
DSCM	Direct Stiffness Calculation Method
EFDD	Enhanced Frequency Domain Decomposition method
FDD	Frequency Domain Decomposition method
FE	Finite Element
FEMU	Finite Element Model Updating method
FFT	Fast Fourier Transform
FPE	Final Prediction Error
FRF	Frequency Response Function
GPS	Global Position System
GSM	Global System for Mobile communication
IGESPAR	Portuguese Authority for the Architecture and Archeological Heritage
IRF	Impulse Response Functions
LNEC	Laboratório Nacional de Engenharia Civil
MAC	Modal Assurance Criteria
MDOF	Multi-Degree Of Freedom
MEMS	Micro Electric Mechanical Systems
MIMO	Multi-Input-Multi-Output algorithm
MISO	Multi-Input-Single-Output algorithm
MSCM	Mode Shape Curvature Method
ND	Non-Destructive
NMD	Normalised Modal Difference
OMA	Operational Modal Analysis
PM	Parameter Method
PP	Peak Picking method
PSD	Power Spectra Density function
RD	Random Decrement
RS	Reference Scenario

SAD	Sum of Absolute Differences
SCE	Sum of Curvature Errors method
SDOF	Singel-Degree Of Freedom
SIMO	Single-Input-Multi-Output algorithm
SISO	Single-Input-Single-Output algorithm
SSD	Square Sum Differences
SSI	Stochastic Subspace Identification method
SSI-DATA	DATA driven stochastic subspace identification
USB	Universal Serial Bus
USI	Unified Significance Indicator
VI	Virtual Instrument
WPD	Wavelet Packet Decomposition
WPS	Wavelet Packet Signature
WSN	Wireless Sensors Networks

Index

Abstract

Resumo

Glossary

1 Introduction

1.1 Motivation for Damage Identification on Masonry Structures 2
1.2 Background of Damage Identification Analysis 3
1.3 Focus of the Thesis....3
1.4 Outline of the Thesis 4

2 Basic Dynamics and Experimental Testing

2.1 Introduction 8
2.2 Basic Dynamics....8
2.2.1 Classical Formulation 9
2.2.2 State-Space Formulation....12
2.2.3 Auto-Regressive Models....15
2.3 Experimental Modal Identification 16
2.3.1 Excitation Mechanisms....16
2.3.2 Response Transducers....17
2.3.3 Data Acquisition Systems....20

2.3.4 Micro-Electro-Mechanical Systems and Wireless Sensor Networks 24
2.3.5 Input-Output Identification Techniques 26
2.3.6 Output-Only Identification Techniques 30
2.3.7 Test Planning 37
2.3.8 Mode Shape Mass Normalization 38
2.4 Environmental and Loading Conditions Influence 39
2.4.1 Linear Regression 41
2.4.2 ARX Models 42
2.5 Conclusions 44

3 Dynamic Based Damage Identification

3.1 Introduction 46
3.2 Historical Overview 48
3.3 General Methods Classification 48
3.4 Review of Selected Methods 51
3.4.1 Non-Model Based Methods 51
3.4.2 Finite Element Modal Updating Method 58
3.5 Conclusions 63
3.5.1 General Remarks 63
3.5.2 Application to Masonry Structures 64

4 Description of an Arch Model and Experimental Tests

4.1 Introduction 68
4.2 Arch Model Description 68
4.3 Preliminary Studies 69
4.3.1 Numerical Prediction for Crack Locations 69
4.3.2 Numerical Estimation of Modal Parameters 70
4.4 Arch Static Damage Tests 71
4.5 System Identification Tests 75
4.5.1 Test planning 75

4.5.2 Reference Scenario Results with Different Stochastic Subspace Identification Techniques 79
4.5.3 Environmental Tests in the Laboratory....85
4.5.4 Mass Scaled Tests....89
4.6 Conclusions....91

5 Damage Identification in the Arch Model
5.1 Introduction....94
5.2 Proposed Approach....94
5.2.1 Selected Methods....94
5.2.2 Calculation of the Modal Curvatures....97
5.3 Preliminary Model Updating Analysis....99
5.4 Numerical Damage Simulation and Identification....102
5.4.1 Damage Identification without Noise....104
5.4.2 Damage Identification with Added Noise....109
5.5 Experimental Damage Identification....111
5.5.1 Analysis with Global Parameters....111
5.5.2 Analysis with Non-Model Based Methods....115
5.5.3 Analysis with the Finite Element Model Updating Method....121
5.6 Conclusions....126
5.6.1 Results with Simulated Damage....126
5.6.2 Results with Experimental Data....127

6 Damage Identification in the Wall Model
6.1 Introduction....130
6.2 Description of the Wall Model....130
6.3 Static Tests for Damage Scenarios....131
6.4 System Identification Tests....139
6.4.1 Numerical Estimation of Modal Parameters....139
6.4.2 Test planning....141
6.4.3 Environmental Tests in the Laboratory....144
6.4.4 Evaluation of the Data Quality....144

6.5 Experimental Damage Identification 147
6.5.1 Analysis with Global Parameters 148
6.5.2 Analysis with Non-Model Based Methods 151
6.5.3 Analysis with the Finite Element Model Updating Method 158
6.6 Conclusions 165

7 Case Studies and Environmental Effects
7.1 Introduction 168
7.2 Proposed Methodology for Damage Identification 168
7.3 Case Study I: Mogadouro Clock Tower 169
7.3.1 Damage and Rehabilitation Works in the Tower 169
7.3.2 Modal Identification Before and After the Rehabilitation Works 171
7.3.3 Structural Assessment 174
7.3.4 Dynamic Monitoring System 184
7.3.5 Automatic Parameter Estimation 186
7.3.6 Environmental and Loading Effects 187
7.4 Case Study II: Church of Monastery of Jerónimos 195
7.4.1 Modal Identification of the Main Nave 197
7.4.2 Modal Identification of Two Columns of the Main Nave 201
7.4.3 Structural Assessment 203
7.4.4 Monitoring Systems 204
7.4.5 Environmental Effects on the Static Behaviour 207
7.4.6 Environmental and Loading Effects on the Dynamic Behaviour 209
7.5 Conclusions 213

8 Conclusions and Future Works
8.1 Conclusions 218
8.1.1 Dynamic Experimental Testing and Damage Identification 218
8.1.2 Laboratory Simulations 219
8.1.3 Case Studies and Environmental and Loading Effects 220
8.2 Future Works 222

References

Annex A

Annex B

Annex C

Annex D

Chapter 1
Introduction

1.1 Motivation for Damage Identification on Masonry Structures

Preservation of the architectural heritage is considered a fundamental issue in the cultural life of modern societies. In addition to their historical interest, monuments significantly contribute to the economy of cities and countries by providing key attractions, see Figure 1.1. Tourism and leisure is a major industry in the 3rd millennium (6 to 10% of the GNP in Europe) and the "cultural" tourism received increasing attention in the last decades. The need of preserving historical constructions is thus not only a cultural requirement but also an economical and developmental demand. Therefore, structural assessment and safety evaluation become significant issues for heritage constructions.



(a) (b)

Figure 1.1 – Examples of moments with significant cultural and economical importance for their countries: (a) Taj Mahal, India; and (b) Monastery of Jerónimos, Portugal.

In the process of preservation of ancient structures, damage evaluation and monitoring procedures by non-destructive methods are particularly attractive, due to the modern context of minimum intervention and respect of the original construction. The use of observational methods, combined with iterative and step-by-step analysis tools, is frequently used, EU-India (2006).

It is known that service loads, environmental and accidental actions may cause damage to structural systems. In this context, life long maintenance plays an important roll. Regular inspections and condition assessment of engineering structures allow programmed repair works and cost-effective management of the infrastructures. In the case of historical constructions, maintenance is even more essential because of their cultural importance, the safety of visitors, potential natural risks and the accumulation of physical, chemical and mechanical damage through time.

Many methods are presented in literature for damage identification based on vibration signatures, but there are few works on their application to masonry-like structures. The current practice of structural health monitoring is still based mainly on visual inspections or condition surveys. During the last decade, software and hardware developments made continuous monitoring possible. Typically, one can install hundreds of sensors in a structure and read the data in real time. The challenge is now focused in what type of information is important to gather from the structural point of view and how the data should be processed and stored for damage analysis.

For the above reasons, it was decided to study damage identification by means of non-destructive procedures or test methods applied to masonry-like structures. The recent developments on system identification techniques as a potential tool for the damage identification, the variety of dynamic based damage identification methods and the importance of the cultural heritage were driving forces of the present work.

1.2 Background of Damage Identification Analysis

Dynamic based damage identification techniques began to be used intensively with the remarkable developments in hardware FFT analyzers, in the 1980's. Historically, there are four main groups of communities which have been using this technology: mechanical engineering, oil industry companies, aerospace engineering and civil engineering. With the same aim, i.e. to detect damage at an early stage in the structures, these groups produced notorious developments in the field. These developments focus on different approaches and test procedures, resulting in a variety of methods and techniques. Until now, no single method has been shown to be efficient in all situations and for all types of structures (Farrar and Doebling, 1998; Choi et al., 2005; and Montalvão et al., 2006).

The mechanical engineering community made remarkable improvements for the task of rotating machinery monitoring. A less successful application of damage detection occurred in the offshore platforms by the oil industry between 1970's and the 1980's. Although remarkable efforts were made to develop dynamic based damage detection methods, the application of the techniques in real case studies was limited. The aerospace community successfully began to use dynamic based damage identification techniques in the earlier 1980's with the space shuttle developments.

In parallel, the civil engineering community started to use the same techniques since the earlier 1980's. Bridge assessment for health monitoring was a first focus of interest, which quickly spread to other constructions. In these structures, the environmental conditions significantly influence the dynamic response and the separation of both effects is still considered a challenge. In literature, several applications on beam structures (steel and concrete), trusses, plates, shells and frames, bridges, buildings and composite materials can be found.

As far as masonry structures are concerned, there are few references in literature dedicated to the problem of damage identification based on dynamic response changes.

1.3 Focus of the Thesis

The thesis addresses damage identification at an early stage by vibration measurements. Initially, a review about dynamic testing and damage identification analysis based on vibration measurements is presented. With respect to experimental testing, besides the description of recent techniques, there is a description on practical issues, like test planning and selection of testing equipment, which are very important for the success of damage identification analysis and are often not adequately discussed. With respect to dynamic based damage identification analysis, different methods were considered for damage identification in masonry structures.

To study the differences between the damage methods, one masonry arch and one masonry wall were constructed in the laboratory. These replicates of historical constructions were built as reference, undamaged, state. Afterwards, progressive damage

was induced and sequential modal identification analysis was performed at each damage stage, aiming at finding adequate correspondence between dynamic behavior and internal crack growth. The dynamic measurements included the records of accelerations and strains in several points of the specimens.

The comparisons between different techniques based on vibrations measurements allowed evaluating which group of methods or which modal information is more adequate to identify damage in masonry constructions. A methodology based on the combination of different methods is proposed for the identification of damage location. The approach presented in the thesis can be considered as a significant contribution for the damage analysis of masonry like structures.

Furthermore, the proposed approach was applied to two monuments in Portugal: the Clock Tower of Mogadouro and the Church of Jerónimos Monastery, in Lisbon. Apart from the detailed description of the monitoring systems, the environmental and loading effects are studied in detail. The aim is to use the dynamic based methods as a part of a health monitoring system to preserve historical constructions. A relevant contribution in this field is the study of environmental and loading effects in the two monuments, where it was possible to conclude that these effects are non-neglected, as they can change significantly the dynamic response. If not properly tackled, these effects can mask any dynamic change from any non-stabilized phenomena.

1.4 Outline of the Thesis

The thesis is organized in eight chapters as follows:

- **Chapter 1** is the introduction to the work, with the motivation, the background, the focus of the thesis, as well as the outline of the text;
- **Chapter 2** presents the state of the art about system identification based on vibration signatures. A brief introduction on dynamics is carried out, followed by the main developments on system identification. Issues addressed include sensor selection, data acquisition systems and test planning. The environmental effects are also discussed and procedures to remove their influence are presented;
- **Chapter 3** presents a state of the art about dynamic based damage identification in structural systems. The main goal is to review the main developments made by researchers during the recent years. Issues addressed are the historical overview of the applicability of damage methods, general classification of methods, and a review of a selected group of methods. Finally, the underlying hypotheses are discussed, concerning the applicability of the existent damage identification methods to masonry-like structures;
- **Chapter 4** presents the description of an arch model and all the experimental tests carried out in the laboratory for damage identification. The arch model was built in the laboratory, and subsequently subjected to programmed and controlled damage. Issues addressed are the preliminary numerical model simulations for static and dynamic behavior of the arch, the description of the static tests series, including the observed damage pattern, the system identification tests on each scenario, the environmental tests to study the influence of temperature and relative humidity inside the laboratory and a series of tests to scale the mode shapes;

- **Chapter 5** presents the damage identification analysis of a masonry arch model. In a first step, an approach to identify the damage based on vibration signatures is addressed. For this purpose, numerical simulations of a cracked arch were adopted instead of the experimental data. The numerical simulation consists of three different finite element models where cracks are incorporated by different procedures. Subsequently, damage identification methods were applied to the experimental data. The damage identification analysis was divided in three groups: global dynamic parameters, non-model based methods and the finite model updating method;
- **Chapter 6** presents the damage identification analysis of a masonry wall model. A description of the model is carried out, followed by the detailed description of the static tests. Next, the dynamic identification tests are addressed. The damage identification analysis is carried out in three phases: global parameters analysis, non-model based methods, and finite element model updating method. The results of each phase are extensively discussed;
- **Chapter 7** presents two cases studies: the Clock Tower of Mogadouro and the Church of Jerónimos Monastery, in Lisbon. A methodology for monitoring and damage identification is proposed based on vibration signatures. For the two cases there is a description of all preceding dynamic analysis before the monitoring task, which includes the installation of the monitoring system, the system identification and subsequent FE model updating analysis for structural assessment. The environmental and loading effects are also addressed. The automatic modal identification procedures to estimate the global modal parameters are presented and numerical models to simulate the structural response are studied;
- **Chapter 8** presents the main conclusions from each chapter and a proposal for future works.

A schematic representation of the outline of thesis is presented in Figure 1.2.

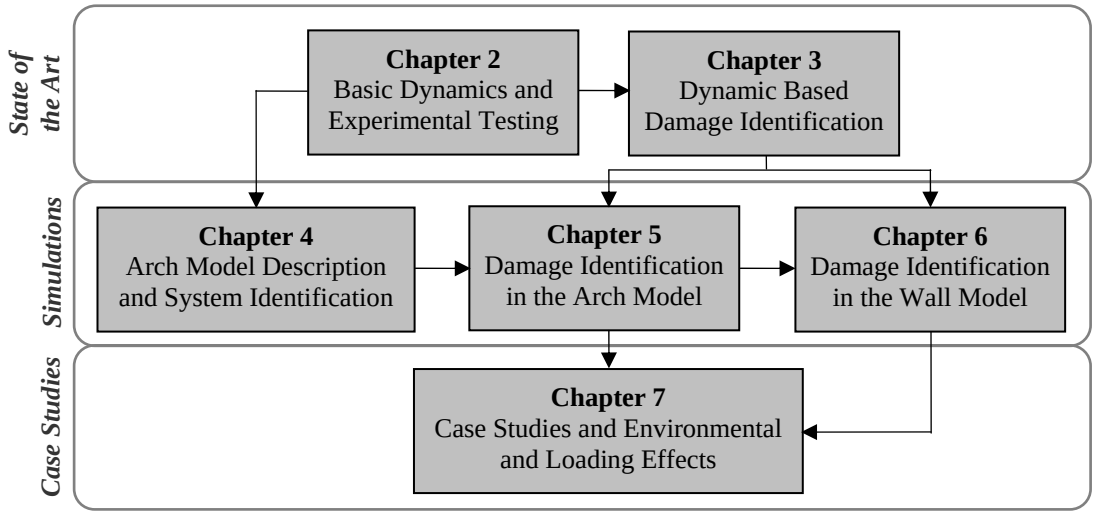


Figure 1.2 – Outline of the thesis.

Chapter 2

Basic Dynamics and Experimental Testing

Abstract

In this chapter a state of the art about system identification based on vibration signatures is presented. First, a brief introduction on dynamics is carried out, followed by the main developments on system identification. Issues addressed include sensors selection, data acquisition systems and test planning. The environmental effects are also discussed and procedures to remove their influence are presented. Finally, a summary is given with conclusions.

2.1 Introduction

The main goal of the present chapter is to review the most important developments in the field of experimental dynamics. Before presenting the different identification methods, a brief introduction on basic dynamics is carried out, helping to introduce concepts and definitions later used. If the dynamic identifications testes are carried out with the aim of damage identification, then the influence of the environmental effects plays a significant role for civil engineering structures, and therefore their removal are also addressed here.

2.2 Basic Dynamics

The theory of structural dynamics defines that a undamped structure with multiple degrees of freedom possesses simple harmonic motion without changing the deflected shape, if free vibration is initiated under special conditions (Chopra, 2001). When every degree of freedom passes through the equilibrium position at the same time, the deflected shape is called a natural mode of vibration, see Figure 2.1. Therefore, a vibration mode can be understood as a vibration applied to a system of multiple degrees of freedom with different amplitudes and deflections.

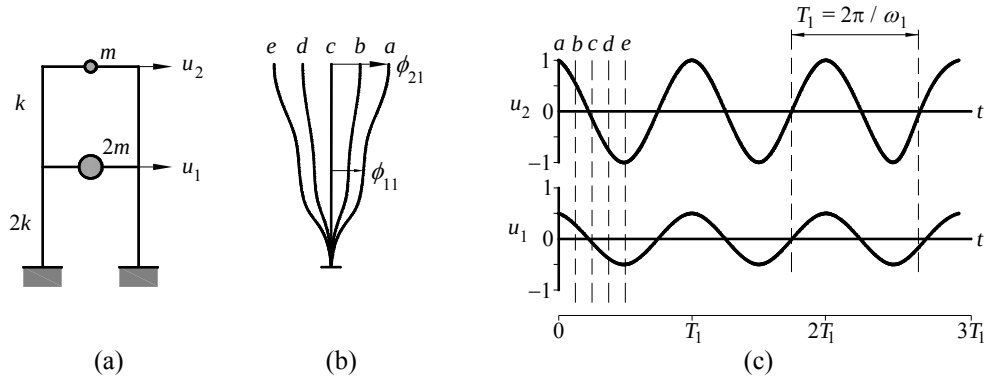


Figure 2.1 – Free vibration of an undamped system (Chopra, 2001): (a) system; (b) and (c) different representations of the first natural vibration mode.

The three main characteristics of dynamic systems are stiffness, damping and mass. For damped systems, energy is dissipated in each cycle of vibration, resulting on the reduction of the amplitudes of motion, until the amplitudes equals to zero in all points. For undamped systems, once the movement is started, the body or the system remains in harmonic motion indefinitely.

Structural systems can also be considerate as discrete or continuous, depending on the level of analysis sought. Normally, civil engineering structures are discretized in a series of key points, being their characterization of movement enough to understand the entire system. Each of these points may have a maximum of six degrees of freedom (three translations and three rotations).

The dynamic response can be studied using two different approaches: a deterministic and a stochastic approach. If the excitation is known and characterized in time, the loads are deterministic and the response can also be treated as deterministic. If the excitation is random, the problem can be analyzed with probabilistic concepts and it is possible to analyze the statistical description of the response (Chopra, 2001).

When mathematical methods are used to characterize the dynamic behavior of the systems, three formulations are possible, namely: the Classical Formulation, the Steady-State Formulation and Auto-Regressive Models. Each of these formulations is presented in the following Sections.

2.2.1 Classical Formulation

2.2.1.1 Single Degree of Freedom Systems

The most important difference between dynamic and static analysis is the time dependency of the dynamic approach. Indeed, the response of the structure (displacements, velocities, accelerations or internal forces) is associated to the accelerations that take place due to inertia forces. In this relation, mass, stiffness and damping play an important role. The motion itself can be expressed by a mathematic expression, using (a) Newton's second law of motion or (b) dynamic equilibrium. If $q(t)$ is defined as the time-dependent displacement of a system with one degree of freedom, the equation of motion is:

$$m\,\ddot{q}(t) + c\,\dot{q}(t) + k_e\,q(t) = p(t) \tag{2.1}$$

where m is mass of the system, c is the damping constant, k_e is the system stiffness and $p(t)$ is the load vector, which is also time-dependant. Here, the time derivates $\dot{q}(t)$ and $\ddot{q}(t)$ represents the velocity and the acceleration of the system, respectively. When an arbitrary force is acting in the system, the solution of this second order differential equation can be obtained by the *Duhamel's integral* (Chopra, 2001), valid for linear systems and given by the following expression:

$$q(t) = \frac{1}{m\,\omega_D}\int_0^t p(\tau)\; e^{-\xi\omega_n(t-\tau)}\sin\left[\omega_D\,(t-\tau)\right] d\tau \quad , \quad t > \tau \tag{2.2}$$

where τ is a reference instant, ω_D is the damped frequency that can be related to the natural frequency ω_n or the natural period T_n $\left(\omega_n = \sqrt{k_e/m} = 2\pi/T_n\right)$ by:

$$\omega_D = \omega_n\sqrt{1-\xi^2} \tag{2.3}$$

and ξ is the damping coefficient, which for civil engineering structures is lower than 20% (Chopra, 2001). The damping coefficient is given by the following expression:

$$\xi = \frac{c}{2m\,\omega_n} \tag{2.4}$$

where c is a damping constant.

Another possibility is to obtain the solution of linear differential equation in the frequency domain, by applying the Fourier transform to the functions on both sides of Eq.(2.1). The Fourier transform $X(\omega)$ of a function $x(t)$ is given by:

$$X(\omega) = \int_{-\infty}^{+\infty} x(t)\; e^{-j\omega t} dt \tag{2.5}$$

where j is the imaginary number ($j^2 = -1$). In the process, $P(\omega)$ and $Q(\omega)$ represents the Fourier transforms of the excitation $p(t)$ and the response $q(t)$, respectively. As the time derivate of the frequency transform functions are given by the product $j\omega$ in the frequency domain, Eq.(2.1) can be recast as:

$$-m\omega^2 Q(\omega)+cj\,\omega\, Q(\omega)+k_e\, Q(\omega)=P(\omega) \tag{2.6}$$

Solving the last equation with respect to $Q(\omega)$ as presented in Eq.(2.7), it can be concluded that the response Fourier transform function directly depends on the excitation and on a complex function $H(\omega)$. This is the so-called Frequency Response Function (FRF), defined as the ratio of the Fourier transforms of the response and the excitation force:

$$Q(\omega)=\frac{P(\omega)}{-m\omega^2+cj\,\omega+k_e}=H(\omega)P(\omega) \tag{2.7}$$

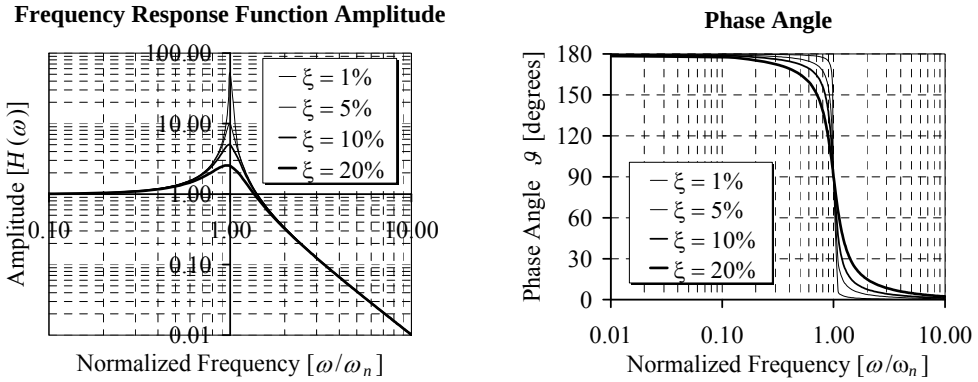
The advantage of this approach is the fact that a deterministic relationship between excitation and response can be established, as given by:

$$H(\omega)=\frac{Q(\omega)}{P(\omega)}=\frac{1}{k_e}\frac{1}{1-(\omega/\omega_n)^2+j[2\xi(\omega/\omega_n)]} \tag{2.8}$$

It is noted that $H(\omega)$ is a complex function and to calculate its amplitude it is necessary to square root the sum of the squares from the real and imaginary parts, which results in

$$|H(\omega)|=\frac{1/k_e}{\sqrt{\left[1-(\omega/\omega_n)^2\right]^2+\left[2\xi(\omega/\omega_n)\right]^2}} \tag{2.9}$$

Figure 2.2a presents the FRF for a single degree of freedom system, with natural frequency ω_n and variable damping coefficient ξ up to 20%. It is easy to conclude that the maximum amplitude value is equal to the abscissa $\omega=\omega_n\sqrt{1-\xi^2}$, the resonant frequency, which is higher for smaller values of ξ.



(a) (b)

Figure 2.2 – Frequency Response Function (FRF): (a) amplitude *vs* normalised frequency; and (b) phase *vs* normalized frequency.

Figure 2.2b shows the phase angle ϑ, defined as equal to the arctangent of the quotient between the imaginary and real parts of Eq.(2.8), also dependent of the frequency domain. The maximum amplitude value shown in Figure 2.2a occurs with a shift of 180º in phase.

Finally, the desired solution $q(t)$ is given by the inverse Fourier transform of $Q(\omega)$, given by:

$$q(t)=\frac{1}{2\pi}\int_{-\infty}^{+\infty}H(\omega)\;P(\omega)\;e^{j\omega t}\,d\omega \tag{2.10}$$

2.2.1.2 Multiple Degree of Freedom Systems

When the system has n degrees of freedom, the equation of movement can be again obtained using the Newton's second law:

$$\boldsymbol{M}\,\ddot{\boldsymbol{q}}(t)+\boldsymbol{C}_2\,\dot{\boldsymbol{q}}(t)+\boldsymbol{K}\,\boldsymbol{q}(t)=\boldsymbol{p}(t) \tag{2.11}$$

where $\boldsymbol{M}$, $\boldsymbol{C}_2$ and $\boldsymbol{K}$ are now the order $n \times n$ matrices of mass, viscous damping and stiffness, with their components m_{ik}, c_{ik} and k_{ik} representing the generalized forces for coordinate i, when an acceleration is applied in the coordinate k, $\boldsymbol{p}(t)$ is the generalized excitation vector and $\boldsymbol{q}(t)$ the generalized response vector.

To solve Eq.(2.11) Fourier transform functions can again be used, establishing the direct relation between excitation and response, similar to Eq.(2.8), through the FRF:

$$\boldsymbol{H}(\omega)=\left[-\omega^2\boldsymbol{M}+j\omega\,\boldsymbol{C}_2+\boldsymbol{K}\right]^{-1} \tag{2.12}$$

The calculation of the FRF is tedious because it is necessary to calculate the complex inverse of the matrix of $n \times n$ for each frequency ω (Caetano, 1992). An alternative solution is the modal approach, which starts from the assumptions of a undamped problem by the homogeneous differential equation:

$$\boldsymbol{M}\,\ddot{\boldsymbol{q}}(t)+\boldsymbol{K}\,\boldsymbol{q}(t)=0 \tag{2.13}$$

A solution of this differential equation is given by:

$$\boldsymbol{q}(t)=\varphi_i e^{\lambda_i t} \tag{2.14}$$

where φ_i are the real eigenvectors (i = 1,…, n) and λ_i^2 are the real eigenvalues, which in case of undamped systems are equal to the natural frequencies ω_i ($\lambda_i = j\omega_i$). Introducing Eq.(2.14) into Eq.(2.13) results in:

$$\left[\boldsymbol{K}-\left(-\lambda_i^{\,2}\right)\boldsymbol{M}\right]\varphi_i=0 \quad \vee \quad \boldsymbol{K}\,\Phi=\boldsymbol{M}\,\Phi\,\Lambda \tag{2.15}$$

The modes are commonly grouped in the modal matrix Φ where each column represents the eigenvectors, and the eigen frequencies ω_i are grouped in a diagonal matrix Λ. The orthogonality properties of the modes shape hold:

$$\Phi^T\,\boldsymbol{M}\,\Phi=\left[\,m_i\,\right] \quad , \quad \Phi^T\,\boldsymbol{K}\,\Phi=\left[\,k_i\,\right] \tag{2.16}$$

where m_i are the modal masses, k_i the modal stiffness and the superscript T denotes transpose. The eigenvectors can also be mass-normalized by the matrix Φ_m, composed by the normalized eigenvalues ($\varphi_{m,i} = \varphi_i/\sqrt{m_i}$), leading to the following relations:

$$\Phi_m^T\,\boldsymbol{M}\,\Phi_m=\boldsymbol{I} \quad , \quad \Phi_m^T\,\boldsymbol{K}\,\Phi_m=\Lambda^2 \tag{2.17}$$

where $\boldsymbol{I}$ is the identity matrix of dimension $n \times n$.

If Eq.(2.15) is pre-multiplied by Φ^T and taking into account the Eq.(2.16), the natural undamped frequencies of each mode i can be obtained similarly to one degree of freedom system problem:

$$\omega_i^2=k_{e,i}/m_i \tag{2.18}$$

Adding now proportional damping to the system, i.e. damping which gives a linear relation between the stiffness and mass, and assuming that the damping matrix can be also diagonalized, it is possible to obtain:

$$\Phi^T \boldsymbol{C}_2 \Phi = \left[c_{i} \right] = \left[2\xi_i \, \omega_i \, m_{i} \right] = \Gamma \left[m_{i} \right] \quad \text{with} \quad \Gamma = \left[2\xi_i \, \omega_{i} \right] \tag{2.19}$$

Introducing the coordinate transformation $\boldsymbol{q}(t) = \Phi \, \boldsymbol{q}_m(t)$, where $\boldsymbol{q}_m(t)$ are the modal displacements, and pre-multipling Eq.(2.11) by Φ^T, the following simplified equation, with all the left diagonal side terms, is obtained:

$$\boldsymbol{I} \, \ddot{\boldsymbol{q}}_m(t) + \Gamma \, \dot{\boldsymbol{q}}_m(t) + \Lambda^2 \, \boldsymbol{q}_m(t) = \left[\frac{1}{m_{i}} \right] \Phi^T \boldsymbol{p}(t) \tag{2.20}$$

Again, if this equation is assumed to be homogeneous, the solution form is equal to the one adopted in Eq.(2.14) and the eigenvalues satisfy the condition:

$$\lambda_i^{\,2} + 2\xi_i \omega_i \lambda_i + \omega_i^{\,2} = 0 \tag{2.21}$$

with the solution:

$$\lambda_i = -\xi_i \omega_i + j\omega_i \sqrt{1-\xi_i^{\,2}} \quad , \quad \lambda_i^{\,*} = -\xi_i \omega_i - j\omega_i \sqrt{1-\xi_i^{\,2}} \tag{2.22}$$

$$\omega_i = \left| \lambda_i \right| \quad , \quad \xi_i = -\operatorname{Re}(\lambda_i) / \left| \lambda_i \right| \tag{2.23}$$

where the superscript * denotes de complex conjugate.

Fourier transform functions can also be used to solve Eq.(2.20), because the equation is similar to the system of one degree of freedom. The response now is related to the solicitation by a FRF in the modal space, in the following form:

$$\boldsymbol{Q}(\omega) = \boldsymbol{H}(\omega) \, \boldsymbol{P}(\omega) \tag{2.24}$$

where the diagonal terms of the FRF is a matrix $n \times n$ given by the expression:

$$\boldsymbol{H}_{(i,k)}(\omega) = \sum_{j=1}^{n} \frac{\varphi_{i,j} \, \varphi_{k,j}}{(\omega_n^2 - \omega^2) + i(2\xi_n \, \omega_n \, \omega)} \quad , \quad i \wedge k = 1,\ldots,n \tag{2.25}$$

This formulation has the advantage that the response can be approximated computing only a few numbers of mode shapes without significant errors, thus with low computational effort.

The deterministic formulation for mass and stiffness can be calculated by extracting the mechanical material characteristics of the structural systems, but the information about damping cannot be calculated with those parameters. In situ experimental tests must be accomplished to determine the modal damping coefficients ξ_i. For further reading about deterministic formulation see Clough and Penzien (1993), Chopra (2001), Ewins (2000) and Maia and Silva (1997).

2.2.2 State-Space Formulation

In the cases that damping is not proportional to the mass and stiffness of the system, e.g. by the presence of a localized damper, the damping matrix cannot be diagonalized and another formulation is needed to obtain the solution. The State-Space Formulation deals with this problem and can also construct mathematical models in which experimental data

can be coupled to discrete models. These characteristics make the state formulation a powerful tool, more adequate to handle stochastic time series and the noise present in the experimental data.

2.2.2.1 Time Continuous Models

The State-Space Formulation transforms the system of n classical second order differential equations of motion, Eq.(2.11), in to $2n$ systems with first order differential equations, by introducing the state vector $\boldsymbol{x}(t)$, the input vector $\boldsymbol{u}(t)$, and the matrices $\boldsymbol{A}_S$ and $\boldsymbol{B}_S$ (Peeters, 2000; Caetano, 2000; and Rodrigues, 2004), where:

$$\boldsymbol{x}(t)=\begin{bmatrix}\boldsymbol{q}(t)\\ \dot{\boldsymbol{q}}(t)\end{bmatrix} \quad , \quad \boldsymbol{A}_S=\begin{bmatrix}\boldsymbol{C}_2 & \boldsymbol{M}\\ \boldsymbol{M} & 0\end{bmatrix} \quad , \quad \boldsymbol{B}_S=\begin{bmatrix}\boldsymbol{K} & 0\\ 0 & -\boldsymbol{M}\end{bmatrix} \tag{2.26}$$

The excitation vector $\boldsymbol{p}(t)$ of Eq.(2.11) suffers a modification by the introduction of the matrix $\boldsymbol{B}_2$, constructed by zeros and ones that specifies the locations of the inputs, and the vector $\boldsymbol{u}(t)$ describing the inputs in time. The new formulation can be written in the following form:

$$\boldsymbol{A}_S\,\dot{\boldsymbol{x}}(t)+\boldsymbol{B}_S\,\boldsymbol{x}(t)=\begin{bmatrix}\boldsymbol{B}_2\\ 0\end{bmatrix}\boldsymbol{u}(t) \tag{2.27}$$

The state equation of the time continuum model is obtained solving Eq.(2.27) with respect to $\dot{\boldsymbol{x}}(t)$:

$$\dot{\boldsymbol{x}}(t)=\boldsymbol{A}_c(t)+\boldsymbol{B}_c\,\boldsymbol{u}(t) \tag{2.28}$$

where $\boldsymbol{A}_c$ is the so called state matrix and $\boldsymbol{B}_c$ the input matrix (the subscript c indicates that they are time continuums), both defined as:

$$\boldsymbol{A}_c=-\boldsymbol{A}_S^{-1}\boldsymbol{B}_S=\begin{bmatrix}0 & I\\ -\boldsymbol{M}^{-1}\boldsymbol{K} & -\boldsymbol{M}^{-1}\boldsymbol{C}_2\end{bmatrix} \quad \text{and} \quad \boldsymbol{B}_c=-\boldsymbol{A}_S^{-1}\begin{bmatrix}\boldsymbol{B}_2\\ 0\end{bmatrix}=\begin{bmatrix}0\\ \boldsymbol{M}^{-1}\boldsymbol{B}_2\end{bmatrix} \tag{2.29}$$

Once matrix $\boldsymbol{A}_c$ is know, all the modal information of the system (natural frequencies, damping coefficients and mode shapes) can be extracted, because the state matrix is related to the complex eigenvectors Ψ and eigen values Λ as follows:

$$\boldsymbol{A}_c=\Psi\,\Lambda\,\Psi^{-1} \tag{2.30}$$

2.2.2.2 The Observation Equation

The State-Space Formulation allows adding experimental data information to the mathematical models, in a sense that the system response cannot be measured in all degrees of freedom. The particularity of the problem is that the response of the system is measured in a few points but it is assumed that the dynamic properties of the entire system are known. For that reason, the state formulation involves a second equation, known as the observation equation, which tries to study the relation between the model and the isolated measured responses.

In the observation equation it is assumed that measurements are made in l locations ($l < n$) and the response vector $\boldsymbol{y}(t)$ can be measured through accelerations, velocities or displacements transducers, and coupled in the following form:

$$\boldsymbol{y}(t) = \boldsymbol{C}_a\,\ddot{\boldsymbol{q}}(t) + \boldsymbol{C}_v\,\dot{\boldsymbol{q}}(t) + \boldsymbol{C}_d\,\boldsymbol{q}(t) \tag{2.31}$$

where the matrices $\boldsymbol{C}_a$, $\boldsymbol{C}_v$ and $\boldsymbol{C}_d$ are locations matrices of acceleration, velocity and displacement, respectively. They are composed by zeros and ones, describing where the measured system response is.

Introducing the state vector of Eq.(2.26) and considering Eq.(2.28), this last equation can be written as:

$$\boldsymbol{y}(t) = \boldsymbol{C}_c\,\boldsymbol{x}(t) + \boldsymbol{D}_c\,\boldsymbol{u}(t) \tag{2.32}$$

where $\boldsymbol{C}_c$ and $\boldsymbol{D}_c$ are the output and direct transmission matrices, respectively, given by the following expressions:

$$\boldsymbol{C}_c = \begin{bmatrix}\boldsymbol{C}_d - \boldsymbol{C}_a\,\boldsymbol{M}^{-1}\boldsymbol{K} & \boldsymbol{C}_v - \boldsymbol{C}_a\,\boldsymbol{M}^{-1}\boldsymbol{C}\end{bmatrix} \quad \text{and} \quad \boldsymbol{D}_c = \boldsymbol{C}_a\,\boldsymbol{M}^{-1}\boldsymbol{B}_2 \tag{2.33}$$

2.2.2.3 The State-Space Model

The time continuum state-space model results from the combination of the state and observation equations, where the responses $\boldsymbol{y}(t)$ can be related to the excitations $\boldsymbol{u}(t)$ by (Peeters, 2000; Caetano, 2000; and Rodrigues, 2004):

$$\begin{aligned}\dot{\boldsymbol{x}}(t) &= \boldsymbol{A}_c\,\boldsymbol{x}(t) + \boldsymbol{B}_c\,\boldsymbol{u}(t)\\ \boldsymbol{y}(t) &= \boldsymbol{C}_c\,\boldsymbol{x}(t) + \boldsymbol{D}_c\,\boldsymbol{u}(t)\end{aligned} \tag{2.34}$$

2.2.2.4 Time Discrete Models

In the formulation above a time continuum variable was adopted. In reality, experimental system identification is done through discrete time series, because it is impossible to have a continuous time record of a system. Therefore, the response is studied in discrete numerical time series with finite time intervals. Another reason to study discrete models is that they are needed to simulate the response when there is no analytical solution and a numerical approach must be used.

Time discrete models require that the continuous response can be represented with a certain fixed sampling period Δt. Then, the time continuum equations can be discretized and solved at every instant t_k, where $t_k = k\Delta t$ and k is an integer. If it is assumed that between each Δt the excitation vector $\boldsymbol{u}(t)$ is constant, the continuous-time state-space model can be converted in the following discrete-time state-space model (Juang, 1994):

$$\begin{aligned}\boldsymbol{x}_{k+1} &= \boldsymbol{A}\;\boldsymbol{x}_k + \boldsymbol{B}\;\boldsymbol{u}_k\\ \boldsymbol{y}_k &= \boldsymbol{C}\;\boldsymbol{x}_k + \boldsymbol{D}\;\boldsymbol{u}_k\end{aligned} \tag{2.35}$$

where $\boldsymbol{x}_k$ is the discrete-time state vector with the sampling displacements and velocities in instant $k\Delta t$, $\boldsymbol{u}_k$ is the sampling excitation vector, $\boldsymbol{y}_k$ is the sampling response vector and the matrices $\boldsymbol{A}$, $\boldsymbol{B}$, $\boldsymbol{C}$ and $\boldsymbol{D}$ are the state, input, output and direct transmission matrices, respectively. The referred matrices are also time discrete and can be related to the equivalent continuous-time matrices by:

$$\boldsymbol{A} = e^{\boldsymbol{A}_c\Delta t} \quad , \quad \boldsymbol{B} = \int_0^{\Delta t} e^{\boldsymbol{A}_c\,\tau}\,d\tau\;\boldsymbol{B}_c = \left(\boldsymbol{A} - \boldsymbol{I}\right)\boldsymbol{A}_c^{-1}\boldsymbol{B}_c \quad , \quad \boldsymbol{C} = \boldsymbol{C}_c \quad , \quad \boldsymbol{D} = \boldsymbol{D}_c \tag{2.36}$$

2.2.2.5 Deterministic-Stochastic State-Space Models

In a more complete approach, noise can be added to the State-Space Formulation. Noise is present in the system identification due to the input perturbations, modeling inaccuracy and disturbances in the transducers and data acquisition systems. To take into account these perturbations, stochastic components have to be included in the state models:

$$\begin{aligned} \boldsymbol{x}_{k+1} &= \boldsymbol{A}\,\boldsymbol{x}_k + \boldsymbol{B}\,\boldsymbol{u}_k + \boldsymbol{w}_k \\ \boldsymbol{y}_k &= \boldsymbol{C}\,\boldsymbol{x}_k + \boldsymbol{D}\,\boldsymbol{u}_k + \boldsymbol{v}_k \end{aligned} \tag{2.37}$$

where $\boldsymbol{w}_k$ is defined as process noise resulted from input perturbations and modeling inaccuracy and $\boldsymbol{v}_k$ is measurement noise due to transducers and data acquisition disturbances. Both stochastic vectors are impossible to measure but statistic properties can be assumed, namely: zero mean and white noise (Peeters, 2000; Caetano, 2000; and Rodrigues, 2004).

For civil engineering systems Eq.(2.37) can be simplified if a stochastic approach is chosen for system identification, i.e. if the ambient vibration response is measure in the system. For those systems it is impossible to distinguish between the excitation terms $\boldsymbol{u}_k$ and the noise terms $\boldsymbol{w}_k$ and $\boldsymbol{v}_k$ (e.g. in case of ambient excitation). The input vector is then absorbed by the noise terms and the formulation is still valid if the inputs are considered as white noise, reading:

$$\begin{aligned} \boldsymbol{x}_{k+1} &= \boldsymbol{A}\;\boldsymbol{x}_k + \boldsymbol{w}_k \\ \boldsymbol{y}_k &= \boldsymbol{C}\,\boldsymbol{x}_k + \boldsymbol{v}_k \end{aligned} \tag{2.38}$$

For further reading about State-Space Formulation, the reader is referred to Peeters (2000), Caetano (2000) and Rodrigues (2004).

2.2.3 Auto-Regressive Models

Another time-discrete formulation is the so called Auto-Regressive Moving Average models (ARMA) or, for multi-degree of freedom, Auto-Regressive Moving Average Vector models (ARMAV). In the case of excitations characterized by white noise stochastic processes, the state vector is eliminated and the response vector is given by the following equation:

$$\boldsymbol{y}_k = \underbrace{-\boldsymbol{A}_1^{AR}\boldsymbol{y}_{k-1} - \boldsymbol{A}_2^{AR}\boldsymbol{y}_{k-2} - \ldots - \boldsymbol{A}_{na}^{AR}\boldsymbol{y}_{k-na}}_{auto-regressive\ part\ (AR)} + \underbrace{\boldsymbol{e}_k + \boldsymbol{C}_1^{MA}\boldsymbol{e}_{k-1} + \boldsymbol{C}_2^{MA}\boldsymbol{e}_{k-2} + \ldots + \boldsymbol{C}_{nc}^{MA}\boldsymbol{e}_{k-nc}}_{moving\ average\ part\ (MA)} \tag{2.39}$$

where $\boldsymbol{y}_k$ has l columns, in correspondence with the measured degrees of freedom, $\boldsymbol{e}_k$ is a stochastic white noise vector process, $\boldsymbol{A}_i^{AR}$ are the parameter matrices of the auto-regressive part and $\boldsymbol{C}_i^{MA}$ are the parameter matrices of the moving average part.

An ARMAV model is an external representation of the input-output relation, which tries to explain the system response in the instant k from the responses in the preceding instants through a stochastic white noise process. In the ARMAV models it is possible to calculate the matrices $\boldsymbol{A}_i^{AR}$ and $\boldsymbol{C}_i^{MA}$ from the matrices which characterizes the state models and to make the inverse process (Peeters, 2000). Knowing the relation between these two formulations it is possible to establish procedures to calculate, from the auto-regressive matrices, the modal system parameters (frequencies, mode shapes and damping coefficients), hence the moving average matrices do not affect the modal parameters.

For further reading about ARMAV models see Andersen (1997), Ljung (1999) and Peeters (2000).

2.3 Experimental Modal Identification

In the preceding Sections, basic dynamics was presented in order to allow to a better understanding of experimental modal identification techniques. In what concerns *in situ* modal identification tests there are three groups of experimental techniques: (a) the input-output vibration tests, where the excitation forces and the vibration response are measured; (b) the output-only tests, where only the response of the system is measured, and (c) the free vibration tests, where the systems are induced with an initial deformation and then are quickly released. The output-only tests also called Operational Modal Analysis (OMA), where the response is measured during service conditions of the structural systems.

Before any discussion about the experimental techniques, it is necessary to describe the characteristics of measurement equipments and the issues of signal processing. Basically, a PC-based data acquisition test equipment is composed by an excitation mechanism, a series of transducers, a signal conditioner, an Analogue to Digital Converter (ADC) incorporated in the data acquisition hardware and a computer to process all the digital signal information. These equipments can be generally divided in three groups: (a) excitation mechanisms; (b) response transducers; and (c) data acquisition systems. The main characteristics of these components are addressed next.

2.3.1 Excitation Mechanisms

The excitation mechanisms frequently used in dynamic tests of civil engineering structures are shakers, impact hammers and drop weight systems. Shakers are used to study stationary dynamic responses and can induce large forces to the structure. They need to be well fixed to the structure for the correct force transmission. Normally, the application of shakers is expensive and sometimes it is necessary to limit the use of the structure; e.g. in case of bridges is necessary to stop the traffic (Caetano, 2000). The others systems are used to study transient responses. They are cheaper to use than mechanical exciters but they have the disadvantage of transmitting low energy to the structure.

There are three types of shakers, namely mechanic, electro-magnetic and electro-hydraulic shakers. The later is presented in Figure 2.3a, but most common mechanism type is the shaker with eccentric masses. This mechanical exciter is composed of two eccentric masses rotating synchronously in plane and generating a sinusoidal force. Figure 2.3b shows an example of a eccentric mass shaker.



(a) (b)

Figure 2.3 – Eccentric mass shaker: (a) example of an electro-hydraulic shaker used on the Z24 bridge (Maeck and De Roeck, 2003); and (b) eccentric mass shaker installer on a roof (Yu, et al., 2004).

The impact hammer is frequently used in mechanical engineering structures, because it gives accurate results with light/medium-weight systems. Generally speaking, the exciter is a hammer with a selected tip for different spectral impact energy, coupled with a sensor to measure the impact force. The impulse depends on the mass of the head, the velocity of the impact and the selected tip, i.e. more rigid tips will induce a shorter impulse force to the structure. Figure 2.4a shows several hammers and Figure 2.4b presents the differences in spectral response by changing the tips.



Figure 2.4 – Impulse hammers (PCB, 2004): (a) different models; and (b) response spectrum depending on the selected tip.

The drop weight system has the advantage to better control the frequency contents of the impacts, by changing the damping properties, and to apply higher energy than the impact hammers, see Figure 2.5.

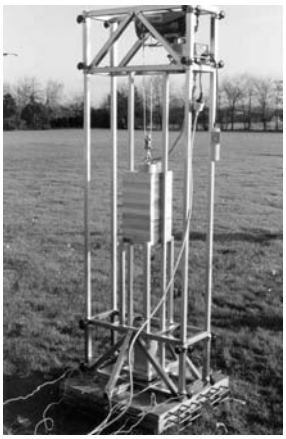


Figure 2.5 – Drop weight system from Catholic University of Leuven (Maeck and De Roeck, 2003).

2.3.2 Response Transducers

A transducer is an equipment able to transform a physic quantity, that usually defines the system response, such as displacements, velocities, accelerations, strains, forces, etc., into a proportional electrical signal, ready to be processed by the data acquisition system. In theory, the measure of the dynamic response can be achieved by any of the above physic quantities. However, displacements are better for low frequency response cases, e.g. civil engineering structures, and acceleration measurements are more adequate for higher frequency components, e.g. machinery (Caetano, 2000).

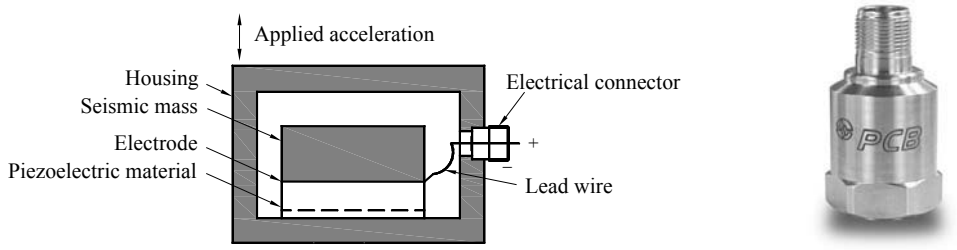
In what concerns civil engineering structures, measuring displacements requests all sensors to be related to an external reference point and, often it is costly to do it. Therefore, test equipments based on accelerometers are usually preferred, providing accurate results

with relatively low cost. Moreover, it is possible to calculate displacements by numerical integration of the acceleration records.

In the following, only acceleration transducers (accelerometers) are presented, while a description of other sensors for civil engineering structures is given in Caetano (2000).

2.3.2.1 Piezoelectric Accelerometers

A piezoelectric accelerometer is one spring-mass-damper system which produces signals proportional to the acceleration in a frequency band below their resonant frequency. The active part of the accelerometer is made of quartz crystals or ceramic materials, which produce an electrical output signal proportional to the acceleration. Figure 2.6a presents a schematic cross section where it is possible to observe the seismic mass attached to the piezoelectric material. When accelerated, the mass m creates a force p directly proportional to the acceleration $\ddot{q}$ according to Newton's law of motion, $p = m\ddot{q}$.



(a) (b)

Figure 2.6 – Piezoelectric accelerometer (PCB, 2004): (a) cross section; and (b) PCB Model 393B12.

Piezoelectric accelerometer generally requires conditioning before being connected to readout, recording, or analysis equipment. This signal conditioning is either remotely located or built into the accelerometer.

Compared with others, the piezoelectric accelerometers have the advantages of not using external power source (active transducers), being stable, having a good signal-to-noise ratio and being linear over a wide frequency and dynamic range. The principal disadvantage concerns the impossibility of measuring the DC components (0 Hz), like the permanent gravity acceleration g. This characteristic is unfavorable to measure very flexible structures, where the natural frequency values can be close to zero; e.g. the 25th of April Tagus River Bridge in Lisbon has a first resonant frequency equal to 0.07 Hz (Rodrigues, 2004). However, there are piezoelectric transducers with a frequency range close to zero and with high sensitivity, which can accurately be used in flexible structures. It is the case of the accelerometer presented in Figure 2.6b, with 10 V/g sensitivity, frequency range form 0.1 to 2000 Hz, dynamic range equal to ±0.5 g and a resolution of 8 μg.

2.3.2.2 Piezoresistive and Capacitive Accelerometers

Piezoresistive and capacitive accelerometers are capable of measuring uniform acceleration signals, which is an advantage with respect to piezoelectrics. They can also respond to varying acceleration events but with a range limited to a maximum of 1000 Hz. They are passive accelerometers, in the sense of requiring the supply of energy to measure accelerations and, generally, they are more expensive than the piezoelectrics.

The piezoresistive accelerometers are formed by a cantilever beam with a given length and a mass on the free end. Strain-gages are glued in the upper and bottom part of the

beam and, when excited, the differential output signals of the strains are proportional to the acceleration.

The capacitive accelerometers are devices similar to the cantilever beam of the piezoresistive transducers. The sensing element consists of two parallel plate capacitors acting in a differential mode. These capacitors operate in a bridge circuit, along with two fixed capacitors, in a way that the differential output measured is proportional to the acceleration. Figure 2.7a shows a schematic cross section of a capacitive accelerometer and Figure 2.7b presents a triaxial accelerometer, which can be configured with 1 V/g sensitivity, frequency range form DC to 150 Hz, a dynamic range equal to ±3 g and a maximum resolution of 30 μg.

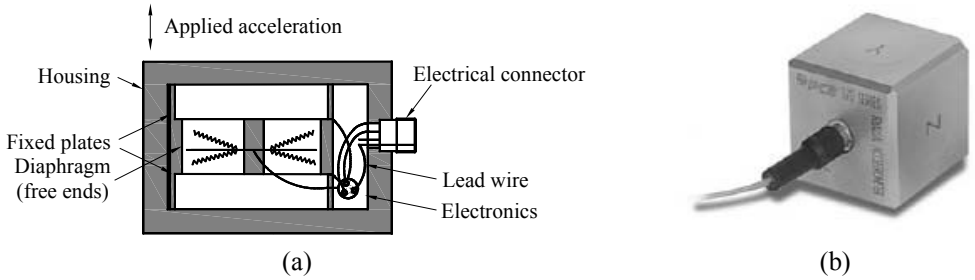


Figure 2.7 – Capacitive accelerometer (PCB, 2004): (a) cross section; and (b) PCB Model 3703.

2.3.2.3 Force-Balance Accelerometers

Like piezoresistive and capacitive accelerometers, force-balance accelerometers are passive transducers and are composed by a mass-spring system, so that, under excitation, they lead to a differential electrical signal proportional to the acceleration. Figure 2.8a shows a schematic representation of the transducer, where one can observe that the mass is fixed through four suspension beams. The mass has an appendix located between two capacitive plates (unit cell). When excited, the mass moves out of the equilibrium position (see Figure 2.8b) and the unit cell forces the mass back to the initial position, through the capacitor plates. The differential voltage required to force the central plate back to its equilibrium position is proportional to the acceleration.

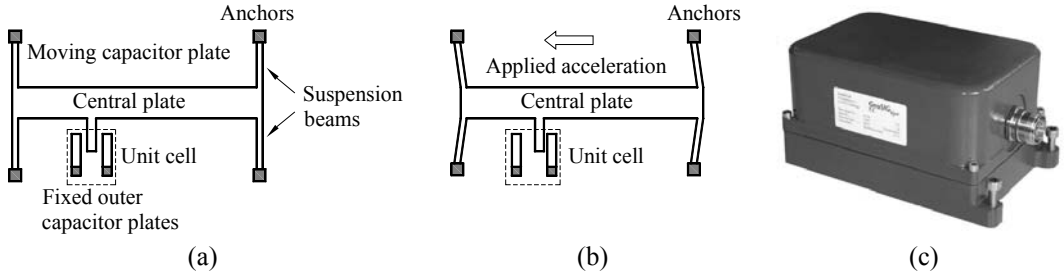


Figure 2.8 – Force-balance accelerometer (Maia and Silva, 1997): (a) mass-spring system in its equilibrium position; (b) deformation due to an applied acceleration; and (c) GEOSIG model AC-63.

Force-balance transducers are widely used in civil engineering to test flexible structures. They are also recommended for ambient vibration tests as they have ruggedness and high sensitivity, as the case of the accelerometer presented in Figure 2.8c, which can be configurable with a dynamic range equal to ±0.5, ±1, ±2 and ±4 g, frequency range from DC to 100 Hz and a maximum resolution of 1 μg. The main disadvantage is the fact that, usually, force-balance accelerometers are more expensive than others transducers.

2.3.3 Data Acquisition Systems

The Data AcQuisition system (DAQ) records the excitation and the response signals through a discrete-time series. Sometimes, it is impossible to directly process the information given by a transducer and signal conditioning is needed to process the given information. Generally, the signal conditioner functions are the following:

- The most common type of conditioning is the amplification of the low level signals to increase the resolution and reduce noise. For the highest possible accuracy, the signal should be amplified so that the maximum voltage range of the conditioned signal equals the maximum input range of the Analogue Digital Converter (ADC);
- Isolate the transducer signals from the computer, because the measured system can contain high-voltage and also to make sure that the measurements are safe from differences in ground potentials or common-mode voltages;
- Filtering the undesired signals from the measured signals. Noise filters are used to increase the measurement accuracy by excluding high frequencies signals that are out of the range of measured system frequencies. Anti-aliasing filters remove all frequencies components that are higher than the input bandwith of the computer board. Both filters are lowpass filters;
- Excite the transducers that need external voltage or excitation (passive transducers);
- Linearization of the nonlinear transducers response during the changes in the measured phenomenon.

In the preceding functions, the most important is the anti-aliasing function, because two signals at different frequencies can produce the same measured signal. This is possible if a low sampling rate is used to measure the response signal. Figure 2.9 illustrates the measurement error produced by the aliasing phenomenon, where a high frequency appears as a low frequency.

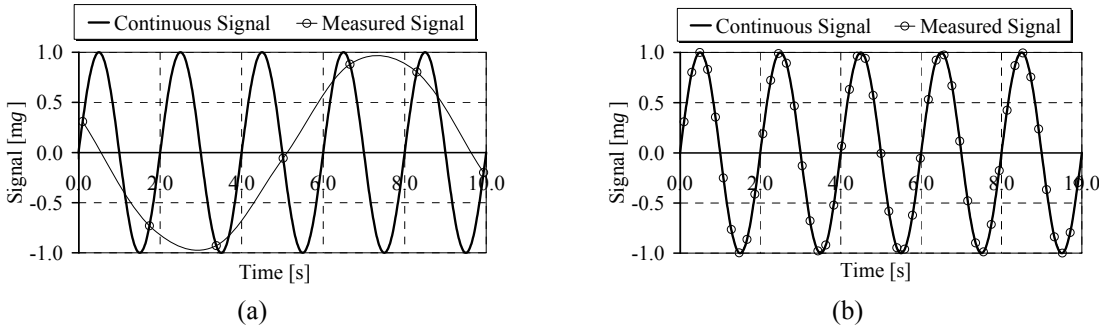


Figure 2.9 – Example of aliasing problem: (a) low sampling rate with aliasing; and (b) desire sampling rate.

To avoid the aliasing problem, a lowpass filter must be used with a sharp cut-off close to the Nyquist frequency (anti-aliasing filter). The Nyquist frequency (f_{Nyq}) is given by the Shannon sampling theorem: the sampling frequency f_S must be twice, and preferably slightly higher (Ventura and Brincker, 2001, recommend a factor of 2.5), the maximum frequency of interest f_{max}:

$$f_S = \frac{1}{\Delta t} \geq 2 \times f_{Nyq} \Leftrightarrow f_S \geq 2 \times f_{\max} \tag{2.40}$$

The Nyquist frequency corresponds to the maximum frequency value, in a range from zero to f_{Nyq}, that the system can correctly analyzed from discrete-time series, with a frequency resolution $\Delta f = 1/T_S$, where T_S is the complete measured time.

The ADC also plays an important role in the DAQ, because solving the sampling problems the digitalizing process must assure the accuracy of the digital signal. The accuracy itself depends on the number of binary digits used to represent the analogue signal (resolution) and the level of the analogue signal with respect to the maximum allowed level of the ADC. A converter of n bits capacity can represent 2^n levels of analogue signal; e.g a system with a 24 bit ADC has a resolution of 0.06 μ and an accuracy of 1.2 μV if a range of ±10 V is used in the ADC.

With respect to ADCs, the issues of sampling rate, multiplexing, differential nonlinearity, relative accuracy, settling time, noise, common mode voltage, maximum sampling rate *vs* bandwith concept, board performance and the analog input/multi-functions boards are also important for an accurate digital converter (Ventura and Brincker, 2001).

Figure 2.10 presents the data acquisition systems used in the experimental tests carried out in the preset work. For further reading on dynamic testing and applications see Ewins (2000) and Maia and Silva (1997).



(a) (b) (c)

Figure 2.10 – Analyses systems: (a) BRUEL model PULSE (www.bksv.com); (b) NATIONAL INSTRUMENTS platform SCXI (www.ni.com); and (c) GEOSIG model GSR-18 (www.geosis.com).

2.3.3.1 Signal Processing

After the acquisition, digital computer processing is also necessary. The signal information enters the computer in time domain but, for practical reasons and computation requirements, frequency domain is preferred. Fourier series plays an important role here, being possible to represent a periodic signal $x(t)$, with a period T, through a infinite series given by:

$$x(t) = \frac{a_0}{2} + \sum_{n=1}^{\infty} \left[a_n \cos\left(\frac{2\pi n}{T} t\right) + b_n \sin\left(\frac{2\pi n}{T} t\right) \right] \tag{2.41}$$

where

$$a_0 = \frac{2}{T}\int_0^T x(t)\, dt \quad , \quad a_n = \frac{2}{T}\int_0^T x(t) \cos\left(\frac{2\pi n}{T} t\right) dt \quad \text{and}$$
$$b_n = \frac{2}{T}\int_0^T x(t) \sin\left(\frac{2\pi n}{T} t\right) dt \tag{2.42}$$

As the signal is discretised with a finite series duration, with N samples of particular values of time (t_k, k = 1, 2,…, N) the Discrete Fourier Transform (DFT) series can obtain by the following expression:

$$x_k = x(t_k) = \frac{a_0}{2} + \sum_{n=1}^{N/2}\left[a_n \cos\left(\frac{2\pi k}{N} n\right) + b_n \sin\left(\frac{2\pi k}{N} n\right)\right] \quad , \quad k = 1, 2, \ldots, N \tag{2.43}$$

where the new a_0, a_n and b_n are given by:

$$a_0 = \frac{2}{N}\sum_{k=1}^{N} x_k \quad , \quad a_n = \frac{1}{N}\sum_{k=1}^{N} x_k \cos\frac{2\pi n k}{N} \quad \text{and} \quad b_n = \frac{1}{N}\sum_{k=1}^{N} x_k \sin\frac{2\pi n k}{N} \tag{2.44}$$

In case of periodic zero mean signals, a_0 is null and the set of the coefficients a_n and b_n are called the spectral or Fourier coefficients, often presented in modulus X_n and phase form ϑ_n:

$$X_n = \sqrt{{a_n}^2 + {b_n}^2} \quad , \quad \vartheta_n = \tan\left(\frac{-b_n}{a_n}\right)^{-1} \tag{2.45}$$

In practice, the DFT can be efficiently calculated using variations from the method of Fast Fourier Transform (FFT) presented by Cooley and Tukey (1965), which significantly reduces the number of mathematic operations in the computation process. But the frequency domain brings an additional problem related with the consequence of taking a finite length of time history on a periodic signal, known as the leakage error.

The leakage error appears when the measuring time is not a integer multiple of the signal period, which always happens in experimental testing. This problem is illustrated in Figure 2.11 which shows two different spectrums of the same periodic signal calculated with different measuring time T_S. In Figure 2.11a T_S is equal to a multiple integer of signal period and the spectrum is a non-zero value only at the expected signal frequency. When random T_S occur, see Figure 2.11b, the frequencies close to the signal frequency are contaminated.

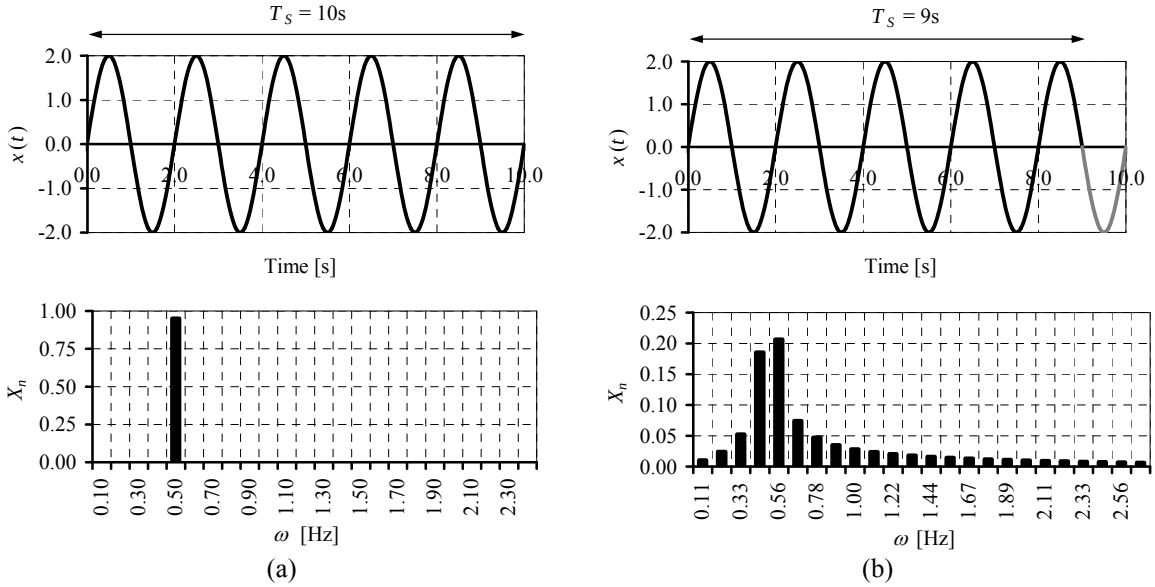


Figure 2.11 – Example of an leakage error: (a) signal and the correspondent spectrum when the complete measuring time is an integer multiple of the signal period; and (b) signal and the correspondent spectrum when the measuring time T_S is not a multiple integer of the signal period, producing the leakage error.

One solution to reduce this problem is to increase the sampling duration T_S, so that the difference between the spectral lines (frequency lines) is very small and, consequently, minimizes the error. But the most used procedure to reduce leakage is the signal transformation by the introduction of a window function, a process so-called windowing. In practice, the signal $x(t)$ is multiplied by a time function $w(t)$ so that the initial and final time series are rescaled, producing a final improved spectrum. Several time functions can be used depending on the analysed signal type. For stationary signals, Hanning or cosine-taper can be used, whereas and for transient signals the exponential time window has a better performance, because the initial part has the most important signal information. For random data the most popular is the Hanning window, defined has:

$$w(t) = \begin{cases} \dfrac{1}{2}\left[1+\cos\left(\dfrac{2\pi t}{T}\right)\right] & , \quad |t| \le \dfrac{T}{2} \\ 0 & , \quad |t| > \dfrac{T}{2} \end{cases} \tag{2.46}$$

Figure 2.12 shows one application of a Hanning window on a periodic signal, where the final improved spectrum can be observed and compared with Figure 2.11b.

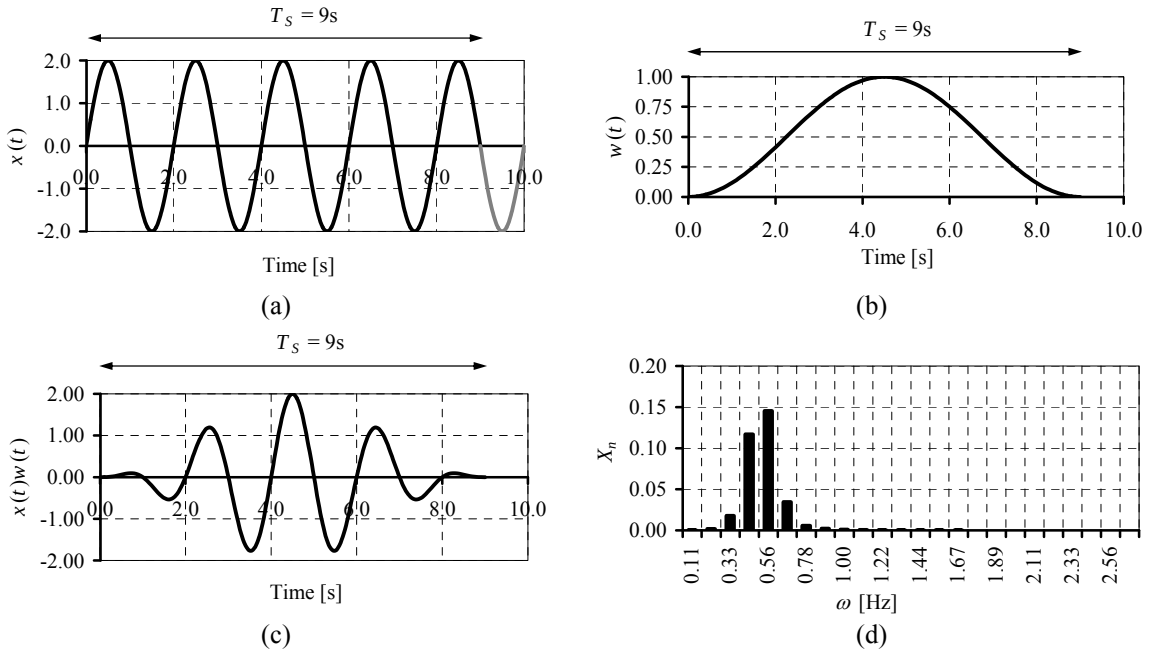


Figure 2.12 – Windowing application: (a) measured signal when the sampling time is not a multiple integer of the signal period; (b) Hanning window; (c) the windowed signal; and (d) the final DFT windowed spectrum.

Another signal conditioning process related with windowing is filtering. The solution of the aliasing problem is solved with a filter similar to a window, except that it is applied in frequency domain instead of time domain. The filtering process is the modification of the spectrum signal through application of different types of window functions. The common filters are low-pass, high-pass, band-limited, narrow-band and notch, see Figure 2.13a.

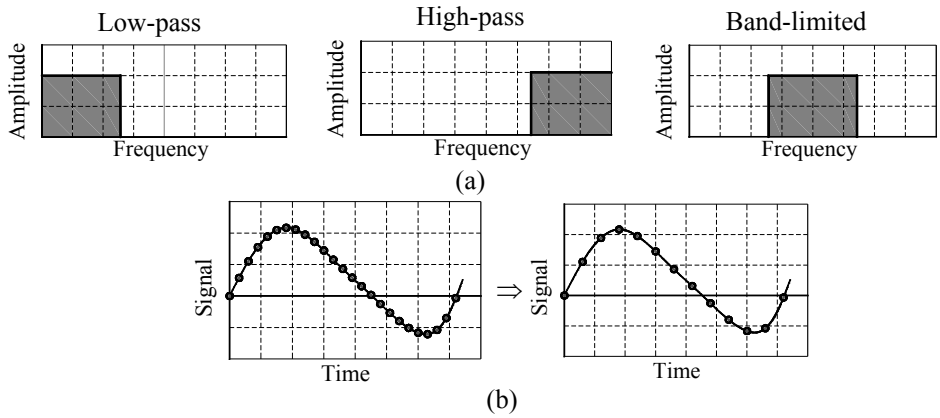


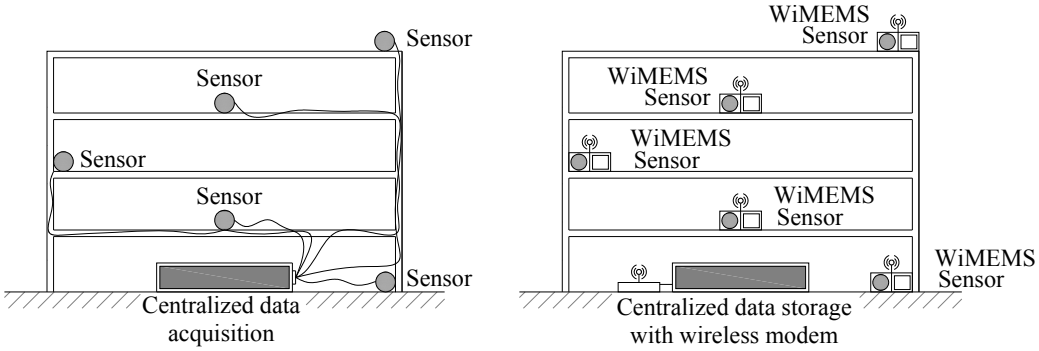
Figure 2.13 – Digital processing: (a) main filters; and (b) decimation by 2 (dots indicating sample data).

Decimation is another common procedure before the application of any modal identification technique. It is the digital alteration of sample frequency of the time signal histories to a lower sampling rate (see Figure 2.13b). This procedure can reduce the number of values in the time histories, resulting in a fast processing time for the modal identification, without the loss of signal quality in a frequency range on interest for the structural system. To avoid the aliasing error in the decimated time series it is important to apply a low-pass filter with a cutoff frequency about 40% of the new sample frequency.

Finally, a particular requirement is referred when random signals are processed by Fourier transforms. Before the experimental signals can be used with confidence, it is necessary to add an averaging process, also known as Welch procedure (Welch, 1967), which involves the signal separation on several individual time records or samples with limited time duration, the application of FFTs for all time records and, finally, the average calculation of every signal transformation, resulting in a final smoothed spectrum. This procedure removes spurious random noise from the signals and gives statistical reliability to the data. However, the adoption of a large number of segments implies short segments in time, and, consequently, when the FFT is applied a decrease of the frequency resolution on the segment analysis is observed. To minimize this problem, the overlap technique associated with the Hanning windowing can be used, resulting in an increase of all segments (by an overlap between them). An overlap of 2/3 is the one that better utilizes the signal information, but it is common to use an overlap of 1/2 on random signals (Rodrigues, 2004).

2.3.4 Micro-Electro-Mechanical Systems and Wireless Sensor Networks

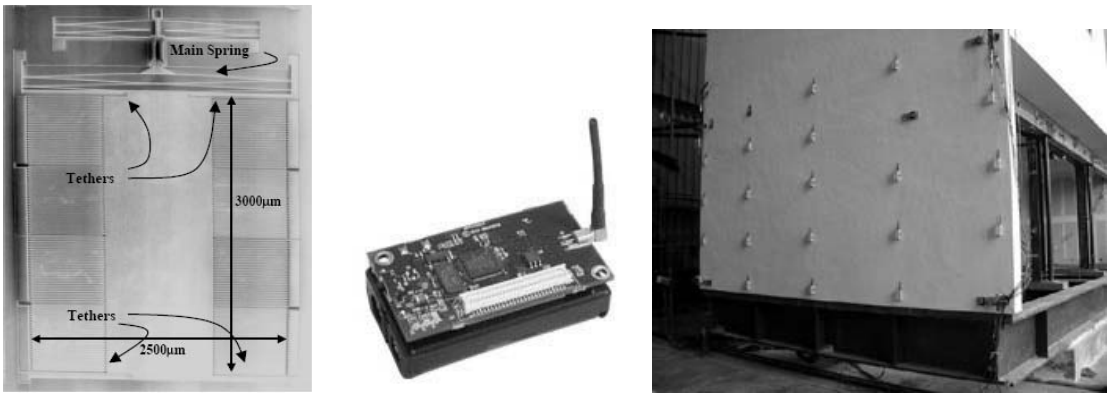
All the presented data acquisition systems and transducers are cable based. Among the problems inherent to these systems are the installation time and cost. Experience allows to conclude that the installation time of a complete measurement system for bridges and buildings, can potentially consume over 75% of the total testing time and installation labour costs can approach well over 25% of the total system cost (Lynch et al., 2002). The installation time can be widely reduced with the implementation of Micro Electric Mechanical Systems (MEMS) based sensors, microprocessors, Wireless Sensors Networks (WSN) and integrated circuits. Figure 2.14 shows the evolution from a cable based measurement system to a flexible wireless system.



(a) (b)

Figure 2.14 – Measurement systems (Lynch et al, 2002): (a) conventional cable based system; and (b) wireless system.

MEMS are the integration of mechanical elements, sensors, actuators, and electronics on a common silicon substrate through nanotechnology (Valoff and Kaiser, 1999). MEMS are devices with a promising future for the measurements and data acquisition systems, because the sensors are very small in size and conditioning and digitalization circuits can be installed on the same board. Figure 2.15a shows one MEMS based accelerometer where it is possible to observe the dimensions involved, and Figure 2.15b presents one wireless unit, which includes power battery, signal conditioning and digitalizing and a wireless connection system.



(a) (b) (c)

Figure 2.15 – MEMS and WSN: (a) MEMS based accelerometer (Valoff and Kaiser, 1999); (b) wireless unit (www.xbow.com); and (c) seismic test of a building with wireless measurement system.

WSN allows testing large structures with large measurement points to analyze both the global and local response of the structures. Crossbow (www.xbow.com) has developed solutions for customers leading recent research initiatives and in the area of seismic structural health monitoring. In a pilot project, wireless accelerometers were mounted on a three story house. The house was built on top of California's largest seismic shaker at the Richmond Field Test Center. Data recorded from 50 wireless accelerometers were used to analyze the structural response to a simulated earthquake. Figure 2.15c shows a seismic shaker, a scale house built on top of it and the wireless sensors.

The main disadvantages of the wireless systems are the low resolution of the transducers at high sampling frequencies and power consumption: by using a 9V battery in a sensor unit, the battery power can run out only in 5 hours.

2.3.5 Input-Output Identification Techniques

The input-output modal identifications techniques were first developed in the areas of Mechanical and Aeronautic Engineering, and then implemented in Civil Engineering around the 1960's. These techniques are based on the control of the input excitation and the measurement of the structural time history response in a set of selected points (see Figure 2.16). The modal parameters (natural frequencies, mode shapes and damping coefficients) are then calculated by estimating the FRFs or the Impulse Response Functions (IRF), either in frequency or time domain. There is also a particular type of tests based on the application of a sinusoidal input, at successive natural frequencies close to the structural resonances. These tests are called tuned-sinusoidal forced tests and they are frequently applied in Civil Engineering structures by the use of eccentric mass shakers.

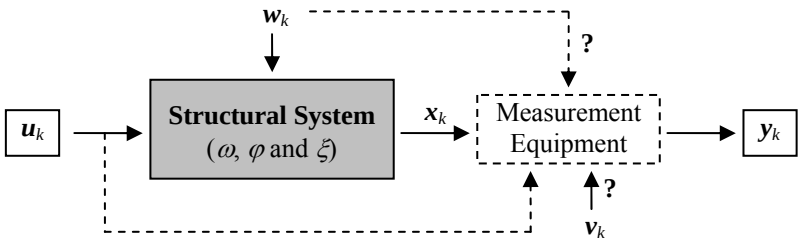


Figure 2.16 – Input-output identification techniques scheme

2.3.5.1 General Classification

The theory and methods of modal system identification based on controlled excitation is well documented by Ewins (2000) and Maia and Silva (1997). The methods can be classified by the type of formulation, number of degrees of freedom, type of estimates and number of inputs/outputs.

Starting from the type of formulation, there are two possibilities: the indirect (modal) and direct formulation. The modal formulation is based on the modal descriptions of structural systems presented in Section 2.2.1. The assumptions are linearity, orthogonally property of the mode shapes and damping $\boldsymbol{C}_2$ proportional to the mass $\boldsymbol{M}$ and stiffness $\boldsymbol{K}$. The direct formulation deals with differential dynamic equilibrium equations and estimates the associated constant coefficients. Some methods are also based on the state-space approach presented in Section 2.2.2.

The formulation has the property of uncoupling the structural response in modal contributions, allowing the accounting of only a few of them in the curve-fitting algorithm. If the fitting algorithm depends on one resonant frequency and damping coefficient to adjust the function to the measured data, the algorithm is called Single Degree Of Freedom (SDOF). On the contrary, if the adjusting process considers several mode shapes these algorithms are called Multiple Degree Of Freedom (MDOF) and, consequently, they are more accurate and more complex to implement.

The type of estimates can only be related to frequency domain with modal formulation. They can be divided in local and global estimates depending on the procedure of mode shape extraction, which can be based on separate fitting of each FRF or on the fitting of the ensemble FRFs.

The number of points to be excited and measured is also important to refer. From the point of view of results accuracy, the ideal is to excite the structures in several points to

induce sufficient energy to extract the largest number of modal information. Difficulties in synchronization and equipment constrain lead often to a single input test. The simpler tests are those with a single input and a single output measured, the so called Single-Input-Single-Output (SISO) identification algorithm. Single input tests have difficulties in inducing all relevant modes and different input locations can be selected, together with different responses treated simultaneously or individually. The first case leads to Single-Input-Multi-Output (SIMO) algorithms, and the second case leads to Multi-Input-Multi-Output (MIMO) algorithms.

Table 2.1 shows the most used system identification algorithms that summarize the methods classification.

Table 2.1 – Classification of typical system identification algorithms, see Caetano, 2000 for details.

	Method	Type of formulation	Type of DOF	Type of estimates	Number of inputs/outputs
Frequency Domain	Peak Picking	Indirect (Modal)	SDOF	Local	SISO
	Circle-fit				
	Inverse				
	Dobson				SISO/SIMO
	Nonlinear LSFD		MDOF	Local Global	SIMO MIMO
	Orthogonal Polynomial				
Tuned-sinusoid	Mau		SDOF	Local	SISO
	Asher's		MDOF	Global	MIMO
Time Domain	Complex Exponential		SDOF	Local	SISO
	LSCE		MDOF	Global	SIMO/MIMO
	Ibrahim				MIMO
	ERA				
	ARMA	Direct			

2.3.5.2 Measurement of the FRFs

According to the first definition of the FRFs, see Eq.(2.8) and Eq.(2.25), having the measured response time history $\boldsymbol{y}(t)$ in the i degree of freedom and of the excitation time history $\boldsymbol{u}(t)$ on the j degree of freedom, the FRF $\boldsymbol{H}_{(i,j)}(\omega)$ can, in theory, be calculated directly from the application of the FRFs to the time histories by (Caetano, 2000):

$$\boldsymbol{H}_{(i,j)}(\omega) = \frac{\boldsymbol{Y}_i(\omega)}{\boldsymbol{U}_j(\omega)} \tag{2.47}$$

where $\boldsymbol{U}$ and $\boldsymbol{Y}$ are the Fourier spectrums of the excitation and the response signals, respectively.

Another process to calculate $\boldsymbol{H}_{(i,j)}(\omega)$ is through the stochastic input-output relations, with respect to cross-spectra density functions between the excitation and the response,

$\boldsymbol{S}_{(i,j)}(\omega)$, and the Power Spectra Density (PSD) functions of the response or the excitation, $\boldsymbol{S}_{(i,i)}(\omega)$ and $\boldsymbol{S}_{(j,j)}(\omega)$, respectively, where the following relations can be observed:

$$\boldsymbol{H}_{(i,j)}(\omega) = \frac{\boldsymbol{S}_{(i,j)}(\omega)}{\boldsymbol{S}_{(j,j)}(\omega)} \quad \text{and} \quad \left|\boldsymbol{H}_{(i,j)}(\omega)\right|^2 = \frac{\boldsymbol{S}_{(i,i)}(\omega)}{\boldsymbol{S}_{(j,j)}(\omega)} \tag{2.48}$$

Once the measurements are discrete in time with Δt spacing, the above equations can only be estimated at discrete frequency values ω on a frequency spacing $\Delta\omega$ defined by the sampling frequency f_S given by Eq.(2.40) and the number of samples N in the time history by:

$$\Delta\omega = \frac{2\pi}{N\, f_S} \tag{2.49}$$

and the FRFs are then calculated as estimation of the real values by (the superscript ^ denotes estimate):

$$\begin{gathered} \hat{\boldsymbol{H}}_{(i,j)}(\omega) = \frac{\hat{\boldsymbol{Y}}_i(\omega)}{\hat{\boldsymbol{U}}_j(\omega)} \quad , \\ \hat{\boldsymbol{H}}_{(i,j)}(\omega) = \frac{\hat{\boldsymbol{S}}_{(i,j)}(\omega)}{\hat{\boldsymbol{S}}_{(j,j)}(\omega)} \quad \text{and} \quad \left|\hat{\boldsymbol{H}}_{(i,j)}(\omega)\right|^2 = \frac{\hat{\boldsymbol{S}}_{(i,i)}(\omega)}{\hat{\boldsymbol{S}}_{(j,j)}(\omega)} \end{gathered} \tag{2.50}$$

where every spectrum $\boldsymbol{S}_{(x1,x2)}$ is given by the following expression:

$$\hat{\boldsymbol{S}}_{(x_1,x_2)}(\omega) = \frac{\boldsymbol{X}_1(\omega)^*\, \boldsymbol{X}_2(\omega)}{N\,\Delta t} \tag{2.51}$$

2.3.5.3 Peak Picking Method

The most well know and used frequency domain method is the Peak Picking (PP) method (Ewins, 2000 and Maia and Silva, 1997) based on the assumption that in the vicinity of a resonant frequency the response is dominated by the resonant mode shape, and consequently there are no contributions of other non-resonant modes. The FRF, see Eq.(2.25), can be substituted by an equivalent FRF of one degree-of-freedom given by:

$$\boldsymbol{H}_{(i,j)}(\omega) = \frac{\varphi_{i,n}\,\varphi_{j,n}}{(\omega_n^2 - \omega^2) + j(2\xi_n\,\omega_n\,\omega)} \tag{2.52}$$

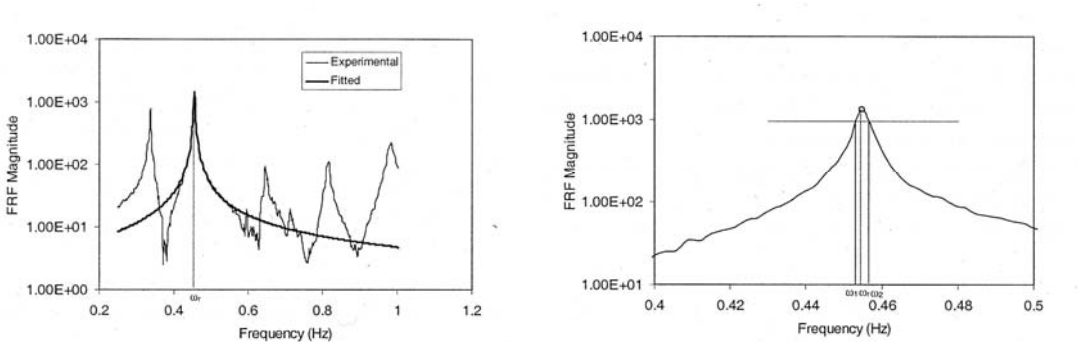
The resonant frequencies ω_n are then associated to the peaks of the FRF amplitude. For damping estimation, the Half-Power Bandwidth method can be used. The method is based on the calculation of the close frequencies, where the square of the amplitude of the FRF is equal to the half of is maximum value:

$$\left|\boldsymbol{H}_{(i,j)}(\omega)\right|^2 = \frac{1}{2}\left|\boldsymbol{H}_{(i,j)}(\omega_n)\right|^2 \tag{2.53}$$

Using the preceding definition, the damping coefficient ξ_n can be approximately calculated by:

$$\xi_n \approx \frac{\omega_2 - \omega_1}{2\omega_n} \tag{2.54}$$

Figure 2.17 shows graphically the procedures to calculate the peak values for the resonant frequencies and the damping coefficients.



(a) (b)

Figure 2.17 – Peak Picking method (Caetano, 2000): (a) fitting of the FRF with one degree of freedom; and (b) estimation of the damping coefficients using the Half Power Bandwidth Method.

Finally, the mode shape vectors are assumed to be real eigenvectors, which can be estimated by taking the peaks values of the set of FRFs and according to Eq.(2.52), by:

$$\left|\boldsymbol{H}_{(i,j)}(\omega_n)\right| \approx \frac{\varphi_{i,n}\,\varphi_{j,n}}{2\xi_n\,\omega_n^{\,2}} \tag{2.55}$$

and calculating the first diagonal terms where the FRFs are related with the input and output measurements at the same location, the eigen components are therefore obtained by:

$$\varphi_{i,n} = \sqrt{2\xi_n\,\omega_n^{\,2}\left|\boldsymbol{H}_{(i,k)}(\omega_n)\right|} \quad \text{and} \quad \varphi_{j,n} = \sqrt{2\xi_n\,\omega_n^{\,2}\left|\boldsymbol{H}_{(i,j)}(\omega_n)\right|}\Big/\varphi_{i,n} \tag{2.56}$$

The results form PP method are highly sensitive to noise and to structural damping, because the estimated mode shapes are calculated only with three points of each FRFs. Others sources of errors on modal estimation can occur when resonant frequencies are in a narrow range, resulting in frequency contamination at the resonant values, or when the FRFs are extremely sharp, and consequently the estimation of damping coefficients has low resolution. Nevertheless, there are procedures that can be used to increase the result accuracies for the modal parameters estimation, as given by Ewins (2000) and Maia and Silva (1997).

2.3.5.4 Practical Implementation of Forced Vibration Tests on Masonry Constructions

In what concerns masonry constructions and independently of the type of forced based identification method, several researchers have been using the input-output identification techniques to estimate modal parameters. It is important to briefly review these works to highlight the main characteristics of these types of techniques when applied to masonry constructions.

Vestroni et al. (1996) presented an analysis of a two storey masonry house excited with steady-state vibration tests with small amplitudes at medium intensity shaking force to estimate its dynamic characteristics. Although the geometry of the building was quite regular, the dynamic response was very complex, with a high number of resonant peaks to analyze. They concluded that it was necessary to adopt a model with a higher number of degrees of freedom, close to the measurement points, to describe the response accurately. From the results of different amplitude of oscillations, the authors could calculate the decrease of the first modal stiffness, indicating the nonlinear behaviour of the structure.

Genovese and Vestroni (1998) also used small force amplitudes oscillations to identify modal parameters. They concluded that the response is sensitive to the characteristics of the input if the excitation and the dynamic behaviour of the structure subjected to increased levels of force are characterized by the decrease of the modal stiffness.

De Sortis et al. (2005), concluded that sinusoidal excitation appears to be more reliable for masonry buildings than the sine sweep excitation. The sine sweep produces both a shift in the peak frequency and an over estimated damping coefficient in comparison to sinusoidal excitation. The reason for this behaviour is the nonlinearity of masonry buildings when close resonant frequencies are present, even at low levels of vibration. Another conclusion was that modal characteristics were dependent on the location of the excitation device and on the kind of load applied.

To conclude, force vibrations techniques have been widely used for modal identification on masonry constructions (Bensalem et al., 1995; Vestroni et al, 1996; Genovese and Vestroni, 1998; Sigmund and Herman, 1998; Zonta, 2000; Modena et al., 2001; Erdogmus and Boothby, 2004; De Sortis et al., 2005). The main problem is adequate excitation equipments. For small structural systems, it is not difficult to develop excitation mechanisms and there are several commercial companies that have them available. But for medium/large systems, like towers, large bridges and heavy buildings, it is difficult and laborious to apply a controlled excitation with appropriate dynamic characteristics.

2.3.6 Output-Only Identification Techniques

The output-only modal identifications techniques or ambient vibration techniques were also developed in the areas of Mechanical and Aeronautic Engineering, but more importance was paid to large civil engineering constructions, such as bridges and towers, in which artificial excitations and the determination of forces constitutes a problem. The techniques are based on the dynamic response measurements of a virtual system under natural (ambient or operational) conditions (see Figure 2.18), and the assumption that the excitations are random nature in time and in the physical space of the structure (or if it is physically local it can gives sufficient energy to excite all the structure).

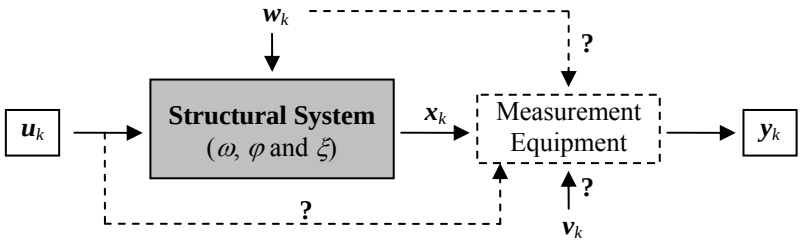


Figure 2.18 – Output-only identification techniques scheme

In this type of identification technique, the main assumption for the excitation of the virtual system is the consideration of the ambient excitations $\boldsymbol{u}_k$ as a stationary Gaussian white noise stochastic process in a frequency range of interest. Due to the nature of the measurement data, the response $\boldsymbol{y}_k$ includes the modal contributions of the ambient forces, the contribution of the structural system and the contribution of the noise signals from undesired sources. Furthermore, the measured response reflects the poles (amplitude picks from the spectral density functions) from the structural system and from the ambient forces, and consequently the identification techniques must have the ability to separate

them. Ivanović et al. (2000) presents a literature review with the bases for the application of these techniques.

2.3.6.1 General Classification

The techniques can be divided into two main groups, depending on the type of data used, namely frequency or time domains. The first group is based on the signal analysis of each measured point (in frequency domain by the application of the FFTs) and on the correlation between the signals. The techniques are also called non-parametric methods. The second group is based on model fitting by the correlation functions or time history series of every measured point in the time domain. The techniques of this group are also called parametric methods.

Generally, frequency domain methods have a faster processing time and are more user friendly, when compared with time domain methods. As a disadvantage, frequency domain methods have difficulties in identifying close frequency values, because they have a limit on the frequency resolution resulting from the FFT process.

Table 2.2 summarizes some relevant output-only identification methods based on Caetano (2000). These methods and others are extensively documented in the work of Rodrigues (2004), who compared sixteen methods on a four story mock-up building. One key conclusion is that there is no singe best method to use on modal identification, because all methods have accurate results when applied conveniently and each method has its own advantages and limitations. Therefore, experience analysts must select the most appropriate method for a given application. Additional comparisons on building modal analysis can be found in the work of Peeters and De Roeck (1999) and Horyna and Ventura (2000) and on bridges in the work of Andersen et al. (1999), Peeters et al. (2002), Magalhães (2004) and Cunha et al. (2004). These researchers also stressed that the damping coefficient estimation is marked by significant differences using different methods.

Table 2.2 – Classification of some relevant output-only identification algorithms (Caetano, 2000).

	Method	Characteristics
Frequency Domain	Peak Picking (PP)	Classical SDOF method
	Frequency Domain Decomposition (FDD)	MDOF method; application of SVD to reduce noise
	Enhanced Frequency Domain Decomposition (EFDD)	MDOF method; application of SVD to reduce noise
	Polimax	MDOF method
Time Domain	Random Decrement (RD)	Operates on time domain series, leading to a free decay curve analysis
	Recussive Techniques (ARMA)	Time series modelling using recursive algorithms
	Maximum Likelihood Methods	Stochastic methods based on the minimization of a covariance matrix
	Stochastic Subspace Identification Methods (SSI-DATA)	Stochastic methods based on the project of state vector on a vector of past realizations

Next, the two identifications techniques used in the test carried out for damage identification purpose are briefly presented.

2.3.6.2 Frequency Domain Decomposition Method

To introduce the Frequency Domain Decomposition (FDD) method, it is important to point out a characteristic of the measured FRFs in the context of ouput-only techniques. As the excitation source is considered as a stationary Gaussian white noise stochastic process, the PSD function of the excitation is considered constant, i.e. $\boldsymbol{S}_{jj}(\omega) = C$, and this assumption influences the third relation presented in Eq.(2.50), given by:

$$\left|\hat{\boldsymbol{H}}_{(i,j)}(\omega)\right|^2 = \frac{\hat{\boldsymbol{S}}_{(i,i)}(\omega)}{C} \tag{2.57}$$

This observation indicates that the FRF peaks according to the resonant frequencies of the structural system can be obtained directly from the peaks of the estimation of PSD functions only of the measurement response.

The FDD method can be visualized as an extension of the PP method, which assumes that resonant frequencies are well spaced in frequency and the contribution of other modes in the vicinity of that resonant frequency is null. The method was presented by Brincker et al. (2000) and the basis of the FDD method is the Singular Value Decomposition (SVD) of the response spectral density matrix, given by:

$$\boldsymbol{S}_y(\omega_k) = \Psi_k \, \Lambda_k \, \Psi_k^H \tag{2.58}$$

where Λ_k is a diagonal matrix with the singular values, positive and real eigenvalues of the matrix $\boldsymbol{S}_y(\omega)$, disturbed in decreasing order. The first singular value corresponds for every frequency the power spectrum of one degree of freedom system in accordance to the significant modes shapes that contributes for the response. Ψ_k is an orthogonal complex matrix where each column contains the mode shape vectors of each spectral peak. The superscript ^{H} denotes the conjugate transpose and the following relation can be established for the matrix Ψ_k:

$$\Psi_k \, \Psi_k^H = \Psi_k^H \, \Psi_k = \boldsymbol{I} \tag{2.59}$$

The next step is the spectrum analysis of the singular values Λ_k for the selection of the resonant peaks and corresponding mode shapes and the evaluation of the model components on the measured degrees of freedom. Figure 2.19a shows the SVD by the FDD method, where fourteen resonant peaks of the structural global modes can be observed in the first singular value. Other evident peaks can be observed in the second and third singular values.

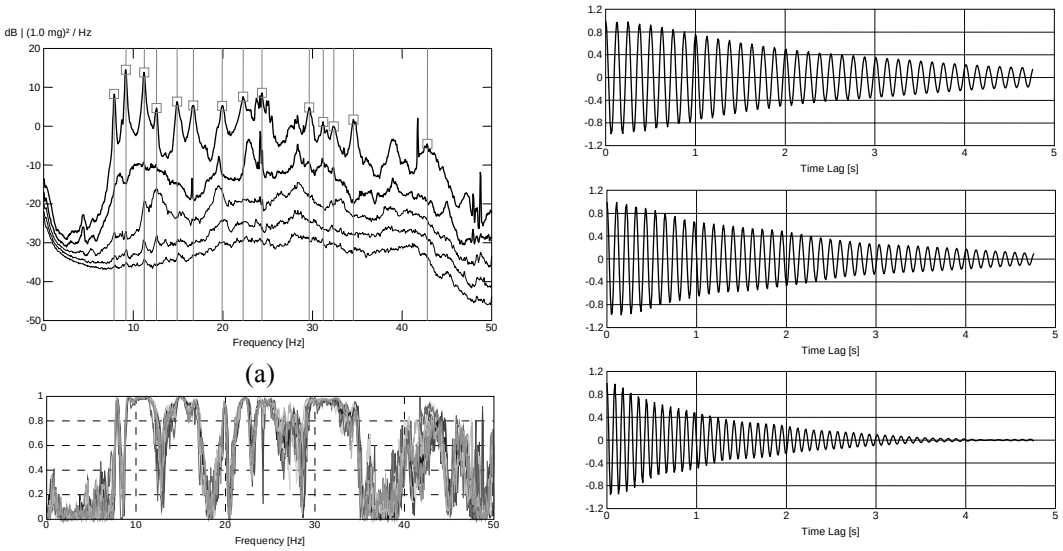


Figure 2.19 – Frequency domain decomposition methods: (a) Single values decomposition of FDD method; (b) coherence of spectral density between the references transducers for all data sets; and (c) auto-correlation functions of single degree of freedom system of EFDD method for the first three selected peaks on (a).

The FDD method suffered an improvement by Brincker et al. (2001) with the Enhanced FDD (EFDD) method. Basically, the first step of the EFDD is equal to the FDD method but the estimation of frequency values and damping coefficients are calculated by the application of inverse FFT of each spectral density function for each mode shape. The obtained auto-correlation response function is now a typical response of a single degree of freedom system with a dynamic response in free vibration (see Figure 2.19c). The intersection with zero provides the natural frequency of each system and the damping coefficients are calculated through logarithmic decrement.

As referred above, output-only methods must have the ability to separate spectral density functions peaks of structural resonant frequencies from other peaks resulting from undesired sources. To assist in the selection of the structural peaks a scalar coherence function between the response of two measured points, $\boldsymbol{y}_i$ and $\boldsymbol{y}_j$, can be used. The values of the coherence function $\gamma^2(\omega)$, given by:

$$\gamma_{i,j}^2(\omega) = \frac{\left|\hat{\boldsymbol{S}}_{y(i,j)}(\omega)\right|^2}{\hat{\boldsymbol{S}}_{y(i,i)}(\omega)\,\hat{\boldsymbol{S}}_{y(j,j)}(\omega)} \tag{2.60}$$

varies from zero to one and indicates, in the frequency domain, the linearity between the two measured signals and the presence of a global mode shape. The values close to one indicate a strong relation between the signals. However, for resonant frequencies resulting from localized modes or from ambient vibration frequencies that do failed to mobilize a global mode, the coherence function value is low (Paultre et al., 1995). Figure 2.19b presents coherence values for the spectral density between two reference points in all measured data sets, and it is possible to observe, when the coherence value is close to one, a clear peak in the first singular value appears in Figure 2.19a.

The implementation of the FDD method is simple. However, this method estimates the resonant frequencies with discrete frequency values with limited precision, due to the fact that the method is based on FFT signal analysis. In particular, difficulties in the estimation can be observed when two close resonant frequencies exist. To increase the

frequency resolution, very large time series can be used for the modal analysis. An alternative is to use the EFDD method, which can surpass the problem because the resonant frequencies and damping coefficients are estimated in time domain, by the application of inverse FFTs.

The FDD and the EFDD are implemented, for example, in the software ARTeMIS (SVS, 2006).

2.3.6.3 Stochastic Subspace Identification Method

The time domain methods and, in particular, the Stochastic Subspace Identification (SSI) method deals directly with time series processing (SSI-DATA, driven stochastic subspace identification). Time domain methods are robust and allow modal parameter estimation with high frequency resolution. On the other hand, the implementation is not as friendly as the FDD method, and more processing time is needed during parameter estimation.

As an example, the SSI-DATA was implemented to analyse civil engineering structures by Peeters (2000) and Rodrigues (2004). The method fits a model directly to the raw times series data, based on the State-Space Formulation already presented in Section 2.2.2 and from the analysis of the response time series. The mathematical model has parameters that can be adjusted to minimise the deviation between the predicted system response and the measured system response (see Figure 2.20a).

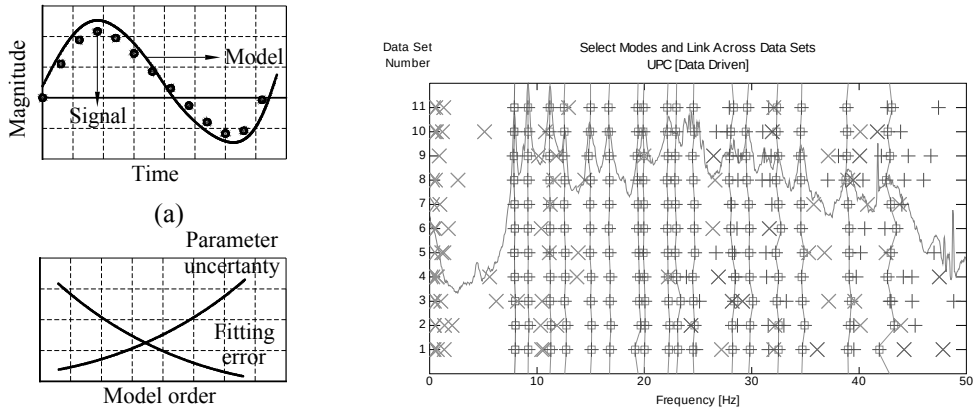


Figure 2.20 – Stochastic Subspace Identification method: (a) model calibration; (b) model parameter estimation dilemma; and (c) data driven with the poles selection through the several test setups.

The main objective of the SSI method is the identification of the state matrix $\boldsymbol{A}$ and the output matrix $\boldsymbol{C}$, see Eq.(2.38), which contain the information about the resonant frequencies, mode shapes vectors and damping coefficients.

For the matrices estimation, the methods uses complex but robust mathematical techniques. The steps are next briefly presented (see Peeters and De Roeck, 1999; Peeters, 2000; Rodrigues, 2004; and Deraemaeker, et al., 2007, for detailed information):

1. Construction of the Hankel matrix $\boldsymbol{h}$ with the past and future information of the output response $\boldsymbol{y}_k$. The output response is arranged in a block Hankel matrix with $2i$ block rows and j columns. The first i blocks have r rows in with respect to the number of reference sensors, and the last i blocks have l rows with respect to the moving sensors. The Hankle matrix has the following form:

$$\boldsymbol{h} = \frac{1}{\sqrt{j}} \left(\begin{array}{cccc} \boldsymbol{y}_0^{ref} & \boldsymbol{y}_1^{ref} & \cdots & \boldsymbol{y}_{j-1}^{ref} \\ \boldsymbol{y}_1^{ref} & \boldsymbol{y}_2^{ref} & \cdots & \boldsymbol{y}_j^{ref} \\ \cdots & \cdots & \cdots & \cdots \\ \boldsymbol{y}_{i-1}^{ref} & \boldsymbol{y}_1^{ref} & \cdots & \boldsymbol{y}_{i+j-2}^{ref} \\ \hline \boldsymbol{y}_i & \boldsymbol{y}_{i+1} & \cdots & \boldsymbol{y}_{i+j-1} \\ \boldsymbol{y}_{i+1} & \boldsymbol{y}_{i+2} & \cdots & \boldsymbol{y}_{i+N} \\ \cdots & \cdots & \cdots & \cdots \\ \boldsymbol{y}_{2i+1} & \boldsymbol{y}_{2i} & \cdots & \boldsymbol{y}_{2i+j-2} \end{array} \right) = \left(\begin{array}{c} \boldsymbol{Y}_p^{ref} \\ \hline \boldsymbol{Y}_f \end{array} \right) = \frac{\text{" past"}}{\text{" future"}}, \tag{2.61}$$

2. LQ factorization of $\boldsymbol{h}$, i.e. the decomposition of the matrix $\boldsymbol{h}$ into a product of other matrices, which when multiplied together gives the original matrix. With the factorization the rows of $\boldsymbol{h}$ are divided in four parts, where the first row is related to the past and the others to the future as follow:

$$\boldsymbol{h} = \boldsymbol{L}\,\boldsymbol{Q}^H = \left(\begin{array}{cccc} \boldsymbol{L}_{11} & 0 & 0 & 0 \\ \hline \boldsymbol{L}_{21} & \boldsymbol{L}_{22} & 0 & 0 \\ \boldsymbol{L}_{31} & \boldsymbol{L}_{32} & \boldsymbol{L}_{33} & 0 \\ \boldsymbol{L}_{41} & \boldsymbol{L}_{43} & \boldsymbol{L}_{43} & \boldsymbol{L}_{44} \end{array} \right) \left(\begin{array}{c} \boldsymbol{Q}_1^H \\ \boldsymbol{Q}_2^H \\ \boldsymbol{Q}_3^H \\ \boldsymbol{Q}_4^H \end{array} \right) \tag{2.62}$$

3. Singular value decomposition of first column of the future $\boldsymbol{L}$ factors:

$$\begin{pmatrix} \boldsymbol{L}_{21} \\ \boldsymbol{L}_{31} \\ \boldsymbol{L}_{41} \end{pmatrix} = \boldsymbol{U}_L\,\Lambda_L\,\boldsymbol{V}_L^H \tag{2.63}$$

and selection the system order n to split the singular vectors and the singular values in two parts, in way that $\boldsymbol{S}_1$ contains the first n singular values:

$$\boldsymbol{U}_L\,\Lambda_L\,\boldsymbol{V}_L^H = \begin{pmatrix} \boldsymbol{U}_1 & \boldsymbol{U}_2 \end{pmatrix} \begin{pmatrix} \boldsymbol{S}_1 & 0 \\ 0 & \boldsymbol{S}_2 \end{pmatrix} \begin{pmatrix} \boldsymbol{V}_1 \\ \boldsymbol{V}_2 \end{pmatrix} \tag{2.64}$$

4. Estimation of the state matrix $\boldsymbol{A}$ and the output matrix $\boldsymbol{C}$ from the observability matrix $\boldsymbol{O}_i$, given by:

$$\boldsymbol{O}_i = \boldsymbol{U}_1\,\boldsymbol{S}_1^{1/2} \tag{2.65}$$

$$\begin{pmatrix} \boldsymbol{A} \\ \boldsymbol{C} \end{pmatrix} = \begin{pmatrix} \boldsymbol{O}_{i-1}^{+} \begin{pmatrix} \boldsymbol{L}_{41} & \boldsymbol{L}_{42} & 0 \end{pmatrix} \\ \begin{pmatrix} \boldsymbol{L}_{21} & \boldsymbol{L}_{22} & 0 \\ \boldsymbol{L}_{31} & \boldsymbol{L}_{32} & \boldsymbol{L}_{33} \end{pmatrix} \end{pmatrix} \begin{pmatrix} \boldsymbol{O}_{i-1}^{+} \begin{pmatrix} \boldsymbol{L}_{21} & 0 & 0 \\ \boldsymbol{L}_{31} & 0 & 0 \\ \boldsymbol{L}_{41} & 0 & 0 \end{pmatrix} \end{pmatrix}^{+} \tag{2.66}$$

The superscript $^+$ denotes the Moore-Penrose pseudo-inverse of a matrix. For system matrices, the last row of the observability matrix is removed;

5. Finally, modal parameters (eigen frequencies Λ, the eigen vectors Φ and the damping coefficients ξ) are estimated from $\boldsymbol{A}$ and $\boldsymbol{C}$ matrix as follows:

$$\begin{aligned} \boldsymbol{A} &= \Psi \Lambda \Psi^{-1} \\ \Phi &= \boldsymbol{C}\, \Psi \\ \xi &= \frac{\mathrm{Re}(\lambda)}{|\lambda|} \end{aligned} \tag{2.67}$$

where $|\cdot|$ denotes the complex modulus.

In all this process, the definition of a reasonable number of model parameters or model order (also known as the state space dimension, which is the dimension of the matrix $\boldsymbol{A}$) is essential, because a small number will not model correctly the dynamic behaviour of the structure, and a large number can over-specify the model and large statistical uncertainties can occur in the model parameters (see Figure 2.20b).

The SSI-DATA is implemented, for example, in the software ARTeMIS (SVS, 2006) and MACEC (Peeters and De Roeck, 1999). Figure 2.20b shows the application of the method where it is possible to identify close frequencies, which did not appear clearly in the FDD method (see Figure 2.19).

2.3.6.4 Practical Implementation of Ambient Vibration Tests on Masonry Constructions

Several researchers have recently used the output-only identification techniques for modal identification of masonry constructions. The robust results associated with the facilities and the economic low cost test and real operating conditions during its daily use makes these techniques very popular. To highlight this fact, a few works are presented below related to masonry constructions.

Jaishi et al. (2003) presented a dynamic characterization of three typical Nepalese temples with ambient vibration analysis. The authors stressed the advantages of output-only techniques and concluded that these techniques are sufficient to identify the most important modes. With PP and SSI methods they could identify six resonant frequencies between 1.5 an 13 Hz, with the first two frequencies closely spaced for symmetrical temples.

On the modal identification of the bell-tower of the Monza Cathedral, Gentile and Saisi (2004) used the PP and FDD methods to estimate the natural frequencies, in a frequency range of 0 to 10 Hz. The excitations were associated to the environmental loads and to the bells ringing. The results show a good agreement between the two methods, in terms of frequencies (maximum difference of 2%) and mode shapes (minimum MAC value of 0.96). Other works on masonry towers are presented by Rebelo et al. (2007), Schmidt (2007) and Ivorra and Pallarés (2007).

Analysis carried out in other masonry constructions where the first resonant frequencies were successfully estimated by the FDD method are presented by Costa et al. (2004) on a masonry arch bridge, Neves et al. (2004) on two-floor houses in Azores, Baptista (2004) at N. Sr.a do Carmo Church, in Lagos and Casarin and Modena (2007) on S. Maria Assunta Cathedral, Italy.

In the dynamic system identification of the Qutub Minar, in New Delhi (Ramos et al., 2006) different acquisition systems with different techniques were used to test the tower. With output-only techniques fourteen natural frequencies and corresponding modes were obtained in a range between 0.78 to 8.67 Hz. The first two mode shapes were very closed, with differences of 0.02 Hz, due to the axisymmetric cross section of the tower.

To conclude, in literature is possible to find several cases of output-only techniques applied to masonry structures with successful results. For heavy masonry structures, the excitation level might be a problem, but based on the author's experience moderate wind or traffic excitations are sufficient to perform accurate modal analysis.

2.3.7 Test Planning

One important aspect that must be addressed in the application of output-only identification techniques is the definition of the test planning, which should ideally comprise six phases:

1. The first phase comprises a modal analysis of a Finite Element (FE) model to have a preliminary idea about the frequency values and the mode shape configurations of the structure. Generally, for masonry constructions, the model must be constructed and mechanical tests can be carried out to characterize the material properties;
2. The second phase refers to the definition of the number of points to measure in accordance with the demand of the dynamic identification test and the preliminary dynamic analysis from the FE model. The number of points to be measured is, in general, larger than the number of available sensors. In this case, a measuring point or a group of points should be chosen as fixed sensors, while the other sensors are moved around the structure (see Figure 2.21);

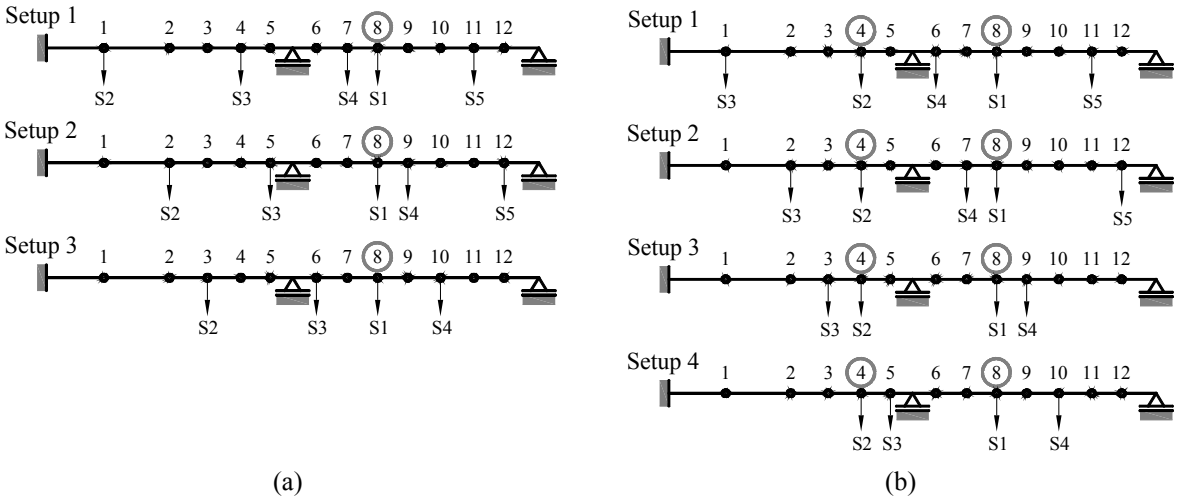


Figure 2.21 – Examples of reference and moving sensors: (a) three test setups with one reference sensor; and (b) four test setups with two reference sensors.

It is important to stress that at least one of the reference points should not coincide with a node[†] of the structural mode shapes, otherwise inaccurate results may occur. Every single measurement step is called a setup or data set, and it is common for a simple dynamic identification to have ten or more setups. Everyone involved in the tests should be informed about all test procedures;

3. In the third phase, before the measurements of each setup, it is first important to proceed with some localized signal measurements to monitor the level of the

[†] A node of a mode shape is a point with zero modal displacement.

signals, to characterize the signal-to-noise ratio and to have an idea about the resonant frequencies involved. This task can be made by a simple FFT of the response measurements in a few key points, e.g. the reference points. After this preliminary identification analysis, changes to the test planning can be necessary to obtain accurate results, such as different sensor types, other positions, the need of additional excitation to increase the signal-to-noise level or, simply, the definition of the sampling frequency and the measurement duration. If the signal-to-noise ratio is very low, additional random excitation can be applied so that results do not suffer significant influences (Peeters, 2000);

4. The fourth phase is the setup measurements. In what concerns the measuring duration, a large number of points should be recorded to have resolution in frequency. A first empirical rule (Rodrigues, 2004) is to consider 2000 times the highest natural period of interest (the lowest frequency), e.g. for a structure with a natural frequency of 2 Hz, the total sampling duration should be, at least, about 17 minutes. Based on practical experience and in case of flexible structures, Caetano (2000) recommends a measuring duration about 30 to 40 times the highest period, times a number of averages varying between 8 and 32. In this case, the record length varies from 2 to almost 11 minutes. Nevertheless, based on the variance error (Bendat and Piersol, 1986) the number of averages in the pre-processing signal analysis should be equal to 100 to have a variance error of 10%. If the frequency resolution is 0.1 Hz, each record segment should have 10 s, plus 100 averages, which results in almost 17 minutes. To conclude and according to the author's own experience, the empirical rule of 1000 times the highest period (with a minimum of 10 min for each setup) can be used to obtain accurate results if the structure is well excited, but the duration must be conveniently defined taking into account the number of available sensors, the number of measurement points and the available time for the complete test;
5. The fifth phase is a preliminary check to quality of the data obtained. In the setup recording phase and between each setup, it is important to check the measured signals of every sensor to avoid data losses or bad signal quality. Before packing all test equipment, it is also desirable to make a preliminary modal analysis in order to be sure that the experimental results have sufficient quality for the success of the modal identification;
6. In the final phase, it is a good practice to study the dynamic behaviour using two or more identification methods. This gives the analyst confidence in the results and can contribute to proceed with more objective test procedures.

2.3.8 Mode Shape Mass Normalization

A consequence of the output-only techniques is the fact that the estimated mode shapes vectors are not mass-normalized or mass-scaled, because the excitation is unknown. From the identification point of view, this does not change the results accuracy. Only when it is necessary to know the mass-normalized modes, which is the case of some vibration based damage identification methods to be discussed in Chapter 3, it is necessary to apply procedures to overcome this difficulty. Two alternatives can be used for the approximated calculation of the scaled modes: (a) the assumption that the mass matrix is known

or (b) the comparison between two dynamic identification tests with and without controlled masses added to the structure.

In the first approach, the mass matrix $\boldsymbol{M}$ can be calculated from a FE model. This procedure is acceptable if sufficient information is known from the structure. Afterwards, the mode shape vectors are normalized from the output-only techniques, see Eq.(2.58) and Eq.(2.67). The normalized mode shapes ϕ_j for each measured mode $\varphi_{j,m}$ can be obtained, see also Eq.(2.17):

$$\phi_j = \alpha_j^m \varphi_j = \frac{1}{\sqrt{m_j}} \varphi_{j,m}, \tag{2.68}$$

where α^m are the normalization factors, proportional to the inverse of the corresponding modal mass m, given by:

$$m_j = \varphi_j^T \boldsymbol{M} \varphi_j \tag{2.69}$$

where the matrix $\boldsymbol{M}$ is calculated from a FE model with condensation techniques.

In the second case, the alternative way is to add controlled masses to the structures, in a sense that mode shapes does not significantly change and the frequency shifts are small, and compare the response without the added masses. This technique was first presented by Parloo et al. (2002) and further Brincker and Andersen (2003) also used to scale modes. The scaled factors can be calculated by (see Parloo et al., 2002):

$$\alpha_j^m \approx \sqrt{-\frac{2\Delta\omega_j}{\omega_j \sum_{j=1}^{m} \varphi_{j,m}^T \Delta\boldsymbol{M} \varphi_{j,m}}} \tag{2.70}$$

where $\Delta\omega_j$ are frequencies shifts and $\Delta\boldsymbol{M}$ are the added mass matrix.

With this technique is possible to scale the modes with a few masses added to the structure. Adding masses near a node is not recommended, because it can change the mode shape configurations. An alternative is to add uniformly distributed masses along the structure. It is also important that added mass are small enough to produce a linear relation between the amount of added mass and the resulting shifts in the resonant frequencies.

2.4 Environmental and Loading Conditions Influence

Before any attempt to identify the presence of damage it is important to evaluate and separate the environmental and the loading effects from the dynamic response of the structure. In fact, it is known that temperature can change the modulus of elasticity in an inverse relation and boundary conditions may also be dependent from temperature. Figure 2.22 shows the temperature dependence of the Z24 Bridge (see Peeters, 2000), in Switzerland, in terms of the first natural frequency. In this case, a different behaviour of the bridge below and upper the 0ºC is clearly obtained. The author concluded that this bilinear behaviour is due to the strong influence of the asphalt on the road pavement on the bridge, which on the cold period significant contributes to the stiffness of the structure. Also Farrar et al. (1994) when study a bridge in US, recorded changes of 5% for the first frequency during a period of 24 hours while, for another bridge, Roberts and Pearson (1998) found that environmental effects could provide a change in the first frequency up to 4% during a period of one year.

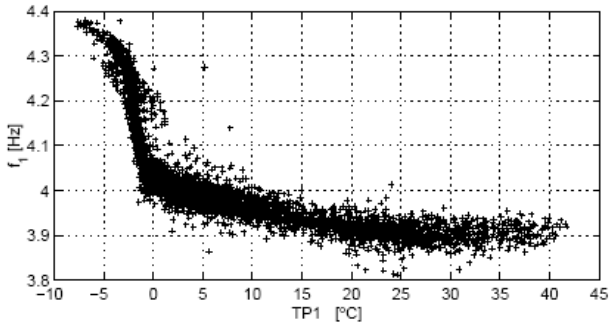


Figure 2.22 – Temperature dependence for the first resonant frequency for the Z24 Bridge (Peeters, 2000).

Soil freezing at the supports may also have a significant influence in the resonant frequencies. Alampalli (1998) reported significant changes in the relative frequencies (40 to 50%) of a small bridge compared with the changes of controlled damage (3 to 8%).

It is also known that the loading source may introduce changes in the dynamic response. Ambient excitations can involve different sources like: traffic, wind, ice actions, waves, stream and earthquakes. Ndambi et al. (2000) found some changes in its identified dynamic properties in the dynamic response of a concrete beam when the type of excitation changed: (a) the resonant frequencies decreased with increasing excitation amplitude; and (b) the modal damping ratios increases with the excitation amplitude. Also Peeters and Ventura (2003) reported some changes in the dynamic response of a bridge depending on using artificial and ambient excitations, or different excitation mechanisms.

In the case of masonry structures, it is expected that also moisture may have an influence on the dynamic behaviour. The possible effect of stiffness and mass change due to the moister is still a challenge to be addressed by the scientific community involved in this field of knowledge.

In the context of vibration based damage identification with output-only measurements, independently of the method used to estimate the modal parameters (frequencies ω, modes φ and damping ξ), the environmental and loading effects should be modeled (filtered) to obtain the final modal parameters (ω', φ' and ξ') for damage identification (see Figure 2.23). This model should give a correlation between the environmental and loading effects and the dynamic response and also should give a confidence interval to assure the presence (detection) of damage.

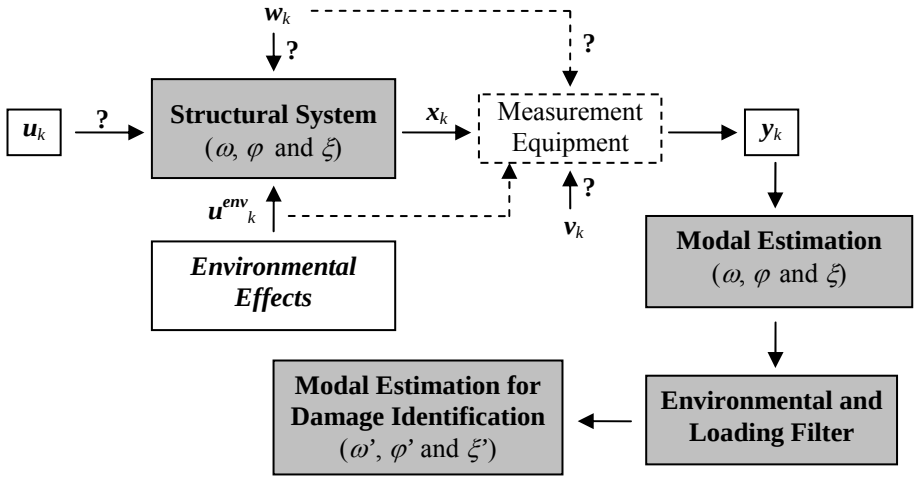


Figure 2.23 – Filtering of environmental and loading influences in output-only system identification for damage detection.

Taking into account the above consideration, the first step before any attempt to model the environmental and loading conditions is to study the correlation between environmental effects $\boldsymbol{u}^{env}{}_k$ and measured dynamic response $\boldsymbol{y}_k$. This can be carried out through the correlation coefficient r_{xy} or the square of the correlation coefficient $r_{xy}{}^2$, which is also known as the coefficient of determination. The estimated correlation coefficient is given by:

$$\hat{r}_{xy} = \frac{\hat{R}_{xy}}{\hat{\sigma}_x \, \hat{\sigma}_y} \tag{2.71}$$

where $\hat{R}_{xy}$ is the estimated covariance given by:

$$\hat{R}_{xy} = \frac{1}{N-1} \sum_{k=1}^{N} \left(x_k - \bar{x}\right) \left(y_k - \bar{y}\right) \tag{2.72}$$

and $\hat{\sigma}_x$ and $\hat{\sigma}_y$ are the estimated standard deviation given by:

$$\hat{\sigma}_x = \sqrt{\frac{1}{N-1} \sum_{k=1}^{N} \left(x_k - \bar{x}\right)^2} \quad \text{and} \quad \hat{\sigma}_y = \sqrt{\frac{1}{N-1} \sum_{k=1}^{N} \left(y_k - \bar{y}\right)^2} \tag{2.73}$$

The absolute value of the correlation coefficient can vary from zero to one, indicating a weak or strong correlation between the two variables. If no correlation (or a weak correlation) is observed between pairs of environmental inputs and dynamic response, for convenience one can reduce the complexity of the environmental filter.

2.4.1 Linear Regression

The simplest model to correlate resonant frequencies and the environmental effects is to use linear or multi-linear regressions by means of the least squares method. The estimated response $\hat{y}_k$ can be model as follows:

$$\hat{y}_k = a_0 + a_1 \, u_{1,k}^{env} + a_2 \, u_{2,k}^{env} + \ldots + e_k \tag{2.74}$$

where the coefficients a_i can be determined by the least square method and e_k are the residuals given by,

$$e_k = y_k - \hat{y}_k \tag{2.75}$$

If the residuals are assumed to be normal distributed, the confidence intervals ci for a estimation $\hat{y}_k \pm ci$ are given by:

$$ci = \pm z\left(1 - \alpha/2\right) \hat{\sigma} \tag{2.76}$$

where $z(1\text{-}\alpha/2)$ is the point on the standard normal density curve such that the probability of observing a value greater than z is equal to $\alpha/2$ (see Figure 2.24).

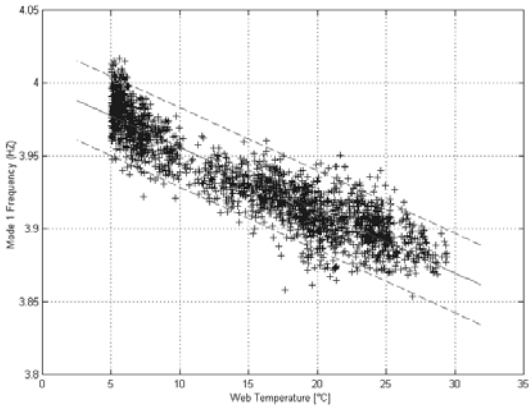


Figure 2.24 – Linear regression for the Z24 Bridge (temperature values between 5 and 30ºC) with confidence intervals (Peeters, 2000).

To increase the model efficiency, it is possible to adopt polynomial or non-linear regressions, but models such as the ones considered here, also called static models, have the disadvantage to be unable to take into account the thermal inertia of the structure, which is an important property in the dynamic response. An alternative is to use autoregressive models or dynamic models.

2.4.2 ARX Models

One simple dynamic model that can be used is the AutoRegressive output with an eXogeneous input part, also called ARX model (Ljung, 1999). In this model the response $\boldsymbol{y}$ (e.g. resonant frequencies) in the instant k does depend not only in the input $\boldsymbol{u}^{env}$ (e.g. temperature) for the same instant, but also on the evolution of the previous inputs and outputs (thermal inertia modelling). The estimated response can be given by:

$$\hat{y}_k + a_1 y_{k-1} + ... + a_{na} y_{k-na} = b_1 u^{env}_{k-nk} + b_2 u^{env}_{k-nk-1} + ... + b_{nb} u^{env}_{k-nk-nb+1} + e_k \tag{2.77}$$

where a_i and b_i are coefficients for the autoregressive and exogeneous part, respectively, na is the autoregressive order, nb the exogeneous order, nk is the number of delays from input to output, and e_k is the unknown residuals that can be assumed Gaussian, see Eq.(2.75). To simplify, Eq.(2.77) can be recast by using a shift operator $q^{-1}y_k = y_{k-1}$:

$$A_q \hat{y}_k = B_q u^{env}_{k-nk} + e_k \tag{2.78}$$

with the operator polynomials A_q and B_q given by:

$$\begin{aligned} A_q &= 1 + a_1 q^{-1} + ... + a_{na} q^{-na} \\ B_q &= b_1 + b_2 q^{-1} + ... + b_{nb} q^{-nb+1} \end{aligned} \tag{2.79}$$

It is common to refer to a ARX model by the orders na and nb, the delay nk, being the model characterized by these three parameters (e.g. ARX[1,2,3]).

Peeters (2000) presented a procedure to model the environmental effects and detect the presence of damage based on an ARX model. The procedure is briefly presented here and includes:

1. The normalization of the inputs and outputs:

$$u^{env}_k = \frac{u^{env,m}_k - \overline{u}}{\sigma_u} \quad \text{and} \quad y_k = \frac{y^m_k - \overline{y}}{\sigma_y} \tag{2.80}$$

where $u_k^{env,m}$ and y_k^m are the measuring values, $\bar{u}$ and $\bar{y}$ are the average values and σ_u and σ_y are the standard deviations;

2. The estimation of several ARX models (e.g. ARX[0,1,0], ARX[2,1,0], ARX[3,1,0], etc.) and their statistical properties;
3. The selection of the "best" model based on quality criteria, like the loss function *V* or the Akaike's Final Prediction Error (*FPE*), see Ljung (1999), given by:

$$V = \frac{1}{N}\sum_{k=1}^{N} e_k^2 \quad \text{and} \quad FPE = V\frac{1+d/N}{1-d/N} \tag{2.81}$$

where *d* is the number of estimated parameters;

4. The simulation of the expected response with the previous selected model;
5. The calculation of simulation error and its statistics;

$$\hat{e}_k = y_k - \hat{y}_k \quad \text{and} \quad \hat{R}_{xy} \tag{2.82}$$

6. The establishing of confidence intervals *ci* and detect the outliers:

$$\left[\hat{y}_k - z(1-\alpha/2)\sqrt{\hat{R}_{xy}} \quad , \quad \hat{y}_k + z(1-\alpha/2)\sqrt{\hat{R}_{xy}}\right] \tag{2.83}$$

Once the prediction is completed, the detection of damage should be carried out by observing frequency shifts that significantly go out of the confident intervals *ci*.

2.5 Conclusions

In this chapter a state of the art about system identification based on vibration signatures was presented. Addressed issues include the basic dynamics, system identification with input-output and output-only techniques, experimental modal testing and environmental effects in the dynamic response of civil engineering structures.

To estimate modal parameters, output-only modal analysis seems to be one of the best techniques and with large applicability to all structure types. One of the most accurate methods is based on the stochastic subspace identification techniques, a time-domain method where the State-Space Formulation is used.

Output-only techniques requires that excitations are reasonably random in time and in the physical space of the structures (or if it is local it can gives sufficient energy to excite the all structure). Even for masonry structures, the robust results obtained, together with simplicity, the low cost and reduced interference with operating conditions make this technique an attractive tool. One disadvantage is the fact that mode shapes are not scaled to the structure mass matrix.

Other important issues related to the system identification are the selection of transducers to measure the dynamic response (e.g. accelerations, strains), the data acquisition system to digitalize and store the signals (response), and adequate test procedures (test planning). With respect to test equipment, the developments on MEMS technology and Wireless Sensors Networks (WSN) are significant, allowing to estimate and to monitor the structural behaviour, in particular, of complex masonry structures that require a large number of sensors. At the moment, few applications are found in the literature with respect to structural monitoring of monuments with MEMS sensors and WSN.

In real case studies and before any attempt to identify the presence of damage, it is important to evaluate and to separate the environmental and the loading effects from the dynamic response of the structures. It is important to “model” these effects because they can change the modal parameters in the same order of magnitude of possible (small) damages. In the case of masonry structures, temperature seems to be the most important environmental effect, but changes in mass and stiffness due to moisture absorption need to be considered in the future.

Chapter 3
Dynamic Based Damage Identification

Abstract

This chapter presents a state of the art about dynamic based damage identification in structural systems. The main goal is to review the developments made by researchers during the past. Issues addressed are historical context of the applicability of damage methods, general methods classification, and a review of a selected group of methods. Finally, the underlying hypotheses are discussed, concerning the applicability of the existent damage identification methods to masonry-like structures.

3.1 Introduction

It is known that service loads, environmental and accidental actions may cause damage to structural systems. With respect to this issue, long life maintenance plays an important roll. Regular inspections and condition assessment of engineering structures allow programmed repair works and cost-effective management of the infrastructures. In historical constructions, maintenance is also essential because of their cultural importance, the safety of visitors, the potential seismic risk and the accumulation of physical, chemical and mechanical damage through the time.

Alterations of geometrical dimensions, boundary conditions and mass, and the degradation of the mechanical properties of materials, including physical damage, or the simultaneously occurrence of all these phenomena, affect the dynamic behaviour of the structures, see Doebling et al. (1996). If the environmental influence is evaluated and separated from the dynamic response of the structure, the damage occurrence can be globally detected. After detection, the next task is to localize the damage and its extension with more detail. Finally, its consequences for the construction should be evaluated.

As far as masonry constructions are concerned, there are very few references in literature dedicated to damage identification based on vibration signatures. The first attempt of Ramos et al. (2005) to establish a relation between the damage progress and the dynamic response of a masonry building was done on a real scale rubble stone masonry structure (see Figure 3.1), built in the "Laboratório Nacional de Engenharia Civil" (LNEC), in Lisbon. This structure was tested in the LNEC shaking table, under the European Union Research Project within the 5th EU framework program, ECOLEADER – Enhancing Seismic Resistance and Durability of Natural Stone Masonry (Sofronie, 2004).

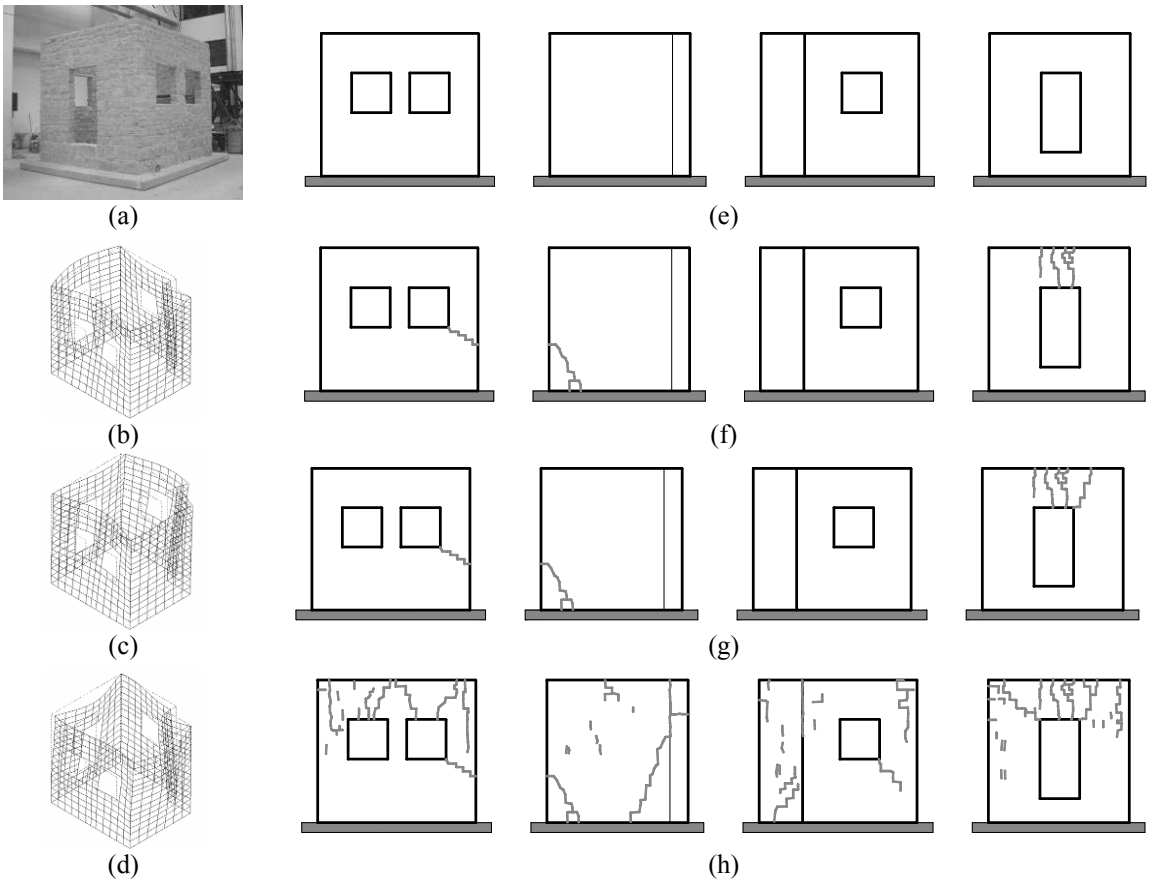


Figure 3.1 – Masonry mock-up: (a) general view; (b), (c) and (d) the first 3 mode shapes; (e) reference and damage scenario A; (f) damage scenario B; (g) damage scenario C; and (h) damage scenario D.

Progressive Damage Scenarios (DS) were induced in the shaking tests, and at each DS, a modal identification was performed with operational modal analysis techniques for comparison with the virgin state of the structure, or the Reference Scenario (RS). The results of this study are presented elsewhere (Ramos et al., 2005). The natural frequencies decreased significantly during the several DS, see Table 3.1, but the relation between the dynamic response and the crack pattern was difficult to analyze.

Table 3.1 – Resonant frequencies for the several damage scenarios [Hz].

Mode Shape	RS	DS_A	DS_B	DS_C	DS_D
1st	15.05	12.28	10.60	7.55	4.62
2nd	19.79	13.97	12.29	9.60	6.13
3rd	20.50	18.30	16.63	12.96	8.71
4th	26.57	21.27	17.60	13.83	12.80
5th	28.91	25.94	19.56	17.58	13.61
6th	36.85	32.87	28.06	23.82	15.40
7th	39.73	33.69	32.06	28.99	21.64

Therefore, it was decided to study simple models and two masonry replicates were built in the Structural Laboratory of University of Minho: one arch and one wall. The replicates were built to better understand the correlation between progressive damage in the structure and the changes in the dynamic response. These analyses will be presented later.

Next, a historical context, a general classification for the methods, a discussion of a selected group of methods, a review of strategies for health monitoring and a reflection on the state of the art are presented.

3.2 Historical Overview

In this field, it is important to stress the work of Doebling et al. (1996), a reference study that summarizes the main works carried out during the last three decades, especially related to civil engineering constructions.

The civil engineering community started to use the dynamic based techniques for damage identification since the earlier 1980's. Bridge assessment for health monitoring was a first motive of interest, but quickly spread to other constructions. In literature, several applications on beam structures (steel and concrete), trusses, plates, shells and frames, bridges, buildings and composite materials can be found.

There are few references in the literature where damage identification based on dynamic response is applied to masonry structures, but in the process of preservation of ancient masonry structures, damage evaluation and monitoring procedures are particularly attractive, due to the modern context of minimum repair and observational methods, with iterative and step-by-step approaches. High-priority issues related to damage assessment and monitoring are global non-contact inspection techniques, improved sensor technology, data management, diagnostics (decision making and simulation), improved global modal dynamic analysis, self-diagnosing / self-healing materials, and improved prediction of early degradation. In this context, vibration based damage identification techniques play an essential roll.

3.3 General Methods Classification

The present work tries to deal with the problem of damage identification by using Global and Local damage identification techniques, which is, indeed, the first possible general classification for the identification methods.

Regarding that classification, is possible to have two categories of methods: (a) the dynamic based damage detection methods, defined as Global methods, because they do not give sufficiently accurate information about the extent of the damage, but they can alert about its presence and define the precise location of it (Chang et al., 2003); and (b) the methods based on visual inspections and experimental tests of acoustic or ultrasonic methods, magnetic field methods, radiograph, eddy-current methods, thermal field methods or others (Doherty, 1987), also called as Local methods. The Local methods need another approach to detect the presence of damage and need that the portion of structure to be inspected is accessible.

From another perspective, to study more carefully the damage identification problem, Worden and Dulieu-Barton (2004) underlined the importance of using exact taxonomy for the precise definition of what constitutes a fault, a damage and a defect in a structure. The authors proposed the following definitions:

- Fault is a state when the structure can no longer operate satisfactorily, caused by an unacceptable reduction in the quality for user requirements;

- Damage is when the structure is no longer operating in its ideal condition, but can still function satisfactorily;
- Defect is inherent in the material and statistically all materials have some unknown amount of defects. This means that the structure can operate in its ideal condition even if the materials contain defects.

The definition above allows a hierarchical relationship: defects can lead to damage and damage leads to fault. This relationship can be used to establish a state when the presence of several damage scenarios means that the structures can no longer operate in a satisfactory manner.

The next step of the methodology for damage identification is to define a classification for the methods and actions used in the process of monitoring and assessing damage. The first classification was presented by Rytter (1993), where four levels of damage assessment were established:

- Detection (Level 1): the method gives a qualitative indication that damage might be present in the structure;
- Localization (Level 2): the method gives information about the probable position of the damage;
- Assessment (Level 3): the method gives an estimate of extent of the damage;
- Prediction (Level 4): the method offers information about the safety of the structure, estimating the residual operating life.

Each level is connected in a hierarchical way, because to pass to the next level it is necessary to know the previous one. It is also stressed that the term damage identification is the conjunction of one or more of the presented levels.

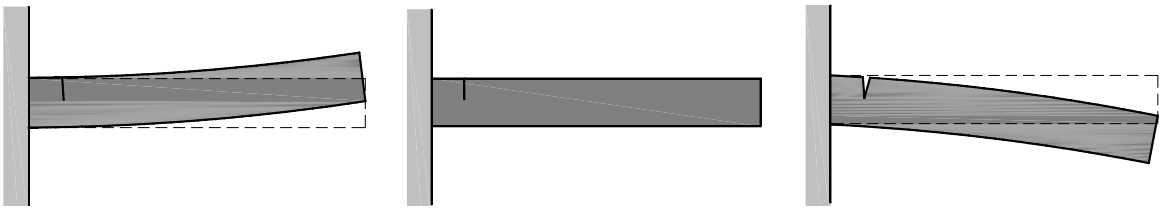
More recently, Worden and Dulieu-Barton (2004) presented a classification where one intermediate level is proposed, leading to a new level 3 and shifting levels 3 and 4 above:

- Classification (new Level 3): the method gives information about the type of damage.

The introduction of the third level seems vital for effective identification of "Prediction" and possibly for "Assessment", since information about the characteristics of damage is necessary to predict the residual operating life time of the structure. Also, all the first four levels need structural observation while the last one can be estimated by numerical analysis. For convenience, the first classification (with four levels) will be used next.

In the literature of vibration based damage identification methods it is common to assume that damage is directly related to a decrease of stiffness and not to any change of mass.

The global vibration methods can be divided in Linear or Nonlinear depending on which type of behavior is assumed after the damage occurrence. If during the dynamic test the crack is assumed to remain open, the response is linear and the method is classified as Linear. In this last classification, the damage can be only associated with changes in boundary conditions, material properties (loss of stiffness) or changes in geometry. On the contrary, the Nonlinear methods take into account the changing stiffness according with the oscillating amplitudes for the simulation of the crack breathing, i.e. when the crack is closed there is a restoration of the original stiffness, see Figure 3.2.



(a) (b) (c)

Figure 3.2 – Crack breathing of a cantilever beam: (a) crack closed with initial stiffness; (b) transitory stage; and (c) crack open with minimum stiffness.

References to Linear methods are often found in the literature. They can also be divided as Model Based or Non-model Based methods, depending whether or not they use numerical models for the damage identification. Model based methods assume that the monitored structure responds in some predetermined manner such as the response described by the Euler-Bernoulli beam theory.

Figure 3.3 presents a few linear methods organized according to the above classification, with the level damage identification, the required data, and if it is required or not a reference scenario. These aspects will be described next, where a selected group of methods will further detailed.

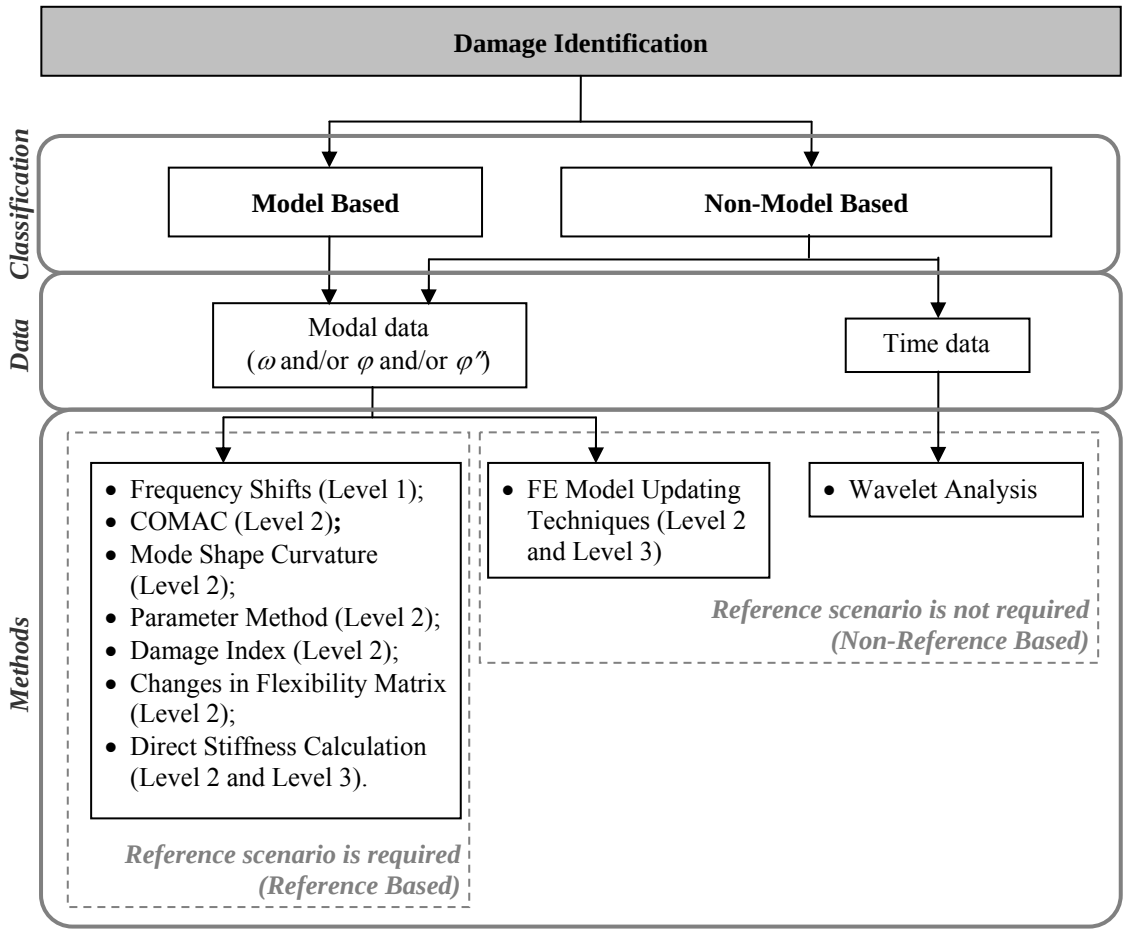


Figure 3.3 – General overview of the damage identification methods.

In the present work it is assumed that the modal identification can be accurately performed with linear modal analyses at very low ambient excitation level, even with the presence of damage. This means that crack breathing effects are negligible.

3.4 Review of Selected Methods

At the moment, there is no single method which gives accurate resulst through all presented levels of damage identification and for all types of structural systems. This is still a challenge for the next decades (Farrar and Doebling, 1998; and Choi et al., 2005). The presentation of all possible methods would be an exhausting task and review papers exists (Doebling et al., 1996; Doebling et al., 1998; Salawu, 1997; Hemez and Doebling, 2001; Chang et al. 2003; and Montalvão et al., 2006). Here, only the most significant dynamic based damage identification methods related to civil engineering structures are addressed. For a more clear presentation, the methods were divided in the following groups:

1. Non-Model Based Methods:
    a) Methods based on wavelet analysis (Non-Reference Based);
    b) Methods based on changes of modal parameters (Reference Based);
    c) Methods based on changes in derivates of modal parameters (Reference Based);
2. Finite Element Model Updating Method (Non-Reference Based).

3.4.1 Non-Model Based Methods

3.4.1.1 Methods Based on Wavelets Analysis

Wavelet analysis methods have become popular because they do not require differentiation of the measured data and it is possible to detect damage only with the existing (damaged) information. These methods are considered as an improvement of Fourier Transform, because they have the ability to analyze the measured data with variable size windows, making possible detection of small singularities that can exist due to damage.

Wavelets are defined as functions that contain waves which drop to zero after some oscillations and have one independent variable. A function with these characteristics is called a "mother wavelet". Different sets are generated from this mother wavelet translated by b and dilated by a, represented as $\chi_{a,b}$. The main idea of this analysis is based on a Continuous Wavelet Transform (*CWT*), which is the integral over time of the wavelet convolution:

$$CWT(a,b) = \frac{1}{\sqrt{a}} \int_{-\infty}^{+\infty} x(t)\, \chi\left(\frac{t-b}{a}\right) dt \;=\; \int_{-\infty}^{+\infty} x(t)\, \chi_{a,b}\; dt \tag{3.1}$$

The results of this transformation are called wavelet coefficients and they show how the function correlates with the signal. It has been found that damage due to a sudden loss of stiffness and the moment of time when it occurs, creates wavelet coefficients with large amplitudes like a spike or an impulse. This procedure is the base of the Wavelet Analysis damage detection.

Wavelet functions are composed of a family of basis functions that are capable of describing a signal in a localized time (or space) and frequency (or scale) domain

(Daubechies, 1992). The main advantage gained by using wavelets is the ability to perform local analysis of a signal, i.e., zooming on any interval of time or space. Wavelet analysis is thus capable of revealing hidden aspects of the data that other signal analysis techniques fail to detect. This property is particularly important for damage detection applications. Many researchers (Wang and McFadden, 1996; Kitada, 1998; Wang and Deng, 1999; Hou et al., 2000; and Ovanesova and Suárez, 2004) presented applications of wavelet transform to detect cracks in frame structures. One possible drawback is that the frequency resolution is quite poor in the higher frequency region. Hence, the method still faces difficulties when discriminating the signals containing close high frequency components.

The Wavelet Packet Decomposition (WPD) is a generalization of the wavelet transform, defined as the linear decomposition of the evaluated function. In WPD the signal is decomposed in approximations and details, these two results are themselves decomposed into another level of decomposition. Then this process is repeated until the required level of accuracy is achieved. Wavelet packets consist of a set of linearly combined wavelet functions. The wavelet packets inherit the properties such as orthonormality and time-frequency localization from their corresponding wavelet functions. A wavelet packet $\chi^i_{j,k}(t)$ is a function with three indices where integers i, j and k are the modulation, dilation and translation parameters, respectively.

At the lower levels of the WPD tree (see Figure 3.4) the results lead to good resolution in time domain but poor resolution in frequency domain. At the higher levels of the tree, the opposite happens and one can detect minor changes in the signals calculating as the higher frequency changes are highlighted.

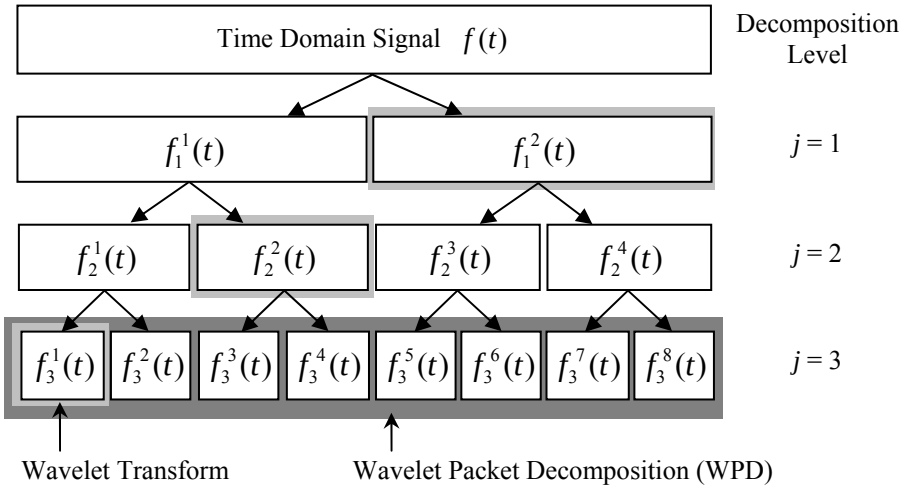


Figure 3.4 – Wavelet packet decomposition over three levels.

The Wavelet Packet Signature (WPS) method, proposed by Chang and Sun (2005), obtains the entropy energy E of the dynamic response at measured points and calculated the spatial WPS by the second derivative of the entropy energy along the structure. The component energies are calculated as follows:

$$E_j^i = \int_{-\infty}^{+\infty} x_j^i(t)^2 dt \tag{3.2}$$

After extracting the WPS from the response measured at various locations, the spatial distribution curvature of the WPS is used for locating damage. Chang and Sun (2005) concluded for a numerical simply supported beam that, according to the difference of the spatial WPS distribution curvature, the damage position could be accurately located and

qualitatively assessed. The advantages of the proposed method are that it does not require an accurate analytical model of the structure, and does not require comparing two different scenarios.

Chang and Sun (2005) also proposed damage indices that are based on wavelet packet analysis. The damage index is calculated from the extraction of the larger energy component E^i_j from two damage scenarios, through either the Sum of Absolute Differences (*SAD*):

$$SAD = \sum_{i=1}^{N} \left| E^i_{j,d} - E^i_{j,u} \right| \tag{3.3}$$

or the Square Sum Differences (*SSD*):

$$SSD = \sum_{i=1}^{N} \left(E^i_{j,d} - E^i_{j,u} \right)^2 \tag{3.4}$$

For further reading on wavelet analysis, the reader is referred to Zabel (2003).

3.4.1.2 Methods Based on Direct Changes of Modal Parameters

The study of damage identification based on vibration signatures started with the observations of shifts in the resonant frequency values. Accurate estimation of these values is crucial for the success of the method. It was found that large civil structures had low sensitivity to changes in the structural configuration, unless the changes were large, because resonant frequencies represents condensed information about the response and also a global property of the structures.

Cawley and Adams (1979) proposed a method based on the calculation of the ratio between frequencies for modes *i* and *j*, $\delta\omega_i/\delta\omega_j$. A grid of possible damage is considered and an error term is defined to correlate the estimated frequencies with the model based predicted frequencies. In the numerical model, the damage is simulated by a local stiffness reduction and a number of mode pairs are considered for each potential damage location. The mode pair that gives the lowest error indicates the location of the damage. One disadvantage of this formulation is that it cannot be applied in cases of multi-damage scenarios.

Later, Brincker et al. (1995), proposed a statistical analysis method to detect damage by frequencies shifts. By estimating the undamaged and the damage condition of the structure for five selected instants of time, the authors define a significance indicator for the j^{th} resonant frequency as:

$$\left(S_f\right)_j = \frac{\omega^u_j - \omega^d_j}{\sqrt{\left(\sigma^u_\omega\right)^2_j + \left(\sigma^d_\omega\right)^2_j}} \tag{3.5}$$

where σ_ω is the estimated standard deviation (resulted from the five system identification tests) of the j^{th} resonant frequency and the super scripts *u* and *d* indicates the undamaged and the damage state, respectively. With this shift scaling, the measured frequencies with higher confidence (low standard deviation) are weighted more heavily in the indicator function. A similar significance indicator is also defined for the estimated damping ratio. The authors define a "Unified Significance Indicator" (USI) by summing the frequency and damping significance indicators over several measured modes. The significance

indicator proved to be a sensitive indicator of structural damage (Level 1), but it is not capable of providing an estimate of damage location (Level 2). The authors state that knowledge of the input signal is not essential for the detection of damage using this technique, which makes output-only modal identification techniques applicable for this method.

Other researchers found significant difficulties when using only the frequency shifts. In fact, damage is a local phenomenon and may not influence significantly the lower frequencies or the global response. If a member is not strained in the global modes, then the damage on that member has no effect on the global resonant frequencies (Chang et al., 2003).

A possible enhancement consists of analysing not only shifts in resonant frequencies but also in the mode shape vectors. Mode shape vectors are spatially distributed quantities and they provide information that can be used to identify damage. In order to have accurate results with these quantities, Farrar and Doebling (1998) stress from the fact that a large number of measurement locations can be required to accurately characterize the mode shapes and to provide sufficient resolution for the damage identification methods.

When results are available from two scenarios, e.g. undamaged and damaged stage, the most well known procedure to study the numerical correlation between two sets of mode shape vectors is to use the Modal Assurance Criteria (MAC) value, given by:

$$MAC_{u,d} = \frac{\left| \sum_{i=1}^{n} \varphi_i^u \, \varphi_i^d \right|^2}{\sum_{i=1}^{n} \left(\varphi_i^u\right)^2 \sum_{i=1}^{n} \left(\varphi_i^d\right)^2} \tag{3.6}$$

where φ^{u} and φ^{d} are the mode shape vectors for the two different stage conditions and n indicates the number of estimated degrees of freedom. The expression leads to a scalar value between zero and one, associated with low and high correlation between the two vectors. The disavantage of using this indicator is the fact that MAC values are global quantities and they are not sensitive to low damage in the structure.

The Normalised Modal Difference (NMD) value is more sensitive to the differences between the shape vectors (Gentile et al., 2001). After the MACs calculation, the NMD can be calculated as:

$$NMD_{u,d} = \sqrt{\frac{1 - MAC_{u,d}}{MAC_{u,d}}} \tag{3.7}$$

A MAC value of 0.99 corresponds to a NMD value of 10%, which means that on average the differences between two modes shapes vectors is about 10%. A MAC of 0.5 corresponds to a NMD equal to 100%. In practice, one might consider that a NMD value less that 33% (MAC value greater than 0.90) between to modes is an indicator of a good correlation between the two modes.

When searching for local information, the Co-ordinate Modal Assurance Criterion (COMAC) can be used for each measuring point i, by the following:

$$COMAC_{i,u,d} = \frac{\left| \sum_{j=1}^{m} \varphi_{i,j}^{u} \; \varphi_{i,j}^{d} \right|^2}{\sum_{j=1}^{m} \left(\varphi_{i,j}^{u}\right)^2 \sum_{j=1}^{m} \left(\varphi_{,ji}^{d}\right)^2} \tag{3.8}$$

where m is the number of estimated mode shapes. If the COMAC value of the measuring point i is closed to one, it means that in the given location the modals displacements are identical.

In the work of Ewins (2000), several techniques based on MAC and COMAC calculations are presented to compare the numerically predicted and experimentally estimated dynamic responses, such as the frequency-scaled MAC plot.

Dong et al. (1994) propose a combination of frequency and mode shape changes through a Parameter based Method (PM) given by following expression:

$$\Delta\varphi = \sum_{j=1}^{m} \left[\varphi_j^d \left(\frac{\omega_j^u}{\omega_j^d} \right) - \varphi_j^u \right] \tag{3.9}$$

Another basic dynamic parameter is the damping coefficient, perhaps the less used parameter for damage identification, but the one that need attention in its study. It is known that the presence of damage alters the energy dissipation mechanism in the structure and, as a consequence, the damping coefficient increases. The major problem is damping estimation, as damping is related to nonlinear phenomena. Another difficulty is the fact that damping is sensitive to the level of structural vibration, see Ndambi et al. (2000). Nevertheless, some researchers are still improving techniques to estimate and to use this parameter in the damage identification problem. Zonta (2000) combined successfully two formulations, viscous and friction behaviour, to model damping and to identify damage. Casas and Aparicio (1994) concluded that there was no clear relation between crack growth and damping increasing. Salawu and Williams (1995) compared the damping parameter before and after strengthening of a concrete bridge and no clear relation could also be established between structural improvement and damping coefficients.

3.4.1.3 Methods Based on Changes in Derivates of Modal Parameters

The quantities derived from the mode shapes (e.g. the mode shape curvature or strain mode shape) and their combination with mode shapes give spatially disturbed and sensitive information about structural differences. These methods are based on the fact that the second derivate of the mode shape vector is more sensitive to structural changes than the modes shapes, and especially to localized phenomena.

For beam and plate-like structures, the mode shape curvature can be related to the strain energy. The curvature and the bending strain at position h from the neutral section axes are related by:

$$\varepsilon = \frac{h}{R} = \kappa h \tag{3.10}$$

where ε is the strain, R is the radius curvature and κ is the curvature equal to $1/R$. The strain can be directly measured, or the mode shape curvature can be calculated from the modal displacements using a numerically central difference theorem, as:

$$\kappa_i = \varphi_i'' \approx \frac{\varphi_{i+1} - 2\varphi_i + \varphi_{i-1}}{(\Delta L)^2}, \tag{3.11}$$

where ΔL is the distance between the points i and $i + 1$.

Pandey et al. (1991) demonstrated that local changes in the beam stiffness are clearly observed by absolute changes in the mode shape curvatures, calculated as the difference between damaged and undamaged stage with the same scale, as follows:

$$\Delta\varphi'' = \sum_{j=1}^{m} \left| \varphi_{d,j}'' - \varphi_{u,j}'' \right| \tag{3.12}$$

This method is the well known Mode Shape Curvature Method (MSCM).

Stubbs et al. (1992) proposed the Damage Index Method (DIM) for beam like structures, based on the decrease in modal strain energy between two degrees of freedom. The damage index $\beta_{i,j}$ is calculated based on the changes in the curvature of the j^{th} mode at location i, and is defined as:

$$\beta_{i,j} = \frac{\left[\int_a^b \left(\varphi_j^{d\,''}(x)\right)^2 dx + \int_0^L \left(\varphi_j^{d\,''}(x)\right)^2 dx\right]}{\left[\int_a^b \left(\varphi_j^{u\,''}(x)\right)^2 dx + \int_0^L \left(\varphi_j^{u\,''}(x)\right)^2 dx\right]} \cdot \frac{\int_0^L \left(\varphi_j^{u\,''}(x)\right) dx}{\int_0^L \left(\varphi_j^{d\,''}(x)\right) dx} \tag{3.13}$$

where $\varphi_j^{u"}(x)$ and $\varphi_j^{d"}(x)$ are the second derivates of the j^{th} mode shape in the undamaged and damaged condition, respectively, L is the length of the structure, and a and b are the locations i and $i + 1$, respectively, which define the limits of a segment where the damage is evaluated in the structure. In this formulation, as the measured mode shapes are only available in a selected number of points, continuous functions of the mode shapes are evaluated by fitting the modal displacements with a cubic polynomial function in the length L. If all m estimated modes are used for the damage identification, the damage index β of a segment i can be defined as:

$$\beta_i = \sum_{j=1}^{m} \beta_{i,j}, \tag{3.14}$$

Finally, the possible damage locations are estimated through the normalized damage index Z_i, assuming that β_i represents a sample population of a normally distributed random variable. The normalized damage index is given by:

$$Z_i = \left(\beta_i - \overline{\beta}_i\right) / \sigma_i, \tag{3.15}$$

where $\overline{\beta}_i$ and σ_i are the mean and standard deviation of the damage indices, respectively. Normalized values greater than two are considered as potential damage segments, Stubbs et al. (1992).

Later, Cornwell et al. (1999) generalized the DIM for plate like structures where the damage index for the sub-region i, k calculated for the j^{th} mode shape is now given by:

$$\beta_{i,k} = \frac{f_{i,k,j}^{d}}{f_{i,k,j}^{u}}, \tag{3.16}$$

where

$$f_{i,k,j}^{d} = \frac{\int_{b_k}^{b_{k+1}} \int_{a_i}^{a_{i+1}} \left(\left(\frac{\partial^2 \varphi_j^d}{\partial x^2} \right)^2 + \left(\frac{\partial^2 \varphi_j^d}{\partial y^2} \right)^2 + 2\nu \left(\frac{\partial^2 \varphi_j^d}{\partial x^2} \right) \left(\frac{\partial^2 \varphi_j^d}{\partial y^2} \right) + 2(1-\nu) \left(\frac{\partial^2 \varphi_j^d}{\partial x \partial x} \right) dx\, dy}{\int_0^b \int_0^a \left(\left(\frac{\partial^2 \varphi_j^d}{\partial x^2} \right)^2 + \left(\frac{\partial^2 \varphi_j^d}{\partial y^2} \right)^2 + 2\nu \left(\frac{\partial^2 \varphi_j^d}{\partial x^2} \right) \left(\frac{\partial^2 \varphi_j^d}{\partial y^2} \right) + 2(1-\nu) \left(\frac{\partial^2 \varphi_j^d}{\partial x \partial x} \right) dx\, dy}, \qquad (3.17)$$

and the analogous term $f^{u}_{i,k,j}$ can be determined with the undamaged mode shapes. Afterwards, Eq.(3.14) and Eq.(3.15) can be used to locate the damage.

One advantage of using the MSCM or the DIM is that mass normalized mode shape vectors are not required. Output-only modal identification techniques can be used to estimate the vectors before and after the damage. One disadvantage is the difficulty in the accurate determination of modal curvature from the experimental modal parameters.

In other to address this problem, Maeck (2003) proposed a Mixed Approach for the calculation of mode shapes curvatures, using smoothing for mode shapes and its derivates, where the measurement noise is filtered through appropriate penalty factors α and β. The penalty factors are calculated form the minimization of an objective function π given by:

$$\pi = \int \frac{\left(v - \varphi_{\exp}\right)^2}{2} dx + \frac{\alpha L^2}{2} \int \left(\psi - \frac{dv}{dx} \right)^2 dx + \frac{\beta L^4}{2} \int \left(\kappa - \frac{d\psi}{dx} \right)^2 dx \qquad (3.18)$$

where, v and $\varphi_{\exp}$ are the calculated and measured modal displacements, ψ are the calculated modal rotations, and κ are the calculated modal curvatures and L is the element length. The results of this technique are promising compared with alternative techniques, like the central difference theorem, b-splines or moving polynomials, and exhibit better performance for the lower modes.

Maeck (2003) also used the preceding modal curvature approach in a Direct Stiffness Calculation Method (DSCM) for damage localization in beam-like structures. The method only uses the estimated resonant frequencies and mode shapes to detect any decrease of the bending and torsional stiffness along the beam, assuming the Bernoulli Hypothesis. The bending and torsional stiffness are derived from the estimated mode shape vectors through the mixed approach. The mass is assumed to be known and the damage is only related to a loss of stiffness. A numerical model is not needed in this method, because the bending and torsional stiffness are calculated by the basic relations between bending stiffness EI and modal bending moment M^m, and torsion stiffness GJ with the modal torsion moment T^m, given by:

$$EI = \frac{M^m}{\partial^2 \varphi^b / dx^2} \text{ and } GJ = \frac{T^m}{\partial \varphi^t / dx} \qquad (3.19)$$

The method provided accurate results for the Level 2 (localization), in the presence of good quality experimental mode shapes, and a rather dense net of measuring points. An approach to calculate the curvatures through fibre optics sensors or strain gauges sensors distributed along the structure, was also addressed, Maeck (2003).

The last group of methods based on derivates of the basic modal parameters uses the dynamically measured flexibility matrix to estimate changes in the stiffness of the structure, here defined as Changes in Flexibility Matrix method (CFM). By definition, flexibility matrix is composed by a set of columns representing the nodal displacement when a unitary static force is applied in one degree of freedom. The flexibility matrix $\boldsymbol{F}$

can be calculated by the inverse of the stiffness matrix or, alternatively, through the estimated mass-normalized mode shapes ϕ_j and resonant frequencies ω_j, given by following:

$$\boldsymbol{F} = \Gamma_m \, \Omega_m^{-1} \, \Gamma_m{}^T = \sum_{j=1}^{m} \frac{1}{\omega_j^2} \, \boldsymbol{\phi}_j \, \boldsymbol{\phi}_j^T \tag{3.20}$$

where Ω_m is the diagonal modal stiffness matrix composed by the square of the resonant frequencies and Γ_m is the mass-normalized mode shape matrix. In practice, this formulation is approximated because only the estimated mode shapes are used, which means $\boldsymbol{F}$ is a synthesized flexibility matrix of the structure. One advantage of the method is the dependence of the inverse of the square of modal frequencies. This results in a sensitive behavior to changes of the modes in a lower frequency range, which are, in practice, the ones that can be estimated, especially by output-only methods. Finally, the damage is located by the damage index vector β given by diagonal terms of the difference between the synthesized flexibility matrices of the damaged and undamaged structure or, alternatively, of the difference from the flexibility matrix derived from a numerical model. The damage index vector is obtained as

$$\beta = diag\left\{ \boldsymbol{F}^{\boldsymbol{d}} - \boldsymbol{F}^{\boldsymbol{u}} \right\} \tag{3.21}$$

Zhang and Aktan (1995) stated that as the sum of all columns in the flexibility matrix represents the deformed shape of the structure under a unitary uniform load, one could use this sum to locate the damage by the application of other methods, like the MSCM.

Pandey and Biwas (1994) tested the method numerically on a beam specimen and concluded that damage localization (Level 2) could be obtained from just the two first estimated mode shapes. Other researchers successfully used this method to locate damage but stressed the difficulty of estimating higher mode shapes in an accurate manner. Another disadvantage is the need of mass-normalized mode shapes ϕ, which requires the knowledge of the excitation force during the modal identification tests.

3.4.2 Finite Element Modal Updating Method

The final approach addressed here is to update the modal parameters based on optimization processes to minimize the residuals between the experimental response and the mathematical response (model based and inverse methods). In simple terms, these methods update the mass, stiffness and damping matrices related to the damaged stage and compare there elements with the analogous elements from matrices of the undamaged stage.

Stubbs et al. (1990) and Stubbs and Osegueda (1990a, 1990b) studied the sensitivity relation between the changes in the stiffness members to changes in the resonant frequencies. A sensitive matrix for the resonant frequencies was constructed numerically and was compared with the estimated frequencies, which allowed the location and magnitude of damage. Nevertheless, the sensitivity method leads to an ill-conditioned problem if the number of modes is much lower than the number of damage parameters.

A wide number of model based methods with a set of common basic equations and different algorithms procedures are presented by Doebling et al. (1996), and taking into account three different aspects: the objective function π to be minimized, the problem constraints and the optimization process. The problems in this class of methods are: (a) the initial structural matrices which incorporate errors; (b) the optimization solution,

which is not unique; and (c) the error minimization process, which often changes the stiffness terms that are not damaged, resulting in a distorted solution (Chang et al., 2003).

Damage identification by means of FE model updating (FEMU), see Figure 3.5, has the advantage of being a general approach. Unlike many other damage identification methods, often developed for specific modal quantities, the algorithm can be applied to any modal feature that is sensitive to damage, such as eigen frequencies, mode shape displacements, modal curvatures, modal strain energy, etc., and their combinations. On the other hand, the technique requires a reliable and adequate FE model that represents reasonably well the real structure. In this field, the work of Friswell and Mottershead (1995) is highlighted.

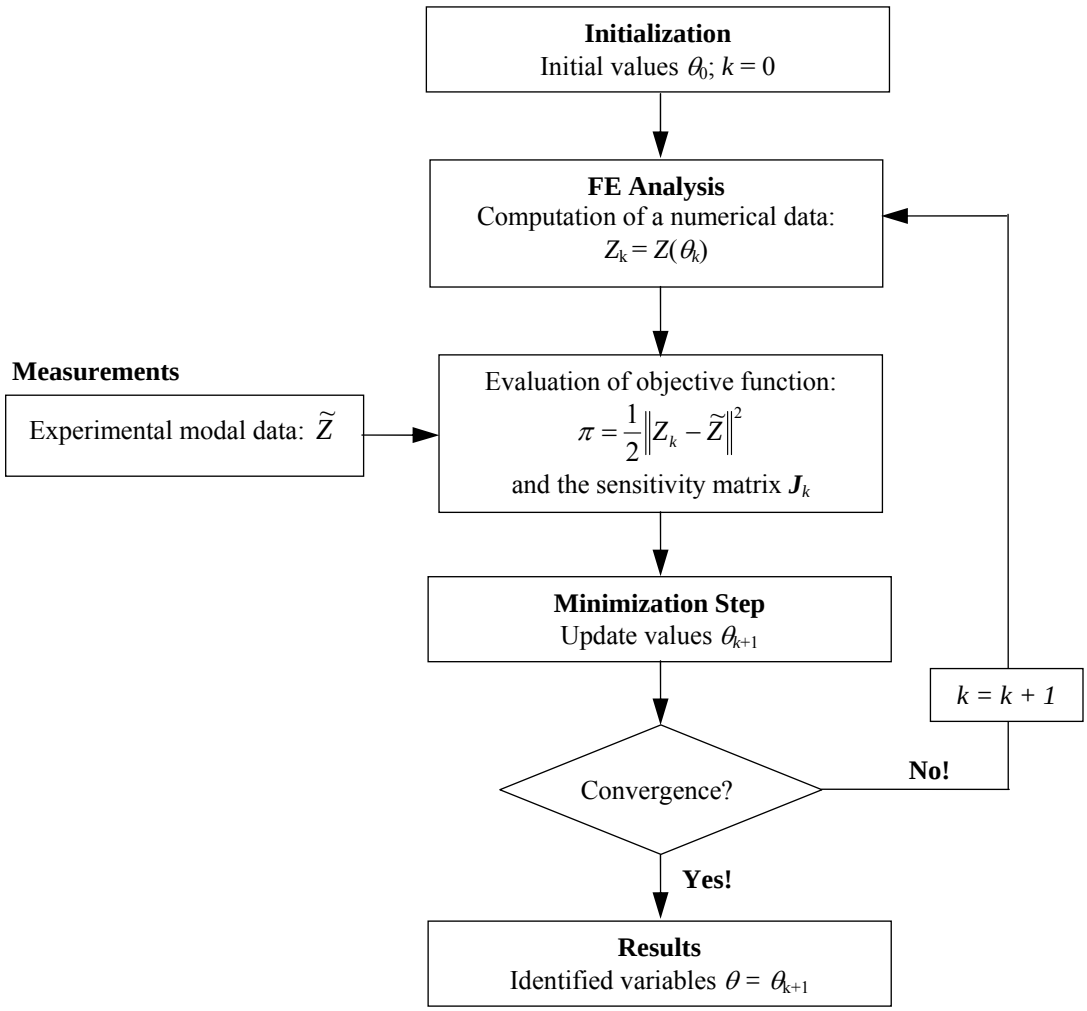


Figure 3.5 – Flowchart of the FE model updating procedure (Teughels, 2004).

3.4.2.1 Objective Function

Generally speaking, the objective function π is stated as a non-linear least square problem by

$$\pi(\theta) = \frac{1}{2}\| r(\theta) \|^2 \tag{3.22}$$

were θ are the updating parameters, r is a vector contained the residuals, and $\| \cdot \|$ denotes the Euclidean norm of a vector.

Gentile and Saisi (2004) used the method presented by Douglas and Reid (1982) to update a FE model of the Monza cathedral bell-tower. The method minimizes the difference between the theoretical and experimental dynamic parameters through a dependence of the natural frequencies (or another modal parameter) on the unknown structural variables X_k (k = 1,2,..., n). The relation between the resonant frequencies and the structural variables are established by the following expression:

$$f_j^{FE}\left(X_1, X_2, ..., X_k\right) = C_j + \sum_{k=1}^{n}\left(A_{j,k} X_k + B_{j,k} X_k^2\right) \tag{3.23}$$

where f_i^{FE} represents the approximation of the j^{th} frequency of the FE model. The established relation indicates that, before any approximation, $2n$+1 constants ($A_{j,k}$, $B_{j,k}$ and C_j) must be calculated, and the minimized model must be calibrated. Engineering judgement is necessary to establish the base value (staring point) X_k^B and the range for each structural variable, more precisely the upper and lower values, X_k^U and X_k^L, respectively.

Since the base, upper and lower values for the updating parameters are established, the constants $A_{j,k}$, $B_{j,k}$ and C_j are calculated by computing the j^{th} resonant frequency f_j^C by changing the initial values. The first equation is constructed by the base values, the second is constructed with the lower value of the first variable, the third with the upper value of the first parameter, and so on until all variables are used for the selected frequencies as follows:

$$\begin{cases} f_j^{FE}\left(X_1^B, X_2^B, ..., X_n^B\right) = f_i^C\left(X_1^B, X_2^B, ..., X_n^B\right) \\ f_j^{FE}\left(X_1^L, X_2^B, ..., X_n^B\right) = f_i^C\left(X_1^L, X_2^B, ..., X_n^B\right) \\ f_j^{FE}\left(X_1^U, X_2^B, ..., X_n^B\right) = f_i^C\left(X_1^U, X_2^B, ..., X_n^B\right) \\ ... \\ f_j^{FE}\left(X_1^B, X_2^B, ..., X_n^L\right) = f_i^C\left(X_1^B, X_2^B, ..., X_n^L\right) \\ f_j^{FE}\left(X_1^B, X_2^B, ..., X_n^U\right) = f_i^C\left(X_1^B, X_2^B, ..., X_n^U\right) \end{cases} \tag{3.24}$$

and

$$\begin{cases} f_m^{FE}\left(X_1^B, X_2^B, ..., X_n^B\right) = f_m^C\left(X_1^B, X_2^B, ..., X_n^B\right) \\ f_m^{FE}\left(X_1^L, X_2^B, ..., X_n^B\right) = f_m^C\left(X_1^L, X_2^B, ..., X_n^B\right) \\ f_m^{FE}\left(X_1^U, X_2^B, ..., X_n^B\right) = f_m^C\left(X_1^U, X_2^B, ..., X_n^B\right) \\ ... \\ f_m^{FE}\left(X_1^B, X_2^B, ..., X_n^L\right) = f_m^C\left(X_1^B, X_2^B, ..., X_n^L\right) \\ f_m^{FE}\left(X_1^B, X_2^B, ..., X_n^U\right) = f_m^C\left(X_1^B, X_2^B, ..., X_n^U\right) \end{cases} \tag{3.25}$$

Once the constants are defined, the method is completed by minimizing the objective function π, given by the following expression:

$$\pi = \frac{1}{2}\sum_{j=1}^{m} W_j r_j^2 \tag{3.26}$$

in which W_j is a weight constant and r_j the residuals given by

$$r_j = f_j^{\exp} - f_j^{FE}\left(X_1, X_2, ..., X_n\right) \tag{3.27}$$

where f_j^{exp} is the j^{th} experimental frequency to be tuned.

In case of the masonry tower study by Gentile and Saisi (2004), the above formulation for the objective function seems to give accurate updating results, but is quite simple and other alternatives can be used.

Much more robust formulation is to accomplish in the objective function directly the errors between the measured and calculated eigen frequencies (ω_j and $\omega_{j,\exp}$), the differences between the measured and calculated modal displacements (φ_j and $\varphi_{j,\exp}$), and errors between measured and calculated modal curvatures (φ''_j and $\varphi''_{j,\exp}$), leading to the following function:

$$\pi = \frac{1}{2}\left[W_\omega \sum_{j=1}^{m}\left(\frac{\omega_j^2 - \omega_{j,\exp}^2}{\omega_{j,\exp}^2} \right)^2 + W_\varphi \sum_{j=1}^{m}\left(\varphi_j - \varphi_{j,\exp}\right)^2 + W_{\varphi''} \sum_{j=1}^{m}\left(\frac{\varphi''_j - \varphi''_{j,\exp}}{\varphi''_{j,\exp}} \right)^2 \right] \tag{3.28}$$

where W_ω, W_φ, and $W_{\varphi''}$ are the diagonal weighting matrices for frequencies, mode shapes and modal curvatures, respectively. The weighting matrices can have different values according to the engineering judgement of the analyzer, but in order to account the measurement and identification errors, they can be calculated with the inverse of the normal variance of each modal quantity (Friswell and Mottershead, 1995):

$$W = \left[diag\left(\sigma_1^2, \sigma_2^2, ..., \sigma_m^2\right) \right]^{-1} \tag{3.29}$$

In Eq.(3.28), both experimental and numerical mode shapes must be normalized in a way that the maximum real value of the modal displacement is equal to one to achieve the same order of the residuals from both, the eigen frequencies and modal curvatures.

Eigen frequencies should always accomplish the objective function. Although they are global parameters, the system identification techniques can estimate them with high accuracy. Higher variance can be found for modal displacements, but still they are spatial information about the structure, and therefore they should also be included in the objective function. The weight of the two modal quantities can be assumed differently, dependent on the engineering point of view.

If modal curvatures are measured, they should also be considered in the optimization. They are very sensitive to local changes in the stiffness, but only in the vicinity of the cross section with changes. If the sensors are installed far away from the section with damage, the modal curvatures are insensitive to damage. As a consequence, if the FE model updating technique is applied to detect damage, the strain sensors should be placed all over the structure in order to locate the damaged section. This is often not possible since it is rather expensive. If only a few strain sensors are available, they should ideally be placed near the potential damaged sections, which implies that these locations are known or assumed beforehand.

3.4.2.2 Optimization Process

For simpler problems (when the objective function has one clear minimum) the algorithms used for the local optimization can be feasibly used, like the ones used in the least squares problems.

In the least square problems the Gradient $\nabla\pi(\theta)$ and the Hessian $\nabla^2\pi(\theta)$ play an important role. The Gradient is constructed from the sensitivity matrix $\boldsymbol{J}$, known as the Jacobian matrix, which is calculated with the first order partial derivates of the residual functions, given by:

$$\boldsymbol{J}(\theta)_{ij} = \frac{\partial r_j(\theta)}{\partial x_i} \quad \text{with} \begin{cases} j = 1,..., m \text{ (rows)} \\ i = 1,..., n \text{ (columns)} \end{cases} \tag{3.30}$$

and the Hessian matrices $\boldsymbol{G}$ by the second order partial derivates of the residual functions, given by:

$$\boldsymbol{G}_j(\theta)_{ik} = \frac{\partial^2 r_j(\theta)}{\partial x_i \, \partial x_k} \tag{3.31}$$

The Gradient and the Hessian of a objectify function have the following form:

$$\begin{aligned} \nabla \pi(\theta) &= \boldsymbol{J}(\theta)^T \, r(\theta) \\ \nabla^2 \pi(\theta) &= \boldsymbol{J}(\theta)^T \, \boldsymbol{J}(\theta) + \boldsymbol{Q}(\theta) \end{aligned} \tag{3.32}$$

with

$$\boldsymbol{Q}(\theta) = \sum_{j=1}^{m} r_j(\theta) \, \boldsymbol{G}_j(\theta) \tag{3.33}$$

Next, the linear or nonlinear least squares algorithms, depending is the residual function *r* is linear or nonlinear, should be used to find the solution. The updating solution is obtained by the minimization of the residuals until a tolerance is obtained. These methods have the disadvantage to be unsuccessful when the objective function has several local minimums.

Teughels (2004) presents a more robust approach using a FE model to update a group of unknown structural parameters by using a new efficient global optimization algorithm, called Coupled Local Minimisers (CLM), to deal with objective functions with several local minimums and one global minimum.

3.4.2.3 Updating Parameters

Since a sensitivity-based optimization algorithm is used to solve the minimization problem, the updating parameters should influence the modal data considerably, otherwise the updated parameters are likely to be poor. Low sensitivities may imply that the information content of the measurements is insufficient to estimate the parameters. However, the reverse is not true. The fact that the modal data are sensitive to a parameter does not imply that this parameter should be included in the updating process. If the parameter is likely to be estimated accurately in the initial FE model (by others experimental tests), there is no reason to update it. Reasonable selection of the updating parameters and engineering judgement are essential to avoid unrealistic and ill-conditioned solutions.

3.5 Conclusions

Structural monitoring and damage identification at the earliest possible stage is an issue that received much attention from scientific community. Damage identification is relevant to all the engineering fields as the service loads and the accidental actions may cause damage to the structural systems. Regular inspections and condition assessment of engineering structures allow programmed repair works and cost-effective management of the infrastructures. In the case of historical constructions, maintenance is even more essential because of their cultural importance, the safety of visitors, the potential seismic risk and the accumulation of physical, chemical and mechanical damage through time.

Dynamic based damage identification methods have been studied in many types of structures, like rotating machinery, aeronautic structures, or civil engineering buildings and bridges. The methods are based on changes of dynamic parameters (eigen frequencies, mode shapes and damping coefficients), typically a decrease in stiffness and an increasing in damping.

3.5.1 General Remarks

In the literature, many methods have been presented for damage identification based on vibration signatures. Most of the methods calculate the differences between the dynamic parameters (eigen frequencies, mode shapes and their derivatives, and the damping coefficients) from different damage scenarios.

Large civil engineering structures have low sensitivity to frequency changes, because resonant frequencies represent condensed information about the response and are also a global property of the structures.

Another global property that can be used for damage identification is the damping coefficient. Damping increases with the presence of damage, because is related to the nonlinear phenomena, but it also increases with the level of vibration and for that reason damping estimation is complex.

As damage is a local phenomenon and may not influence significantly the lower frequencies or the global response, it is important to estimate higher modes and to have accurate information about modal displacements. For these reasons, the methods based on changes on the mode shapes or modal curvatures (or the combination of all responses, e.g. frequencies, modes shapes and modal curvatures) are more successful.

Most of the methods consider the Euler-Bernoulli beam theory. Few of them estimate damage by modal curvatures, more sensitive to structural changes than the modes shapes. The difficulty is to measure accurately the modal strains (modal curvatures) or to derivate accurately the modal curvatures from the modal displacements. In any case, to estimate damage a sufficient number of measuring points is necessary in order to have enough spatial resolution of the mode shapes.

Table 3.2 presents the reviewed dynamic based methods with their damage level, the need of a reference scenario and the requirement information from the structures.

Table 3.2 – Dynamic based damage identification methods

Method	Expected Damage Level	Comparison to a Reference Scenario	Time Information	Modal Information				
				ω	φ	φ''	ϕ	ϕ''
Unified Significance Indicator (USI)	Level 1	Yes		•				
Wavelet Package Decomposition (WPD)	Level 2 and 3	No	•					
COMAC	Level 2	Yes			○	○	○	○
Parameter Method (PM)	Level 2	Yes		•	○	○	○	○
Mode Shape Curvature Method (MSCM)	Level 2	Yes				○		○
Damage Index Method (DIM)	Level 2	Yes				○		○
Direct Stiffness Calculation Method (DSCM)	Level 2 and 3	No		•	•	○	○	○
Change in Flexibility Matrix method (CFM)	Level 2 and 3	Yes		•			•	○
Finite Element Model Updating method (FEMU)	Level 2 and 3	No		○	○	○	○	○

○ – Optional; • - Required; Level 1 – Detection; Level 2 – Localization; Level 3 – Assessment.

Most of the methods give only the possible location of the damage, while damage assessment is only obtained by few methods, being unclear if they work with all type of structures.

USI only gives the information about the presence of damage. Wavelet analysis methods (WPD) deals directly with time-domain data and do not need a mathematical model to extract the necessary information. The method became popular because it does require two different damage scenarios. The COMAC, PM, MSCM, DIM, and DSCM have the advantage that they can be applied with the estimated results from the output-only system identification techniques, as they do not need mass scaled mode shapes. On the contrary, CFM requires scaled modes to compute the flexibility matrix. Both groups of methods are simple to implement and thus not require significant computation efforts. Modal updating techniques (FEMU) are probably the most robust method, allowing more flexibility with respect to required information. However, reasonable selection of the updating parameters and engineering judgement are essential to avoid unrealistic and ill-conditioned solutions.

3.5.2 Application to Masonry Structures

Damage on masonry structures are mainly cracks, foundation settlements, material degradation and excessive deformations. When cracks occur, generally they are localized, splitting the structures in macro-blocks. The use of dynamic based methods to identify the damage is an attractive tool to use in this type of structures due to the modern requirements of unobtrusiveness, minimum physical intervention and respect of the original construction. The assumption that damage can be associated with the decrease of stiffness seems to be reasonable to this type of structures.

Many methods are presented in literature for damage identification based on vibration signatures, but there are few works on the application to masonry-like structures. The current practices of structural health condition are based mainly on visual inspections or condition surveys. During the last decade, software and hardware developments made continuous monitoring possible. Typically, one can install hundreds of sensors in a structure and read the data in real time. The challenge now is focused in what type of information is important from the structural point of view and how the data should be processed and stored for the damage analysis. The developments in the MEMS and WSN are promising technologies in this field, in particular to historical masonry structures.

Concerning monitoring the historical masonry structures, this task can be possibly divided in four phases, involving global and local damage identification approaches:

1. The first phase is the collection of all the possible data of the structure, including the historic information, geometrical and topographic survey, damage survey, the mechanical materials characterization with ND tests, a global dynamic modal test and a numerical model analysis for static and dynamic calibration. This is the first approach to the structural behaviour and health condition at the time "zero";
2. In the second phase the health monitoring can be performed with a limited number of sensors (e.g. a pair of reference accelerometers, strain gauges at critical sections, temperature and humidity sensors, etc). Data should be stored periodically and the monitoring system should be able to send immediate alarms. The presence of damage should be observed by the global modal parameters;
3. In the third phase, if an alarm is triggered a full-scale dynamic survey with more sensors and measuring points should be performed. In this phase, the "health condition" of a structure is studied with more detail. Damage identification methods should be applied to the structure after filtering the environmental and loading effects. The aim of the dynamic methods is to confirm and locate the (possible) damage in a global way;
4. In the last phase, a local approach with complementary non-destructive tests should be performed to locally classify and assess the damage. This can be realized with sonic tests or radar tests, depending on the access conditions of the structure and the type of damage sought. This local approach can give a better identification of damage.

Chapter 4

Description of an Arch Model and Experimental Tests

Abstract

This chapter presents the description of an arch model and all the experimental tests carried out in the laboratory for damage identification. The arch model was built in the laboratory where programmed and controlled damage was applied. Issues addressed here are the preliminary numerical model simulations for static and dynamic behavior of the arch, the description of the static tests series, including the observed damage pattern, the system identification tests on each scenario, the environmental tests to study the influence of temperature and relative humidity inside the laboratory and a series of tests to scale the mode shapes. Finally, the conclusions that emerged from the experimental tests are presented.

4.1 Introduction

In this chapter a description of the arch model and all the laboratory tests carried out in the Structural Laboratory of the Civil Engineering Department of the University of Minho are presented. Although only the results from the dynamic identification tests were used for the damage identification analysis based on vibration measurements, it is important to describe with detail the experimental tests involved, stressing the relevance of test planning for the success of damage identification analysis.

4.2 Arch Model Description

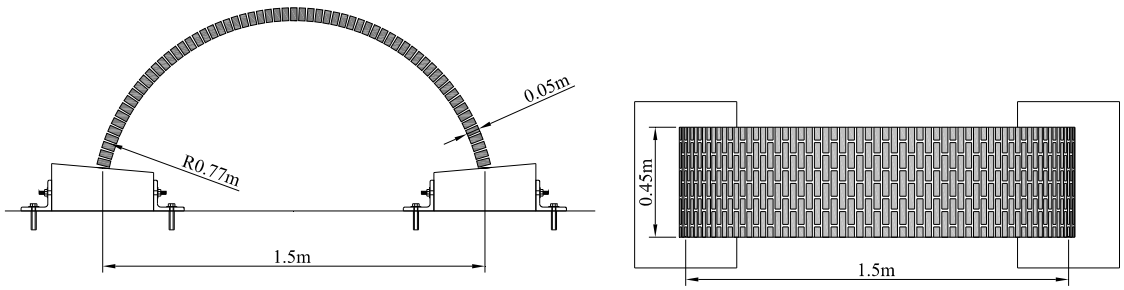
One replicate of an ancient masonry arch was built with clay bricks with $100 \times 50 \times 25$ mm^3, handmade in the Northern area of Portugal. The clay bricks have low compressive strength and are bounded using Mapei® mortar with poor mechanical properties, trying to be representative of the materials used in historical constructions. Figure 4.1 presents some images of the replicate construction. Details about the mechanical properties of these materials are given in Basilio (2007).



(a) (b) (c)

Figure 4.1 – Arch model: (a) and (b) the starting and the ending of the arch, respectively, and (c) the arch finished.

The arch has a semicircular shape with a radius of 0.77 m. It has a span equal to 1.50 m, a width equal to 0.45 m, and a thickness equal to 0.05 m. The thickness of the joints is about 0.5 cm. The arch rests in two concrete abutments fixed to the ground floor with bolts. The geometrical details are presented in Figure 4.2.



(a) (b)

Figure 4.2 – Arch geometry: (a) front view (b) top view.

The load stages/damage scenarios were produced with the application of a static point load located at a quarter span, where the lowest safety factor is obtained (Huerta, 2001). The load was applied with increasing magnitudes, being removed after each Damage

Scenario (DS). This assumption tries to represent the situation of temporary exceptional loading in the lifetime of the structure (e.g. a heavy truck passing in a bridge or an earthquake) and assumes that cracks can partially close after the exceptional event. The assumption makes the task of damage identification more difficult but more challenging, considering obviously that damage will be difficult to detect with a visual inspection. All the tests were carried out in 2005, between October and December, and after 60 days of the arch construction.

4.3 Preliminary Studies

Before the application of the controlled load stages/DS, several tests and analyses were performed to better understand the static and dynamic structural behavior of the arch. These studies included the numerical prediction of the crack locations, and the numerical estimation of modal parameters.

4.3.1 Numerical Prediction for Crack Locations

A Finite Element (FE) model was used to predict the possible location of damage. The numerical model was built with 8 noded plane stress elements in DIANA (2006) FE package. To simulate the nonlinear behavior of masonry, a standard smeared cracking model was used, incorporating a tension cut-off, tension softening and shear retention.

The simulation tries to represent a monotonically increasing load applied until the collapse. It should be stressed that the results are qualitatively and they were useful only to predict the possible crack location. For that reason a sensitivity analysis was performed by changing the tensile strength of the masonry material.

The arch was modeled as a continuous and homogeneous material with a Young's modulus equal to 4.0 GPa, a Poisson coefficient equal to 0.2, a mass density equal to 1930 kg/m^3, a tensile strength f_t equal to 0.05, 0.10, 0.20 and 0.40 MPa, a fracture energy equal to 10% of the tensile strength (in N/mm), and a shear retention factor equal to 0.10. The concrete abutments were assumed linear elastic with a Young's modulus equal to 30.0 GPa, a Poisson coefficient equal to 0.2, a mass density equal to 2500 kg/m^3. Four different analyses were performed to evaluate if the location of cracks moves by changing the tensile strength.

Figure 4.3 summarizes the results of the four analyses. Although the static response is different according to the tensile strength all the analyses show four cracks (hinges) at ultimate load stage. The numerical crack sequence is the following: the first crack appears in the intrados below the load application point; the second crack appears in the intrados at the right support; the third crack appears in the extrados, approximately in a symmetrical position with the first crack; and the last crack appears in the extrados closed to the left support. During the experimental static tests, especial attention was therefore paid to these predicted crack locations.

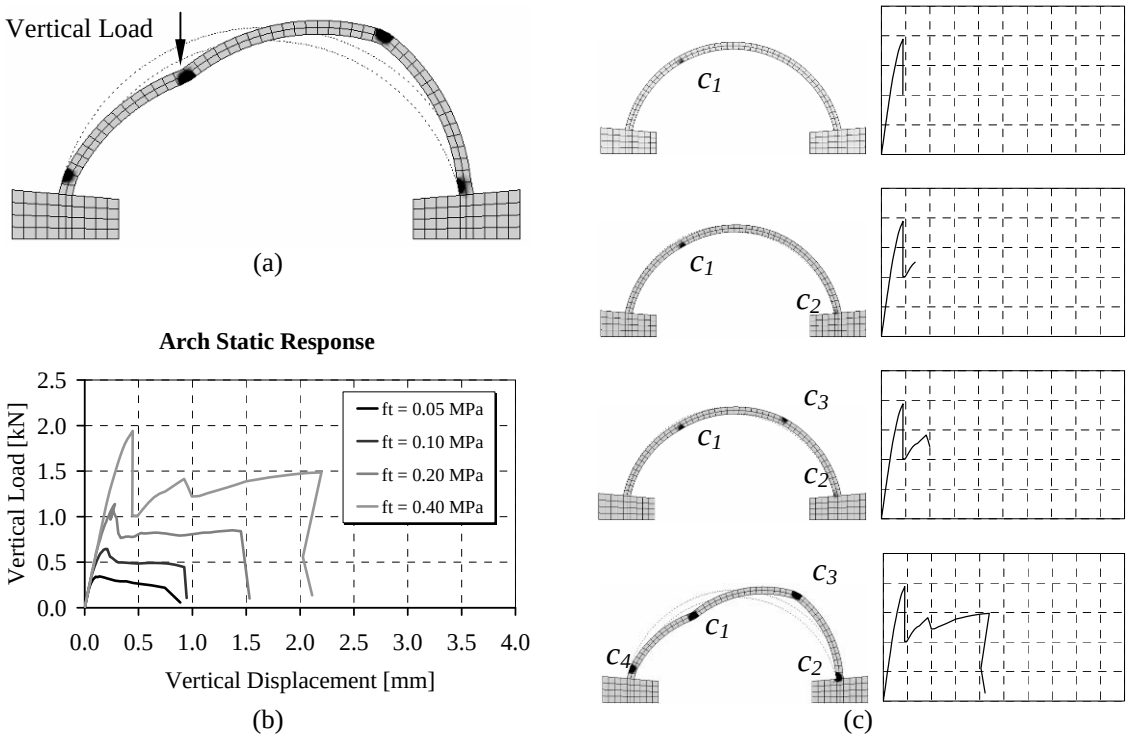


Figure 4.3 – Numerical crack prediction: (a) crack pattern (principal strains) for the ultimate load stage of the model with tensile strength of 0.40 MPa; (b) static response of the arch; and (c) the crack sequence.

4.3.2 Numerical Estimation of Modal Parameters

For the numerical estimation of modal parameters a 3D FE model with 20 noded brick elements was prepared in DIANA (2006) FE package. This analysis was performed to better define the dynamic experimental tests. As operational modal analysis was chosen for parameter estimation (with reference and moving sensors) it is important to select the location for the reference transducers and the number of points to measure, in order to have enough resolution in the mode shapes.

The 3D model was chosen so that all the modes could be estimated, including the out-of-plane and torsion modes. The elastic properties were equal to the previous plane stress model. Figure 4.4 shows the results in terms of frequency values and mode shape configurations for the first twelve modes. The range of frequencies starts from 36 up to 335 Hz. There is only one pair of close frequencies, namely 291.53 and 291.93 Hz for the 10^{th} and 11^{th} modes, respectively. Therefore, it was expected to measure experimentally, at least, ten well spaced frequencies.

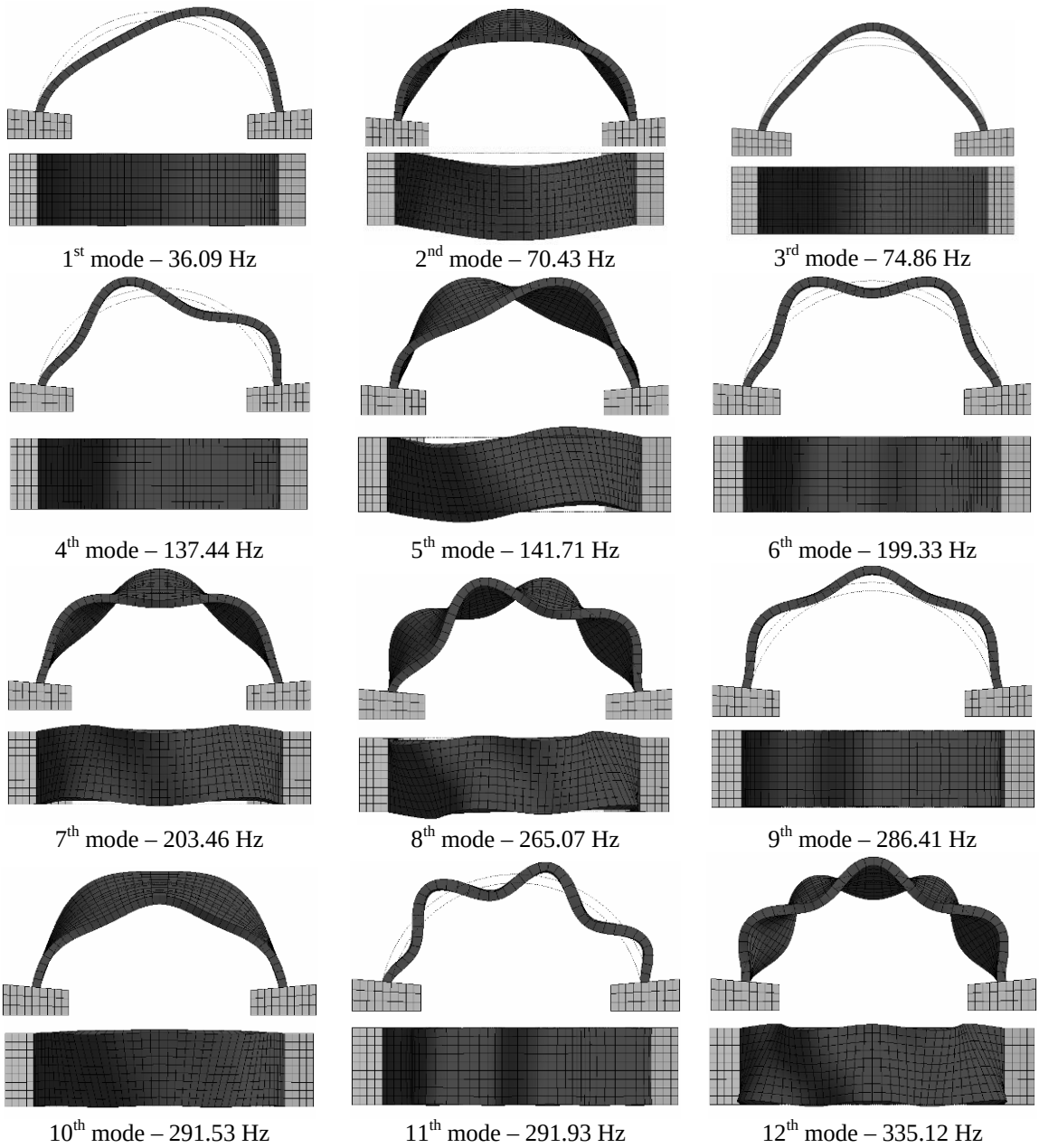
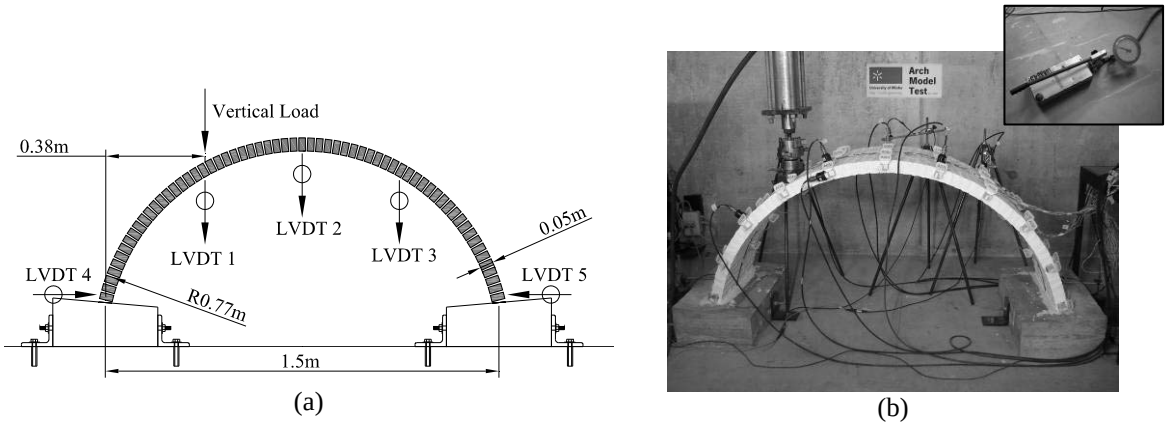


Figure 4.4 – Numerical modal estimation (mode shapes and frequency values).

4.4 Arch Static Damage Tests

The selected sensors for the static tests were five LVDTs and one load cell. The LVDTs and the load cell were resistive transducers with sufficient accuracy to measure the static response.

The static test apparatus was based in the numerical static analysis presented above and the work of Basilio (2007). The measuring points in the arch are presented in Figure 4.5a. The key aspect was to measure the vertical displacement just below the load application and the load value. All the remaining LVDTs were disposed symmetrically, including horizontal ones to capture any horizontal movement at the supports. The tests were carried out with load-control by means of a hydraulic jack, see Figure 4.5b.



(a) (b)

Figure 4.5 – Arch static tests: (a) location of the measuring points; and (b) view of the test apparatus.

Progressive and controlled damage was applied by statically increasing loads able to reach different DS. The loads were applied and removed with linear branches for all the levels. Between each DS, modal identification analysis using output-only (ambient or natural vibration) techniques were carried out, where the ambient temperature and humidity were also recorded, to evaluate possible environmental effects on the dynamic response.

Eight DS were induced by the loads on the arch. Figure 4.6 and Figure 4.7 shows the response of the model during the consecutive static tests before and after the first crack, respectively. The tests results in terms of load displacement diagrams indicate a clear loss of stiffness upon reloading, with visible load drops with crack opening.

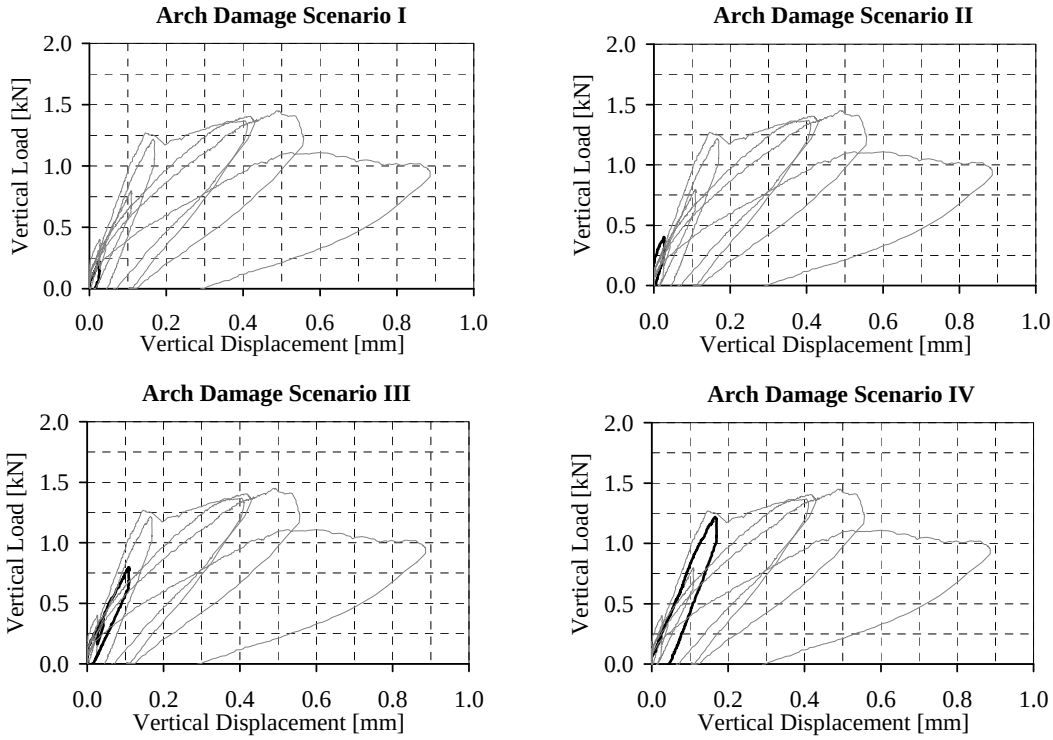


Figure 4.6 – Arch static response before the first crack.

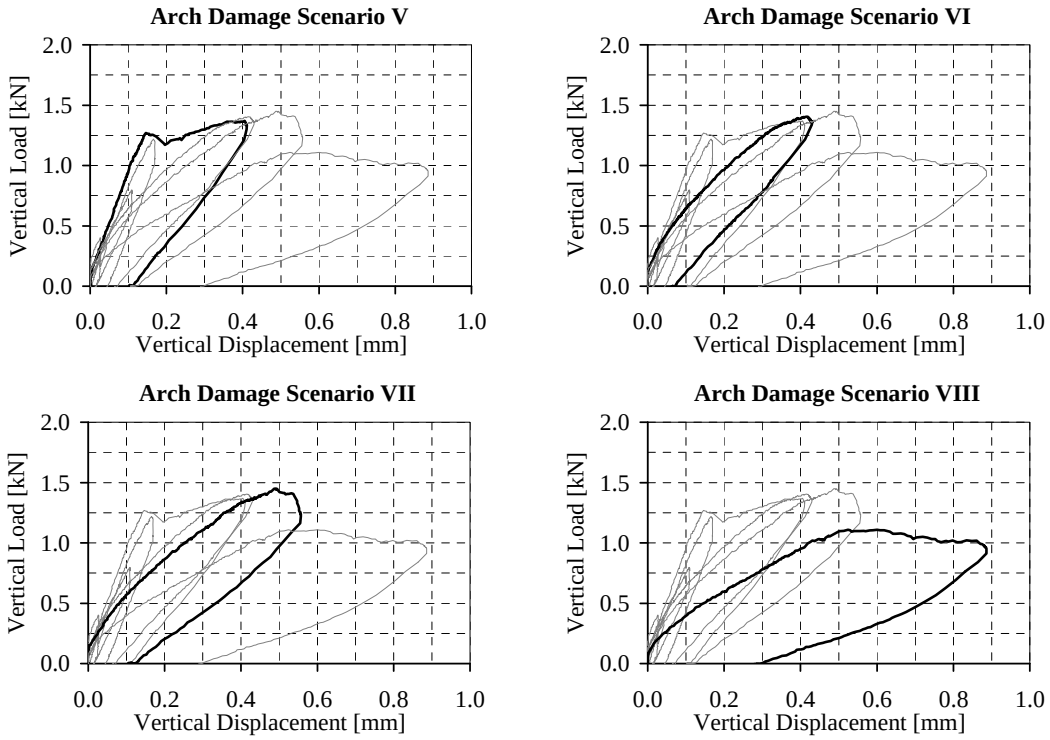


Figure 4.7 – Arch static response after the first crack.

Figure 4.8 presents the resulting crack patterns in the arch and the position of the dynamic transducers. Four cracks were found in agreement with the numerical crack prediction. However, it was impossible to register the full crack sequence.

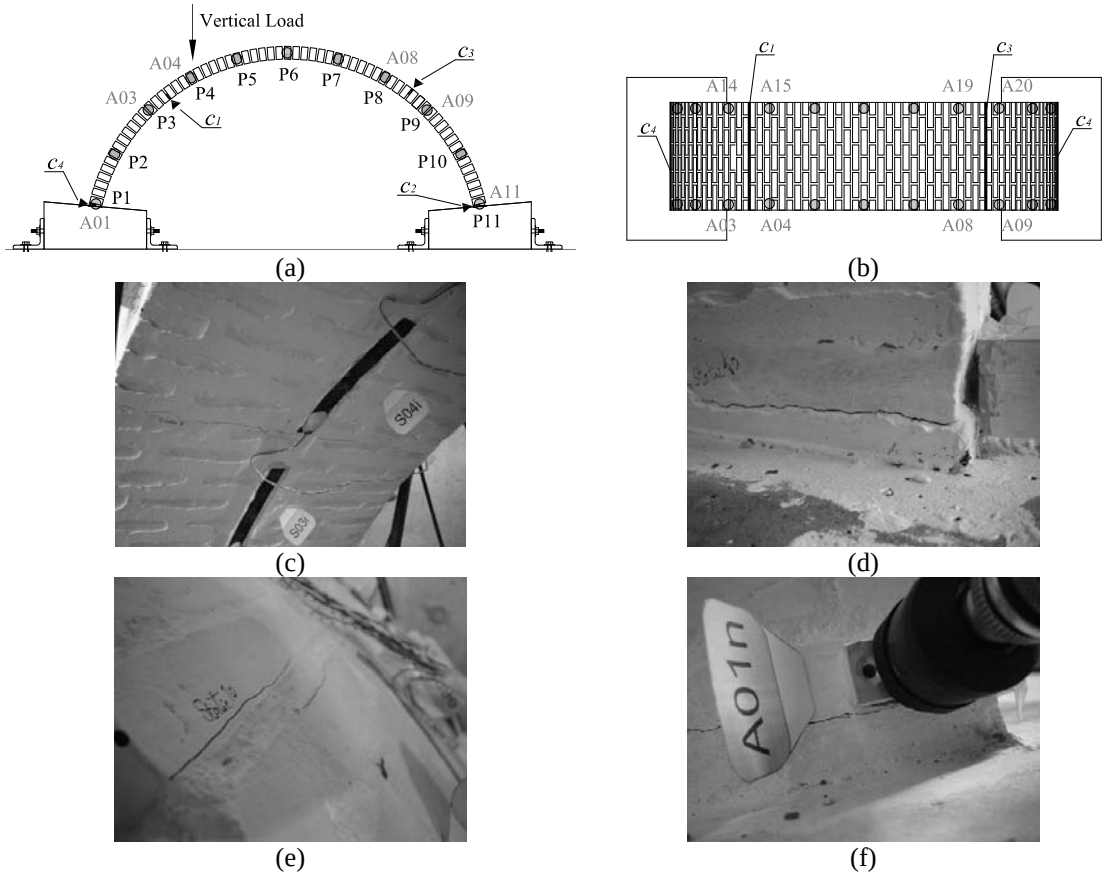


Figure 4.8 – Arch damage: (a) and (b) crack location; (c) crack c_1; (d) crack c_2; (e) crack c_3; and (f) crack c_4.

The first crack to appear (c_1) was located between the positions P3 and P4 (accelerometers A03 and A04) and not below the load application point, see Figure 4.8a. The crack appears in the intrados, as expected, but it was only visible during the loading branch of the DS_{VI}, although it is evident that it has occurred on DS_V, given the loss of stiffness in the static tests.

Crack c_2 was located in position P11 (right support in the measuring point A11) in the intrados, crack c_3 was located between P8 and P9 (measuring point A08 and A09) in the extrados, and the crack c_4 was located at positions P1 (left support in the measuring point A01) in the extrados. Occurrence of these cracks was impossible to detect. They became visible in the loading range of DS_{VIII}. This can be explained by the fact that the self-weight of the arch is a stabilizing action and almost fully closes the cracks at the equilibrium position. The decision to stop each static test after DS_V was based on the sound of a crack that suddenly opens. Therefore, the designation c_1 to c_4 presented here do not try to represent the real crack sequence, which is unknown.

It should be stressed that the maximum remaining crack opening after the entire testing program was 0.05 mm and the maximum crack depth in the loading branch of the tests was 30 mm (more than half of the arch thickness) for crack c_1.

Analyzing now in detail the stiffness during the several tests presented in Figure 4.9a, after the occurrence of the crack c_1 it was possible to observe a decrease of stiffness. Here, a loading and unloading stiffness can be defined, where static tests allow measuring the rapidly varying loading stiffness k^l and the dynamic tests only measure the slowly varying unloading stiffness k^u, see Figure 4.9b and c. As a result, dynamic tests are less sensitive than static tests to identify structural damage.

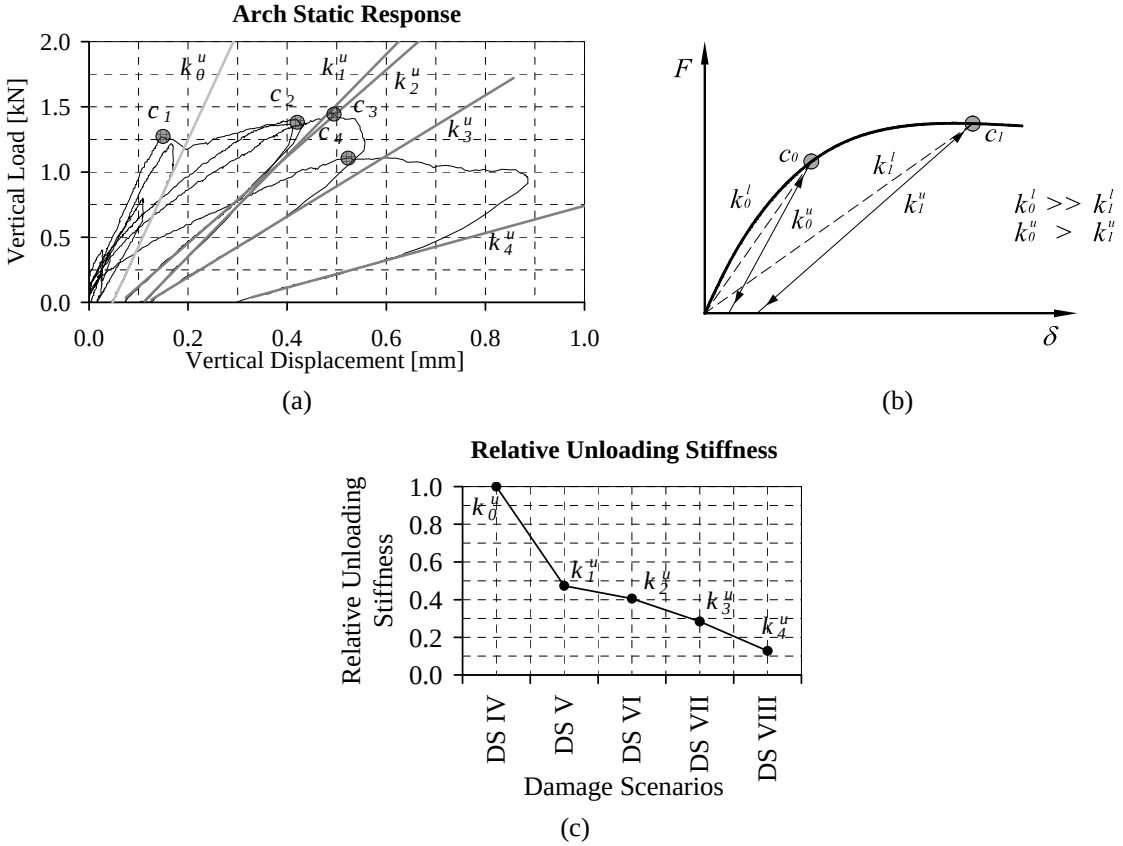


Figure 4.9 – Stiffness decrease: (a) possible sequence of cracks and gradual stiffness decrease; (b) difference between the loading and the unloading stiffness; and (c) relative unloading stiffness variation.

4.5 System Identification Tests

The system identification tests were carried out according to the test planning described next. To estimate the modal parameters the stochastic subspace identification techniques were chosen based on the discussion given in Chapter 2. Before the identification of the several DS, one qualitatively analysis was performed on the Reference Scenario (RS) by a comparison between different stochastic subspace identification tools. Finally, environmental and mass-scaled tests are presented.

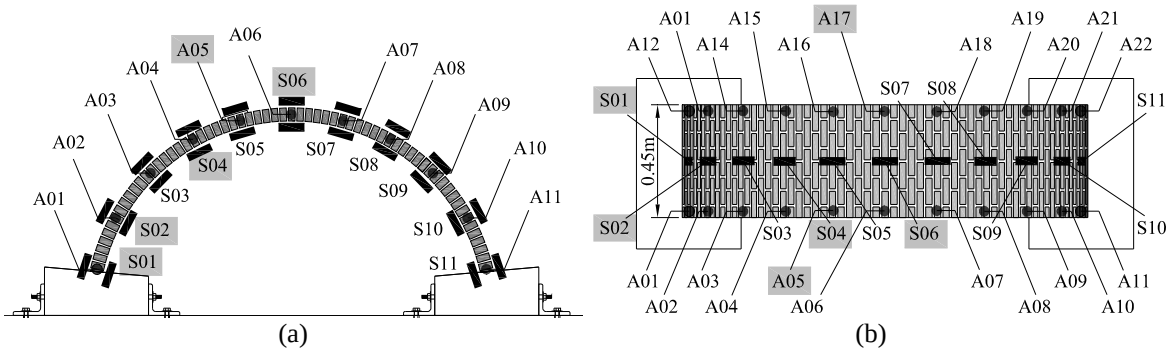
4.5.1 Test planning

4.5.1.1 Sensors Selection and Location

The selected sensors for the dynamic tests were accelerometers and strain gauges. The accelerometers were selected because they have good accuracy for the dynamic response. The strain gauges were chosen to measure directly dynamic strains for the direct estimation of modal curvatures. The obvious reason is to have more modal information for the damage identification analysis. The discussion about the sensors location is necessary to acquire good quality data. In the next section a detailed description of the test equipment is presented.

From the preliminary numerical analysis, it was possible to conclude that all modes have significant modal displacements in the arch plane. In the out-of-plane direction only the numerically predicted 2nd and 5th modes have significant modal displacements. For this reason, it was decided to measure accelerations only in the in-plane direction, and, for convenience, in the normal and tangential directions on each location. It was also decided to measure both edges of the arch (front and back edges) to estimate the torsion modes and to detect any asymmetric behavior.

According to the configuration of the twelve numerical mode shapes, the best points for the reference transducers (points which have significant modal displacements in all modes) is at ¼ span for some modes and at ½ span for other modes. In order to have a better resolution in the modal estimation, two positions were selected to be the reference points for accelerations in the front and back edges (four sensors) and four strain gauges in the extrados and intrados (eight sensors). Figure 4.10 shows the location of the measuring points where the reference points are given in a grey box. The designation A*i* is for accelerometers and S*i* is for strain gauges.



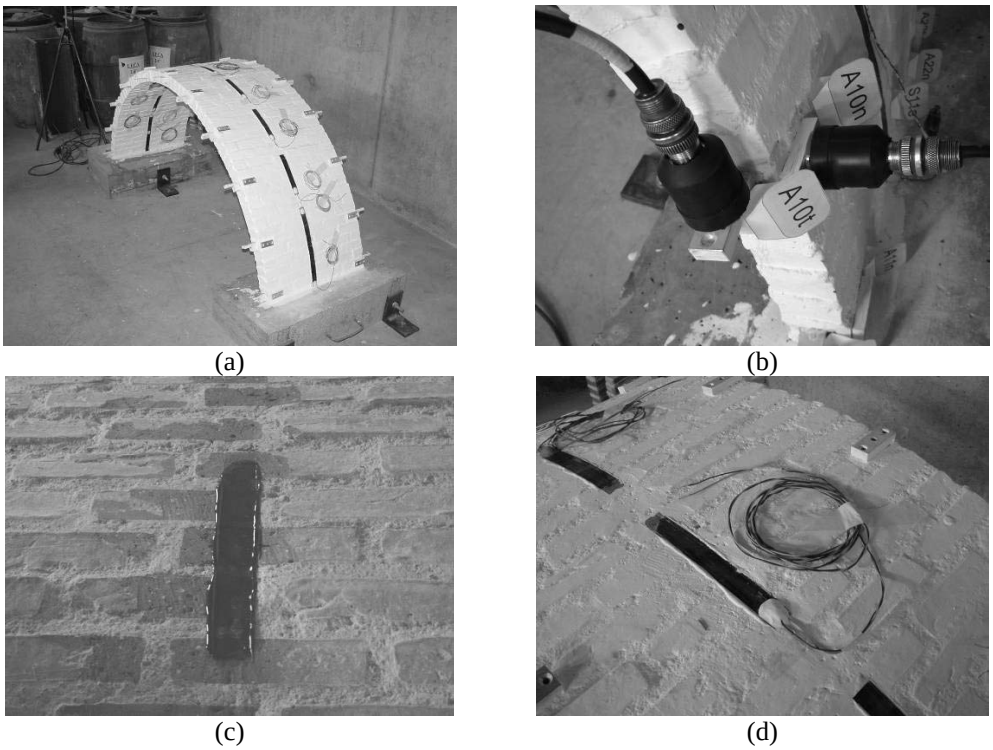
(a) (b)

Figure 4.10 – Location of the measuring points for the dynamic tests: (a) front view; and (b) top view. A*i* indicates accelerometers and S*i* indicates strain gauges. Boxed-values in grey are the reference points.

In the case of the strain gauges, as an attempt to study the possibility to measure strains for dynamic modal analysis, it was decided to measure only the middle line of the arch on both sides; in the intrados and the extrados. This means that the torsion modes will not be (or very weakly) present in the strains measurements.

Regarding the mode shapes resolution, aiming at a clear definition of the modal displacements, it was decided to measure 11 points uniformly distributed along the arch (spaced approximately 1/8 of the arch maximum dimension). This resolution is enough to have the complete definition for the twelve estimated modes and is feasible from the practical point of view, as too many points are unpractical and expensive for experimental tests in real structures. Those 11 points were materialized along two lines at the edges for the accelerometers and along the middle line for the strain gauges. In total, 44 different directions for accelerations and 22 strain points were measured.

Figure 4.11 shows images of the sensors location in the arch. The accelerometers were bolted to aluminum plates that were directly glued in the arch edges to perform the normal and tangential measurements. The dimension of the strain gauges is shown in detail in Figure 4.11c and d. The length of 12 cm is justified to have representative information of the masonry behavior. This way, the strain gauge crosses, at least, three bricks.



(a) (b)

(c) (d)

Figure 4.11 – Sensors location: (a) general view; (b) normal and tangential directions for accelerations; (c) strain gauges surface base across 3 bricks; and (d) strain gauges glued and ready to be measured.

4.5.1.2 Test Equipment, Test Sequence and Location of Specimen in the Laboratory

The dynamic acquisition system was composed by 8 uniaxial piezoelectric accelerometers, with a bandwidth ranging from 0.15 to 1000 Hz (5%), a dynamic range of ±0.5 *g*, a sensitivity of 10 V/*g*, 8 μ*g* of resolution and 210 g of weight, connected by coaxial cables to a data acquisition system with a 16 bit ADC, provided with anti-aliasing filters in the amplification cards for both strains and accelerations. The digitalized band for the ADC was adjusted for each type of tests in other to have good data resolution.

The 22 strain gauges were of 120 Ω resistance, glued in the masonry by a thin epoxy layer to smooth the arch surface on the desired measurement location. The strain gauges were connected to the data acquisition system with one quarter bridge configuration. This configuration gives lower resolution (a half bride doubles the resolution) but has the advantage to allow separate connections, which can be useful if a crack crosses one strain gauge. The strain measurements arrangement allows detecting any crack that could cross a strain gauge at one side of the arch and to proceed with the data acquisition at the opposite side.

The estimated maximum frequency of interest was around 330 Hz and it was decided to analyze the structure up to a frequency three times greater. Using the Nyquist theorem a sampling frequency of 2000 Hz was therefore fixed. For all the identification tests, 10 setups with four reference sensors in positions A05 and A17 (see Figure 4.10) and four moving sensors were carried out, as it can be seen in Figure 4.12 and Table 4.1. Also the strains measurements were carried out in a sequential process, taking as a reference the strains in positions S01, S02, S04 and S06 (see Table 4.2).

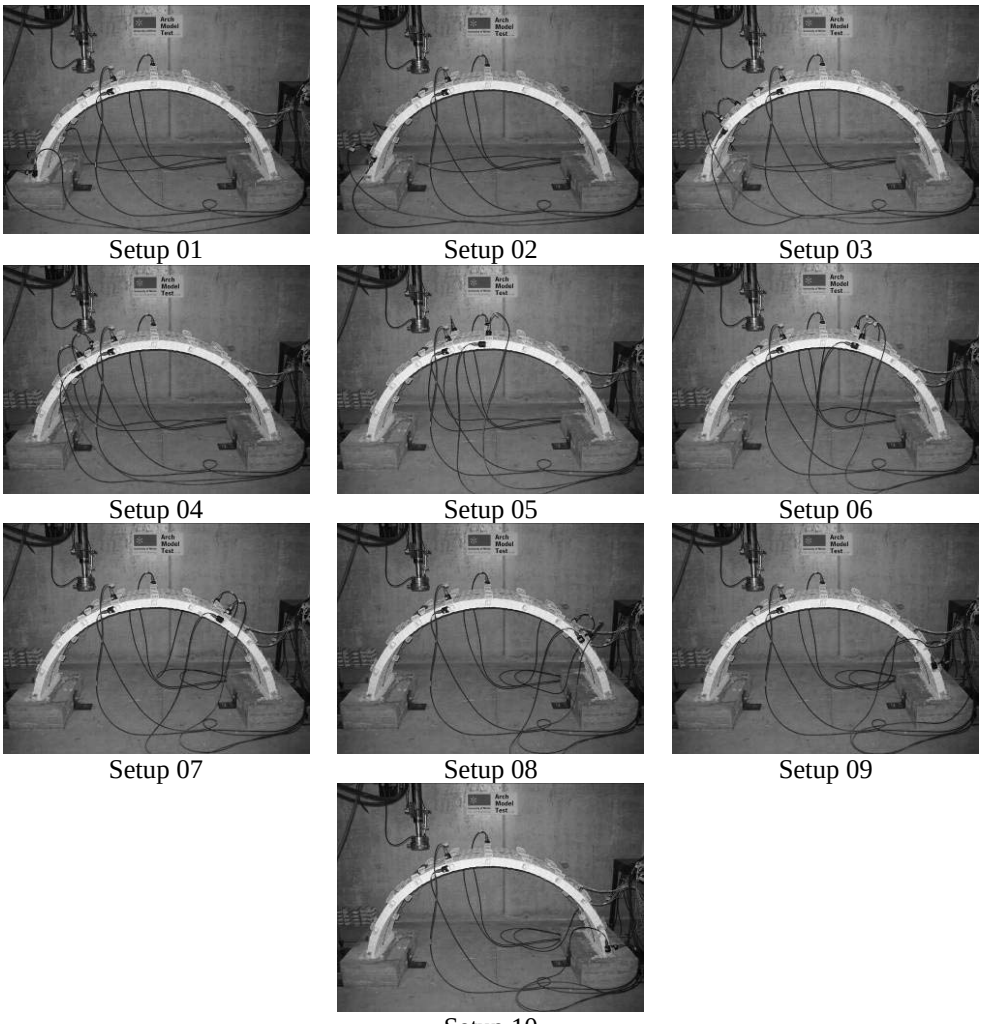


Figure 4.12 – Dynamic test sequence, with the different setups and two reference positions (four sensors).

Table 4.1 – Test setups for accelerometers (n and t indicates normal and tangential directions, respectively).

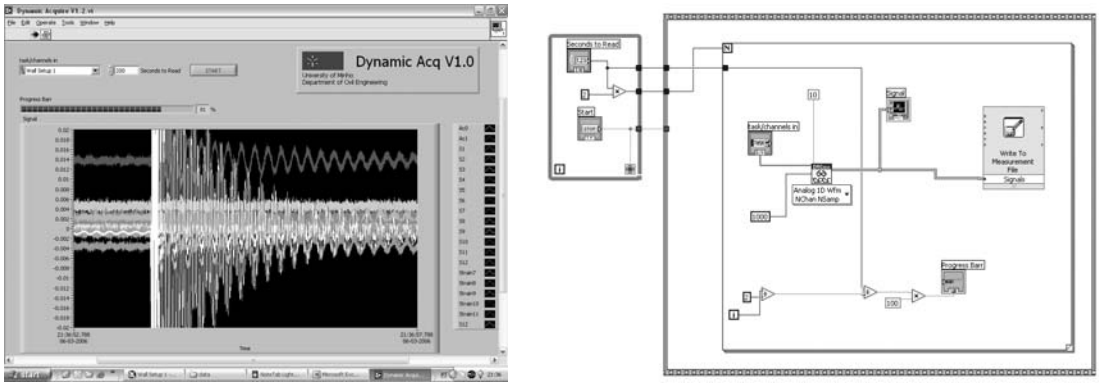
Setup	Ref. 1	Ref. 2	Ref. 3	Ref. 4	Mov.1	Mov. 2	Mov. 3	Mov. 4
1	A05t	A05n	A17t	A17n	A01t	A01n	A12t	A12n
2	A05t	A05n	A17t	A17n	A02t	A02n	A13t	A13n
3	A05t	A05n	A17t	A17n	A03t	A03n	A14t	A14n
4	A05t	A05n	A17t	A17n	A04t	A04n	A15t	A15n
5	A05t	A05n	A17t	A17n	A06t	A06n	A16t	A16n
6	A05t	A05n	A17t	A17n	A07t	A07n	A18t	A18n
7	A05t	A05n	A17t	A17n	A08t	A08n	A19t	A19n
8	A05t	A05n	A17t	A17n	A09t	A09n	A20t	A20n
9	A05t	A05n	A17t	A17n	A10t	A10n	A21t	A21n
10	A05t	A05n	A17t	A17n	A11t	A11n	A22t	A22n

Table 4.2 – Test setups for strain gauges[†].

Setup	Ref.1	Ref.2	Ref.3	Ref.4	Mov.1	Mov.2	Mov.3	Mov.4
1*	S01	S02	S04	S06	S07	S08	S10	S11
2*	S01	S02	S04	S06	S03	S05	S9	–

* – measured at the same time as setups 1 and 2 for accelerometers (see Table 4.1).

On each test, time segments were recorded with a complete measuring time equal to 2000 times the first (highest) period of the structure, with a minimum duration equal to 60 s. The allowed number of channels in the data acquisition system was equal to 24 and they were all used during the test setups, which means that it was necessary to store 48000 (24×2000) data points per second during one minute or more. To avoid loss of data, one simple Virtual Instrument (VI) from LabVIEW (2006) was built to acquire the data and store it in the hard drive of a Pentium® IV Laptop. The data was automatically stored in an ASCII file, in which each column corresponds to one channel. Figure 4.13 shows the front panel and the block diagram of the VI.



(a) (b)

Figure 4.13 – LaVIEW VI: (a) front panel; and (b) block diagram.

The location of the specimen inside the laboratory was chosen according to the frequency range of interest and the natural frequencies of the concrete supporting slabs of the laboratory. The ambient noise was measured in several locations with the sensors

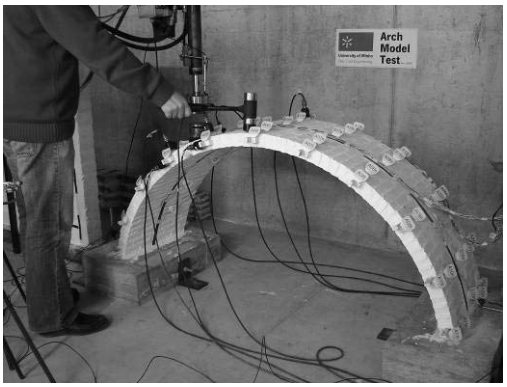
[†] Note that the strain gauges are fixed in the structure but the data acquisition system only allowed to read 16 strain gauges channels simultaneously, while 22 were glued to the arch. Thus, two different setups were required.

attached to the slabs. A place at the basement of the laboratory was selected because the ambient noise spectrum was flat in the frequency range of interest, although it was necessary to prohibit the use of any sort of electrical rotating equipement inside the laboratory during the dynamic tests.

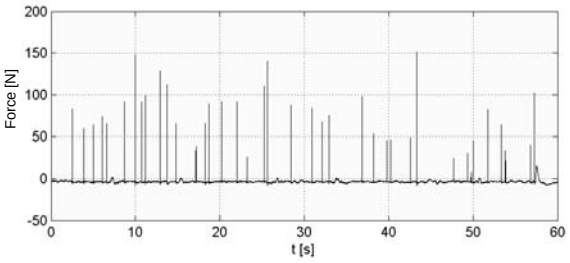
4.5.1.3 Types of Excitation

Another important issue to address is the excitation type during the identification tests. The intention was to validate if damage could be identified with ambient excitations or require stronger excitation. The ambient vibrations in the laboratory were not strong enough to excite the structure sufficiently to identify modal strains. Therefore, the modal identification tests at each load stage/DS were carried out by two different excitation types: (a) natural and ambient noise present in the laboratory; and (b) random impact excitation in space and in time (not recorded), induced by a hammer with 2.5 kg of mass. The impact forces were about 5% of the arch mass. It should be stressed that random impact excitation could violate the white noise assumption of the output-only modal analysis, but this type of exogeneous inputs were used successfully by others researchers, e.g. Reynders and De Roeck (2006), and Cantieni (2006).

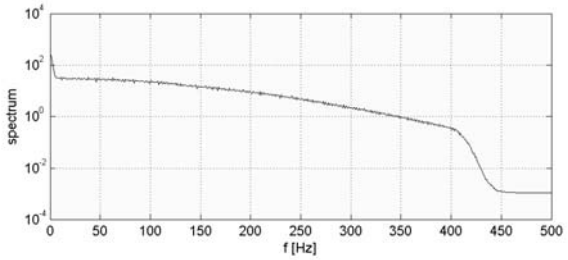
Figure 4.14 presents the impact time history of one test and the respective power spectrum, where one can see that for frequencies under 200 Hz the spectrum is almost flat, indicating that this type of excitation should not reduce the quality of the estimation results.



(a)



(b)



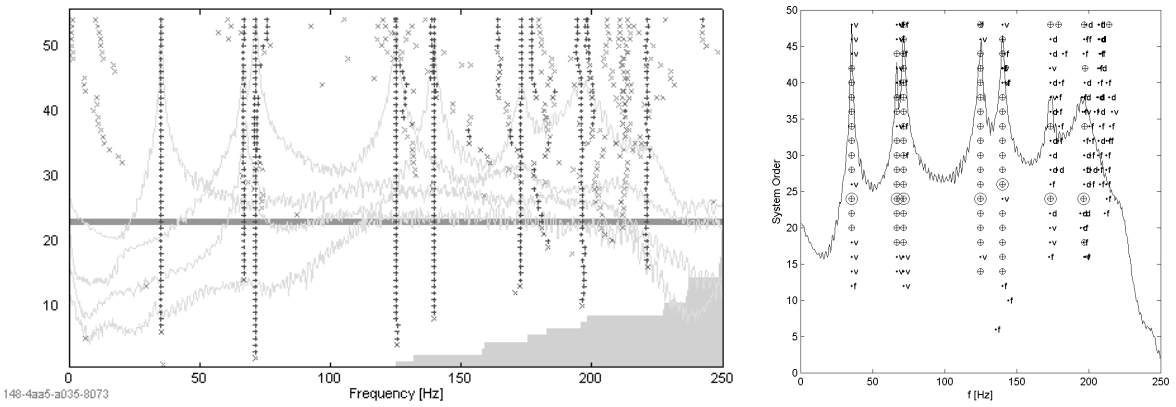
(c)

Figure 4.14 – Random impact excitation: (a) impact tests; (b) impact time history; and (c) impact spectrum.

4.5.2 Reference Scenario Results with Different Stochastic Subspace Identification Techniques

Two different tools were used to analyze the data quality of the dynamic tests. It was not intended to compare the tools, but to have a qualitatively idea about the experimental data to be used later in the damage identification analysis. The SSI techniques selected here were the SSI/Principal Component method available in ARTeMIS Extractor software (SVS, 2006) and the SSI/Ref method implemented in the MACEC tool from Catholic University of Leuven (Peeters and De Roeck, 1999). Seven mode shapes were easily estimated with ambient and randomly distributed impact tests. Note that in the preliminary

analysis twelve modes were expected to be estimated, but the experimental results show that only the first seven modes can be adequately estimated with the adopted excitation. Figure 4.15 shows the stabilization diagrams for both analyses.



(a) (b)

Figure 4.15 – Stabilization diagrams for SSI techniques: (a) ARTeMIS; and (b) MACEC.

The results in terms of frequency values and damping coefficients are presented in Table 4.3 and Table 4.4 for the ambient and random excitation tests, respectively. Both standard deviation (σ) and Coefficient of Variation (CV) are presented for the same modal parameters: frequency ω and damping ξ. In general, the random impact excitation tests have lower standard deviation values, indicating a possible better modal estimation. Nevertheless, the high CV values for the damping in all cases should be stressed as possible less accurate results. The damping values depend on the excitation mechanism and in the nonlinear phenomena, but one can conclude that an average value of 0.6% can be observed for all modes and all analyses. As it will be shown later, the damping will be carefully used as a qualitatively indicator in the damage identification analysis.

Table 4.3 – Results from the ambient excitation test.

Modes	ARTeMIS Estimation						MACEC Estimation					
	ω [Hz]	σ_ω [Hz]	CV_ω [%]	ξ [%]	σ_ξ [%]	CV_ξ [%]	ω [Hz]	σ_ω [Hz]	CV_ω [%]	ξ [%]	σ_ξ [%]	CV_ξ [%]
1	35.59	0.20	0.57	0.44	0.20	45.18	35.35	0.82	2.33	0.27	0.19	69.81
2	67.30	0.46	0.69	0.53	0.12	22.50	66.67	0.68	1.02	0.69	0.26	37.35
3	72.11	0.38	0.53	0.88	0.90	101.92	72.27	0.98	1.36	0.91	0.37	40.21
4	125.74	0.65	0.52	0.59	0.10	17.53	125.20	0.53	0.42	0.84	0.20	24.11
5	140.08	0.89	0.63	0.46	0.31	66.76	139.83	0.61	0.44	1.27	0.27	21.61
6	173.38	1.63	0.94	0.83	0.33	39.02	173.73	0.97	0.56	1.14	0.60	52.17
7	199.32	2.91	1.46	1.84	0.65	35.39	197.09	2.04	1.04	2.94	1.43	48.62

Table 4.4 – Results from the random impact excitation test.

Modes	ARTeMIS Estimation						MACEC Estimation					
	ω [Hz]	σ_ω [Hz]	CV_ω [%]	ξ [%]	σ_ξ [%]	CV_ξ [%]	ω [Hz]	σ_ω [Hz]	CV_ω [%]	ξ [%]	σ_ξ [%]	CV_ξ [%]
1	35.21	0.12	0.33	0.51	0.08	15.94	35.24	0.55	1.57	0.12	0.04	31.72
2	66.58	0.36	0.55	0.64	0.09	14.68	66.43	0.60	0.90	0.35	0.02	6.00
3	71.16	0.21	0.30	0.72	0.14	19.21	71.24	0.73	1.02	0.20	0.05	23.24
4	124.52	0.74	0.60	0.79	0.10	12.32	124.05	0.72	0.58	0.71	0.08	11.67
5	138.94	0.90	0.65	0.73	0.22	30.11	138.92	0.69	0.50	0.83	0.34	41.28
6	172.54	0.84	0.49	1.11	0.30	27.38	172.36	1.17	0.68	0.92	0.42	45.88
7	196.76	2.13	1.08	2.55	0.94	36.98	196.84	2.43	1.24	1.23	0.43	35.31

Table 4.5 and Figure 4.16 summarize the results concerning the frequency values and the mode shape configurations through the MAC values. It is stressed that the results are highly accurate for frequencies and modal displacements, as the maximum error between the resonant frequency values is about 1% and the MAC values are greater than 0.94 (except for mode 4 in the same ambient vibration condition). However, it should be also stressed differences for the modal configuration of the seventh mode shape at middle span and at the left support.

Table 4.5 – Frequency comparison between different SSI analyses.

Modes	Ambient Excitation				Random Impact Excitation			
	ARTeMIS [Hz]	MACEC [Hz]	Diff. [%]	MAC	ARTeMIS [Hz]	MACEC [Hz]	Diff. [%]	MAC
1	35.59	35.35	0.67	0.97	35.21	35.23	–0.06	0.97
2	67.30	66.67	0.94	0.94	66.58	66.43	0.23	0.95
3	72.11	72.27	–0.22	0.94	71.16	71.24	–0.11	0.94
4	125.74	125.20	0.43	0.78	124.52	124.05	0.38	0.98
5	140.08	139.83	0.18	0.97	138.94	138.92	0.01	0.99
6	173.38	173.73	–0.20	0.95	172.54	172.38	0.09	0.95
7	199.32	197.09	1.12	0.96	196.76	196.83	–0.04	0.95

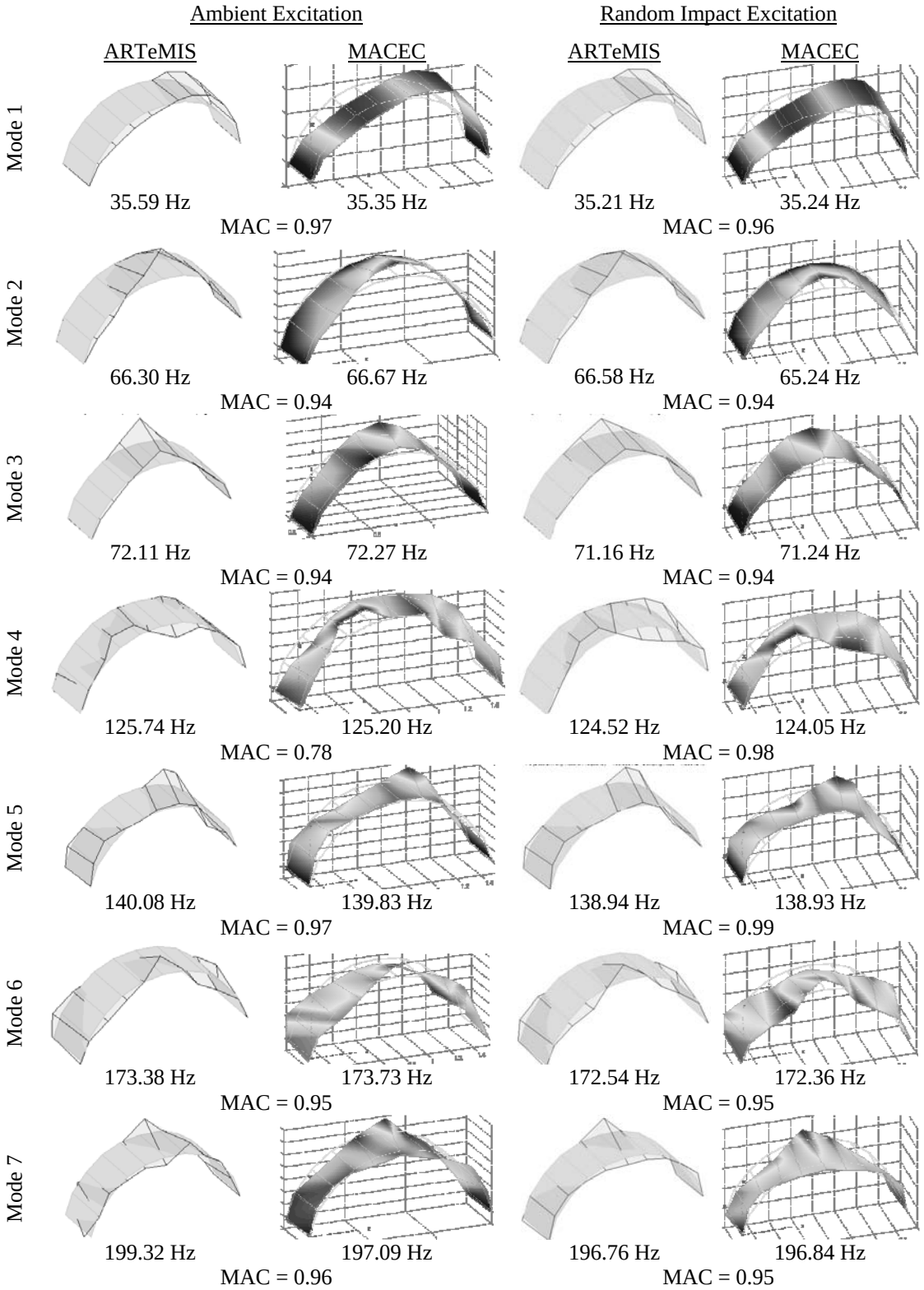


Figure 4.16 – Mode shape configurations for all the analyses.

As strains were measured on 11 points in the extrados and intrados of the arch centre line, it was also possible to estimate directly the curvature mode shapes. As mentioned before, the curvatures were only estimated with accuracy in the case of randomly

distributed impact excitation tests, because the signal-to-noise ratio was too small for ambient vibration excitation.

Figure 4.17 presents the estimated modal curvatures with the two adopted processing tools. Larger differences seem to be found in this case. It is also noted that the extreme values in curvature mode shape 1 are much higher than other modes. This is due to the fact that mode 1 is basically in plane and the other modes involve torsion, meaning that the curvature values at the centre line of the arch are much lower than the values at the edges.

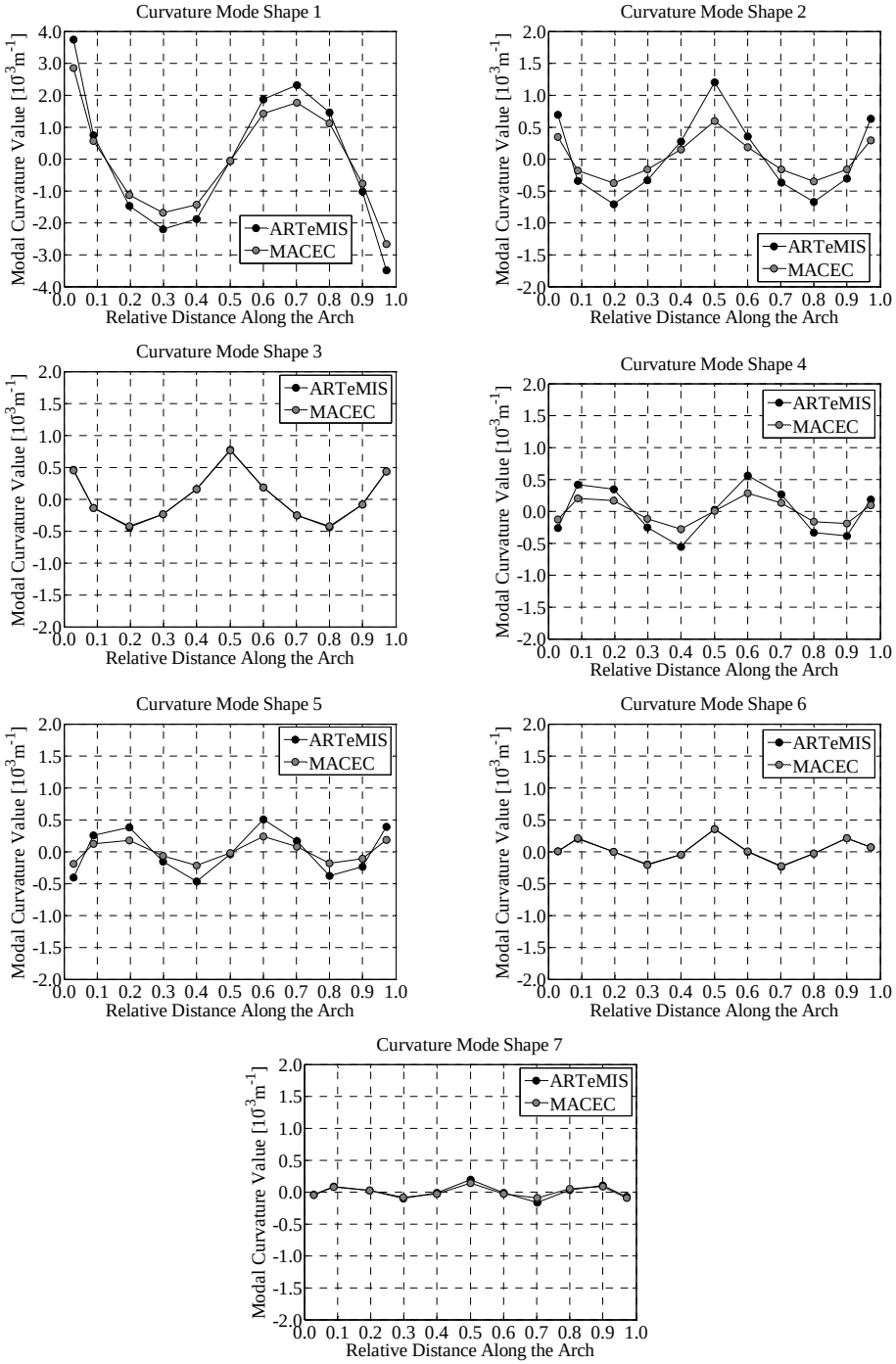


Figure 4.17 – Curvature mode shapes estimated by the two SSI analyses. Note that the results for curvature mode shape 3 and 6 are almost coincident and the difference is not apparent in the graphics.

Figure 4.18 presents the normalized modal curvatures, i.e. the maximum real value of the modal curvature is equal to one. With the normalized curvatures the symmetry or anti-

symmetry of the modes along the arch is stressed. The fact that perfect symmetry of the results is not obtained indicates that geometrical imperfections might be present in the arch. Note also the almost perfect coincidence of the measured curvatures after normalization of the response.

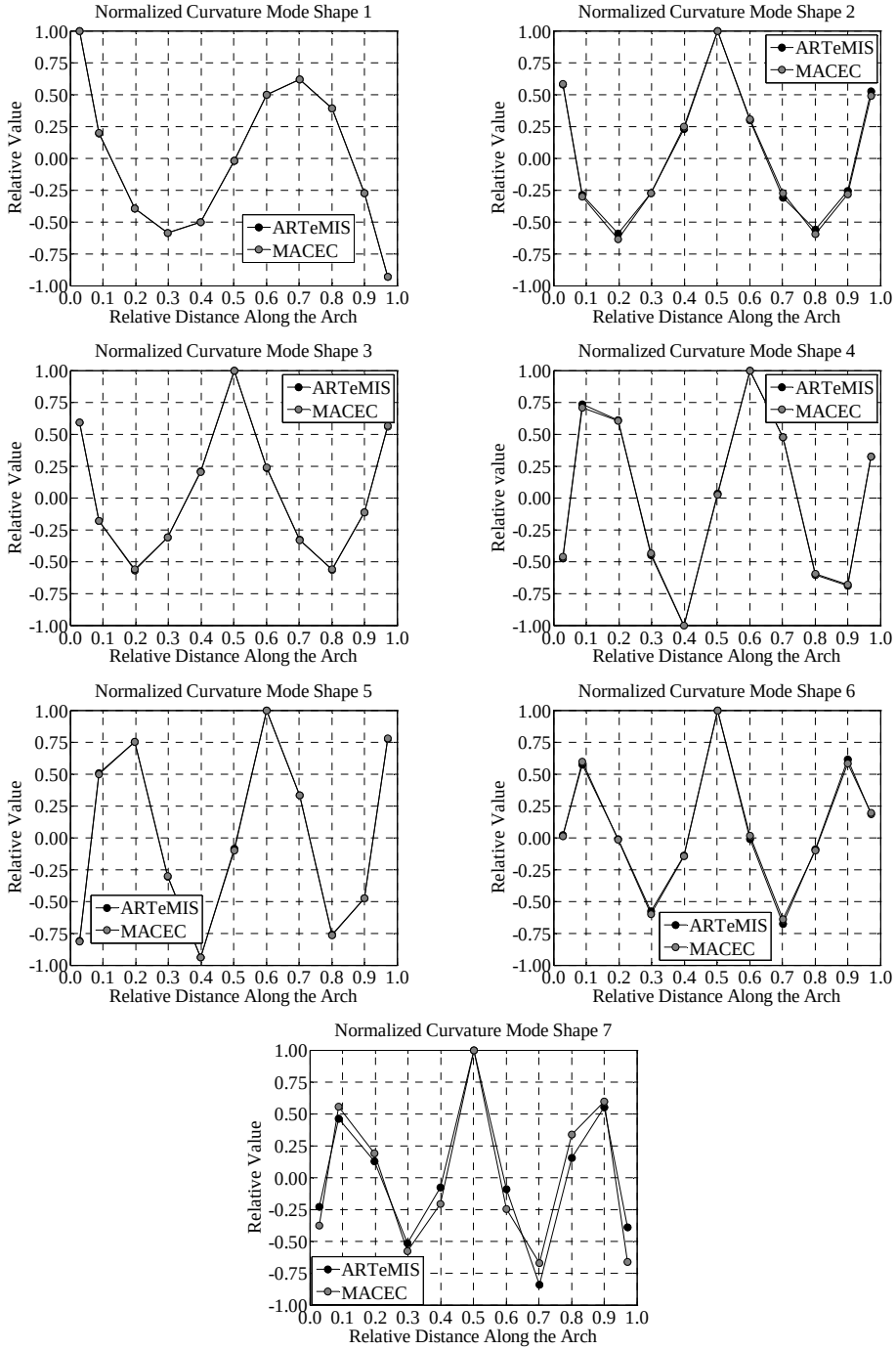


Figure 4.18 – Normalized curvature mode shapes estimated by the two SSI Analyses.

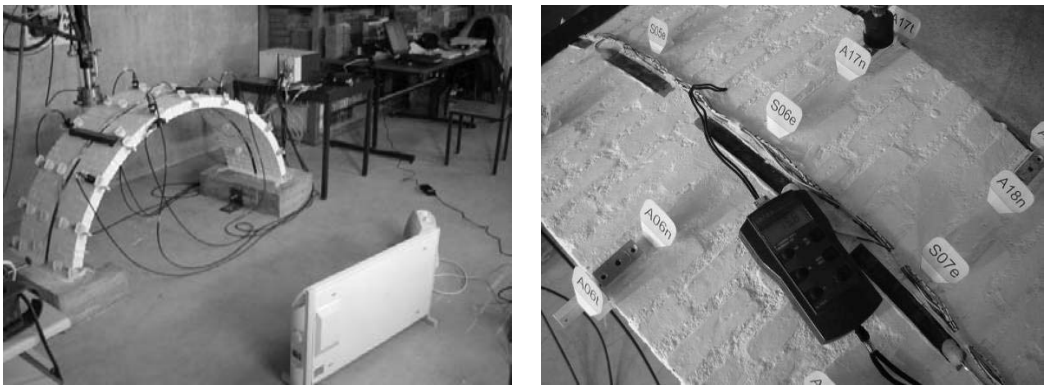
The modal curvatures are valuable quantities for subsequent damage identification analysis under the assumption of Euler-Bernoulli hypotheses: The bending stiffness and the normal stiffness are directly related to the curvatures and the average strains in the arch, respectively.

To conclude, the results seem to be accurate and in good agreement for both analyses. No significant differences were found for the seven resonant frequencies. In the case of

modal displacements and modal strains, differences were found for the seventh mode shape. In the later damage identification analysis, for frequency comparison all the seven frequencies will be taking in to account, while for mode shape comparison only the first six modes will be considered.

4.5.3 Environmental Tests in the Laboratory

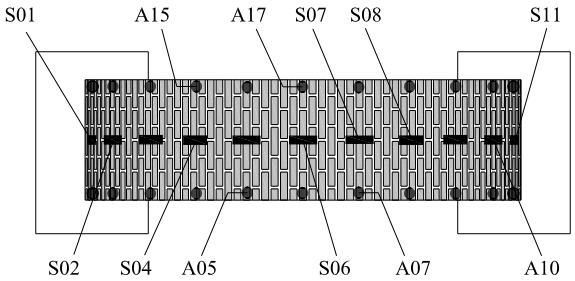
To investigate the influence of temperature and relative air humidity to the arch model inside the laboratory, a series of tests was performed to evaluate their effects on the virgin structure. Due to variations of heating and ventilation it was observed that the air temperature in the laboratory could change 3ºC in one hour (the approximate time of one entire group of test setups per specimen). Even if the thermal inertia of the arch significantly reduces the temperature change in the structure, an induced temperature variation with two heating devices close to the arch was carried out (see Figure 4.19a). The surface temperature, the air temperature and relative air humidity were then measured (see Figure 4.19b) with an accuracy of ±0.1ºC for temperature and ±1% for the relative air humidity.



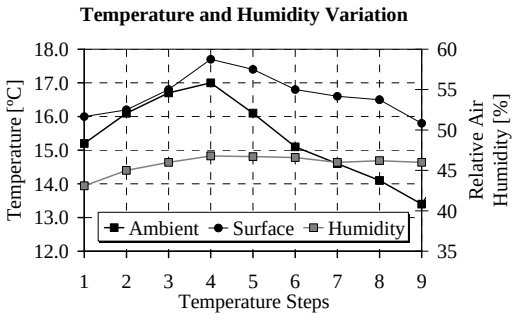
(a) (b)

Figure 4.19 – Environmental tests: (a) location of the heating devices near the arch; and (b) the surface temperature test equipment.

Nine temperature steps were performed in 2 hours. On every step, acceleration records of 60 s were acquired with the acceleration transducers in positions A05, A07, A15 and A17, and with strain gauges in positions S01, S02, S04, S06, S07, S08, S10 and S11 (see Figure 4.20a). During the cycle, the ambient temperature amplitude was equal to 3.6ºC, while the surface temperature amplitude was equal to 1.9ºC. The relative air humidity changed 6%. Figure 4.20 shows the temperature and the relative humidity variation along the tests.



(a)



(b)

Figure 4.20 – Environmental tests inside the laboratory: (a) sensors location; and (b) temperature and humidity variation.

Table 4.6 and Table 4.7 present the results for the first six mode shapes in terms of the frequency values for all the temperature steps and according to the excitation type. For the ambient vibration tests the average standard deviation value is equal to 0.46 Hz and for the random impact excitation tests the average standard deviation is equal to 0.19 Hz. This demonstrates that marginal variations for the frequency values are found on both types of excitation.

Table 4.6 – Resonant frequencies for the ambient vibration measurements [Hz].

Test	Ambient Temp.	Surface Temp.	Relative Humidity	Mode 1	Mode 2	Mode 3	Mode 4	Mode 5	Mode 6
1	15.2	16.0	43.1	35.315	66.936	71.797	125.491	139.439	174.652
2	16.1	16.2	45.0	35.334	67.975	71.893	126.565	139.736	174.129
3	16.7	16.8	46.0	35.369	66.825	71.551	125.080	139.529	173.204
4	17.0	17.7	46.8	35.133	67.694	71.870	125.146	139.548	173.651
5	16.1	17.4	46.7	35.376	67.870	71.824	125.054	139.392	173.508
6	15.1	16.8	46.6	–	–	–	–	–	–
7	14.6	16.6	46.0	35.318	66.932	71.660	124.874	139.461	173.106
8	14.1	16.5	46.2	35.608	66.182	71.414	124.960	139.405	173.375
9	13.4	15.8	46.0	35.430	66.393	71.750	125.455	139.766	173.712
Average	15.4	16.6	45.8	35.360	67.101	71.720	125.328	139.535	173.667
σ	1.2	0.6	1.2	0.132	0.675	0.167	0.546	0.144	0.511
CV [%]	7.9	3.7	2.5	0.374	1.005	0.233	0.435	0.104	0.294

Table 4.7 – Resonant frequencies for the random impact excitation measurements [Hz].

Test	Ambient Temp.	Surface Temp.	Relative Humidity	Mode 1	Mode 2	Mode 3	Mode 4	Mode 5	Mode 6
1	15.2	16.0	43.1	35.178	66.936	70.762	123.861	138.435	172.521
2	16.1	16.2	45.0	35.144	67.975	70.971	124.147	138.537	172.394
3	16.7	16.8	46.0	35.018	66.825	70.817	124.025	138.382	172.405
4	17.0	17.7	46.8	35.022	67.694	70.692	123.687	138.268	171.718
5	16.1	17.4	46.7	–	–	–	–	–	–
6	15.1	16.8	46.6	35.000	67.870	70.577	123.686	138.073	171.565
7	14.6	16.6	46.0	34.973	66.932	70.627	123.958	138.370	171.728
8	14.1	16.5	46.2	35.017	66.182	70.714	124.009	138.336	172.315
9	13.4	15.8	46.0	35.001	66.393	70.856	124.105	138.365	172.925
Average	15.4	16.6	45.8	35.044	67.101	70.752	123.935	138.346	172.196
σ	1.2	0.6	1.2	0.074	0.675	0.128	0.176	0.135	0.475
CV [%]	7.9	3.7	2.5	0.212	1.005	0.181	0.142	0.097	0.276

Table 4.8 presents the coefficients of determination r^2 between environmental effects and the resonant frequencies. The values are lower than 0.6, demonstrating the poor correlation between rapidly changing environmental effects and dynamic properties.

Table 4.8 – Coefficients of determination.

Mode	Ambient Excitation			Random Impact Excitation		
	Ambient Temp.	Surface Temp	Relative Humidity	Ambient Temp.	Surface Temp	Relative Humidity
1	0.323	0.067	0.025	0.057	0.203	0.130
2	0.525	0.306	0.014	0.304	0.082	0.270
3	0.132	0.002	0.003	0.011	0.295	0.011
4	0.055	0.012	0.130	0.100	0.348	0.082
5	0.006	0.179	0.355	0.004	0.288	0.052
6	0.000	0.199	0.067	0.103	0.596	0.004

Figure 4.21 and Figure 4.22 show the relative frequency variation due to the temperature changes for the ambient and random impact excitation, respectively. The very low changes in the dynamic response and the thermal inertia effect reducing the surface temperature amplitude are confirmed.

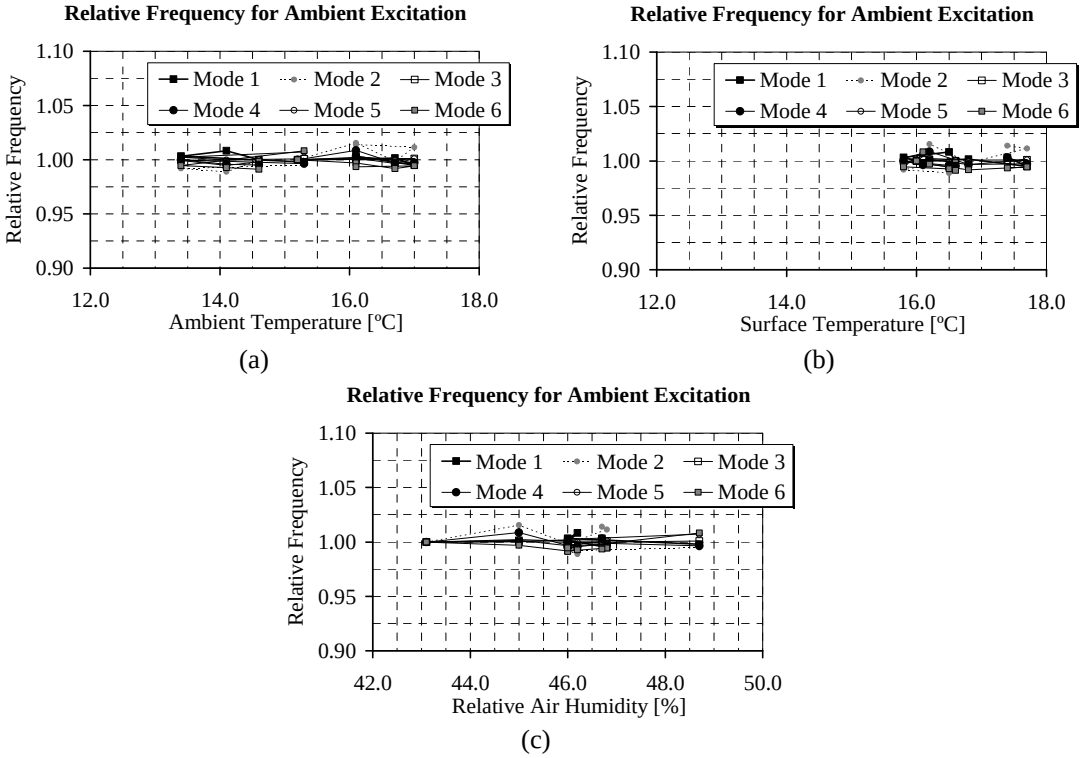


Figure 4.21 – Frequency relative variation for the ambient excitation: (a) with ambient temperature; (b) with surface temperature; and (c) with the relative air humidity.

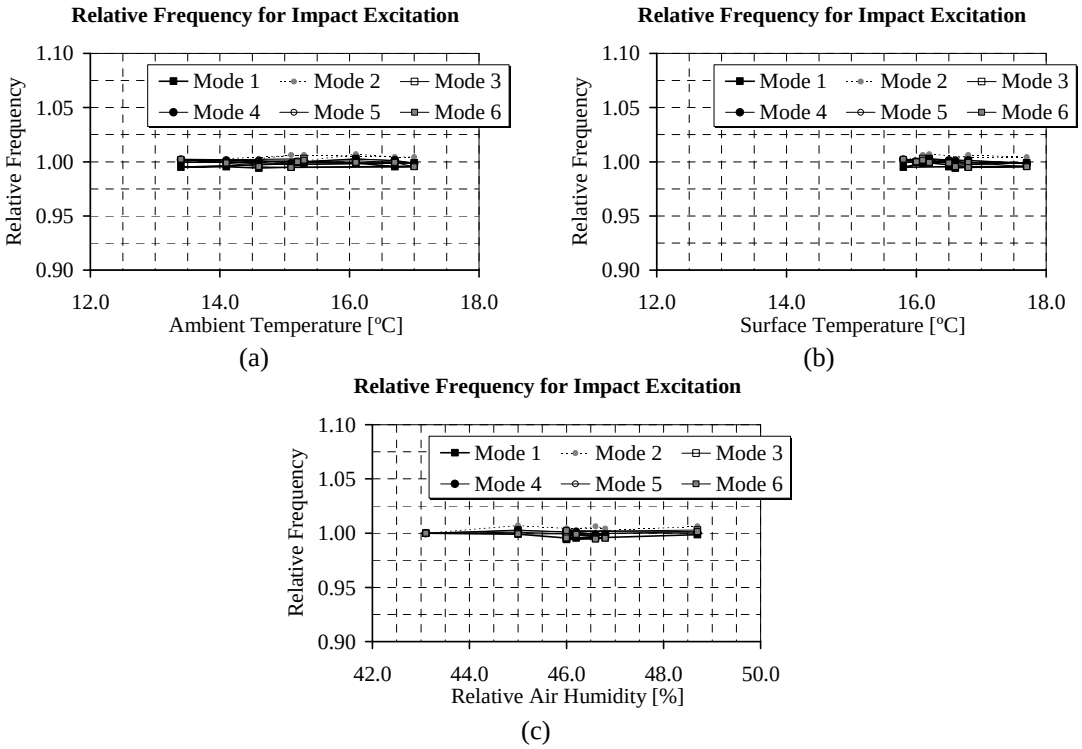


Figure 4.22 – Frequency relative variation for the random impact excitation: (a) with ambient temperature; (b) with surface temperature; and (c) with the relative air humidity.

From Figure 4.21 and Figure 4.22 it was possible observe that the rapidly changes of the environmental effects inside the laboratory can be neglected, as the relative frequency variation is less than 2%. These tests also show the reliability and repetitivity of the frequency measurements, with CV values lower than 1% (see also Table 4.6 and Table 4.7).

Additional confirmation of the results reliability is through the almost unit values for the diagonal MAC values between the modes shape of first temperature test and the following ones, presented in Table 4.9 and Table 4.10 for the ambient and random excitation, respectively.

Table 4.9 – Diagonal MAC values for the ambient excitation measurements (compared with Test 1).

	Test 2	Test 3	Test 4	Test 5	Test 7	Test 8	Test 9
Mode 1	1.00	1.00	1.00	1.00	1.00	1.00	1.00
Mode 2	1.00	1.00	1.00	1.00	1.00	1.00	1.00
Mode 3	1.00	1.00	1.00	0.99	1.00	1.00	1.00
Mode 4	1.00	1.00	1.00	0.95	1.00	1.00	1.00
Mode 5	0.98	0.99	0.99	0.92	0.99	0.99	1.00
Mode 6	1.00	1.00	1.00	0.97	1.00	1.00	0.98

Table 4.10 – Diagonal MAC values for the random impact excitation measurements (compared with Test 1).

	Test 2	Test 3	Test 4	Test 6	Test 7	Test 8	Test 9
Mode 1	1.00	1.00	1.00	1.00	1.00	1.00	1.00
Mode 2	1.00	1.00	1.00	1.00	1.00	1.00	1.00
Mode 3	1.00	1.00	1.00	1.00	1.00	1.00	1.00
Mode 4	1.00	1.00	1.00	1.00	1.00	1.00	1.00
Mode 5	1.00	1.00	1.00	1.00	1.00	1.00	1.00
Mode 6	1.00	1.00	1.00	1.00	1.00	1.00	1.00

About the influence of the long-term changes of the environmental effects, Figure 4.23 presents the average values calculated for each group of test setups for the dynamic identification of each DS. The temperature values were around 16ºC with almost no variation along the three months of damage tests. However, a significant variation for the relative air humidity was observed. The humidity amplitude value was the double of the amplitude during the environmental tests and with a total mean value equal to 51%. Although the amplitude was much larger in this case, it is expected for values of that order that the dynamic response of the arch do not change significantly. To conclude, it is assumed that the environmental effects inside the laboratory can be neglected in the later damage identification analysis.

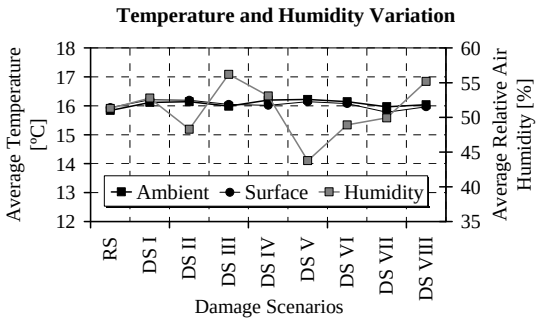
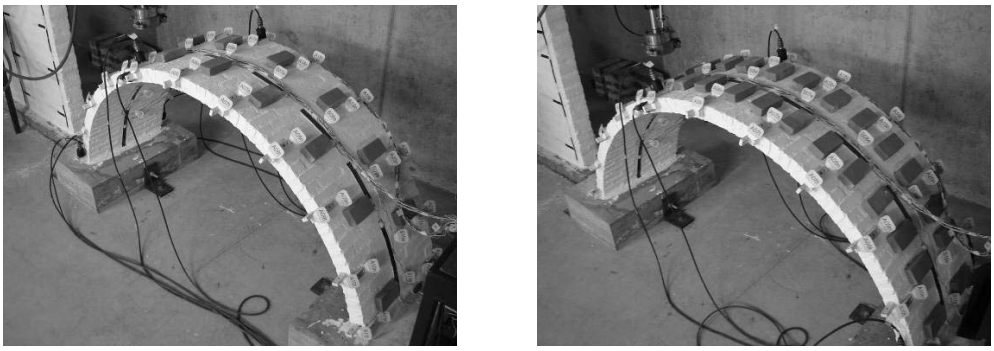


Figure 4.23 – Average environmental effects along the damage scenarios.

4.5.4 Mass Scaled Tests

Damage identification methods may require mass-scaled modes. As the system identification is to be carried out with output-only techniques, the method suggested by Parloo et al. (2002) was adopted to scale the mode shapes.

Two tests were performed with approximately 5 and 10% of added masses uniformly distributed along the arch, see Figure 4.24. The masses were materialized by adding bricks to the top of the arch. Plasticine (modeling clay) was placed between the bricks and the arch to avoid noise contamination in the signals.



(a) (b)

Figure 4.24 – Tests for scaling the mode shapes: (a) and (b) with 5 and 10% of added masses, respectively.

The method developed by Parloo et al. (2002) calculates the scale factors assuming that the shifts in frequencies are small and the modes shapes do not change significantly with the added masses. Therefore, the scale factor α^m for each mode j can be calculated by the following expression:

$$\alpha^m{}_j \approx \sqrt{-\frac{2\Delta\omega_j}{\omega_j \sum_{i=1}^{N} \varphi_{i,j}^T \; \Delta \boldsymbol{M}_i \; \varphi_{i,j}}} \tag{4.1}$$

where ω_j are the frequencies, φ_j are the un-scaled mode shapes, $\Delta\boldsymbol{M}$ is the added mass matrix calculated using the added masses in the structure, and N the number of mass changes used.

The results of this technique are presented in Table 4.11. The differences between the scale factors are lower than 14%, on average. Lower differences may be found for the case of randomly impact excitation, indicating that the structure was properly excited. It should be stressed here that for the correct scale factors calculation all the degrees of freedom should be measured to obtain the correct values. For the case of the arch model, only the in plane directions were measured, and therefore the results might be close to the real values only when the modes have manly in plane mode shape components (modes 1, 3, 4, 6 and 7).

Table 4.11 – Comparison with the scaled factors.

Mode Shape	Ambient Excitation			Randomly Impact Excitation			5% Mass	10% Mass
	5% Mass	10% Mass	Diff. [%]	5% Mass	10% Mass	Diff. [%]	Diff. [%]	Diff. [%]
1	0.0969	0.1022	–5.47	0.1147	0.1109	3.31	–18.37	–8.51
2	0.2025	0.2132	–5.28	0.2333	0.2316	0.73	–15.21	–8.63
3	0.2592	0.2433	6.13	0.2357	0.2235	5.18	9.07	8.14
4	0.1492	0.1447	3.02	0.1352	0.1371	–1.41	9.38	5.25
5	0.2161	0.2016	6.71	0.1826	0.1783	2.35	15.50	11.56
6	0.1134	0.1367	–20.55	0.1213	0.1240	–2.23	–6.97	9.29
7	0.0969	0.1022	–5.47	0.1147	0.1109	3.31	–18.37	–8.51
Average			| 7.52 |			| 2.65 |	| 13.27 |	| 8.56 |

4.6 Conclusions

This Chapter describes a masonry arch model adopted in the thesis for damage identification analysis and all the experimental tests carried out in the laboratory. Several damage scenarios were imposed to the arch by load increasing static tests. After each static test, dynamic identification tests were performed with the aim of using the modal parameters in the subsequent dynamic based damage identification analysis. Issues addressed here includes the preliminary numerical analysis for definition of possible crack locations and expected mode shapes and frequency range of interest, the arch static and dynamic tests with progressive and controlled damage scenarios, a series of dynamic tests to study the environmental effects in the arch response, and a final series of tests to scale the mode shapes with added masses.

The preliminary numerical analyses using a finite element model significantly contributed to estimate the arch structural response and for the planning of static and dynamic tests.

In the static tests eight damage scenarios were induced by controlled loads. The damage in the specimen was characterized by four cracks, very difficult to visualize. For this reason, it was not possible to register the crack sequence, although the static response exhibits an evident decrease of stiffness.

After each static test, a system identification test campaign with output-only techniques was carried out. The dynamic test planning was discussed in detail, including the sensors selection and location, the data acquisition system and the place in the laboratory for the execution of the tests. Accelerations and strains were measured in the specimen, and the strains were used to directly estimate the modal curvatures.

Two different types of excitation were used in the dynamic tests: ambient noise inside the laboratory and random impact excitation in time and in space. The reasons to use these excitations were that it was intended to study if damage could be identified with ambient excitations only and that with ambient excitations it was not possible to estimate the curvatures mode shapes from the measured strains.

For the dynamic identification of the undamaged condition (reference scenario), two stochastic subspace identification techniques, implemented in two different software tools, were used to qualitatively validate the experimental data. No significant differences were found between the results from the two tools, indicating that the modal parameters to be used in the damage analysis were estimated accurately.

Concerning the frequencies and mode shape values, no significant differences were found between the two different excitations. The analyses performed indicated that the first six mode shapes of the structure were well estimated, and can be used in the dynamic based damage identification analysis.

In the case of damping values, the results from the random impact excitation tests have lower coefficients of variation, but still the damping results need to be considered as less accurate results. The damping values depend on the excitation mechanism and on nonlinear phenomena, therefore they should be carefully used as qualitatively indicators for damage identification analysis.

The modal curvatures were accurately estimated for the case of random impact excitation. Therefore, they can be used for damage identification if the Euler-Bernoulli hypotheses are assumed. In this case, the bending and normal stiffness are directly related to the curvatures and the average strains in the arch, respectively.

To study the possible environmental influence inside the laboratory, a series of dynamic tests varying the ambient temperature were carried out before the application of damage scenarios. During the tests, the air temperature, the surface temperature of the structure and the relative air humidity were measured, but no influence or correlation could be found between the rapidly changing environmental effects and the dynamic response.

Finally, a method to scale the mode shapes to the mass matrix was adopted experimentally. The method solves the problem that output-only system identification techniques do not provide mass-scaled modes. By adding controlled masses to the structure it is possible to scale the modes with output-only techniques by comparing the two conditions. The results from a series of tests with the arch in its undamaged condition indicated that modes can be scaled with 5% of added masses uniformly distributed, if the structure is well excited. This method is useful when scaled modes are required for damage identification analysis.

Chapter 5
Damage Identification in the Arch Model

Abstract

This Chapter presents the damage identification analysis of the arch model. In a first step, an approach to identify the damage based on vibration signatures is addressed. For this purpose, numerical simulations of crack arch were adopted instead of the experimental data. The numerical simulation consists of three different finite element models, where cracks are incorporated by different procedures. Subsequently, damage identification methods were applied to the experimental data. The damage identification analysis was divided in three groups: global dynamic parameters, non-model based methods and the finite model updating method. Finally, the conclusions emerging from the damage analyses are presented.

5.1 Introduction

Historical masonry structures are built with materials exhibiting significant variations in properties and internal structure, and have a complex geometry. Therefore, the selection of appropriate models for structural analysis is delicate (Lourenço, 2001). The combination of quantitative methods with qualitative approaches is necessary, where the experience of the analyst is of much relevance, Binda and Saisi (2001). Different structural models provide different answers and not fully coincident results, Lourenço (2001), EU-India (2006), which is not necessarily a major concern. The existence of a group of methods should be understood as an added value in capturing difficult phenomena and in assisting the decision process.

In this context, an approach for damage identification is presented next using a series of numerical simulations to evaluate its applicability to the arch model. After the simulations, the approach is applied to the experimental results from the arch damage tests. Finally, the conclusions of the damage analyses are presented.

5.2 Proposed Approach

Based on the previous Chapters, a group of methods was selected for damage identification analysis. A first issue is to study the applicability of the methods to masonry-like structures. A second issue is to obtain a wide perspective of the problem and conclusions on damage identification, taking into account that different methods provide different results. If significant damage is present in the structure, the results provided from different methods would converge in the identification, giving more confidence to the analyst. It is noted that the present approach is a part of the third phase proposed in the framework of monitoring historical masonry structures, addressed in Chapter 3.

The methods will be used in a different and stepwise approach, according to the levels of the damage identification process presented in Chapter 3. From the point of view of the applicability of dynamic based identification methods to masonry-like structures, the aspects under consideration are the possibilities of detection (Level 1), localization (Level 2) and assessment (Level 3).

5.2.1 Selected Methods

The selected methods for validation and comparison are:

- The Unified Significance Indicator (USI);
- The COMAC values;
- The Parameter Method (PM);
- The Mode Shape Curvature Method (MSCM);
- The Damage Index Method (DIM);
- The Sum of all Curvature Errors method (SCE);
- The Changes in Flexibility Matrix method (CFM);

- The Finite Element Model Updating method (FEMU).

With exception of USI, all methods have one common aspect; they all use spatial modal information of the structure, through mass-scaled or non-scaled mode shapes ϕ and φ, respectively (or/and through mass-scaled or non-scaled curvatures mode shapes ϕ'' and φ'', respectively).

For convenience, the expressions of each method, already introduced in Chapter 3, are again repeated with brief details.

The USI will be used as a Level 1 approach, together with the analysis of the changes in the global modal quantities (e.g. frequencies ω, damping ξ, MACs, and NMDs). The USI is presented in Eq.(5.1), where the standard deviation σ_ω for both undamaged and damaged conditions will be extracted from the stochastic modal estimation results. Here, it is noted that the subscript *u* refers to undamaged state and the subscript *d* refers to damaged state.

$$USI = \sum_{j=1}^{m} \left(S_f\right)_j \quad \text{with} \quad \left(S_f\right)_j = \frac{\omega_j^u - \omega_j^d}{\sqrt{\left(\sigma_\omega^u\right)_j^2 + \left(\sigma_\omega^d\right)_j^2}} \tag{5.1}$$

For the Level 2 approach, all the others methods will be used. The COMAC values of each degree of freedom will be calculated for displacement mode shapes and curvature mode shapes, by the following expressions:

$$COMAC^{\varphi}{}_{i,u,d} = \frac{\left|\sum_{j=1}^{m} \varphi_{i,j}^u \, \varphi_{i,j}^d\right|^2}{\sum_{j=1}^{m}\left(\varphi_{i,j}^u\right)^2 \sum_{j=1}^{m}\left(\varphi_{,ji}^d\right)^2} \quad \text{and} \quad COMAC^{\varphi''}{}_{i,u,d} = \frac{\left|\sum_{j=1}^{m} \varphi_{i,j}''^u \, \varphi_{i,j}''^d\right|^2}{\sum_{j=1}^{m}\left(\varphi_{i,j}''^u\right)^2 \sum_{j=1}^{m}\left(\varphi_{,ji}''^d\right)^2} \tag{5.2}$$

The PM will also be used with displacement and curvature mode shapes given by:

$$\Delta\varphi = \sum_{j=1}^{m}\left[\varphi_j^d\left(\frac{\omega_j^u}{\omega_j^d}\right) - \varphi_j^u\right] \quad \text{and} \quad \Delta\varphi'' = \sum_{j=1}^{m}\left[\varphi_j''^d\left(\frac{\omega_j^u}{\omega_j^d}\right) - \varphi_j''^u\right] \tag{5.3}$$

where curvature PM seems to be more sensitive to damage than the equivalent parameter computed using displacements.

The MSCM will be calculated by the following expression:

$$\Delta\varphi'' = \sum_{j=1}^{m}\left|\varphi_{d,j}'' - \varphi_{u,j}''\right| \tag{5.4}$$

with the unslaced curvature mode shapes φ''_d and φ''_u in the same scale, and the Sum of all Curvature Errors method (SCE) will be calculated by:

$$SCE = \sum_{j=1}^{m}\left|\frac{\left(\varphi_{d,j}'' - \varphi_{u,j}''\right)}{\varphi_{u,j}''}\right| \tag{5.5}$$

For the DIM the expressions are the following:

$$Z_i = \left(\beta_i - \overline{\beta}_i\right)/\sigma_i \quad , \quad \text{with} \quad \beta_i = \sum_{j=1}^{m}\beta_{i,j} \ \text{ and} \tag{5.6}$$

$$\beta_{i,j} = \frac{\left[\int_a^b \left(\varphi_j^{d\,''}(x)\right)^2 dx + \int_0^L \left(\varphi_j^{d\,''}(x)\right)^2 dx\right]}{\left[\int_a^b \left(\varphi_j^{u\,''}(x)\right)^2 dx + \int_0^L \left(\varphi_j^{u\,''}(x)\right)^2 dx\right]} \cdot \frac{\int_0^L \left(\varphi_j^{u\,''}(x)\right) dx}{\int_0^L \left(\varphi_j^{d\,''}(x)\right) dx} \tag{5.7}$$

To achieve also a Level 3 approach, the CFM will be applied and a variant for the modal curvatures will be calculated. In this case, the index β_i will be computed as follows:

$$\beta_i = diag\left\{\boldsymbol{F}^{d} - \boldsymbol{F}^{u}\right\} \quad \text{with} \quad \boldsymbol{F} = \sum_{j=1}^{m} \frac{1}{\omega_j^2}\,\phi_j\,\phi_j^T \quad \text{or} \quad \boldsymbol{F} = \sum_{j=1}^{m} \frac{1}{\omega_j^2}\,\phi_j''\,\phi_j''^T \tag{5.8}$$

The last method to be considered will be the FEMU as a Level 2 and 3 approache. The Finite Element (FE) package DIANA (2006) will be used to estimate the numerical modal parameters require in an objective function π including frequency and mode shape information, as follows:

$$\pi = \frac{1}{2}\sum_{j=1}^{m}\left[W_\omega\left(\frac{\omega_j^2 - \omega_{j,\exp}^2}{\omega_{i,\exp}^2}\right)^2 + W_\varphi\left(\varphi_j - \varphi_{j,\exp}\right)^2\right] \tag{5.9}$$

The FEMU will be used in a two-step approach: first, a band of elements with different Young's modulus around the measuring points will be used to globally localize the damage (see Figure 5.1a). With the eleven sets of elements adopted, the updating parameters will be the respective Young's modulus with adequate ranges.

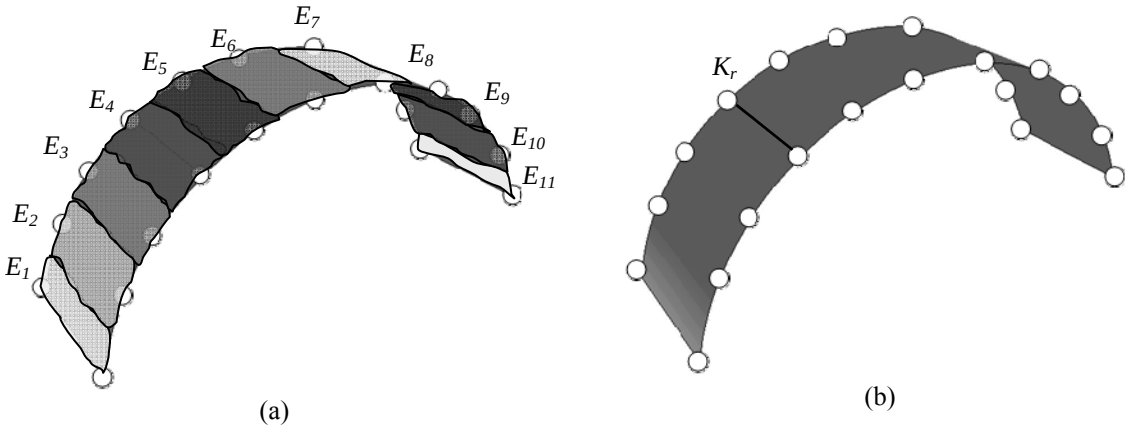


Figure 5.1 – Two step FEMU approach: (a) global updating analysis; and (b) local updating analysis.

To better localize the damage the Young's modulus at each set of element *k* will be normalized by the following expression:

$$Z_k = \left(E_k - \overline{E}\right) / \sigma_E \tag{5.10}$$

where $\overline{E}$ is the average value for all Young's modulus and σ_E is the standard deviation. The areas with *Z* values higher than 2 will be considered as possible damage location (Level 2), similar to values adopted in the DIM by Stubbs et al. (1992).

Afterwards, as a second step, if a selected area is pin-pointed as a damage location, a subsequent updating analysis will be carried out with local rotational spring elements in a single line to better simulate a localized crack (see Figure 5.1b). In this second updating analysis the stiffness of the springs K_r will be the updating parameter, expected to give information about the damage extension (Level 3).

The above methods were chosen because they require similar modal quantities: frequencies and/or mode shapes and/or modal curvatures. Table 5.1 presents the list of selected methods, the expected level to attain and the type of information required.

Table 5.1 – Selected damage identification methods.

Method	Expected Damage Level	Comparison to a Reference Scenario	Modal Information				
			ω	φ	φ''	ϕ	ϕ''
Unified Significance Indicator (USI)	Level 1	Yes	•				
COMAC	Level 2	Yes		○	○	○	○
Parameter Method (PM)	Level 2	Yes	•	○	○	○	○
Mode Shape Curvature Method (MSCM)	Level 2	Yes			○		○
Damage Index Method (DIM)	Level 2	Yes			○		○
Sum Curvature Errors method (SCE)	Level 2	Yes			○		○
Change in Flexibility Matrix method (CFM)	Level 2 and 3	Yes	•			•	○
Finite Element Model Updating (FEMU)	Level 2 and 3	No	○	○	○	○	○

○ – Optional; • – Required.

5.2.2 Calculation of the Modal Curvatures

Modal curvatures, if not measured experimentally, can be calculated from the derivatives of the modal displacements. In the case of a curved beam (see Figure 5.2), it is necessary to take into account the initial curvature $1/R$ in order to have accurate results, where R is the radius of curvature.

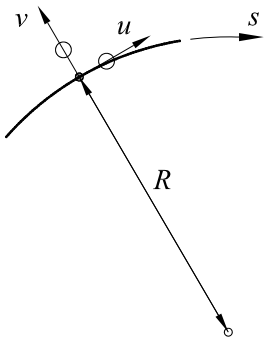


Figure 5.2 – Variables for the curvature calculation in the case of a curved beam.

The rotations ψ at a certain point are related with the normal v and tangential u displacements by:

$$\psi = \frac{u}{R} + \frac{dv}{ds} \tag{5.11}$$

and the curvatures κ are given by:

$$\kappa = \frac{d\psi}{ds} = \frac{du}{ds} \cdot \frac{1}{R} + \frac{d^2v}{ds^2} \tag{5.12}$$

In the above relations it is necessary to know the first and second derivatives of the tangential and normal displacements, which can be numerically calculated by the central difference theorem, or the second order approximation, as:

$$\psi_i = \varphi_i' \approx \frac{\varphi_{i+1} - \varphi_{i-1}}{2\Delta L} \quad \text{and} \quad \kappa_i = \varphi_i'' \approx \frac{\varphi_{i+1} - 2\varphi_i + \varphi_{i-1}}{(\Delta L)^2} \tag{5.13}$$

where ΔL is equal to the distance between the points i and $i + 1$.

It is noted that, in order to reduce the errors in the numerical calculations, the derivatives can be approximated with a quadratic polynomial or fourth order approximation, as:

$$\psi_i = \varphi_i' \approx \frac{-\varphi_{i+2} + 8\varphi_{i+1} + 8\varphi_{i-1} + \varphi_{i-2}}{12\Delta L} \tag{5.14}$$

and

$$\kappa_i = \varphi_i'' \approx \frac{-\varphi_{i+2} + 16\varphi_{i+1} - 30\varphi_i + 16\varphi_{i-1} - \varphi_{i-2}}{12(\Delta L)^2} \tag{5.15}$$

To study the performance of the different order approximations, their results were compared with the theoretical values of a straight Euler-Bernoulli beam. Two different support conditions were considered: simply supported and fully supported. Rotations and curvatures were calculated in 11 points, which is the same number of measuring points of the arch. For convenience, a beam length L = 1 m, a bending stiffness EI = 1 kNm^2, and a uniformly distributed load equal to 1 kN/m were considered. The theoretical and the numerical results for rotations and curvatures are presented in Figure 5.3 for simply and fully supported beams.

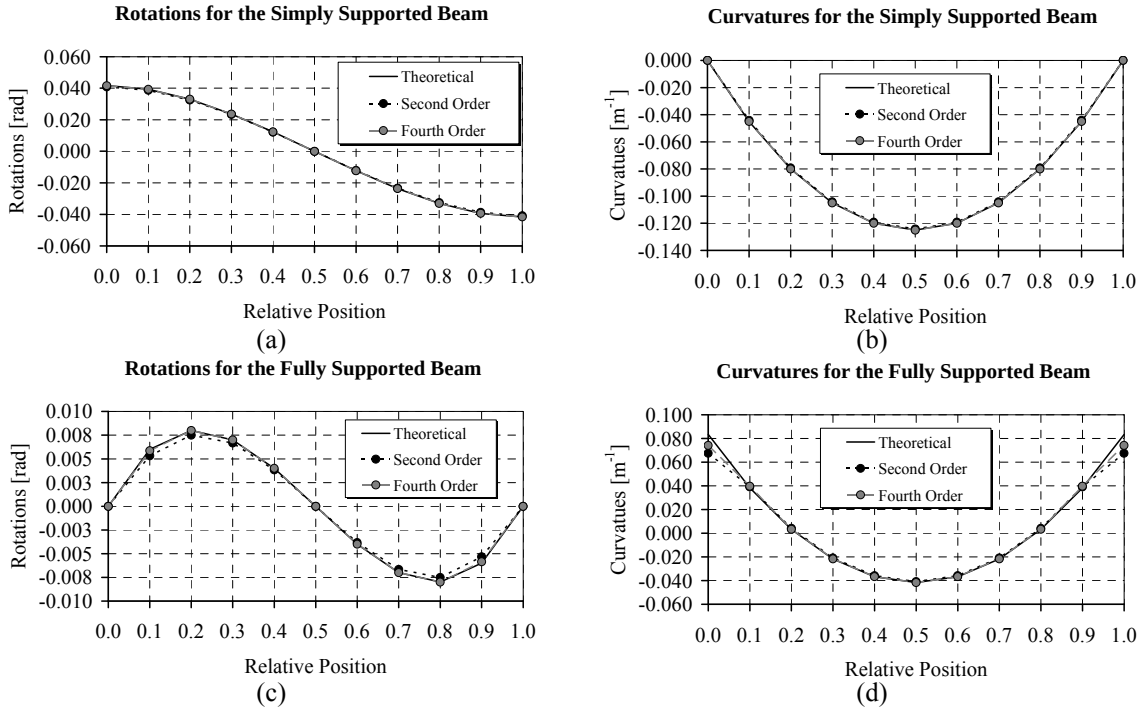


Figure 5.3 – Theoretical and approximation results for a simply and fully supported beam: (a) rotations; and (b) curvatures.

Figure 5.4 presents the comparison between the relative errors for rotations and curvatures for the beams. In general, the simply supported case has neglectable errors

(lower than 2%) and better results because the number of points used are the double of the points used in the fully supported beam, i.e. the fully supported beam is equivalent to a simply supported beam with $L/2$. The fourth order approximation is indeed the one with lowest relative errors and better approximation. In the fully supported case, the errors are considerable (up to 25%), particularly in the case of the curvatures, meaning that the 11-point resolution is insufficient for a second order approximation. Taking into account the results, the fourth order approximation in ΔL will be used to calculate the modal curvatures when judged necessary.

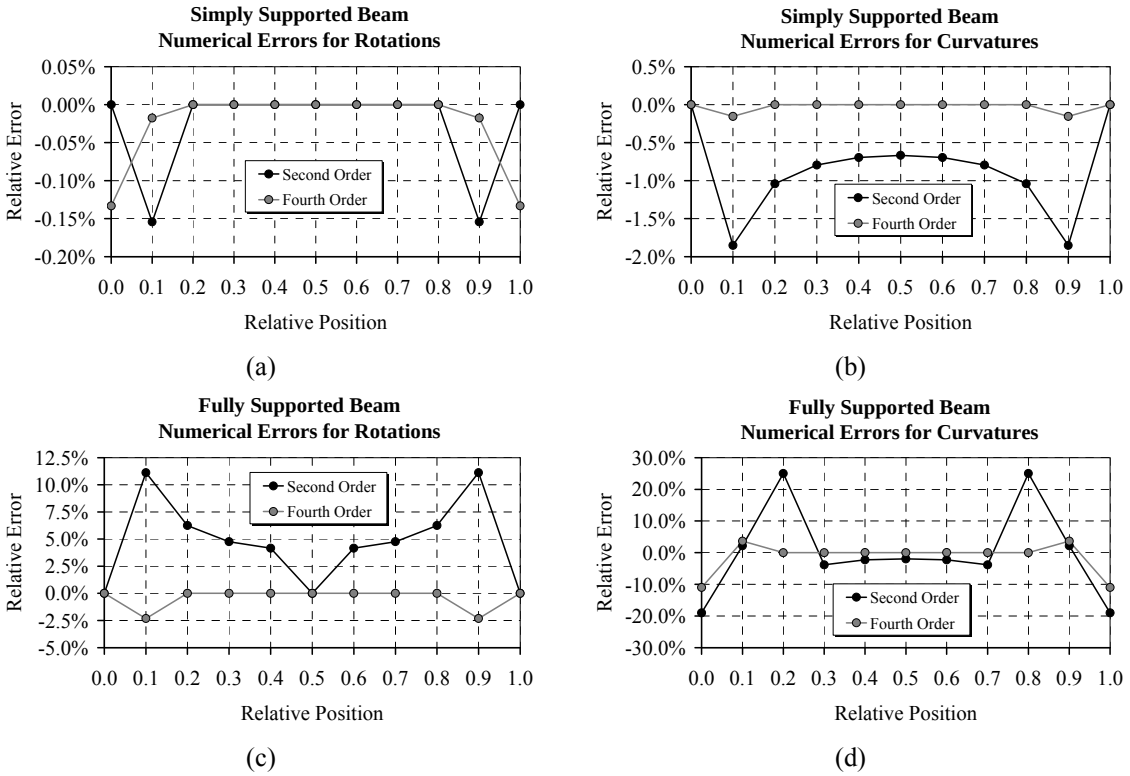


Figure 5.4 – Results comparison: (a) and (b) for the simply supported beam; and (c) and (d) for the fully supported beam. Note that the vertical scale is not constant.

5.3 Preliminary Model Updating Analysis

Before the application of the selected damage methods to the numerical damage simulations, one model updating analysis was performed with the aim to assess the arch dynamic behavior in its undamaged condition or Reference Scenario (RS). This task was carried out as a first approach to understand the real arch dynamic behavior. A nonlinear least square method implemented in MatLab (2006), function `lsqnonlin`, was used to minimize the objective function π, composed by the residuals formed by the relative error between the numerical and experimental frequencies and the difference between the numerical and experimental mode shapes, given by:

$$\pi = \frac{1}{2}\left[\sum_{j=1}^{m_\omega} W_{\omega,j}\left(\frac{\omega_j^2 - \omega_{j,\exp}^2}{\omega_{j,\exp}^2}\right)^2 + \sum_{j=1}^{m_\varphi}\left(\varphi_j - \varphi_{j,\exp}\right)^2\right] \tag{5.16}$$

where m_ω denotes the number of eigen frequencies taken into account, m_φ is the number of normalized eigen modes to taken into account and $W_{\omega,j}$ is a weighting diagonal matrix for

the frequency values, which introduces the uncertainties in the measurements (only for frequency estimation), a variant of what was proposed by Friswell and Mottershead (1995), given by:

$$W_{\omega,j} = \left[diag\left(CV_1, CV_2, ..., CV_m\right)\right]^{-1} \tag{5.17}$$

where CV is the coefficient of variation ($CV_i = \sigma_i / \omega_i$) calculated with the standard variation obtained from the several tests setups on the system identification analysis. In Eq.(5.16) experimental and numerical mode shapes are normalized, in a way that the maximum real value of the modal displacement is equal to one, in order to be comparable with the residuals from the frequency values normalized by the experimental results.

The selection of the optimization parameters was carried out taking into account the geometrical survey of the arch in its virgin state. Different optimization analyses were performed by changing the range updating parameters, including boundary conditions, geometrical imperfections and orthotropic behavior for masonry material. The best analysis has ten updating parameters described in Figure 5.5 and Table 5.2, and the objective function has 4 eigen frequencies and 6 eigen modes ($m_\omega = 4$ and $m_\varphi = 6$). In this analysis the total global geometry of the model depends on the geometrical position of updating parameters $P2_x$, $P3_z$, $P4_x$, $P6_x$, $P7_z$ and $P8_x$, and the supports were considered fully constrained. The experimental results to tune were the RS with ambient vibration calculated with ARTeMIS software (SVS, 2006), presented in Chapter 4. For all the analysis, the tolerance for the residuals and the updating parameters in the objective function was equal to 1.0×10^{-6} and the Jacobian increment was equal to 1%. Sensible constraints were applied to the geometrical updating parameters in order to avoid unrealistic results for the final values.

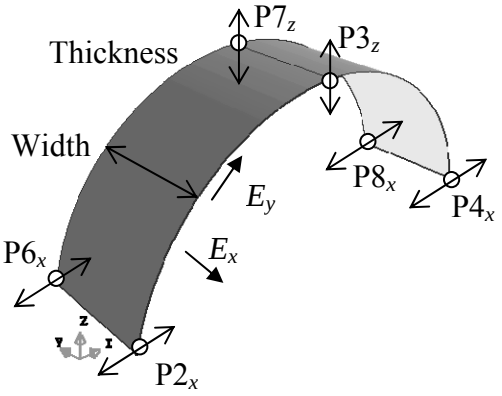


Figure 5.5 – Updating parameters.

Table 5.2 – Updating parameters and initial, possible range and final values.

Updating Parameters	Initial Values	Lower Bound	Upper Bound	Final Values	Difference [%]
E_y [GPa]	3.9000	0.1950	6.4740	3.7901	–2.82
$P2_x$ [m]	–0.7625	–0.7473	–0.7778	–0.7475	–1.97
$P4_x$ [m]	0.7625	0.7473	0.7778	0.7652	+0.35
$P3_z$ [m]	0.7625	0.7473	0.7778	0.7775	+1.97
$P6_x$ [m]	–0.7650	–0.7497	–0.7803	–0.7678	+0.37
$P8_x$ [m]	0.7650	0.7497	0.7803	0.7799	+1.95
$P7_z$ [m]	0.7650	0.7497	0.7803	0.7498	–1.99
Thickness [m]	0.0480	0.0408	0.0504	0.0501	+4.37
E_x/E_y	1.0000	0.5000	1.5000	1.1272	+12.72
Width [m]	0.4500	0.4410	0.4590	0.4431	–1.53

One main conclusion emerging from the optimization analysis is that the arch dynamic response is very sensitive to geometry changes. The final values of the updating parameters are presented in fifth column of Table 5.2, were it is stressed that the value of 3.79 GPa for the Young's modulus in the *y* direction and the orthotropic properties for the material are essential to attain good results. The differences between the final and the initial values are rather small, as can be seen in the last column of Table 5.2.

Other results of the updating analysis are presented in Figure 5.6, in Figure 5.7, and Table 3.3. Figure 5.6a shows the global results of the MAC matrix, the NMD values, the comparison between the experimental and numerical frequencies and the residuals history of the objective function π, including the number of iterations. Figure 5.6b shows the COMAC values for all measured degrees of freedom in the front and back edges of the arch. The results seem acceptable if the complexity of the material is taken into account. The null COMAC values at positions 1 and 11 are due to the fixed constraints used in the numerical model, and, for these positions, the experimental modal results are close to zero. Figure 5.7a shows the modes shape configurations, which are in agreement with the numerical and experimental modes presented in Chapter 4. Figure 5.7b presents the differences between the experimental and the numerical mode shapes. In general, a good correspondence between the modes can be observed, although local modal components are not always well tuned, especially for higher modes. Finally, Table 3.3 presents the frequencies results, the MAC values and the NMD values for the first six modes. The maximum frequency error is 10.3% for the 6th mode shape, but for others mode shapes the maximum error is about 3%. Considering the average values for the frequency errors (3.67%), MAC values (0.91) and NMD values (0.30) the results are considered acceptable.

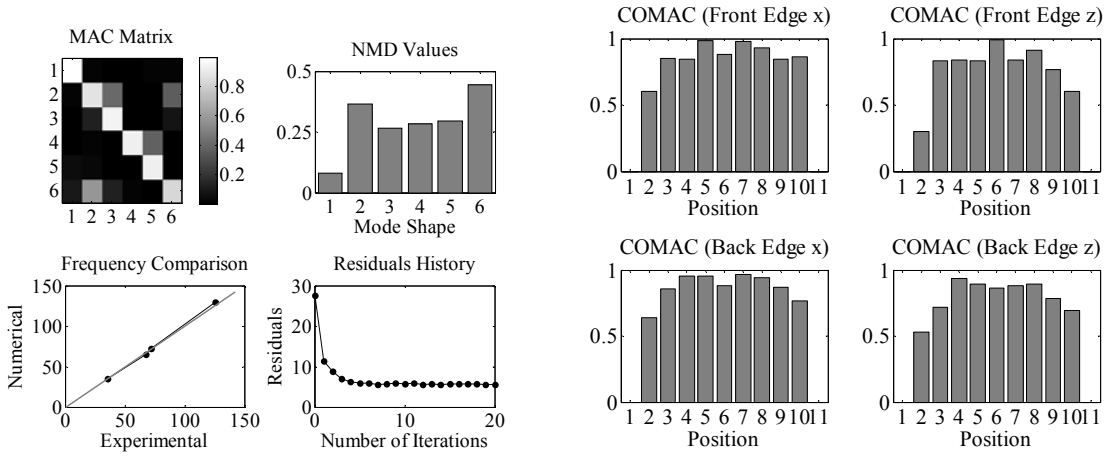


Figure 5.6 – Results from the optimization analysis: (a) MAC matrix, NMD values, frequency values comparison and residuals history; and (b) COMAC values for all the measured DOFs.

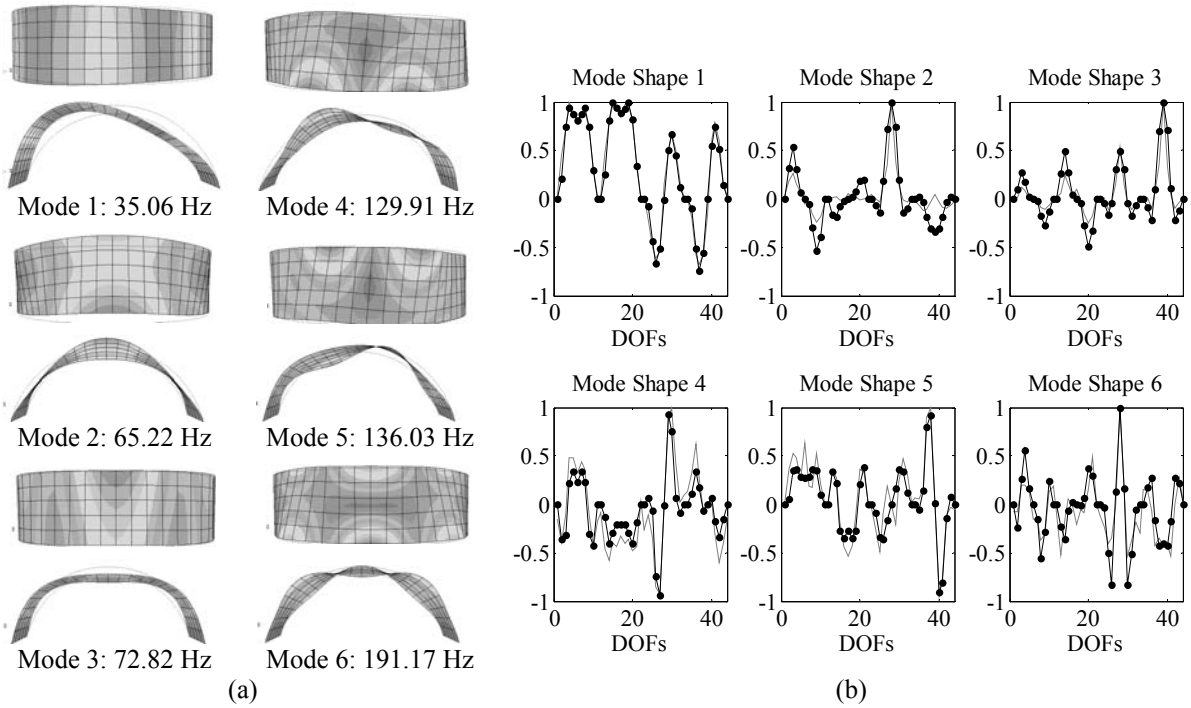


Figure 5.7 – Numerical mode shapes: (a) top and lateral views; and (b) differences between updated experimental DOFs (11 positions, time two edges times two directions), with experimental (grey line) and numerical (marker line) values.

Table 3.3 – Comparison between experimental and updated results.

Mode Shape	Experimental [Hz]	FEM [Hz]	Error [%]	MAC	NMD
1st	35.59	35.06	1.50	0.99	0.09
2nd	67.30	65.22	3.09	0.87	0.39
3rd	72.11	72.82	–0.98	0.93	0.28
4th	125.74	129.91	–3.32	0.93	0.28
5th	140.08	136.03	2.89	0.92	0.29
6th	173.38	191.17	–10.26	0.84	0.44
		Average	| 3.67 |	0.91	0.30

Another interesting observation emerging from the comparison between numerical and experimental dynamic estimation is the asymmetries for modes (see Figure 5.7) that were symmetrical in the preliminary numerical estimation presented in Chapter 4. This further indicates possible geometrical or material imperfections.

5.4 Numerical Damage Simulation and Identification

To analyze the performance of the select damage methods, crack simulations with three numerical models were studied. In Model A the crack was simulated using a line of spring elements between two opposite measuring points, in the front and back edge of the arch, see Figure 5.8a. In Model B, the crack was localized between two pairs of opposite measuring points, see Figure 5.8b, again with spring elements. In Model C, the crack was simulated by means of a Young's modulus reduction in a band of elements with 0.10 m length, see Figure 5.8c.

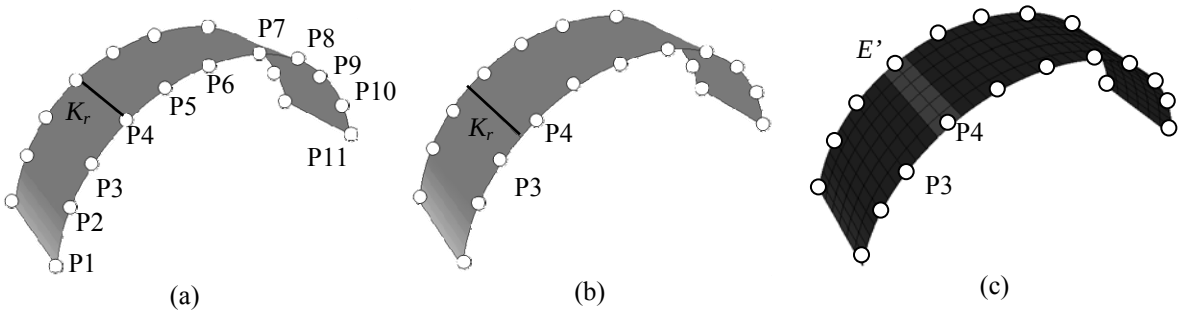


Figure 5.8 – Numerical models: (a) Model A; (c) Model B; and (c) Model C.

In models A and C the crack location was at position P4 and in model B between the positions P3 and P4 (in the real position of crack c_1 of the experimental tests, presented in Chapter 4). The aim of the two different locations in models A an B is to study if the selected methods can locate damage in the vicinity of the simulated damage, even if the measurements were not in the exact position of the simulated damage.

On each model, three different Damage Scenarios (DS_I, DS_{II}, DS_{III}) were simulated by three different crack depths. The crack depths were equal to 7.5, 15 and 30 mm, which correspond to cross section reductions of 15, 30 and 60%, respectively. Note that the arch thickness is equal to 50 mm.

The spring stiffness K_r of the models A and B was calculated from facture mechanics, Chondros et al (1998). The rotational spring flexibility F_r of a beam with a height h and with a crack depth a is given by the following expression:

$$F_r = 6\pi \left(1-\nu^2\right) h\, \Pi(\alpha) / EI \tag{5.18}$$

where ν is the Poisson ratio, EI is the beam proportional stiffness and $\Pi(\alpha)$ reads:

$$\begin{aligned}\Pi(\alpha) = {} & 0.6272\alpha^2 - 1.04533\alpha^3 + 4.5948\alpha^4 - 9.973\alpha^5 + 20.2948\alpha^6 - \\ & - 33.035\alpha^7 + 47.1063\alpha^8 - 40.7556\alpha^9 + 19.6\alpha^{10}\end{aligned} \tag{5.19}$$

Here, α is the ratio between the crack depth and the beam height ($\alpha = a/h$). Finally the spring stiffness K_r is calculated by the inverse of the flexibility F_r. For the case of the arch model, Figure 5.9 presents one abacus where it is possible to observe the stiffness decrease with the increase of crack depth, plotted in a semi-logarithm scale. An approximated linear relation can be observed for crack depths higher than 10 mm ($\alpha > 20\%$).

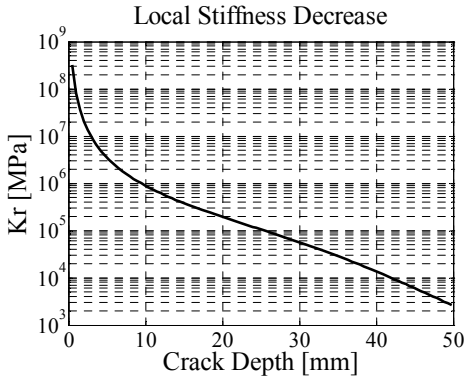


Figure 5.9 – Local stiffness decrease depending on the crack depth for the arch model.

For Model C, equivalent modulus of elasticity E' was calculated to reproduce the frequency results obtained in the model A.

Finally, it is noted that in this damage identification analysis the modal displacements used were in the same of the experimental tests, namely displacements in the normal and tangential arch directions.

5.4.1 Damage Identification without Noise

The first damage analysis was carried out considering the curvatures calculated in the middle line of the arch, exactly as they were measured in the experimental tests by strain gauges. Because DIANA (2006) does not have the option to calculate the curvatures directly from the results of the eigen problem analysis, the numerical curvatures were obtained by a static analysis where the loads were applied as prescribed displacements on each degree of freedom *i*. For every mode shape *j*, the applied prescribed displacements $\delta_{i,j}$ were proportional to resonant frequencies, with the following relation:

$$\delta_{i,j} = \varphi_{i,j} \big/ \omega_j^2 \tag{5.20}$$

5.4.1.1 Analysis with Global Parameters

Table 5.4, Table 5.5 and Table 5.6 present the global response in terms of frequencies shifts and MAC values through all the damage scenarios. The first seven modes shapes were considered and, on each DS_i, the values are compared with the RS, or the undamaged condition. In all the models, changes are significant only for the frequencies shifts in DS_{II} and DS_{III}. Frequency shifts have higher values for the first mode shape, which are in plane. Frequency shifts seem thus to be a good indicator for the presence of damage (Level 1). On the contrary, MAC values are insensitive to damage.

Table 5.4 – Global results for Model A.

Mode	RS	DS_I			DS_{II}			DS_{III}		
	ω [Hz]	Δ_ω [Hz]	Error [%]	MAC	Δ_ω [Hz]	Error [%]	MAC	Δ_ω [Hz]	Error [%]	MAC
1	35.06	–0.15	0.43	1.00	–0.60	1.74	1.00	–2.83	8.20	1.00
2	65.22	–0.01	0.02	1.00	–0.02	0.03	1.00	–0.06	0.09	1.00
3	72.82	–0.09	0.13	1.00	–0.36	0.51	1.00	–1.57	2.22	1.00
4	129.91	–0.11	0.09	1.00	–0.40	0.31	1.00	–1.51	1.17	1.00
5	136.03	–0.11	0.08	1.00	–0.41	0.31	1.00	–2.00	1.52	0.99
6	191.17	–0.24	0.13	1.00	–0.85	0.46	1.00	–3.11	1.67	0.99

Table 5.5 – Global results for Model B.

Mode	RS	DS_I			DS_{II}			DS_{III}		
	ω [Hz]	Δ_ω [Hz]	Error [%]	MAC	Δ_ω [Hz]	Error [%]	MAC	Δ_ω [Hz]	Error [%]	MAC
1	35.06	–0.15	0.43	1.00	–0.59	1.71	1.00	–2.80	8.12	1.00
2	65.22	–0.03	0.05	1.00	–0.11	0.17	1.00	–0.42	0.64	1.00
3	72.82	–0.24	0.34	1.00	–0.91	1.29	1.00	–3.77	5.32	0.99
4	129.91	–0.04	0.03	1.00	–0.14	0.11	1.00	–0.52	0.40	1.00
5	136.03	0.00	0.00	1.00	–0.02	0.02	1.00	–0.09	0.07	1.00
6	191.17	–0.34	0.18	1.00	–1.26	0.67	1.00	–4.67	2.50	1.00

Table 5.6 – Global results for Model C.

Mode	RS ω [Hz]	DS$_I$ Δ_ω [Hz]	DS$_I$ Error [%]	DS$_I$ MAC	DS$_{II}$ Δ_ω [Hz]	DS$_{II}$ Error [%]	DS$_{II}$ MAC	DS$_{III}$ Δ_ω [Hz]	DS$_{III}$ Error [%]	DS$_{III}$ MAC
1	35.06	–0.14	0.41	1.00	–0.59	1.71	1.00	–2.82	8.17	1.00
2	65.22	–0.14	0.21	1.00	–0.51	0.78	1.00	–1.77	2.71	1.00
3	72.82	–0.10	0.14	1.00	–0.42	0.59	1.00	–1.94	2.74	1.00
4	129.91	–0.20	0.15	1.00	–0.77	0.60	1.00	–3.13	2.42	1.00
5	136.03	–0.14	0.11	1.00	–0.58	0.44	1.00	–3.13	2.38	0.99
6	191.17	–0.38	0.20	1.00	–1.47	0.79	1.00	–5.99	3.21	0.99

5.4.1.2 Analysis with Non-Model Based Methods

From the selected damage methods presented in Section 5.2.1, the USI was excluded because standard variations cannot be calculated in the numerical analysis. The results for the three models (A, B, and C) and the three DS$_i$ (DS$_I$, DS$_{II}$, and DS$_{III}$) are presented in Annex A. As an example, Figure 5.10 and Figure 5.11 shows the results for Model B (crack between positions P3 and P4) and DS$_I$ (7.5 mm crack depth), which is a challenging damage analysis.

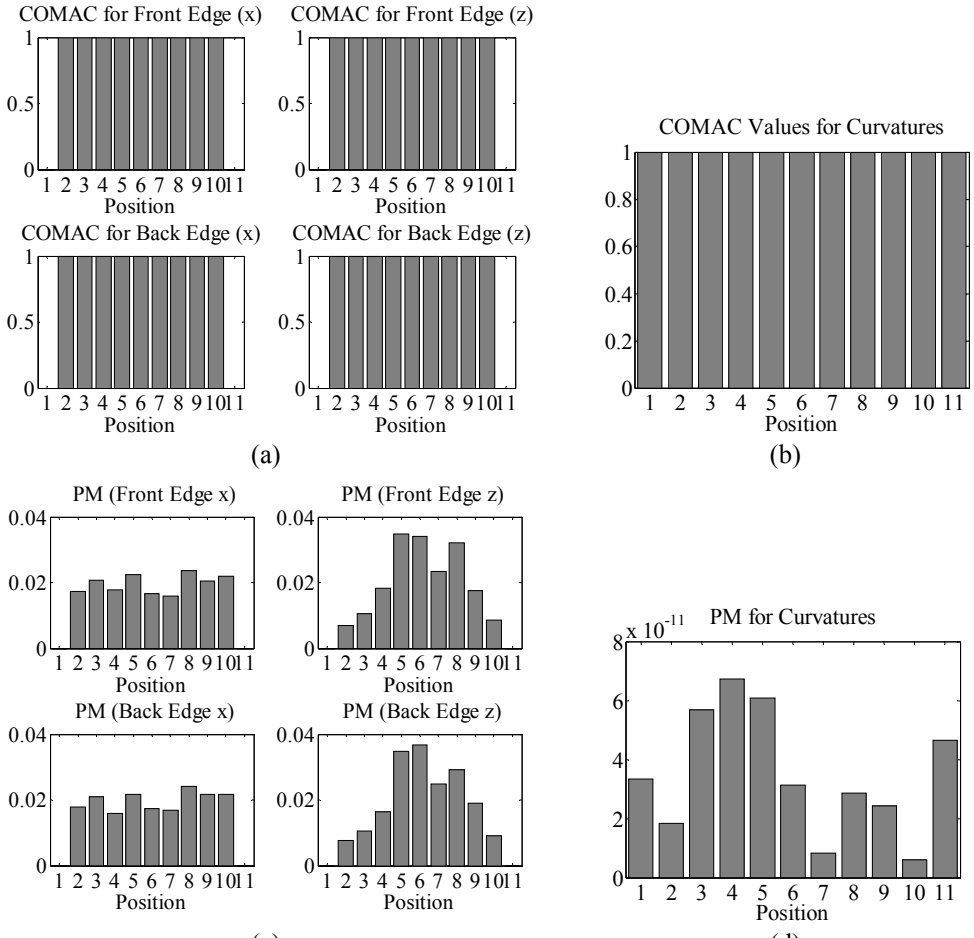


Figure 5.10 – Damage analysis of Model B for DS$_I$: (a) and (b) COMAC for curvatures; (c) and (d) PM.

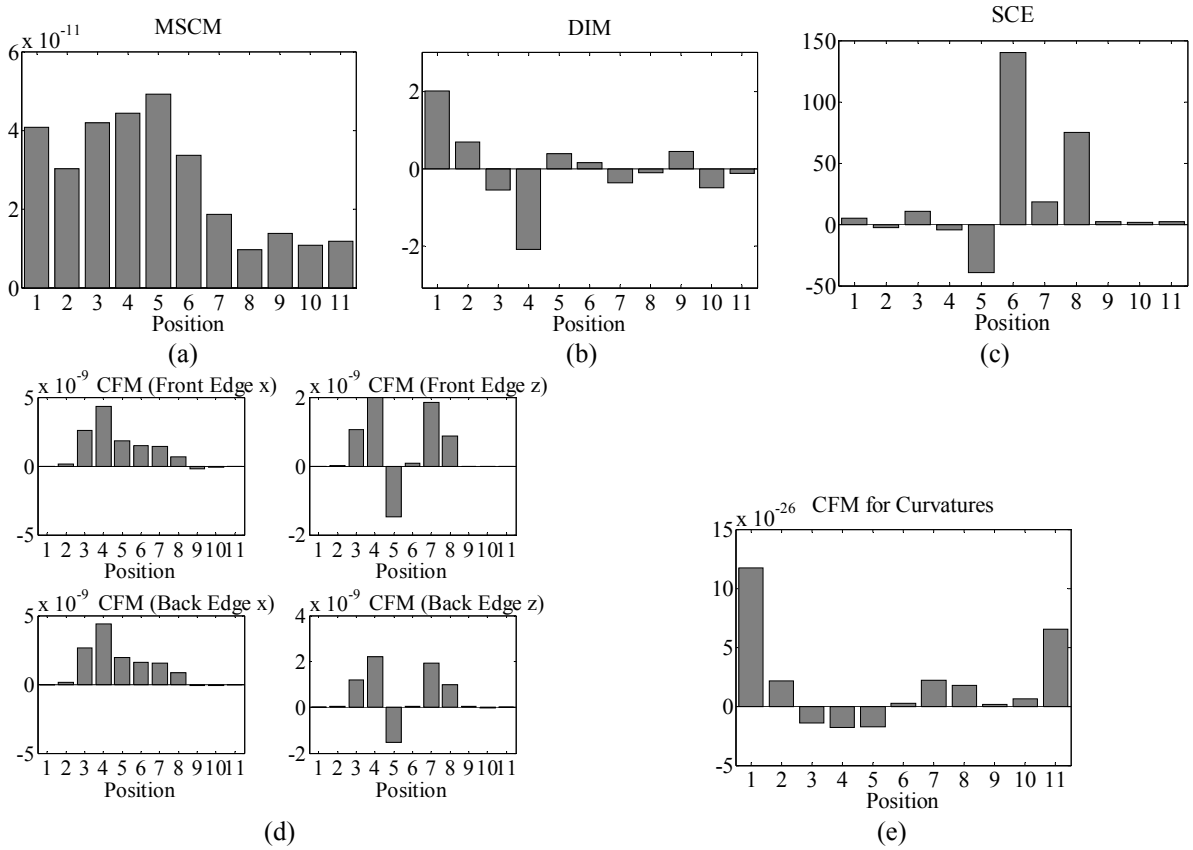


Figure 5.11 – Damage analysis of Model B for DS_i: (a) MSCM; (b) DIM; (c) SCE; and (d) and (e) CFM for modal displacements and curvatures, respectively.

From this particular simulation, the following conclusions emerged:

- COMAC values are insensitive to damage for modal displacements and modal curvatures, as illustrated in Figure 5.10a and b;
- The PM is inconclusive for modal displacements (see Figure 5.10c). For modal curvatures it is possible to visualize damage around position P4, as shown in Figure 5.10d;
- The MSCM is inconclusive because protuberances can be observed from positions 1 to 6, see Figure 5.11a;
- The DIM indicates a possible damage for positions P1 and P4, see Figure 5.11b;
- The SCE give inaccurate results for damage localization, see Figure 5.11c;
- The results for modal displacements of the CFM, see Figure 5.11d, indicate a clear damage location at position P4 for the *x* direction and two possible positions at location P4 and P7 for the *z* direction. In case of modal curvatures, presented in Figure 5.11e, damage is incorrectly indicated at positions P1 and P11.

For others simulations similar results can be found, i.e. some methods can provide the location of damage, others are inconclusive, see Annex A. In general, the results improve with the depth of the crack and better results can be obtained with the methods that use modal curvatures. As modal curvatures are calculated in the centre line of the arch, the amplitudes are small, with the exception of the first mode shape. If the curvatures are

calculated in both arch edges, even approximately with the fourth order central difference, the damage localization for the PM (with curvatures), the MSCM, the DIM, and the CFM (with curvatures) is more accurate, see also Annex A. Figure 5.12 shows the results of the example above recalculated using the curvatures at the arch edges, where damage at position P4 is clear. In the subsequent analysis, it was decided to use the curvatures calculated in the arch edges by the fourth order central difference theorem.

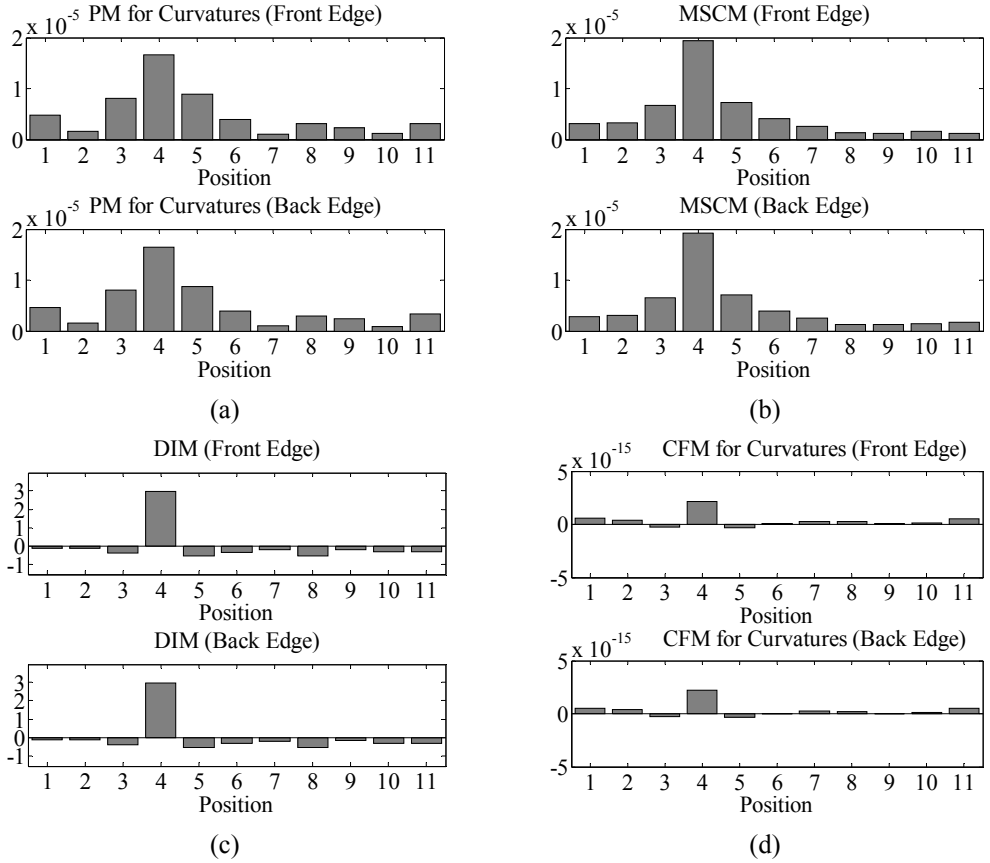


Figure 5.12 – Damage methods with curvatures calculated in the arch edges: (a) PM for modal curvatures; (b) MSCM; (c) DIM; and CFM for modal curvatures.

Another aspect to highlight is the variance of the numerical scale factors among the several damage scenarios. Table 5.7 presents the errors between each DS and the RS. As the simulated damage increase also, in general, the errors increase. The higher error was observed for the 1th mode and is around 8%. This is important for the case of the CFM, because mass-scaled modes are required, see Eq.(5.8). In the experimental results, the modes were scaled only for the RS (see Chapter 4). Therefore, the results from the CFM can be contaminated with these errors, resulting in inaccurate results.

Table 5.7 – Numerical scale factors among the several damages scenarios.

Mode Shape	RS	Model A			Model B			Model C		
		DS_I Error [%]	DS_{II} Error [%]	DS_{III} Error [%]	DS_I Error [%]	DS_{II} Error [%]	DS_{III} Error [%]	DS_I Error [%]	DS_{II} Error [%]	DS_{III} Error [%]
1	0.1184	–0.15	–1.42	–7.45	–0.09	–1.08	–8.26	–0.14	–1.22	–6.44
2	0.1749	–0.13	–0.49	–2.16	0.49	–0.15	–3.30	–0.02	–0.10	–0.70
3	0.2202	–0.15	–0.57	–2.34	1.11	0.76	–1.10	–0.05	–0.22	–1.03
4	0.2335	0.20	0.71	–0.42	0.81	1.08	2.14	0.13	0.51	–3.68
5	0.1902	0.32	0.32	0.00	2.43	2.58	1.83	0.23	–0.03	–2.50
6	0.2913	–0.12	–0.44	–2.98	0.92	1.38	2.66	0.01	–0.04	–2.19

5.4.1.3 Analysis with Finite Element Model Updating Method

The last method to be applied is the FEMU method, using the two approaches presented in Section 5.2.1. Figure 5.13 presents two tentative analyses with the global approach for the case of models A and B with DS_I. Different constraints in the updating parameters were used. In the first case, constraints were kept wide, in a way that Young's modulus could vary between 5% and 600% of the value obtained by the first updating analysis presented in Table 5.2. In the second case, the Young's modulus could vary only between 5% and 100%. This implies that the undamaged stiffness is unknown in the first case, while it is upper bounded by the initial value in the second case. In both cases, it was possible to localize the damage at position P4, but with a better performance for the case when the initial stiffness distribution is known (see Figure 5.13b and d).

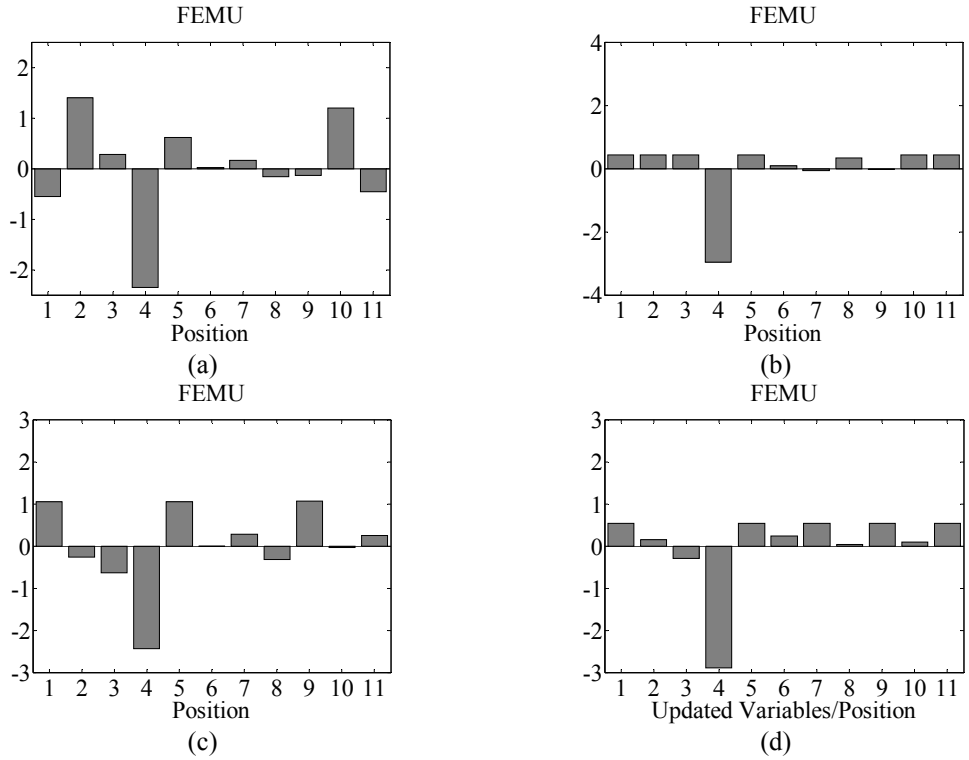


Figure 5.13 – FEMU global results with DS_I: (a) and (b) with unknown and known initial stiffness distribution for Model A, respectively; and (c) and (d) with unknown and known initial stiffness distribution for Model B, respectively.

Table 5.8 presents the results with the second local approach for Model A. In this approach only two updating parameters were selected: the Young's modulus and the local

stiffness K_r at the simulated crack (see Figure 5.8a). The initial values for the Young's modulus and for the local stiffness were equal to 5.0 GPa and 1×10^6 MPa (infinite stiffness), respectively. The modulus of elasticity was used as an updating parameter just to be a quality indicator of the updating analysis. The results in terms of the local stiffness are accurate, as the maximum error is equal to 1.7% for the DS_{III}.

Table 5.8 – Local FEMU analysis of Model A.

Damage Scenarios	K_r Simulated [MPa]	K_r Updated [MPa]	K_r Error [%]	E_y Simulated [GPa]	E_y Updated [GPa]	E_y Error [%]	Average ω Errors [%]	MAC Average	NMD Average
DS_I	1.586	1.566	1.30	3.790	3.795	–0.14	| 0.06 |	1.00	< 0.01
DS_{II}	0.382	0.383	–0.30	3.790	3.772	0.47	| 0.30 |	1.00	< 0.01
DS_{III}	0.057	0.056	1.65	3.790	3.620	4.63	| 2.26 |	1.00	< 0.01

Table 5.9 shows the results for the case of Model B, where again is possible to observe accurate damage quantification, confirming that is possible, in this case, to quantify the damage (Level 3) with the FEMU.

Table 5.9 – Local FEMU analysis of Model B.

Damage Scenarios	K_r Simulated [MPa]	K_r Updated [MPa]	K_r Error [%]	E Simulated [GPa]	E Updated [GPa]	E Error [%]	Average ω Errors [%]	MAC Average	NMD Average
DS_I	1.586	1.560	1.63	3.790	3.796	–1.58	| 0.11 |	1.00	< 0.01
DS_{II}	0.382	0.387	–1.31	3.790	3.765	0.66	| 0.43 |	1.00	< 0.01
DS_{III}	0.057	0.056	1.65	3.790	3.605	4.48	| 3.01 |	1.00	< 0.01

5.4.2 Damage Identification with Added Noise

To study the influence of measuring and computational noise present in the modal data for the damage analysis, simulated random noise was added to the dynamic modal parameters. The noise was added by the multiplication of the modal result X by a constant error and by a random number with zero mean and standard deviation equal to one, according to the following expression:

$$X_{noise} = X + Error \cdot X \cdot random \tag{5.21}$$

Two levels of noise were studied. In the first level, values for the constant error of 0.25 and 1.0% were considered for frequencies and mode shapes, respectively. In the second level, 0.5 and 2.0% constant errors were considered for the same modal quantities. The error for modal displacements was kept four times higher than for frequencies due to the reason that frequencies can be estimated more accurately than modal displacements. Annex A presents the results for the two noise levels and for Model B (damage between positions P3 and P4).

As an example of the noise influence, Figure 5.14 and Figure 5.15 compare the results for the MSCM and the DIM for DS_I, with different noise levels. For the MSCM the noise masks the simulated location with other contaminated locations. With DIM the added noise also changes results but damage can still be localized around position P4. Concerning the influence of noise level in other methods, the COMAC values remain insensitive. The PM and the CFM for displacements is inconclusive and for curvatures only in some cases is possible to localize the damage. The FEMU seems to be the most robust, especially when

the stiffness distribution is known. For all the damage scenarios with noise, FEMU was the only method able to detect accurately the damage. Therefore, it is expected that damage analysis with experimental modal results is rather difficult due to the presence of noise.

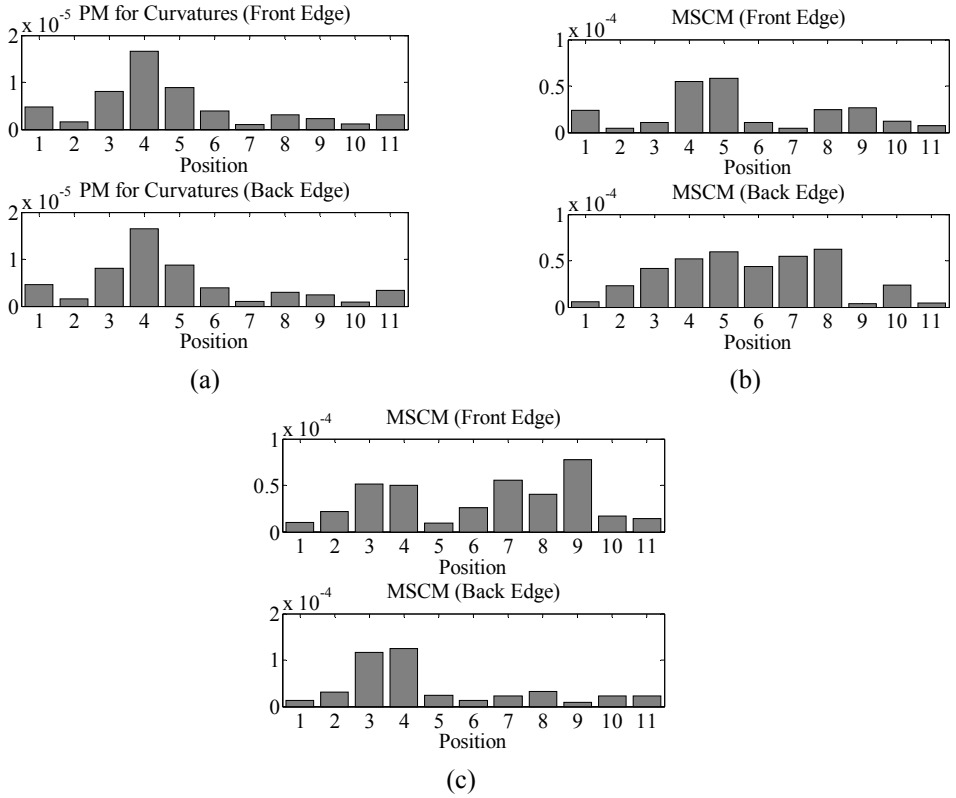


Figure 5.14 – Damage analysis with noise for MSCM: (a) without noise; (b) first and (c) second noise level.

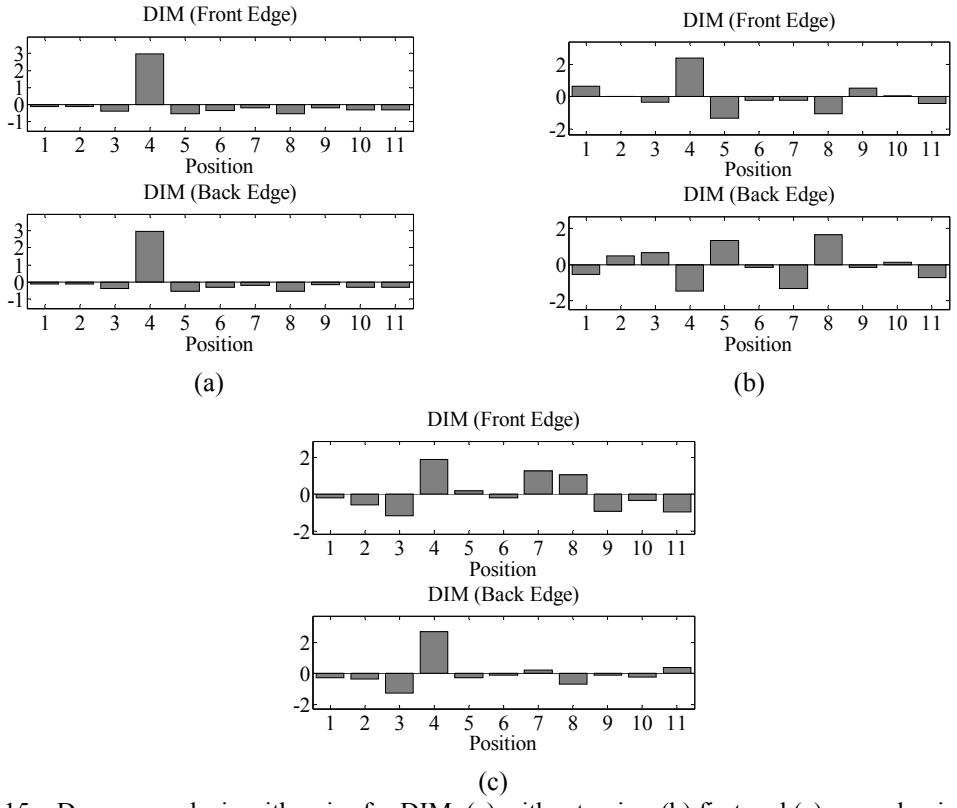


Figure 5.15 – Damage analysis with noise for DIM: (a) without noise; (b) first and (c) second noise level.

5.5 Experimental Damage Identification

The following Sections describe the damage analysis over the eight experimental DS induced by increasing external loading. First, the analysis with global parameters is presented, followed by the damage analysis with non-model based methods. Finally, the analysis with FEMU is addressed.

5.5.1 Analysis with Global Parameters

For all the identification analyses the tool ARTeMIS (SVS, 2006) was used to estimate the modal parameters with the SSI/Principal Component method. Table 5.10 and Table 5.11 present the frequency results for the consecutive DS and for the two types of excitation, ambient and random distributed impacts, respectively. The frequency values are presented together with the value $\pm 2\sigma_\omega$ as a 95% confidence interval, and the frequency differences Δ_ω to the RS. It is stressed that small increase in the frequency values are found before the occurrence of the first crack. This is due to the normal adjustments of the structure with the applied load, mainly at the supports and masonry joints. Considering the seven estimated frequencies, the first significant frequency decrease, i.e. higher that $2\sigma_\omega$ (given in a grey box), happens around DS_V, except for mode 6 with ambient excitation. In fact, the first significant change in the static stiffness (see Chapter 4) also appears in this scenario. In the subsequent scenarios it is also possible to observe significant frequency decreases. The maximum difference varies between 6.3 and 19.0 Hz and between 9.1 and 21.1 Hz for the ambient and random impact excitation, respectively.

Table 5.10 – Frequency results for the arch model with ambient excitation.

Damage Scenario	Mode 1			Mode 2			Mode 3			Mode 4		
	ω [Hz]	$2\sigma_\omega$ [Hz]	Δ_ω [Hz]	ω [Hz]	$2\sigma_\omega$ [Hz]	Δ_ω [Hz]	ω [Hz]	$2\sigma_\omega$ [Hz]	Δ_ω [Hz]	ω [Hz]	$2\sigma_\omega$ [Hz]	Δ_ω [Hz]
RS	35.59	0.40	–	67.30	0.93	–	72.11	0.76	–	125.74	1.30	–
DS_I	35.55	0.31	–0.05	67.51	0.83	0.21	71.80	0.38	–0.30	125.69	1.91	–0.05
DS_{II}	35.55	0.24	–0.04	67.39	1.11	0.09	71.83	1.06	–0.28	125.79	2.03	0.05
DS_{III}	35.42	0.31	–0.17	67.47	1.19	0.17	71.66	0.94	–0.45	125.75	2.21	0.01
DS_{IV}	35.15	0.24	–0.44	67.11	0.88	–0.19	71.33	0.58	–0.78	126.01	1.09	0.28
DS_V†	33.72	0.32	–1.87	65.68	0.72	–1.62	69.36	0.60	–2.75	124.48	1.60	–1.25
DS_{VI}	33.19	0.34	–2.40	64.91	1.02	–2.39	68.56	0.58	–3.55	123.58	1.37	–2.16
DS_{VII}	31.49	0.44	–4.10	63.08	1.29	–4.22	65.72	0.69	–6.39	121.97	1.83	–3.77
DS_{VIII}	28.09	0.62	–7.50	58.44	1.40	–8.86	62.61	0.93	–9.50	119.44	1.76	–6.30

† - Damage scenario in which the first crack was detected in the static tests.

Table 5.10 (cont.) – Frequency results for the arch model with ambient excitation.

Damage Scenario	Mode 5			Mode 6			Mode 7		
	ω [Hz]	$2\sigma_\omega$ [Hz]	Δ_ω [Hz]	ω [Hz]	$2\sigma_\omega$ [Hz]	Δ_ω [Hz]	ω [Hz]	$2\sigma_\omega$ [Hz]	Δ_ω [Hz]
RS	140.08	1.77	–	173.38	3.26	–	199.32	5.82	–
DS_I	139.76	3.57	–0.31	174.10	2.54	0.72	197.44	3.96	–1.88
DS_{II}	140.48	1.89	0.40	175.27	2.34	1.90	199.87	5.13	0.55
DS_{III}	139.94	2.05	–0.13	174.62	2.61	1.25	199.00	4.62	–0.31
DS_{IV}	139.58	2.70	–0.50	174.31	2.37	0.93	198.80	5.96	–0.52
DS_V†	135.68	5.65	–4.40	173.24	3.56	–0.13	188.78	3.32	–10.54
DS_{VI}	136.10	3.66	–3.98	171.55	2.38	–1.83	185.93	4.05	–13.39
DS_{VII}	132.81	3.10	–7.27	167.64	3.34	–5.74	188.25	4.93	–11.07
DS_{VIII}	127.44	2.64	–12.64	156.24	2.75	–17.13	180.27	5.19	–19.04

† - Damage scenario in which the first crack was detected in the static tests.

Table 5.11 – Frequency results for the arch model with random impact excitation.

Damage Scenario	Mode 1			Mode 2			Mode 3			Mode 4		
	ω [Hz]	$2\sigma_\omega$ [Hz]	Δ_ω [Hz]	ω [Hz]	$2\sigma_\omega$ [Hz]	Δ_ω [Hz]	ω [Hz]	$2\sigma_\omega$ [Hz]	Δ_ω [Hz]	ω [Hz]	$2\sigma_\omega$ [Hz]	Δ_ω [Hz]
RS	35.21	0.23	–	66.58	0.73	–	71.16	0.43	–	124.52	1.49	–
DS_I	35.17	0.23	–0.03	66.67	0.77	0.09	71.22	0.49	0.06	124.55	1.51	0.04
DS_{II}	35.17	0.30	–0.03	66.72	0.85	0.14	71.25	0.61	0.08	124.64	1.66	0.12
DS_{III}	35.11	0.24	–0.09	66.73	0.80	0.14	71.14	0.55	–0.02	124.65	1.48	0.14
DS_{IV}	34.83	0.24	–0.38	66.45	0.80	–0.14	70.76	0.40	–0.40	124.49	1.29	–0.02
DS_V†	33.20	0.34	–2.00	64.62	0.79	–1.96	68.33	0.66	–2.83	123.10	1.35	–1.42
DS_{VI}	32.42	0.28	–2.78	63.84	0.73	–2.75	67.18	0.74	–3.98	122.14	1.45	–2.38
DS_{VII}	30.17	0.41	–5.04	61.29	0.72	–5.30	64.06	0.86	–7.10	120.26	1.55	–4.26
DS_{VIII}	26.13	0.66	–9.07	55.28	0.98	–11.30	61.33	0.67	–9.83	117.59	1.46	–6.92

† - Damage scenario in which the first crack was detected in the static tests.

Table 5.11 (cont.) – Frequency results for the arch model with random impact excitation.

Damage Scenario	Mode 5			Mode 6			Mode 7		
	ω [Hz]	$2\sigma_\omega$ [Hz]	Δ_ω [Hz]	ω [Hz]	$2\sigma_\omega$ [Hz]	Δ_ω [Hz]	ω [Hz]	$2\sigma_\omega$ [Hz]	Δ_ω [Hz]
RS	138.94	1.80	–	172.55	1.69	–	196.76	4.25	–
DS_I	138.93	1.82	–0.02	173.41	1.98	0.86	196.13	3.90	–0.63
DS_{II}	138.99	1.91	0.05	173.30	1.94	0.76	196.83	3.14	0.06
DS_{III}	138.86	1.70	–0.08	173.12	1.81	0.57	196.71	2.64	–0.06
DS_{IV}	138.33	1.79	–0.61	172.88	1.97	0.33	196.30	2.82	–0.47
DS_V†	135.61	1.90	–3.33	171.10	2.15	–1.44	193.43	4.50	–3.33
DS_{VI}	134.31	1.90	–4.63	169.54	1.87	–3.01	186.10	3.86	–10.67
DS_{VII}	130.71	1.89	–8.24	163.93	1.96	–8.61	182.37	3.22	–14.39
DS_{VIII}	125.95	1.52	–12.99	151.43	2.37	–21.11	176.33	3.07	–20.43

† - Damage scenario in which the first crack was detected in the static tests.

Figure 5.16a and c show the progressive frequency decrease with increasing damage. The residual frequencies in the last DS are between 0.78 and 0.95, and 0.74 and 0.95 of the original frequency value for the ambient and random impact excitations, respectively. Here is noted that the term “relative frequency” has been used for the relation between the

frequency in the DS and the original frequency in the RS. Again, the first notorious frequency shift is observed in DS_V, and it is more significant for the lower modes.

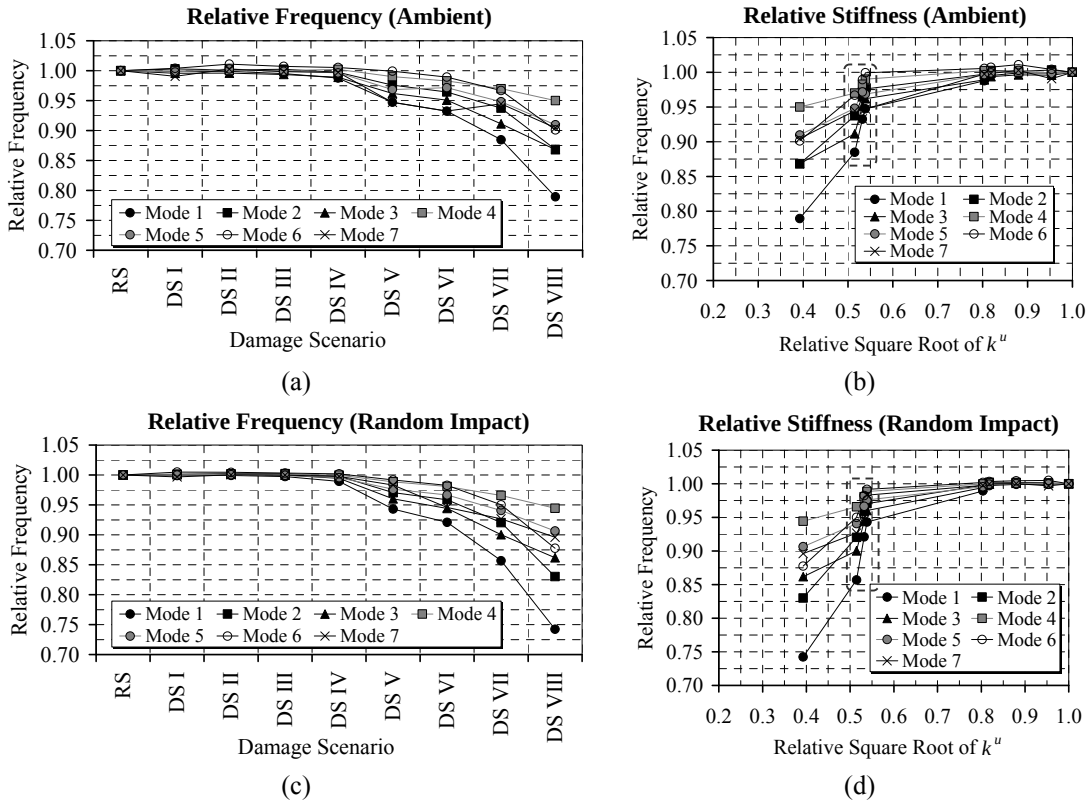


Figure 5.16 – Different damage scenarios: (a) and (b) relative values for the frequencies and square root stiffness for ambient excitation, respectively; and (c) and (d) relative values for the frequencies and square root stiffness for random impact excitation, respectively.

Figure 5.16b and d shows the relative square root of the unloading stiffness k^u, calculated in Chapter 4, *versus* the relative frequency values calculated to the RS. The changing point is clearly at DS_V, where the relative square stiffness decreases more than 20%. In these figures it is possible to observe a general nonlinear relation between the two quantities, but with a zoom from DS_V to DS_{VII} (see the dashed squares in Figure 5.16b and d) is possible to observe a linear relation between the two quantities with the exception of mode 7, see Figure 5.17. As the two quantities are square root proportional ($\omega \propto \sqrt{k/m}$), and no significant mass changes was carried out, the results seem to be acceptable.

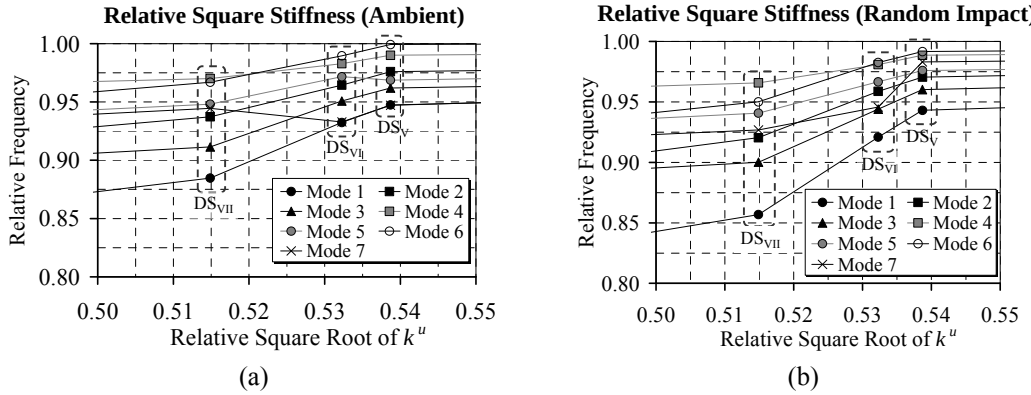


Figure 5.17 – Relative square root stiffness values for the DS_V to DS_{VII}: (a) ambient excitation; and (b) random impact excitation.

Table 5.12 and Table 5.13 present the additional global modal parameter to be studied: the damping coefficient. As referred in Chapter 3, it is difficult to estimate experimentally this parameter, but for the case of the arch a significant increase on its value with the progressive damage can be observed for both types of excitation. The average value for the 7 modes starts in 0.8 and 1.0% and ends in 1.24 and 1.62% for the ambient and random impact excitations, respectively.

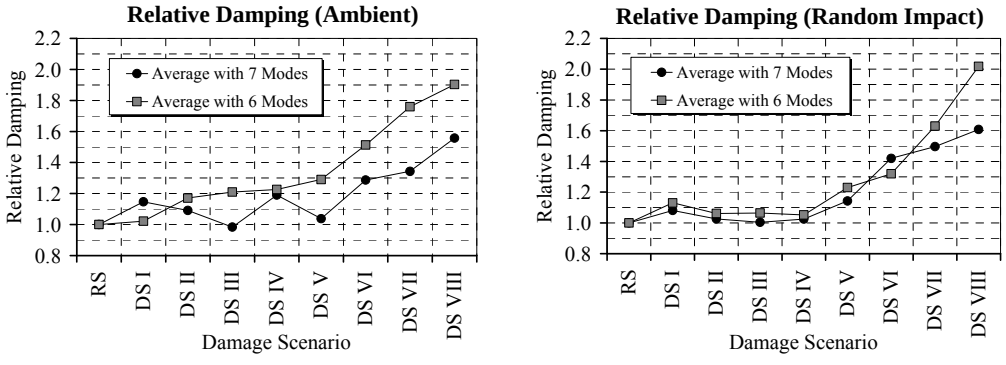
Table 5.12 – Damping results for the ambient excitation [%].

Mode	RS	DS_I	DS_{II}	DS_{III}	DS_{IV}	DS_V	DS_{VI}	DS_{VII}	DS_{VIII}
1	0.44	0.61	0.50	0.93	0.60	0.84	0.75	1.17	1.51
2	0.53	0.73	0.72	0.87	0.84	0.72	0.63	0.95	1.23
3	0.88	0.58	0.70	0.76	0.56	0.46	0.72	1.04	1.17
4	0.59	0.57	0.55	0.77	0.59	0.84	0.80	0.89	0.95
5	0.46	0.64	0.93	0.51	0.96	0.78	1.62	1.33	1.11
6	0.83	0.69	0.97	0.69	1.03	1.18	1.14	1.19	1.15
7	1.84	2.58	1.71	0.97	2.05	0.97	1.52	0.92	1.58
Average	0.80	0.91	0.87	0.78	0.95	0.83	1.03	1.07	1.24

Table 5.13 – Damping results for random impact excitation [%].

Mode	RS	DS_I	DS_{II}	DS_{III}	DS_{IV}	DS_V	DS_{VI}	DS_{VII}	DS_{VIII}
1	0.51	0.55	0.52	0.55	0.62	0.85	0.97	1.38	2.12
2	0.64	0.75	0.69	0.78	0.73	0.82	0.96	1.38	2.07
3	0.72	0.88	0.90	0.87	0.88	1.08	1.15	1.32	1.09
4	0.79	0.80	0.81	0.78	0.79	0.82	0.83	0.86	0.90
5	0.73	0.72	0.64	0.64	0.63	0.75	0.78	0.88	0.98
6	1.11	1.40	1.22	1.18	1.09	1.23	1.26	1.53	1.94
7	2.55	2.54	2.46	2.29	2.49	2.52	4.07	3.22	2.25
Average	1.01	1.09	1.03	1.01	1.03	1.15	1.43	1.51	1.62

Figure 5.18 presents the average relative damping values for the first 6 and for all the modes. As observed with frequencies, is possible to observe the increasing in DS_V, with the exception for the average values with all the modes in the case of ambient vibration. In the case of the average with the first 6 modes the final damping values, on average, are two times the initial ones.



(a) (b)

Figure 5.18 – Relative damping values: (a) ambient excitation; and (b) random impact excitation.

As a conclusion, observing the global modal results, it seems that the modal properties of the masonry specimen are sensitive to the damage progress and no significant

differences were found between the two cases of excitation. In both types, damage was detected in DS_V and it is coincident with the significant decrease observed in the static results. This fulfils the first level (detection) of the damage identification process. Concerning the type of structure analyzed, the result seems promising, because other tests in literature report smaller changes for frequency values, see for instance Doebling et al. (1996).

5.5.2 Analysis with Non-Model Based Methods

Starting with the results from the USI method, Figure 5.19 shows for both types of excitation the results for the comparisons with the RS and the relative comparisons for each consecutive DS. In this analysis all the seven estimated frequencies were considered, together with the standard deviations presented in Table 5.10 and Table 5.11. One conclusion is the difference in the order of values before and after DS_V, confirming the significant change that happened in this scenario. The USI values in DS_{VI} are significant to DS_V and the last two DS show a significant increase. These results indicate that when the USI is calculated for the several scenarios, the detection of damage (Level 1) is possible, and they confirm the results obtained with the global parameters. In case of no information about the modal history, the detection of damage with USI might be difficult, because no reference values in the undamaged condition exist.

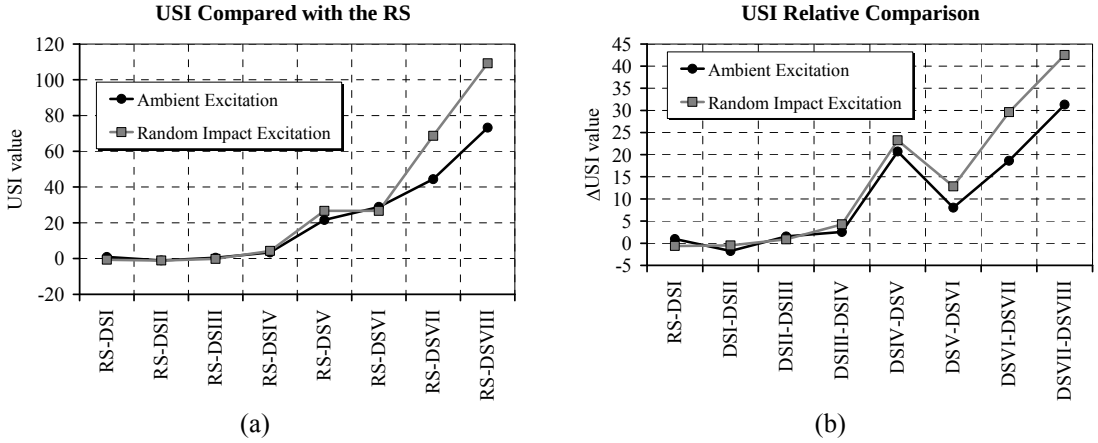


Figure 5.19 – USI results: (a) Compared with the RS; and (b) relative comparison.

Concerning the others non-model based methods (COMAC, PM, MSCM, DIM, SCE and CFM) two assumptions were made in order to increase the results quality. The first assumption is that the values close to zero of curvature mode shape were neglected in order to avoid contamination in the results. This way, only significant values for curvatures are compared, which makes the analysis more reliable. The second assumption is that not all modes were considered. As the seventh mode shape was not well estimated, see Chapter 4, the analyses were carried out using only the first six modes. For some cases, even an enhanced analysis with a lower number of modes was performed.

5.5.2.1 Results with Measured Curvatures

The results for the application of the selected methods based on measured curvatures with random impact excitation are extensively presented in Annex B. The six modes were considered and results include the comparison of each DS_i to the RS, the relative comparison for each consecutive DS_i, and the comparison with DS_{III} as a new undamaged reference.

The following conclusions are possible from the results:

- The COMAC values calculated for modal displacements and modal curvatures are inconclusive, or are insensitive to the damage location, in agreement with the numerical simulation analysis presented in Section 5.4.1;
- The PM, the MSCM, the DIM and the SCE gave similar results and were able to locate the damage in the vicinity of the experimental crack locations;
- The majority of the results from CFM were inconclusive. Only for the final DS the results with modal curvatures are coincident with the MSCM. This might be related to the fact that the modes used in this analysis were scaled to the mass matrix with the scale factors of the RS, see Chapter 4.

As an illustration of the preceding conclusions, Figure 5.20 and Figure 5.21 present the results for the relative comparison between DS_{IV} and DS_V, where a damage occurs at positions P1 and P11 for the PM, MSCM and CFM for modal curvatures, and a damage occurs at position P1 and P7 for the DIM and SCE.

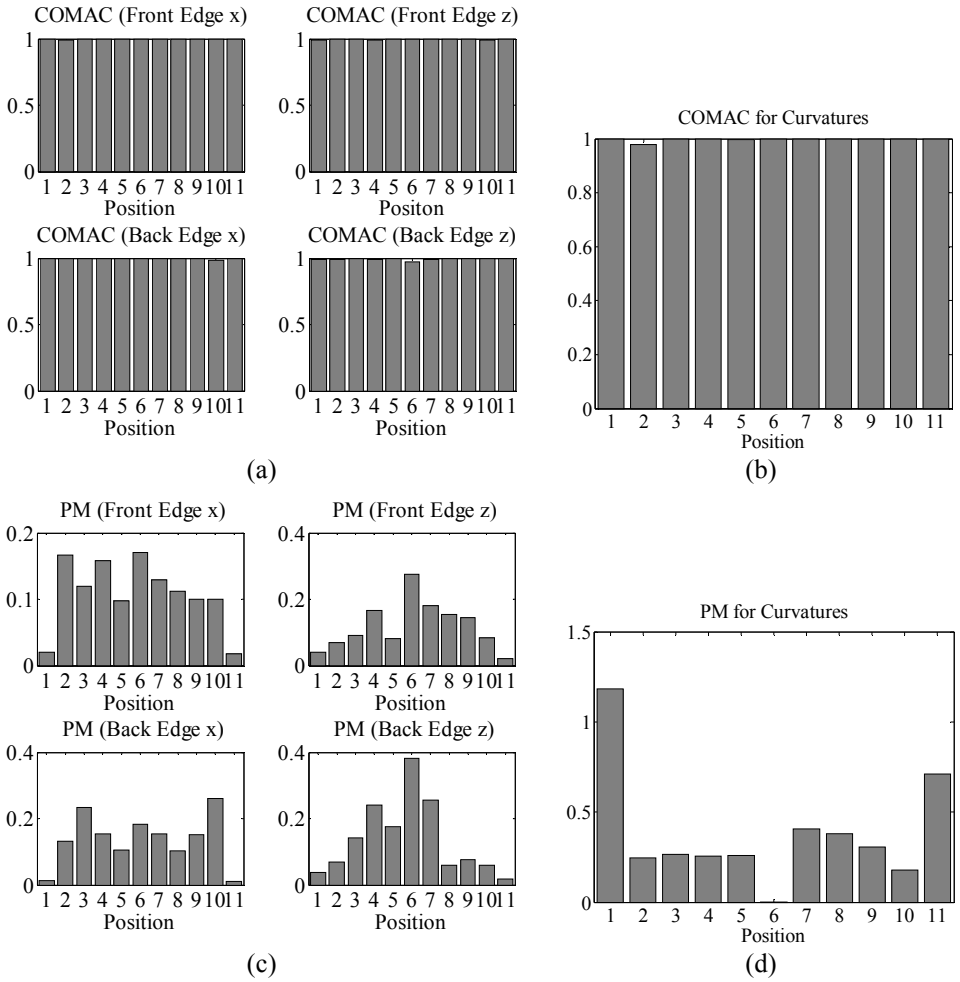


Figure 5.20 – Results with measured curvatures for the comparison between DS_{IV} and DS_V: (a) COMAC values for modal displacements; (b) COMAC values for modal curvatures; (c) PM values for modal displacements; and (d) PM values for modal curvatures.

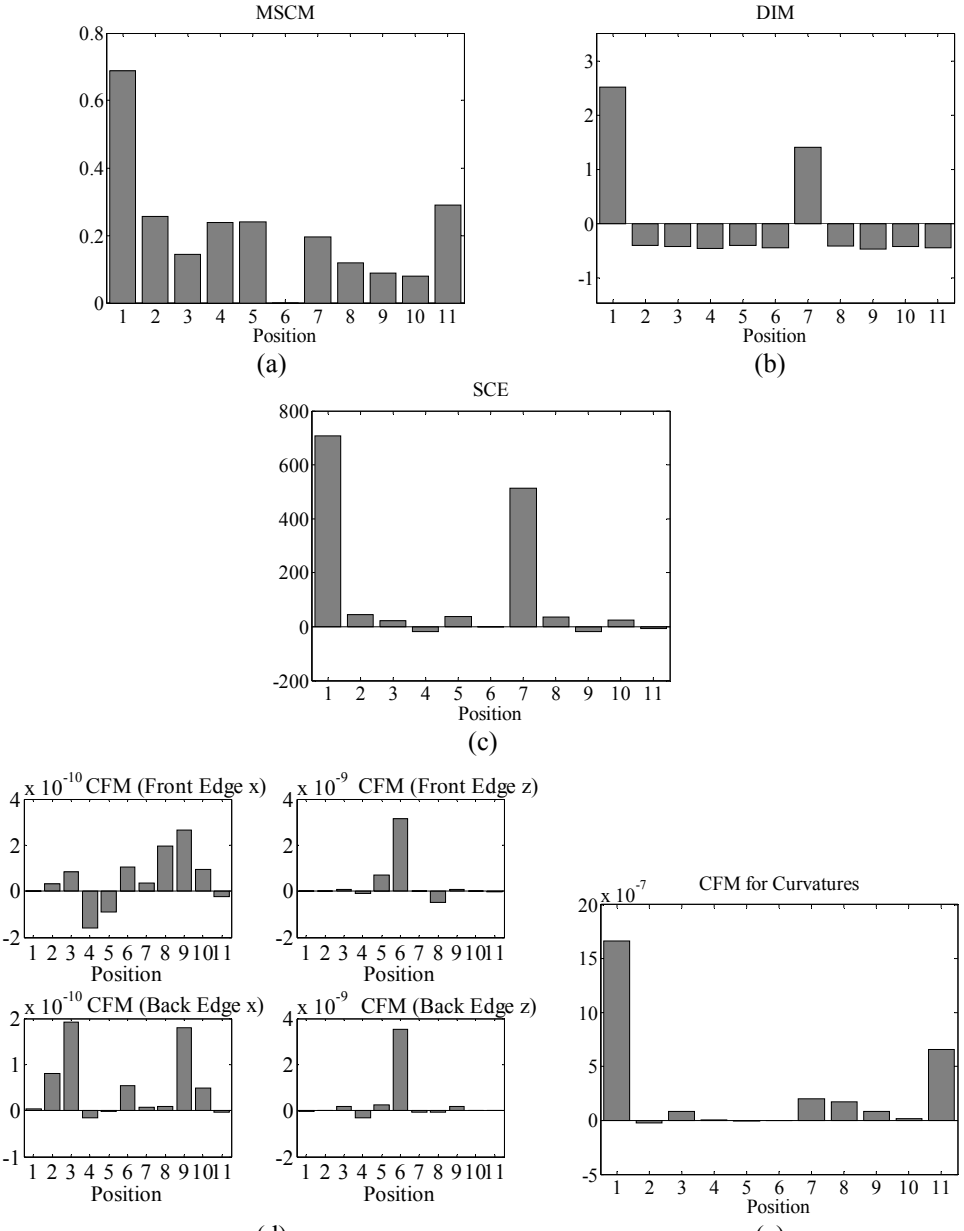


Figure 5.21 – Results with measured curvatures for the comparison between DSI_V and DS_V: (a) MSCM; (b) DIM; (c) SCE; (d) CFM for modal displacements; and (e) CFM for modal curvatures.

Considering the above conclusions, the definition of the damage location was based in three criteria with the decreasing importance: (a) at least a correlation between two of the methods which gave similar results, namely the PM, the MSCM, the DIM and the SCE, should occur; (b) only the values greater than two will be considered as potential damage in the DIM, Stubbs et al. (1992); and (c) there should be also a correlation between the damage in the four referred methods and the remaining others. Considering these criteria, Figure 5.22 shows the damage location analysis, where it is possible to conclude the following:

- The analysis based on the RS (see Figure 5.22a), shows the first crack c_1 (see Chapter 4) even before the notorious occurrence of damage in DS_V. All the cracks were located in the vicinity of the observed experimental positions, namely at positions P1, P3, P9 and P11;

- For the case of consecutive comparisons with the previous configurations (see Figure 5.22b), the cracks were located in the same positions. The third comparison (DS_{III}-DS_{IV}), a possible location at position P7 is indicated. Although it was not possible to see any crack in the vicinity of this measuring point, it is possible that some micro cracks have appeared in this area and, due to stress redistributions, never reached a macro crack;
- In the last analysis DS_{III} is used as a new undamaged reference (see Figure 5.22c) and only three cracks were located at positions P1, P9 and P11. The crack at position P3/P4 was not located because it is only possible to localize it with the comparison between DS_{II} and DS_{III}. The same comments apply for the damage at position P7.

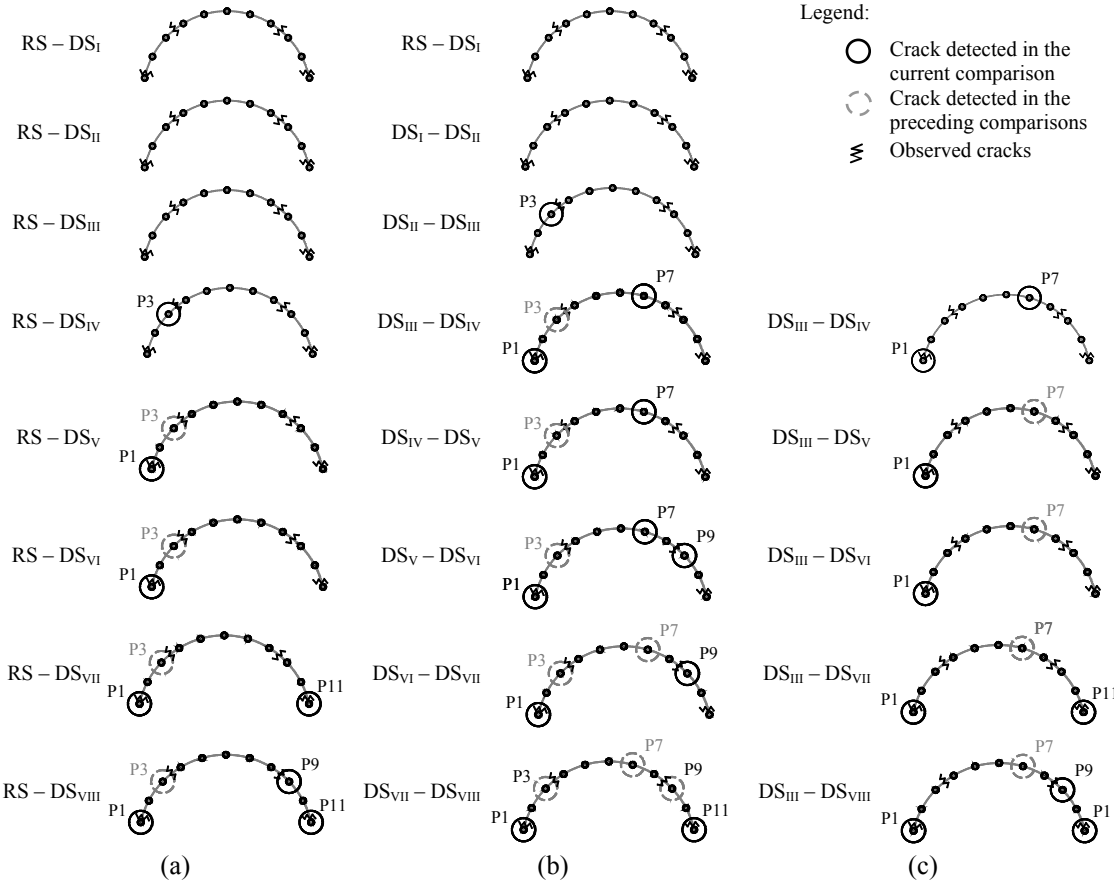


Figure 5.22 – Damage location with measured curvatures: (a) comparison with the RS; (b) relative comparison with each consecutive DS; and (c) comparison with DS_{III}.as a new undamaged reference

5.5.2.2 Results with Calculated Curvatures Derived from Modal Displacements

The preceding analysis was repeated for the curvatures calculated from the modal displacements at the arch edges with the ambient excitation. For each mode, two modal curvatures were obtained for the front and back edges of the arch. The curvatures were computed with the fourth order central difference theorem (see Section 5.2.2) and fully supported boundary conditions were assumed. Only five modes (2^{nd} to 6^{th}) were considered in order to obtain enhanced results. The aim of this analysis is to study the possibility of using only modal displacements estimated by ambient excitation for damage localization.

The results are extensively presented in Annex B. The conclusions related to the performance of methods with measured curvatures given in the section above apply for this

analysis, with the exception of better results for the COMAC values (calculated for the modal curvatures) and for the PM. Figure 5.23 shows again the results for the comparison between DS_{IV} and DS_V where the analysis indicates that damage might be present in positions P4 and P8. However, it should be stressed here that these results have lower quality than the results calculated with the measured curvatures, therefore damage is more difficult to localize due to noise in the computations.

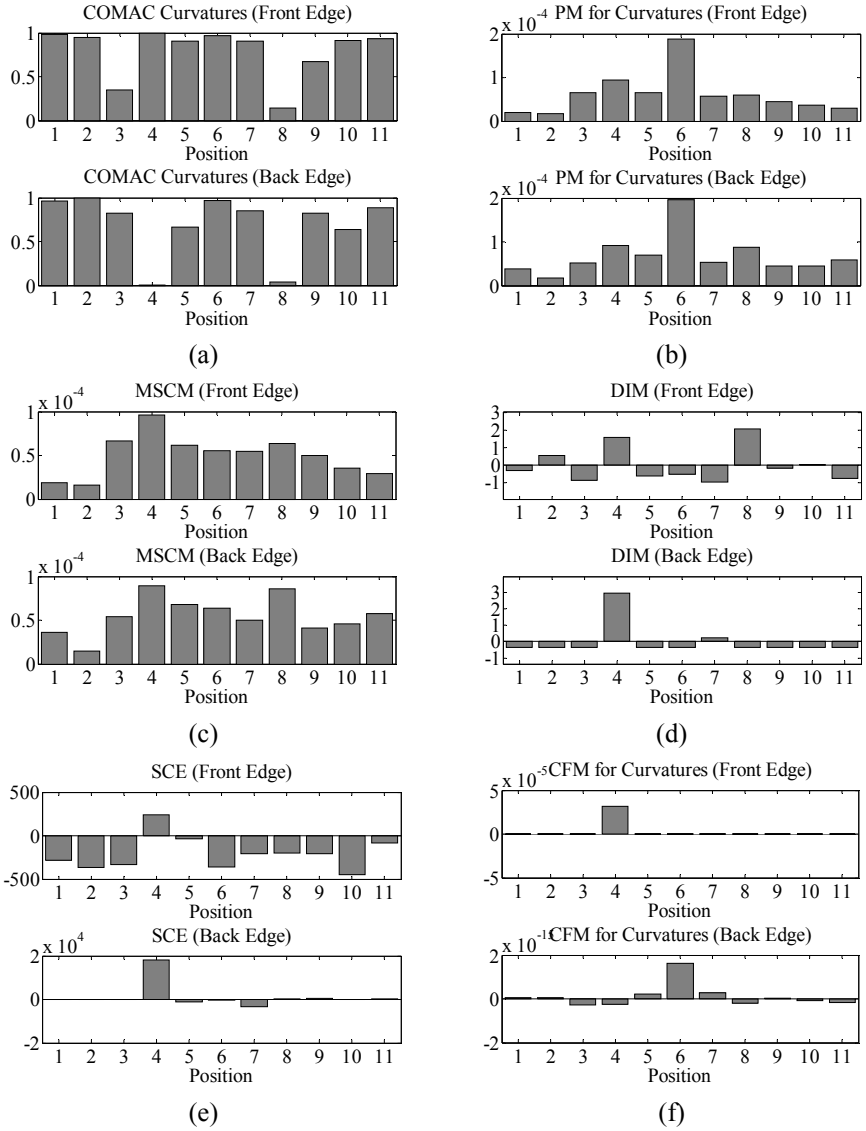


Figure 5.23 – Results with calculated curvatures for the comparison between DS_{IV} and DS_V: (a) COMAC values for modal curvatures; (b) PM for modal curvatures; (c) MSCM; (d) DIM; (e) SCE; and (f) CFM for modal curvatures.

For damage localization, the three criteria addressed above were again taking into account. The results are presented in Figure 5.24, where it is possible to conclude the following:

- The analysis based on the RS (see Figure 5.24a) was able to locate the four cracks at positions P1, P3/P4, P8 and P10. The first crack appeared in the comparison with DS_I, which is an earlier localization of damage. This might be related to a low stiffness distribution in the structure even without the presence of cracks;

- For the case of consecutive comparisons with the previous configurations (see Figure 5.24b), again all the predicted cracks were located in the vicinity of the experimental cracks (P2, P3/P4, P8 and P10). In this analysis the positions P6 and P7 also appear as potential damage locations, possibly due to micro-cracking or computational noise in the modal estimation and curvature calculation;
- In the analysis using DS_{III} as a new undamaged reference (see Figure 5.24c), again the cracks were localized at positions P2, P3/P4, P8 and P10, showing that if a DS close to the first crack occurrence is chosen for RS, the damage can be accurately localized.

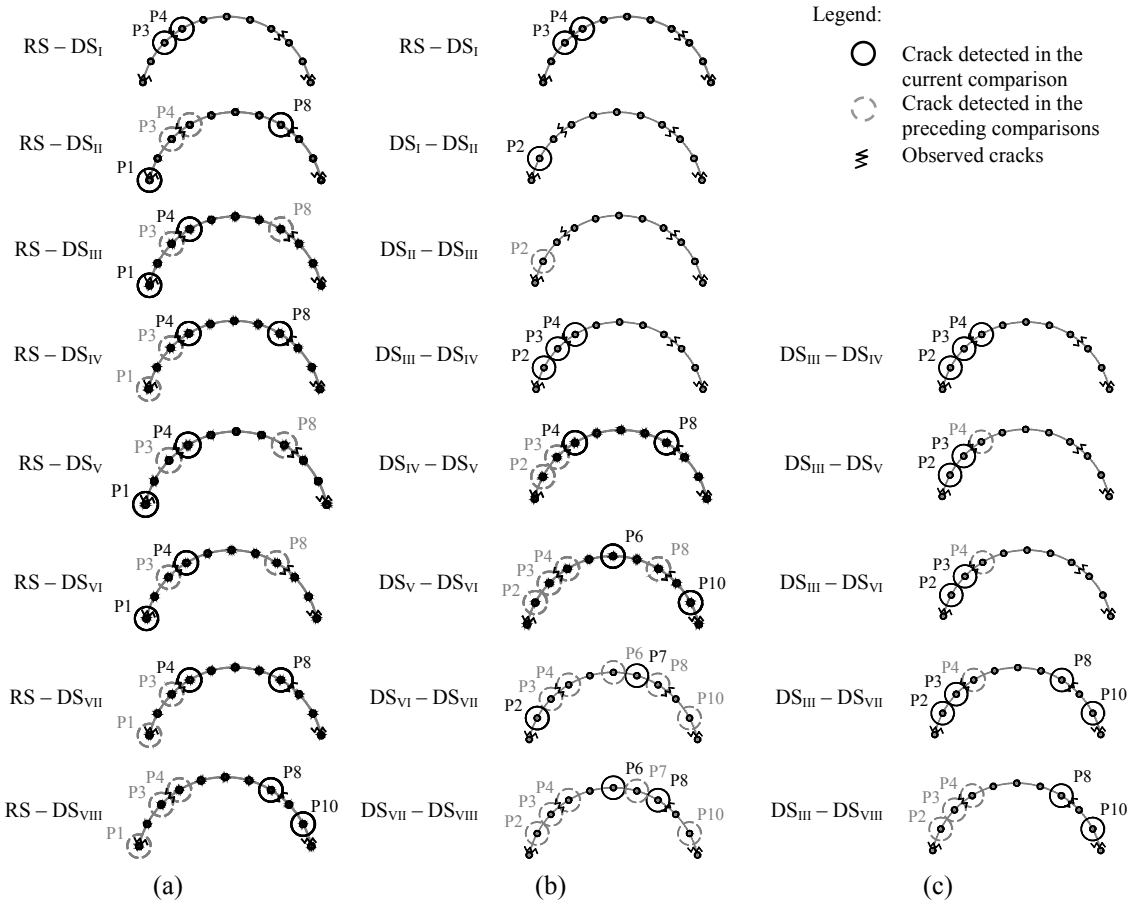


Figure 5.24 – Damage location with calculated curvatures: (a) comparison with the RS; (b) relative comparison with each consecutive DS; and (c) comparison with DS_{III}.

5.5.2.3 Crack Sequence

With respect to the crack sequence, there is no exact agreement between the different analyses and different methods, as shown in Figure 5.25. But there is a trend to the following sequence: first crack, c_1, at position P3/P4, second crack, c_2, at position P1, third crack, c_3, at position P8/P9, and fourth crack, c_4, at position P11. The sequence is not coincident with the one predicted with the numerical static analysis, presented in Chapter 4, and, experimentally, only the crack c_1 could be detected as the first occurrence. But the sequence is possible if a variance of 20% in the mechanical properties of the material is considered (Oliveira, 2003). It is noted that masonry presents a wide scatter in

mechanical properties and different failure mechanism can be obtained with similar failure loads, only by slight variations on the matrial properties, Lourenço (1998).

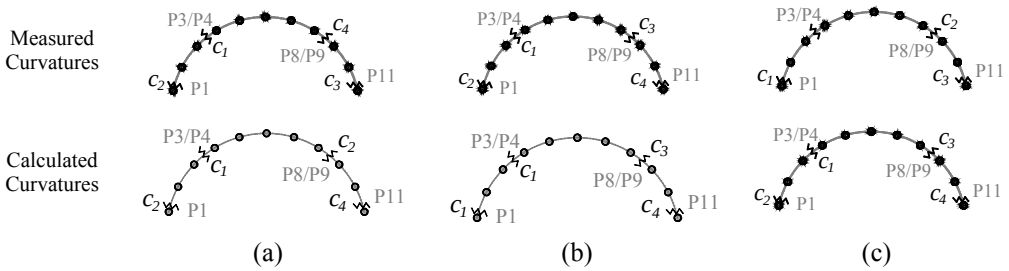


Figure 5.25 – Crack sequence using calculated and measured curvatures: (a) comparison with the RS; (b) relative comparison with each consecutive DS; and (c) comparison with DS_{III}.as new reference

5.5.3 Analysis with the Finite Element Model Updating Method

As performed in the numerical crack simulation, the two step approach presented in Section 5.3 is now used to apply the FEMU method to the experimental data. In the first step, two models were used to, globally, localize the damage (Level 2) and on the second step a third model with rotational spring elements was used to assess the damage (Level 3). In both steps, models with shell elements with eight nodes were used, similarly to the model used in the preliminary model updating analysis.

5.5.3.1 Global Localization

The difference between the two models used for the damage localization is the size for the bands of elements with different Young's modulus (11 updating parameters). The models are presented in Figure 5.26, where it is possible to visualize the different bands widths and the measuring point locations. The size of the bands for the first model (Model L) varies between 0.20 and 0.25 m and for the second (Model T) between 0.07 and 0.11 m.

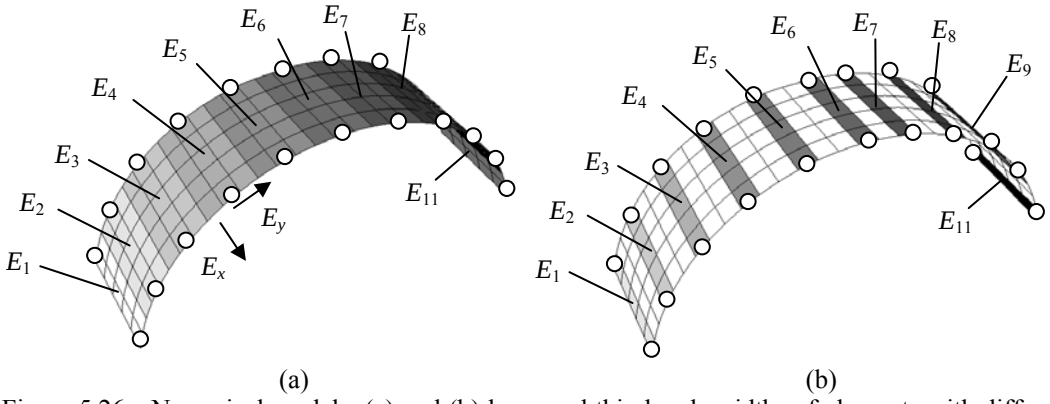


Figure 5.26 – Numerical models: (a) and (b) large and thin bands widths of elements with different Young's modulus, respectively.

The procedures presented in Section 5.3 were used for the model updating analysis. For the objective function, six eigen frequencies and six mode shapes ($m_\omega = 6$ and $m_\varphi = 6$) were considered in order to have more equations than updating parameters. The experimental model information to tune was always from the ambient excitation tests, as no significant differences were found between the modal parameters from the two types of excitation.

The FEMU was applied only to the DS_i with frequencies lower that the observed in the RS. The starting Young's modulus for all bands was the same as the preliminary model updating analysis (E_y = 3.79 GPa and E_x/E_y = 1.13). The upper bounds for the updating parameters were fixed at 3.79 GPa and the lower limit at 5% of the initial value.

The results for all the DS_i studied are presented in Annex B. In general, only two cracks were localized at position P3/P4 and P8/P9. Figure 5.27 shows the results for the two analyses in the case of DS_{IV}. With large bands (see Figure 5.27a), the crack is indicated to be at position P9, but with thin bands (see Figure 5.27b) two possible cracks are indicated at positions P4 and P8. Comparing these results with the ones from the non-model based methods, a correspondence is found with the same DS calculated using curvatures information. However, the cracks at the supports were impossible to localize with the FEMU. A first possible reason for unsuccessfully damage identification can be the higher number of updating parameters (eleven unknowns) for the available experimental modal data used in the objective function π (six frequencies plus six modes gives 12 equations). A second reason can be that the objective function might have several local minimums.

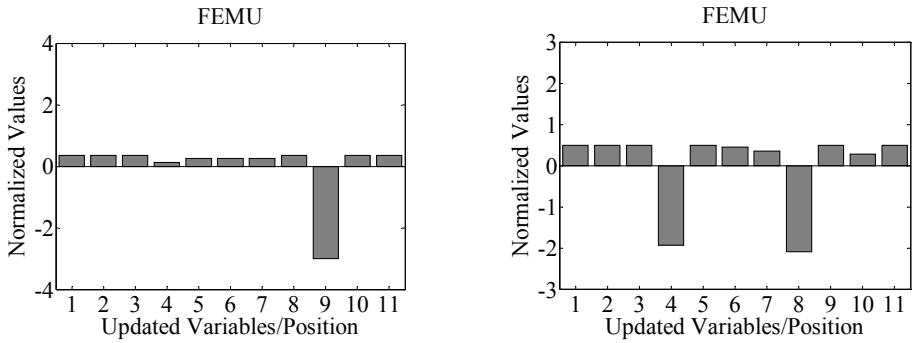


Figure 5.27 – FEMU applied to DS_{IV}: (a) L model; and (b) T model.

Table 5.14 shows the relative Young's modulus values for the two models. For the case of Model L, the relative values decrease until 39 and 19% for the bands in the vicinity of the positions P3 and P8, respectively. For the Model T, the values decrease until 9 and 6% for the bands near the positions P4 and P9, respectively.

Table 5.14 – Relative Young's Modulus.

Updating Variables / Position	Model L					Model T				
	DS_{IV}	DS_V	DS_{VI}	DS_{VII}	DS_{VIII}	DS_{IV}	DS_V	DS_{VI}	DS_{VII}	DS_{VIII}
E_1 / P1	1.00	0.96	1.00	1.00	0.79	1.00	1.00	1.00	1.00	1.00
E_2 / P2	1.00	1.00	1.00	1.00	1.00	1.00	0.99	1.00	1.00	1.00
E_3 / P3	1.00	0.68	1.00	0.58	0.39	1.00	1.00	0.56	1.00	1.00
E_4 / P4	0.97	1.00	0.50	1.00	1.00	0.50	0.30	0.30	0.16	0.09
E_5 / P5	0.99	0.99	1.00	1.00	1.00	1.00	1.00	1.00	1.00	1.00
E_6 / P6	0.99	0.99	0.99	0.99	0.99	0.99	0.99	0.99	0.99	0.99
E_7 / P7	0.99	0.73	1.00	1.00	1.00	0.97	1.00	1.00	1.00	1.00
E_8 / P8	1.00	1.00	1.00	0.30	0.19	0.47	0.55	0.43	1.00	1.00
E_9 / P9	0.61	0.79	0.52	1.00	1.00	1.00	0.53	0.70	0.18	0.06
E_{10} / P10	1.00	1.00	1.00	1.00	1.00	0.95	0.71	0.80	0.41	0.68
E_{11} / P11	1.00	1.00	1.00	1.00	1.00	1.00	1.00	1.00	1.00	0.98
Average ω errors [%]	2.91	3.20	3.08	3.06	4.04	3.35	2.62	2.72	2.42	2.83
Average MAC values	0.82	0.83	0.81	0.74	0.66	0.87	0.90	0.89	0.85	0.83
Average NMD values	0.44	0.43	0.46	0.62	0.75	0.36	0.31	0.33	0.40	0.44

Table 5.14 also presents the average frequency errors and the average for MAC values and for NMD values. Better results were found for the case of the Model T, indicating that thin band widths can improve the results as they simulate better the localized cracks. However, it should be stressed that even if the average results for the frequency errors are acceptable, the average results for the MAC values are not close to one and the average NMD values are higher that 33%. This indicates that not all the mode shapes were updated with acceptable results for the modal configurations. As an example, Figure 5.28 presents the agreement between the experimental and the updated modes, where it is possible to observe a good agreement for modes 1, 2, 3 and 6 and a poor correlation for other modes.

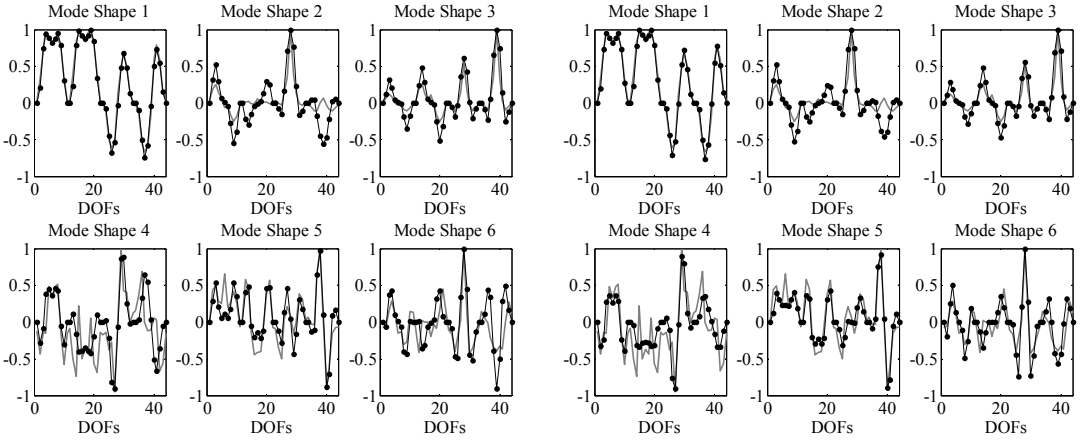


Figure 5.28 – Mode shape comparison FEMU applied to DS_{IV}: (a) Model L; and (b) Model T.

5.5.3.2 Damage Assessment

In the second step of FEMU, a third numerical model with rotational spring elements located at positions P1, P4, P8 and P11 was used to tune the experimental data by two different updating analyses. In the first analysis, only the spring elements at position P4 and P8 (the ones indicated as potential damage localizations in the fist step of FEMU) were considered as updating parameters, and others springs were simulated with infinite stiffness. Also the Young's modulus in the *y* direction (see Figure 5.29a) was considered as updating parameter, only for better quality of results. In the second analysis, all the rotational spring elements were taken as updating parameters (see Figure 5.29b). The Young's modulus was suppressed in order to keep a low number of updating variables. The other procedures in the updating analysis were kept the same as in the preceding step of FEMU.

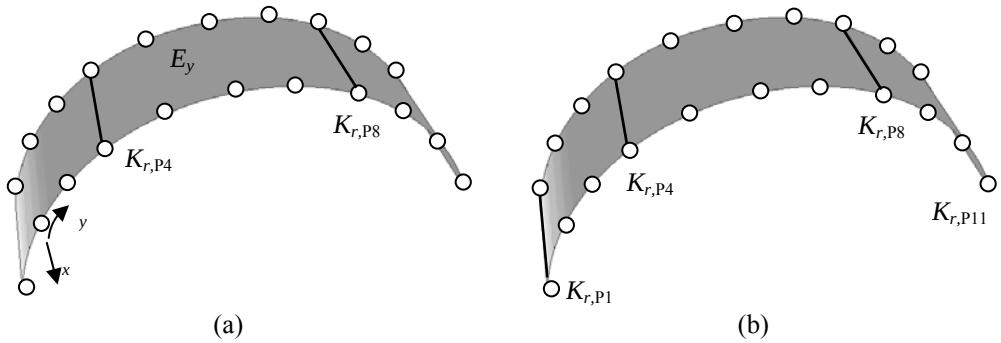


Figure 5.29 – Numerical models: (a) and (b) large and thin bands of elements with different Young's modulus, respectively.

Table 5.15 shows, for the first damage location analysis, the updated values for each variable and the estimated crack depth, calculated according to the fracture mechanics method, presented in Section 5.4. The table also shows the average values for the frequency errors, MAC and NDM values. From the results, one can conclude that, according to the numerical model, the first significant crack appears at position P8 at DS_{IV} and DS_V, and then at position P4. The maximum estimated crack depth was equal to 32.6 mm at position P4. The crack depth is in the order of the experimental results for this crack location (see Section 4.4). It is noted that once the crack at location P4 opens, the crack at location P8 stabilizes or even partially closes.

Table 5.15 – First location analysis.

Damage Scenarios	E_y		$K_{r,P4}$		$K_{r,P8}$		Average ω Errors	Average MAC values	Average NMD values
	Modulus [GPa]	Error [%]	Local Stiffness [MPa]	Crack Depth [mm]	Local Stiffness [MPa]	Crack Depth [mm]	[%]		
RS	3.79	–	1×10^6	–	1×10^6	–	3.67	0.91	0.30
DS_{IV}	3.79	<0.01	1×10^6	–	937.51	0.29	3.55	0.78	0.51
DS_V	3.79	<0.01	750.09	0.32	0.23	20.29	2.65	0.78	0.52
DS_{VI}	3.78	–0.01	0.09	32.13	0.45	14.27	3.09	0.77	0.53
DS_{VII}	3.54	–6.27	0.09	31.74	0.25	19.29	3.39	0.70	0.71
DS_{VIII}	3.19	–9.84	0.03	32.62	0.26	19.11	3.43	0.67	0.79

Another result to highlight is the value of the Young's modulus used to obtain better agreement in the results. The change with respect to the original value starts to be significant after DS_{VII}, indicating that is necessary to vary the modulus in order to have acceptable frequency tuned results. The conclusions in the first step of FEMU from the frequency errors and average MAC and NDM values remain valid. Again, there is a difficulty to adjust the experimental modes shapes to the numerical ones. The MAC values are less than 0.8 and the NMD higher than 50%.

The second location analysis (with the four springs) was carried out with the information emerged from the non-model based methods, namely with the existence of four cracks in the arch at positions P1, P3/P4, P8/P9 and P11. In this analysis, only three cracks were located and assessed at positions P1, P4 and P8. The estimated crack depths in the final DS were equal to 21.1, 30.4 and 0.3 mm for the same positions, respectively.

Table 5.16 – Second location analysis (values of the updating parameters).

Damage Scenarios	$K_{r,P1}$		$K_{r,P4}$		$K_{r,P8}$		$K_{r,P11}$	
	Local Stiffness [MPa]	Crack Depth [mm]	Local Stiffness [MPa]	Crack Depth [mm]	Local Stiffness [MPa]	Crack Depth [mm]	Local Stiffness [MPa]	Crack Depth [mm]
RS	1×10^6	–	1×10^6	–	1×10^6	–	1×10^6	–
DS_{IV}	1×10^6	–	1×10^6	–	1×10^6	–	1×10^6	–
DS_V	915.52	0.29	1×10^6	–	976.38	0.28	1×10^6	–
DS_{VI}	1.31	8.26	36.61	1.51	750.14	0.32	1×10^6	–
DS_{VII}	97.02	0.91	953.02	0.28	952.87	0.28	1×10^6	–
DS_{VIII}	0.21	21.08	0.04	30.37	999.29	0.28	1×10^6	–

In this analysis it was also difficult to tune the modes shapes. Table 5.17 presents the average values for the frequency errors, MAC and NMD, which compared with the first location analysis, presents similar quality results.

Table 5.17 – Second location analysis (average values for frequencies, MAC, and NMD).

Damage Scenarios	Average ω Errors [%]	Average MAC values	Average NMD values
RS	| 3.56 |	0.78	0.51
DS_{IV}	| 3.19 |	0.78	0.52
DS_{V}	| 3.50 |	0.76	0.54
DS_{VI}	| 4.61 |	0.68	0.75
DS_{VII}	| 4.14 |	0.67	0.79
DS_{VIII}	| 3.56 |	0.78	0.51

From the two step approach with FEMU, it is possible to conclude that the updating analysis did not provide accurate results, on the contrary to the damage analysis of the numerical crack simulation presented in Section 5.4. A non explored procedure to increase the tuned results is to add in the objective function π the modal curvatures. Modal Curvatures prove to be useful information in the damage identification analysis for the case of non-model based methods. Note that this procedure was not used because DIANA (2006) does not have the option to calculate the curvatures directly from the results of the eigen problem analysis.

The difficulties of tuning the numerical model to the experimental mode shapes can be explained by the sensitivity of the dynamic response of the numerical model to the geometry, as addressed in Section 5.3. Another possible explanation for the low quality of the results is the residual deformation of the arch on each static test (see Chapter 4), which changes the geometry of the arch for each damage scenario. If the geometry is taken as an updating parameter for each DS, together with groups of spring elements to simulate localized cracks, the updating analysis will be tedious and complex, leading possibly to ill-conditioned solutions. Such analysis is hardly acceptable from a practical point of view and, if it is confirmed in real cases, is unreasonable to apply, being not pursued here.

5.6 Conclusions

In this chapter the damage identification analysis of a masonry arch model was presented. First, a selection of methods available in literature was made. The methods were combined in a qualitative approach with the aim to capture difficult phenomena and in assisting the decision of damage identification analysis. The methods were validated with a series of numerical simulations before being applied to the experimental modal data.

The selected methods are again presented in Table 5.18, together with the expected damage identification level, the need of a reference scenario and the require experimental modal information.

Table 5.18 – Selected damage identification methods.

Method	Expected Identification Level	Comparison to a Ref. Scenario	Modal Information				
			ω	φ	φ''	ϕ	ϕ''
Unified Significance Indicator (USI)	Level 1	Yes	•				
COMAC	Level 2	Yes		○	○	○	○
Parameter Method (PM)	Level 2	Yes	•	○	○	○	○
Mode Shape Curvature Method (MSCM)	Level 2	Yes			○		○
Damage Index Method (DIM)	Level 2	Yes			○		○
Sum of the Curvature Errors method (SCE)	Level 2	Yes			○		○
Change Flexibility Matrix method (CFM)	Level 2 and 3	Yes	•			•	○
Finite Element Model Updating method (FEMU)	Level 2 and 3	No	○	○	○	○	○

○ – Optional; • – Required; Level 1 – Detection; Level 2 – Localization; Level 3 – Assessment.

The selected methods, with the exception of the Unified Significance Indicator (USI), have one common aspect: they use spatial modal information of the structure, through mass-scaled or non-scaled mode shapes ϕ and φ, respectively (or/and through mass scaled or non-scaled curvatures mode shapes ϕ'' and φ'', respectively). The methods can be easily applied to masonry-like structures and, when applied in combination, they give information about the detection (Level 1), the localization (Level 2) and possibly the assessment (Level 3). In the case of non-measured curvatures, a procedure based on the central difference theorem for curved beams was used.

5.6.1 Results with Simulated Damage

Before damage identification using the experimental data, numerical crack simulations were carried out to evaluate the proposed approach. Three different finite element models were used to simulate cracks at different positions, and with three different crack depths, namely 15, 30 and 60% of the arch thickness. Two different results from the modal curvatures were also studied; the curvatures calculated in the centre line of the arch, as in

the experimental tests, and those calculated in the arch edges, derived from the modal displacements by the central difference theorem.

The first updating analysis to tune the undamaged condition allowed verifying that the arch dynamic response is very sensitive to geometry. A relative high number of updating parameters, such as the orthotropic behavior of the masonry material and several geometrical deviations, were used to have acceptable optimization results.

The results from the frequency values show that damage was detected after the second crack depth (15% of the arch thickness). With respect to the spatial modal information, the curvatures calculated in both arch edges are more sensitive to damage than the curvatures calculated with respect to the middle of the arch. This is due to the fact that higher modes have torsional and/or out-of-plane components.

With respect to the performance of the selected methods, the MAC and COMAC values were insensitive to damage for modal displacements and modal curvatures values. The Parameter Method (PM) was inconclusive for modal displacements, but for modal curvatures it was possible to locate the simulated damage. The others methods that used modal curvatures, namely the Mode Shape Curvature Method (MSCM), the Damage Index Method (DIM), the Sum of the Curvature Errors method (SCE), and the Change in Flexibility Matrix method (CFM), were able to localize accurately the damage. The last method used was the Finite Element Modal Updating method (FEMU) and it was able to locate and to assess the damage accurately.

An issue to highlight is the variation of the numerical scale factors in the different damage scenarios. As the simulated damage increases, in general, the errors also increase. This is important for the case of the CFM which requires mass-scale modes. In the experimental results, the modes were scaled only for the undamaged condition. Therefore, the CFM results can be contaminated with these errors, leading to inaccurate results.

Finally, in the numerical crack simulations, analyses with noise added to the modal data were also carried out. In this case, only the FEMU was able to detect accurately the damage, where it is possible to conclude that damage identification analysis with experimental modal results can be rather difficult due to the presence of noise.

5.6.2 Results with Experimental Data

After the comparison with the numerical data, the damage identification analysis was applied to experimental data. The damage analysis was divided in three groups: global parameters, non-model based methods and FEMU method.

The global parameter results from the damage scenarios revealed that modal properties of the masonry specimen were sensitive to induced damage. In terms of frequency results, the values significantly decrease at progressing damage, more than reported for other structures in the literature. The damping coefficient significantly increases after the occurrence of the first crack in the arch, although it can be an ambiguous parameter to use for damage detection due to dependence on other factors. It is again noted that MAC values were insensitive to damage.

The damage analysis with non-model based methods was divided in two groups of experimental modal data: the analysis with measured curvatures and the analysis with calculated curvatures, derived from the modal displacements. On each group, three different analyses were carried out by changing the reference scenario. The analysis with measured curvatures gives more accurate results, although it should be stressed that a

similar crack pattern could be identified with calculated curvatures. The analysis changing the reference scenarios gave the same final crack pattern, and a crack sequence based in the damage analysis was presented.

With respect to the performance of the non-model based methods, the presence of damage was easily identified with the USI. Nevertheless, it should be stressed that if no information about the history of modal information exists, the detection of damage with USI might be difficult, because no reference values in the undamaged condition are available. The COMAC values were insensitive to damage. The PM, the MSCM, the DIM and the SCE gave similar results and they were able to locate the damage in the vicinity of the experimental crack locations. The results from CFM were generally inconclusive due to the fact that mode shapes were not mass-scaled in the different damage scenarios.

The FEMU method was applied in a two step approach in order to localize and assess the damage. It was possible to conclude that the updating analysis did not give reliable results, neither to localize nor to assess damage, in opposition to the damage analysis of the numerical crack simulations. The difficulties to tune the numerical model to the experimental modal data can be explained by the sensitivity of the dynamic response of the model to the global geometry. Therefore, a large number of updating parameters would be required to tune each damage scenario, leading to a tedious and complex updating analysis, with likely ill-condition solutions.

Finally, for the case of the arch model, the damage could be successfully detected and localized based on dynamic changes, especially if modal curvatures are taken into account, as cracks were localized at a very early stage. Whenever possible, these quantities should be measured in real structures. It is also stressed that not all the methods could always capture the location of damage and there is no single method that worked for all damage scenarios. The reasons might be related to the presence of noise in the modal data, resulting from measurements and computations. The usage of different methods with adequate criteria to localize damage proves to be a best approach.

Chapter 6
Damage Identification in the Wall Model

Abstract

This Chapter presents the damage identification analysis of a masonry wall subjected to increasing loading. First, a description of the wall model is carried out, followed by the detailed description of the static tests. Next, the dynamic identification tests are addressed. The damage identification analysis is carried out in three phases: global parameters analysis, non-model based methods, and finite element model updating method. The results of each phase are extensively discussed and, finally, the conclusions emerging from the damage analyses are presented.

6.1 Introduction

This Chapter presents the damage analysis of the second specimen built in the laboratory: the wall model. The wall model was built after carrying out the test in the arch model but before the completion of the entire set of damage identification analyses. Therefore, only part of the experience gained in the first test campaign could be used in the wall model tests.

For the sake of conciseness, not all the analyses carried out in the wall model are presented here. Preliminary tests and immediate processing of results are essential for the success of the damage analysis, but, in order to give more attention to the damage identification analysis, only selected information will be presented here.

Next, a description of the wall model will be made, followed by a discussion of the static tests to induce damage in the structure and the details of dynamic identification tests. Finally, the damage analysis will be addressed together with the resulting conclusions.

6.2 Description of the Wall Model

The wall model was built with clay bricks with $210 \times 105 \times 55$ mm^3, handmade in the Northern area of Portugal. The adopted clay bricks have low compression strength and the adopted Mapei® mortar for the joints has low mechanical properties for the joints, trying to be representative of the materials used in the historical constructions. Figure 6.1 presents images of the wall construction and its geometry.

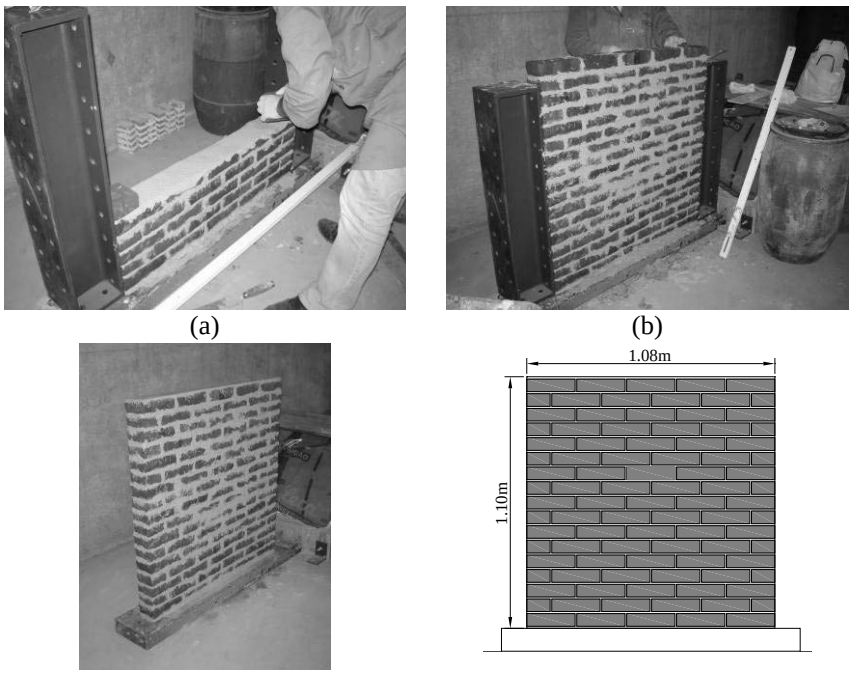


Figure 6.1 – Wall model: (a) and (b) starting and completion, respectively; (c) general view; and (d) geometry.

The wall has a length equal to 1.08 m, a height equal to 1.10 m, and a thickness equal to 0.105 m, which matches the bricks thickness. The thickness of the joints is about 1.0 cm.

The wall rests in a steel beam fixed to the ground floor with bolts and all tests were carried out in 2006, between January and March, and after 60 days of the wall construction.

6.3 Static Tests for Damage Scenarios

Fourteen Damage Scenarios (DS) were induced with the application of two static forces: a constant vertical force to replicate existing vertical compressive stresses and a horizontal force to produce shear stresses. The vertical load was transmitted through a group of three steel beams with appropriate devices to distribute uniformly the load to the wall. The last beam was direct glued to the wall. The in-plane stresses were applied with the aim of producing bending and shear cracks, i.e. to reproduce the common crack pattern present in the masonry piers that suffer earthquake actions. To achieve several controlled cracks, three series of static tests were carried out. In Series A, the horizontal load was applied in the top of the wall, see Figure 6.2a, and b, and, in Series B and C, the horizontal load was applied at half of the wall height, see Figure 6.2c, and d. The difference between Series B and C is the level of compressive stresses, which was higher in the second case. The vertical force was always applied in the same position with an average stress value of 0.5 MPa for Series A and B and 1.5 MPa for Series C.

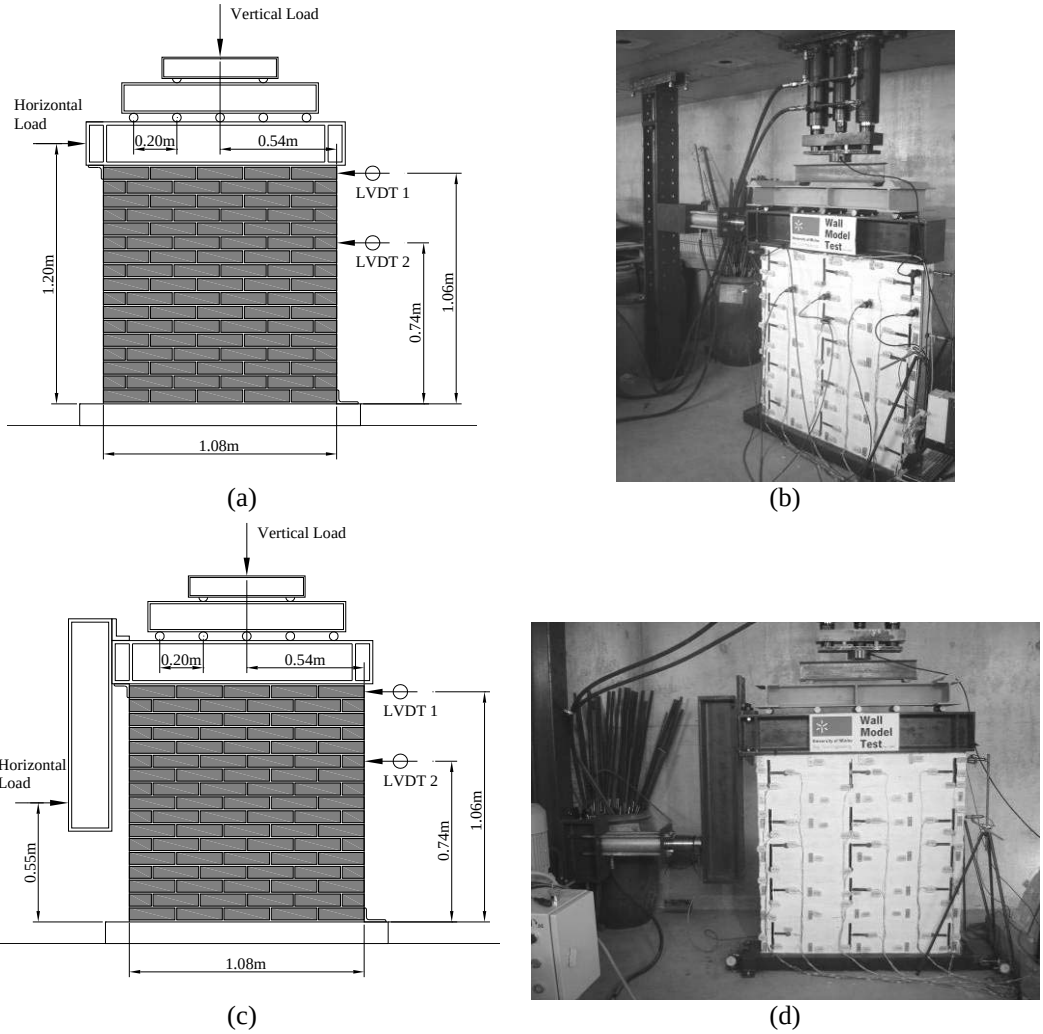


Figure 6.2 – Wall static tests: (a) and (b) location of the measuring points and a static test of Series A; (c) and (d) location of the measuring points and a static test of Series B and C.

On each series, the horizontal load was applied with linearly increasing magnitude, while the vertical force was kept constant. The forces were removed in all DS for the damage identification analysis, which simulates, to some extent, an overload during an extreme event, such as earthquake.

Two LVDTs and two load cells were selected to measure the static response. The LVDTs and the load cells were resistive transducers with adequate accuracy to measure the static response. The selected measuring points on the three series of tests are presented in Figure 6.2a and c. The horizontal displacement at the top of the wall is measured by LVDT 1. LVDT 2 was located above the mid-height of the wall to capture any horizontal sliding, and the vertical load was measured continuously to control the compressive stresses. The tests were carried out in load-control by means of hydraulic actuators, see Figure 6.2b and d.

On Series A five DS were produced, namely $DS_{I\text{-}A}$, $DS_{II\text{-}A}$, $DS_{III\text{-}A}$, $DS_{IV\text{-}A}$ and $DS_{V\text{-}A}$. Figure 6.3 shows the response of the model during the subsequent static tests, where the horizontal displacement indicated corresponds to the maximum or top value (LVDT 1).

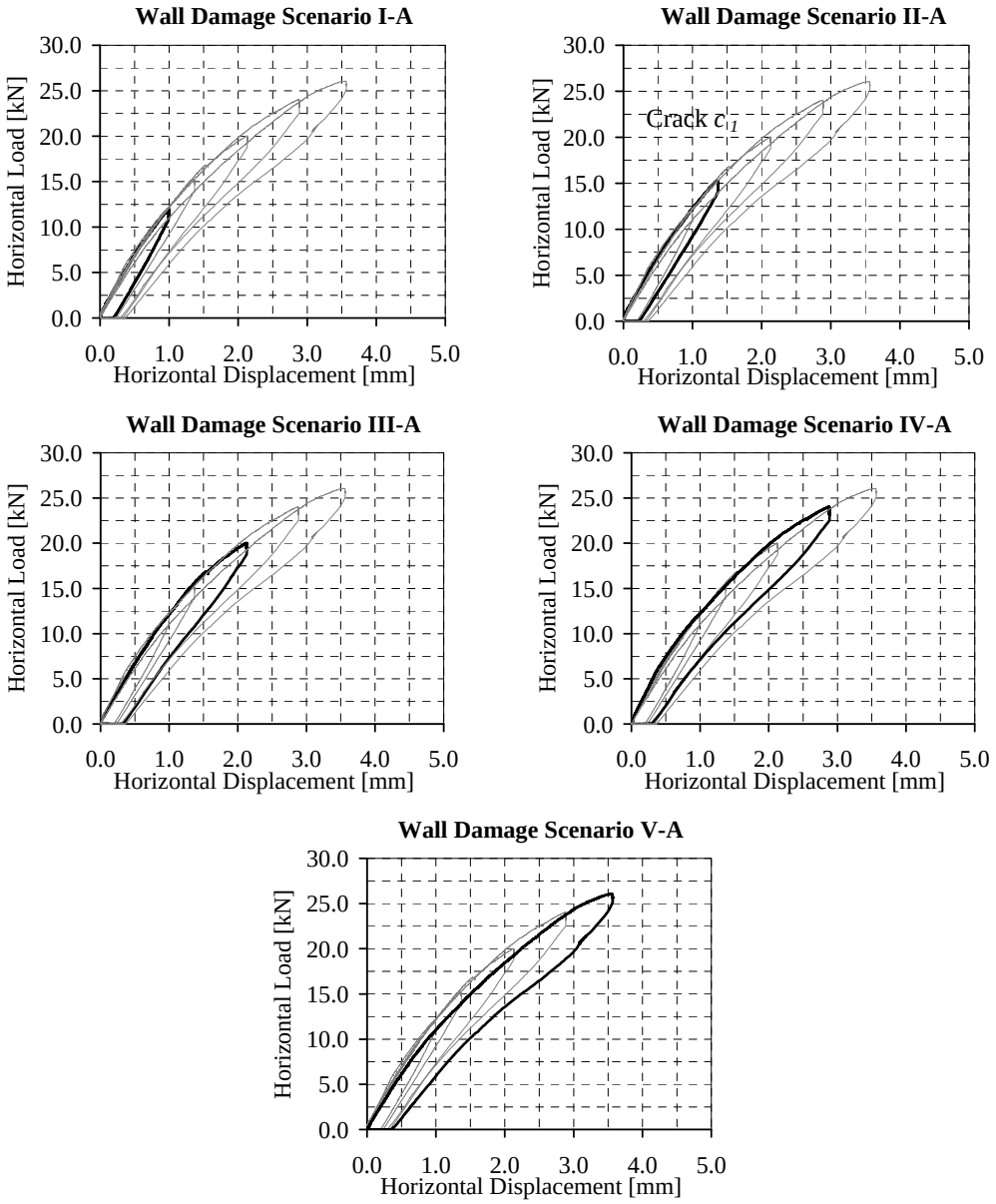


Figure 6.3 – Wall static response during Series A.

Figure 6.4 presents the Reference Scenario (RS) and the crack patterns of each DS, together with the position of the dynamic transducers. The first visible bending crack (c_1) occurred at the front bottom side of the wall in $DS_{II\text{-}A}$, with a maximum opening less than 0.05 mm. The crack increased its length in the subsequent DS and reached a maximum opening equal to 0.10 mm in the front side and 0.05 mm in the back side of the wall.

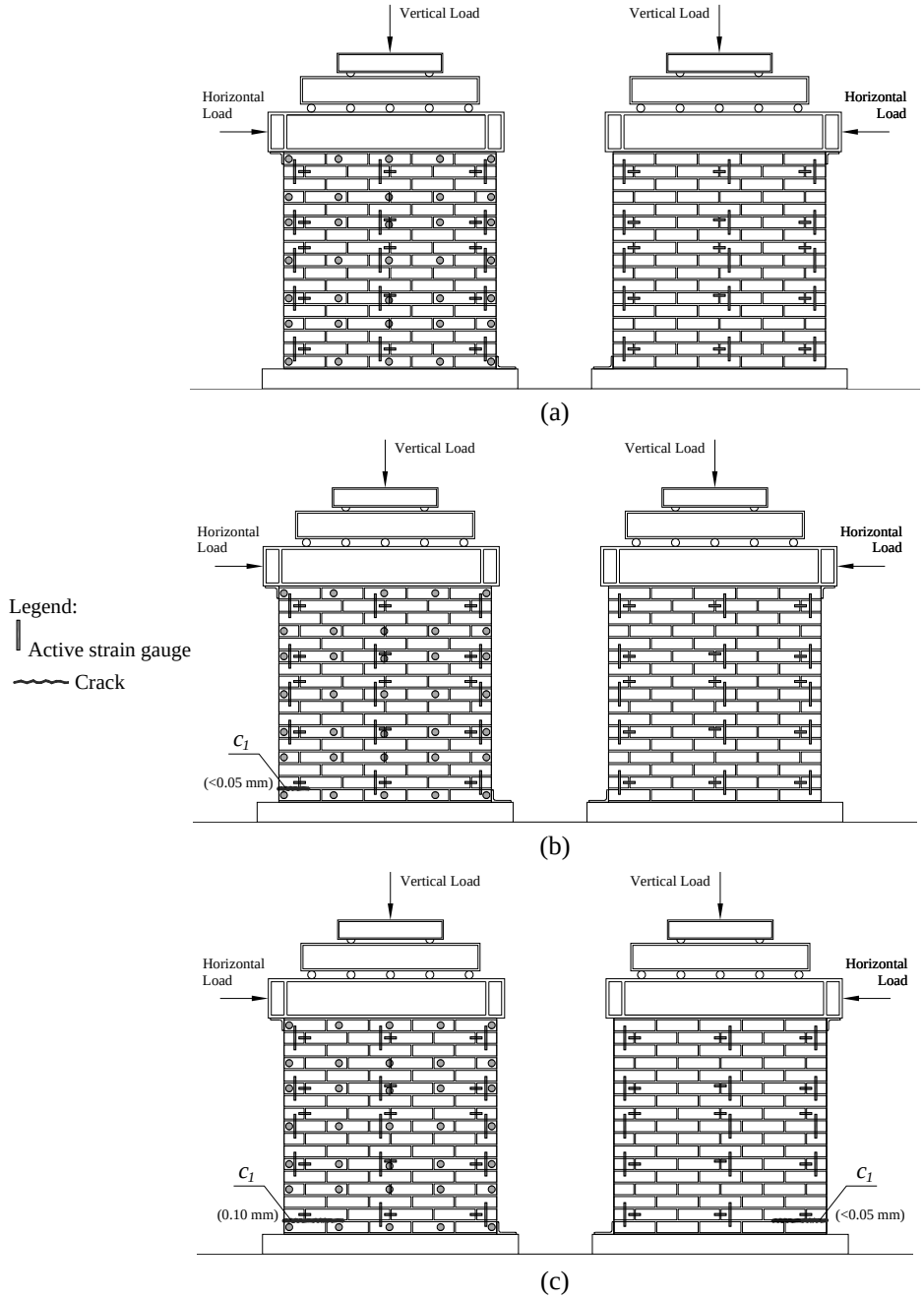
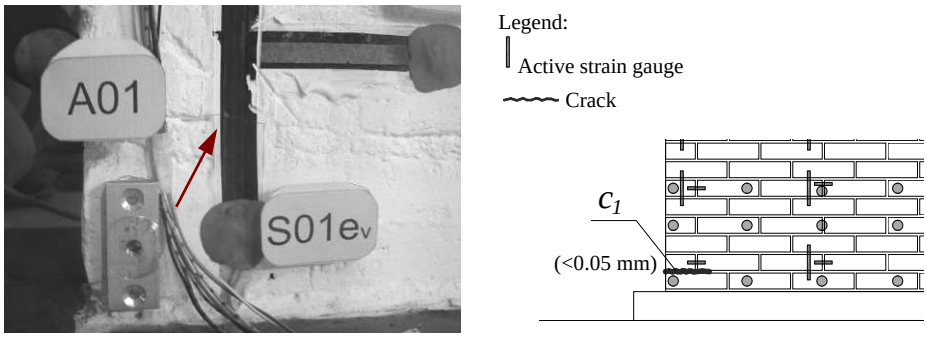


Figure 6.4 – Front and back view of the crack pattern of Series A: (a) RS_A and $DS_{I\text{-}A}$; (b) $DS_{II\text{-}A}$; and (c) $DS_{III\text{-}A}$, $DS_{IV\text{-}A}$ and $DS_{V\text{-}A}$.

It should be stressed that the first crack broke one vertical strain gauge in the front side of the wall, see the missing strain gauges in Figure 6.5, but the strain gauge at the back side and in the same position was still able to measure strains. Figure 6.5 shows the crack at $DS_{V\text{-}A}$, where the difficulties to visualize the crack with a 0.10 mm opening are obvious. Without painting the specimen in white colour, the crack visualization would be hardly difficult.



(a) (b)

Figure 6.5 – Damage in Series A ($DS_{V\text{-}A}$): crack across the strain gauge; and (b) schematic representation

On Series B, again five DS were produced, namely $DS_{I\text{-}B}$, $DS_{II\text{-}B}$, $DS_{III\text{-}B}$, $DS_{IV\text{-}B}$ and $DS_{V\text{-}B}$. Figure 6.6 shows the response of the model during the subsequent static tests. The horizontal displacement indicated corresponds to the top value. Note that although the vertical load has the same value, the horizontal load is now at different position and therefore the static response is also different.

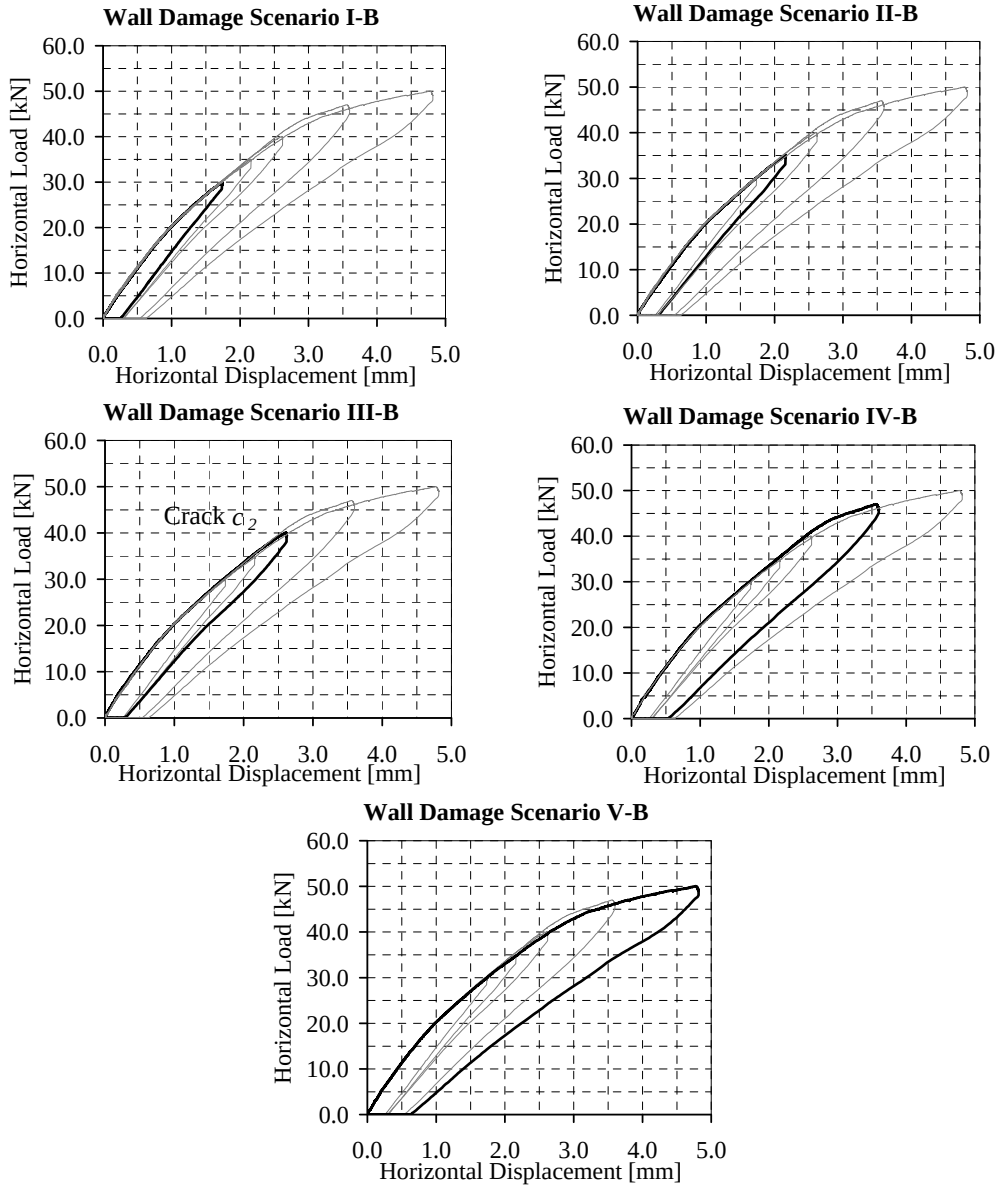


Figure 6.6 – Wall static response during Series B.

Figure 6.7 and Figure 6.8 present the respective crack patterns in the wall for Series B. In this case, crack c_1 in RS_B has a length higher than in the $DS_{V\text{-}A}$, see Figure 6.4c, due to the necessary adjustments in the test setup. In $DS_{III\text{-}B}$ a new visible bending crack (c_2) occurred at top of the wall, in an opposite position with respect to crack c_1, see Figure 6.7c. The new crack started with a maximum opening of 0.05 mm and ended with 0.10 mm at $DS_{V\text{-}B}$. In the last DS the first crack at the bottom (c_1) increased its extent to the complete wall length and its maximum opening to 2.00 mm, see Figure 6.8, but without sliding of the wall. In the last DS the lateral drift, calculated as the quotient between the lateral maximum displacement divided by the wall height (%), was about 4%, which is the double of the typical value reported by others researchers, see Vasconcelos (2005). This indicates that the wall was most likely failing in rocking. In this series, the crack c_1 broke more three vertical strain gauges at front and back side of the wall (see the missing strain gauges). Figure 6.9 shows the two cracks in the wall at the final DS of Series B.

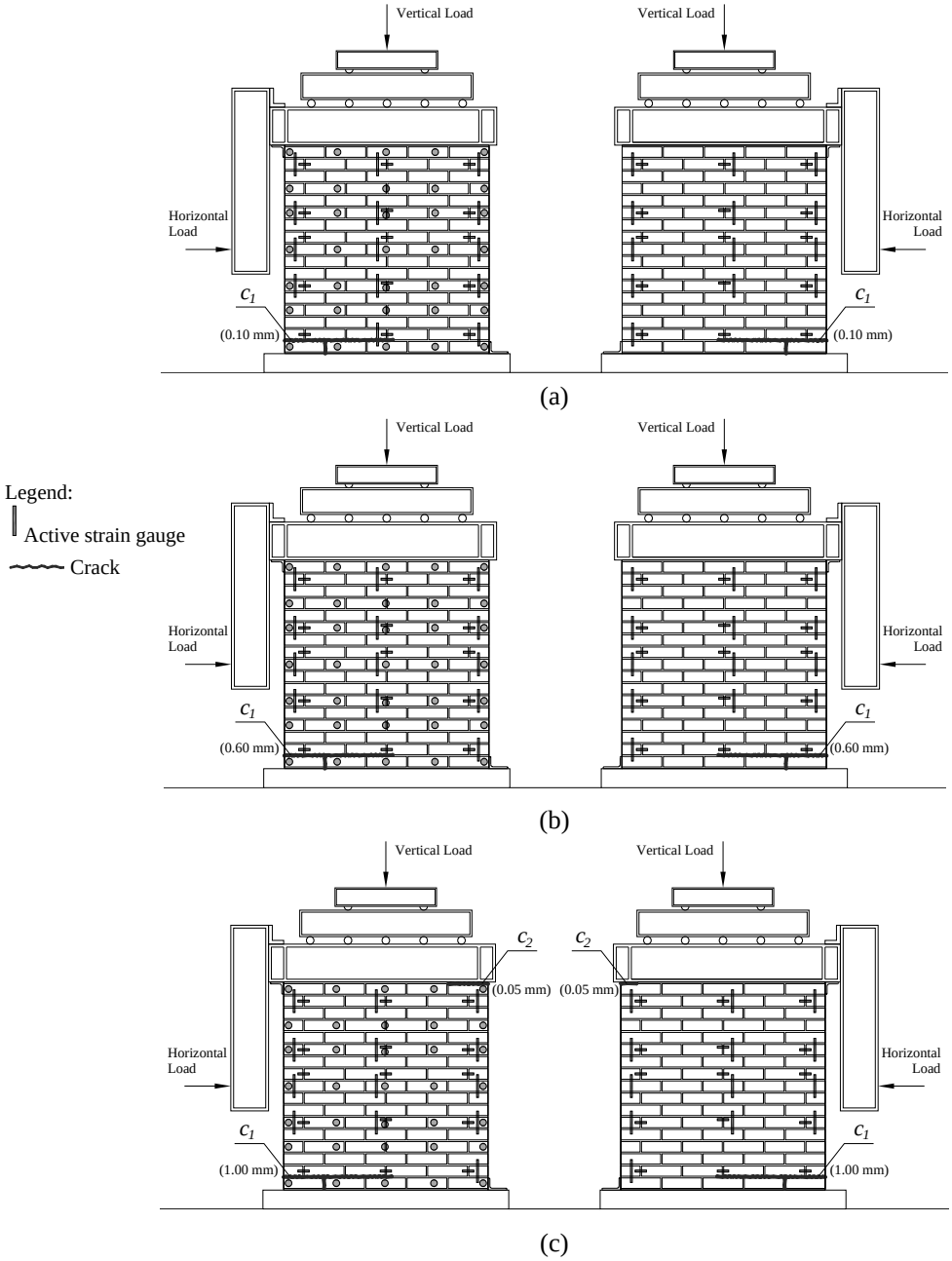


Figure 6.7 – Front and back view of the crack pattern of Series B: (a) RS_B and $DS_{I\text{-}B}$; (b) $DS_{II\text{-}B}$; and (c) $DS_{III\text{-}B}$.

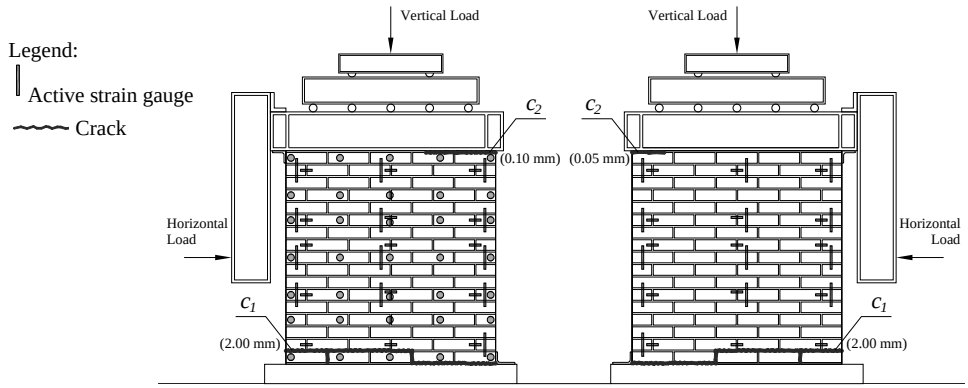
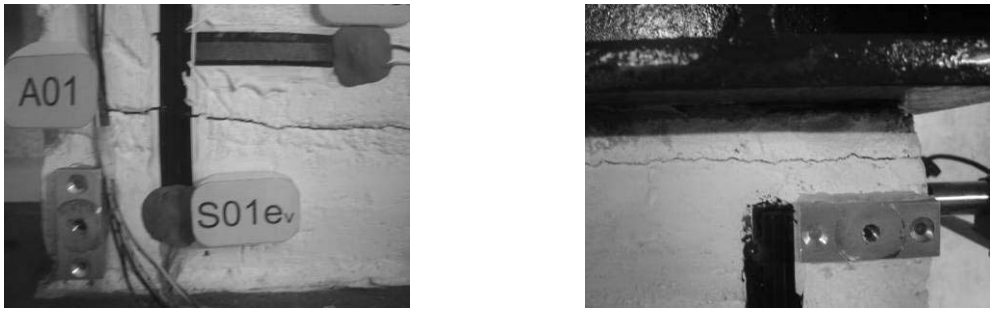


Figure 6.8 – Front and back view of the crack pattern $DS_{IV\text{-}B}$ and $DS_{V\text{-}B}$ of Series B



(a) (b)

Figure 6.9 – Damage in Series B ($DS_{V\text{-}A}$): (a) crack c_1; and (b) crack c_2

As no shear crack was observed in the wall, on the third series of tests the vertical compression load was increased and four DS were produced, namely $DS_{I\text{-}C}$, $DS_{II\text{-}C}$, $DS_{III\text{-}C}$, and $DS_{IV\text{-}C}$. Figure 6.10 presents the static response during all DS. In this series a shear crack c_3 was occurred at $DS_{II\text{-}C}$.

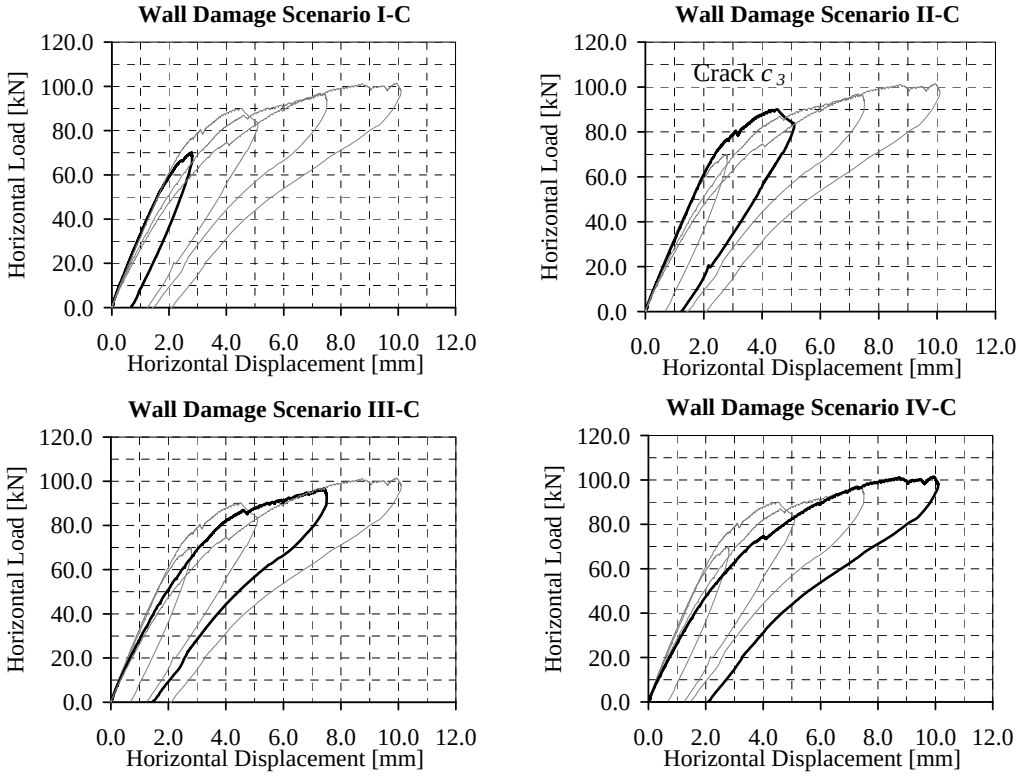


Figure 6.10 – Wall static response during Series C.

The occurrence of crack c_3 is obvious by the visible load drops with crack opening in the respective static response. Note that here the designation c_3 is related to a group of diagonal shear cracks that, together, compose one diagonal macro crack through units and joints. The different static response of the model due to increasing vertical load should also be noted. In the last DS, the lateral drift was about 9%, a very high value resulting from the combination of shear and rocking behaviour.

Figure 6.11 and Figure 6.12 present the crack patterns of the last series. The shear crack c_3 started to be visible in $DS_{II\text{-}C}$ with a maximum opening of 0.50 mm, see Figure 6.11b. In the final DS the maximum opening was equal to 1.20 mm, see Figure 6.12. The bending cracks c_1 and c_2 did not increase the value of the maximum opening.

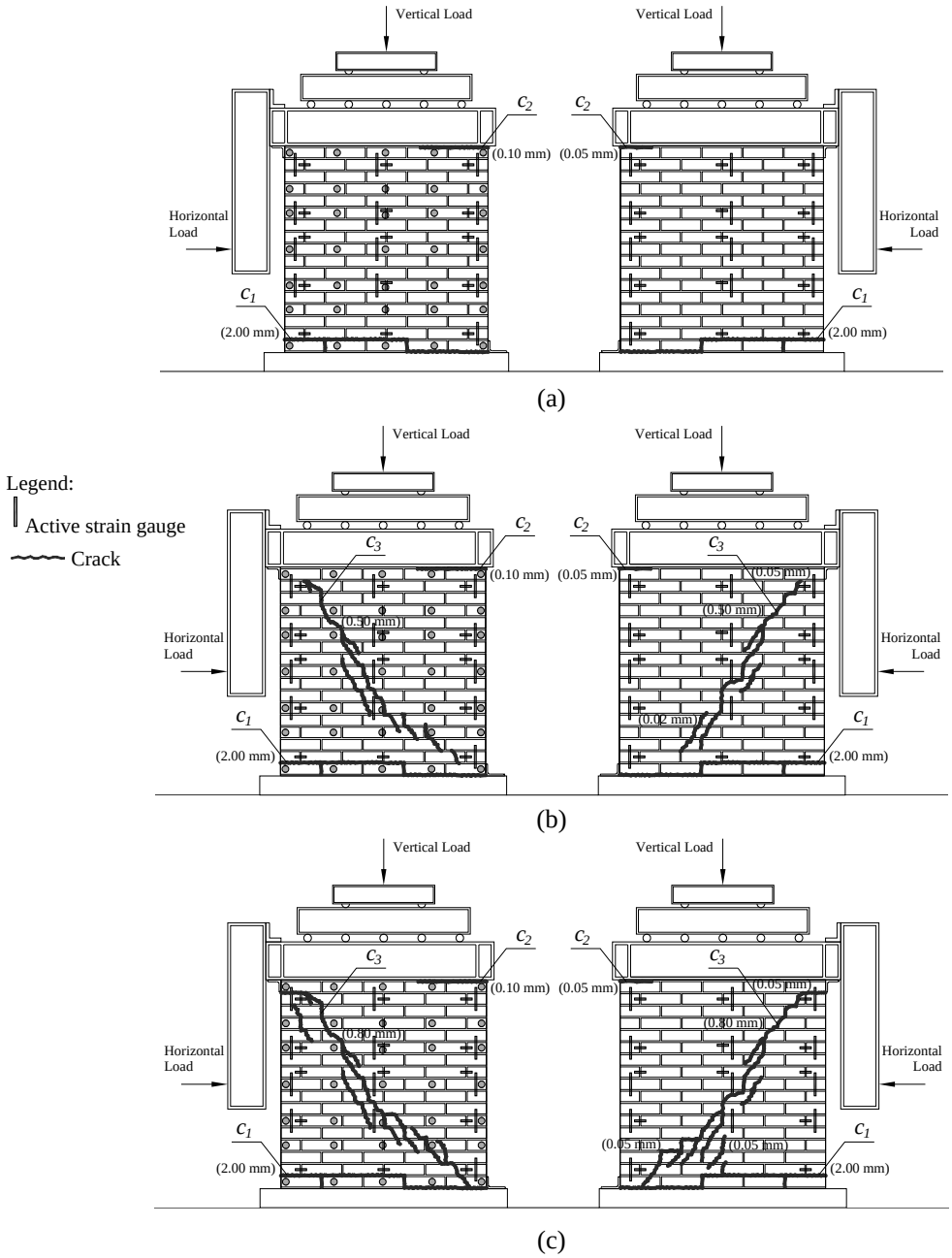


Figure 6.11 – Front and back view of the crack pattern of Series C: (a) RS_C and $DS_{I\text{-}C}$ (b) $DS_{II\text{-}C}$; and (c) $DS_{III\text{-}C}$.

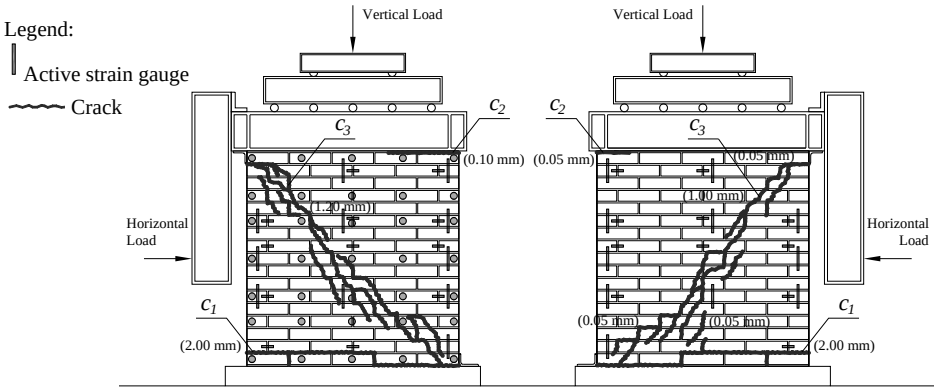
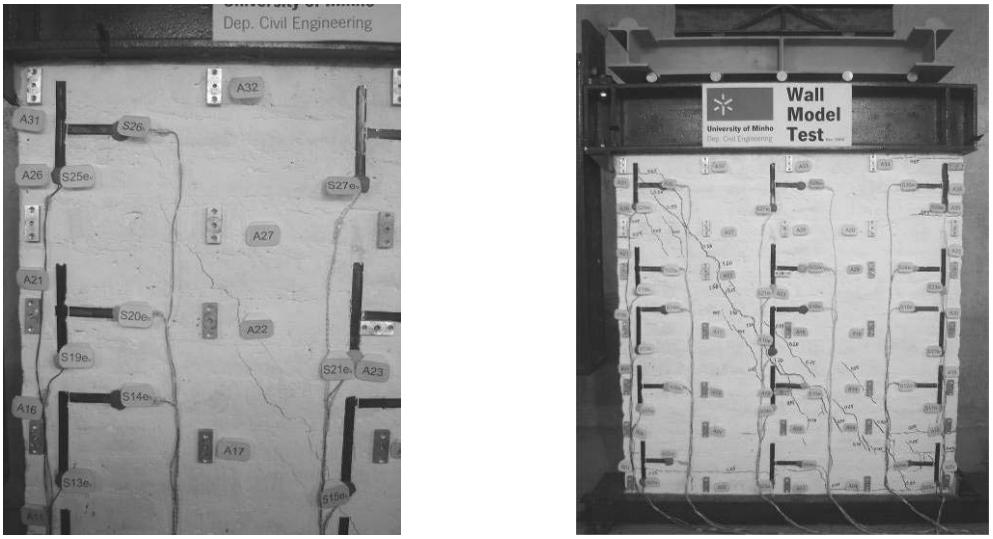


Figure 6.12 – Front and back view of the crack pattern of $DS_{IV\text{-}C}$ for Series C.

Figure 6.13 presents images of the observed cracks in Series C. The crack pattern was practically symmetric in both sides of the wall and additional ten strain gauges were broken (fourteen in total).



(a) (b)

Figure 6.13 – Damage in Series C: (a) crack c_3 in $DS_{II\text{-}C}$; and (b) final crack pattern. Note that, in the second picture, the cracks were drawn with a black marker in order to be visible.

Analyzing now the unloading stiffness during the several tests, presented in Figure 6.14a to Figure 6.14c, it is possible to observe that the stiffness decreases with increasing damage. Note that the stiffness cannot be compared from series to series due to the different tests configurations, but on each series it is possible to observe a continuous stiffness decrease. The larger stiffness loss was observed in Series C from $DS_{I\text{-}C}$ to $DS_{II\text{-}C}$, when the shear crack c_3 occurred, see Figure 6.14c and d.

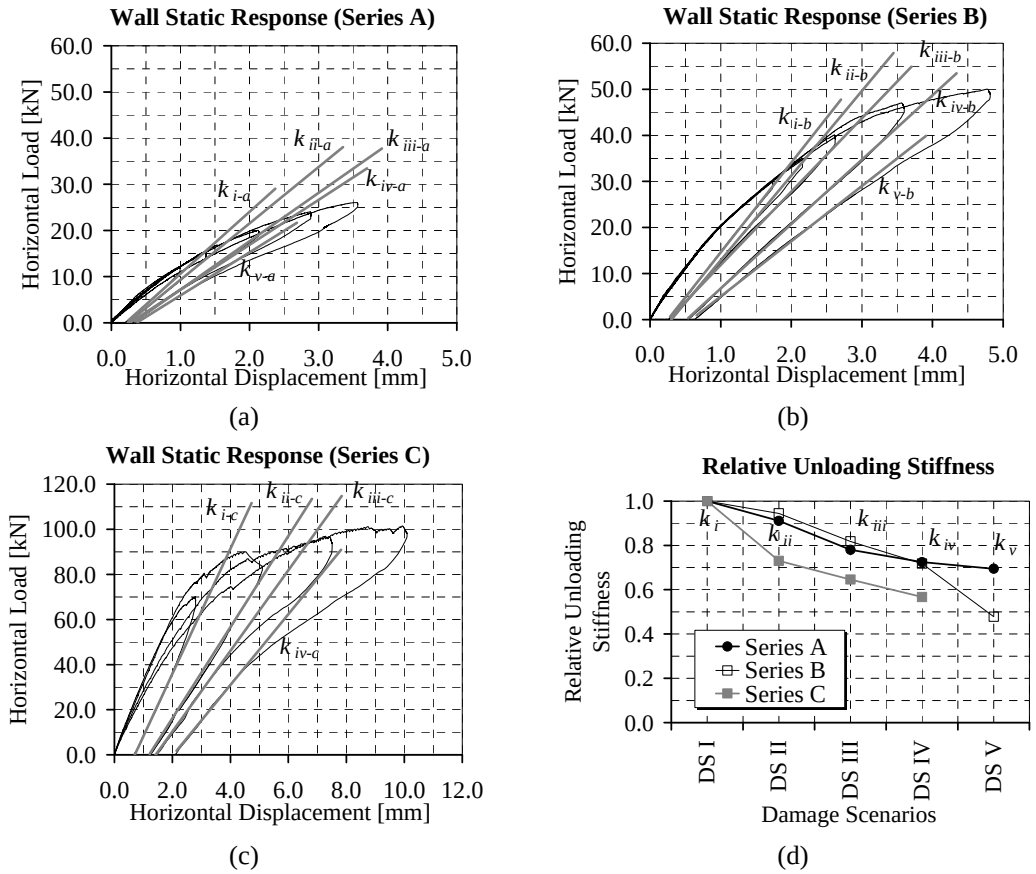


Figure 6.14 – Unloading stiffness decreasing in the wall model. Note that the scales are different on Series C.

6.4 System Identification Tests

As carried out in Chapter 5, between each DS, modal identification analysis using output-only techniques was performed. To evaluate the possible environmental effects on the dynamic response, the ambient temperature and the relative air humidity were also measured.

Next, the preliminary system identification analysis using a numerical model will be described, followed by a discussion on the test planning. A qualitatively analysis using a comparison between different stochastic subspace identification tools will be addressed for the RS_A.

6.4.1 Numerical Estimation of Modal Parameters

Even if presented here, this analysis was performed before the static tests to better define the dynamic experimental tests. The DIANA (2006) Finite Element (FE) package was used to built a 3D FE model with 8 noded shell elements. Note that a 3D model was chosen so that all the modes could be estimated. The elastic properties of the masonry material were: Young's modulus equal to 1.0 GPa, Poisson coefficient equal to 0.2, and mass density equal to 1875 kg/m^3. The steel beam on the top of wall, glued to the last mortar joint, was also simulated with a Young's modulus equal to 210.0 GPa, Poisson

coefficient equal to 0.3, and a weigh including all the tests apparatus. The bottom boundary was considered fully constrained.

Two different test configurations were considered: the test configuration of Series A and the test configuration of Series B and C. Figure 6.16 shows the results in terms of frequency values and mode shape configurations for the first twelve modes of Series A. The range of frequencies starts from 6.72 up to 216.01 Hz. All the frequencies are well spaced. There are three modes with modal components only in the wall plane, namely the 4th, the 8th and 10th mode. The out-of-plane modes present almost perfect symmetry.

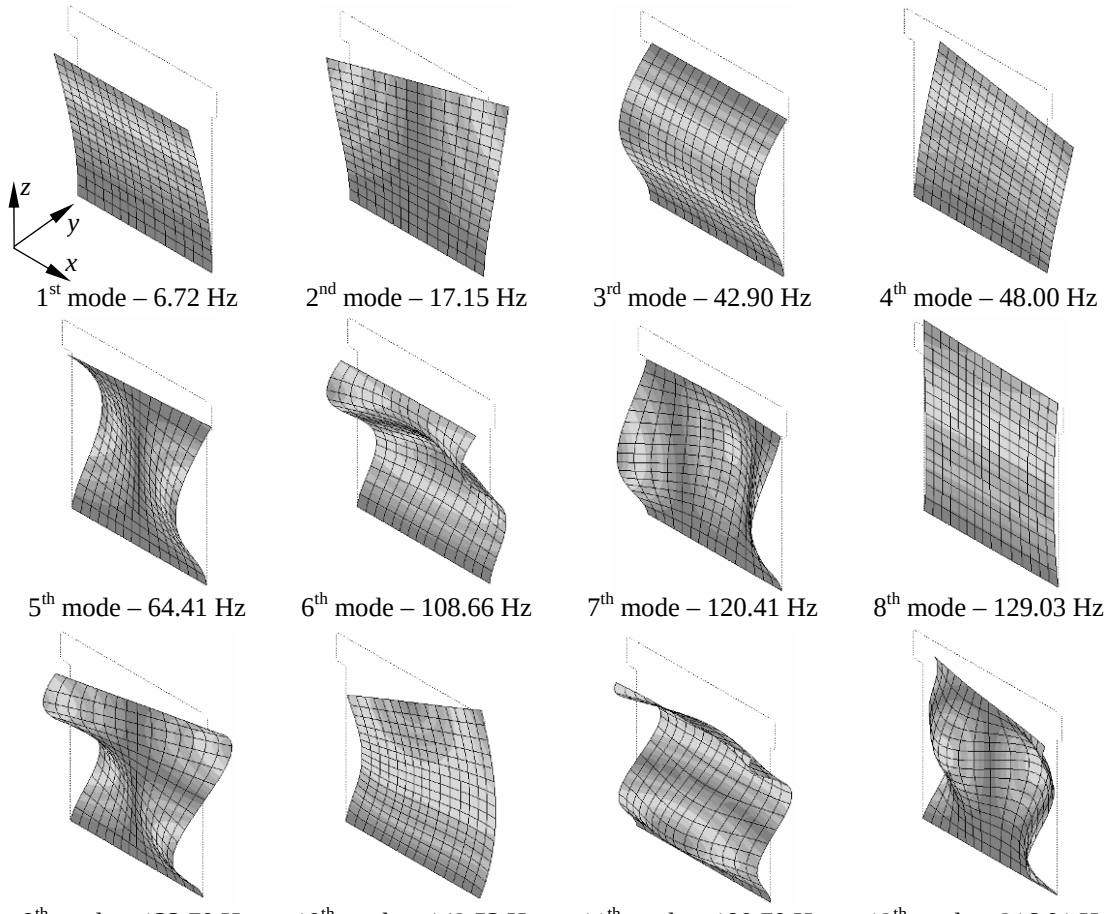


Figure 6.15 – Numerical modal estimation for Series A (mode shapes and frequency values). Note that only the elements with the masonry material are presented here.

Figure 6.16 shows the same results for the case of test configuration of Series B and C. In this case, a drop of the frequency values is observed due to the added vertical beam to the test apparatus for the application of the horizontal force. The frequency range starts now from 5.88 up to 165.09 Hz, with well spaced values. Because of the eccentricity of the steel beams, the modes with out-of-plane components are not symmetric. The modes with in-plane components are the 4th, the 7th and the 10th mode.

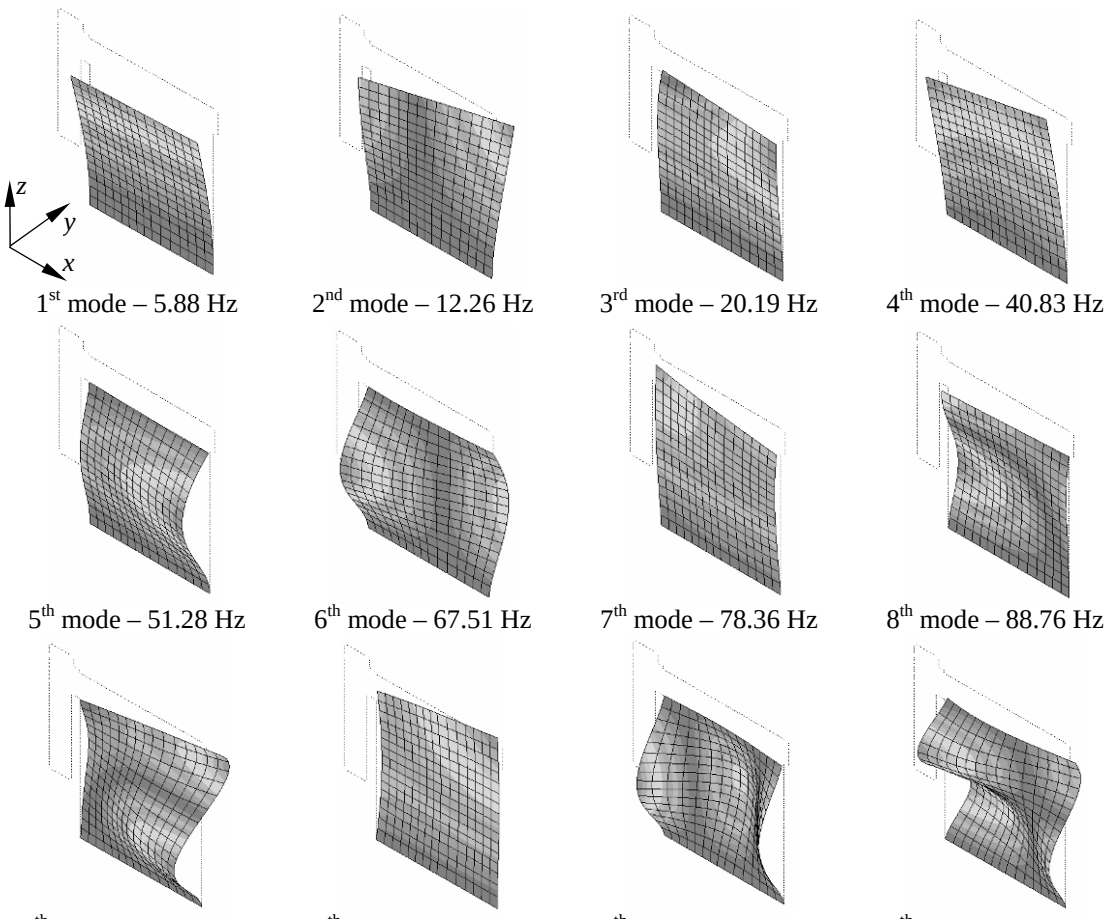


Figure 6.16 – Numerical modal estimation for Series B and C (mode shapes and frequency values). Note that only the elements with the masonry material are presented here.

6.4.2 Test planning

The selected sensors for the dynamic tests were the same as in Chapter 4: accelerometers and strain gauges with quarter bridge configuration. The same dynamic acquisition system was used with a sampling frequency of 2000 Hz.

From the preliminary numerical analysis, it was possible to conclude that nine modes have significant out-of-plane modal displacements, including the first three modes. For this reason, it was decided to measure accelerations only in the out-of-plane direction. A regular grid of five vertical lines and seven horizontal lines was chosen for the accelerometers. In the case of the strains gauges, it was decided to use an array of three vertical lines and five horizontal lines. Figure 6.17 shows the location of the measuring points where the reference points are given in a grey box. The selection of the reference points was carried out according to the configuration of the twelve numerical mode shapes. The designation A*i* is for accelerometers and S*i* is for strain gauges.

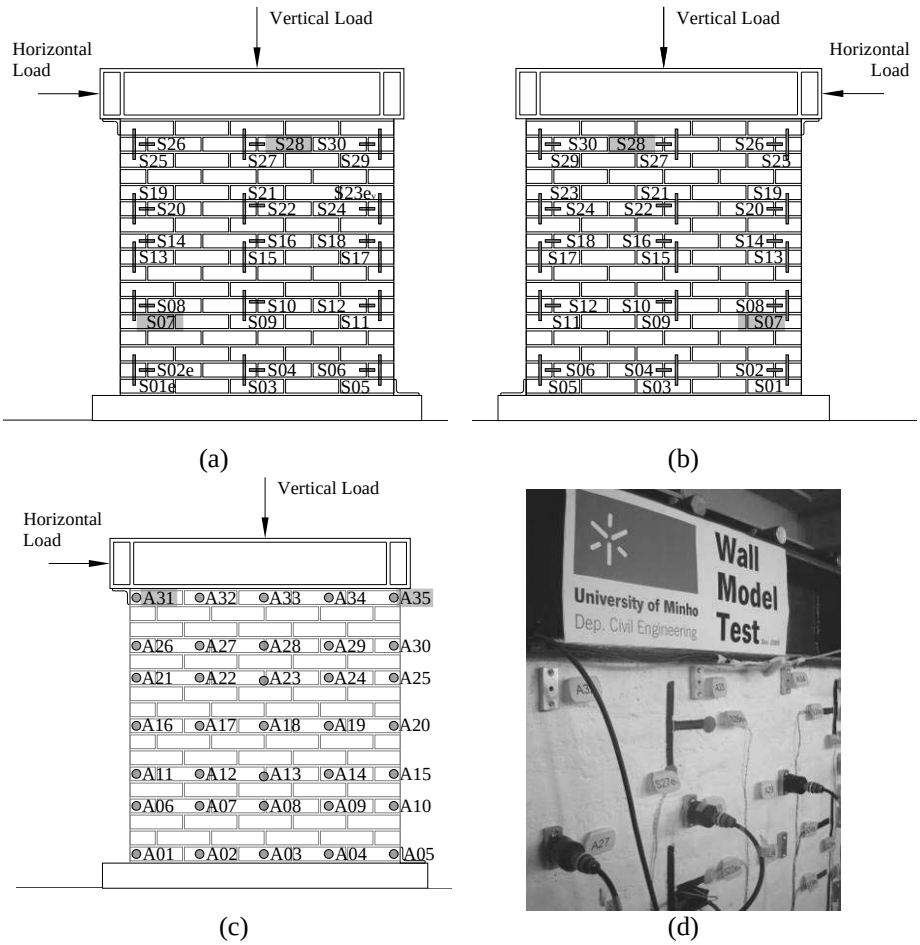


Figure 6.17 – Location of the measuring points for the dynamic tests: (a) and (b) location of strain gauges in the front and back side, respectively; (c) location of the accelerometers in the front view; and (d) detail of the different transducers. A*i* indicates accelerometers and S*i* indicates strain gauges. Boxed-values in grey are the reference points.

The accelerometers were bolted to aluminum plates that were directly glued to the wall. The vertical strain gauges have 12 cm of length and the horizontal strain gauges have 6 cm of length. This way, the vertical strain gauge crosses, at least, three joints and the horizontal strain gauge only one joint. The specimen was located in the Laboratory near the arch model presented in Chapter 4.

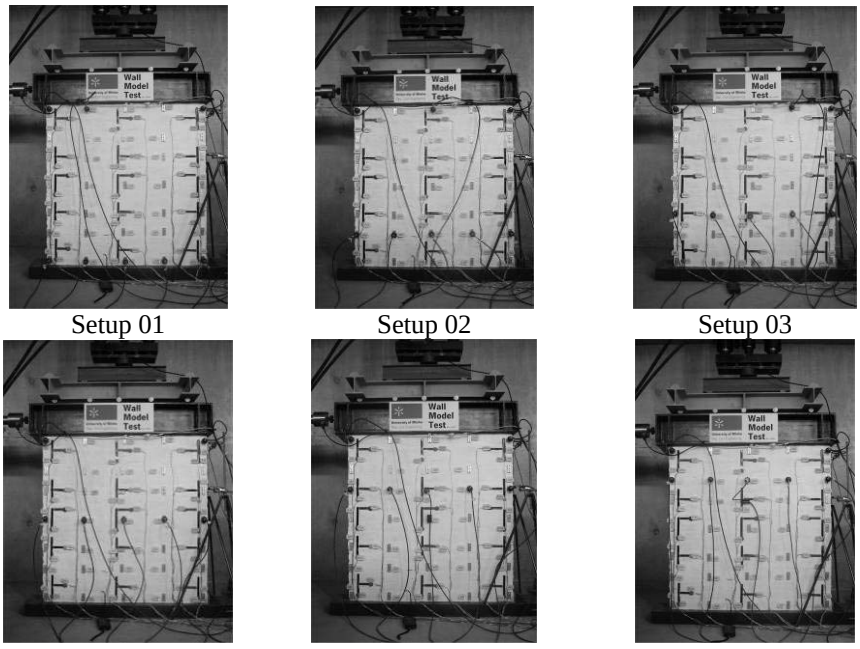
The dynamic identification tests were carried out in 13 test setups divided into two groups, see Table 6.1 and Table 6.2. The first group corresponds only to acceleration measurements with the reference transducers at positions A31 and A35, see Figure 6.17c and Figure 6.18. The strains measurements were acquired in the second group. For the second case, the reference sensors for accelerations were kept, and two reference sensors for strains at positions S07 and S28 were added, see Figure 6.17a and b, and Table 6.2. It was decided to separate accelerations from strains because sharp frequency peaks around 50 Hz were observed in a preliminary dynamic test. On each test setup, time segments were recorded with a complete measuring time equal to 2000 times the first (highest) period of the structure, with a minimum duration equal to 6 minutes.

Table 6.1 – Test setups for accelerometers.

Setup	Ref. 1	Ref. 2	Mov.1	Mov. 2	Mov. 3	Mov. 4	Mov. 5	Mov. 6
1	A31	A35	A01	A02	A03	A04	A05	A32
2	A31	A35	A06	A07	A08	A09	A10	A33
3	A31	A35	A11	A12	A13	A14	A15	A34
4	A31	A35	A16	A17	A18	A19	A20	–
5	A31	A35	A21	A22	A23	A24	A25	–
6	A31	A35	A26	A27	A28	A29	A30	–

Table 6.2 – Test setups for strain gauges[†].

Setup	Ref. 1	Ref. 2	Ref.3	Ref.4	Mov.1	Mov.2	Mov.3	Mov.4
7	A31	A35	S07	S28	S07	S28	S07	S28
8	A31	A35	S07	S28	S05	S06	S08	S7
9	A31	A35	S07	S28	S09	S10	S11	S12
10	A31	A35	S07	S28	S13	S14	S15	S16
11	A31	A35	S07	S28	S17	S18	S19	S20
12	A31	A35	S07	S28	S21	S22	S23	S24
13	A31	A35	S07	S28	S25	S26	S39	S30



Setup 01 Setup 02 Setup 03

Setup 04 Setup 05 Setup 06

Figure 6.18 – Dynamic test sequence, with the different setups and two reference positions (two sensors).

As performed in the arch model described in Chapter 4, two different excitation types were used during the identification tests: (a) natural and ambient noise present in the laboratory; and (b) random impact excitation in space and in time. The impact forces were about 2% of the specimen mass. Figure 6.19 presents the impact time history of one test and the respective power spectrum, where one can see that for frequencies less than 200 Hz

[†] The strain gauges are fixed to the structure but the data acquisition system only allowed to read 16 strain gauges channels simultaneously, while 60 strain gauges were glued to the wall. Thus, seven different setups were required.

the spectrum is almost flat, but has a sharp peak around 50 Hz. This might indicate that resonant frequencies close to the 50 Hz can be contaminated with electrical noise. During the dynamic identification tests several procedures were carried out to minimize this noise, although it was always present in the signals.

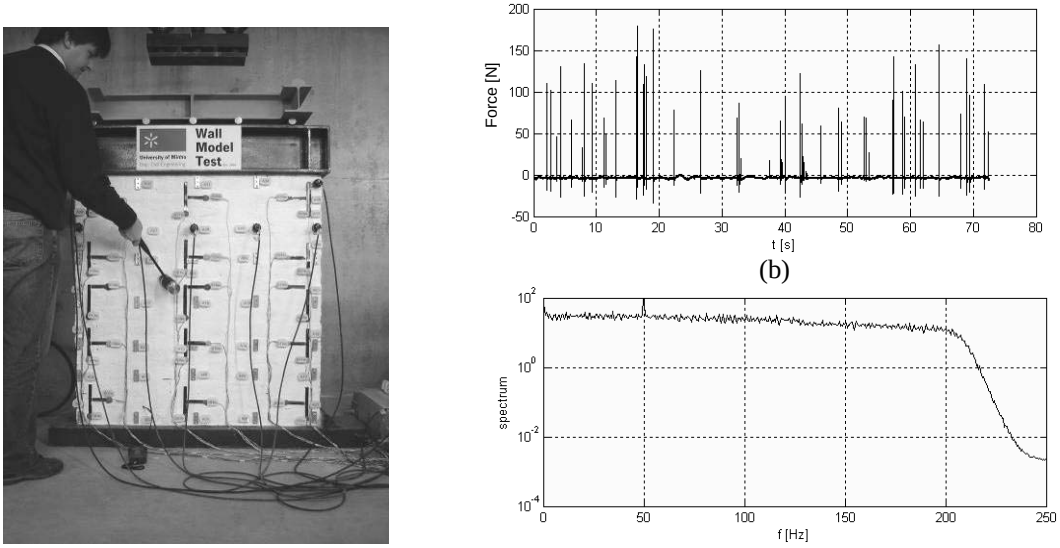


Figure 6.19 – Random impact excitation: (a) impact tests; (b) impact time history; and (c) impact spectrum.

6.4.3 Environmental Tests in the Laboratory

About the influence of the long-term changes of the environmental effects inside the laboratory, Figure 6.20 presents the average values for ambient and surface temperature and relative air humidity measured for each DS. The average temperature values were about 17ºC with a low increasing trend. The average humidity is about 69% with ±7% of maximum amplitude. As considered in Chapter 4 for the arch model, it is expected for values of that order that the dynamic response of the wall does not change significantly and therefore it is assumed that the environmental effects inside the laboratory can be neglected in the subsequent damage identification analysis.

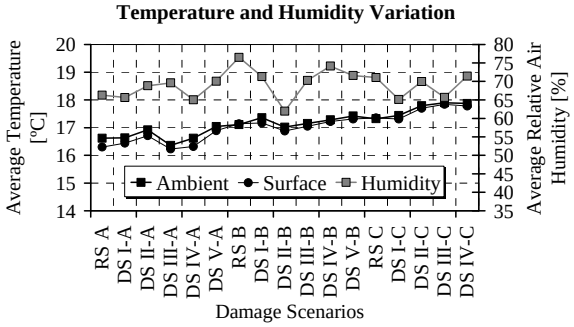


Figure 6.20 – Average environmental effects along the damage scenarios

6.4.4 Evaluation of the Data Quality

In order to evaluate the quality of the experimental data, two different tools were used to estimate the dynamic properties for the RS_A (Series A). Again, the SSI/Principal

Component method available in ARTeMIS Extractor software (SVS, 2006) and the SSI/Ref method implemented in the MACEC tool from Catholic University of Leuven (Peeters and De Roeck, 1999) were selected for parameter estimation.

From the numerical simulation twelve modes were expected to be estimated, but, in practice, only four experimental modes could be accurately estimated. The noise present in the data did not allow the estimation of higher modes.

Table 6.3 and Table 6.4 present the frequency values ω, the damping ξ with the standard deviations σ and Coefficient of Variations CV for the ambient and random excitation tests, respectively. Comparing the values from the two tools on each excitation type, the frequency results seem acceptable with no significant standard deviation values. The random impact excitation tests have lower standard deviation values, indicating a possible better modal estimation. For the case of the damping coefficient, the high CV values in all excitation types should be stressed, indicating possible less accurate results. As mention before, the damping values depend on the excitation mechanism and in the nonlinear phenomena. For the case of ambient excitation, the average value is equal to 2%, while for the random impact excitation an average value is 4.9%.

Table 6.3 – Results from RS_A with ambient excitation test.

Modes	ARTeMIS Estimation						MACEC Estimation					
	ω [Hz]	σ_ω [Hz]	CV_ω [%]	ξ [%]	σ_ξ [%]	CV_ξ [%]	ω [Hz]	σ_ω [Hz]	CV_ω [%]	ξ [%]	σ_ξ [%]	CV_ξ [%]
1	5.21	0.06	1.11	0.57	0.21	37.06	5.17	0.03	0.64	0.70	0.17	24.73
2	19.93	0.16	0.80	0.97	0.38	39.44	20.61	1.49	7.22	0.76	0.53	70.65
3	33.33	1.47	4.41	2.96	0.45	15.11	33.41	1.61	4.82	2.76	0.73	26.62
4	67.06	3.14	4.67	3.45	0.85	45.68	64.57	1.47	2.27	3.51	0.43	12.21

Table 6.4 – Results from RS_A with random impact excitation test.

Modes	ARTeMIS Estimation						MACEC Estimation					
	ω [Hz]	σ_ω [Hz]	CV_ω [%]	ξ [%]	σ_ξ [%]	CV_ξ [%]	ω [Hz]	σ_ω [Hz]	CV_ω [%]	ξ [%]	σ_ξ [%]	CV_ξ [%]
1	5.01	0.02	0.48	2.69	0.24	9.03	5.02	0.02	0.45	1.88	0.26	13.60
2	19.73	0.05	0.27	0.96	0.05	4.11	19.73	0.04	0.19	1.48	1.25	84.32
3	41.62	0.37	0.89	7.19	0.37	5.15	41.24	0.55	1.85	8.80	0.86	9.82
4	57.39	0.49	0.86	7.78	0.49	6.30	57.65	0.92	1.60	8.09	1.61	19.91

Comparing the values from the two different excitation types, significant differences between frequency values were found, especially for the third and fourth modes. In the beginning, it was thought that these frequencies were not from the same modes, but observing the mode shape configurations presented in Figure 6.21, it is possible to verify that those frequencies are from the same modes. This might be related to the high nonlinear dynamic behavior of the wall for the two different excitations levels. Figure 6.21 also compares the results concerning the MAC values on both type of excitation. It is stressed that the modal displacements are only accurate for case of the random impact excitation, as the minimum MAC value is about 0.96. Observing the modes from the ambient excitation, significant differences were found for the second and fourth modes, indication that these modes were not properly estimated. Therefore, in the damage identification analysis carried out next, for frequency comparison both excitation results will be used (ambient and random impact), but when modal displacements are required only the random impact excitation results will be used.

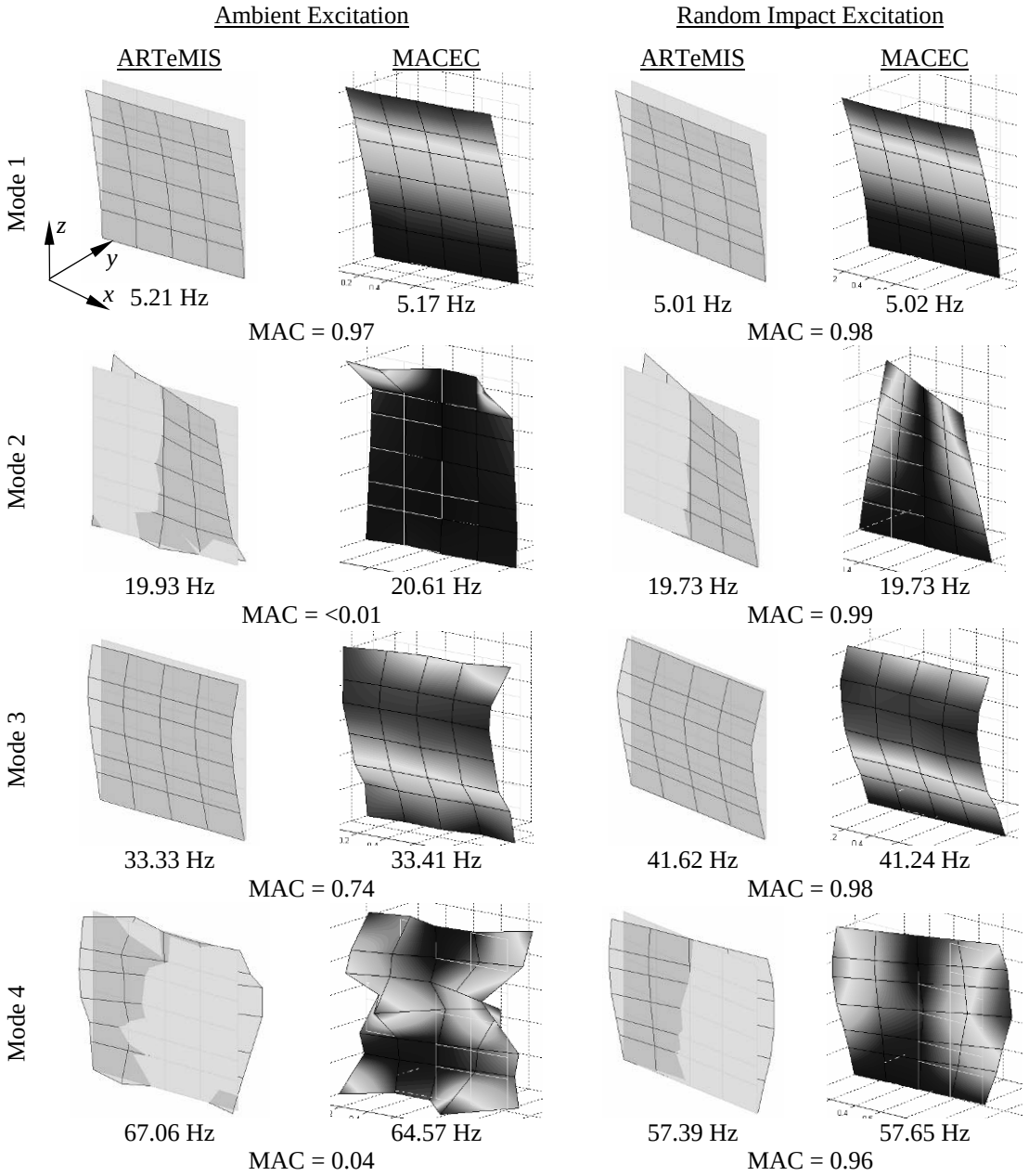


Figure 6.21 – Mode shape configurations for all the analyses

As strains were measured in the wall, it was also possible to estimate directly the curvature mode shapes. The curvatures were estimated only for the case of randomly distributed impact excitation tests, because the signal-to-noise ratio for ambient vibration excitation was too small.

No significant differences were found between the two tools. Figure 6.22 presents the estimated modal curvatures with ARTeMIS (SVS, 2006). The curvatures measured in *x* direction have higher values than the curvatures in the *z* direction. Analysing in detail the curvatures in the *x* direction, it is possible to observe a non symmetric behaviour of the wall, especially at the bottom part, imperceptible with the modal displacements, indicating that the wall might have geometrical or material defects. As concluded in Chapter 5, the modal curvatures will be valuable quantities for subsequent damage analysis if the Euler-

Bernoulli hypothesis is assumed; the bending and normal stiffness are directly related to the curvatures and the average strains in the wall, respectively.

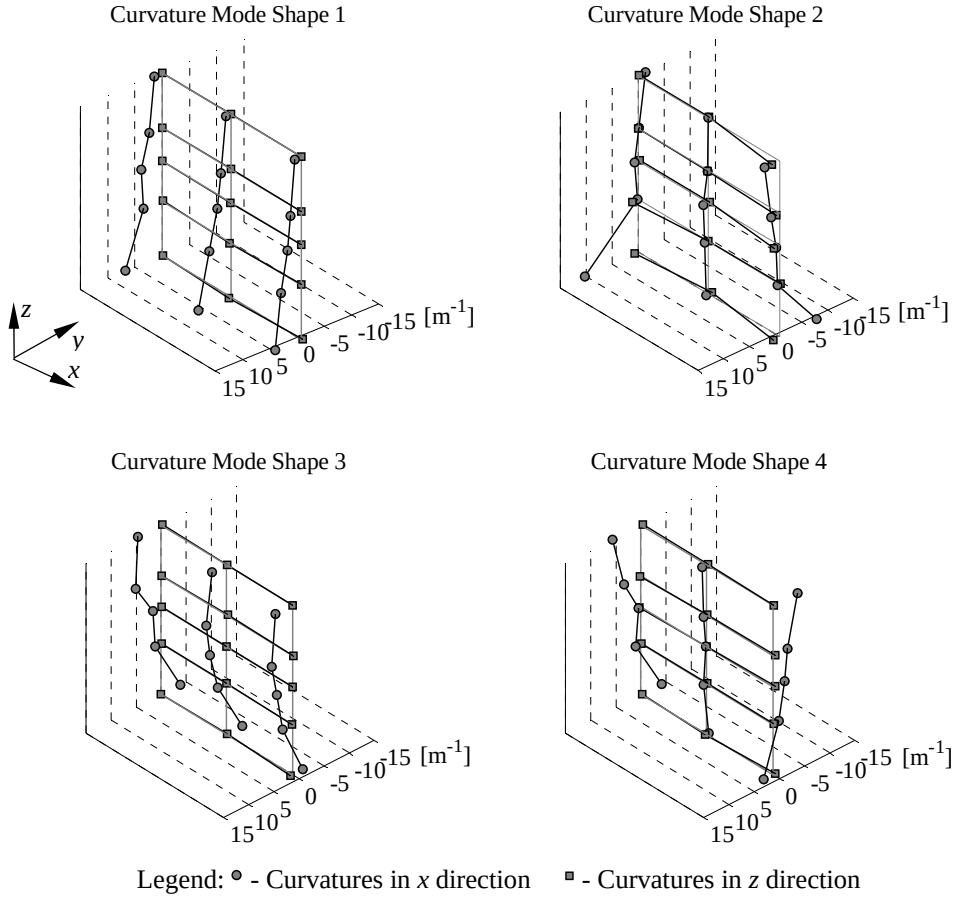


Figure 6.22 – Curvature mode shapes estimated by ARTeMIS.

6.5 Experimental Damage Identification

The following Sections describe the damage identification analysis over the three series of DS induced in the wall. The analysis was carried out taking into account the conclusions of the preceding Chapters. As performed in Chapter 5, a group of damage methods was selected aiming at providing an adequate approach for analysis. Methods that performed unacceptably in Chapter 5 were no longer included in this chapter. The selected methods are (see Chapter 3 for details):

- The Unified Significance Indicator (USI);
- The COMAC values;
- The Parameter Method (PM);
- The Mode Shape Curvature Method (MSCM);
- The Damage Index Method (DIM);
- The Sum of all Curvature Errors method (SCE);
- The FE Model Updating method (FEMU).

Next, the analysis with global parameters is presented first, followed by the damage analysis with non-model based methods. Finally, the analysis with FEMU is addressed.

6.5.1 Analysis with Global Parameters

The SSI/Principal Component method implemented in the tool ARTeMIS (SVS, 2006) was used to estimate the modal parameters for all the fourteen DS. Table 6.5 and Table 6.6 present for the three test series the frequency results for the two types of excitation, ambient and random distributed impacts, respectively. The frequency values are presented together with the value $\pm 2\sigma_\omega$ as a 95% confidence interval, and the frequency differences Δ_ω to the respective RS. Note that, as identified visually, the crack c_1 appeared in $DS_{II\text{-}A}$, the crack c_2 appeared in $DS_{II\text{-}B}$ and the crack c_3 appeared in the $DS_{II\text{-}C}$. As occurred in the arch model, small increase in the frequency values were observed on each test series before the occurrence of the cracks. This is due to the normal adjustments of the structure with the applied load, mainly at the wall support and masonry joints. Analysing the frequency shifts, there is an evidence of decreasing values after the observed cracks. The significant frequency decrease, i.e. higher that $2\sigma_\omega$ (given in a grey box), where around the DS where the crack was visually localized, with exception of mode 1 of Series A and mode 2 of Series C for the ambient excitation tests, and for mode 4 of Series A and mode 1 of Series B for the random impact excitation.

Table 6.5 – Frequency results for the wall model with ambient excitation.

Damage Scenario	Mode 1			Mode 2			Mode 3			Mode 4		
	ω [Hz]	$2\sigma_\omega$ [Hz]	Δ_ω [Hz]	ω [Hz]	$2\sigma_\omega$ [Hz]	Δ_ω [Hz]	ω [Hz]	$2\sigma_\omega$ [Hz]	Δ_ω [Hz]	ω [Hz]	$2\sigma_\omega$ [Hz]	Δ_ω [Hz]
RS_A	5.21	0.12	–	19.93	0.32	–	33.33	2.94	–	67.06	6.27	–
$DS_{I\text{-}A}$	5.22	0.16	0.01	20.00	0.17	0.07	33.59	2.38	0.26	65.16	4.75	–1.90
$DS_{II\text{-}A}$ †	5.26	0.35	0.05	19.93	0.39	0.00	32.34	0.86	–0.99	65.83	3.51	–1.23
$DS_{III\text{-}A}$	5.11	0.46	–0.10	19.81	0.24	–0.12	32.70	0.94	–0.63	64.14	1.95	–2.92
$DS_{IV\text{-}A}$	5.00	1.25	–0.20	19.77	0.90	–0.16	31.02	1.57	–2.31	62.35	2.41	–4.71
$DS_{V\text{-}A}$	4.74	0.82	–0.46	19.42	0.40	–0.51	30.20	1.18	–3.13	61.97	2.23	–5.09
RS_B	4.19	0.10	–	13.54	0.18	–	20.06	0.28	–	41.50	1.32	–
$DS_{I\text{-}B}$	4.22	0.19	0.03	13.69	0.22	0.15	19.94	0.22	–0.12	41.22	1.02	–0.28
$DS_{II\text{-}B}$	4.16	0.14	–0.03	13.55	0.23	0.01	19.90	0.08	–0.16	39.36	1.32	–2.14
$DS_{III\text{-}B}$ †	4.15	0.06	–0.04	13.48	0.07	–0.06	19.91	0.12	–0.15	38.16	0.97	–3.34
$DS_{IV\text{-}B}$	4.01	0.15	–0.17	13.07	0.19	–0.47	19.17	0.27	–0.89	37.85	0.35	–3.65
$DS_{V\text{-}B}$	3.58	0.13	–0.61	12.63	0.12	–0.91	18.62	0.25	–1.44	34.68	2.73	–6.82
RS_C	3.41	0.45	–	12.49	0.05	–	18.29	0.12	–	35.63	1.12	–
$DS_{I\text{-}C}$	3.46	0.07	0.06	12.44	0.07	–0.05	18.24	0.07	–0.05	35.38	0.26	–0.25
$DS_{II\text{-}C}$ †	3.54	0.29	0.13	11.72	0.15	–0.77	17.56	0.18	–0.73	34.41	0.37	–1.22
$DS_{III\text{-}C}$	2.99	0.05	–0.42	10.82	0.16	–1.67	16.76	0.19	–1.53	33.11	0.33	–2.52
$DS_{IV\text{-}C}$	2.81	0.09	–0.60	9.27	0.20	–3.22	16.03	0.30	–2.26	32.52	2.78	–3.11

† - Damage scenario in which the cracks were identified by visual observation

Table 6.6 – Frequency results for the wall model with random impact excitation.

Damage Scenario	Mode 1			Mode 2			Mode 3			Mode 4		
	ω [Hz]	$2\sigma_\omega$ [Hz]	Δ_ω [Hz]	ω [Hz]	$2\sigma_\omega$ [Hz]	Δ_ω [Hz]	ω [Hz]	$2\sigma_\omega$ [Hz]	Δ_ω [Hz]	ω [Hz]	$2\sigma_\omega$ [Hz]	Δ_ω [Hz]
RS_A	5.01	0.05	–	19.73	0.11	–	41.62	0.74	–	57.39	0.98	–
$DS_{I\text{-}A}$	4.97	0.03	–0.04	19.48	0.55	–0.25	43.44	1.36	1.82	58.91	1.65	1.52
$DS_{II\text{-}A}$ †	4.93	0.03	–0.08	19.55	0.08	–0.18	42.38	3.28	0.76	59.29	2.23	1.90
$DS_{III\text{-}A}$	4.82	0.16	–0.19	19.38	0.06	–0.35	40.81	0.77	–0.81	58.52	2.91	1.13
$DS_{IV\text{-}A}$	4.94	0.43	–0.07	19.22	0.04	–0.51	38.87	0.55	–2.75	55.94	0.47	–1.45
$DS_{V\text{-}A}$	4.10	0.18	–0.90	18.98	0.16	–0.75	29.52	1.34	–12.10	55.05	3.76	–2.34
RS_B	3.76	0.05	–	13.06	0.04	–	19.21	0.10	–	41.65	0.27	–
$DS_{I\text{-}B}$	3.79	0.04	0.04	13.13	0.05	0.07	19.27	0.09	0.06	41.94	0.14	0.29
$DS_{II\text{-}B}$	3.74	0.09	–0.01	13.12	0.02	0.06	19.16	0.07	–0.05	41.22	0.32	–0.43
$DS_{III\text{-}B}$ †	3.75	0.31	0.00	13.12	0.10	0.06	19.21	0.25	0.00	41.05	0.51	–0.60
$DS_{IV\text{-}B}$	3.60	0.33	–0.16	12.62	0.11	–0.44	18.39	0.23	–0.82	40.84	0.89	–0.81
$DS_{V\text{-}B}$	3.36	1.23	–0.40	12.24	0.13	–0.82	17.85	0.22	–1.36	40.69	0.94	–0.96
RS_C	2.79	0.35	–	12.23	0.17	–	17.83	0.28	–	36.14	0.42	–
$DS_{I\text{-}C}$	2.91	0.27	0.12	12.01	0.15	–0.22	17.39	0.25	–0.44	35.23	1.06	–0.91
$DS_{II\text{-}C}$ †	2.95	0.07	0.16	11.22	0.18	–1.01	16.84	0.30	–0.99	33.00	1.20	–3.14
$DS_{III\text{-}C}$	2.64	0.12	–0.15	10.35	0.11	–1.88	16.08	0.11	–1.75	32.90	0.98	–3.24
$DS_{IV\text{-}C}$	2.52	0.08	–0.28	8.74	0.24	–3.49	15.36	0.18	–2.47	31.93	0.22	–4.21

† - Damage scenario in which the cracks were identified by visual observation

Concerning the average relative frequency values, calculated with the four estimated frequencies for each test series, Figure 5.23 and Figure 5.24 show the progressive frequency decrease with increasing damage and the correlation with the square root of the unloading stiffness k^u, calculated in the static tests. The lower residual values for the average frequency were observed for the Series C, see Figure 5.23a and Figure 5.24a. Note that it was in this series that the diagonal shear crack c_3 appeared. This might indicate that the dynamic behaviour of the wall is more sensitive to shear cracks than to bending cracks. For Series A the average residual frequency values in the last DS were between 0.86 and 0.93 of the original average frequency value for the ambient and random impact excitations, respectively. For Series B, the same results were between 0.88 and 0.93, and for Series C, the same results were between 0.82 and 0.84. Here is noted that the term "relative frequency" has been used for the relation between the frequency in the DS and the original frequency in the RS.

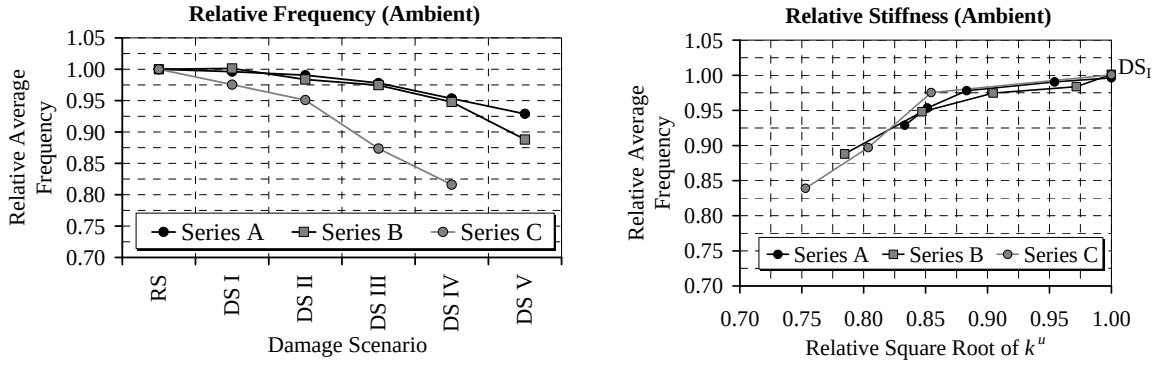
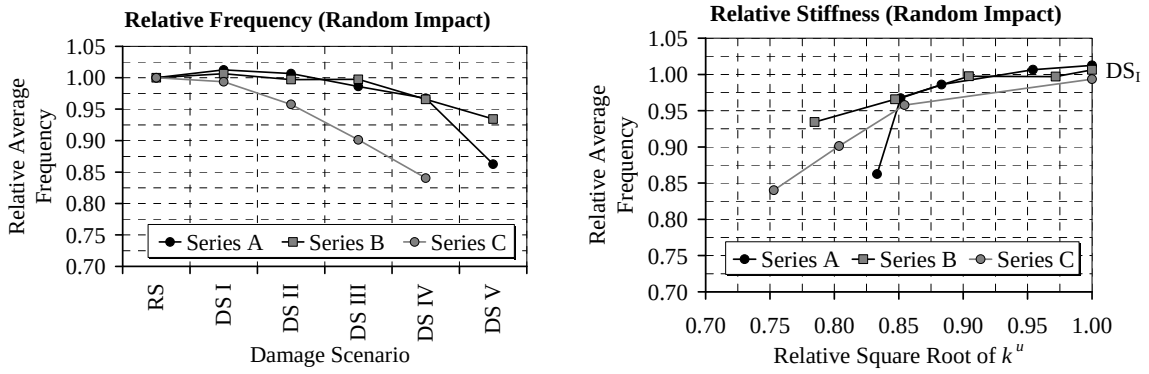


Figure 5.23 – Different damage scenarios for ambient excitation tests: (a) relative frequency values; and (b) relative square root of the unloading stiffness *versus* the relative frequencies values.



(a) (b)

Figure 5.24 – Different damage scenarios for random impact excitation tests: (a) relative frequency values; and (b) relative square root of the unloading stiffness *versus* the relative frequencies values.

Analysing the correlation between the square root of the relative unloading stiffness, calculated in the static tests, and the relative frequency values, the results presented in Figure 5.23b and in Figure 5.24b demonstrates a linear trend between the two quantities after the occurrence of cracks on each test series. Note that no significant mass changes was carried out in the specimen during the several DS.

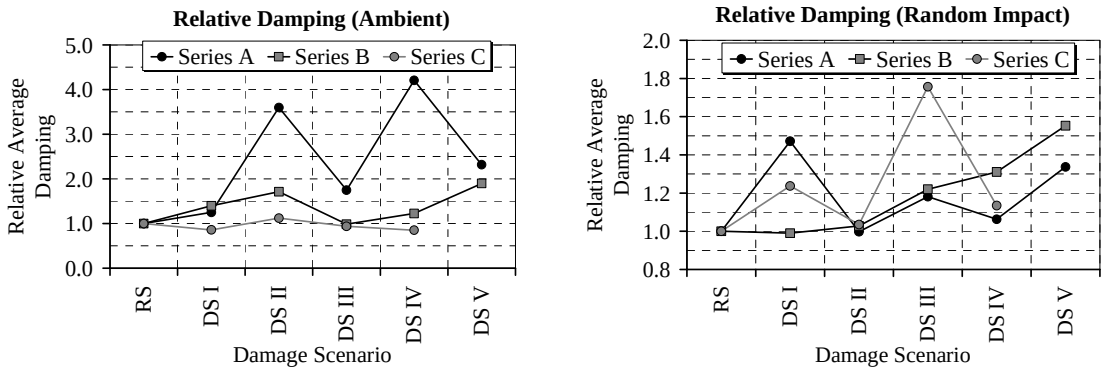
Table 6.7 presents the damping coefficient as a second global modal parameter to be studied, even if the damping values were difficult to estimate experimentally. The drops from the last DS of Series A to the first DS of Series B, and from the last DS of Series B to the first DS of Series C should be noted. The average damping values from the random impact excitation are, on average, two times larger that the values from the ambient excitation, confirming that damping depends on the level of excitation, and is an ambiguous parameter to use for damage identification analysis.

Table 6.7 – Damping results for the wall model [%].

Damage Scenario	Ambient Excitation					Random Impact Excitation				
	ξ_1	ξ_2	ξ_3	ξ_4	Average	ξ_1	ξ_2	ξ_3	ξ_4	Average
RS_A	0.57	0.97	2.96	0.85	1.99	2.69	0.96	7.19	7.78	4.66
$DS_{I\text{-}A}$	1.42	0.99	2.56	0.73	1.78	1.88	3.36	8.50	3.98	4.43
$DS_{II\text{-}A}$†	5.04	2.82	4.03	1.07	4.05	2.20	1.11	8.47	6.60	4.59
$DS_{III\text{-}A}$	1.82	1.50	4.21	0.93	2.59	3.30	1.17	8.81	8.23	5.38
$DS_{IV\text{-}A}$	6.30	3.03	5.18	2.14	4.38	3.81	1.06	5.83	7.17	4.47
$DS_{V\text{-}A}$	3.29	1.93	2.09	1.68	2.51	6.09	1.15	5.71	8.53	5.37
RS_B	0.83	0.90	0.95	0.74	1.59	2.79	1.34	1.83	4.69	2.66
$DS_{I\text{-}B}$	1.67	1.87	0.84	0.55	1.67	2.68	1.21	1.72	5.41	2.76
$DS_{II\text{-}B}$	2.95	0.98	1.28	1.33	2.09	3.38	1.23	1.69	4.99	2.82
$DS_{III\text{-}B}$†	0.91	0.79	0.83	1.66	1.64	4.45	1.22	1.55	7.15	3.59
$DS_{IV\text{-}B}$	1.28	1.17	1.18	0.46	1.67	4.52	1.33	1.70	7.99	3.88
$DS_{V\text{-}B}$	3.68	0.88	1.01	2.60	2.42	6.70	1.55	2.58	5.83	4.16
RS_C	1.38	0.96	0.78	1.16	1.59	2.68	1.81	2.16	2.87	2.38
$DS_{I\text{-}C}$	1.47	0.66	0.89	0.46	1.19	4.15	1.42	2.04	4.79	3.10
$DS_{II\text{-}C}$†	1.50	0.88	1.55	0.25	1.38	3.43	1.60	2.15	2.82	2.50
$DS_{III\text{-}C}$	1.57	0.82	1.02	0.33	1.22	7.23	1.65	2.06	7.05	4.50
$DS_{IV\text{-}C}$	1.53	0.76	0.85	0.48	1.12	4.14	1.88	2.08	2.85	2.74

† - Damage scenario in which the cracks were identified by visual observation

Figure 6.25 presents the average relative damping values for the three series of tests. Observing the graphs, one can conclude that there is some trend for increasing damping through the DS, but the difficulties in the experimental estimation do not allow a final conclusion.



(a) (b)

Figure 6.25 – Relative damping values: (a) ambient excitation; and (b) random impact excitation.

To conclude about the global parameter results, and in agreement with the conclusions observed in the arch model case for the same study, it seems that the modal properties of the masonry specimen are sensitive to the damage progress, especially when frequency changes are studied. In all the test series, damage was detected around the respective DS where the cracks were visualized. Nevertheless, it should be stressed that the detection of damage (Level 1) was not so accurate as in the case of the arch model, due to the difficulties in parameter estimation.

6.5.2 Analysis with Non-Model Based Methods

The first non-model based method to apply was the USI method. Figure 6.26 shows, for both types of excitation and for the three series, the results for the comparisons with the RS and the relative comparisons for each consecutive DS. When compared with the RS, there is an increase of the USI values with progressive damage. The USI values also increase with test series sequence, indicating that the severity of damage was increasing with the static tests, in agreement with the observed damage presented in Section 6.3. For the case of relative comparison, it is also possible to observe higher sensitive of the Series C, the one with shear cracks. In all the series there were few DS before the occurrence of the cracks, leading to no clear jumps in the USI values. Nevertheless, the detection of damage (Level 1) with USI is evident.

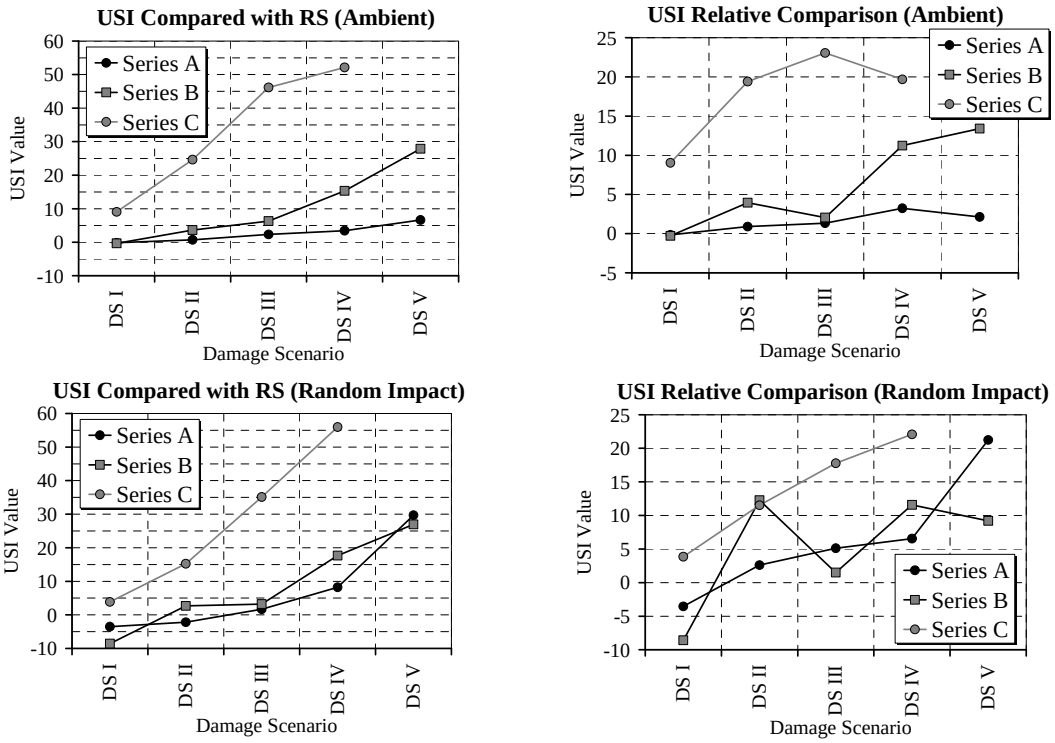


Figure 6.26 – USI results for ambient and random impacts: (a) compared with the RS; and (b) relative comparison for each consecutive DS.

As carried out in damage identification analysis of the arch model (see Chapter 5), for the application of COMAC, PM, MSCM, DIM and SCE the curvature mode shape values close to zero were neglected in order to avoid noise contamination in the results. The methods were applied only for the case of random impact excitation. The results are extensively presented in Annex C. For all the test series, four estimated modes were considered. The results include the comparison of each DS_i to the RS and the relative comparison for each consecutive DS_i.

To help the results interpretation in the damage localization analyses (Level 2), Figure 6.27 presents the location of the measuring points for accelerations (35 points) and strains (15 points). Note that for case of strains, the pair of transducers glued in the two sides of the wall at the same location is represented by a single measuring point.

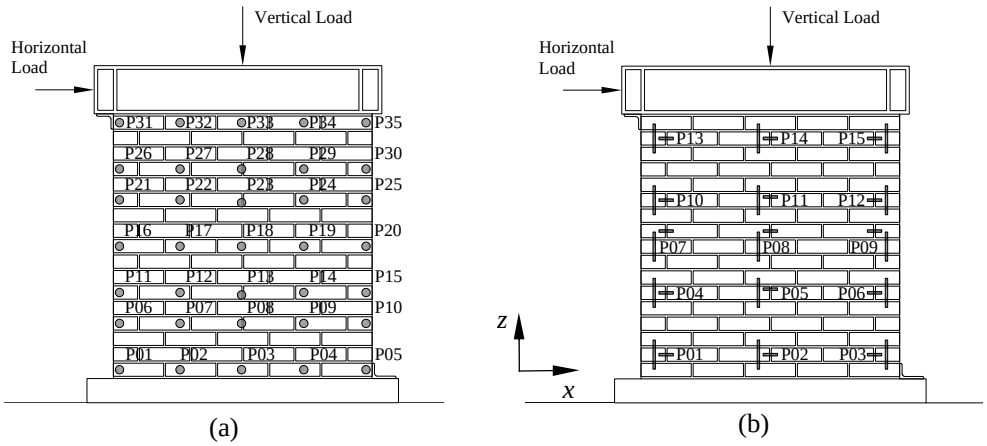


Figure 6.27 – Location of measuring points: (a) for accelerometers; and (b) for strain gauges

Concerning the performance of the non-model based methods, the following conclusions emerged from the results:

- For all the series the COMAC values calculated for modal displacements gave protuberances at the bottom of the wall, mainly until the second level of the measuring points (see Figure 6.27a). According to the visual damage, the crack c_1 at the bottom totally changes the boundary conditions of the wall, and when this happens significant changes in the modal configurations are possible;
- In the case of COMAC values, calculated for modal curvatures in the *x* direction, there is a trend to pinpoint the first three points (P01, P02 and P03) as possible damage locations. For the case of COMAC values calculated in the *z* direction some comparisons gave the same results as MSCM, DIM and SCE, but for other comparisons the results were inconclusive or inaccurate;
- The PM calculated for modal displacements gave inconclusive or inaccurate results;
- The PM calculated for modal curvatures, the MSCM, the DIM and the SCE gave similar results, with better agreement for the last three methods. They were able to locate the damage in the vicinity of the experimental crack locations.

As an example of the preceding conclusions, Figure 6.28 and Figure 6.29 present the results for the relative comparison between RS_A and $DS_{III\text{-}A}$, where the damage is mainly pinpointed at the bottom of the wall for COMAC values. The PM results calculated for modal displacements are inconclusive. For the case of PM calculated for modal curvatures and MSCM, the positions P1, P2 and P10 for the DIM are pinpointed as potential damage, as the locations P02 and P10 for the SCE.

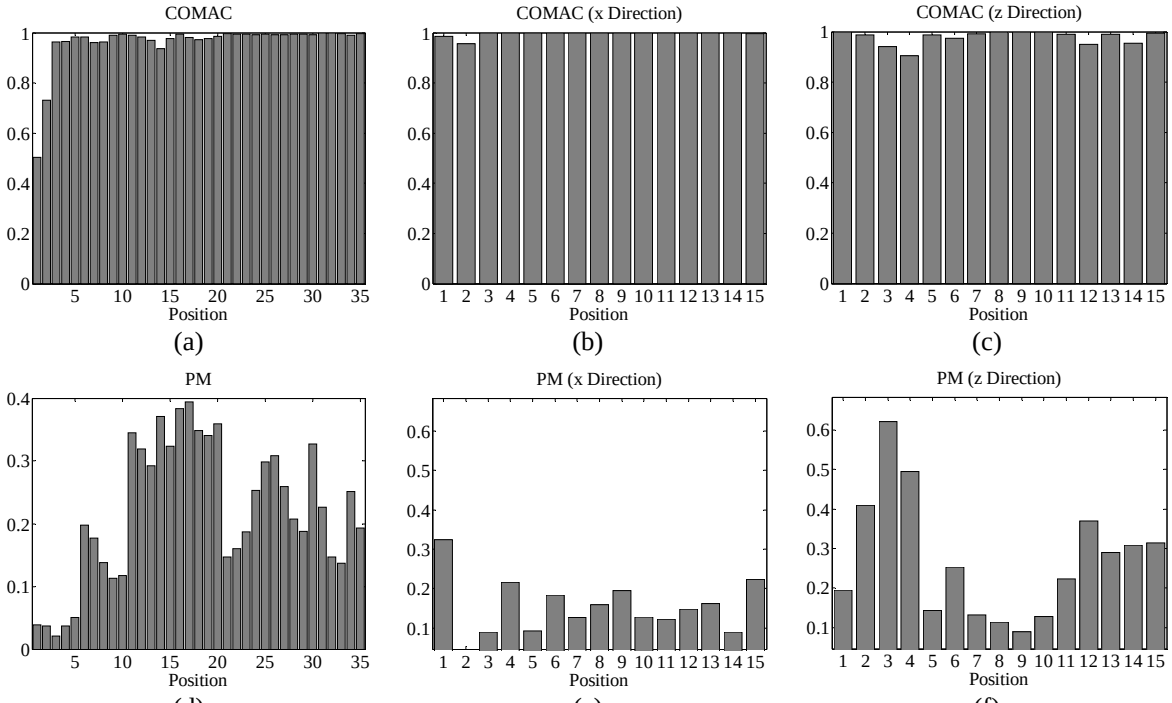


Figure 6.28 – Results with measured curvatures for the comparison between RS_A and $DS_{III\text{-}A}$: (a) COMAC values for modal displacements; (b) and (c) COMAC values for modal curvatures in the *x* and *z* direction, respectively; (d) PM for modal displacements; and (e) and (f) PM for modal curvatures in the *x* and *z* direction, respectively.

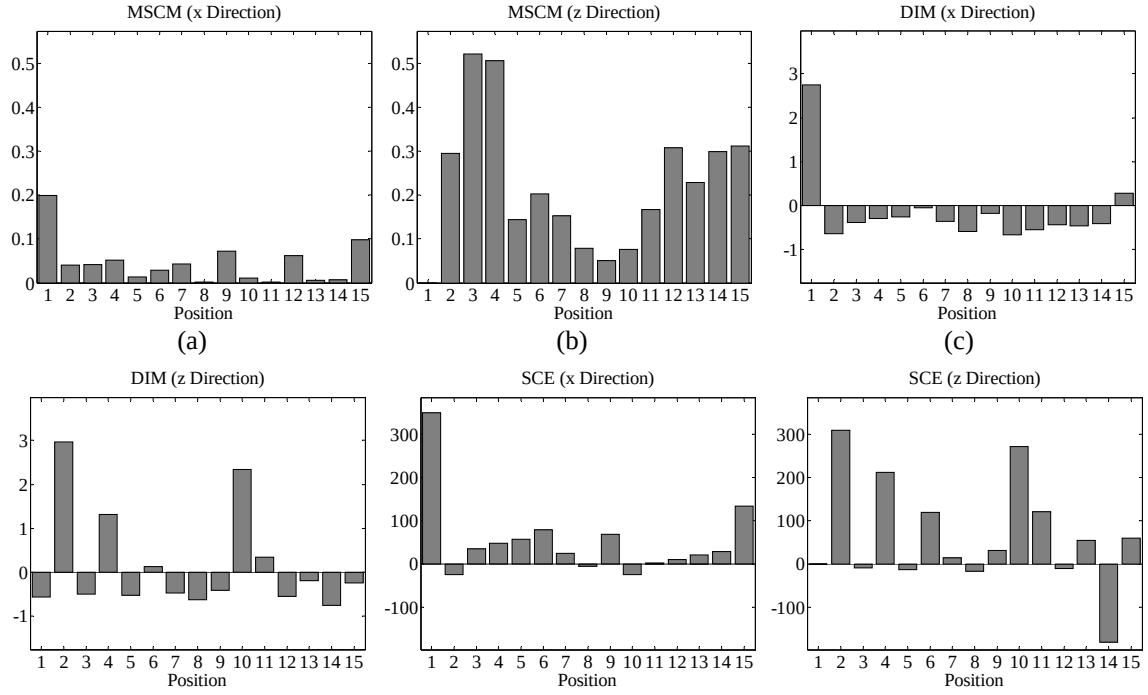
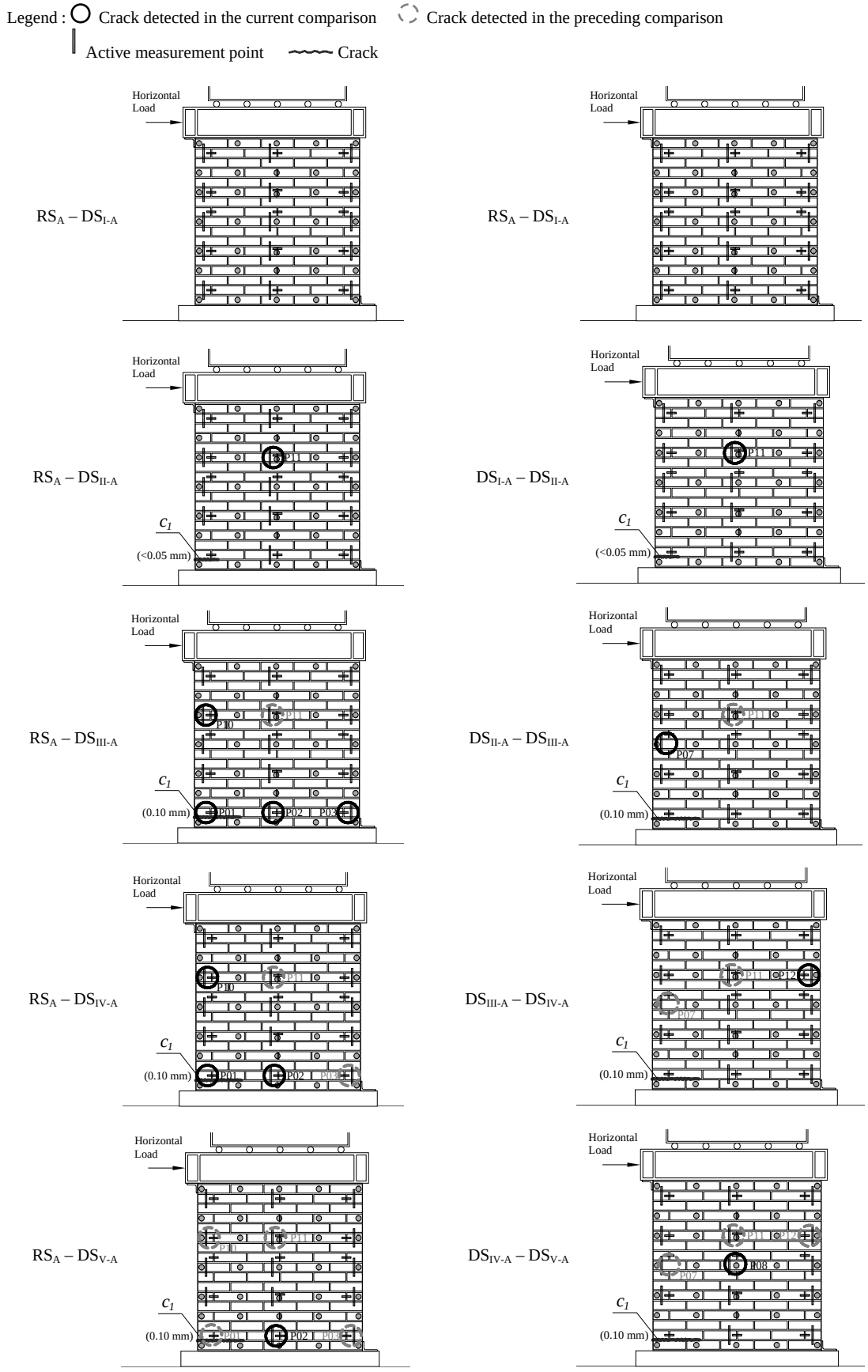


Figure 6.29 – Results with measured curvatures for the comparison between RS_A and DS_{III-A}: (a) and (b) MSCM for curvatures in the *x* and *z* direction, respectively; (c) and (d) DIM for curvatures in the *x* and *z* direction, respectively; and (e) and (f) SCE for curvatures in the *x* and *z* direction, respectively.

Considering the above conclusions and the experience gained in Chapter 5, the definition of the damage location was based in two criteria with decreasing importance: (a) at least a correlation between two of the methods which gave similar results, namely the PM calculated for modal curvatures, the MSCM, the DIM and the SCE, should occur; and (b) only the values greater than two will be considered as potential damage in the DIM, Stubbs et al. (1992). Considering these criteria, Figure 6.30, Figure 6.31 and Figure 6.32 present the damage location analysis for the test series A, B and C, respectively. The results presented correspond to two different strategies where the RS was changing.

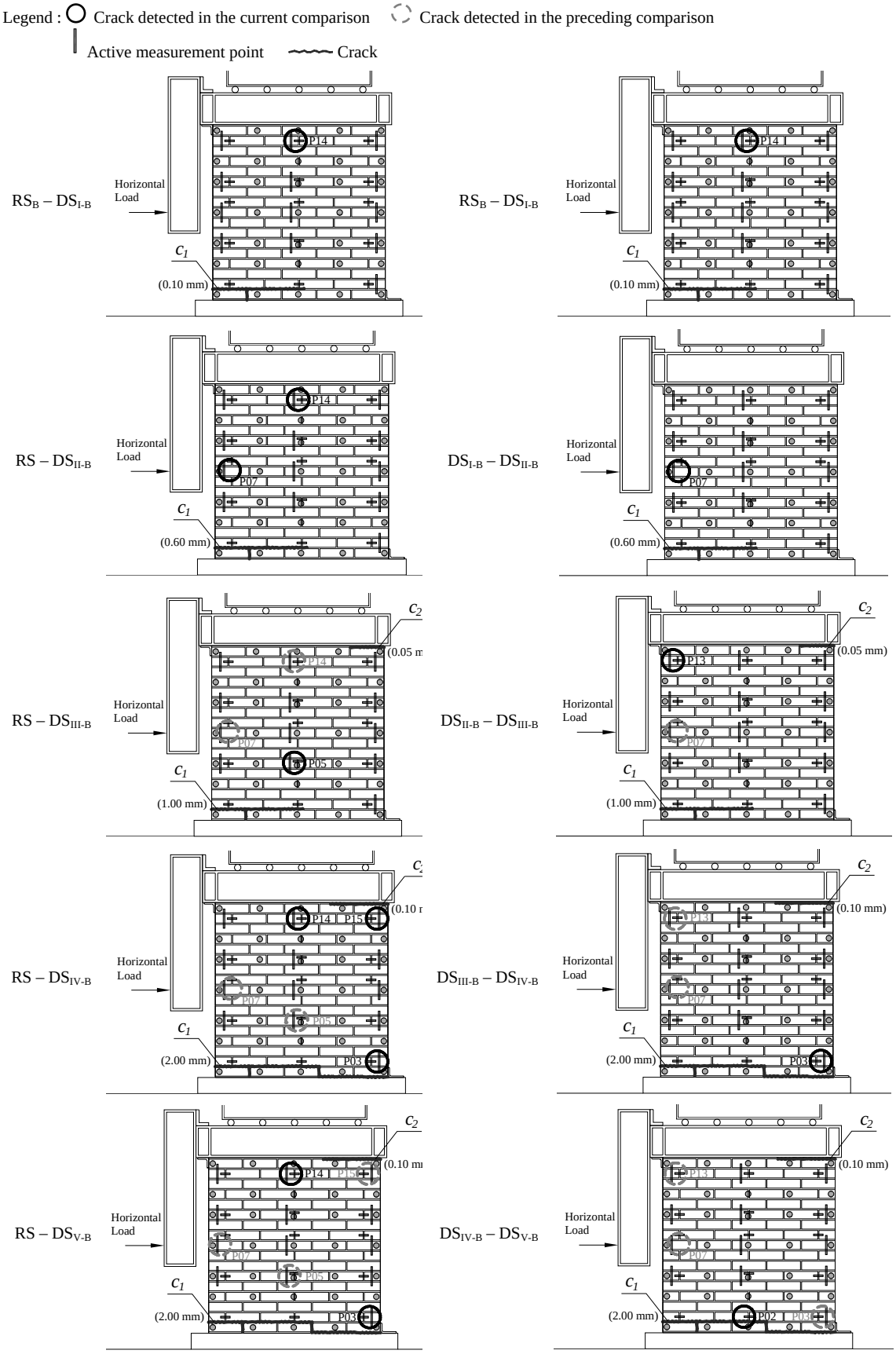
The following conclusions emerged from the analysis with the comparisons to the RS:

- In case of Series A, see Figure 6.30a, although the first visual crack c_1 appeared in DS_{II-A}, the damage could be localized only for DS_{III-A}. Some points are pinpointed with damage, such as P10 and P11, but no visual cracks could be seen in these locations;
- In case of Series B, see Figure 6.31a, the right localization occurred again one DS after of the occurrence of crack c_2. The crack c_1 was localized for DS_{IV-B}. As happened with the preceding series, some points are pinpoint for damage locations, where no visible cracks were seen, namely, P05 and P07;
- In case of Series C, see Figure 6.32a, all the indicated damage locations are close to the observed cracks, including the localization of crack c_3 in the same DS where it was possible to visualize it first (DS_{II-C}), with the exception of point P06. The indication of damage in point P06 can be justified due to large changes in the modal curvatures in its vicinity. In fact, the wall was divided into two macro-blocks, and point P6 is near the edges of one macro-block.



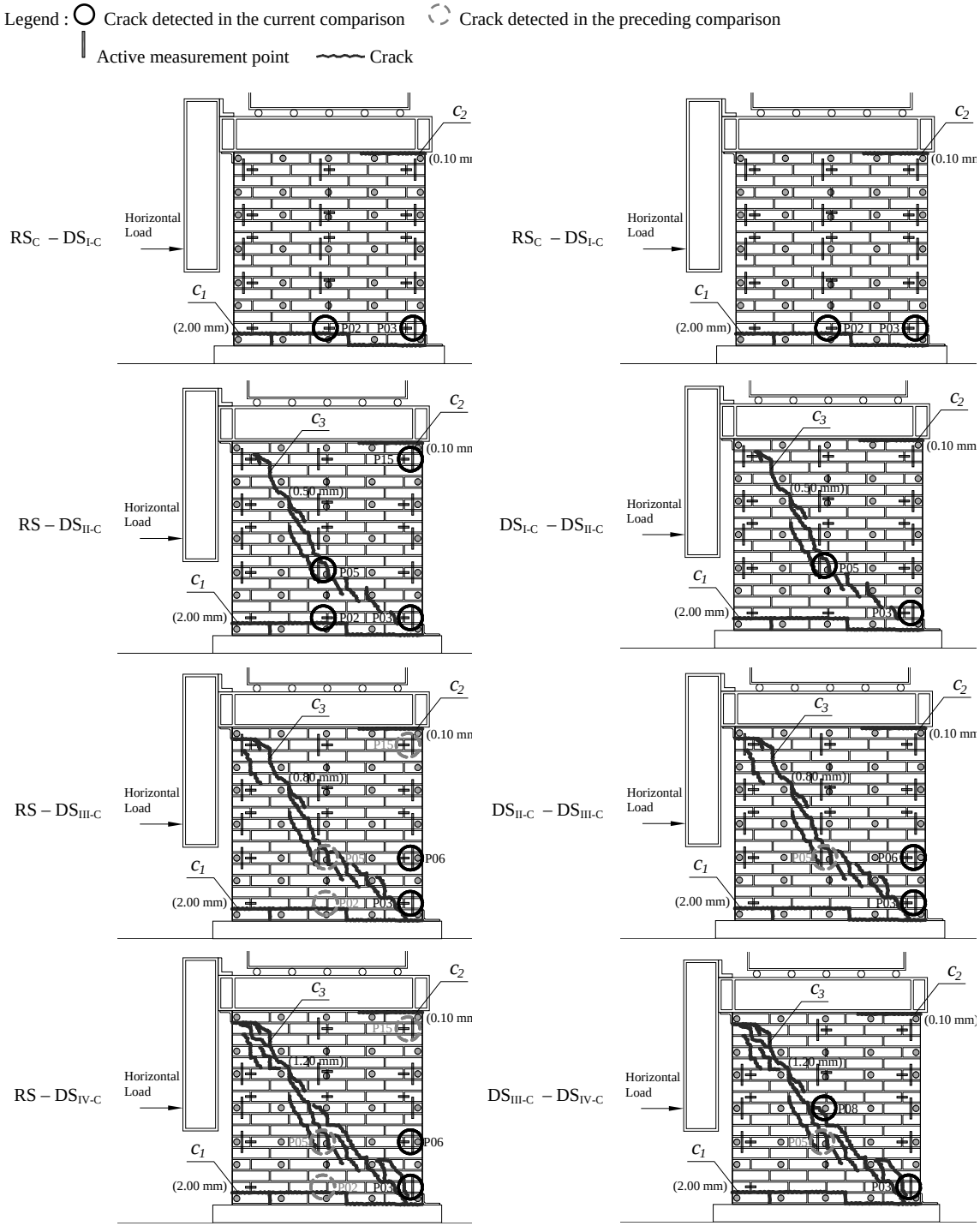
(a) (b)

Figure 6.30 – Damage location with measured curvatures for Series A: (a) comparison with the RS$_A$; and (b) relative comparison with each consecutive DS.



(a) (b)

Figure 6.31 – Damage location with measured curvatures for Series B: (a) comparison with the RS_B; and (b) relative comparison with each consecutive DS.



(a) (b)

Figure 6.32 – Damage location with measured curvatures for Series C: (a) comparison with the RS_C; and (b) relative comparison with each consecutive DS.

For the case of consecutive comparisons with the previous configurations (see Figure 6.30b, Figure 6.31b and Figure 6.32b) poor results were obtained, with the exception of Series C. This indicates that significant differences between modal data are required for better damage localization.

Finally and with respect to the crack sequence, the comparison with the RS allowed replicating the crack sequence c_1, c_2 and c_3 with the non-based methods.

6.5.3 Analysis with the Finite Element Model Updating Method

The FEMU was applied to the FE models used for the numerical estimation of the modal parameters (presented in Section 6.4.1), with the aim of globally localizing the damage (Level 2). As performed in the arch model analysis, the nonlinear least square method implemented in MatLab (2006), function `lsqnonlin`, was used to minimize the objective function π, composed by the residuals formed by the relative error between the numerical and experimental frequencies and the difference between the numerical and experimental mode shapes, given by:

$$\pi = \frac{1}{2}\left[W_\omega \sum_{j=1}^{m_\omega} \left(\frac{\omega_j^2 - \omega_{j,\exp}^2}{\omega_{j,\exp}^2} \right)^2 + W_\varphi \sum_{j=1}^{m_\varphi} \left(\varphi_j - \varphi_{j,\exp} \right)^2 \right] \tag{6.1}$$

where m_ω denotes the number of eigen frequencies taken into account, m_φ is the number of normalized eigen modes taken into account and W_ω and W_φ are weighting diagonal matrices for the frequencies and mode shapes, respectively. Note that experimental and numerical mode shapes are normalized in a way that the maximum real value of the modal displacement is equal to one, in order to be comparable with the residuals from the frequency values normalized by the experimental results.

The FEMU analysis was divided in two steps. For each series, firstly, one updating analysis was performed to update the undamaged condition (RS), and secondly several analysis were carried out to update the DS where visible cracks were observed in the static tests. The analysis for the RS and the damage localization analysis are presented next.

6.5.3.1 Modal Updating of the Reference Scenarios

The updating parameters for the three reference scenarios are presented in Figure 6.33. In RS_A, the Young's modulus E, the shear modulus G and the steel masses M from the test apparatus were updated. In RS_B one parameter was added, namely the Young's modulus E_1 at the base of the wall, in a band of elements (see Figure 6.33b), to better model the crack c_1. For RS_C the updated parameters were the global Young's modulus E, the global shear modulus G, the Young's modulus E_1 at the base of the wall to model the crack c_1, and the Young's modulus E_2 at the top of the wall to model the crack c_2. In all models the supports were considered fully constrained.

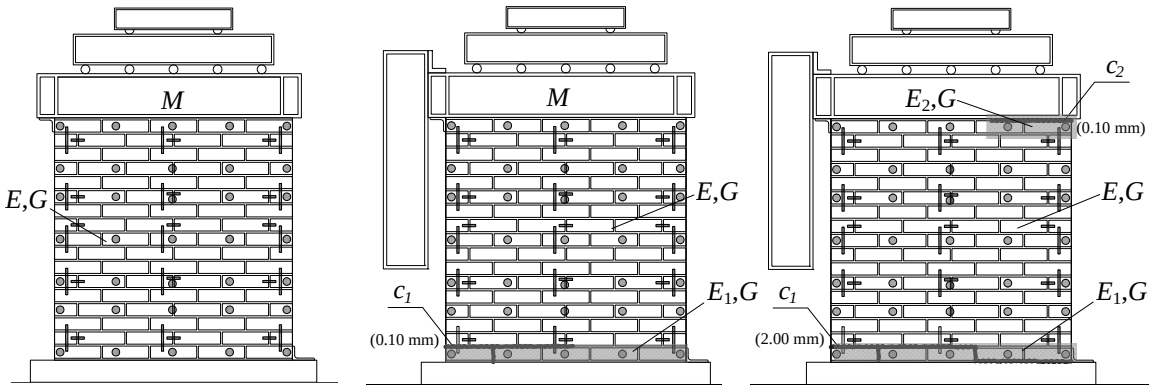


Figure 6.33 – Updating parameters for the RS: (a), (b) and (c) for RS_A, RS_B and RS_C, respectively.

For all the analyses the objective function had four eigen frequencies and four eigen modes ($m_\omega = 4$ and $m_\varphi = 4$), with exception of the RS_A analysis which took only three eigen frequencies ($m_\omega = 3$ and $m_\varphi = 4$) due to difficulties in the optimization, as it will be shown later. The experimental results to tune were the ones obtained from random impact excitation. The tolerance for the residuals and the updating parameters in the objective function was equal to 1.0×10^{-6} and the Jacobian increment was equal to 1%. Boundary constraints were applied to the updating parameters in order to avoid unrealistic results for the final values.

Table 6.8 presents, for the three updating analysis, the updating parameters, the boundary values, the final and updated values and the difference between the initial and final values. From the final values it can be observed that the Young's modulus *E* suffers a decreasing of 75% from RS_A to RS_B and does not change significantly from RS_B to RS_C. Another important conclusion is that for having accurate results the shear modulus has to be much higher than expected, between 81 and 93% of the Young's modulus.

Table 6.8 – Updating parameters and initial, possible range and final values for the three test series.

RS	Updating Parameters	Initial Values	Lower Bound	Upper Bound	Final Values	Difference [%]
RS_A	*E* [GPa]	1.000	0.050	11.000	1.360	+35.993
	G/E [–]	0.500	0.025	0.925	0.925	+84.999
	M [kg]	135.000	121.500	148.500	133.056	–1.440
RS_B	*E* [GPa]	1.360	0.068	1.360	1.033	–24.006
	E_1 [GPa] (crack c_1)	1.360	0.068	1.360	0.202	–85.116
	M [kg]	210.000	189.000	231.000	210.749	–4.330
	G/E [–]	0.400	0.020	0.920	0.772	+93.106
RS_C	*E* [GPa]	1.360	0.068	1.360	0.972	–28.547
	E_1 [GPa] (crack c_1)	1.360	0.068	1.360	0.083	–93.878
	E_2 [GPa] (crack c_2)	1.360	0.068	1.360	0.016	–98.807
	G/E [–]	0.400	0.020	0.920	0.875	+118.770

The results in terms of frequency values, MAC values and NMD values are presented in Table 6.9. The high accuracy of the results should be stressed, as the average frequency error is lower than 5% for RS_A (even lower than 2.5% if only the first three frequencies are taken into account) and lower than 1% for the cases of RS_B and RS_C. The MAC values are almost close to one and the average NMD is lower than 10%.

Table 6.9 – Comparison between experimental and updated results.

RS	Mode Shape	Experimental [Hz]	FEM [Hz]	Error [%]	MAC	NMD
RS_A	1st	5.01	5.17	–3.27	1.00	0.04
	2nd	19.73	19.13	3.04	0.99	0.08
	3rd	41.62	41.07	1.33	0.99	0.11
	4th†	57.39	63.33	–10.35	0.97	0.16
			Average	| 4.50 |	0.99	0.10
RS_B	1st	3.76	3.78	–0.62	1.00	0.04
	2nd	13.06	12.95	0.81	1.00	0.04
	3rd	19.21	19.22	–0.03	1.00	0.06
	4th	41.65	41.64	0.02	0.99	0.12
			Average	| 0.37 |	0.99	0.07
RS_C	1st	2.79	2.81	–0.63	1.00	0.05
	2nd	12.23	12.15	0.65	0.99	0.07
	3rd	17.83	17.99	–0.91	1.00	0.06
	4th	36.14	35.85	0.79	0.99	0.10
			Average	| 0.75 |	0.99	0.07

† - Frequency value not included in the objective function π

As an example of the good agreement obtained, Figure 6.34 presents for the case of RS_B the comparison between experimental and numerical frequencies, the residuals history of the objective function π, the COMAC values for all measured degrees of freedom in the *y* direction, the numerical mode shapes and the differences between experimental and the numerical mode shapes. The COMAC values are almost one with exception of the first degrees of freedom at the bottom of the wall. A good correspondence between the modes can be observed in Figure 6.34e, although local modal components are not well tuned for the fourth mode.

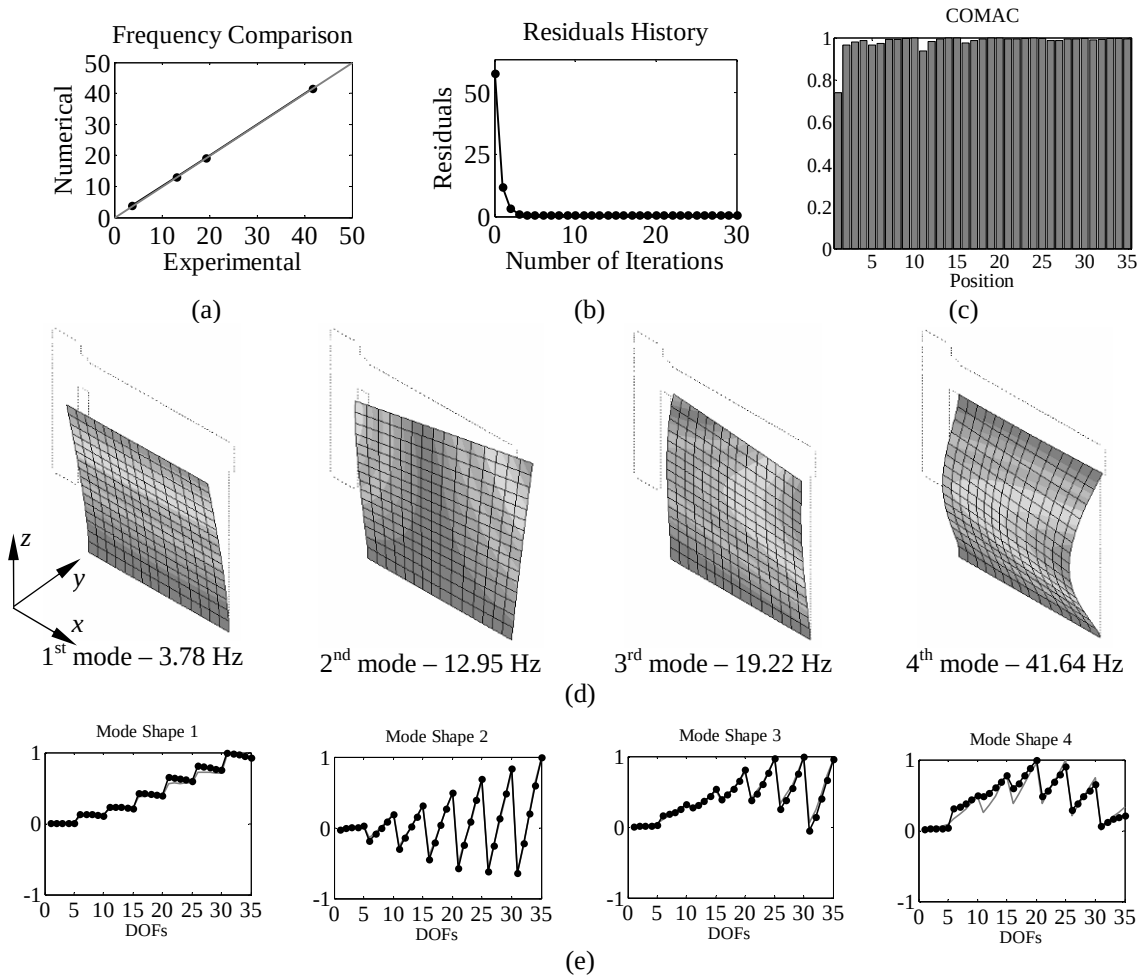
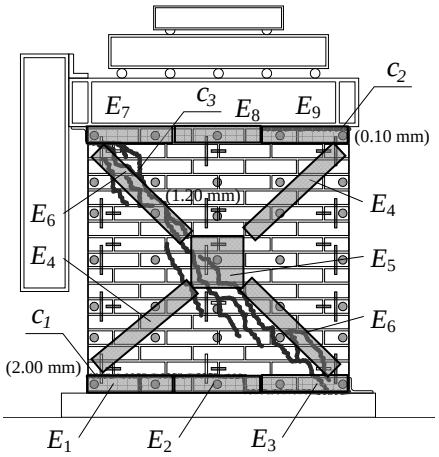


Figure 6.34 – Results from the optimization analysis of RS_A: (a) frequency values comparison; (b) residuals history; (c) COMAC values for all the measured DOFs (d) mode shapes; and (e) differences between updated experimental DOFs in the y direction, with experimental (grey line) and numerical (marker line) values.

6.5.3.2 Damage Localization

The damage localization with FEMU was carried out with an approach similar to the one used for the arch model. For all the tests series, eight thin bands of elements and one square of elements with different Young's modulus as updating parameter were considered. Figure 6.35 shows the selected bands for the damage localization, together with the final crack pattern of test Series C.



(c)

Figure 6.35 – Updating parameters for damage localization.

Three bands were aligned in the horizontal direction at the bottom of the wall as updating parameters E_1, E_2 and E_3, see Figure 6.35. Two interrupted bands were used in the diagonal direction forming an X and were considered as updating parameters E_4 and E_6. The square of elements at the center of the wall was considered as an updating parameter E_5. The last three bands were at the top of the wall, again in horizontal direction as updating parameters E_7, E_8, and E_9. The bands distribution in the wall tries to cover the most likely crack pattern in piers due to seismic actions. The size of the bands is approximately 75 mm and the square has sides of 150 mm.

Additionally and to better localize damage, the Young's modulus at each set of elements k will be normalized by the following expression:

$$Z_k = \left(E_k - \overline{E}\right) / \sigma_E \tag{6.2}$$

where each E_k is equal to the ratio between the final $E_{f,k}$ and the initial $E_{i,k}$ value of the correspondent updating parameter, $\overline{E}$ is the average value for all ratios and σ_E is the standard deviation.

The number of eigen frequencies and the number of mode shapes in the objective function was the same as in the updating analysis for the RS. To emphasize the frequency results, the diagonal values of the weighting matrices W_ω and W_φ were equal to five and one, respectively.

The FEMU was applied only to the DS with cracks visually observed. For each series and for all bands the starting Young's modulus was equal to the values obtained from the RS model updating analysis. The upper bounds were kept equal to the initial value and the lower bounds equal to 5% of the initial value.

The results for all test series are presented in Annex C. Table 6.10 summarizes the relative values of the Young's modulus for Series A and B. On the table, the qualitative results of the average frequency errors, and average values for the MAC, NMD and COMAC are also presented. For the case of Series A, the observed damage was at position E_1 (crack c_1, see also Figure 6.35) and the final relative results indicate that damage is at position E_1/E_2. For the case of Series B, the visible damage was at positions E_1, E_2, E_3 and E_9 (cracks c_1 and c_2, respectively) and the relative values pinpoint the element bands E_1, E_2, E_3, E_6, E_8, and E_9. These results are consistent with the observed damage, with the exception of position E_6. The average values demonstrate that all updating analyses had good results, as the average frequency errors are lower than 4.7%, the average MAC values

are almost one, the average NMD values are lower than 10% and the average COMAC values are higher than 0.95.

Table 6.10 – Updating results for Series A and B.

Updating Variables / Band of Elements	Relative Values of Series A				Relative Values of Series B		
	DS_{II-A}	DS_{III-A}	DS_{IV-A}	DS_{V-A}	DS_{III-B}	DS_{IV-B}	DS_{V-B}
E_1 (Bottom part)	1.00	1.00	0.65	0.41	1.00	1.00	0.72
E_2 (Bottom part)	0.69	0.22	1.00	0.45	1.00	0.80	0.93
E_3 (Bottom part)	0.77	0.76	1.00	0.90	1.00	0.94	0.48
E_4 (Diagonal)	1.00	1.00	1.00	0.92	1.00	1.00	1.00
E_5 (Central part)	1.00	1.00	1.00	0.94	1.00	1.00	1.00
E_6 (Diagonal)	1.00	1.00	1.00	0.95	1.00	1.00	0.86
E_7 (Upper part)	0.51	1.00	1.00	0.98	1.00	1.00	1.00
E_8 (Upper part)	1.00	1.00	1.00	1.00	0.74	0.12	0.01
E_9 (Upper part)	1.00	1.00	1.00	1.00	0.26	0.11	0.38
Average ω errors [%]	| 3.96 |	| 2.21 |	| 1.61 |	| 4.73 |	| 1.52 |	| 1.94 |	| 1.50 |
Average MAC values	0.99	0.99	0.99	0.99	0.99	0.99	0.99
Average NMD values	0.10	0.08	0.08	0.07	0.07	0.07	0.08
Average COMAC values	0.95	0.98	0.95	0.98	0.98	0.97	0.98

To further study the damage localization, Figure 6.36 and Figure 6.37 present the relative and the normalized results for two analysis of the test Series A and B. From the comparison between the two types of graphics, an accurate localization is observed if the normalized negative values for the updating parameters are taken into account. For the later, the location E_1, E_2 and E_6 of test Series B are not pinpointed with damage, but only the locations E_3, E_8 and E_9, which are consistent with the crack growth.

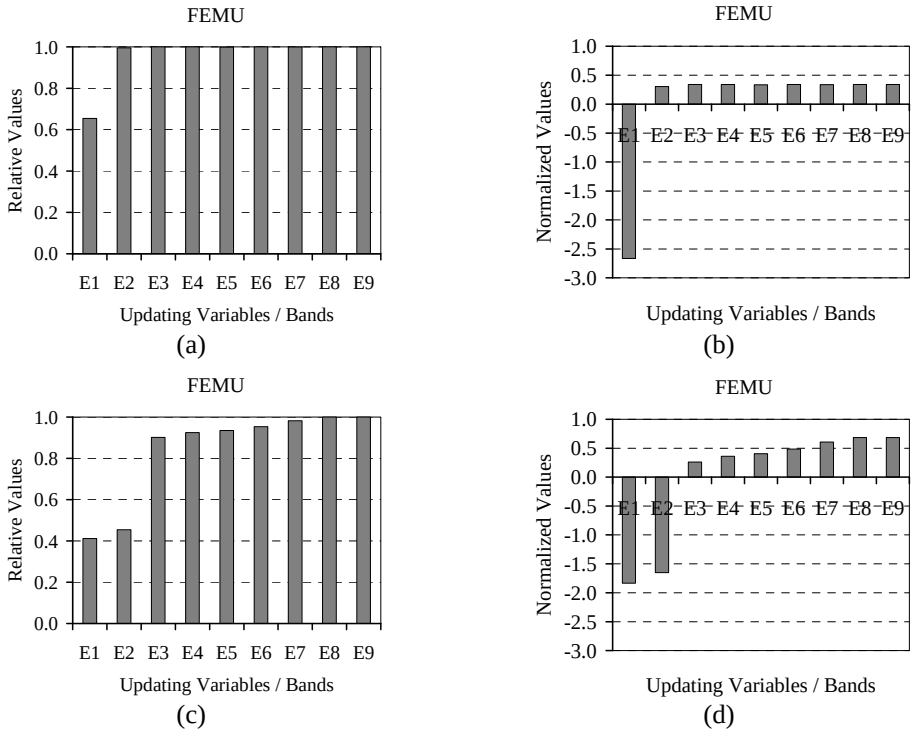


Figure 6.36 – FEMU applied to Series A: (a) and (b) the relative and normalized values for the Young's modulus for the DS_{IV-A}; and (c) and (d) the relative and normalized values for the Young's modulus for the DS_{V-A}.

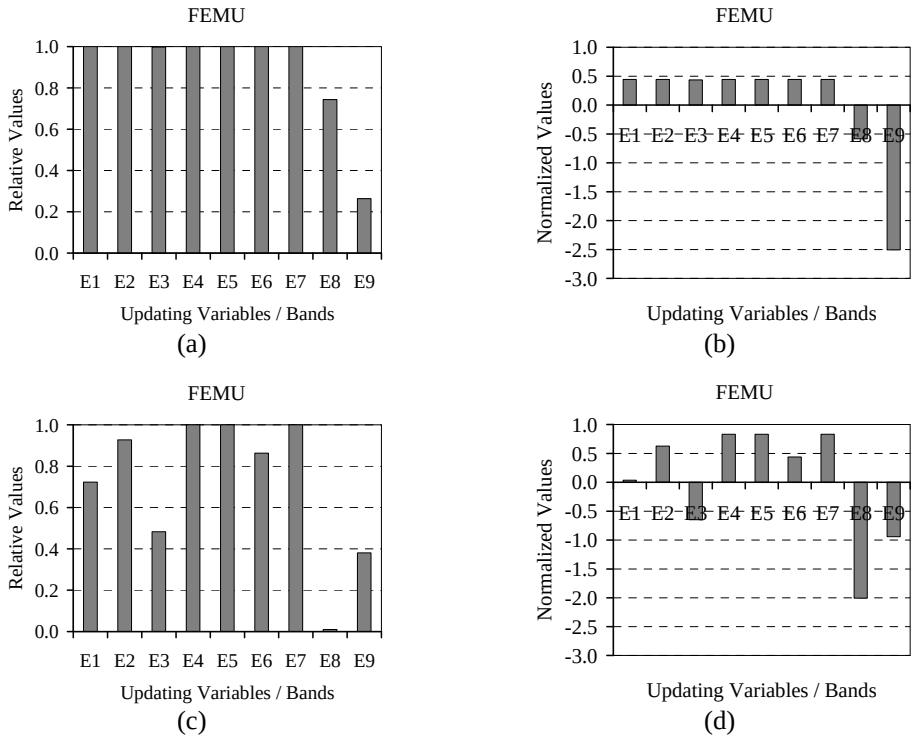


Figure 6.37 – FEMU applied to Series B: (a) and (b) the relative and normalized values for the Young's modulus for the $DS_{III\text{-}B}$; and (c) and (d) the relative and normalized values for the Young's modulus for the $DS_{V\text{-}B}$.

The same analyses were carried out for test Series C and the results are presented in Table 6.11 and Figure 6.38. In this last series, the damage was expected to be localized at position E_5 and E_6 (crack c_3) and it was also expected to observed the crack growth at positions E_8 and E_9 (crack c_2). This damage pattern was obtained with the updating analysis $DS_{II\text{-}C}$ and $DS_{III\text{-}C}$. In the last updating analysis ($DS_{IV\text{-}C}$) the results were not consistent with the observed cracks, as damage at position E_4 was also pinpointed by the normalized updating parameters values, see Figure 6.38d. This might be related to the large differences between the RS_C and the last DS of test Series C. With respect to the qualitative results, the average values are of the same order of magnitude of the previous analyses of Series A and B, indicating that experimental results were successfully tuned.

Table 6.11 – Updating results for Series C.

Updating Variables / Band of Elements	Relative Values		
	$DS_{II\text{-}C}$	$DS_{III\text{-}C}$	$DS_{IV\text{-}C}$
E_1 (Bottom part)	1.00	0.98	1.00
E_2 (Bottom part)	1.00	1.00	1.00
E_3 (Bottom part)	1.00	1.00	1.00
E_4 (Diagonal)	1.00	0.53	0.01
E_5 (Central part)	0.07	0.05	0.01
E_6 (Diagonal)	1.00	0.08	0.01
E_7 (Upper part)	0.91	0.85	0.51
E_8 (Upper part)	0.03	0.09	0.29
E_9 (Upper part)	0.69	0.78	0.36
Average ω errors [%]	| 3.07 |	| 0.89 |	| 2.51 |
Average MAC values	0.99	0.99	0.97
Average NMD values	0.07	0.07	0.09
Average COMAC values	0.98	0.98	0.96

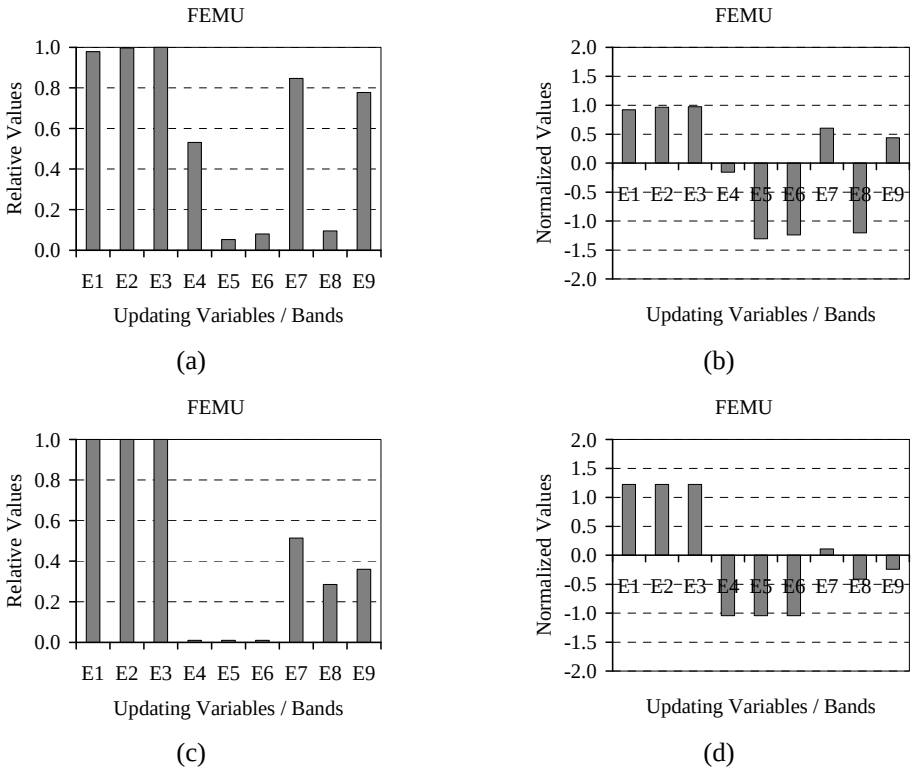


Figure 6.38 – FEMU applied to Series C: (a) and (b) the relative and normalized values for the Young's modulus for the $DS_{III\text{-}C}$; and (c) and (d) the relative and normalized values for the Young's modulus for the $DS_{IV\text{-}C}$.

To conclude, the FEMU prove to be a good method in the damage localization analysis, as the results pinpointed the vicinity of the observed damage position and it was also possible to observe the crack growth and the sequence c_1, c_2 and c_3.

6.6 Conclusions

This chapter presents the damage identification analysis of a masonry wall model. First, a description of the model was made, followed by the detailed description of the static tests. Next, the dynamic identification tests were addressed. The damage identification analysis was carried out in three parts: global parameters analysis, non-model based methods, and finite element model updating method. The results of each part were extensively discussed.

Fourteen damage scenarios were induced by static tests. The static tests were divided into three tests series with different testing conditions to induce several cracks in the wall. From the analysis of the static results it was possible to observe the progressive stiffness decrease with the crack growth. In the end of the static tests, three cracks could be observed: two resulted from bending moments and one resulted from shear stresses.

After each static test, the dynamic system identification analysis was marked by noise in measurements. Mainly, the effects of the electrical noise in the data could not be totally removed after several test procedures. Therefore, only the frequencies lower that 50 Hz for the case of the random impact excitation tests could be well estimated. The reason for inaccurate results in the case of ambient excitation test could be related to the high number of steel elements in the test apparatus.

The damage identification analysis of the global parameters shows that modal properties of the wall were sensitive to induced damage. The frequency values significantly decrease with progressive damage. The changes are higher than reported for other structures in the literature. Concerning the damping coefficient, there is a trend to its increase with progressive damage, but due to difficulties in parameter estimation the results did not allow a final conclusion.

The damage analysis with non-model based methods was carried out only with measured curvatures. Two different approaches were performed by comparing each damage scenario with the reference scenario, and by comparing each consecutive damage scenario. For all test series, the comparison with the reference scenario proves to be more efficient. All the three observed cracks could be localized with the non-model based methods. The crack sequence was also attained.

The data used in the non-model based methods were mainly the curvatures measured directly from the strain gauges. This type of sensor to measure the strains is not the best solution. Although it was possible to estimate accurately the curvatures mode shapes, once the sensors break due to a crossing crack, they cannot continue recording. A system based on two fixed points, with large deformation capacity, or optical measurements would be preferable, since cracking “strains” can be measured.

Concerning the performance of the non-model based methods, the presence of damage was easily identified with the Unified Significance Indicator method, although the number of damage scenarios before the cracks was insufficient to allow a clear detection of damage in time. The COMAC values and the Parameter Method calculated with modal displacements are insensitive to damage. Better performance was observed with COMAC with measured curvatures. The COMAC and the Parameter Method calculated for modal curvatures, the Mode Shape Curvature Method, the Damage Index Method and the Sum of all the Curvatures Errors method gave similar results, with better agreement for the last

three methods, as they were able to locate the damage in the vicinity of the experimental crack locations.

The Finite Element Model Updating method was applied to globally localize the damage. First and for the three tests series, the reference scenarios were tuned with successful results. Second, each damage scenario where visible cracks were observed was tuned by varying the Young's modulus of predefined bands of elements. For all the test series it was possible to localize the damage in the vicinity of the cracks location. There is only one updating analysis where the pinpointed damage is not totally consistent with the observed damage. Nevertheless, the accurate updating results in terms of numerical convergence and the observed crack growth and sequence through the damage scenarios should be stressed.

To conclude and for the case of the wall model, the damage could be successfully detected and localized based on dynamic changes. The measured modal curvatures proved to be useful information for damage identification analysis.

Chapter 7

Case Studies and Environmental Effects

Abstract

This chapter presents two real cases studies of the techniques developed in this thesis: the Clock Tower of Mogadouro and the Church of Jerónimos Monastery, in Lisbon. First, a methodology for monitoring and damage identification in the case studies is proposed, based on vibration signatures. For the two cases there is a description of a preliminary dynamic analysis before the monitoring task, which assists in the decision of sensor location for the monitoring system, the system identification itself and subsequent FE model updating analysis for structural assessment. The environmental and loading effects are also addressed. The automatic modal identification procedures to estimate the global modal parameters are presented and numerical models to simulate the structural response are studied. Finally, the emerging conclusions are discussed.

7.1 Introduction

Two monuments in Portugal are being monitoring by the University of Minho: the Clock Tower of Mogadouro and the Church of Jerónimos Monastery, in Lisbon. Vibration sensors and combined temperature and relative air humidity sensors are installed in the two monuments. Operational modal analysis is being used to estimate the modal parameters, followed by statistical analysis to evaluate the environmental and loading effects on the dynamic response. The aim is to explore damage identification by vibration signatures at an early stage as a part of a health monitoring process to preserve these historical constructions.

This chapter presents the preliminary dynamic analysis before the monitoring task, which assists in the decision of sensor location for the monitoring system, the system identification itself and subsequent FE model updating analysis for structural assessment and the environmental and loading effects on the modal parameters.

7.2 Proposed Methodology for Damage Identification

As described in Chapter 3, current practice of structural health monitoring is based mainly on periodic visual inspections or condition surveys but, during the last decade, software and hardware developments made continuous monitoring possible, Chang et al. (2003). Typically, one can install hundreds of sensors in a structure and read the data in real time. Therefore, the present focus of interest is what type of information is important from the structural point of view and how should the data be processed and stored for damage analysis, Londoño (2006)?

Concerning monitoring of historical masonry structures, it is proposed that this task can be divided in four phases:

- The first phase is the data collection of the structure, including the historical information, geometrical and topographic survey, damage survey, the mechanical materials characterization of materials with Non Destructive (ND) tests, a global dynamic modal test and a numerical model analysis for static and dynamic calibration. This is the first approach to the structural behaviour in the assumed healthy condition at time “zero”;
- In the second phase the health monitoring plan can resort to a limited number of sensors (e.g. a pair of reference accelerometers, strain gauges at critical sections, temperature and humidity sensors, etc). Data should be stored periodically and the monitoring system should be able to send an alarm. Environmental and loading effects should be studied and the presence of damage should be detected by the global modal parameters;
- In the third phase, after alarm triggering, a full-scale dynamic survey with more sensors and measuring points should be performed. In this phase the “health condition” of a structure is studied with more detail. Damage identification methods should be applied to the structure after filtering the environmental effects. The aim of the dynamic methods is to confirm and locate the (possible) damage in a global way;

- In the last phase, a local approach with visual and complementary ND tests should be performed to locally assess the damage and classify it. This can be carried out with sonic test or radar tests, depending on the access conditions of the structure. This local approach can give a better definition of damage.

The global and local approach should be considered as complementary tasks. For the case of historical constructions these two approaches seem to be suitable, since they are ND procedures to evaluate the health conditions.

The following sessions present two case studies of the University of Minho, where the first two phases of the preceding methodology were already applied. For the third phase, the approaches presented in Chapters 5 and 6 should be applied.

7.3 Case Study I: Mogadouro Clock Tower

The Mogadouro Clock Tower is located inside the castle perimeter of Mogadouro (see Figure 7.1), a small town in the Northeast of Portugal. It has a rectangular cross section of 4.7×4.5 m^2 with and interior hole of 2.5×2.3 m^2, and a height equal to 20.4 m. It was built in stone masonry with granite and shale, with dry joints at the corners and with mortar joints in the central part of the walls. The walls have, on average, 1 m of thickness and are composed by an irregular tridimensional bond of stones.



Figure 7.1 – The clock tower and the Mogadouro castle.

On the top, the roof body is supported by eight columns, creating two windows per façade with about 0.9×2.0 m^2. The tower has two entrances at the lower level and at 3.5 m height, in the South and West façades, respectively.

It was not possible to find detailed historical information about the tower, but it is believed that it was built after the year of 1559, to serve as a bell tower of the "Misericordia" church, located Southwest of the tower.

7.3.1 Damage and Rehabilitation Works in the Tower

Due to lack of maintenance, severe damage was observed in the tower in 2004. The damage was characterized by cracks, material degradation, out-of-plane displacements, loss of material in some parts, and biological growth, see Figure 7.2. The most severe damage was a pair of cracks in the East and West façade, see Figure 7.2b and d, that divided the box cross section of the tower in two separated U bodies, leading to a lower safety condition. A geometrical survey of the structure with photogrammetry software allowed registering all anomalies and dimensions. The dimensions of the structural survey have an error about ±5 cm.

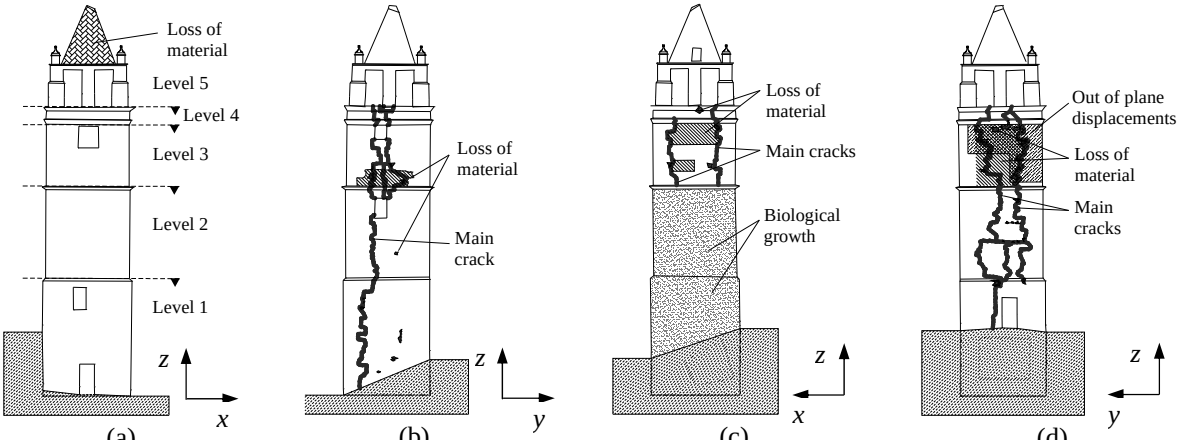




Figure 7.2 – Damage in the tower: (a), (b), (c) and (d) South, East, North and West façades, respectively; and (e) and (f) severe cracks at East and West façade, respectively; (g) inner crack in the West façade; and (h) example of loss of material.

To re-establish the tower safety, consolidation works were carried out in 2005. The remedial treatment included: injections for the walls consolidation, replacement of deteriorated materials and the installation of tie-rods at two levels with very light prestressing stress. In the tie-rods it was applied a low tensile stress. Mainly, the function of the tie-rods is to become active if the cracks reopen. Figure 7.3 shows images of the rehabilitation works and the final view of the tower.

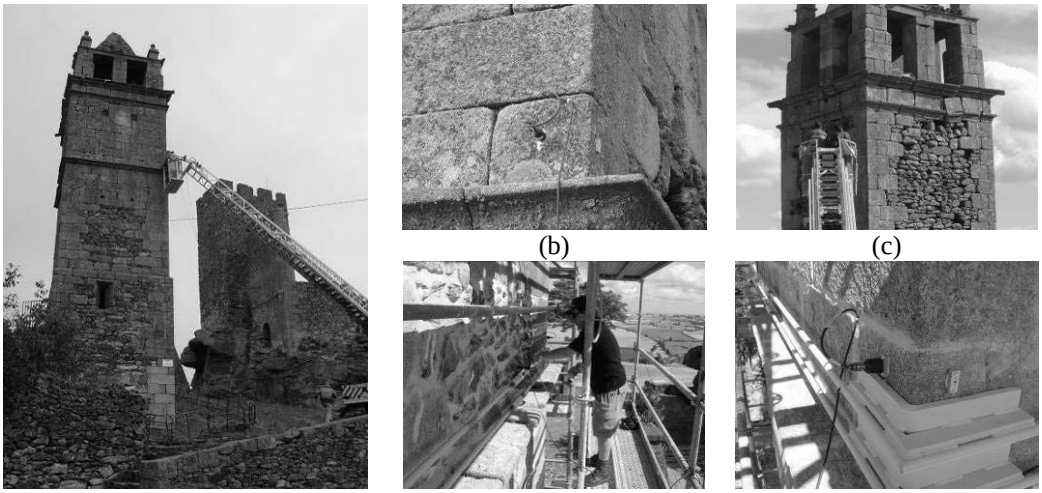


Figure 7.3 – Rehabilitation works in the tower: (a) scaffolding for the work execution; (b) general view of the intervention; and (c) detail of the tie-rods, above the cornices of level 3 and level 4 indicated in Figure 7.2a.

7.3.2 Modal Identification Before and After the Rehabilitation Works

In the case of the Mogadouro Tower, damage was evident and a dynamic based damage identification analysis to detect its presence was not necessary. Nevertheless, the dynamic based methods could be used to locate and to assess the damage. Therefore, two dynamic modal identification tests were performed before and after the structural rehabilitation. The aim was to compare the response of the tower with different structural conditions in order to localize the damage, to archive qualitatively the extent of damage present before the rehabilitation works, and to evaluate the efficiency of the rehabilitation works.

To study the dynamic response, output-only techniques were used to estimate the modal parameters. The ambient excitation from wind and traffic was used to excite the structure. Figure 7.4 presents some images of the ambient vibration dynamic tests. It should be stressed that the tests were carried out before the laboratory campaigns presented in Chapter 4, 5, and 6. Therefore, not all the knowledge that resulted from the laboratorial campaigns was applied to these tests.



(a) (b) (c) (d) (e)

Figure 7.4 – Dynamic tests and example of sensor locations: (a), (b) and (c) before rehabilitation works; and (d) and (e) after rehabilitation works.

The first system identification analysis was performed in October, 2004, and the second analysis was performed in June, 2005. Each campaign took two days of measurements. Due to safety conditions, the measurements from the first tests were only taken outside the tower and with the help of a movable platform, see Figure 7.4a. In order to obtain comparable results, the number of measuring points and their location were kept the same in the second dynamic test. The scaffolding for the rehabilitation works was used to access the measuring points, see Figure 7.4d.

In total, 54 points were selected to measure accelerations in the out-of-plane direction of the walls. Figure 7.5 presents the selected points on each façade (in the designation *Xi*, *X* corresponds to the measuring direction (S)outh, (E)ast, (N)orth or (W)est and *i* to the point number). The points were divided in three horizontal levels. There was no vertical alignment between the points due to the existing cracks in the façades. The intention was to acquire accelerations in both sides of the cracks to possibly measure the relative displacements in both sides of the crack. The upper part of the tower (Level 5,

see Figure 7.2a) was not measured because it was with difficult access and, as a first approach, it was not considered important to capture the global dynamic response.

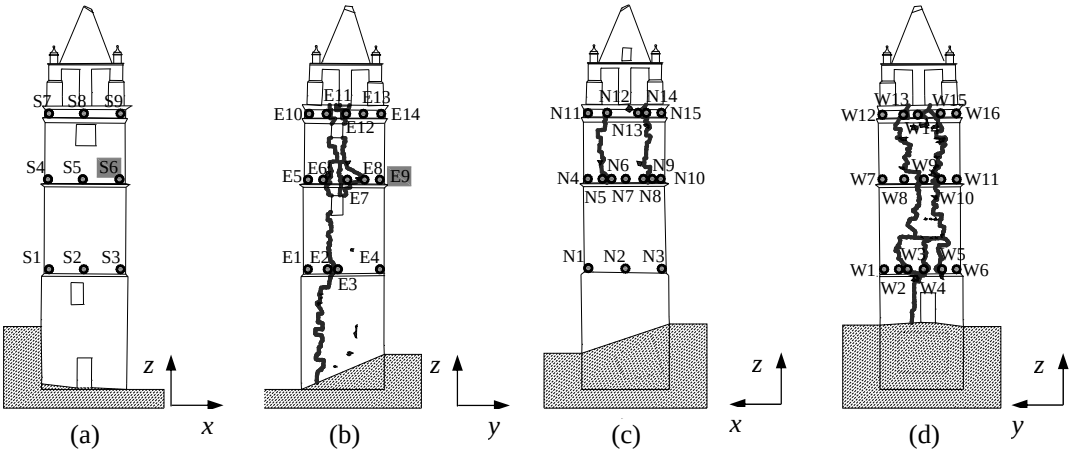


Figure 7.5 – Measuring points: (a), (b), (c) and (d) South, East, North and West façades, respectively. Reference sensors are indicated inside a grey box.

For the measurements, the dynamic acquisition system was composed by 4 uniaxial piezoelectric accelerometers, with a bandwidth ranging from 0.15 to 1000 Hz (5%), a dynamic range of ±0.5 g, a sensitivity of 10 V/g, 8 μg of resolution and 210 g of weight, connected by coaxial cables to a front-end data acquisition system with a 24 bit ADC, provided with anti-aliasing filters. The front-end was connected to a laptop by an Ethernet cable. The accelerometers were bolted to aluminum plates that were glued with epoxy to the stones.

As the acquisition system had only 4 available channels, 27 test setups were necessary to record the accelerations in the 54 measured points. Table 7.1 presents the test setups with the reference sensors at positions S06 and E09 (see Figure 7.5) and the moving sensors.

Table 7.1 – Test setups for the Mogadouro Clock Tower.

Setup	Ref. 1	Ref. 2	Mov. 1	Mov. 2
1	S06	E09	S01	S02
2	S06	E09	S03	S04
3	S06	E09	S05	S07
4	S06	E09	S08	S09
5	S06	E09	E01	E02
6	S06	E09	E03	E04
7	S06	E09	E05	E06
8	S06	E09	E07	E08
9	S06	E09	E10	E11
10	S06	E09	E12	E13
11	S06	E09	E14	–
12	S06	E09	N01	N02
13	S06	E09	N03	N04
14	S06	E09	N05	N06

Setup	Ref. 1	Ref. 2	Mov. 1	Mov. 2
15	S06	E09	N07	N08
16	S06	E09	N09	N10
17	S06	E09	N11	N12
18	S06	E09	N13	N14
19	S06	E09	N15	–
20	S06	E09	W01	W02
21	S06	E09	W03	W04
22	S06	E09	W05	W06
23	S06	E09	W07	W08
24	S06	E09	W09	W10
25	S06	E09	W11	W12
26	S06	E09	W13	W14
27	S06	E09	W15	W16

A preliminary FE dynamic analysis estimated ten frequencies between 2 and 15 Hz. Therefore and for each test campaign, a sampling frequency of 256 Hz was chosen to acquire the response. The total sampling time on each setup was equal to 10 minutes and 40 seconds (2000 times the highest period).

The parameters were estimated before and after rehabilitation works by comparing the results from two different methods: the Enhanced Frequency Domain Decomposition method (EFDD) and the Stochastic Subspace Identification (SSI) method (Principal Component), implemented in ARTeMIS (SVS, 2006). Table 7.2 summarizes the results obtained for the first seven modes in terms of frequency and damping values estimated by the SSI method. Comparing the two structural conditions, there was a significant increase of frequency values (on average 50%) and a significant decrease for damping coefficients, from an average value of 2.2 to 1.5% (40% decrease, on average).

Table 7.2 – Dynamic response before and after the rehabilitation.

Mode Shape	Before		After		Δ_ω	Before		After		Δ_ξ
	ω [Hz]	CV_ω [%]	ω [Hz]	CV_ω [%]	[%]	ξ [%]	CV_ξ [%]	ξ [%]	CV_ξ [%]	[%]
1st	2.15	1.85	2.56	0.21	+19.28	2.68	219.51	1.25	0.13	–53.26
2nd	2.58	1.05	2.76	0.30	+6.70	1.71	94.02	1.35	0.17	–21.00
3rd	4.98	0.69	7.15	0.27	+43.67	2.05	65.33	1.20	0.14	–41.32
4th	5.74	1.56	8.86	0.47	+54.37	2.40	24.27	1.31	0.13	–45.72
5th	6.76	1.13	9.21	0.21	+36.13	2.14	31.74	1.16	0.12	–45.65
6th	7.69	2.94	15.21	2.24	+97.87	2.33	55.98	2.54	0.24	+9.11
7th	8.98	1.21	16.91	1.40	+88.27	2.30	46.39	1.49	0.23	–35.07
Average values	–	1.49	–	0.73	+49.47	2.23	76.75	1.47	0.17	–40.34*

* - Average value calculated only with negative differences

The global parameter results are consistent with the two structural conditions, i.e. the structure after rehabilitation has a new and higher stiffness, and the non-linear phenomena effects in the damping coefficients are reduced. Nevertheless, it should be stressed that damping also depends on the level of vibration. For the first campaign the tests were performed only with low traffic excitation, while for the second campaign the structure was excited by moderate wind and low traffic. Analyzing the Coefficient of Variation CV, it is possible to observe that for the second campaign the results have lower CV values, less than 0.73%, on average, for frequency values and less than 0.17%, on average, for damping coefficients, indicating a better estimation.

Figure 7.6 presents the comparison between the experimental mode shapes in the two conditions, as well the MAC values.

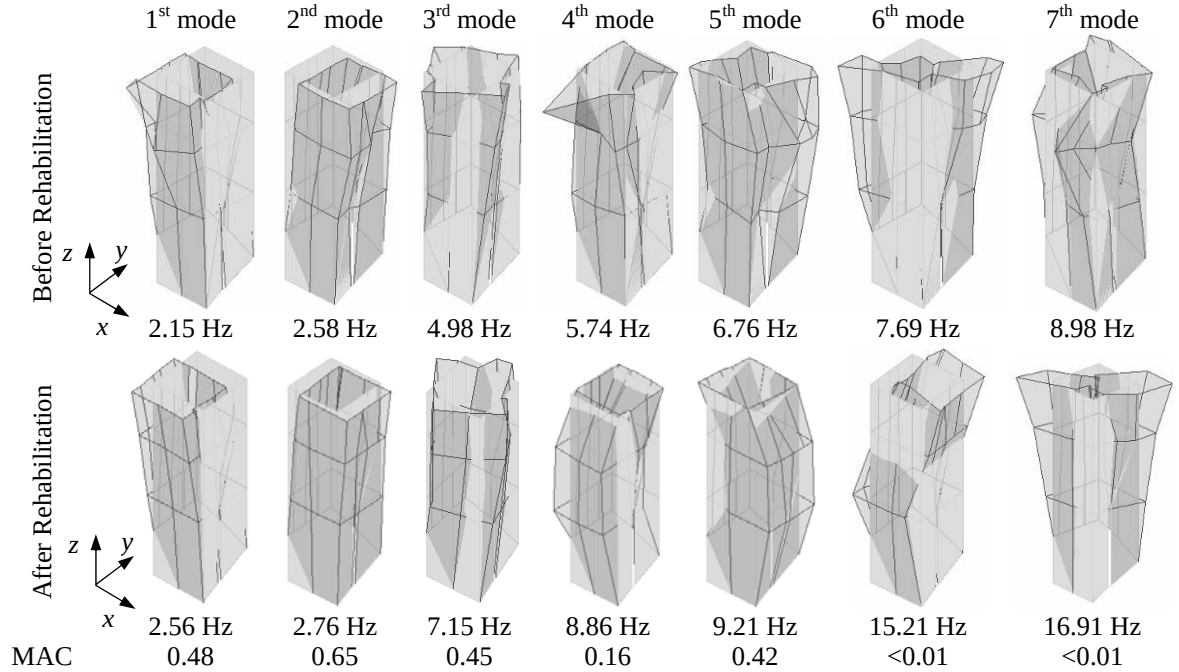


Figure 7.6 – Experimental mode shapes and MAC values before and after rehabilitation works.

From the comparison between the two structural conditions it is possible to observe a similar mode configuration for the first five modes, but with a weak correlation, as the MAC values are lower than 0.65. For sixth and seventh modes there is an exchange in the modes order.

Analyzing the modal displacements, local protuberances can be observed in the areas close to the cracks and in the upper part before the rehabilitation. This is due to the presence of severe damage. The structure only behaves monolithically after the rehabilitation.

Taking into account the previous results, it is possible to conclude that the structure suffered a significant structural intervention and the strengthening works were efficient. One can also conclude that the presence of damage changed the dynamic behaviour significantly with respect to the possible original structure. The challenge now is to verify if the cracks were stabilized with the intervention by means of a dynamic monitoring system.

7.3.3 Structural Assessment

Aiming at a better understanding of the two structural conditions and to better evaluate the efficiency of the strengthening, FE analyses were also addressed. The numerical structural assessment was carried out by the application of the FE Model Updating method (FEMU), see Chapter 3 for details. The nonlinear least square method implemented in MatLab (2006), function `lsqnonlin`, was used together with FE package DIANA (2006) to compute the numerical modes. The objective function π to be minimized is composed by the residuals formed with calculated and experimental frequencies and mode shapes, given by:

$$\pi = \frac{1}{2}\left[\sum_{j=1}^{m_\omega} W_\omega \left(\frac{\omega_j^2 - \omega_{j,\exp}^2}{\omega_{j,\exp}^2}\right)^2 + \sum_{j=1}^{m_\varphi} W_\varphi \left(\varphi_j - \varphi_{j,\exp}\right)^2\right] \tag{7.1}$$

where m_ω denotes the number of eigen frequencies taken into account, m_φ is the number of normalized eigen modes taken into account and W_ω and W_φ are weighting diagonal matrices for the frequencies and mode shapes, respectively. Note that in Eq.(7.1) experimental and numerical mode shapes are normalized in a way that the maximum real value of the modal displacement is equal to one, in order to be comparable with the residuals from the frequency values normalized by the experimental results.

The second term of the objective function was computed with 24 degrees-of-freedom. The selected degrees-of-freedom are those at the corners of the tower, as shown in Figure 7.7.

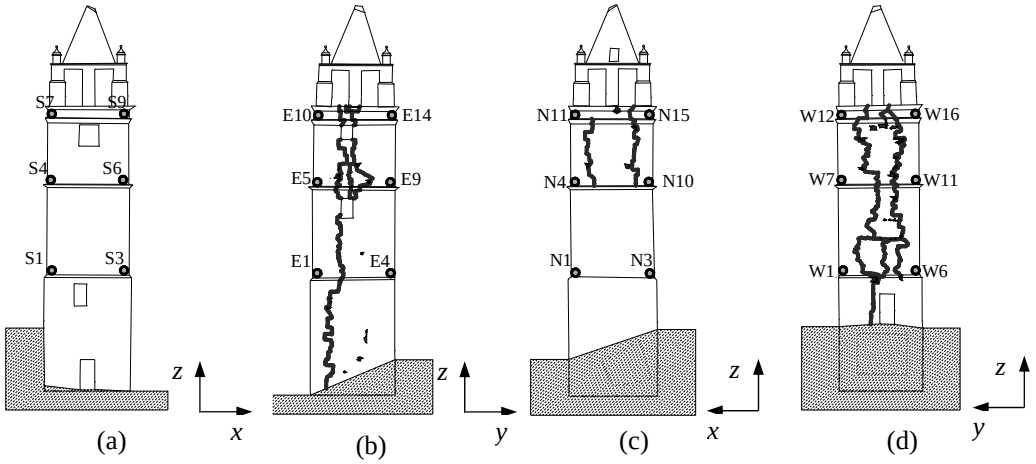


Figure 7.7 – Selected degrees-of-freedom for the objective function: (a), (b), (c) and (d) South, East, North and West façades, respectively.

The objective function was computed with the first five eigen frequencies and first five eigen modes ($m_\omega = 5$ and $m_\varphi = 5$). The tolerance for the residuals and the updating parameters increments in the objective function was equal to 1.0×10^{-6} and the Jacobian increment was equal to 1%. Boundary constraints were applied to the updating parameters in order to avoid unrealistic results.

Since the results of the second experimental modal analysis (strengthened condition) were better estimated, it was decided to start the updating analysis for the case of the strengthened condition and subsequently update the unstrengthened condition.

7.3.3.1 Analysis after Rehabilitation

The optimization analysis was performed in a step-by-step approach, where the updating parameters and procedures were chosen according to the results obtained in each step, in a progressive understanding about the dynamic behavior of the tower. In the strengthened condition, it was assumed that no cracks were present in the tower. The first model was a 3D shell elements model, with 8 noded elements to model the walls and with 6 noded elements to model the roof. The shell model was chosen to simplify the analysis, but after five optimization steps it was decided to use also a second 3D model with brick (20 noded) elements to better simulate the corners of the walls and the geometry of the last level (upper part). The 6 noded shell elements were also used in the second model, but only to model the planar surfaces of the roof. The second model analysis took only two steps. Here, it is noted that shell elements are not capable of reproducing accurately the corner stiffness and the relation thickness/length of the wall suggest the need for 3D elements, as shown by Lourenço at al. (2007).

Figure 7.8 shows the five steps with the shell elements model, where the updating parameters are also indicated. The five steps correspond to five analyses, starting with analysis Shell A_s and ending with analysis Shell E_s, where s indicates the strengthened condition. The initial and final values of the updating parameters, together with indicators of each optimization, are presented in Table 7.3. Next, the main conclusions of each step are addressed.

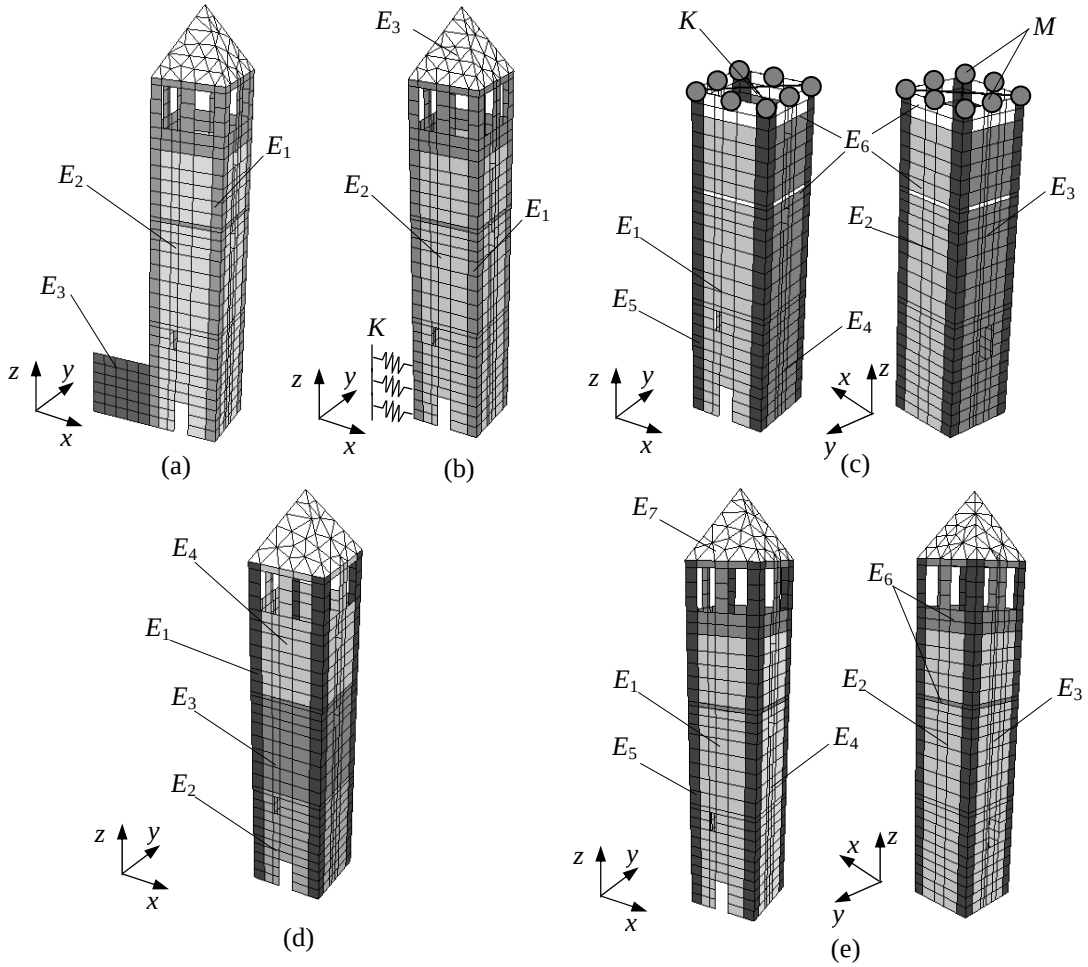


Figure 7.8 – Updating parameters for the shell elements model: (a) analysis Shell A_s; (b) analysis Shell B_s; (c) analysis Shell C_s; (d) analysis Shell D_s; and (e) analysis Shell E_s.

Table 7.3 – Results for the Shell analysis after rehabilitation.

Analysis	Updating Parameters	Initial Values	Final Values	Average ω Error [%]	Average MAC	Average NMD	Average COMAC
Shell A_s	E_1 [GPa] (Corners)	1.000	1.155	| 3.46 |	0.87	0.54	0.85
	E_2 [GPa]	1.000	1.751				
	E_3 [GPa] (Lateral wall)	1.000	0.997				
Shell B_s	E_1 [GPa] (Corners)	1.000	0.911	| 4.31 |	0.99	0.08	0.99
	E_2 [GPa]	1.000	2.580				
	E_3 [GPa] (Roof)	1.000	10.998				
	K [GPa.m] (Lateral wall)	0.001	0.011				
Shell C_s	E_1 [GPa] (South)	2.000	1.123	| 13.82 |	0.99	0.10	0.98
	E_2 [GPa] (North)	2.000	3.533				
	E_3 [GPa] (West)	2.000	1.469				
	E_4 [GPa] (East)	2.000	3.619				
	E_5 [GPa] (Corners)	2.000	1.186				
	E_6 [GPa]	2.000	7.231				
	M [ton] (Concentrated)	1.500	2.193				
	K [GPa.m] (Bars)	10.000	34.707				
Shell D_s	E_1 [GPa] (Corners)	2.000	11.949	| 12.50 |	0.89	0.33	0.85
	E_2 [GPa] (Level 1)	2.000	0.790				
	E_3 [GPa] (Level 2)	2.000	0.254				
	E_4 [GPa] (Level 3)	2.000	2.000				
Shell E_s	E_1 [GPa] (South)	2.000	1.467	| 2.59 |	0.99	0.11	0.98
	E_2 [GPa] (North)	2.000	4.227				
	E_3 [GPa] (West)	2.000	1.919				
	E_4 [GPa] (East)	2.000	4.711				
	E_5 [GPa] (Corners)	2.000	0.575				
	E_6 [GPa]	2.000	4.327				
	E_7 [GPa] (Roof)	2.000	3.900				

In first step (analysis Shell A_s), three different Young's modulus were chosen as updating parameters, namely the modulus E_1 of the masonry material at the corners, the modulus E_2 of the masonry material at the middle of the walls, and the modulus E_3 of the lateral wall at the base of the tower, which was assumed to have strong influence on the dynamic behavior, see Figure 7.8a. A different material at the corners was considered by two reasons. First, the visual survey indicates that the masonry types is different at these areas, and, second, to better model the stiffness at the corners, as the shell elements are unable to replicate the additional stiffness at these points.

The starting values for all the updating parameters were equal to 1.0 GPa and the Young's modulus for the masonry material of the roof was also kept equal to 1.0 GPa. The Poisson coefficient for all the materials was equal to 0.2. The mass density of the material at the corners was equal to 2400 kg/m^3. For the middle walls the mass density was equal to 2200 kg/m^3 and for the roof equal to 2000 kg/m^3. The tie-rods were not included in the model because in a preliminary updating analysis it was concluded that they change the dynamic behavior of the tower only marginally. The bottom elements were considered fully constrained.

Concerning the results of the first step, the final values for the updating parameters indicate that the masonry material in the walls should have a value equal to 1.75 GPa, the material at the corners should have a value equal to 1.15 GPa, and the material of the wall at the base should have the final value of 1.0 GPa. Although the average frequency errors with these updating variables was about 3.5%, the MAC values were equal to 0.87, the average NMD values were equal to 54% and the average COMAC values were equal to 0.85 (see Table 7.3), indicating that the modes configuration were not so well tuned.

In the second step (analysis Shell B_s), the material at the roof was included in the group of updating parameters (new material E_3) and the wall was replaced by springs with axial stiffness K, see Figure 7.8b. The results concerning the modes correlation increased significantly, as the MAC and the COMAC average values are almost one and the average NMD is equal to 8%, see Table 7.3, but the average frequency errors increase to 4.3%, the final value for the roof (E_3) is about 11 GPa, four times higher than the material for the masonry walls in general (E_2), and the material at the corners (E_1) has a low Young's modulus than the material in general. This is an unexpected result. During this analysis it was possible to conclude that the upper part of the tower, including the roof, significantly change the dynamic behavior, while the effect of the lateral wall at the base could be neglected.

Therefore, in the next step (analysis Shell C_s), the upper part was replaced by two bars with axial stiffness K and a group of concentrated masses M, see Figure 7.8c. The elastic supports to simulate the lateral wall at the bottom were removed and the Young's modulus of the walls in the four façades was considered as independent updating parameters. E_1, E_2, E_3 and E_4 are the Young's modulus of the South, North, West and East façades, respectively. The masonry material at the corners E_5 and the better masonry type areas E_6 at two levels in the upper part were also included as updating parameters. The results for this case show a good correlation between experimental and numerical mode shapes, but difficulties to tune the frequencies were observed (the average errors were about 14%). For convenience, the initial values were changed in order to have a fast optimization analysis.

In the fourth step (analysis Shell D_s), an attempt to model the tower with three different Young's modulus, according to the height of the walls, was carried out, see Figure 7.8d, but again with successful updating results.

In the last step with the shell elements model (analysis Shell E_s), the roof was again modeled and included as an updated parameter E_7. The materials of the walls in the four façades (E_1, E_2, E_3 and E_4) were considered as independent variables, as well the material at the corners (E_5) and the areas with better masonry type (E_6), see Figure 7.8e.

The global updating results for this case seems acceptable, as the average frequency errors is about 2.6%, the average MAC and COMAC values are close to one and the average NMD is about 11%, see Table 7.3. Nevertheless, it should be stressed that the final values for the Young's modulus of the North and East façades are almost three times higher than the modulus of the South and West façades. According to the visual inspection of the masonry, presented in Figure 7.9, it was expected to find higher values for the Young's modulus in the South and East façades, and similar values for the North and West façades. Note that the walls thickness does not change in height and is approximately the same for the four façades. The fact that the North façade is three times stiff than the South façade is dubious, and it was also expected that the Young's modulus of roof would be lower than the Young's modulus of the material of the façades. Therefore, the final values for the updating parameters with the shell element models were judged as possibly unrealistic. The difficulties to model the upper part of the structure, with large sensitive to the dynamic response, might be the reason for the possibly incoherent values.

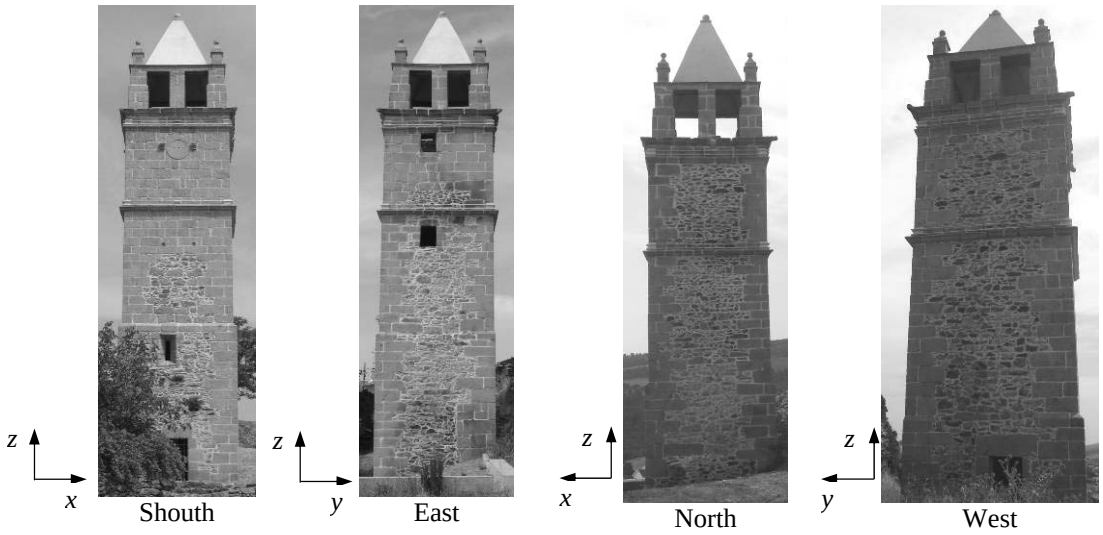


Figure 7.9 – Stone ensemble (the inner ensemble is similar to the middle areas of North and West façades).

To proceed with the updating analysis, a 3D model with brick (20 noded) elements was prepared with a better representation of the upper part. The model is presented in Figure 7.10a with the same updating parameters as the last analysis with the shell elements, see Figure 7.8e. The planar roof surfaces were modeled with 6 noded shell elements to simplify the mesh.

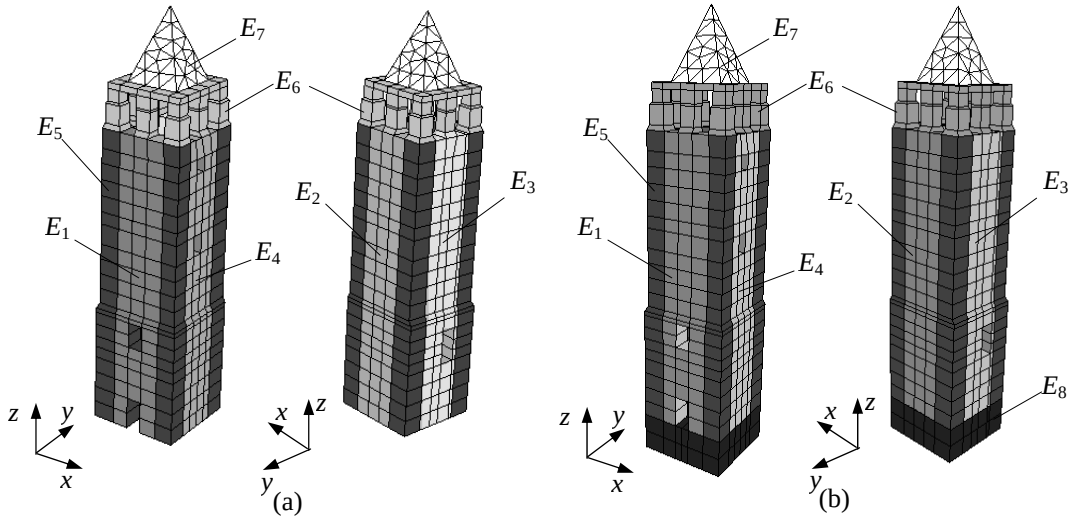


Figure 7.10 – Updating parameters for the brick models: (a) analysis Brick A_s; and (b) analysis Brick B_s.

On this second model, two steps were carried out and the results are presented in Table 7.4. On the first step (analysis Brick A_s), the results were considered unacceptable, because the Young's modulus of the roof material was twenty times higher than the masonry material in general, and the average frequency errors were about 6%. In the second step (analysis Brick B_s) and in order to better tune the frequency results, two meters of foundation were modeled by walls with the same thickness as the façades, see Figure 7.10b. The Young's modulus of the foundation material was also included as updating parameter E_8. For convenience, the initial values were change in order to have a fast optimization analysis. The simulation of the foundation was considered crucial for the optimization. The final values were acceptable, as the average frequency error is about 2%, the average MAC and COMAC values is almost one, the average NMD values is equal to 12%, and, most important, the relation between the modulus of elasticity of the different parts is reasonable.

Table 7.4 – Results for the Brick analysis after rehabilitation.

Analysis	Updating Parameters	Initial Values	Final Values	Average ω Error [%]	Average MAC	Average NMD	Average COMAC
Brick A_s	E_1 [GPa] (South)	2.000	1.368	| 6.30 |	0.96	0.16	0.96
	E_2 [GPa] (North)	2.000	2.238				
	E_3 [GPa] (West)	2.000	0.971				
	E_4 [GPa] (East)	2.000	0.621				
	E_5 [GPa] (Corners)	2.000	2.255				
	E_6 [GPa]	2.000	21.232				
	E_7 [GPa] (Roof)	2.000	21.976				
Brick B_s	E_1 [GPa] (South)	1.000	1.974	| 2.10 |	0.98	0.12	0.98
	E_2 [GPa] (North)	1.000	2.210				
	E_3 [GPa] (West)	1.000	1.075				
	E_4 [GPa] (East)	1.000	0.804				
	E_5 [GPa] (Corners)	1.000	3.875				
	E_6 [GPa]	1.000	1.210				
	E_7 [GPa] (Roof)	1.000	0.195				
	E_8 [GPa] (Foundation)	1.000	5.997				

With respect to Young's modulus variation, the South and North façades have values around 2 GPa, and the East and West façades have values around 1 GPa. The differences from one to two are acceptable if the heterogeneity of masonry is taken into account, but still a relative higher value for the South wall was expected. The material at the corners has higher stiffness, about 4 GPa, and the areas with better masonry type have values of the same order of the masonry walls in general. The roof has a lower value around 0.2 GPa and the foundation 6 GPa, which is a higher value but, at the same time, acceptable due to the lack of survey of the foundations and the high material compaction at the base and the soil confinement.

Other results regarding the correlation between the experimental and the numerical results can be observed in Figure 7.11, which presents the modes and frequencies comparison and the residuals history. Figure 7.12 presents the tuned modes and the frequency values, where it is possible to observe that the upper part of the structure has a flexible behavior due to the presence of the windows.

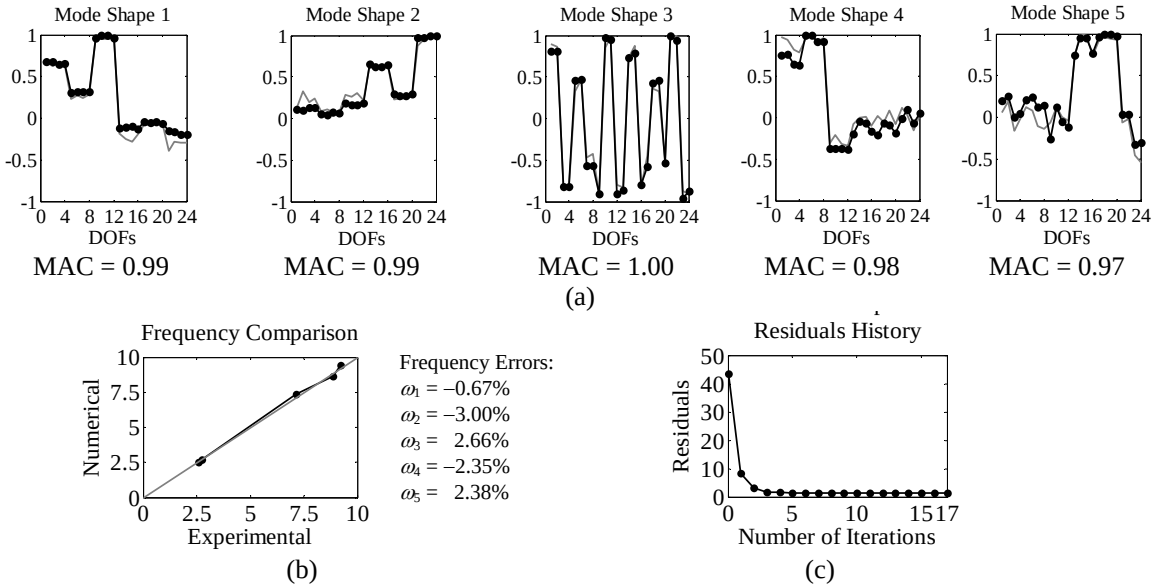
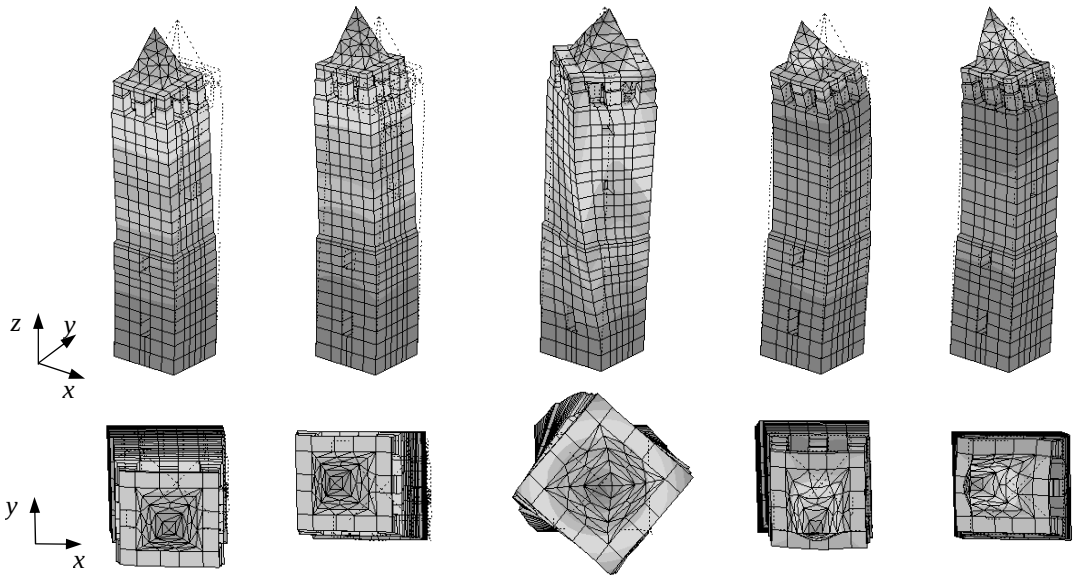


Figure 7.11 – Results from the optimization analysis Brick B_s: (a) differences between updated experimental DOFs, with experimental (grey line) and numerical (marker line) values; (b) frequency values comparison; and (c) residuals history.



Mode 1 (2.54 Hz) | Mode 2 (2.68 Hz) | Mode 3 (7.33 Hz) | Mode 4 (8.62 Hz) | Mode 5 (9.36 Hz)

Figure 7.12 – Numerical mode shapes after rehabilitation (analysis Brick B_s).

7.3.3.2 Analysis before Rehabilitation

For the analysis in the unstrengthened condition, the brick elements model of analysis Brick B_s was again tuned with the same updating parameters, see Figure 7.10b. As a continuation of the previous analysis, the adopted initial values were equal to the final values of the strengthened condition. Only two step analyses were made, the Brick A_d and Brick B_d, where the designation d corresponds to the damaged condition. The correspondent updating results for the two steps are presented in Table 7.5.

Table 7.5 – Results for the Brick analysis before rehabilitation.

Analysis	Updating Parameters	Initial Values	Final Values	Average ω Error [%]	Average MAC	Average NMD	Average COMAC
Brick A_d	E_1 [GPa] (South)	1.974	0.710	| 3.81 |	0.90	0.31	0.85
	E_2 [GPa] (North)	2.210	2.210				
	E_3 [GPa] (West)	1.075	0.310				
	E_4 [GPa] (East)	0.804	0.283				
	E_5 [GPa] (Corners)	3.875	3.870				
	E_6 [GPa]	1.210	0.392				
	E_7 [GPa] (Roof)	0.195	0.082				
	E_8 [GPa] (Foundation)	5.997	5.997				
Brick B_d	E_1 [GPa] (South)	1.974	0.687	| 3.64 |	0.90	0.31	0.85
	E_2 [GPa] (North)	2.210	2.210				
	E_3 [GPa] (West)	1.075	0.302				
	E_4 [GPa] (East)	0.804	0.276				
	E_5 [GPa] (Corners)	3.875	3.870				
	E_6 [GPa]	1.210	0.380				
	E_7 [GPa] (Roof)	0.195	0.083				
	E_8 [GPa] (Foundation)	5.997	5.997				

Observing the results of the first step (analysis Brick A_d) it can be concluded that is necessary to reduce significantly the Young's modulus of the walls in order to have good correlation between the experimental and numerical results, with the exception of the North façade (E_2), the masonry material at the corners (E_5) and the foundation material (E_8). The average frequency error is about 3.8%, the average MAC and COMAC values is about 0.9 and the average NMD value 31%. Note that the experimental dynamic identification analysis was carried out with low ambient excitation, which makes it more difficult to estimate the modal parameters and with local protuberances in the mode shapes due to the presence of severe damage. Therefore the global results could be acceptable, but the unvarying value for the Young's modulus of the North façade (E_2) was questioned.

On the second step (analysis Brick B_d) the same updating parameters were kept and the mass density of the walls was discussed again. In fact, the mass of the walls suffered an approximate increase of 1.5% due to the material addition and the injection works. As the stiffness and the mass is square root proportional to the frequencies ($\omega = \sqrt{k/m}$), it was decided to update only the Young's modulus, i.e. the stiffness, keeping constant the values for the mass and avoiding unrealistic results. Therefore, for the tower in its damaged condition, the mass densities were reduced 1.5%. With the new mass distribution, almost the same results were obtained, allowing concluding that the mass change due to the works is not so significant for the dynamic response. The average frequency errors is about 3.6% and the others results for the correlation between the mode shapes were in the same order of magnitude as in the previous analysis, see Table 7.5.

Figure 7.13 presents other results for the final analysis Brick B_d in terms of correlation between the measured and calculated degrees of freedom, the frequency comparison and the residuals history. In terms of frequency comparison the results are accurate but in terms of mode shape correlations the fourth and fifth modes were not very well tuned, as it can be observed by the differences between the two vectors.

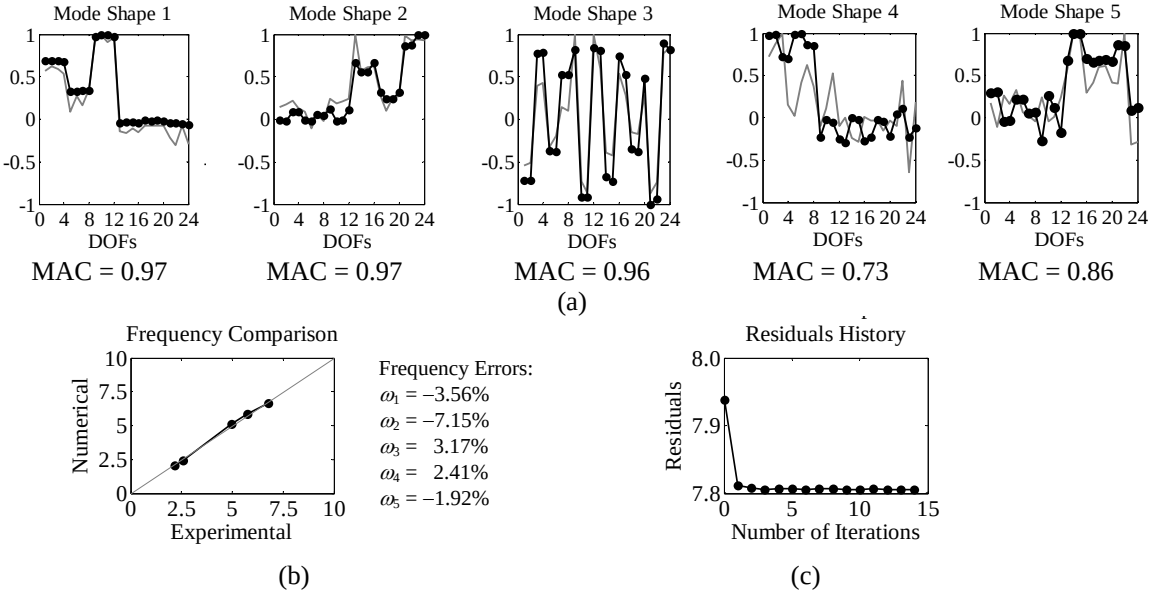
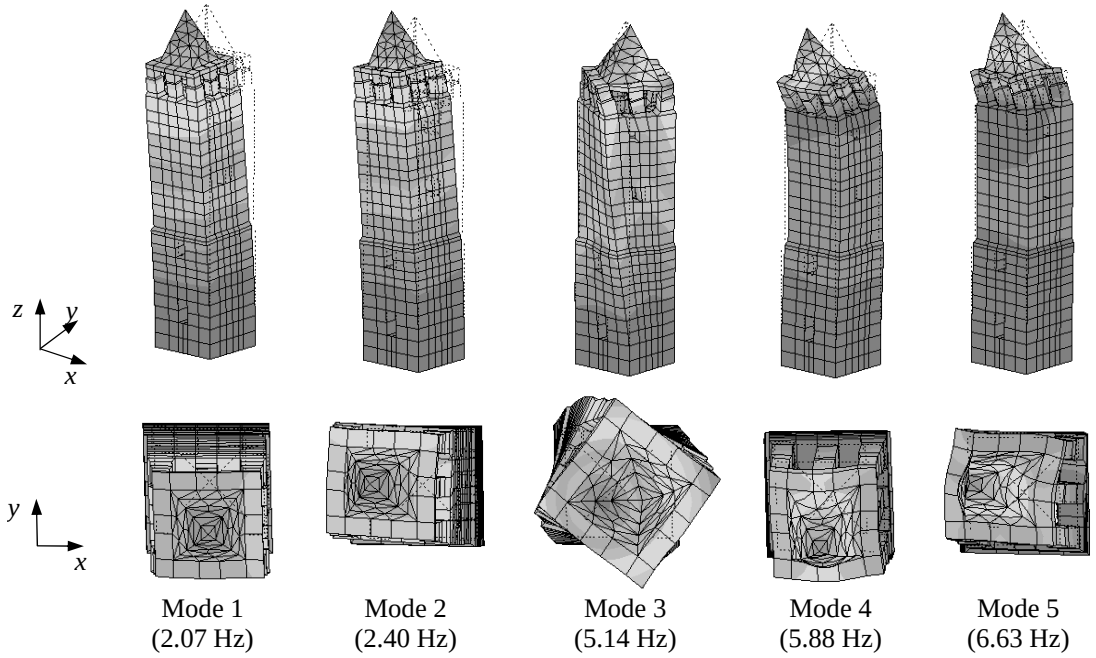


Figure 7.13 – Results from the optimization analysis Brick B_d: (a) differences between updated experimental DOFs, with experimental (grey line) and numerical (marker line) values; (b) frequency values comparison; and (c) residuals history.

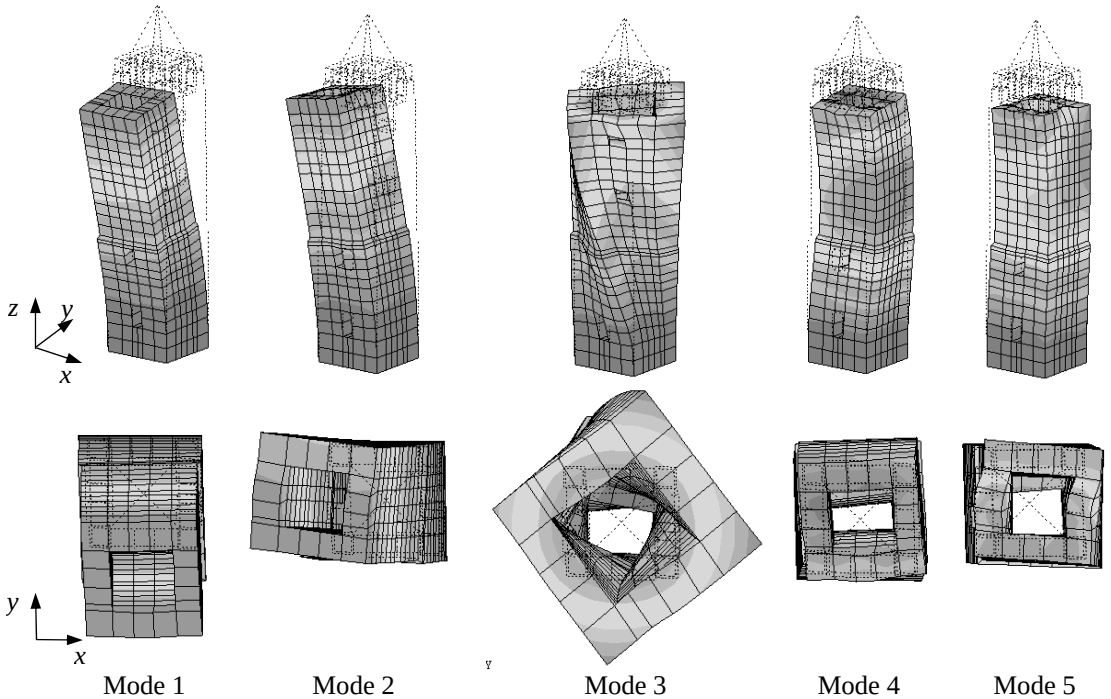
Figure 7.14 presents the numerical mode shapes, where is possible to observe two relevant different parts in the structure, the main body composed by the walls (up to the fourth level, see Figure 7.2a), and the upper part of the tower (the fifth level). The later has

more flexible behavior, especially for the higher modes, being much relevant for the dynamic behavior of the tower. Figure 7.15 presents the same results but only for the first four levels of the tower with a higher magnification factor. Here, it is possible to observe the influence of the upper part on the top of the fourth level and the unsymmetrical shape of the bending modes.



Mode 1 (2.07 Hz) | Mode 2 (2.40 Hz) | Mode 3 (5.14 Hz) | Mode 4 (5.88 Hz) | Mode 5 (6.63 Hz)

Figure 7.14 – Numerical mode shapes before rehabilitation (analysis Brick B_d).



Mode 1 | Mode 2 | Mode 3 | Mode 4 | Mode 5

Figure 7.15 – Numerical mode shapes before rehabilitation (analysis Brick B_d with a magnification factor equal to 2.5 previous results).

Finally and after the two steps analysis, it was tried to model the localized cracks in the East and West façades, with the Young's modulus as a new pair of updating parameters. The results were not as accurate as the Brick B_d analysis, indicating that the

extent of damage was so high that it was necessary to consider the whole wall with a low Young's modulus to model the damage.

7.3.3.3 Comparison between the Two Structural Conditions

As the aim of the FE model updating analysis was to localize and to assess damage in the tower and to evaluate the efficiency of strengthening, the final values of the updating parameters before and after the strengthening are now compared and discussed. Table 7.6 presents again the final results together with the difference and the relative values of the updating parameters. All the updating variables suffered a significant increase, with exception of the material at the corners (E_5), at the foundation (E_8), and at the North wall (E_2). As discussed before, for the corners and for the foundation these results are acceptable because the stone masonry at the corners was better than in the central parts of the walls, and the foundation material tries to represent not only the structural element but also the boundary conditions at the base. For the North wall a Young's modulus increase was expected, but in the strengthened condition the North wall had a higher Young's modulus, which might indicate that the wall was in better condition than the others. The other updating variables on average they increased three times the initial value. This indicates that the damage on the tower was severe on the central parts of the South, East and West façades and at the upper part of the tower. These areas in the structure are the ones which suffer large mortar loss due to deterioration, meaning that the results can be acceptable. Finally, one can conclude that the strengthening works were efficient at re-establishing the tower safety.

Table 7.6 – Comparison between the two updated analysis, after and before rehabilitation.

Updating Parameters	Before Rehabilitation [GPa]	After Rehabilitation [GPa]	Difference [GPa]	Relative Values
E_1 [GPa] (South)	0.687	1.974	+1.287	2.87
E_2 [GPa] (North)	2.210	2.210	–	1.00
E_3 [GPa] (West)	0.302	1.075	+0.773	3.56
E_4 [GPa] (East)	0.276	0.804	+0.528	2.91
E_5 [GPa] (Corners)	3.870	3.875	+0.005	1.00
E_6 [GPa]	0.380	1.210	+0.830	3.18
E_7 [GPa] (Roof)	0.083	0.195	+0.112	2.35
E_8 [GPa] (Foundation)	5.997	5.997	–	1.00

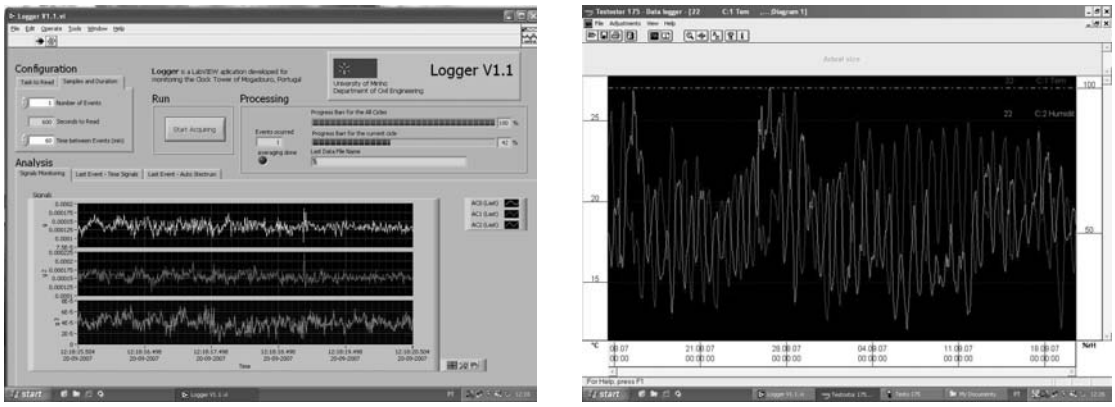
7.3.4 Dynamic Monitoring System

With the FE analysis for structural assessment in the case of the strengthened condition, the first phase of the monitoring methodology for damage identification presented in Section 7.2 was accomplished. The second phase is the dynamic monitoring task, which can be performed with a limited number of sensors. This task has been carried out since April, 2006. The aim is to evaluate the environmental and loading effects and to detect any possible non stabilized phenomena in the structure (damage), by studying the global dynamic parameters.

A low-cost monitoring system was chosen for this task. The system is composed by three piezoelectric accelerometers, connected by coaxial cables to a USB data acquisition card with 24 bits resolution, provided with anti-aliasing filters, which is connected to a Pentium II® laptop with an uninterruptible power supply device. The LabView (2006) software was used to measure and acquire accelerations. In parallel, a combined sensor connected to the laptop through serial cable is recording the ambient temperature and

relative air humidity. The environmental data is acquired in the laptop by interface software provided by the supplier of the combined sensor.

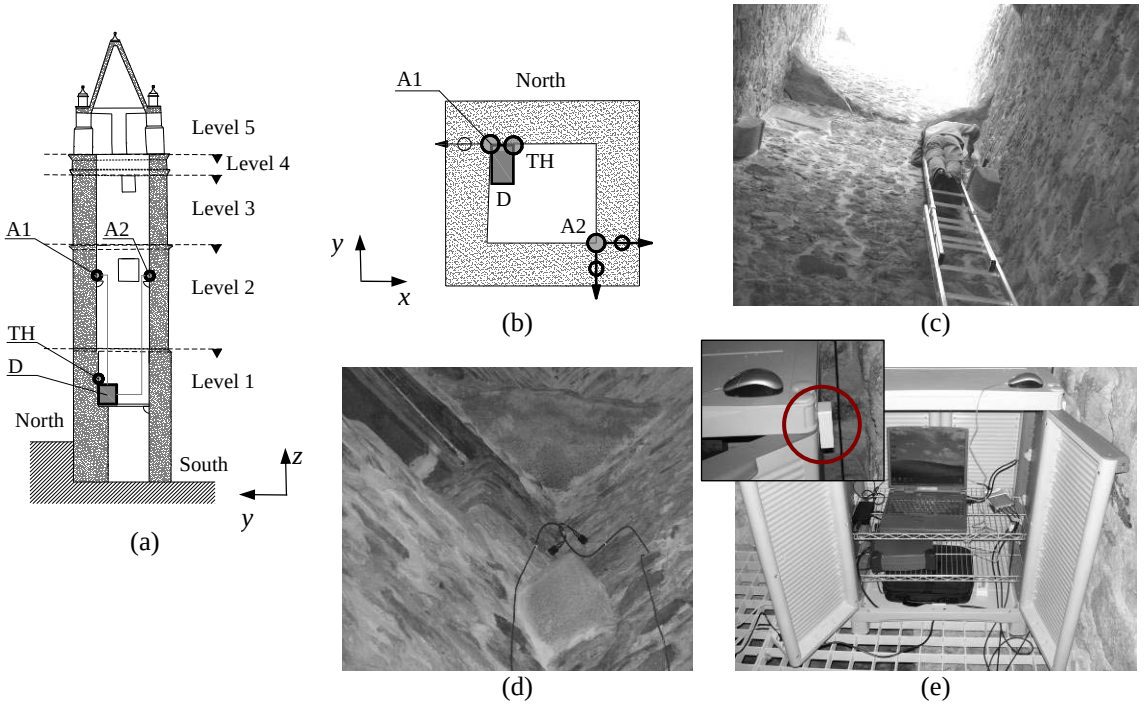
In the LabView (2006) software, a Virtual Instrument (VI) was especially developed for this purpose. The VI has the name of Logger and every hour acquires 10 minutes of ambient vibrations in the three channels with a sampling frequency of 100 Hz, without any triggering. The data is then saved in ASCII files with the general file name `Date_Time_EventNumber.txt`. The temperature and the relative air humidity are measured every hour and, after download the data, is saved in a single ASCII file. The front-end panel for the two systems is presented in Figure 7.16.



(a) (b)

Figure 7.16 – The acquisition software: (a) the front-end for accelerations; and (b) front-end for temperature and relative air humidity.

For convenience, the monitoring system was installed inside the tower, see Figure 7.17. Consequently, there is a difference between the outside and the inside temperature and relative air humidity values, although the tower is not totally closed and the wind can easily penetrate into the tower.



(a) (b) (c) (d) (e)

Figure 7.17 – Dynamic monitoring system: (a) measuring positions and the datalogger; (b) measured directions for accelerations; (c) installation of accelerometer at position A1; (d) accelerometers at position A2; and (e) datalogger (D) and environmental sensor (TH).

Two points (A1 and A2) were selected in the middle of Level 2 to acquire accelerations in three directions, see Figure 7.17a and b. In this way, all the mode shape components of the first five eigenfrequencies can be studied, including the torsion mode. The environmental measurements are acquired in the point TH, close to the datalogger (D).

The monitoring task has been performed in several campaigns (data series). Up to now, ten data series were record in the tower, from April 2006 to August 2007, leading to a full cycle of one year with about 5300 events, see Table 7.7. Because the system does not have a remote connection and the hard disc has only 60 Gigabytes space, it is necessary to, periodically, download the data to an external drive. Initially, it was planed to have one month per yearly season (four per year), but after the analysis of the first results it was decided to acquire as much data as possible to have continuum series of results.

Table 7.7 – Series of data from the monitoring system.

Data Series	From	To	Number of Events
I	12-Apr-06	12-May-06	600
II	21-Jul-06	14-Aug-06	575
III	09-Sep-06	02-Oct-06	600
IV	13-Oct-06	26-Oct-06	321
V	01-Dec-06	21-Dec-06	480
VI	21-Dec-06	15-Jan-07	600
VII	13-Feb-07	10-Mar-07	600
VIII	27-Mar-07	04-May-07	900
IX	22-May-07	24-May-07	54
X	18-Jul-07	07-Aug-07	622

7.3.5 Automatic Parameter Estimation

For modal estimation, an automatic procedure based on SSI/Ref method (Peeters and Roeck, 1999) was implemented in MatLab. However, the automatic procedure needs a preliminary manual estimation of a few numbers of events to better establish limit values for the automatic estimation.

In the manual identification, six to ten data files are selected to better analyze the modal results. A maximum state-space model order equal to 50 is fixed. This number corresponds to 25 structural vibration modes and is expected to exceed the true model order significantly. Although this parameter does not have a direct repercussion on the analysis results, selecting a relatively large number helps to visualize and to stabilised trends in the stabilisation diagrams (see Chapter 2 for details). Next, eigenfrequency intervals, damping intervals and a reference mode shape vector are established. Normally, the damping coefficient interval for all the modes was between 0.5 and 3%.

Finally, the automatic procedure is applied to all the events with the same range of model order. Afterwards and to avoid unreal modes, for every event file the selection of the correct model order in the stabilisation diagram is carried out by selecting the model that gives the frequencies and the damping values in the expected intervals, and gives the best MAC values (always greater than 0.95).

7.3.6 Environmental and Loading Effects

The study of the environmental and loading effects was initially based on the assumption that the modal response is changed by three independent variables: temperature, relative air humidity and the level of excitation. For the later and for every event, it was decided to use the average Root Mean Square (RMS) value of the three acceleration channels. The RMS is a useful quantity to measure the magnitude of a varying quantity x with a N number of values that can have positive and negative sign, such as waves, and is calculated as follows:

$$\text{RMS} = \sqrt{\frac{1}{N}\sum_{i=1}^{N} x_i^2} \tag{7.2}$$

The statistical results of the three variables are presented in Table 7.8. The average values for temperature, relative air humidity and RMS are about 14ºC, 67% and 0.021 mg, respectively. The standard deviation σ and the Coefficient of Variation (CV) is also presented, where the large variability is stressed, especially for the RMS as the CV value is about 90%. With respect to the extreme values, the minimum and maximum values are 1 and 32ºC for temperature, 10 and 100% for relative air humidity, and 0.005 mg and 0.25 mg for RMS.

Table 7.8 – Statistical results.

	Inputs			Outputs					
Results	Temperature [ºC]	Humidity [%]	RMS [mg]	ω_1 [Hz]	ξ_1 [%]	ω_2 [Hz]	ξ_2 [%]	ω_3 [Hz]	ξ_3 [%]
Average	14.37	67.62	0.0207	2.45	1.77	2.65	1.77	7.00	1.54
σ	6.73	21.99	0.0186	0.05	0.45	0.05	0.45	0.06	0.45
CV [%]	46.85	32.53	89.83	2.15	25.30	2.03	25.16	0.83	28.90
Maximum	32.34	99.90	0.2525	2.59	3.00	2.79	3.00	7.19	2.98
Minimum	0.77	10.15	0.0047	2.32	0.51	2.52	0.50	6.88	0.51

From this statistical analysis the low level of excitation during the whole monitoring period should be stressed. Unless there is wind blowing, the tower does not suffer regular and significant excitation from traffic or other human sources, since Mogadouro is a small populated town. During the night periods, it is difficult to estimate accurately the modal parameters due to the low signal to noise ratio, and it was only possible to estimate automatically a large number of events for the first three modes.

The statistical results of the estimated modal parameters are also presented in Table 7.8. In this case, the average for the three frequencies is about 2.45, 2.65 and 7.00 Hz, with the same order of variability, and with CV values between 1 and 2%. The average damping is about 1.77% for the two first coefficients and 1.54 for the third coefficient. For damping a higher variability was observed, as the CV value varyes from 25 to 29%.

The results from the automatic estimation are presented in detail in Annex D, together with the environmental and loading variables. Figure 7.18 presents, for the first mode shape, the variation of the frequency results with the environmental and loading conditions and the variation of the damping results with the temperature along the whole monitoring period. Observing the frequency versus temperature effect it is possible to visualize a positive relation between the variables and the annual cyclic effect, see Figure 7.18a.

For the humidity, when the values are around 100%, the temperature values are lower and also the frequency values, see Figure 7.18b. This corresponds to the raining season mainly in Autumn and Winter. Concerning the loading effect, see Figure 7.18c, it is not possible to observe any relation between the excitation level and the frequency values in this graph. Finally, damping values presents a large variability, between 1 and 3%, and do not exhibit a clear relation with the temperature.

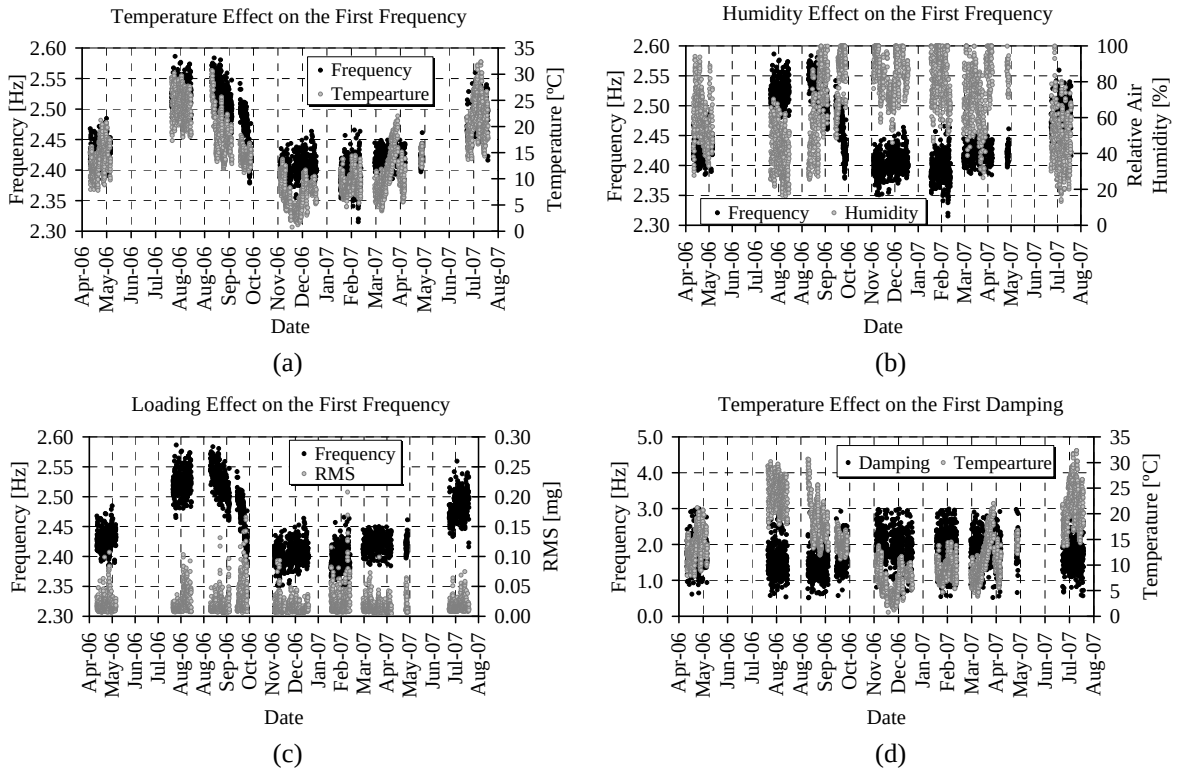


Figure 7.18 – Results for the first mode shape: (a) frequency and temperature varing; (b) frequency and humidity varing; (c) frequency and RMS varing; and (d) damping and temperature varing.

To better analyze the relation between the variables and the first frequency values, Figure 7.19, Figure 7.20, and Figure 7.21 present in detail the history of the ten data series for temperature, humidity and loading effects, respectively. In general, there is a positive relation between temperature and frequency, and a negative relation between humidity and frequency and between level of excitation and frequency. Concerning the temperature relation, from the first to the second series (from the Spring to the Summer, 2006) it is possible to observe a frequency shift from an average value of 2.4 Hz to an average value of 2.5 Hz, which corresponds to a significant shift of about 4% in frequency. In the first data series the temperature ranges from 8 to 21ºC and for the second series the temperature ranges from 17 to 30ºC. For the same data series, the relative air humidity ranges from 25 to 95% in the first series and from 15 to 70% in the second series. Although there is a range overlap in the two series, there is no linear transition. This indicates that another phenomenon was present and it was decided to acquire as much as possible a continuum data series to study this frequency shift.

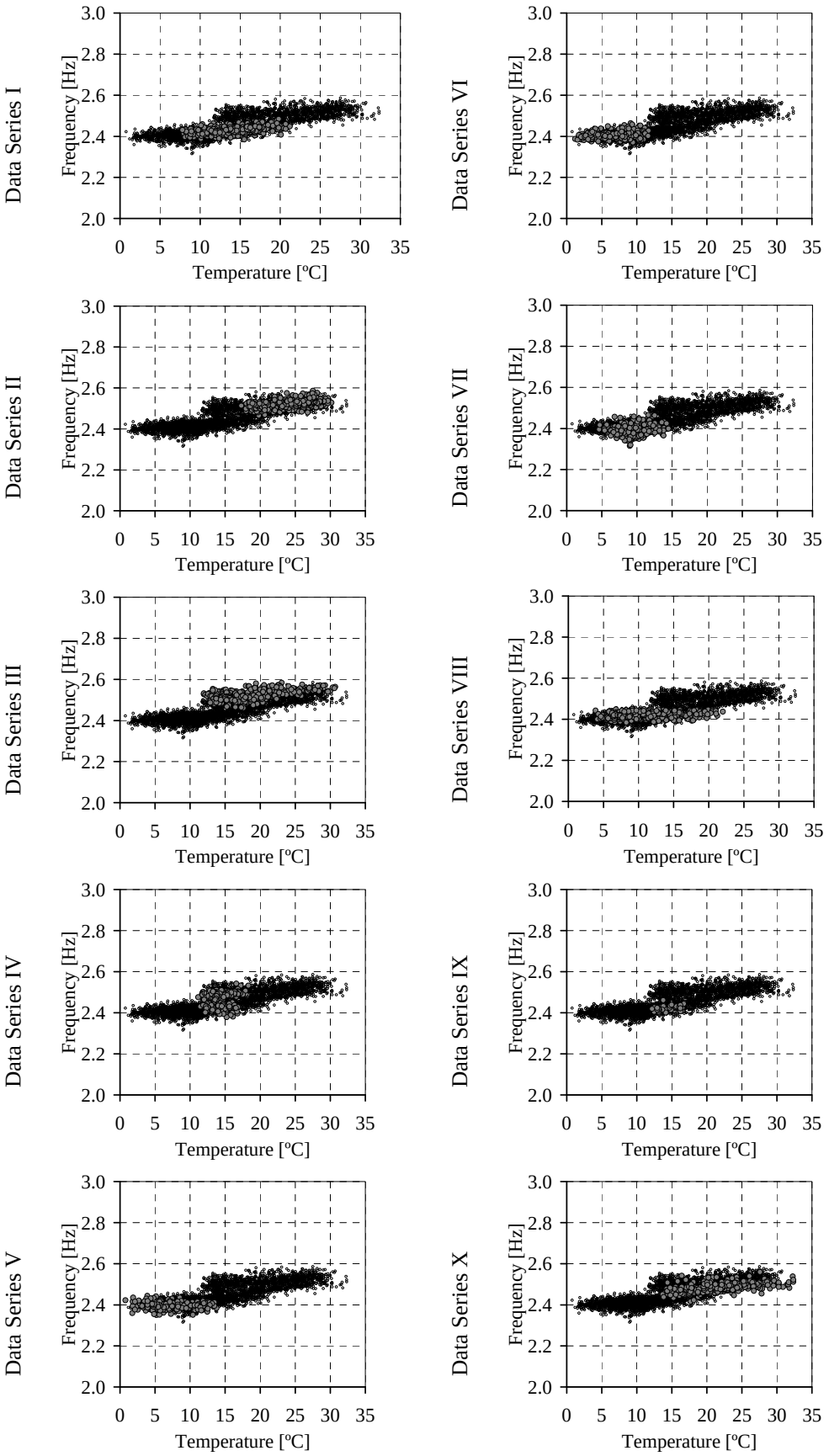


Figure 7.19 – Frequency versus tempearute through each data series (the corresponding data series is presented in grey dots, while the black dots include all data seies).

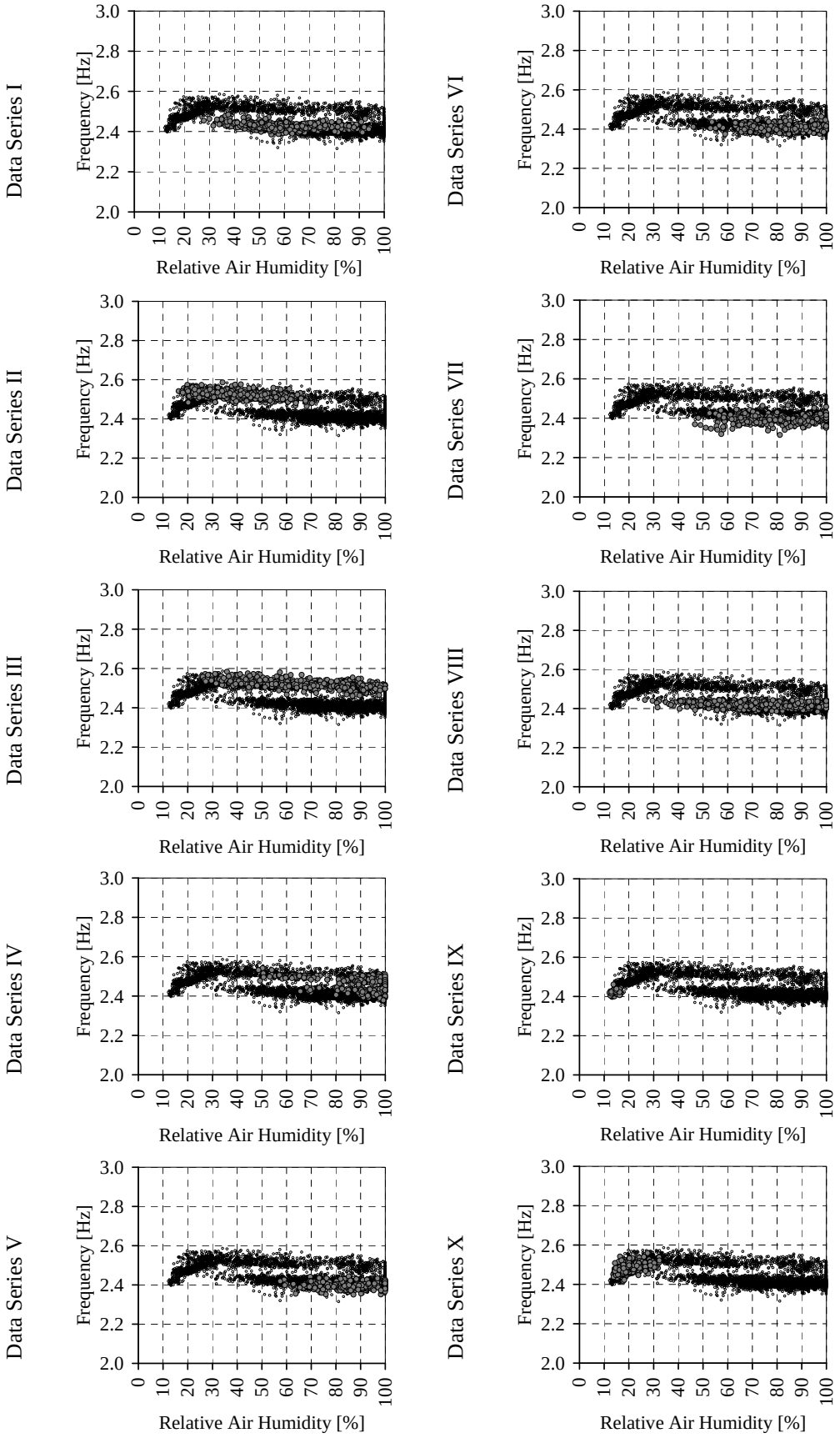


Figure 7.20 – Frequency versus humidity through each data series (the corresponding data series is presented in grey dots, while the black dots include all data seies).

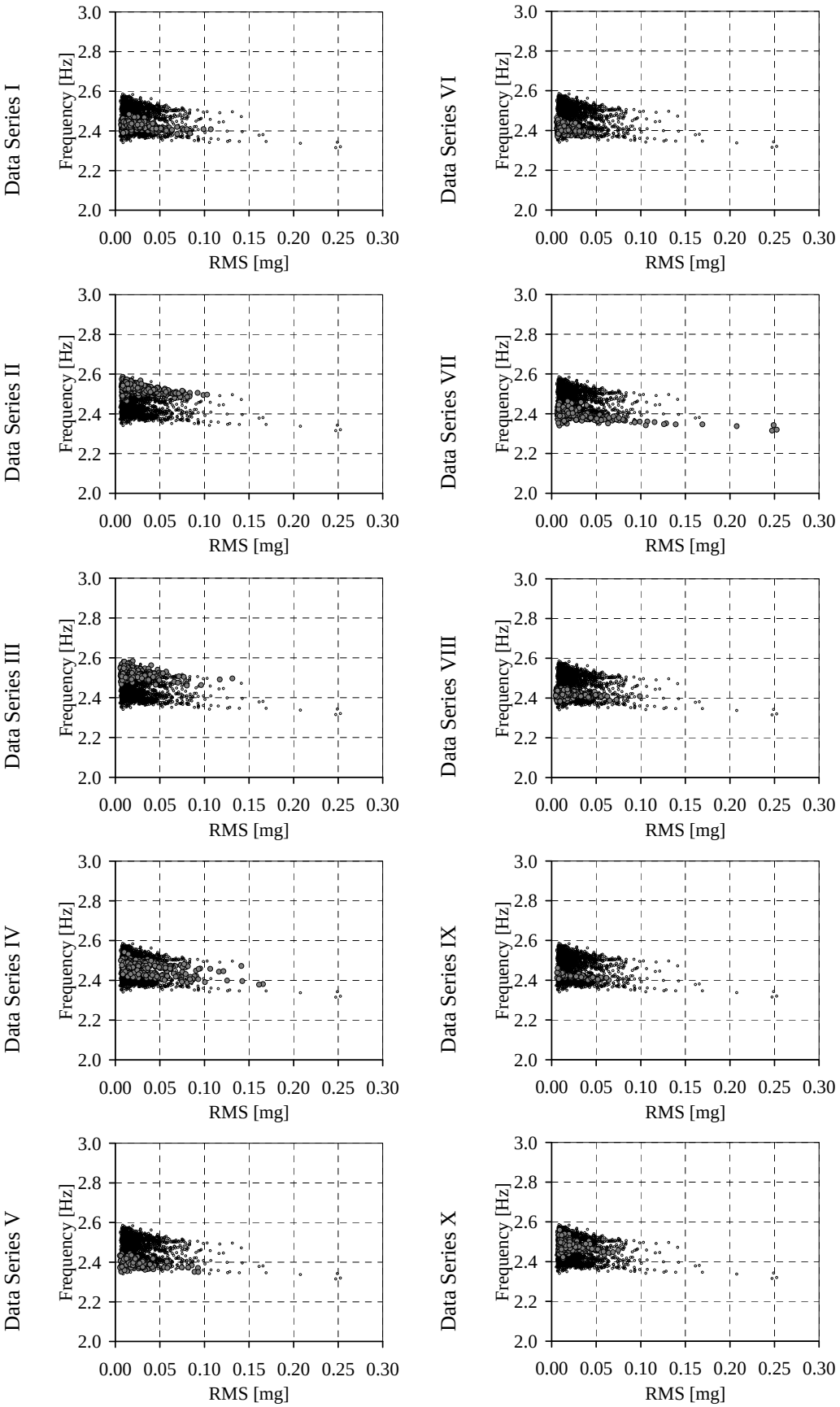


Figure 7.21 – Frequency versus excitation level through each data series (the corresponding data series is presented in grey dots, while the black dots include all data seies).

The initial frequency shift becomes clear in the Data Series IV (Autumn, 2006), where a negative frequency shift happened with the same order, see also Figure 7.22. In fact, during this series the temperature did not change significantly, while the relative air humidity after 18th of October is close to 100%, the first raining season on the site. After 22nd of October the frequency values decrease linearly with humidity almost constant. This indicates that the structure absorbs water and the mass changes, reducing the frequency values because the two quantities are inverse related. It can also occur that water leads to a stiffness reduction, at least in the lime mortars. The inverse phenomenon is observed in the last series (Summer, 2007), see Figure 7.19 and Figure 7.20.

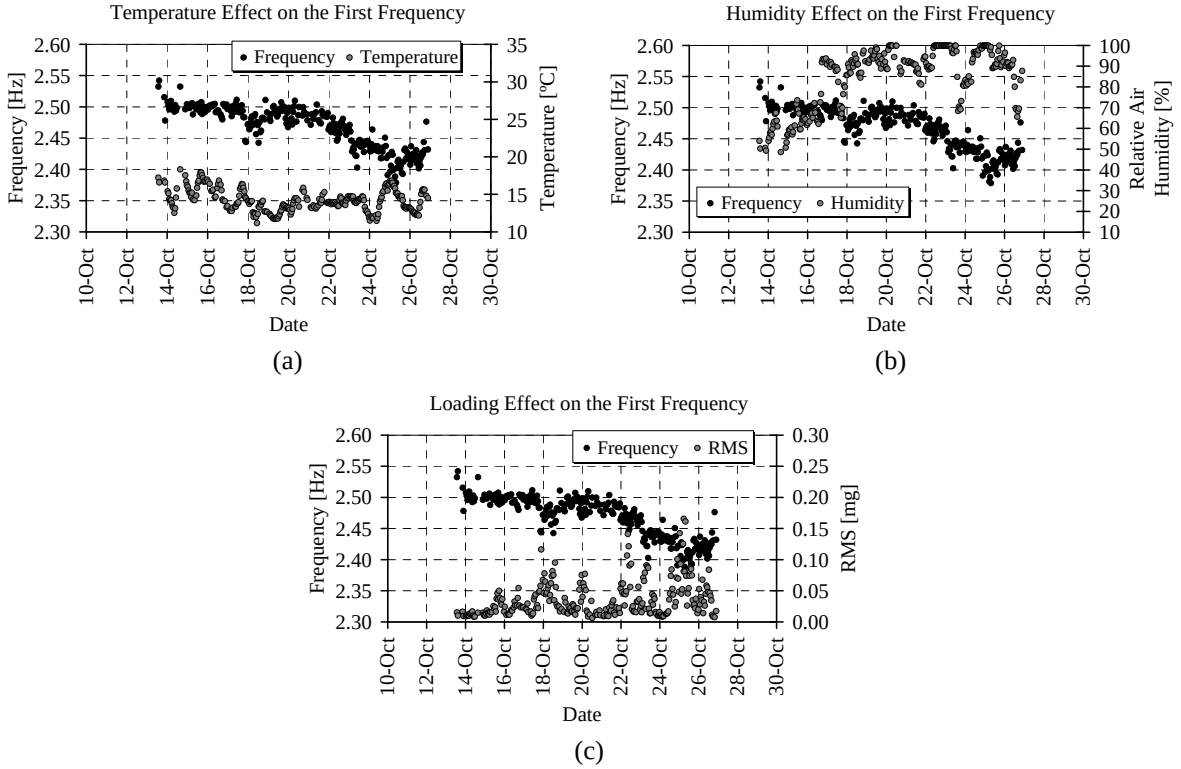


Figure 7.22 – Data Series IV (Autumn, 2006): (a) Frequency versus temperature; (b) Frequency versus humidity; and (c) Frequency versus level of excitation.

Figure 7.22c shows the instantaneously frequency decrease when the excitation level is high. With respect to this aspect, it should be stressed that a trend for a linear relation between these two quantities exists and can be observed in Figure 7.21. For RMS values higher than 0.05 mg the variance for the data decreases, indicating that the structure is well excited and the mode shapes are well estimated.

Concerning the other modes, similar conclusions apply, see Annex D, although the frequency shifts due to raining are not so evident for the third mode as they are for the first two modes.

As no damage was observed in the structure during the monitoring period, the main conclusion emerging from the results is not the larger structure sensitivity to the relative air humidity but to the rain. To monitor this phenomenon, humidity sensors should be placed inside the four façades, at different elevation levels. In order to better study the distribution of the humidity inside the walls, on each measuring point three sensors should be placed along the thickness of the walls, see Figure 7.23. Additionally, to evaluate the tower mass change due to rain, load cells or flat jacks test equipment can be also installed at the bottom of the walls in order to measure the changes in the compressive stresses.

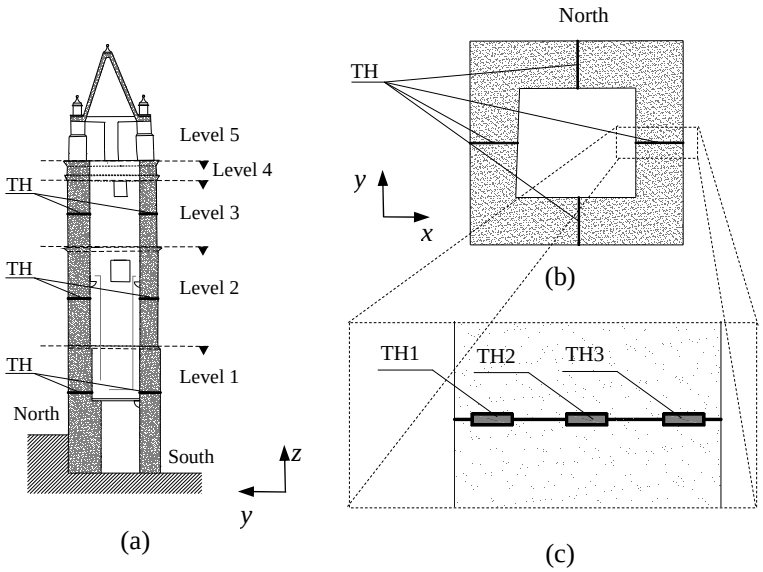


Figure 7.23 – Proposal for humidity sensors to measure water absorption: (a) measuring at three different levels; (b) measuring in the four façades; and (c) measuring along the wall thickness.

Since the environmental and the loading variables are changing the modal parameters of the tower, an attempt to model the dynamic response according to the three variables was carried out. It was decided to use a procedure similar to the one used by Peeters (2000) with AutoRegressive output with an eXogeneous input parts models (ARX models), already introduced in Chapter 2. Here, ARX models with multiple inputs and a single output (MISO models) were computed in MatLab (2006), function `arx`, to model each frequency value. The multivariable ARX model with n inputs u and one output y is presented by:

$$A_q \, \hat{y}_k = B_q \, u_{k-nk}^{env} + e_k \tag{7.3}$$

where A_q is a scalar with the delay operator q^{-1}, B_q is a matrix $1 \times n$, and e is the unknown residuals. For convenience, to model the response and to establish the confidence intervals the synthesis of the approach used by Peeters (2000), with the appropriated changes for the present case, is briefly reviewed:

1. Normalized inputs and outputs:

$$u_{k,Temp}^{env} = \frac{u_{k,1}^{env,m} - \overline{u}_1}{\sigma_{u,1}} \quad , \quad u_{k,RMS}^{env} = \frac{u_{k,2}^{env,m} - \overline{u}_2}{\sigma_{u,2}} \quad , \quad u_{k,Hum}^{env} = \frac{u_{k,3}^{env,m} - \overline{u}_3}{\sigma_{u,3}}$$
$$\text{and} \quad y_{k,\omega} = \frac{y_k^m - \overline{y}}{\sigma_y} \tag{7.4}$$

   where $u_{k,i}^{env,m}$ and y_k^m are the measured values, $\overline{u}_i$ and $\overline{y}$ are the average values and $\sigma_{u,i}$ and σ_y are the standard deviations;

2. Estimate ARX models (e.g. ARX[0,1,2,3,0,0,0]) and their statistical properties;

3. Select the "best" model based on quality criteria, like the loss function V, the Akaike's Final Prediction Error (*FPE*), see Ljung (1999), and the coefficient of determination $\hat{r}_{xy}^2$, given by:

$$V = \frac{1}{N}\sum_{k=1}^{N} e_k^2 \quad , \quad FPE = V\frac{1+d/N}{1-d/N}, \quad \text{and} \quad \hat{r}_{xy}^2 = \left(\frac{\hat{R}_{xy}}{\hat{\sigma}_x\,\hat{\sigma}_y}\right)^2 \tag{7.5}$$

where d is the number of estimated parameters and $\hat{R}_{xy}$ is the estimated covariance given by Eq.(2.72);

4. Simulate the expected response with the previous selected model;
5. Calculate the simulation error and its statistics;

$$\hat{e}_k = y_k - \hat{y}_k \quad \text{and} \quad \hat{R}_{xy} \tag{7.6}$$

6. Establish the confidence intervals *ci* and detect the outliers:

$$\left[\hat{y}_k - z(1-\alpha/2)\sqrt{\hat{R}_{xy}} \quad , \quad \hat{y}_k + z(1-\alpha/2)\sqrt{\hat{R}_{xy}}\right] \tag{7.7}$$

As the damping results present a high variability, the preceding approach was applied only for the frequency values and only for the events with RMS higher than 0.025 mg. In this way, only the best estimated results were used in the model, leading to lower variability. The best fitting ARX models are presented in Table 7.9, where they are compared with the multiple linear regression models (static models). The results with dynamic models for the two first mode shapes are better than the static models, since there is a significant reduction for the loss function V and the FPE, and there is a significant increase for the coefficient of determination r^2. For the third mode shape there is an improvement with the dynamic models, but not as significant as for the first two modes. Thus, for the case of the first two modes, the ARX models explains about 83% of the frequency variability, while for the third model it can only explain 31%.

Table 7.9 – Comparison between ARX and static regression MISO models (see Annex D for the model parameters).

Mode	ARX Model				Static Regression Model			
	n_a , n_b , n_k	V	FPE	r^2	n_a , n_b , n_k	V	FPE	r^2
1	3 , 2 2 4 , 0 0 0	0.043	0.044	0.837	0 , 1 1 1 , 0 0 0	0.318	0.320	0.682
2	4 , 1 2 4 , 0 0 0	0.065	0.066	0.819	0 , 1 1 1 , 0 0 0	0.345	0.347	0.655
3	5 , 2 3 5 , 0 0 0	0.459	0.485	0.309	0 , 1 1 1 , 0 0 0	0.717	0.725	0.282

Figure 7.24 shows the fitting models through the normalized frequency and simulated errors with the 95% confidence intervals *ci*. For the two first mode shapes is possible to observe the reasonable fitting of the ARX model. In general, the model represents the frequency variation, but does not takes into account the water absorption phenomenon, because the relative humidity variation does not totally represent that change. For the third mode the fitting is not so good, as the variability of the error is large. This might indicate that the third frequency (torsion mode) was not estimated accurately for all the events or its value is not sensitive to the three considered variables. Furthermore, for damage detection the first two dynamic models can be used and the damage is detected by frequency shifts that significantly go outside the confident intervals *ci*. To end, it should be stressed that the calibration period of one year might be not enough for having a tuned model. A longer period of, at least, three years should be used for calibration in order to have a reliable model for frequency prediction.

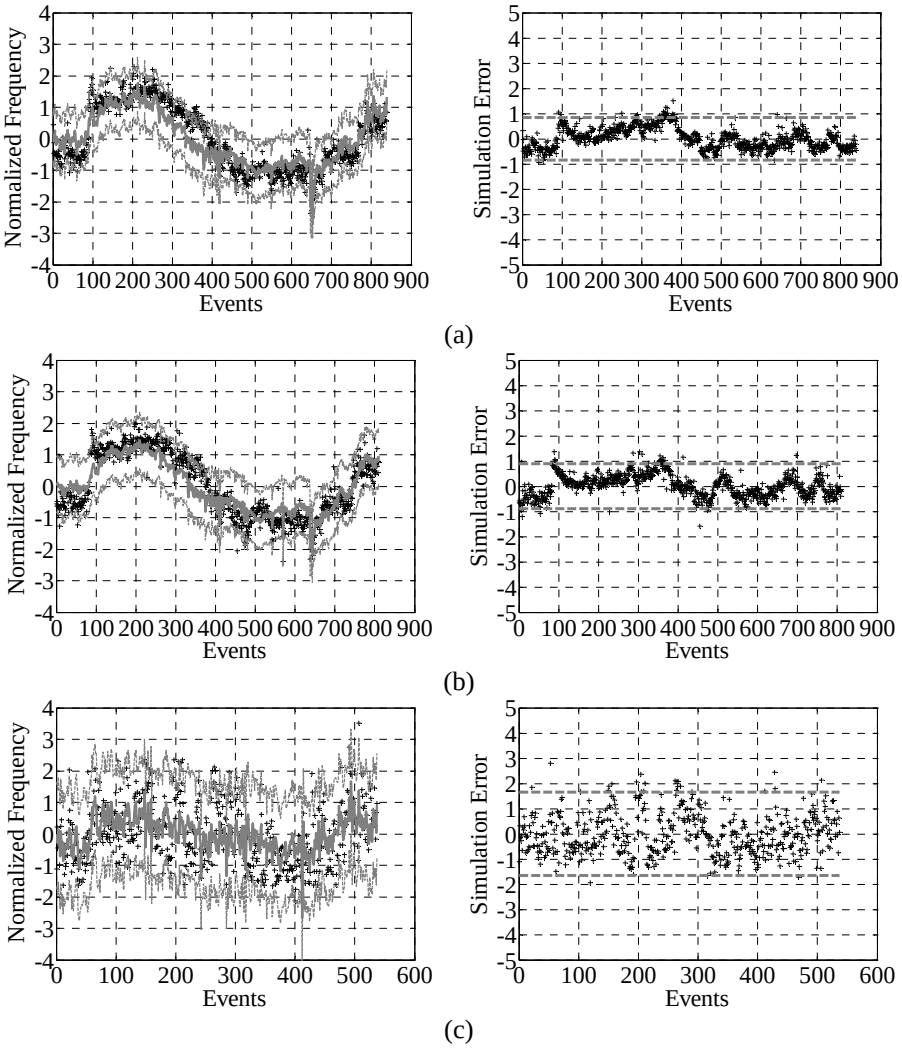


Figure 7.24 – ARX models: (a) mode shape 1; (b) mode shape 2; and (c) mode shape 3.

7.4 Case Study II: Church of Monastery of Jerónimos

The Monastery of Jerónimos, located in Lisbon, is one of the most famous Portuguese monuments, see Figure 7.25. The Monastery is, probably, the crown asset of Portuguese architectural heritage dating from the 16th century.



(a) (b)

Figure 7.25 – Monastery of Jerónimos: (a) General view of the Monastery of Jerónimos and the Empire Square; and (b) the outside view of the church.

The monumental compound has considerable dimensions in plan, more than 300×50 m^2, and an average height of 20 m (50 m in the towers). The monastery evolves around two courts.

The church of the Monastery, see Figure 7.26, was built in the Gothic style that was lately introduced in Portugal, incorporating a specific national influence. The so-called "Manueline" style (after King D. Manuel I), exhibits a large variety of architectural influences and erudite motives. An interesting aspect is that the vaults springs from one external wall to the other, supported in slender columns (see Figure 7.26a and b) that divide almost imperceptibly the naves. From the traditional art, only the proportions and roof remain, being the concepts of space and structure novel. The fusion of the naves in the present Church is more obvious than in other manifestations of spatial Gothic. For this purpose, arches are no longer visible, the slightly curved vault comprises a set of ribs and the fan columns reduce significantly the free span. Additional information about the church can be found in Genin (1995) and Genin (2001).

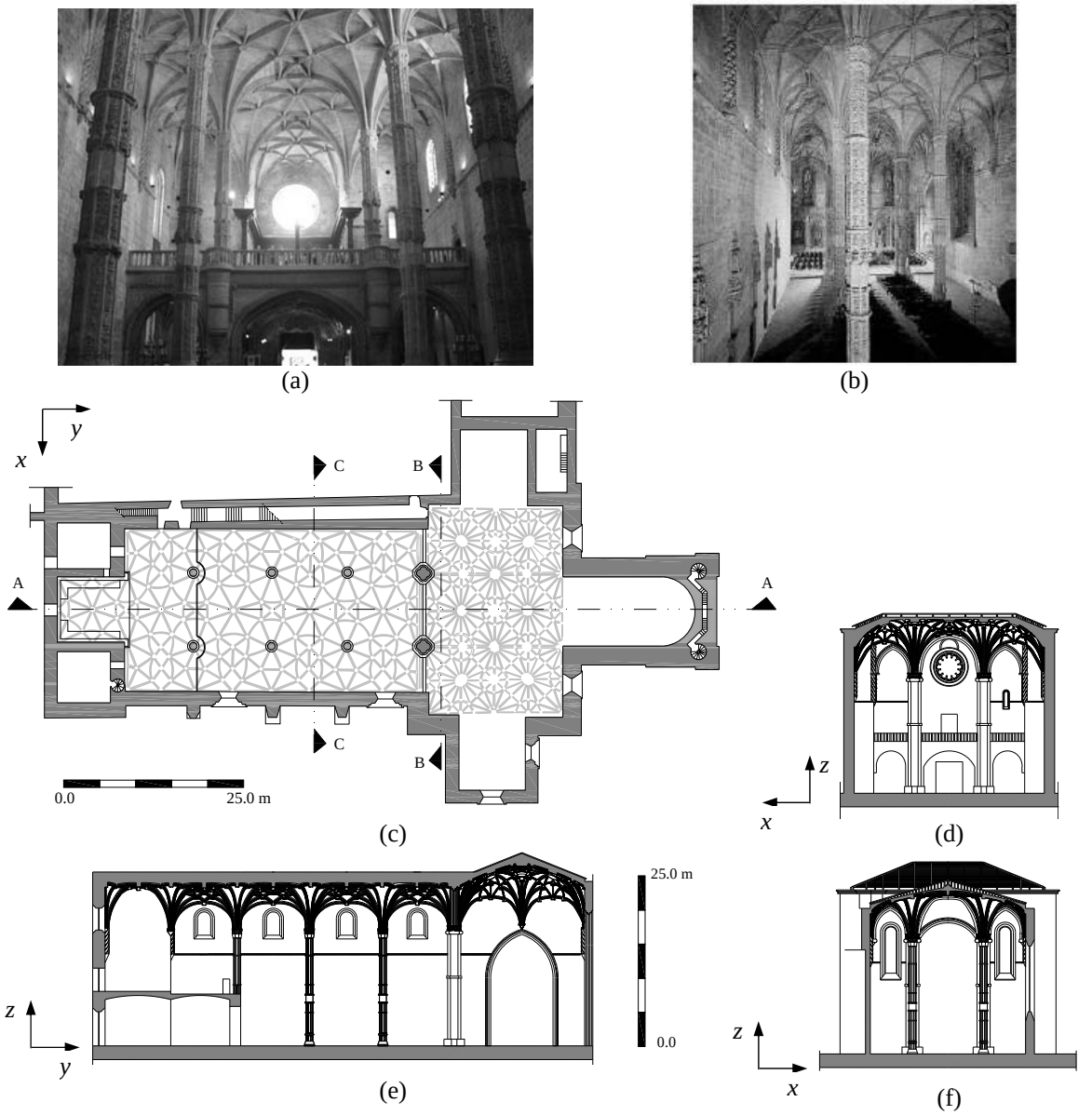


Figure 7.26 – Church of Monastery of Jerónimos: (a) inside view of the choir; (b) aspect of the three naves (c) plan; (d) section A-A; (e) section B-B; and (f) section C-C.

Several studies have been performed to understand the structural behavior of the church, through visual inspections, ND testing, and numerical simulation, see Mourão (2001), Mun (2002), Oliveira (2002), Lourenço and Krakowiak (2003), Oliveira et al. (2005), Lança (2006), and Lourenço et al. (2007). From the different analyses it was possible to conclude the following: (a) the possible collapse of the church nave occurs with a failure mechanism involving the columns and the vaults; (b) the possible collapse of the transept occurs with a failure mechanism involving the external walls and the vaults; (c) the compressive strength of masonry is a key factor for the structural response; and (d) the columns of the nave are too slender.

Apart from the above conclusions, it is stressed that the church has been in use for some hundred years with moderate damaged ribs, and moderate tilting of the columns and sidewalls. Given the cultural importance of the construction, the safety of the users, the seismic risk and the accumulation of physical, chemical and mechanical damage, complementary ND testing was proposed in the framework of the Asia-wide Programme "EU-India Economic Cross Cultural Programme" (EU-India, 2006). The activity includes an integrated plan of tests and the installation of monitoring systems, which involves the following tasks:

- Characterization of the seismic loads in accordance with the local soil conditions and foundations of the structure;
- Definition of experimental tests in situ and in the laboratory to better estimate the material properties (modulus of elasticity and compressive strength) of the columns, vaults and rubble material;
- Execution of sonic and radar tests to detect possible damage inside the columns;
- Detailed inspection for the columns and vaults with the aim to detect aspects potentially dangerous from the structural safety point of view;
- Execution of numerical models for the analysis of the entire structure of the nave under seismic loading, to be calibrated by the experimental tests;
- Execution of a dynamic modal identification analysis to calibrate the numerical models and to estimate the modulus of elasticity;
- Installation of two continuous monitoring systems for static and dynamic structural observation, for helping to understand the complex behavior of the structure and to detect any progressive movements or the presence of damage.

All the tasks above were implemented in the church and were fundamental for better understanding the structure and assess its safety. The tasks belong to the first and second phase of the approach presented in Section 7.2. In the following Sections, the tasks related to dynamic identification and monitoring will be discussed.

7.4.1 Modal Identification of the Main Nave

The first part of the church to be dynamically tested was the main nave where output-only modal identifications techniques were used to estimate the modal parameters: resonant frequencies, mode shapes and damping coefficients. Two techniques were applied to compare the experimental dynamic parameters obtained and have more accurate results. The Enhanced Frequency Domain Decomposition (EFDD) and the Stochastic Subspace Identification (SSI) method (see Chapter 2), both implemented in the software ARTeMIS

(SVS, 2006) where selected for results comparison. For the data acquisition, two clock synchronized strong motion recorders with two triaxial force balance accelerometers were used. The measurement equipment is the same used for the dynamic monitoring system and is presented later in more detail.

From a preliminary numerical model with a simplified three-dimensional beam element model built in SAP2000 (2005), see Figure 7.27, the first expected mode shape was governed by the local effect of the slender columns. The first expected frequency was around 1.37 Hz and the first ten modes were under 2 Hz, but during the preliminary measuring tests the energy peaks in the spectrums could only be observed for frequencies values between 3 and 20 Hz.

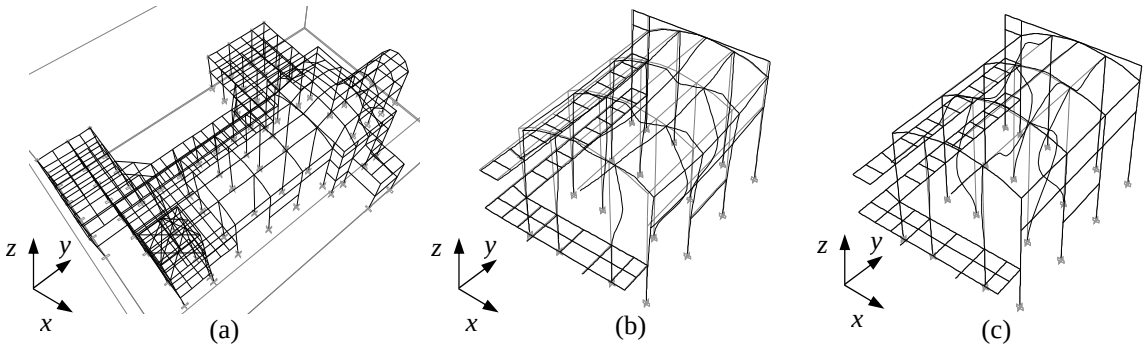


Figure 7.27 – Prelininary numerical model: (a) entire element mesh; (b) first mode shape at 1.37 Hz; and (c) second mode shape at 1.62 Hz.

According to the results of the numeric modal analysis, thirty points on the top of the main nave were selected to measure the acceleration response, see Figure 7.28. Ten points are located on the top of the external walls with the purpose to measure the nave boundaries and also the global dynamic response of the church. The other points are located either on the top of the columns or on the top of the vault keys. As sequential measuring tests (29 test setups) were necessary, with one reference and one moving sensor, a preliminary test campaign was carried out on the roof to assure a good selection of the reference point. From the first measurements, it could be concluded that point P1 was the one with more significant signal vibration amplitudes for all the frequency peaks. For every measured point and whenever possible, the roof tiles were removed and the sensor was placed directly on the top of the nave (extrados) to avoid any possible noise contamination from the roof structure, as can be observed in Figure 7.28b. Each data setup was recorded with a sampling frequency equal to 200 Hz and with a total sampling duration of 10 minutes. All the test setups were carried out in two days (20^{th} and 21^{st} of April, 2005) at an average ambient temperature of 18ºC.

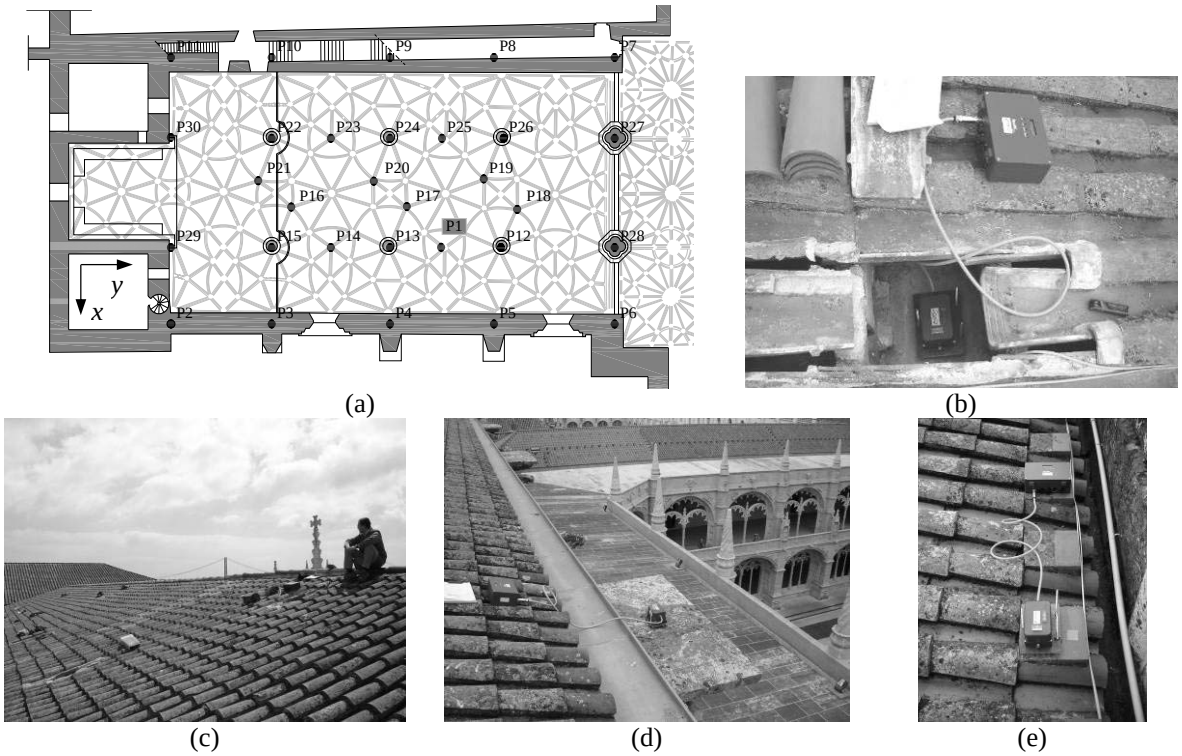


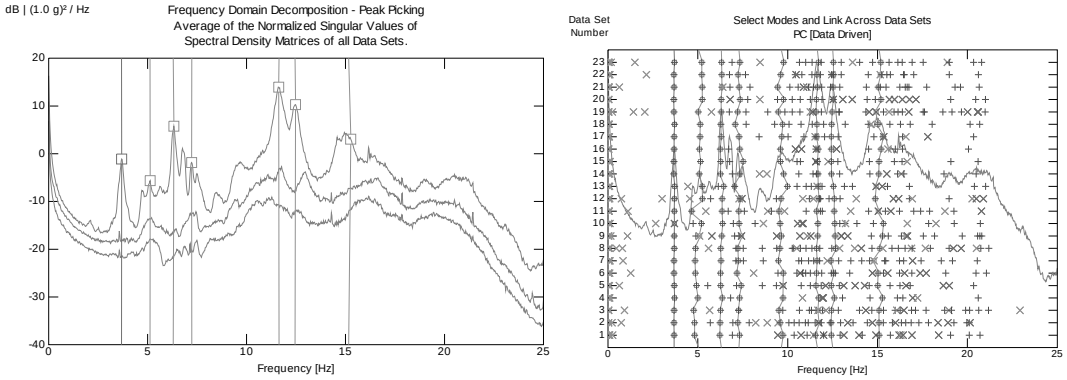
Figure 7.28 – Measurement points: (a) in plan location; (b) the reference transducer; and (c), (d) and (e) measurement at several points with the moving transducer.

Table 7.10 summarizes the eight estimated mode shapes through the two experimental output-only techniques, in terms of resonant frequencies, damping coefficients and Modal Assurance Criteria (MAC). In what concerns the resonant frequencies, the values range from 3.7 to 15.1 Hz and no significant differences could be found between the two methods. The same cannot be stated for the damping coefficients, where, on average, the differences are equal to 160%. The MAC values are discussed later in the text.

Table 7.10 – Comparison with the estimated modal parameters of the main nave.

Mode Shape	ω [Hz]		ξ [%]		MAC
	EFDD	SSI	EFDD	SSI	
Mode 1	3.69	3.68	2.34	1.26	0.99
Mode 2	5.12	5.04	1.11	2.68	0.92
Mode 3	6.29	6.30	1.00	0.82	0.67
Mode 4	7.23	7.29	0.77	1.44	0.67
Mode 5	9.67	9.65	1.10	1.45	0.62
Mode 6	11.64	11.65	1.20	1.46	0.36
Mode 7	12.45	12.51	1.25	1.19	0.71
Mode 8	14.99	15.09	1.31	2.77	0.49

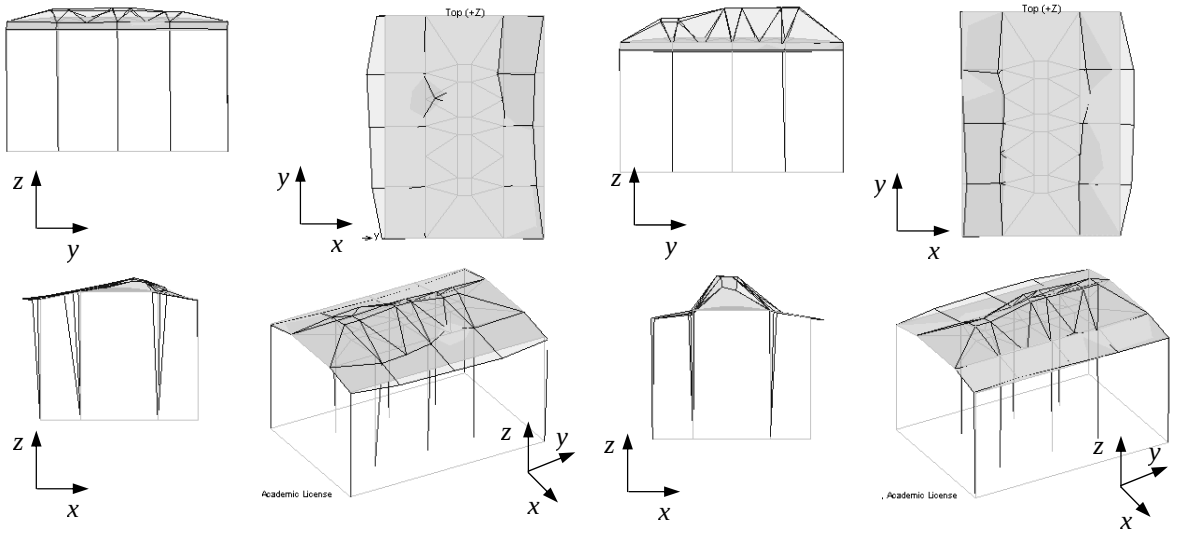
Figure 7.29a presents the average of the first three normalized singular values of the spectral density matrix of the EFDD method, where the eight resonant frequencies can be identified. Figure 7.29b presents the data driven diagram of all data setups for the SSI method. In this case, only the lower resonant frequencies are easy to find, but due to the need of a higher state dimension for the models estimation, a large number of stabilized poles appears, resulting in a complex diagram. This fact allows confirming the difficulties to estimate the higher modes of the nave by using ambient vibration measurements.



(a) (b)

Figure 7.29 – Estimation diagrams: (a) EFDD method; and (b) SSI method.

Figure 7.30 shows the mode shape configuration for the first two modes. As it was observed in the preliminary numeric analysis (see Figure 7.27), the dynamic response of the main nave is influenced by the dynamic response of the slender columns. The first mode shape is a global mode of the church, while the second is a local mode, governed by vertical components of the nave in its central part due to the slender columns. The mode configurations are essentially composed by components in *x* (north-south) and *z* (vertical) directions.



(a) (b)

Figure 7.30 – Experimental mode shape results from EFDD method: (a) first mode shape at 3.7 Hz; and (b) second mode shape at 5.1 Hz.

As referred above, Table 7.10 presents MAC values calculated for the eight mode shape vectors obtained from two modal techniques. Observing the table values, the two first mode shapes are highly correlated (values closed to one), but for the others the value decreases, to a minimum of 0.36. This fact is a result of the difficulties in the estimation of higher modes with ambient vibration measurements, as discussed previously.

Nevertheless, this modal identification seems to be acceptable if the structural complexity of the nave is taken into account. Even if the mode shape and damping coefficients estimation is not very accurate for the higher modes, the resonant frequencies were accurately estimated by the two experimental techniques.

7.4.2 Modal Identification of Two Columns of the Main Nave

As a second step on the dynamic identification of the church, two columns of the main nave were studied. For this case, an acquisition system with different accelerometer types was selected. Twelve uniaxial piezoelectric accelerometers with a bandwidth ranging from 0.15 to 1000 Hz (5%), a dynamic range of ±0.5 g, a sensitivity of 10 V/g, 8 μg of resolution and 210 g of weight were used. The accelerometers were connected by coaxial cables to a front-end data acquisition system with a 16 bit ADC, provided with anti-aliasing filters. The front-end was connected to a laptop by a USB cable.

The selected columns were the two slender columns C_1 and C_2, close to the transept, see Figure 7.31a and b. On each column, accelerations were measured in five levels. On each level, measurements were carried out in three directions in order to estimate not only the bending modes, but also the torsion modes. The setup of the tests is graphically presented in Figure 7.31c, where it is possible to observe the position of the sensors in two test setups. The measurements were taken with a sampling frequency of 100 Hz and the total sampling time was about 10 minutes.

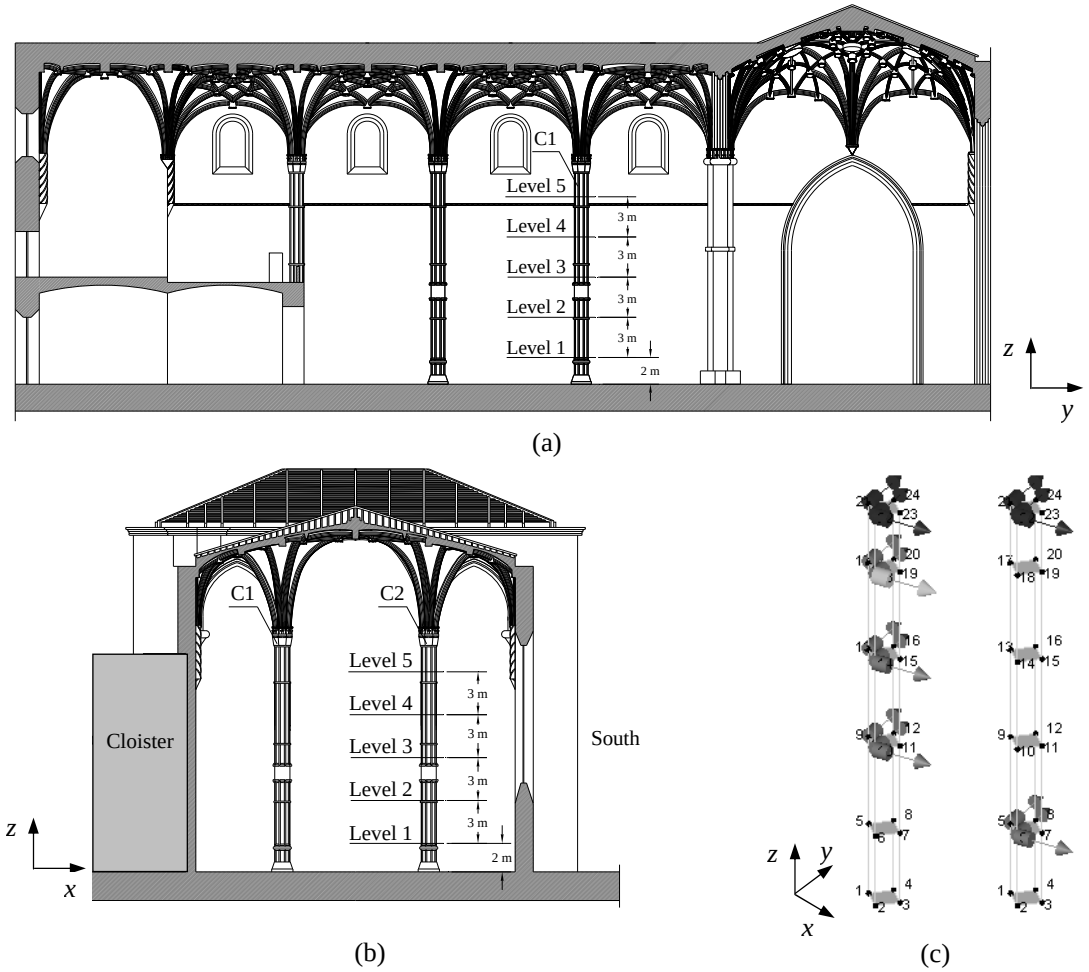


Figure 7.31 – Columns test planning: (a) and (b) location of the columns and the measuring levels; and (c) the two test setups (reference sensors in dark gray at the top).

To perform the tests, an elevation platform was used to access the upper part of the columns, see Figure 7.32a. The accelerometers were bolted to wood cubes fixed to the columns by a rope around the perimeter of the column, see Figure 7.32b. The rope was

provided with a system to attach firmly the cubes to the stones. The acquisition system was at the ground floor and between the columns, see Figure 7.32c. The tests were carried out in two days, one for each column, during 22nd and 23rd of November, 2005, with a stable temperature inside the church around 16ºC.



(a) (b) (c) (d)

Figure 7.32 – Columns dynamic tests: (a) setup1 in column C2; (b) biaxial accelerometer; (c) measuring system; and (d) excitation with impacts.

During the experimental tests difficulties were found to excite conveniently the columns. In the beginning, ambient vibrations were used to excite and then, to increase the signal-to-noise ratio, excitation with an impact hammer was used, see Figure 7.32d. Unfortunately, non of the approaches could lead to a good estimation.

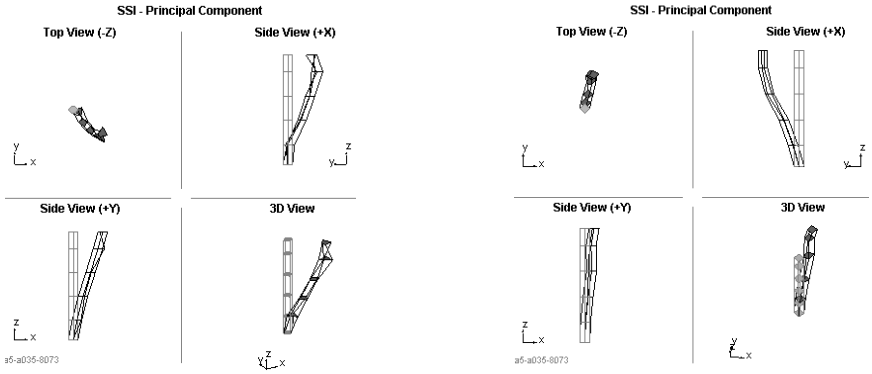
Table 7.11 shows the estimated frequency and damping values, with the respective standard deviations. Some of the global frequencies estimated in the nave are present in the table, but many local modes were identified. In the column C1 five modes could be identified, and in the column C2 nine modes could be identified. It should be stressed that column C1 is the one with highest stiffness constraints, as the column is closer to the monastery cloister, which increases the stiffness of the structure in that area, compared with the South wall, close to column C2.

Table 7.11 – Comparison between the results from the two columns.

Mode	Frequency				Damping			
	Column C1		Column C2		Column C1		Column C2	
	ω [Hz]	σ_ω [Hz]	ω [Hz]	σ_ω [Hz]	ξ [Hz]	σ_ξ [Hz]	ξ [Hz]	σ_ξ [Hz]
Mode 1	–	–	3.80	0.21	–	–	4.83	0.10
Mode 2	–	–	6.28	0.01	–	–	2.29	2.33
Mode 3	7.12	0.01	7.24	0.03	4.00	0.06	0.67	0.52
Mode 4	7.52	0.08	7.36	0.02	5.01	0.42	1.49	0.18
Mode 5	–	–	8.39	0.04	–	–	2.04	0.30
Mode 6	–	–	10.77	0.15	–	–	1.38	0.79
Mode 7	11.40	0.25	11.67	0.07	2.28	2.83	1.75	0.98
Mode 8	12.38	0.08	12.44	0.12	3.81	0.26	2.75	2.30
Mode 9	–	–	14.04	0.01	–	–	1.27	0.34
Mode 10	16.20	0.22	–	–	4.61	0.34	–	–

Concerning the mode shapes, differences were found between modes with close frequency values, as can be seen in Figure 7.33 for the case of the frequency close to 7.2 Hz. The fact that there are non coincident values in the frequency of the two columns and the fact that there are modes in the columns that do not appear in the nave might indicate that the slender columns can have an independent local behavior from each other

and also an independent behavior from the nave, which makes the structure rather complex to analyze.

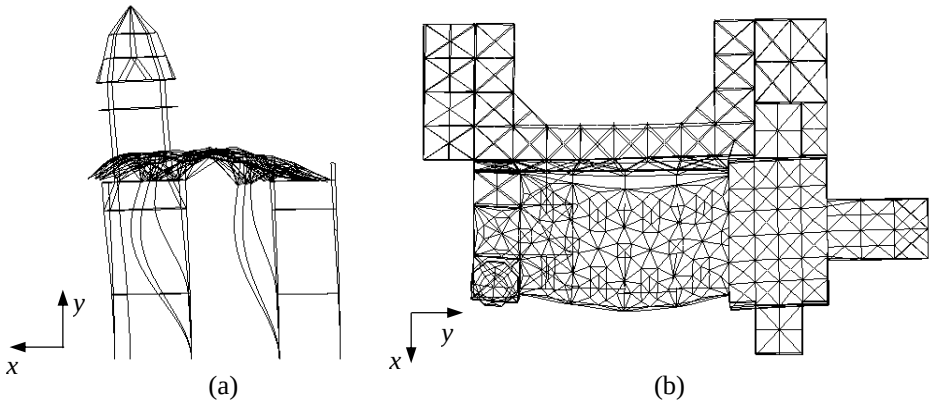


Mode 1 – 7.121 Hz (b) Mode 3 – 7.242 Hz (a)

Figure 7.33 – Columns mode shape comparison: (a) column C1; and (b) column C2.

7.4.3 Structural Assessment

Due to the complexity of the structure and the difficulties in the modal estimation analysis, a simplified beam FE model built in DIANA (2006) FE package was manually tuned to the dynamic experimental results. The updating parameters were the modulus of elasticity of the columns, the modulus of elasticity of the main nave and the boundary conditions of the columns. The dynamic response is mostly governed by the slender columns, as many local modes appear in the results. The first mode shape of the numerical model is presented in Figure 7.34. Table 7.12 shows the first eight frequencies after tuning for the first frequency. The results obtained for the modulus of elasticity were 30 GPa for the columns and 12 GPa for the masonry. The columns were finally considered as full constrained. The high value for modulus of elasticity of the columns can be explained by the high compressive stresses that are present due to the small cross section and by the fact that the columns are made of solid stone blocks. It is noted that the value of the modulus of elasticity of the masonry is also rather high and no clear explanation can be found.



(a) (b)

Figure 7.34 – First mode numerical mode shape at 3.79 Hz.

Table 7.12 also presents the comparison between the numerical and the experimental frequencies, together with some comments. Considering the complexity of the structure, the results seem acceptable. The tuned FE model was further used for a dynamic seismic analysis to assess the safety condition of the church, Roque (2007).

Table 7.12 – Comparison between the results from the two columns.

Modes	Experimental		Numerical	
	ω [Hz]	Comment	ω [Hz]	Comment
1	3.68	Main nave (*x*)	3.79	Main nave (*x*)
2	5.04	Main nave (*x*)	5.06	Tower (*x*)
3	–	–	5.20	Tower (*y*)
4	–	–	5.34	Columns and main nave (*x*)
5	–	–	5.76	
6	–	–	6.13	
7	6.28	Column C2 (*y*)	6.23	Columns and main nave (*y*)
8	6.30	Main nave (*y*)	6.32	

7.4.4 Monitoring Systems

Regarding the results from the preliminary investigations, two monitoring systems, static and dynamic, were installed in the main nave of the church with the following purposes: (a) to better understand the structural behavior of the complex construction; (b) to identify any progressive phenomenon; (c) to detect damage at an early stage; (d) to calibrate the boundary constraints and the modulus of elasticity of numerical models, which take into account the environmental effects; and (e) to be useful for possible future structural strengthening improvements and health monitoring programs.

The monitoring systems are long term installations with continuum data records and seasonal reports. The type and location of the sensors and cables was studied in order to minimize the visual impact in the interior of the church, in close cooperation with IGESPAR former IPPAR, Portuguese Authority for the Architectural Heritage, the responsible institution for the monument. It is stressed that because of the limited budget, the number of sensors installed is low, even if the monitoring systems are prepared for possible future sensors increase.

Due to the different technical characteristics and sampling rates of the data acquisition, the dynamic monitoring system is physically separated from the static monitoring system. Next, a description of the two systems is presented.

7.4.4.1 Static Monitoring System

The static monitoring system aims at measuring deformations of two columns in the main nave, ambient and surface temperature, relative air humidity and wind velocity and direction. The measurement system is focused on the columns structural observation because, as concluded in the preliminary studies, Lourenço and Krakowiak (2003), these elements are essential for the nave structural behavior.

The static monitoring system, see Figure 7.35, is composed by:

- Six temperature sensors (TS1 to TS6), with a measurement range from –20 to +100ºC and measurement resolution of 0.2ºC. Four sensors were installed in the North and South walls and two sensors were installed on the top of the columns and in the nave extrados, see Figure 7.35c;
- Two uniaxial tilt meters (TL1 and TL2), with a measurement range of ±1.5º and a resolution of 0.03º. The two tilt meters were installed on the top of the columns with larger vertical out-of-plumbness (see Figure 7.35d) and in the

extrados of the nave. The measurement orientation is the transverse direction of the nave (*y* direction), see Figure 7.35;

- One combined sensor to measure temperature and relative air humidity (TH). The temperature range is from –20 to +70ºC, with a resolution of 0.2ºC, and the relative air humidity range is from 0 to 100%, with a resolution of 2%;
- One ultrasonic 2D anemometer (W) to measure the wind velocity and direction, with an operating temperature between –35° to +70°C, and operating humidity between 5% and 100%, a wind velocity range between 0 and 60 m/s, with a resolution of 0.01 m/s, and a wind direction range of 360º, with a resolution of 1º;
- One datalogger (D) for the data acquisition and data record, with a Global System for Mobile (GSM) communication device, which allows data remote downloading by phone line. The data logger is located inside an ambient protection box in the bell tower, see Figure 7.35e.

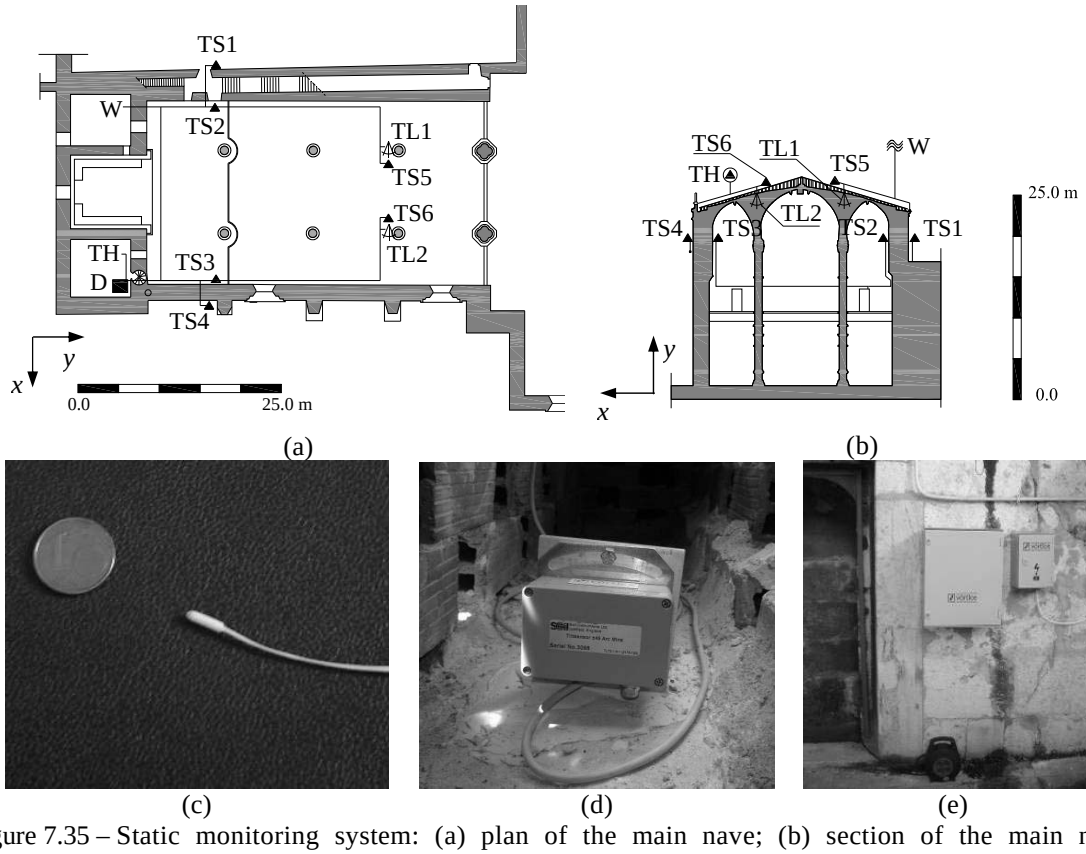


Figure 7.35 – Static monitoring system: (a) plan of the main nave; (b) section of the main nave; (c) temperature sensor; (d) tiltmeter sensor; and (e) datalogger.

It was decided not to include any crackmeter in the static system because cracks could not be observed in the vaults. However, it is important to carry out and extensive survey to evaluate the state of conservation/deterioration of the vaults joints due to recurrent fall of mortar and stone pieces from the nave vault. A visual inspection with an elevation platform able to reach the vault is being planned to evaluate the state of conservation of the nave. Afterwards, crackmeters can be possibly added to the monitoring system, if necessary.

The sampling rate of the static system is one sample per hour. This rate is considered sufficient to observe the temperature variation during one day cycles. The temperature sensors are distributed in the structure to evaluate the effect of the temperature gradient in

the response of the structure. The main static system is in operation since October, 2005. The combined sensor of temperature and relative air humidity and the wind velocity and direction sensor were installed later, on April, 2007.

7.4.4.2 Dynamic Monitoring System

The dynamic system is in operation since April, 2005. The system is composed by two strong motions recorders with 16 bits ADC analyzers provided with batteries. One triaxial force balance accelerometer is connected to each recorder by cable. The accelerometers have a bandwidth form DC to 100 Hz, a dynamic range ±1 g, a sensitivity of 10 V/g and an operating temperature range from –20 to 70ºC. The two devices connected (sensor and analyzer) give a final resolution of 8 μg.

Two points were selected to install the sensors (see Figure 7.36): one sensor (A1) was installed on the base of the structure near the chancel, and the other sensor (A2) on the top of the nave and in the extrados, in the same location of point P1 of the modal identification analysis of the nave. The sampling frequency is equal to 100 Hz.

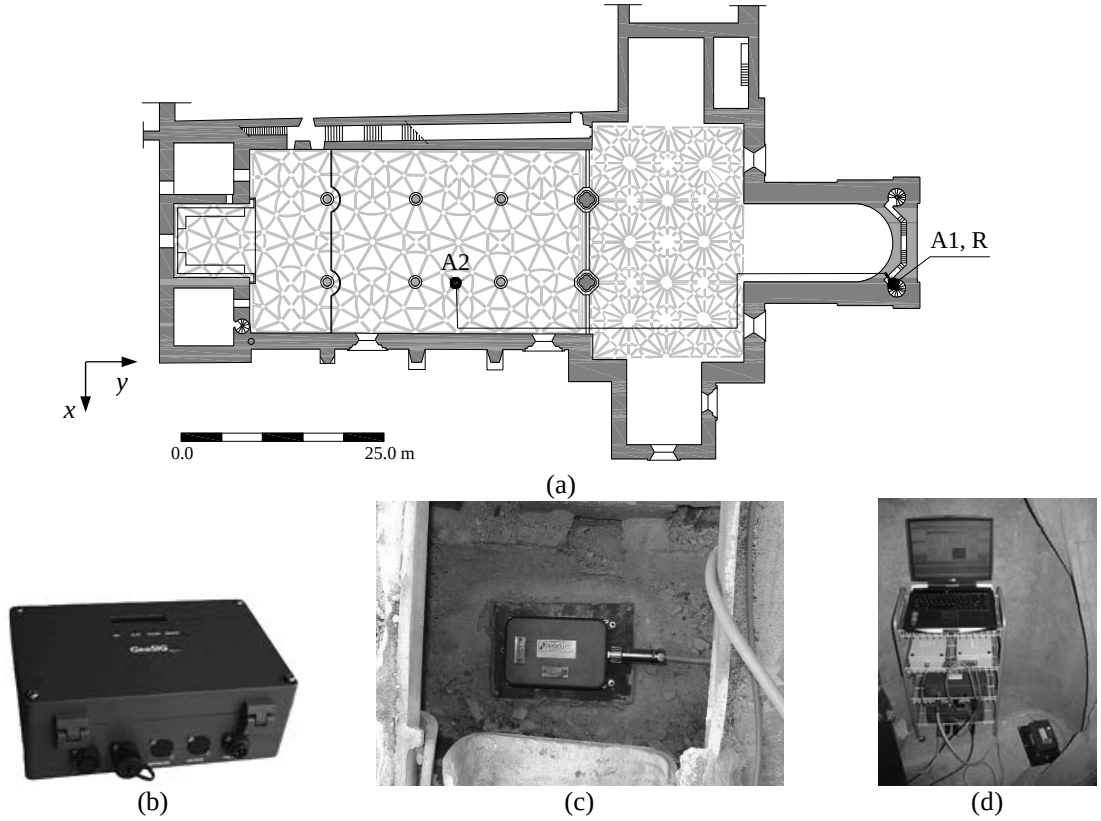


Figure 7.36 – Dynamic monitoring system: (a) location of the sensors; (b) strong motion recorder; (c) accelerometer on the main nave, and (d) battery of recorders and the base accelerometer.

The two recorders (R) were installed near sensor A1, see Figure 7.36a and d. They are connected by an enhanced interconnection network, which allows a common trigger and time programmed records. Each recorder works independently and the data are stored locally. The recorder connected to sensor A1 is the master recorder and enables the synchronization and updates the internal clock of the slave recorder, which in this case is the recorder connected to sensor A2. If, in the future more recorders are added to the system, the same network can be extended to the new apparatus. There is also the possibility to connect the network recorders to a Global Position System (GPS) for clock synchronization and also to connect to a phone modem for data transfer. This solution was

not adopted, because the amount of information in the data files is too large, which would increase significantly the costs and the maintenance of the system.

The actual number of sensors installed in the church is not enough to monitor the dynamic behavior of the church by mode shape changes. So, during a first phase and until further sensor upgrade, the dynamic monitoring system was carried out by in terms of resonant frequencies with the following schedule:

- The recorders are activated for low accelerations levels, which means that when a micro tremor occurs on the site (or strong winds) the dynamic response of the two points is measured;
- Every month, a record of 10 minutes is performed in the two recorders in order to detect frequency shifts. This allows to separate the influence of environmental conditions and to compare through time the consecutive dynamic responses before and after the occurrence of significant events;
- Seasonally, 10 minutes records in every hour and during one complete day are performed to observe, again, the influence of environmental conditions in the dynamic response of the church.

7.4.5 Environmental Effects on the Static Behaviour

Concerning the environmental effects on the static response, Figure 7.37 shows the variation of the rotations for the two columns the time and the correlation between temperature and the rotations. A clear influence of the temperature on the static response was found. Here, only the temperature effect is presented because there is no sufficient data to correlate with others environmental effects, like the relative air humidity and the wind velocity and direction.

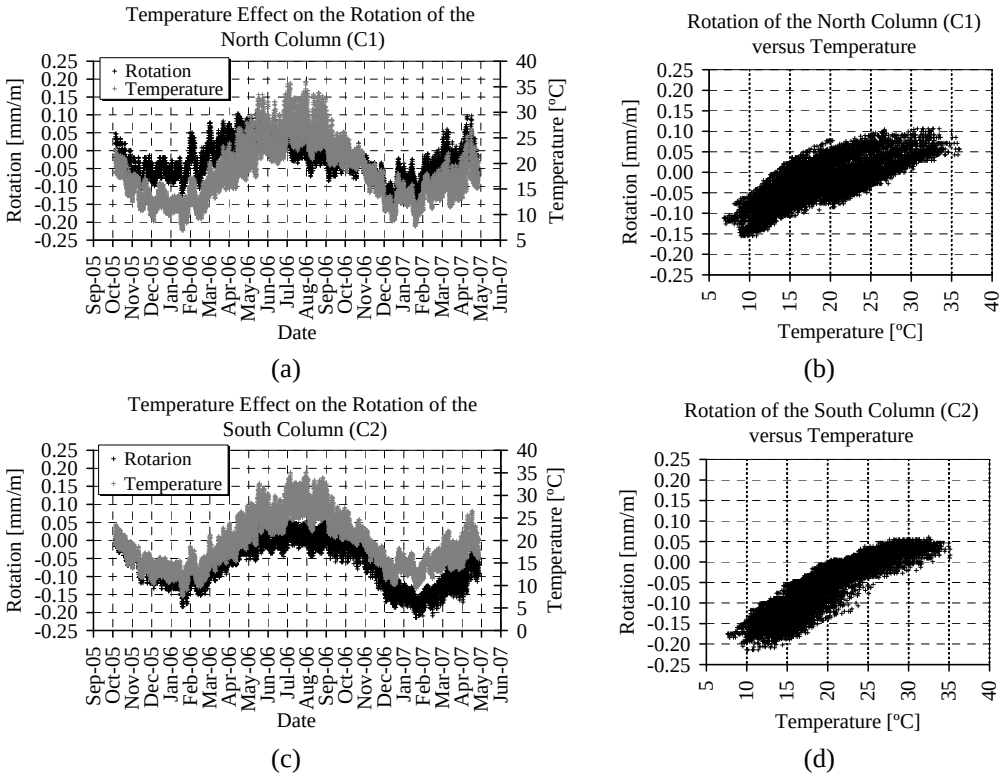


Figure 7.37 – Environmental effects on the static response: (a) and (b) for the North column (C1); and (c) and (d) for the South column (C2).

Since almost two cycles of one year were recorded, a dynamic ARX model and a static regression were calculated for the first year of monitoring. The results from the two analyses were compared in terms of efficiency and a simulation for the second year of monitoring was carried out and compared with the monitoring data, towards the evaluation of the model and the detection of unstable phenomenon.

Table 7.13 shows the parameters of the computed models for the two columns, together with the loss function V, the FPE and the coefficient of determination r^2. For the two columns, the ARX model gave better results as the statistical parameters V and FPE decreased for columns C1 and the coefficient of determination increased for the two columns.

Table 7.13 – Comparison between ARX and static regression SISO models (see Annex D for the model parameters).

Column	Model	n_a , n_b , n_k	V	FPE	r^2
C1	Static Regression Model	0 , 1 , 0	0.470	0.470	0.530
	ARX Model	1 , 4 , 0	0.013	0.013	0.585
C2	Static Regression Model	0 , 1 , 0	0.012	0.012	0.888
	ARX Model	3 , 3 , 3	0.012	0.012	0.921

Figure 7.38a and c compares the monitoring results with the results of the ARX models for the two columns. The ARX model for the column C2 seems to be the one with better correlation because the 95% confidence intervals in the simulation errors are lower, see Figure 7.38b and d. The reason might be related with the presence of more noise in the monitoring results of column C1.

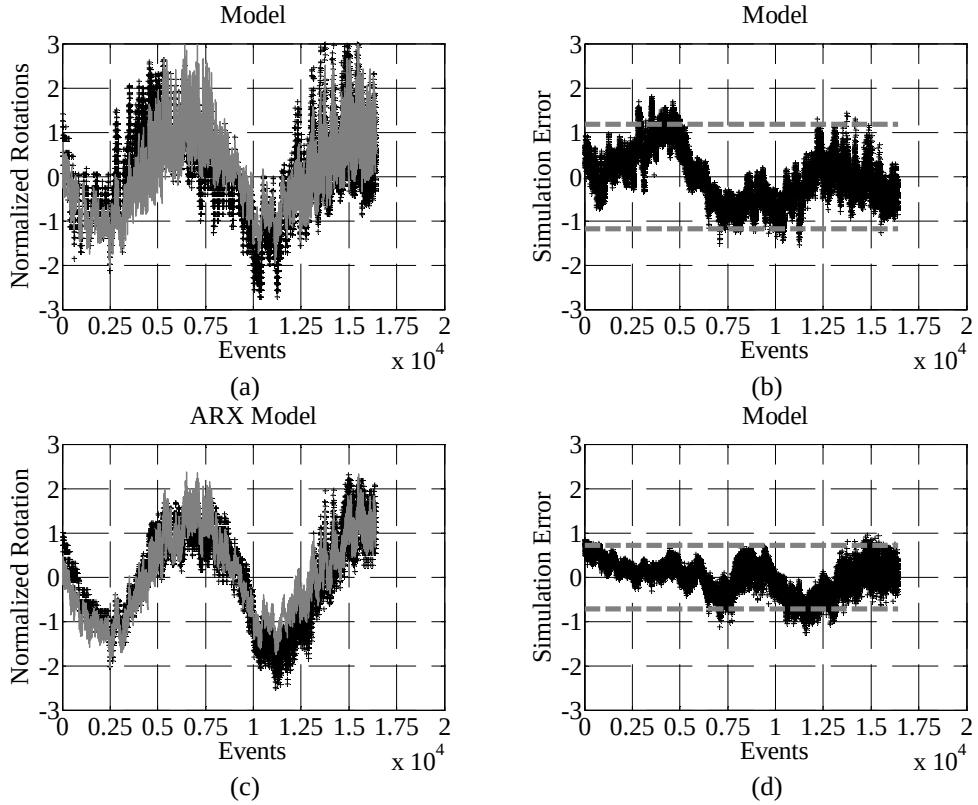


Figure 7.38 – ARX models for the columns: (a) ARX [1,4,0] model for the column C1; (b) the simulation error for the column C1; (c) ARX [3,3,3] model for the column C2, and (d) the simulation error for the column C2.

As introduced before, the ARX models were calibrated for half of the monitoring data. The comparison with the monitoring results with the simulated ones shows a good correlation, as no significant change occurred in the static response of the columns and the simulation errors are still inside the initial confident intervals.

7.4.6 Environmental and Loading Effects on the Dynamic Behaviour

For the study of the environmental and loading effects all data acquired in the strong motion recorders were used. Up to now, 1300 events were acquired: 28% of which corresponds to programmed events with 10 minutes of total sampling duration, and 72% correspond to triggered events, with an average sampling duration of 1 minute and 15 seconds.

To estimate the modal parameters, the procedure described previously for the Mogadouro Clock Tower was carried out. It should be stressed that in the modal parameter estimation only the first, the third and the fourth mode shapes of the nave were successful estimated. The majority of the triggered events occurred during working hours, due to the road traffic, special events inside the church (like mass or concerts), and minor earthquakes. With respect to programmed events, it is noted that it was more difficult to estimate the modal parameters during the night period, due to the low ambient excitation level.

To study the environmental and loading effects only the temperature and the RMS of the signals were taken into account, as there is no sufficient information for the others variables (humidity and wind). The statistical results for the temperature, the RMS and the estimated frequencies and damping coefficients are presented in Table 7.14. The average values for temperature and RMS is about 16ºC and 14 μg, respectively. High variability was observed in these two quantities, as can be seen through the standard deviation σ and the CV. In terms of extreme values, the minimum and maximum values are 7 and 34ºC for temperature (inside the roof of the church and under the tiles), and 8 μg and 761 μg for RMS.

Table 7.14 – Statistical results.

Results	Inputs		Outputs					
	Temperature [ºC]	RMS [μg]	ω_1 [Hz]	ξ_1 [%]	ω_3 [Hz]	ξ_3 [%]	ω_4 [Hz]	ξ_4 [%]
Average	15.64	14.41	3.74	2.19	6.37	1.45	7.24	1.38
σ	4.96	22.72	0.08	0.76	0.16	0.75	0.10	0.72
CV [%]	31.73	157.63	2.08	34.58	2.57	52.08	0.01	0.53
Maximum	34.39	761.29	4.08	3.99	6.96	3.97	7.58	3.99
Minimum	7.27	8.11	3.60	0.52	6.20	0.50	7.00	0.50

Concerning the statistical results of the modal parameters, the low variability for frequencies and the high variability for damping coefficients should be stressed, as the CV value is lower than 2.6% for frequencies and higher than 35% for damping. Once more and in practice, the difficulties of damping estimation make this parameter a unreliable quantity for damage detection.

The graph with the results for frequencies and the graphs for studying the correlation between the frequencies and the environmental and loading effects are presented in Annex D. Here, only the results for the first mode shape will be discussed. Figure 7.18 presents the variation for frequency, temperature and RMS and the correlation between the frequency and the temperature, and the correlation between frequency and

RMS. Observing the graphs, it can be concluded that for the case of the nave the temperature effect is significant and that the level of excitation can be neglected. There is also a trend for a bilinear relation between temperature and frequency, with an apex for a temperature around 18ºC. This trend occurs for all the estimated frequencies, see Annex D.

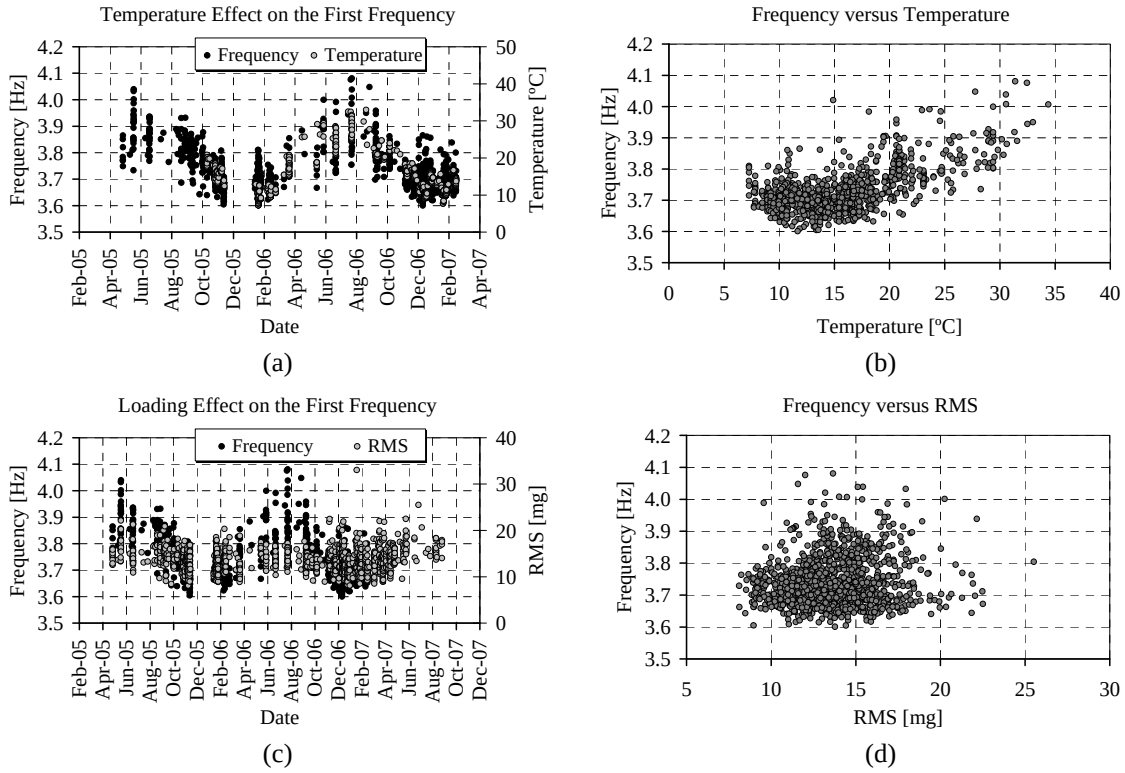


Figure 7.39 – Results for the first mode shape: (a) frequency and temperature variation; and (b) frequency versus temperature; (c) frequency and RMS variation.

As no continuum series were recorded in the monitoring system, modeling of thermal inertia is rather difficult and only the static regression models were used. From the observed bilinear trend, two linear regressions for temperature values lower and higher than 17.5ºC were adopted. Figure 7.40 shows the static models for the three estimated frequencies by correlating the two quantities, temperature and frequency, and by plotting in time the evolution of the frequencies and the model with the 95% ($\pm 2\sigma$) confidence intervals.

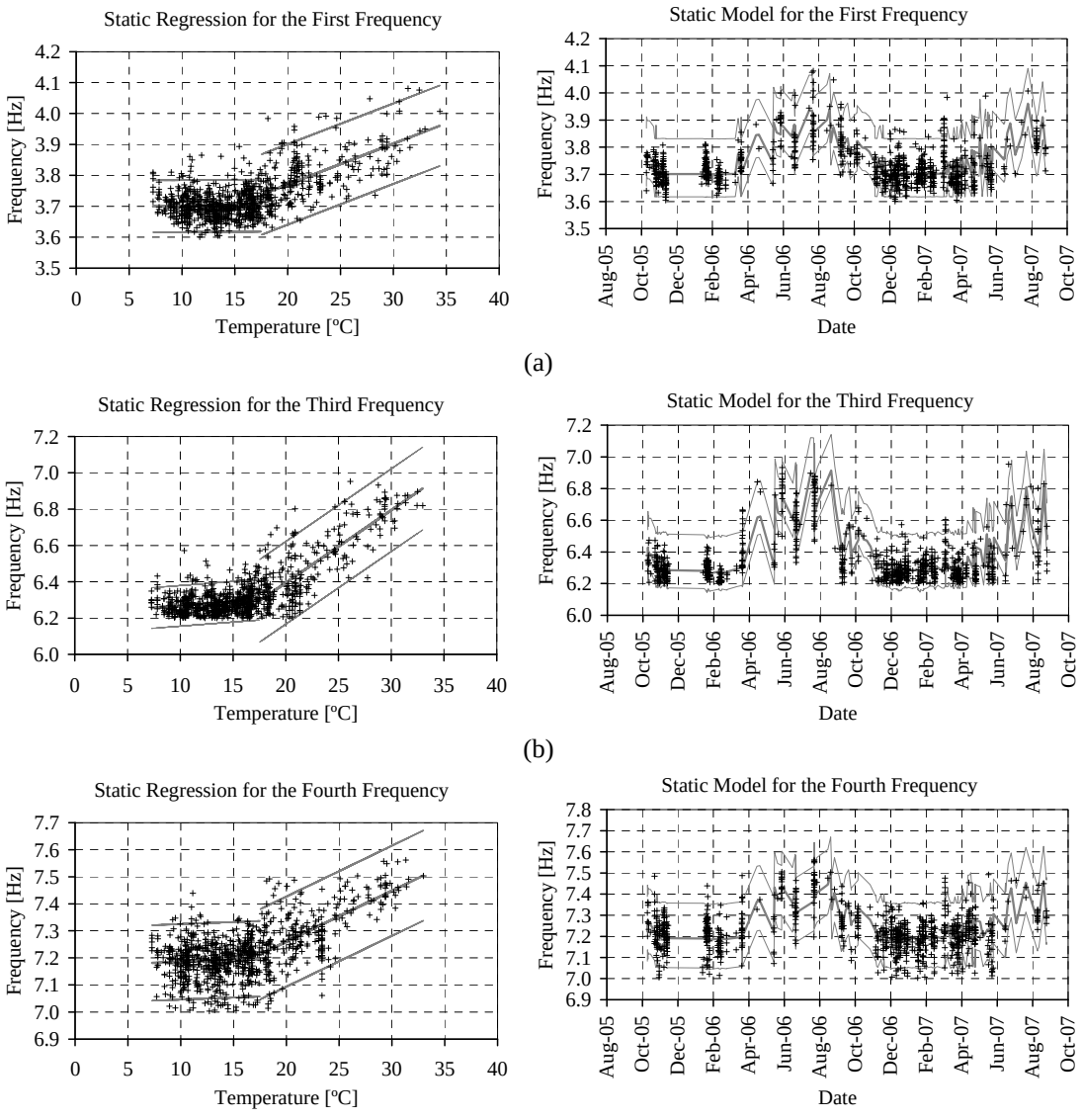


Figure 7.40 – Static models for dynamic response: (a), (b) and (c) for the first, third and fourth frequency, respectively.

The results show that the bilinear static model follows the evolution of the frequencies but a significant number of outliers can be observed in Figure 7.41, where the residuals between the natural frequencies and the simulated frequencies are shown. This indicates that others environmental effects need to be studied to better model the dynamic response. Nevertheless, no damage seems to be detected during the monitoring period.

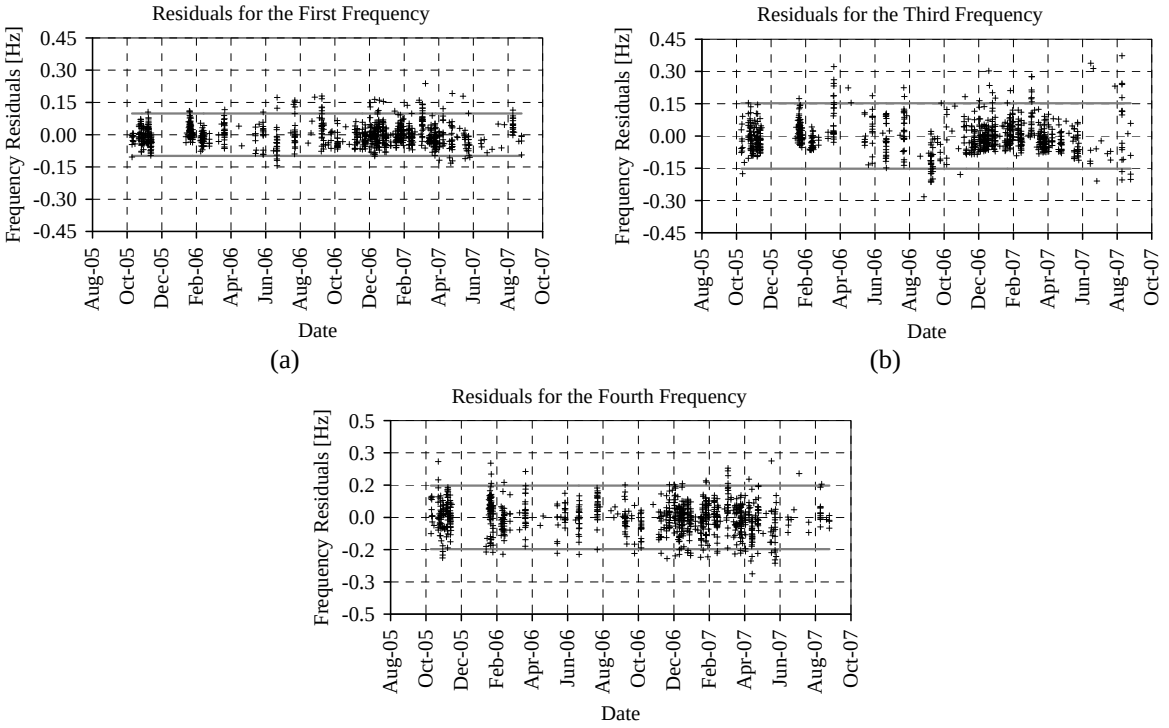


Figure 7.41 – Residuals history: (a), (b) and (c) for the first, third and fourth frequency, respectively.

Finally, it should be stressed that in 12 February, 2007, at 10:35 am a 5.8 magnitude earthquake, with an intensity V, occurred in the Southwest of Lisbon. The permanent staff of the monument felt the ground shake. No visitors were inside the church because on Mondays the church is closed to public. The strong motions recorders acquired the signals, as can be observed in Figure 7.42a. The peak of the frequency contents of the elastic response spectra was in the range of the estimated natural frequencies, see Figure 7.42b, but the three estimated natural frequencies did not suffer any significant shift, as can be observed through Figure 7.40 and Figure 7.41. Therefore, no damage in the structure occurred due to this minor earthquake.

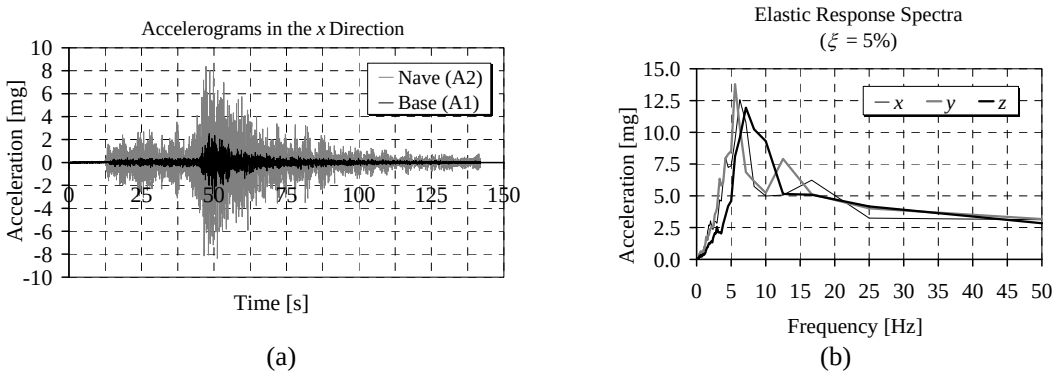


Figure 7.42 – Small earthquake in February, 2007: (a) the accelerograms in the *x* direction (transversal) at the base and at the nave; and (b) the elastic response spectra of the seismic event.

7.5 Conclusions

In this chapter cases studies in to two Portuguese monuments under monitoring were presented: the Clock Tower of Mogadouro and the Church of Jerónimos Monastery, in Lisbon. Aiming at damage identification at an early stage, the methodology for monitoring presented in Chapter 3 was followed. Firstly, there is a description of a preliminary dynamic analysis before the monitoring task, the installation of the monitoring system, the system identification and subsequent FE model updating analysis for structural assessment. Secondly, the environmental and loading effects were studied and the automatic modal identification procedures to estimate the global modal parameters were addressed.

From the Mogadouro Clock Tower the following conclusions emerged:

- With the comparison between the modal response of the tower, before and after rehabilitation, it was possible to conclude that the structure suffered significant structural strengthening and that the damage before rehabilitation significantly changed the dynamic behaviour of the tower;
- The tower structural assessment, by means of FE model updating techniques, demonstrate that the correct definition of the structure, including the foundations, is crucial for having good correlation between the experimental and numerical modal results;
- The comparison between the Young's modulus used for the updating analysis of the unstrengthened and strengthened conditions allowed concluding that damage was severe in most parts of the tower, with exception of the North façade and the corners. The damage was located in areas which suffer large mortar loss due to deterioration;
- A low-cost monitoring system was installed in the tower and has been measuring the dynamic response, as well the environmental effects, during a period of one year. Ten data series were analyzed and they allowed concluding that the environmental effects significantly change the dynamic response of the structure. Mainly, the water absorption of the walls in the beginning of the raining seasons changes about 4% the frequencies. The significant influence of moister inside the walls on the dynamic response of masonry structures is not so well reported in literature, as the changes are always appointed to others environmental effects or loading conditions, such as temperature and excitation level;
- The ambient temperature, the relative air humidity and the excitation level were correlated to the resonant frequencies. Multiple linear regression models were compared with Auto Regressive outputs with eXogeneous input models (ARX models) in order to evaluate the environmental and loading effects. The results indicates that ARX models can better simulate the natural frequencies, but others sensors to measure the water absorption inside the walls are necessary, to better simulate the dynamic response and to detect the presence of damage. A proposal for new humidity sensors was made;
- Apparently, no damage was observed by global modal parameters changes during the monitoring period.

From the Church of Jerónimos Monastery the following conclusions emerged:

- The modal identification of the nave and the columns indicates that the structure exhibits a rather complex behavior. The modal response is characterized by local modes on the slender columns. Difficulties were found during the experimental modal tests with output-only techniques to estimate accurately the modal parameters, due to the low signal-to-noise ratio in the structure. An additional identification test with an excitation device, like a drop weight system or a small shaker, could be useful for a better definition of the dynamic response;
- Since the structure is rather complex, the results of a numerical beam model were manually tuned to the experimental modal results. The model confirmed the significant influence of the slender columns on the dynamic response of the nave;
- For better studying of the complex behavior of the church and to detect the presence of damage, two monitoring systems were installed in the church nave and they have been acquiring the static and dynamic response during a period of two years;
- From the static monitoring system it was possible to visualize the significant influence of the temperature on the static response. ARX models were computed to simulate the static response and were used to detect damage, by using half of the data to calibrate the model and using the other half to simulate the static response and to detect damage. No damage was observed so far;
- With the dynamic monitoring system it was observed that temperature has a significant effect on the dynamic response, while the excitation level could be neglected. The temperate and frequencies exhibit a bilinear correlation, with frequencies varying almost 6%, on average;
- Because the monitoring system was designed with a different aim, no continuum data series were record. Therefore, only static linear regression models were applied to the data. The results of a bilinear regression follows the evolution of the experimental frequencies, but a significant number of outliers could be observed, indicating that others environmental effects need to be studied to better model the dynamic response. Nevertheless, no damage was detected during the monitoring period, even with the occurrence of a small earthquake on February, 2007, that hit the structure with a maximum Peak Ground Acceleration (PGA) of 2.5 mg.

From the experience with the two cases, the proposed methodology for damage identification seems to be useful and applicable to masonry structures, especially to historical constructions. The frequency observation seems to be a reliable quantity for damage detection.

Concerning the damping coefficients, in the two cases it was considered as unreliable quantity for damage detection. Although it was shown that, in the case of the Mogadouro tower, a high level of excitation leads to a better estimation, the variability of this quantity makes its use not recommended.

The aspects presented in this chapter need clearly further research. Different modal analysis and continuum monitoring data for a better definition of the structural response of the case studies is planned. Comparison with other systems based on Micro Electro Mechanical Systems (MEMS) in integrated Wireless Sensors Networks (WSN) needs to be addressed aiming at evaluating the use of new technologies, capable of helping in the protection of architectural heritage buildings.

Chapter 8

Conclusions and Future Works

8.1 Conclusions

This thesis addressed the problem of damage identification in masonry structures at early stage by means of vibration measurements. The work was divided in three phases: (a) a review of basic dynamics and experimental testing and a review of damage identification methods by means of vibration measurements; (b) two laboratory simulations with replicates of masonry structures, one arch and one wall, to better study the changes of the dynamic response with progressive damage; and (c) the application of the knowledge gained with the laboratory tests on two cases studies, one tower and one church, with the evaluation of the environmental and loading effects on the dynamic response of the case studies. Next, the main conclusions from the thesis are presented, together with remarks for future works.

8.1.1 Dynamic Experimental Testing and Damage Identification

To estimate modal parameters, output-only modal analysis is an attractive tool for historical masonry structures, as it is a non-destructive technique. One of the most accurate methods is based on the stochastic subspace identification techniques, a time-domain method where the State-Space Formulation is used. Those techniques require random excitations, normally obtained with ambient noise, which makes the estimation simple, cost-effective and reduces the interference with operating conditions of the structures. One disadvantage is the fact that mode shapes are not scaled to the structure mass matrix, although there are procedures to give approximate scale factors by means of controlled added masses into the structures.

In the literature, many methods have been presented for damage identification based on vibration signatures. The methods can be classified in four levels, according the type of information that they can give about damage, namely its presence (detection), its location and its extent on the structure, and the prediction of the remaining life of the structure. The detection is carried out by frequency changes, while the location is usually obtained by differences between mode shapes and their derivatives from different damage scenarios. The assessment of its extent is only obtained by few methods, being unclear if these work with all type of structures.

Large civil engineering structures have low sensitivity to frequency changes, because resonant frequencies represent condensed information about the response and are also a global property of the structures. Another global property is the damping coefficient. Damping increases with the presence of damage because it is related to the nonlinear phenomena, but it also increases with the level of vibration and, for that reason, damping estimation is difficult and most of the times presents large variability, which makes this parameter not much used for damage detection.

In real case studies and before any attempt to identify the presence of damage, it is important to evaluate and separate the environmental and the loading effects from the dynamic response of the structures. It is important to “model” these effects because they can change the modal parameters in the same order of magnitude of possible (small) damage.

As damage is a local phenomenon, it is important to estimate accurately the mode shapes or the curvature mode shapes in order to localize it. Therefore, a sufficient number

of measuring points is necessary for having enough spatial resolution of the modes. Once accurate information is available, the methods based on changes in the mode shapes or modal curvatures (or the combination of all responses, e.g. frequencies, mode shapes and modal curvatures) are more successful in the damage identification analysis.

8.1.2 Laboratory Simulations

Before the damage analysis on the masonry replicates, preliminary studies on the specimens, which included the cracked simulation analysis using Finite Element (FE) models, the discussion of the sensor types, sensor positions in the specimens and the test planning, significantly contributed to understand the dynamic response of the replicates and the results interpretation in the damage identification analysis.

During the several damage scenarios, induced by controlled loads in the replicates, it was possible to observe that natural frequencies were sensitive to progressive damage. Although the damage in the specimens was very difficult to visualize, the static response exhibits an evident decrease of stiffness and the natural frequency values decrease significantly. The problem of the damage detection was solved only with the frequency shifts observation.

Compared with frequency values, the estimated damping values presented a large variability, and therefore they were considered as less accurate quantities for damage detection, even if a trend to increase at progressive damage was observed.

As the modal curvatures were considered potential information for damage localization, two different sensors were used in the specimens: accelerometers and strain gauges to record directly the modal curvatures. Because the level of excitation with ambient noise inside the laboratory was not enough to estimate accurately the modal curvatures, a second type of excitation with random impacts, in time and in space of the replicates, was carried out. The measurements with strain gauges were accurate, and the information extracted with these sensors proved to be crucial for the damage localization.

The damage localization analysis itself was carried out by a combination of different methods using a qualitative approach. The aim is to capture the difficult phenomena of damage by basing the decision on different results. The selected methods can be divided in two groups: non-model based methods and model based methods. The non-model based methods studied were the Unified Significance Indicator (USI), the COMAC values for modal displacements and modal curvatures, the Parameter Method (PM), the Mode Shape Curvature Method (MSCM), the Damage Index Method (DIM), the Sum of the Curvature Errors method (SCE), and the Change Flexibility Matrix method (CFM). The model based method studied was the FE Model Updating method (FEMU).

For the case of the arch model, the damage could be successfully located only with the non-model based methods. The methods that take into account the modal curvatures were able to localize the cracks at a very earlier stage. The crack sequence was also attained. The difficulties to tune a numerical model to the experimental modal data were the reason for the unsuccessful location analysis with the model based method. A large number of updating parameters would be required to tune each damage scenario, leading to a tedious and complex updating analysis, with likely ill-condition solutions.

For the case of the wall model, damage could be successfully located with both groups of methods. Once again, the measured modal curvatures proved to be useful information for damage identification analysis, even if more noise was present in the modal data and

did not allow estimating the higher modes of the specimen. The crack sequence was also attained.

During the strains measurements of the wall model, it was possible to conclude that strain gauges are not the best solution to measure stains at progressive damage. Although it was possible to estimate accurately the curvatures mode shapes, once the sensors break due to a crossing crack, they cannot continue recording. A system based on two fixed points, with large deformation capacity, or optical measurements, is a better solution since cracking "strains" can be measured.

Concerning the applicability of the different methods in both specimens, it should be stressed that not all the methods could always capture the location of damage and there is no single method that worked for all damage scenarios. The reasons might be related to the presence of noise in the modal data, resulting from measurements and computations. The usage of different methods with adequate criteria to localize damage proves to be a best approach. The chosen criteria was the combination of the results from the PM calculated with curvature mode shapes, the MSCM, the DIM and the SCE, because their results were most of the times coincident.

Finally, damage assessment could not be achieved with reliable results in both specimen analyses.

8.1.3 Case Studies and Environmental and Loading Effects

The current practice of structural health monitoring is based mainly on visual inspections or condition surveys. Concerning monitoring of historical masonry structures, it was proposed that this task can possibly involve global and local damage identification approaches. Dynamic measurements are to be used for an initial structural assessment, for continuous monitoring, for damage detection, and for global damage localization. The local damage assessment is to be carried out with different non-destructive techniques, such as sonic tests or radar tests, if damage is detected in the preceding global phase.

The proposed methodology was applied to two real case studies in Portugal, the Clock Tower of Mogadouro and the Church of Jerónimos Monastery, in Lisbon, where initial structural assessment and global damage detection was carried out.

For the case of Mogadouro Clock Tower, the following main conclusions emerged:

- The assessment of the tower, by means of FE model updating techniques, demonstrates that the correct definition of the structure, including the foundations, is crucial to have good correlation between experimental and numerical modal results;
- A low-cost monitoring system was installed in the tower and has been measuring the dynamic response, as well the environmental effects, during a period of one year. The results allowed concluding that the environmental effects significantly change the dynamic response of the structure. Mainly, the water absorption of the walls in the beginning of the raining seasons, or the drying process in the summer, changes the natural frequencies around 4%. The significant influence of moisture inside the walls on the dynamic response of masonry structures is not well reported in the literature, as the changes are always attributed to other environmental effects or loading conditions, such as temperature and excitation level;

- The ambient temperature, the relative air humidity and the excitation level were correlated to the natural frequencies. Multiple linear regression models were compared with Auto Regressive outputs with eXogeneous input models (ARX models) in order to evaluate the environmental and loading effects. The results indicate that ARX models can better simulate the natural frequencies, but sensors to measure the water absorption inside the walls are needed to better simulate the dynamic response and to detect the presence of damage. A proposal for the addition of new humidity sensors was made.

For the case of the Church of Jerónimos Monastery, the following main conclusions emerged:

- The modal identification of the nave and the columns indicates that the structure exhibits a rather complex behavior. The modal response is characterized by local modes on the slender columns. Difficulties were found during the experimental modal tests with output-only techniques to estimate accurately the modal parameters, due to the low signal-to-noise ratio in the structure. An additional identification test with an excitation device, like a drop weight system or a small shaker, could be useful for a better definition of the dynamic response;
- With the dynamic monitoring system it was observed that temperature has a significant effect on the dynamic response, while the excitation level could be neglected. The temperate and natural frequencies exhibit a bilinear correlation, with three natural frequencies varying almost 6%, on average. Humidity sensors were also installed in the monitoring system to address the possible moisture effect on the dynamic response, but up to now there is insufficient data to correlate the two quantities;
- Static linear regression models were applied to correlate temperature to the natural frequencies. The results of a bilinear regression follows the evolution of the measured frequencies, but a significant number of outliers could be observed, indicating that others environmental effects need to be studied to better model the dynamic response. Nevertheless, no damage was detected during the monitoring period, even with the occurrence of a small earthquake on February, 2007, that hit the structure with a maximum Peak Ground Acceleration (PGA) of 2.5 mg.

From the experience with the two cases studies, the proposed methodology for damage identification seems to be useful and applicable to historical masonry structures. The natural frequency observation seems to be a reliable approach for damage detection, although no damage occurred in the two case studies or was not detected by vibrations measurements.

Concerning the damping coefficients, it was considered as a unreliable quantity for damage detection. Although it was shown that, in the case of the Mogadouro tower, a high level of excitation leads to a better estimation of damping, the variability of this quantity makes its use not recommended for the two cases studies.

8.2 Future Works

With respect to damage detection, during this work damping coefficient was marked as a less accurate modal parameter. Although it is evident that increasing damping is related to a damage progress, the current estimation techniques cannot give reliable results, making this parameter of little use. Further investigation on damping estimation is needed.

For damage localization, it seems that measuring the modal curvatures is a good approach for the success of the damage identification analysis. Research on non-contact measurements systems, such as systems based on two fixed points, with large deformation capacity, or optical measurements, is recommended. The existing systems are too expensive and they are only capable to measure accurately the modal curvatures in small areas of the structures.

The monitoring task of the two historical constructions reported in Portugal will continue to be studied. Different modal analysis and additional monitoring data will be carried out. New sensors should be added to the existing monitoring systems, especially to measure water absorption inside masonry walls.

Although it is almost impossible to induce real damage on historical constructions, to evaluate the efficiency of the global dynamic approach discussed in this thesis, one valuable analysis could be the controlled addition of “positive” damage, by means of adding tie-rods or other structural elements and their subsequent removal, to change the dynamic response of the two case studies. Alternatively to the stiffness increase, the addition of controlled masses can also change the dynamic response. This is considered one of best possibilities, aiming at evaluating the approach presented in this thesis on real historical case studies.

In the case of masonry structures, it was shown that temperature is not always the most important environmental effect. Changes in mass and stiffness due to moisture absorption need to be considered in future. Static and dynamic laboratorial tests with varying temperature and varying humidity should be carried out on specimens for better comprehension of their influence on the dynamic response.

The comparison with the results obtained with the existing monitoring systems used in the two case studies and the results by other systems based on Micro Electro Mechanical Systems (MEMS) in integrated Wireless Sensors Networks (WSN) needs to be addressed, aiming at evaluating the use of new technologies, capable of helping in the protection of architectural heritage buildings.

Finally and during the last decade, software and hardware developments made continuous monitoring possible. Typically, one can install a large number of sensors in a structure and read the data in real time. The challenge now is focused in what type of information is important from the structural point of view and how the data should be processed and stored for damage analysis. Further research on data fusion, management system, risk analysis, and decision-making is needed to better use the fast developments of those technologies on the preservation of heritage constructions.

References

A

Alampalli, S. (1998): Influence of in-service Environment on Modal Parameters, Proceedings of IMAC XVI, 16th International Modal Analysis Conference, Santa Barbara, CA, USA, pp. 111-116

Andersen, P. (1997): Identification of Civil Engineering Structures using Vector ARMA Models, PhD Thesis, Aalborg University, Denmark

Andersen, P.; Brincker, R.; Peeters, B.; De Roeck, G.; Hermans, L.; and Krämer, C. (1999): Comparison of System Identification Merthods Using Ambient Bridge Test Data, Proceedings of IMAC XVII, the 17th International Modal Analysis Conference, Kissimee, USA

B

Baptista, M.A.; Mendes, P.; Afilhado, A.; Agostinho, L.; Lagomarsino, S.; and Victor, L.M. (2004): Ambient Vibration Testing at N. Sra. do Carmo Church, Preliminary Results, Proceedings of the Fourth International Seminar on Structural analysis of Historical Constructions, Padova, Italy, Vol. 1, pp. 483-488

Basilio, I. (2007): Strengthening of Arched Masonry Structures with Composite Materials, PhD thesis, University of Minho

Bendat, J.; and Piersol, A. (1986): Random Data: Analysis and Measurement Procedures, 2nd Edition, John Wiley & Sons

Bensalem, A.; Fairfield, C.; and Sibbald, A. (1995): Non-destructive Testing for Arch Bridge Assessment", Proceedings of the First International Conference on Arch Bridges, Bolton, UK. 3-6 September

Binda, L.; and Saisi, A. (2001): Non Destructive Testing Applied to Historic Buildings: The Case of Some Sicilian Churches, Proceedings of the 3rd International Seminar of Historical Constructions, Guimarães, Portugal, University of Minho, pp. 29-46

Brincker, R.; and Andersen, P (2003): A Way of Getting Scaled Mode Shapes in Output-Only modal Testing, Proceedings of the 21th International Modal Analysis Conference, Kissimee, USA, paper No. 141 (CD-ROM)

Brincker, R.; Andersen, P.; Kirkegaard, P.H.; and Ulfkjaer, J.P. (1995): Damage Detection in Laboratory Concrete Beams. Proceedings of the 13th International Modal Analysis Conference, Vol. 1, pp. 668-674

Brincker, R.; Ventura, C.; and Andersen, P. (2001): Damping Estimation by Frequency Domain Decomposition, Proceedings of IMAC XIX, the 19th International Modal Analysis Conference, Kissimee, USA

Brincker, R.; Zhang, L.; and Andresen, P. (2000): Modal Identification from Ambient Responses using Frequency Domain Decomposition, Proceedings of the 18th Internation Seminar on Modal Analysis, San Antonio, Texas, 7-10 February

C

Caetano, E. (1992): Identificação Experimental de Parâmetros Dinâmicos em Sistemas Estruturais, Master Thesis, Engineering Faculty of University of Porto, Portugal

Caetano, E. (2000): Dynamic of Cable-stayed Bridges: Experimental Assessment of Cable-Structure Interaction, PhD Thesis, Engineering Faculty of University of Porto, Portugal

Cantieni, R. (2006): Office floor vibrations: modal parameter identification and vibration monitoring, Proceedings of ISMA 2006, Leuven, September 18-20, pp. 2937-2948

Casarin, F.; and Modena, C. (2007): Dynamic Identification of S. Maria Assunta Cathedral, Reggio Emilia, Italy, Proceedings of the 2nd Int. Operational Modal Analysis Conference, Copenhagen, Denmark, April 30 - May 2, 2007, pp. 637-644

Casas, J.R.; and Aparicio, A.C. (1994): Structural Damage Identification From Dynamic Test Data, Journal of Structural Engineering, Vol. 120, No. 8, pp. 2437-2450

Cawley, P.; and Adams, R.D. (1979): The Locations of Defects in Structures from Measurements of Natural Frequencies, Journal of Strain Analysis, Vol. 14 No. 2, pp. 49-57

Chang, C.C.; and Sun, Z. (2005): Structural Damage Localization using Spatial Wavelet Packet Signature, Smart Structures and Systems, Vol. 1(1), pp.29-46

Chang, P.C.; Flatau, A.; and Liu, S.C. (2003): Review Paper: Health Monitoring of Civil Infrastructure, Structural Health Monitoring, Vol. 2 (3), pp. 257-267

Choi, S.; Park, S.; and Stubbs, N. (2005): Non-destructive Damage detection in Structures using Changes in Compliance, International Journal of Soils and Structures, n.42, pp. 4494-4513

Chondros, T.G.; Dimarogonas, A.D. and Yao, J. (1998): A Continuous Cracked Beam Vibration Theory, Journal of Sound and Vibration, 215(1), pp. 17-34

Chopra, A.K. (2001): Dynamics of Structures, Theory and Applications to Earthquake Engineering, Second Edition, Prentice Hall

Clough, R.W.; and Penzien, J. (1993): Dynamics of Structures, Second Edition, McGraw-Hill international Editions

Cooley, J.W.; and Tukey, J.W. (1965) An Algorithm for the Machine Calculation of Complex Fourier Series, Mathematics of Computation, Vol. 19(90), pp. 297-311

Cornwell, P.; Doebling, S.W.; and Farrar, C.R. (1999): Application of the Strain Energy Damage Detection Method to Plate Like Structures, Journal of Sound and Vibration 224(2), pp. 359-374

Costa, C.; Arêde, A.; and Costa, A. (2004): Caracterização Dinâmica e Análise da Ponte da Lagocinha, Proceedings of the 6º Congresso de Sismologia e Engenharia Sísmica, University of Minho, Portugal, pp. 931-942

Cunha, A.; Caetano, E.; Brincker, R.; and Andersen, P. (2004): Identification from Natural Response of Vasco da Gama Bridge, Proceedings of IMAC XXII, the 22th International Modal Analysis Conference, Dearborn, USA

D

De Sortis, A.; Antonacci, E.; and Vestroni, E. (2005): Dynamic identification of a masonry building using forced vibration tests, Engineering Structures, Vol. 27, pp. 155-165

Deraemaeker A.; Reynders, E.; De Roeck, G.; and Kullaa, J. (2007): Vibration-based structural health monitoring using output-only measurements under changing environment, Mechanical Systems and Signal Processing, article in press, doi:10.1016/j.ymssp.2007.07.004

DIANA (2006): DIANA-9 Finite Element Analysis, User's Manual - Release 9, TNO, Netherlands

Doebling, S.W.; Farrar C.R. and Prime, M.B. (1998): A Summary review of vibration-based damage identification methods, The Shock and Vibration Digest, no. 30(2), pp.91-105

Doebling, S.W.; Farrar C.R.; Prime, M.B.; and Shevitz D. (1996): Damage identification and health monitoring of structural and mechanical systems from changes in their vibration characteristics: a literature review, Los Alamos National Laboratory, NM, 132 p.

Doherty, J.E. (1987): Nondestructive Evaluation, Handbook on Experimental Mechanics, A.S. Kobavashi Edt., Society for Experimental Mechanics, Chapter 12

Dong C., Zhang, P.Q.; Feng, W.Q.; and Huang, T.C. (1994): The Sensitivity Study of the Modal Parameters of a Cracked Beam, in Proceedings of the 12th International Modal Analysis Conference, pp. 98–104

Doubechies, I. (1992): Ten Lectures on Wavelets, CBS-NSF Regional Conferences in Applied Mathematics

Douglas, B.M.; and Reid, W.H (1982): Dynamic Tests and System Identification of Bridges, ASCE Journal of the Structural Division, Vol. 108, No. 10, October 1982, pp. 2295-2312

E

Erdogmus, E.; and Boothby, T.E. (2004): Validated Structural Analysis of Gothic Vaulted Systems, Proceedings of the Fourth International Seminar on Structural analysis of Historical Constructions, Padova, Italy, Vol. 1, pp. 421-428

EU-India (2006): Benchmarking on the Seismic Behaviour of the Qutb Minar, deliverables of the project “Improving the Seismic Resistance of Cultural Heritage Buildings”, from the Asia-wide Programme “EU-India Economic Cross Cultural Programme”, Project Contract N° ALA/95/23/2003/077-122, 55 p.

Ewins, D.J. (2000): Modal Testing, Theory, Practice and Aplication, Second Edition, Research Studies Press LTD, Baldock, Hertfordshire, England

F

Farrar, C.R. and Doebling, S.W. (1998): Damage Detection and Evaluation II – Field Applications to Large Structures, Modal Analysis and Testing, Júlio Silva and Nuno Maia (Editors), NATO Science Series E, Vol. 363, Kluwer Academic Publishers, London, pp 345-378

Farrar, C.R.; Baker, W.E.; Bell, T.M.; Cone, K.M.; Darling, T.W.; Duffey, T.A.; Eklund, A.; and Migliori, A. (1994): Dynamic Characterization and Damage Detection in the I-40 Bridge over the Rio Grande, Los Alamos National Laboratory, NM, 153 p.

Friswell, M.I. and Mottershead, J.E. (1995): Finite Element Model Updating in Structural Dynamics, Kluwer Academic Publishers, Dordrecht, The Netherlands

G

Genin, S.M (1995): Descriptive study of the vault in the Church of the Monastery of Santa Maria de Belém in Lisbon (in French), M.Sc. Thesis, Katholiek Universiteit Leuven, Belgium

Genin, S.M. (2001): The nave vault of the Hieronymites Monastery Church in Lisbon, Proceedings of Historical Constructions 2001, Eds. P. Lourenço and P. Roca, University do Minho, Guimarães, p. 293-302

Genovese, F.; and Vestroni, V. (1998): Identification of Dynamic Characteristics of Masonry Building, Proceedings of European Conference on Earthquake Engineering, Paris, France

Gentile, C.; and Saisi, A. (2004): Dynamic-based F.E. Model Updating to Evaluate Damage in Masonry Towers, Proceedings of the 4th International Seminar on Structural analysis of Historical Constructions, Padova, Italy, Vol. 1, pp. 439-449

Gentile, C.; Martinez, F.; and Cabrera (2001): Dynamic assessment of a curved cable-stayed bridge at the Malpensa 2000 Airport, Milan, Italy, Structural Engineering International, (1), pp. 52–58

H

Hemez, F.M.; and Doebling, S.W. (2001): Review and Assessment of Model Updating for Nonlinear, Transient Dynamics, Mechanical Systems and Signal Processing, 15(1) pp. 45-74

Horyna, T.; and Ventura, C. (2000): Summary of HCT Building Ambient Vibration Data Analyses, Proceedings of IMAC XVIII, the 17th International Modal Analysis Conference, San Antonio, USA

Hou, Z.; Noori, M.; and St. Amand, R. (2000): Wavelet-Based Approach for Structural Damage Detection, Journal of Engineering Mechanics, Vol. 126, No. 7, July 2000, pp. 677-683

Huerta, S. (2001): Mechanics of Masonry Vaults: the Equilibrium Approach, Proceedings of the 3rd International Seminar of Historical Constructions, Guimarães, Portugal, University of Minho, pp. 47-70

I

Ivanović, S.S.; Trifunac, M.D.; Novikova, E.I.; Gladkov, A.A.; and Todorovska, M.I. (2000): Ambient vibration Tests of a Seven-story Reinforced Concrete Building in Van Nuys, California, Damaged by the 1994 Northridge Earthquake, Soil Dynamics and Earthquake Engineering, 19, pp. 391-411

Ivorra, S.; and Pallarés, F. (2007): A Masonry Bell-Tower Assessment by Modal Testing, 2nd Int. Operational Modal Analysis Conference, Copenhagen, Denmark, April 30 - May 2, 2007, pp. 269-276

Ivorra, S.; Palomo, M.J.; Verdú, G.; and Pallarés, F. (2004): A First Approach to Study an 18th Century Belltower, Proceedings of the Fourth International Seminar on Structural Analysis of Historical Constructions, Padova, Italy, Vol. 1, pp. 429-437

J

Jaishi B.; Ren W.-X.; Zong Z.-H.; and Maskey P.N. (2003): Dynamic and Seismic Performance of Old Multi-Tiered Temples in Nepal, Engineering Structures, Vol. 25, Number 14, pp. 1827-1839(13)

Juang, J-N (1994): Applied System Identification. Prentice Hall Englewood Cliffs, New Jersey, USA

K

Kitada, Y. (1998): Identification of nonlinear Structural Dynamic Systems using Wavelets, Journal Engineering Mechanics, ASCE, 124(10), pp. 1059-1066

L

LabVIEW (2006): LabVIEW User Manual, Release 8.0, National Instruments, USA

Lança, P. (2006): Structural analysis of multi-ribbed vaults: Application to the high choir of Jerónimos Monastery (in Portuguese), MSc of Structural Engineering, University of Minho (www.civil.uminho.pt/masonry)

Ljung, L. (1999): System Identification: Theory for the User, Second edition, Prentice Hall, Upper Saddle River, NJ, USA

Londoño, N.A. (2006): Use of Vibration Data for Structural Health Monitoring of Bridges, PhD Thesis, Carleton University, Ottawa, Canada

Lourenço, P.B. (1998): Sensitivity Analysis of Masonry Structures, Proceedings of the 8th Canadian Masonry Symposium, Jasper, Canada, pp. 563-574

Lourenço, P.B. (2001): Analysis of Historical Constructions: From Thrust-Lines to Advanced Simulations, Proceedings of the 3rd International Seminar on Historical Constructions, Guimarães, Portugal, pp. 91-116

Lourenço, P.B.; and Krakowiak, K.J. (2003): Avaliação da estabilidade das abóbadas da Igreja do Mosteiro dos Jerónimos, Report 03-DEC/E-02, University of Minho

Lourenço, P.B.; Krakowiak, K.J.; Fernandes, F.M.; and Ramos, L.F. (2007): Failure analysis of Monastery of Jerónimos, Lisbon: How to learn from sophisticated numerical models?, Engineering Failure Analysis, 14(2), pp. 280-300

Lynch, J.P.; Law, K.H.; Kiremidjian, A.S.; Kenny, T.; and Carryer, E. (2002): A Wireless Modular Monitoring System For Civil Structures, Proceedings of IMAC XX, the 20th International Modal Analysis Conference, Los Angeles, CA, USA

M

Maeck, J. (2003): Damage Assessment of Civil Engineering Structures by Vibration Monitoring, PhD Thesis, Catholic University of Leuven, Belgium

Maeck, J.; and De Roeck, G. (2003): Description of Z24 Benchmark. Mechanical Systems and Signal Processing, 71(1) pp. 127-131

Magalhães, F. (2004): Identificação Modal Estocástica para Validação Experimental de Modelos Numéricos, Master Thesis, Engineering Faculty of University of Porto, Portugal

Maia, N.M.; and Silva, J.M. (1997): Theoretical and Experimental Modal Analysis, Research Studies Press LTD, England

MATLAB (2006): MATLAB User Manual, Release 7.2, The MathWorks, USA

Modena, C.; Franchetti, P.; Zonta, D.; Menga, R.; Pizzigalli, E.; Ravasio, F.; Muti, M.; Meloni, R.; and Bordone, G. (2001): Static and Dynamic Analyses of "Maniace Castle" in Siracusa-Sicily, Proceedings of the 3rd International Seminar on Historical Constructions, Guimarães, Portugal, pp. 933-942

Montalvão, D.; Maia, N.M.M.; and Ribeiro, A.M.R. (2006): A Review of Vibration-based Structural Health Monitoring with Special Emphasis on Composite Materials, The Shock and Vibration Digest, Vol. 38, No. 4, pp. 295-324

Mourão, S. (2001): Study of the seismic behaviour of the monumental compound of Monastery of Jerónimos (in Portuguese), MSc of Structural Engineering, University of Minho (www.civil.uminho.pt/masonry)

Mun, M. (2002): Estudo da constituição das abóbadas da Igreja do Mosteiro dos Jerónimos através de sondagem com radar e métodos complementares de diagnóstico, Relatório 176/2002, Laboratório Nacional de Engenharia Civil, Lisboa

N

Ndambi, J.M.; Peeters, B.; Maeck, J.; De Visscher, J.; Wahab, M.A.; Vantomme, J.; De Roeck, G.; and De Wilde, W.P. (2000). Comparison of techniques for modal analysis of concrete structures, Engineering Structures, 22, pp. 1159-1166

Neves, N.; Costa, A.; and Arêde, A. (2004): Identificação Dinâmica e Análise do Comportamento Sísmico de um Quarteirão Localizado da Cidade da Horta - Ilha do Faial, Proceedings of the 6º Congresso de Sismologia e Engenharia Sísmica, University of Minho, Portugal, pp. 943-956

O

Oliveira, D.V. (2003): Experimental and Numerical Analysis of Blocky Masonry Structures Under Cyclic Loading, PhD Thesis, Universidade do Minho, 211 p. (www.civil.uminho.pt/masonry)

Oliveira, D.V.; Ramos, L.F.; Lourenço, P.B.; and Roque, J. (2005): Structural monitoring of the Monastery of Jerónimos, Proceeding of the International Conference on the 250th Anniversary of the 1755 Lisbon Earthquake, Lisbon, p. 466-473

Oliveira, M.M.P. (2002): Prospecção por radar na Igreja dos Jerónimos, Relatório nº 177/2002, Laboratório Nacional de Engenharia Civil, Lisboa

Ovanesova, A. V.; and Suárez, L. E. (2004): Applications of wavelet transforms to damage detection in frame structures, Engineering Structures, Vol. 26(1), January 2004, pp. 39-49

P

Pandey, A.K.; and Biswas, M. (1994): Damage Detection in Structures Using Changes in Flexibility, Journal of Sound and Vibration, Vol. 169, No. 1, pp. 3-17

Pandey, A.K.; Biswas, M.; and Samman, M.M. (1991): Damage Detection from Changes in Curvature Mode Shapes, Journal of Sound and Vibration, Vol. 145, No. 2, pp. 321-332

Parloo, E.; Verboven, P.; Guillame, P.; and Van Overmeire, M. (2002): Sensitivity-Based Operational Mode Shape Normalization, Mechanical Systems and Signal Processing, Vol. 16, N. 5, pp 757-767

Paultre, P.; Proulx, J.; and Talbot, M. (1995): Dynamic Tests Procedures for Highway Bridges Using Traffic Loads, Journal of Structural Engineering, Vol. 121(2), pp. 362-376, ASCE

PCB (2004): Product Catalog, PCB Piezotronics, Inc. - Vibration Division

Peeters, B. (2000): System Identification and Damage Detection in Civil Engineering, PhD Thesis, Catholic University of Leuven, Belgium

Peeters, B.; and De Roeck, G. (1999): Reference-Based Stochastic Subspace Identification for Output-Only Modal Analysis. Mechanical Systems and Signal Processing, 13(6), pp. 855-878

Peeters, B.; and Ventura, C. (2003). Comparative Study of Modal Analysis Techniques for Bridge Dynamic Characteristics, Mechanical Systems and Signal Processing, 17(5), pp. 965–988

Peeters, B.; De Roeck, G.; Caetano, E.; and Cunha, A. (2002): Dynamic Study of the Vasco da Gama Bridge, ISMA 2002 International Conference on Noise and Vibration Engineering, Leuven, Belgium

R

Ramos, L.F.; Casarin, F.; Algeri, C.; Lourenço, P.B.; and Modena, C. (2006): Investigations Techniques Carried out on the Qutb Minar, New Delhi, India, Proceedings of the 5th International Conference of Structural Analysis of Historical Constructions, New Delhi, November 6-8, 2006, Vol. 1, pp. 633-640

Ramos, L.F.; Lourenço, P.B.; and Costa, A.C. (2005): Operational Modal Analysis for Damage Detection of a Masonry Construction, Proc. 1th Int. Operational Modal Analysis Conference, Copenhagen, Denmark, April 24-26, 2005, pp. 495-502

Rebelo, C.; Júlio, E.; and Costa, D. (2007): Modal Identification of the Coimbra University Tower, Proceedings of the 2nd Int. Operational Modal Analysis Conference, Copenhagen, Denmark, April 30 - May 2, 2007, pp. 177-184

Reynders, E.; and De Roeck; G. (2006): Reference-Based Combined Deterministic-Stochastic Subspace, Proceedings of ISMA 2006, Leuven, September 18-20, pp. 3035-3046

Roberts G.P.; and Pearson A.J. (1998): Health monitoring of structures - towards a stethoscope for bridges, Proceedings of ISMA 23, the International Conference on Noise and Vibration Engineering, Leuven, Belgium

Rodrigues, J. (2004): Identificação Modal Estocástica, Métodos de Análise e Aplicações em Estruturas de Engenharia Civil, PhD Thesis, Engineering Faculty of University of Porto, Portugal

Roque, J. (2007): Metodologia integrada para avaliação e mitigação da vulnerabilidade sísmica das construções históricas em alvenaria: A igreja dos Jerónimos como caso de estudo, PhD Thesis, University of Minho, Portugal

Rytter, A. (1993): Vibration Based Inspections of Civil Engineering Structures, PhD Thesis, Departement of Building Technology and Structural Engineering, University of Aalborg, Denmark

S

Salawu, O.S. (1997): Detection of Structural Damage through Changes in Frequency: a Review, Engineering Structures, Vol. 19, No. 9, pp. 718-723

Salawu, O.S.; and Williams, C. (1995): Review of Full-scaled Testing of Bridge Structures, Engineering Structures, Vol. 17, No. 2, pp. 113-121

SAP2000, (2005): SAP2000 Advanced User Manuals, Release 10.0.5, CSI Computers & Structures, Inc.

Schmidt, T. (2007): Dynamic Behaviour of Twin Bell Towers, Proceedings of the 2nd Int. Operational Modal Analysis Conference, Copenhagen, Denmark, April 30 - May 2, 2007, pp. 261-268

Sigmund, V.A.; and Herman, K. (1998): Dynamic Characteristics as Indicators of Structural Integrity, Proceedings of Saving Buildings in Central and Eastern Europe, IABSE, Berlin 4-5 June

Sofronie, R.A. (2004): Seismic Strengthening of Masonry in Buildings and Cultural Heritage, Proceedings of the 6º Congresso Nacional de Sismologia e Engenharia Sísmica, Guimarães, University of Minho, 14 t0 16 of April, 2004, pp. 81-100

Stubbs, N.; and Osegueda, R. (1990a): Global Non-Destructive Damage Evaluation in Solids, Modal Analysis, The International Journal of Analytical and Experimental Modal Analysis, 5(2), pp. 67-79

Stubbs, N.; and Osegueda, R. (1990b): Global Damage Detection in Solids – Experimental Verification, Modal Analysis, The International Journal of Analytical and Experimental Modal Analysis, 5(2), pp. 81-97

Stubbs, N.; Broome, T.H.; and Osegueda R. (1990): Non-destructive Construction Error Detection in Large Space Structures, AIAA Journal, 28(1), pp. 146-152

Stubbs, N.; Kim, J.T.; and Topole, K. (1992): An efficient and Robust Algorithm for Damage Localization in Offshore Platforms, Proceedings ASCE 10th Structures Congress, pp. 543-546

SVS (2006): ARTeMIS Extractor Pro User Manual, Release 3.5, Structural Vibration Solutions, Aalborg, Denmark

T

Teughels, A. (2004): Inverse Modelling of Civil Engineering Structures Based on Operational Modal Data, PhD Thesis, Catholic University of Leuven, Belgium

V

Valoff, S.; and Kaiser, W.J. (1999): Presettable Micromachined MEMS Accelerometers, Proceedings of the 12th IEEE International Conference on Micro Electro Mechanical Systems (MEMS'99)

Vasconcelos, G.F.M. (2005): Behaviour of Dry-stone Masonry Walls under Combined Loading, PhD Thesis, University of Minho, Portugal

Ventura, C.; and Brincker, R. (2001): Modal Identification of Output-Only Systems, MI Course Notes

Vestroni, F.; Beolchini, G.C.; Antonacci, E.; and Modena, C. (1996): Identification of Dynamic Characteristics of Masonry Buildings from Forced Vibration Tests, Proceedings of the 11th World Conference on Earthquake Engineering

W

Wang, Q.; and Deng, X. (1999): Damage Detection with Spatial Wavelets, International Journal of Soils and Structures, Vol. 36(24), pp. 3443-3468

Wang, W.J.; and McFadden, P.D. (1996): Application of Wavelets to Gearbox Vibration Signals for Fault Detection, Journal of Sound and Vibration, Vol. 192(5), May 1996, pp. 927-939(13)

Welch, P.D. (1967): The use of Fast Fourier Transform for the Estimation of Power Spectra: a Method based on Time Averaging over short Modified Peridograms, IEEE Transaction on Audio and Electro-Acoustics, AU-15(2)

Worden, K.; and Dulieu-Barton, J.M. (2004): An Overview of Intelligent Fault Detection in Systems and Structures, Structural Health Monitoring, Vol. 3(1), pp. 85-98

Y

Yu, E.; Whang, D.H.; Venogupal, R.; Stewart, J.P.; and Wallace, J.W. (2004): Force-Vibration Testing using the Linear Shaker Seismic Simulation (LSSS) Testing Method, 13th World Conference on Earthquake Engineering, August 1-6, Vancouver, B.C., Canada, paper no.2206

Z

Zabel, V. (2003): Applications of Wavelet Analysis in System Identification, PhD, Faculty of Civil Engineering, Bauhaus-University

Zhang, Z.; and Aktan, H. M. (1995): The Damage Indices for Constructed Facilities, Proceedings of the 13th International Modal Analysis Conference, Tennessee, (2), pp. 1520–1529

Zonta, D. (2000): Structural Damage Detection and Localization by Using Vibrational Measurements, PhD Thesis, University of Bologna, Italy

Annex A

Annex of Chapter 4

Index of Annex A

A.1 Numerical Crack Simulation with Curvatures Calculated in the Middle Line of the Arch A.3
A.1.1 Model A – Crack at Position 4 ..... A.3
A.1.2 Model B – Crack between Positions 3 and 4 ..... A.6
A.1.3 Model C – Crack at Position 4 ..... A.9
A.2 Numerical Crack Simulation with Curvatures Calculated in the Arch Edges A.12
A.2.1 Model A – Crack at Position 4 ..... A.12
A.2.2 Model B – Crack between Positions 3 and 4 ..... A.15
A.2.3 Model C – Crack at Position 4 ..... A.18
A.3 Numerical Crack Simulation for Model B – Crack between Positions 3 and 4 – with Noise A.21
A.3.1 0.25% Noise for Frequencies and 1% Noise for Modal Displacements A.21
A.3.2 0.5% Noise for Frequencies and 2% Noise for Modal Displacements A.24

A.1 Numerical Crack Simulation with Curvatures Calculated in the Middle Line of the Arch

A.1.1 Model A – Crack at Position 4

A.1.1.1 Damage Scenario I (7.5 mm Crack Depth)

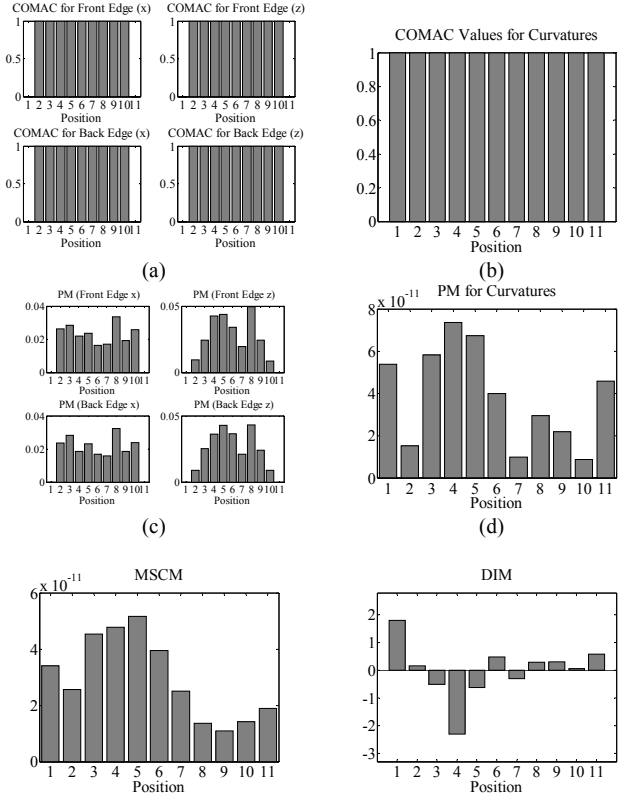


Figure A.1 – Model A, Damage Scenario I: (a) COMAC values for modal displacements; (b) COMAC values for modal curvatures; (c) PM for modal displacements; (d) PM for modal curvatures; (e) MSCM; and (f) DIM

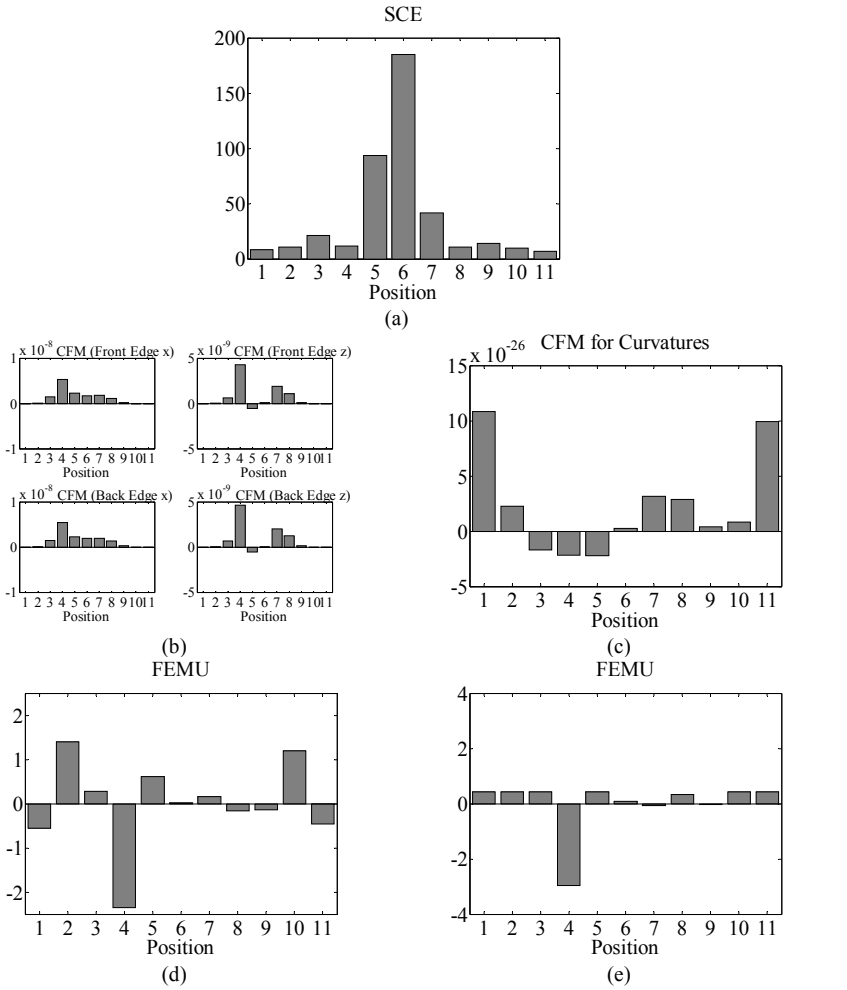


Figure A.2 – Model A, Damage Scenario I: (a) SCE; (b) CFM for modal displacements; (c) CFM for modal curvatures; (d) FEMU with unknown initial mechanical properties; and (e) FEMU with known initial mechanical properties

A.1.1.2 Damage Scenario II (15 mm Crack Depth)

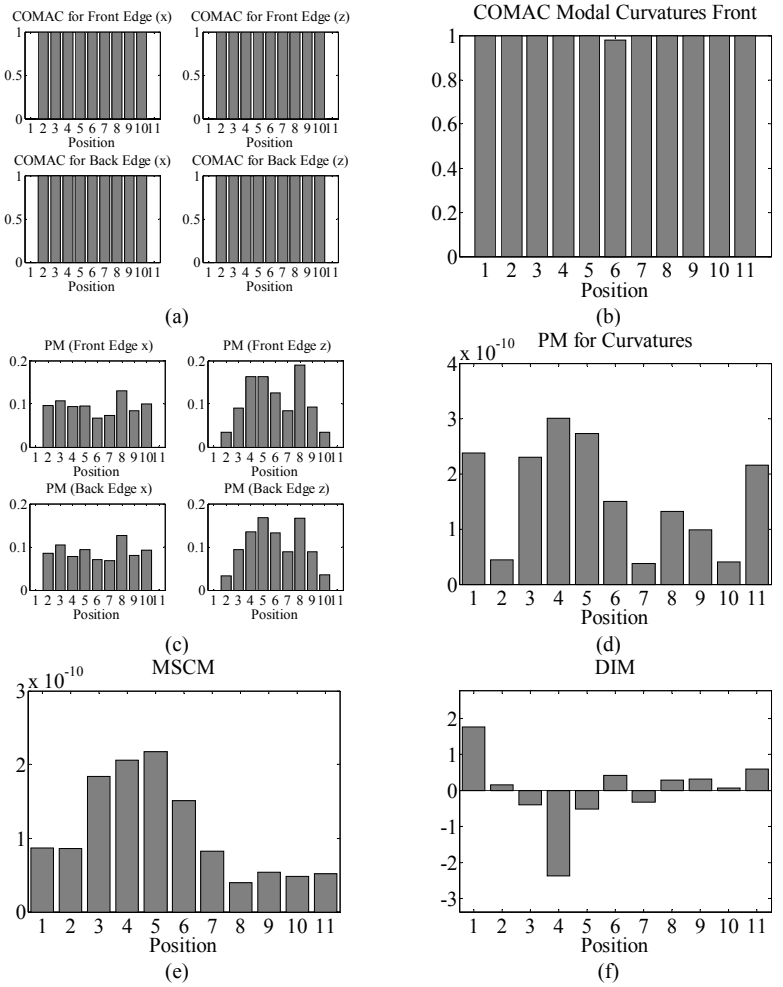


Figure A.3 – Model A, Damage Scenario II: (a) COMAC values for modal displacements; (b) COMAC values for modal curvatures; (c) PM for modal displacements; (d) PM for modal curvatures; (e) MSCM; and (f) DIM

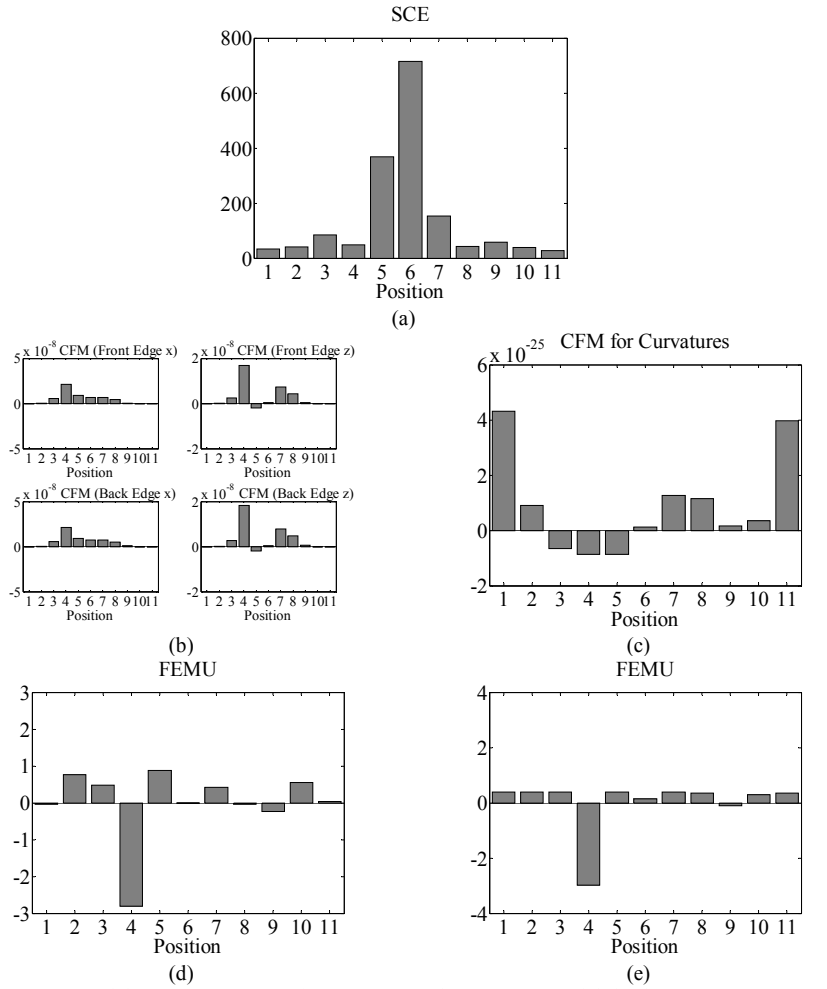


Figure A.4 – Model A, Damage Scenario II: (a) SCE; (b) CFM for modal displacements; (c) CFM for modal curvatures; (d) FEMU with unknown initial mechanical properties; and (e) FEMU with known initial mechanical properties

A.1.1.3 Damage Scenario III (30 mm Crack Depth)

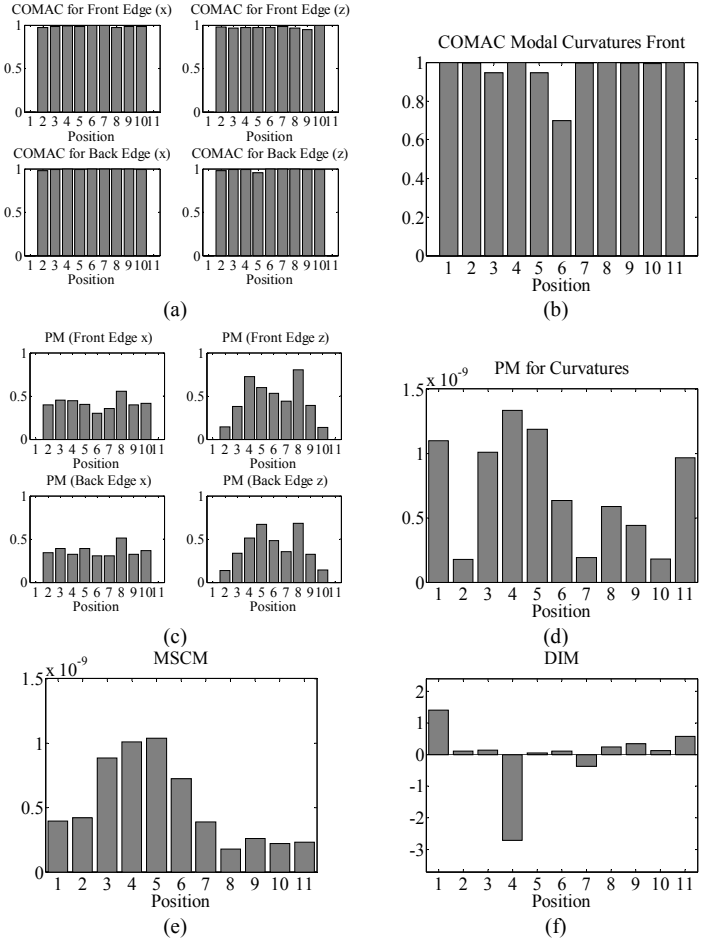


Figure A.5 – Model A, Damage Scenario III: (a) COMAC values for modal displacements; (b) COMAC values for modal curvatures; (c) PM for modal displacements; (d) PM for modal curvatures; (e) MSCM; and (f) DIM

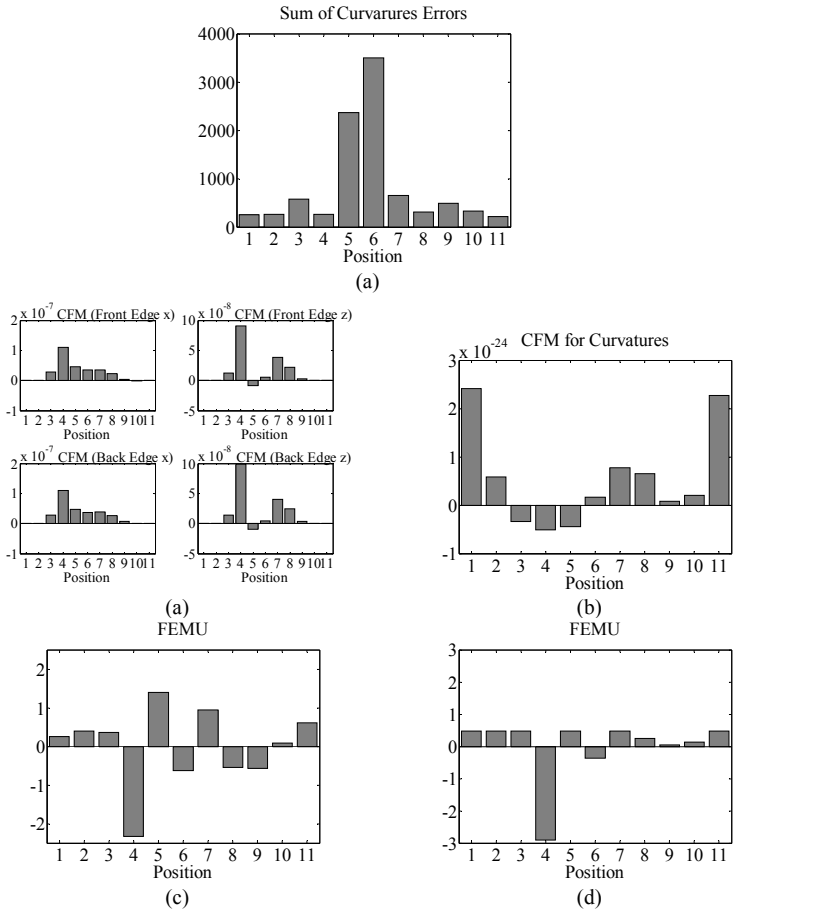


Figure A.6 – Model A, Damage Scenario III: (a) SCE; (b) CFM for modal displacements; (c) CFM for modal curvatures; (d) FEMU with unknown initial mechanical properties; and (e) FEMU with known initial mechanical properties

A.1.2 Model B – Crack between Positions 3 and 4

A.1.2.1 Damage Scenario I (7.5 mm Crack Depth)

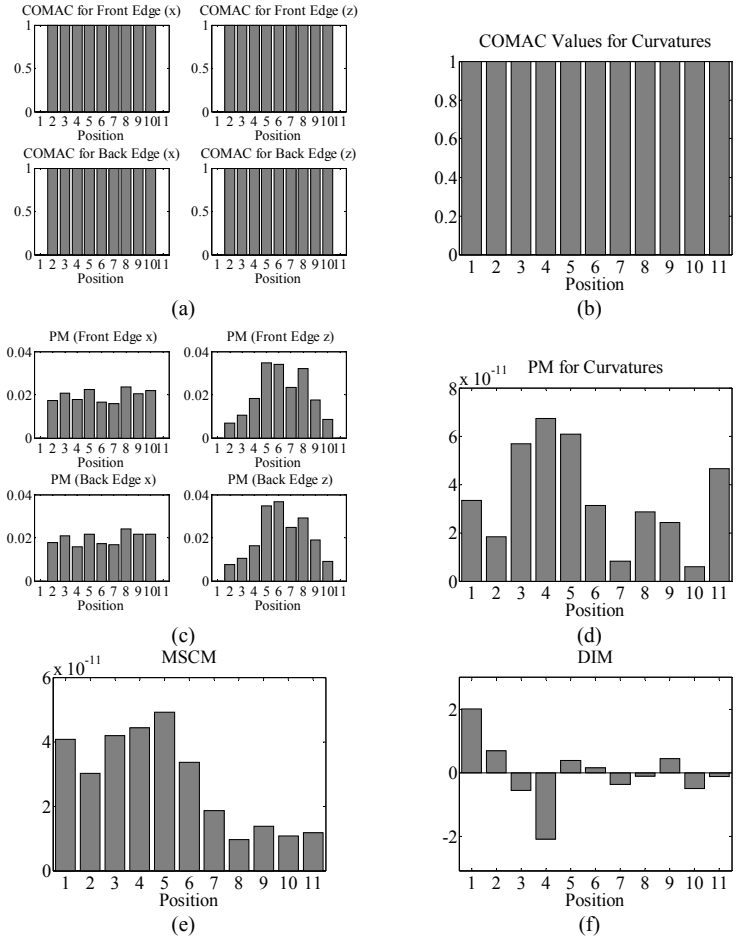


Figure A.7 – Model B, Damage Scenario I: (a) COMAC values for modal displacements; (b) COMAC values for modal curvatures; (c) PM for modal displacements; (d) PM for modal curvatures; (e) MSCM; and (f) DIM

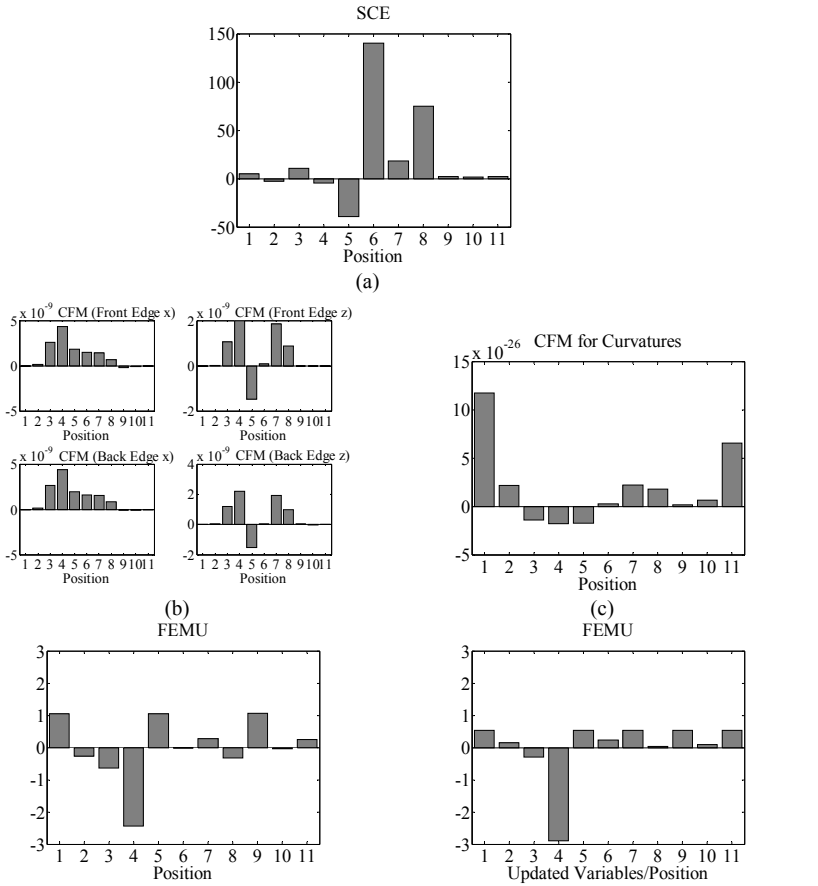


Figure A.8 – Model B, Damage Scenario I: (a) SCE; (b) CFM for modal displacements; (c) CFM for modal curvatures; (d) FEMU with unknown initial mechanical properties; and (e) FEMU with known initial mechanical properties

A.1.2.2 Damage Scenario II (15 mm Crack Depth)

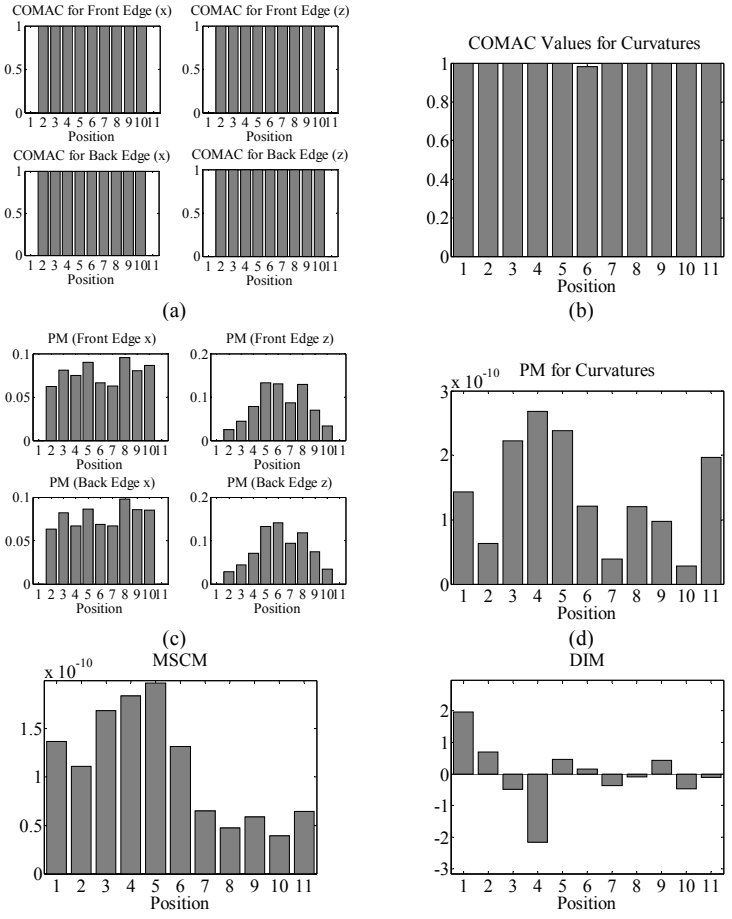


Figure A.9 – Model B, Damage Scenario II: (a) COMAC values for modal displacements; (b) COMAC values for modal curvatures; (c) PM for modal displacements; (d) PM for modal curvatures; (e) MSCM; and (f) DIM

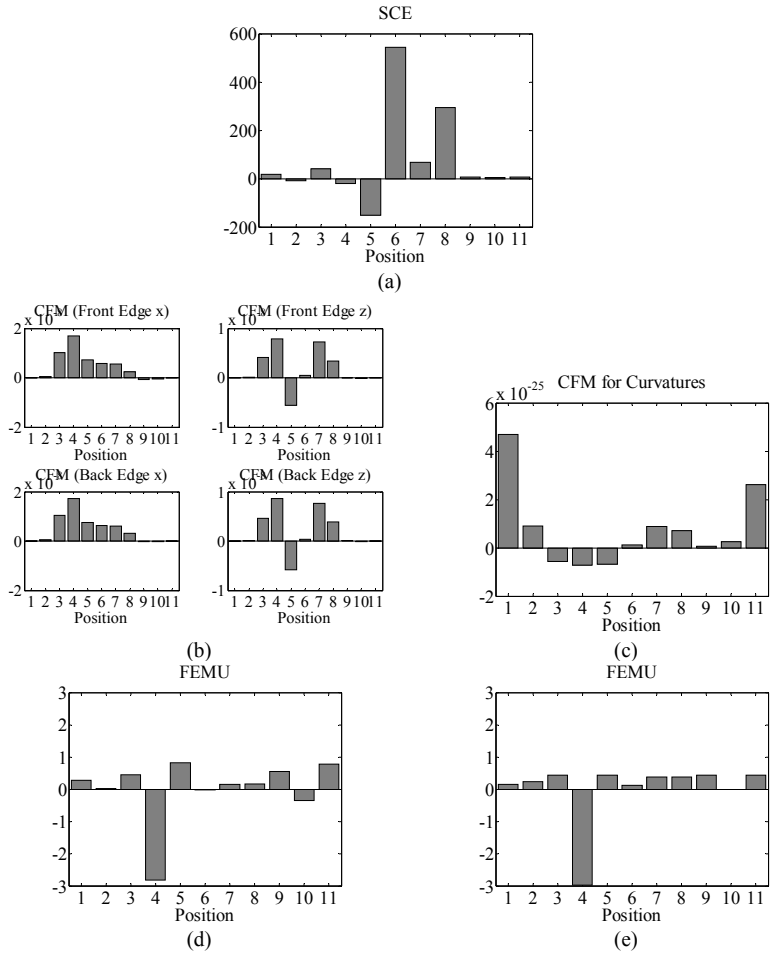


Figure A.10 – Model B, Damage Scenario II: (a) SCE; (b) CFM for modal displacements; (c) CFM for modal curvatures; (d) FEMU with unknown initial mechanical properties; and (e) FEMU with known initial mechanical properties

A.1.2.3 Damage Scenario III (30 mm Crack Depth)

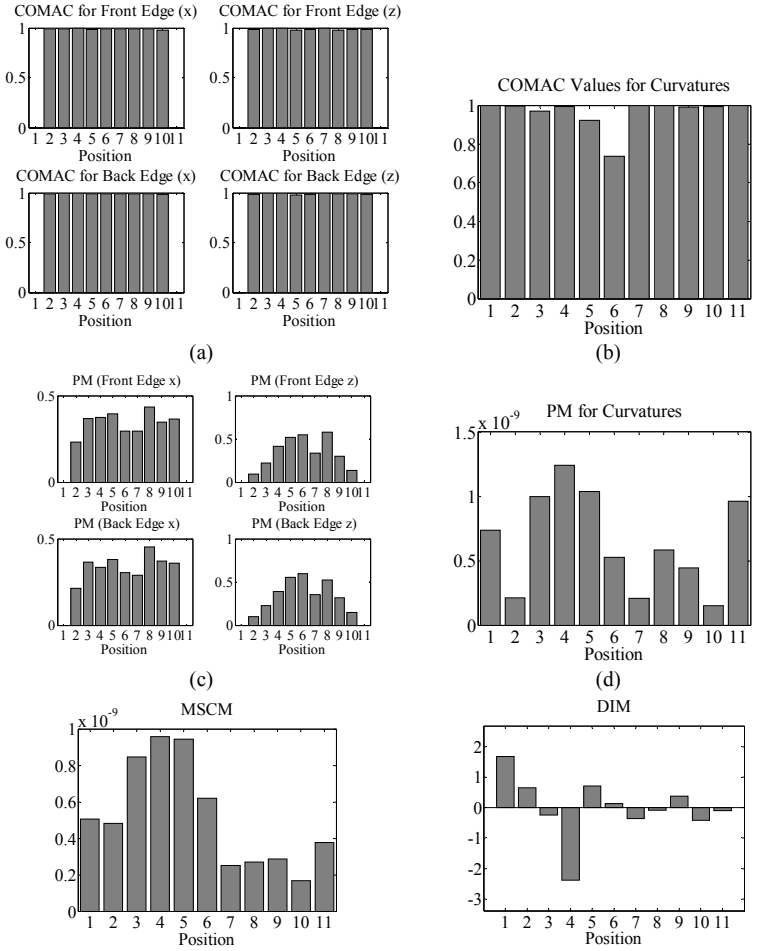


Figure A.11 – Model B, Damage Scenario III: (a) COMAC values for modal displacements; (b) COMAC values for modal curvatures; (c) PM for modal displacements; (d) PM for modal curvatures; (e) MSCM; and (f) DIM

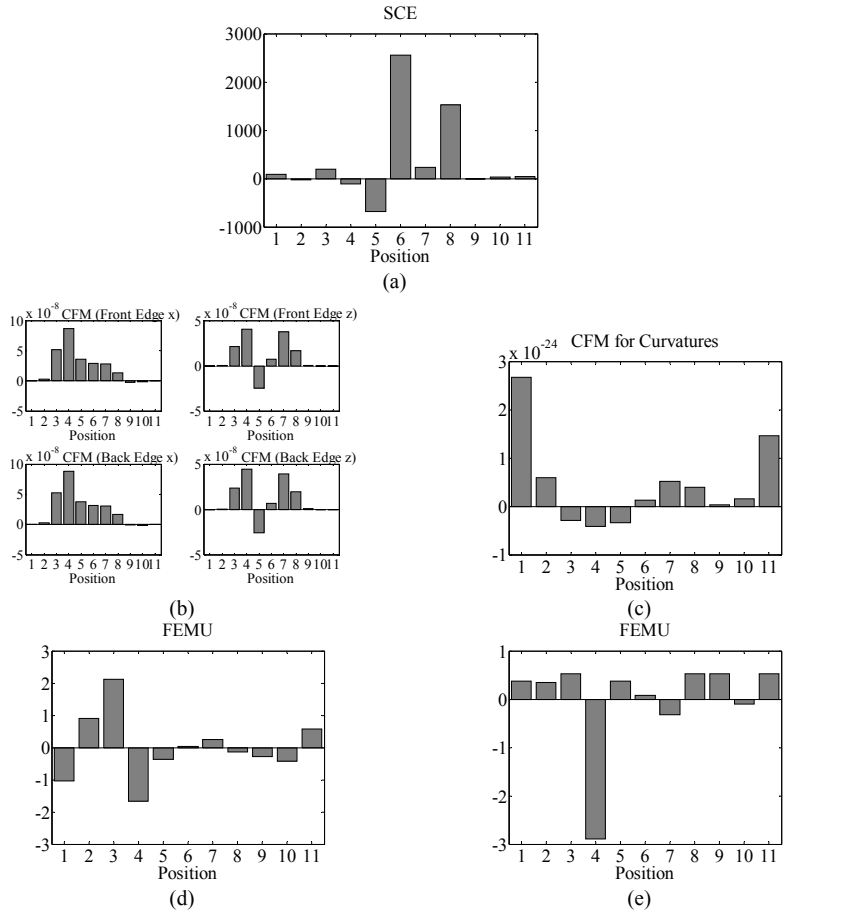


Figure A.12 – Model B, Damage Scenario III: (a) SCE; (b) CFM for modal displacements; (c) CFM for modal curvatures; (d) FEMU with unknown initial mechanical properties; and (e) FEMU with known initial mechanical properties

A.1.3 Model C – Crack at Position 4

A.1.3.1 Damage Scenario I (7.5 mm Crack Depth)

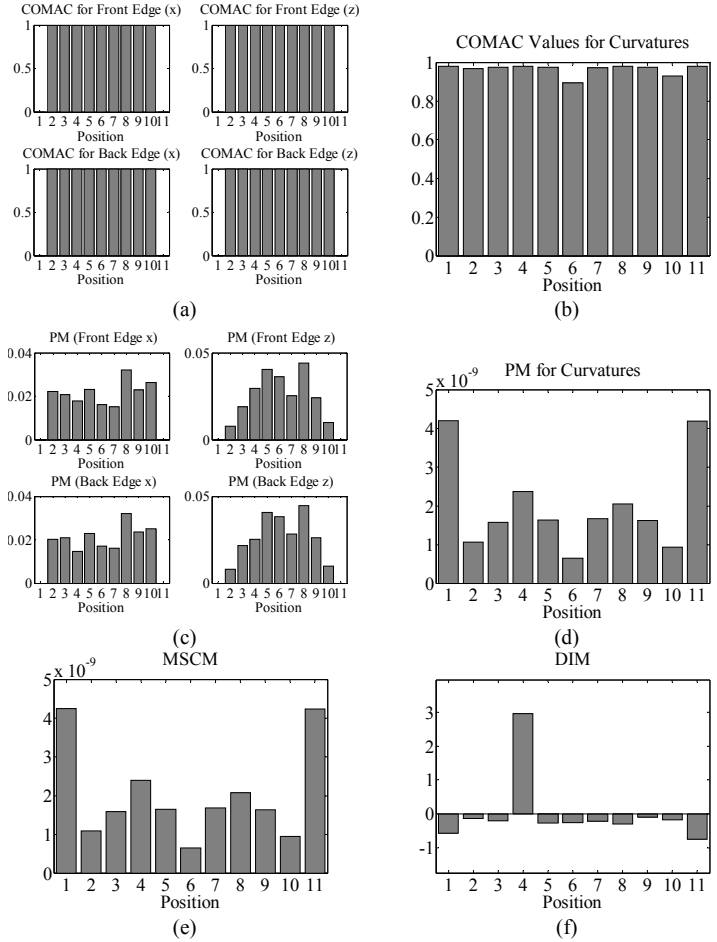


Figure A.13 – Model C, Damage Scenario I: (a) COMAC values for modal displacements; (b) COMAC values for modal curvatures; (c) PM for modal displacements; (d) PM for modal curvatures; (e) MSCM; and (f) DIM

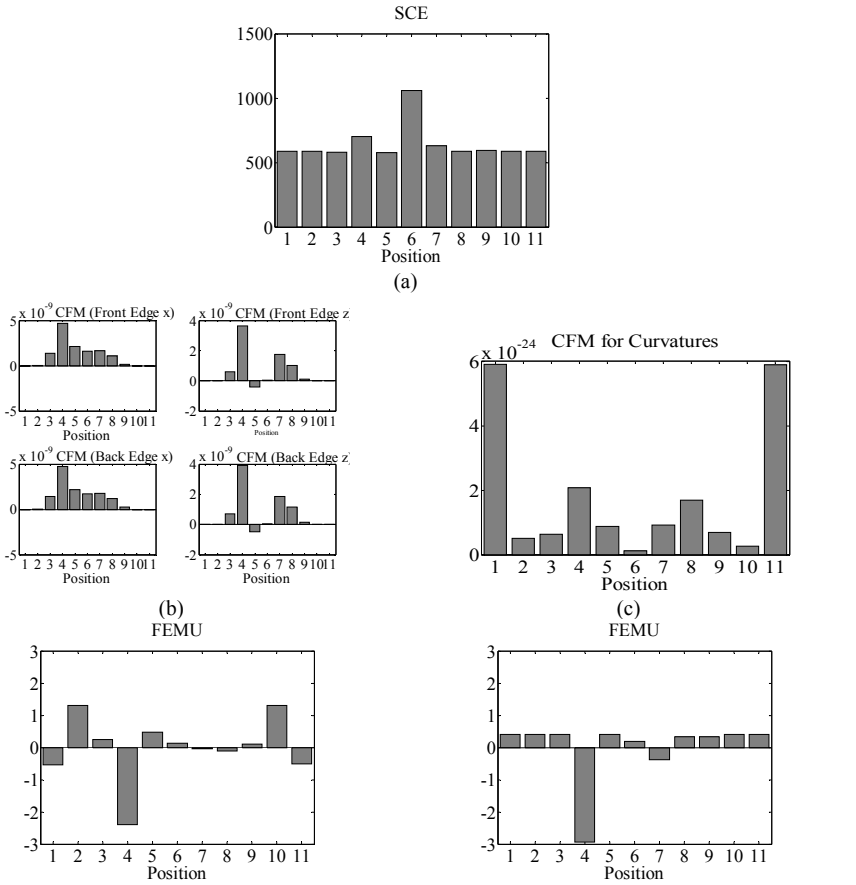


Figure A.14 – Model C, Damage Scenario I: (a) SCE; (b) CFM for modal displacements; (c) CFM for modal curvatures; (d) FEMU with unknown initial mechanical properties; and (e) FEMU with known initial mechanical properties

A.1.3.2 Damage Scenario II (15 mm Crack Depth)

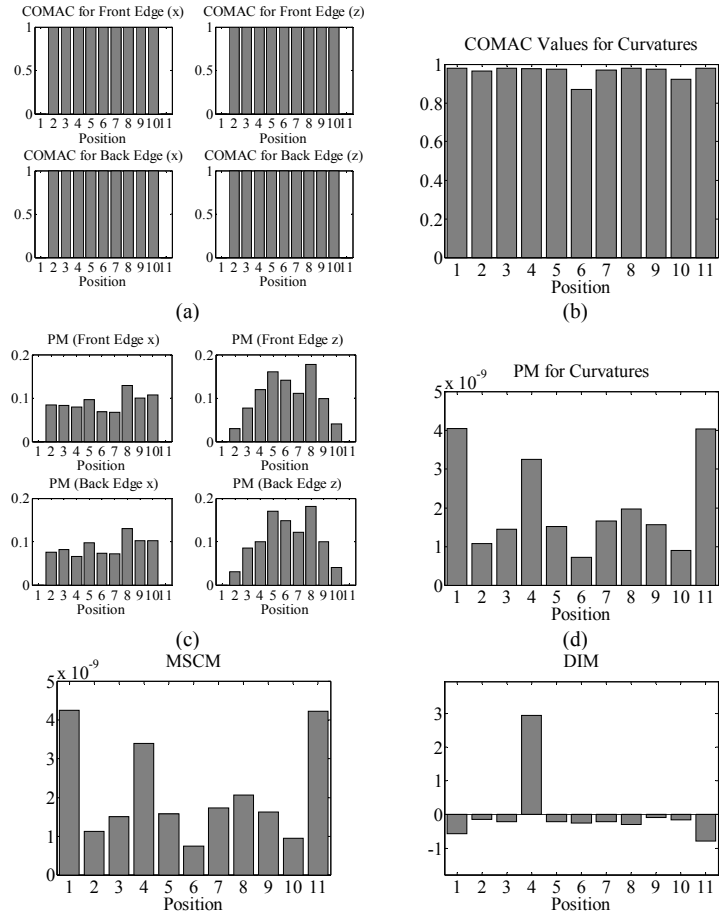


Figure A.15 – Model C, Damage Scenario II: (a) COMAC values for modal displacements; (b) COMAC values for modal curvatures; (c) PM for modal displacements; (d) PM for modal curvatures; (e) MSCM; and (f) DIM

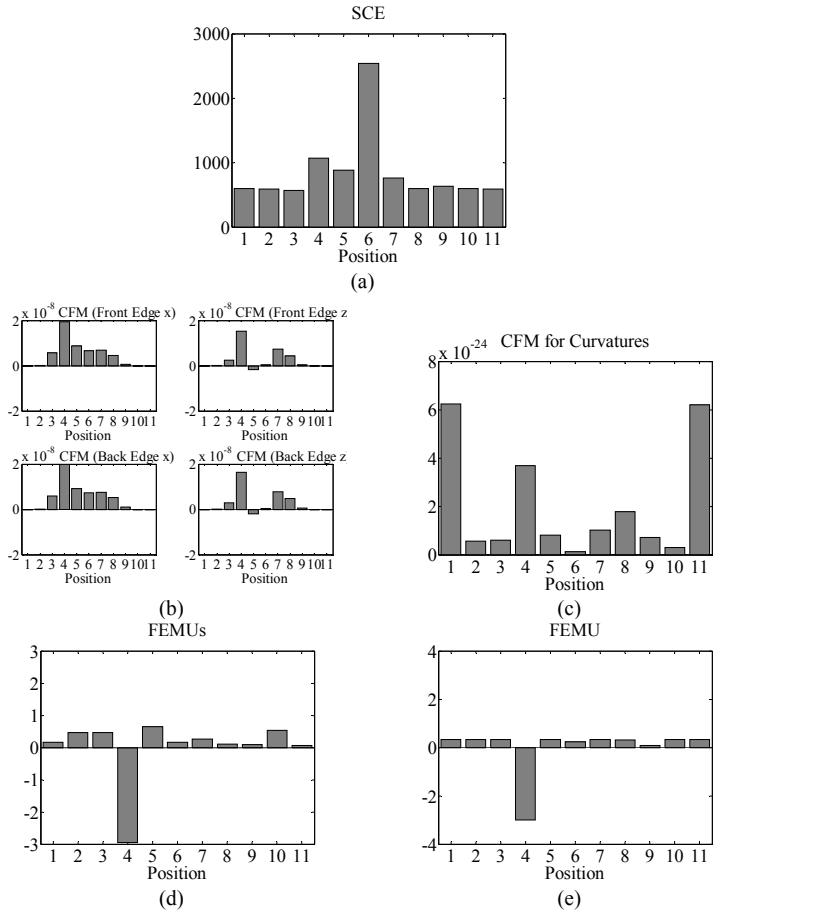


Figure A.16 – Model C, Damage Scenario II: (a) SCE; (b) CFM for modal displacements; (c) CFM for modal curvatures; (d) FEMU with unknown initial mechanical properties; and (e) FEMU with known initial mechanical properties

A.1.3.3 Damage Scenario III (30 mm Crack Depth)

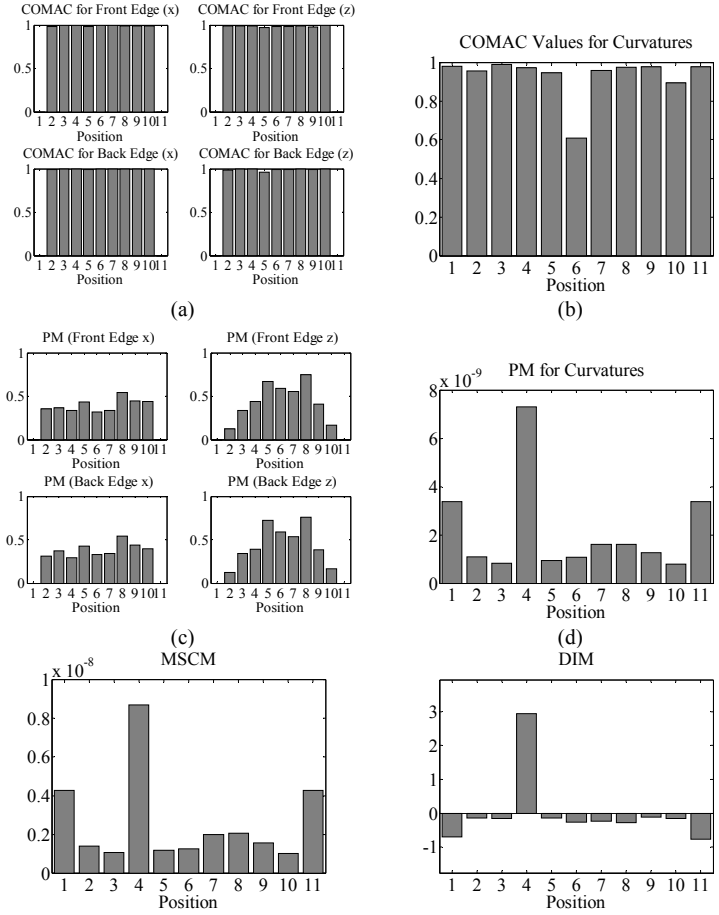


Figure A.17 – Model C, Damage Scenario III: (a) COMAC values for modal displacements; (b) COMAC values for modal curvatures; (c) PM for modal displacements; (d) PM for modal curvatures; (e) MSCM; and (f) DIM

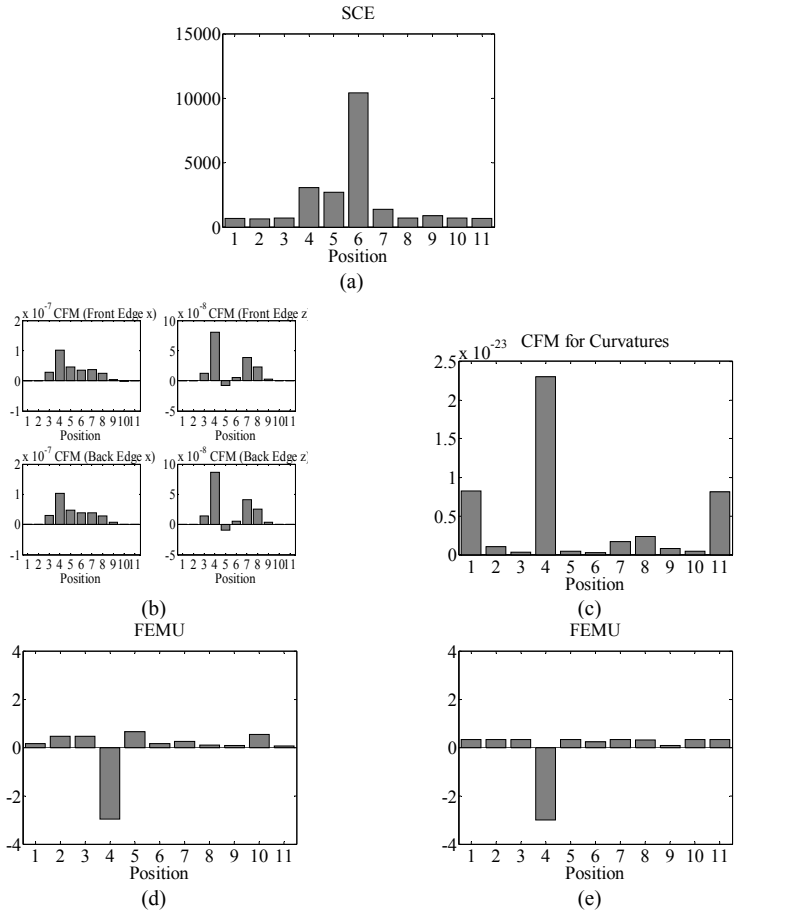


Figure A.18 – Model C, Damage Scenario III: (a) SCE; (b) CFM for modal displacements; (c) CFM for modal curvatures; (d) FEMU with unknown initial mechanical properties; and (e) FEMU with known initial mechanical properties

A.2 Numerical Crack Simulation with Curvatures Calculated in the Arch Edges

A.2.1 Model A – Crack at Position 4

A.2.1.1 Damage Scenario I (7.5 mm Crack Depth)

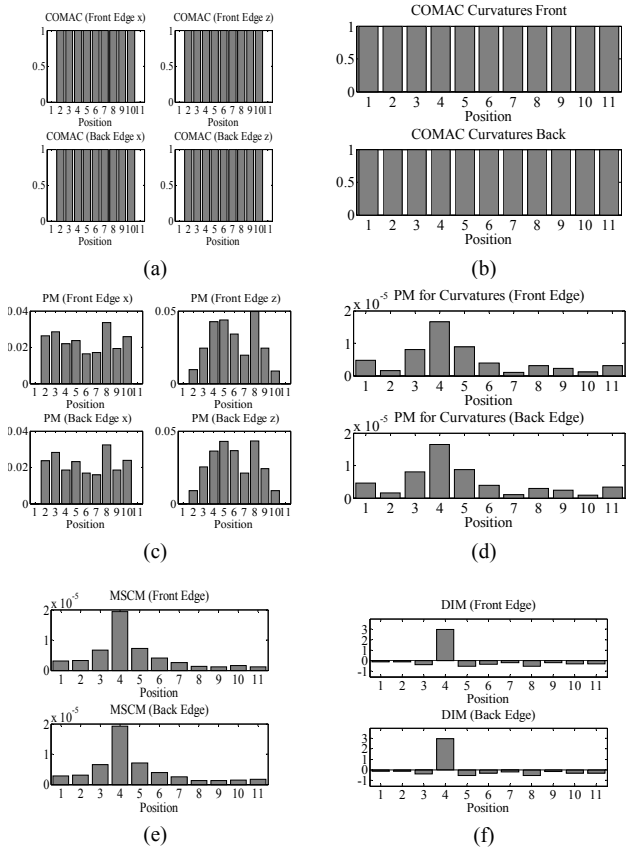


Figure A.19 – Model A, Damage Scenario I: (a) COMAC values for modal displacements; (b) COMAC values for modal curvatures; (c) PM for modal displacements; (d) PM for modal curvatures; (e) MSCM; and (f) DIM

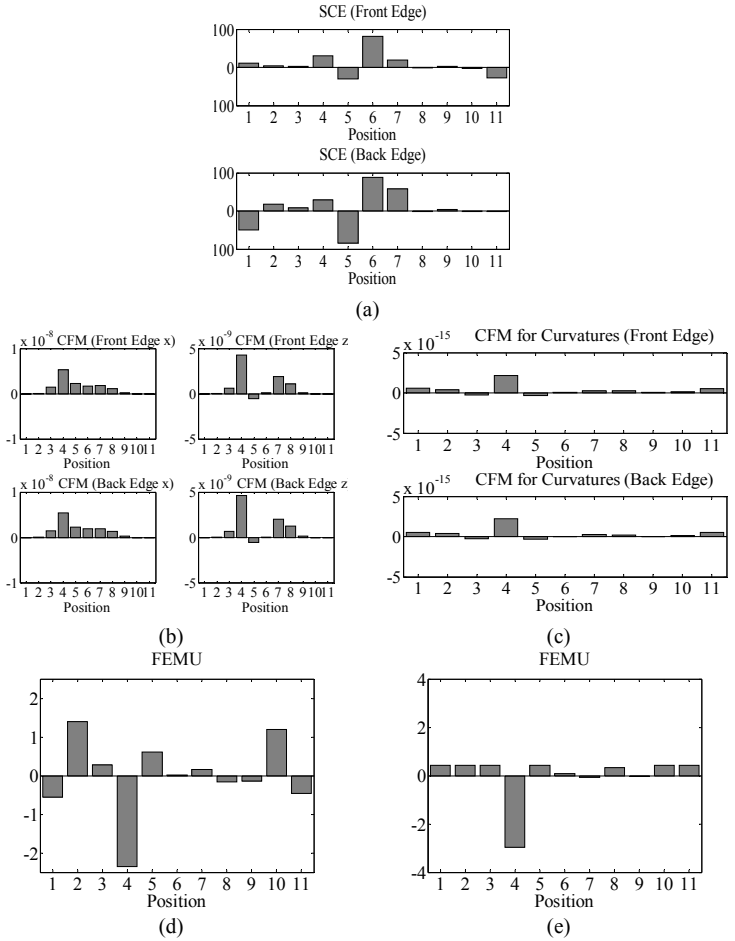


Figure A.20 – Model A, Damage Scenario I: (a) SCE; (b) CFM for modal displacements; (c) CFM for modal curvatures; (d) FEMU with unknown initial mechanical properties; and (e) FEMU with known initial mechanical properties

A.2.1.2 Damage Scenario II (15 mm Crack Depth)

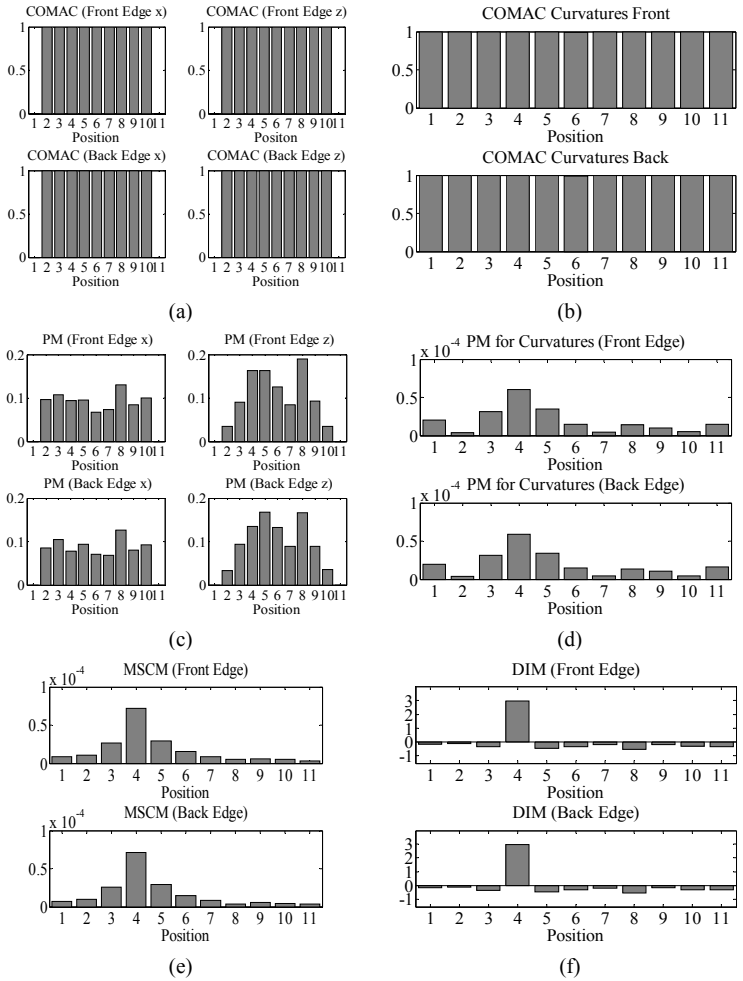


Figure A.21 – Model A, Damage Scenario II: (a) COMAC values for modal displacements; (b) COMAC values for modal curvatures; (c) PM for modal displacements; (d) PM for modal curvatures; (e) MSCM; and (f) DIM

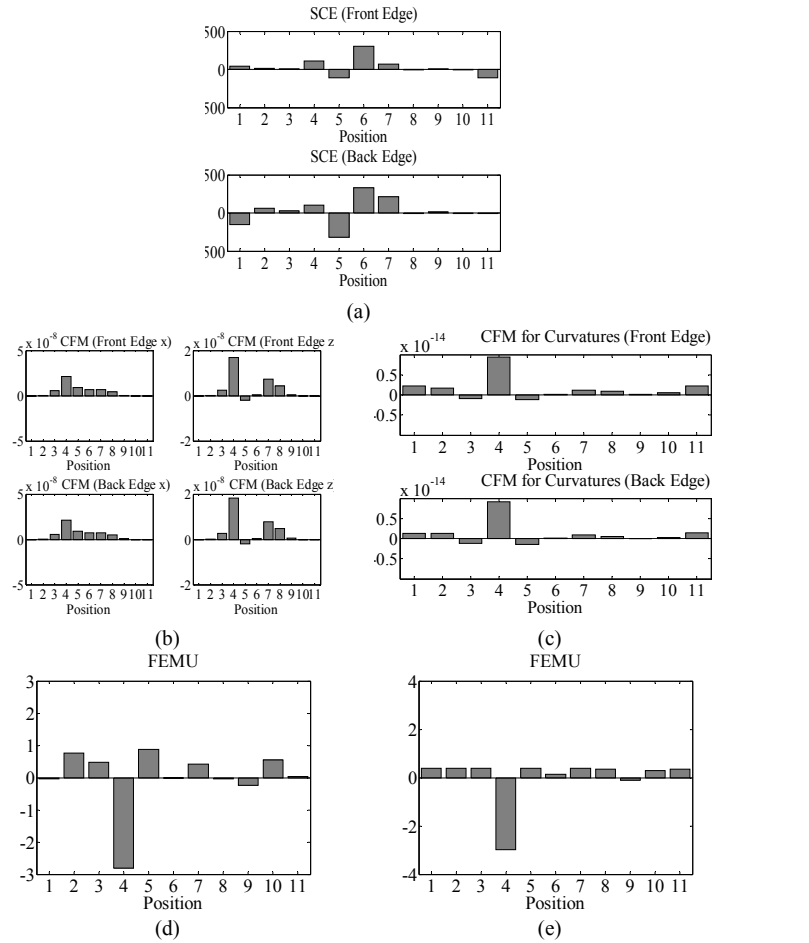


Figure A.22 – Model A, Damage Scenario II: (a) SCE; (b) CFM for modal displacements; (c) CFM for modal curvatures; (d) FEMU with unknown initial mechanical properties; and (e) FEMU with known initial mechanical properties

A.2.1.3 Damage Scenario III (30 mm Crack Depth)

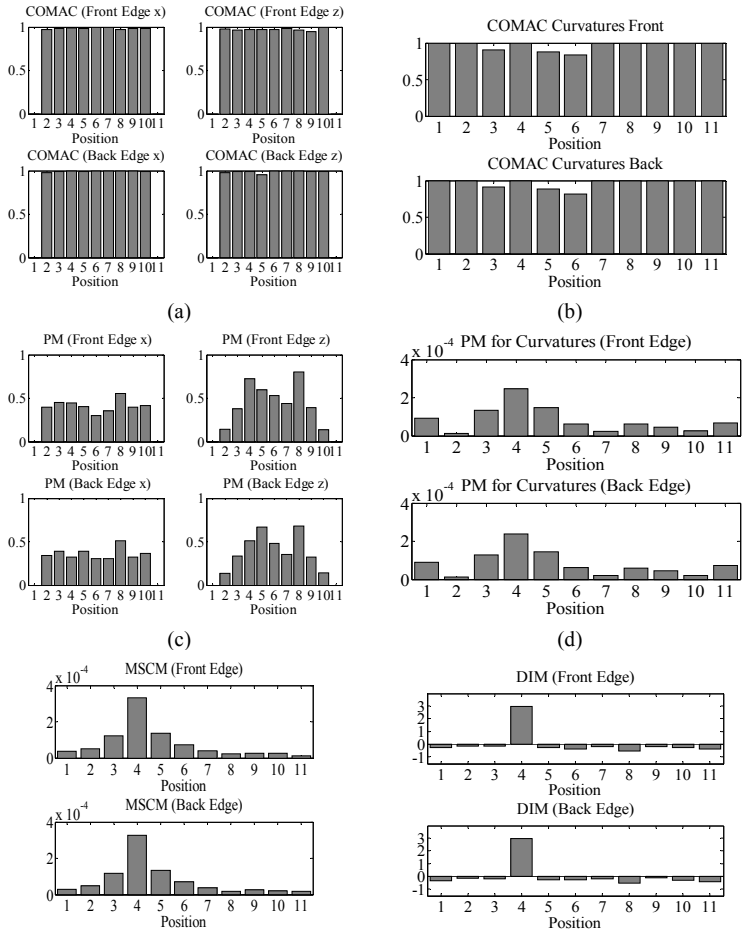


Figure A.23 – Model A, Damage Scenario III: (a) COMAC values for modal displacements; (b) COMAC values for modal curvatures; (c) PM for modal displacements; (d) PM for modal curvatures; (e) MSCM; and (f) DIM

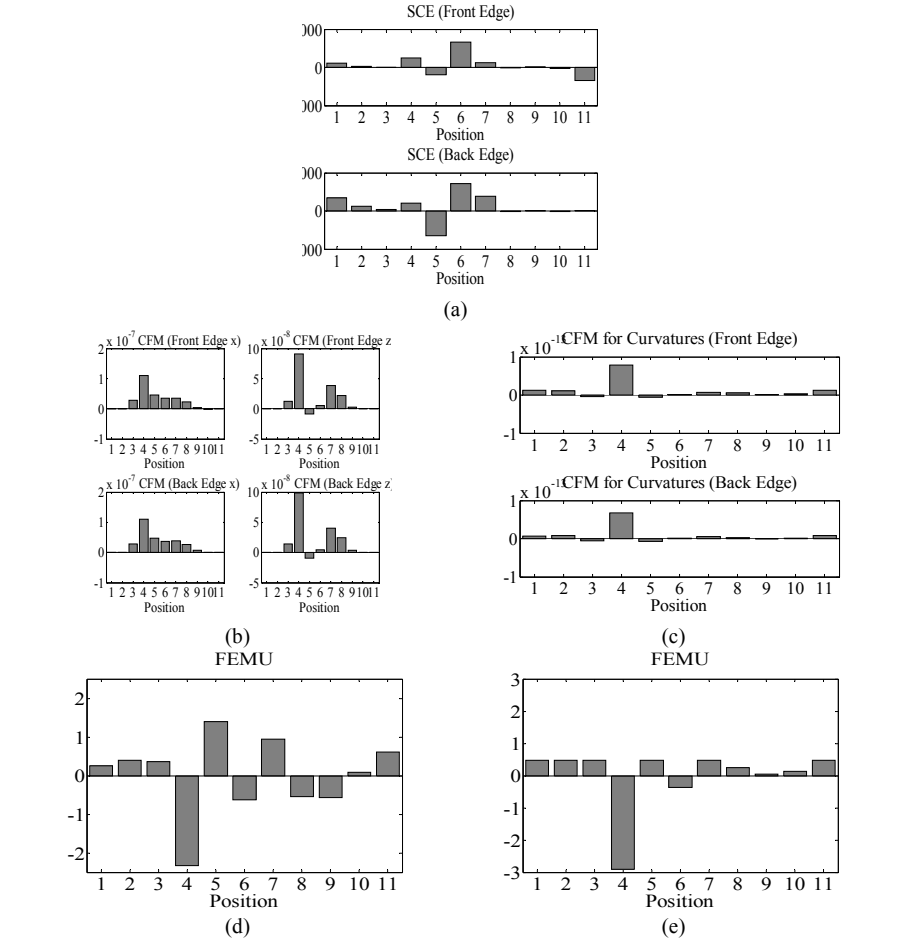


Figure A.24 – Model A, Damage Scenario III: (a) SCE; (b) CFM for modal displacements; (c) CFM for modal curvatures; (d) FEMU with unknown initial mechanical properties; and (e) FEMU with known initial mechanical properties

A.2.2 Model B – Crack between Positions 3 and 4

A.2.2.1 Damage Scenario I (7.5 mm Crack Depth)

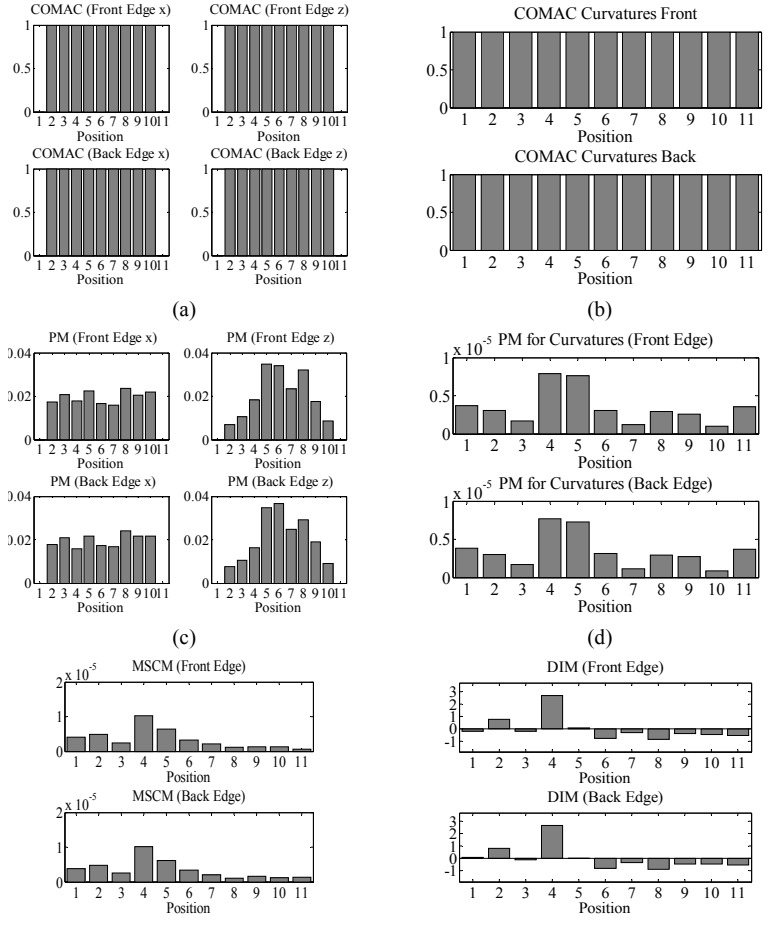


Figure A.25 – Model B, Damage Scenario I: (a) COMAC values for modal displacements; (b) COMAC values for modal curvatures; (c) PM for modal displacements; (d) PM for modal curvatures; (e) MSCM; and (f) DIM

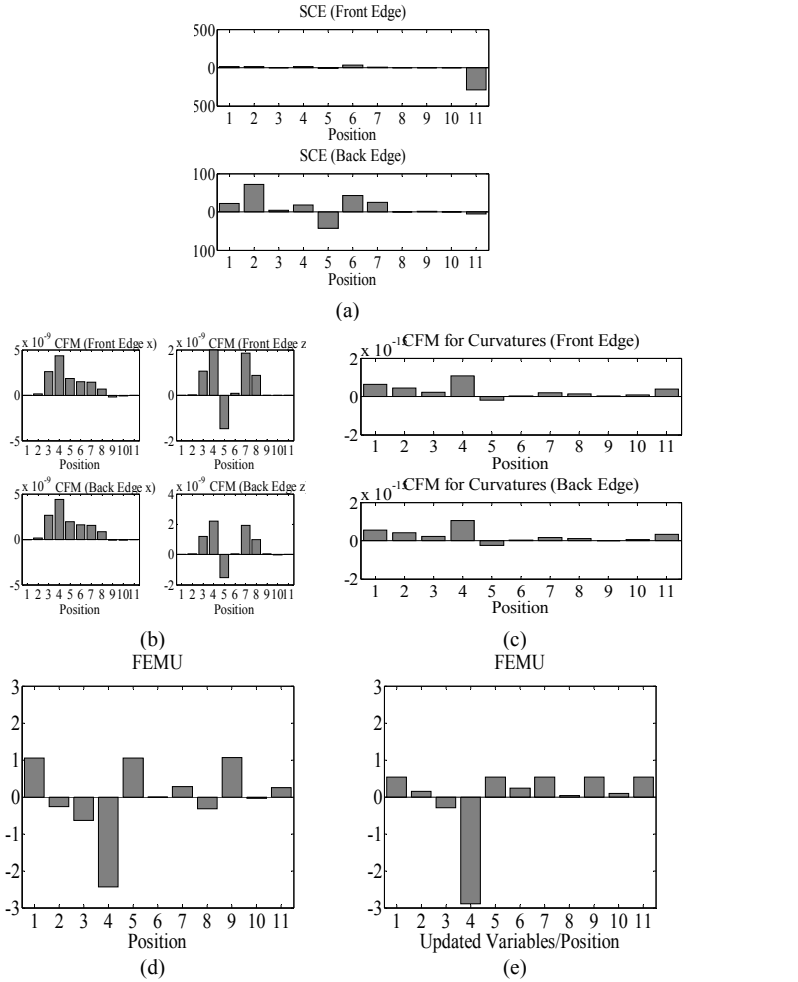


Figure A.26 – Model B, Damage Scenario I: (a) SCE; (b) CFM for modal displacements; (c) CFM for modal curvatures; (d) FEMU with unknown initial mechanical properties; and (e) FEMU with known initial mechanical properties

A.2.2.2 Damage Scenario II (15 mm Crack Depth)

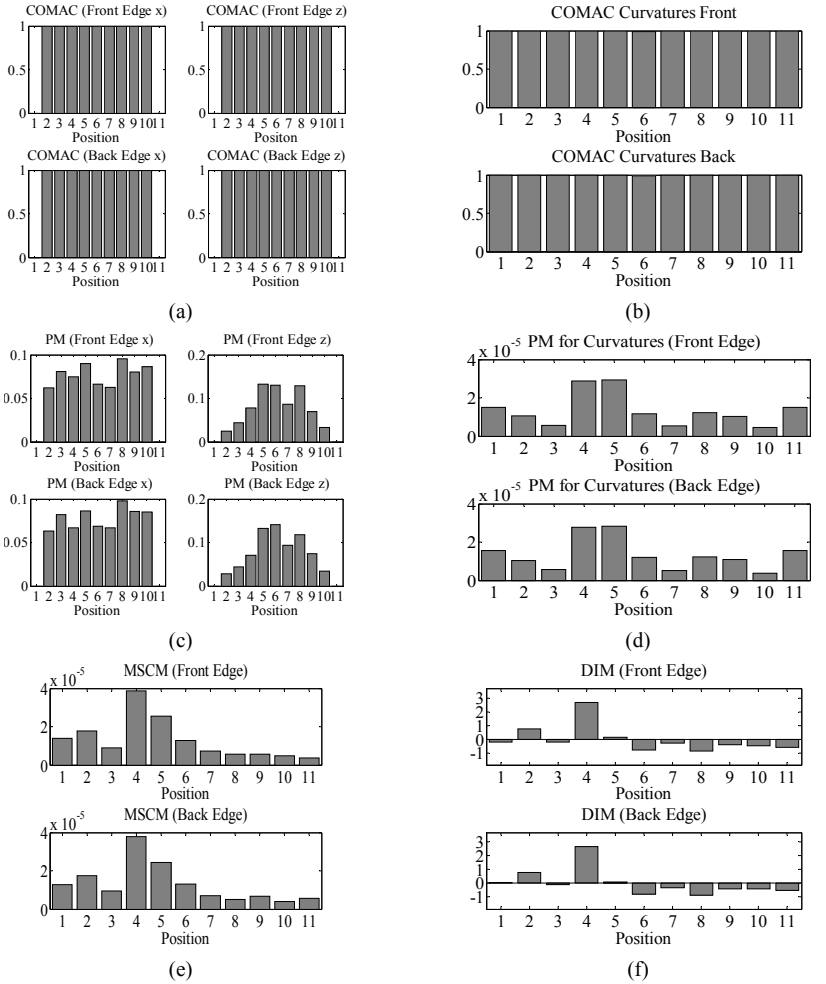


Figure A.27 – Model B, Damage Scenario II: (a) COMAC values for modal displacements; (b) COMAC values for modal curvatures; (c) PM for modal displacements; (d) PM for modal curvatures; (e) MSCM; and (f) DIM

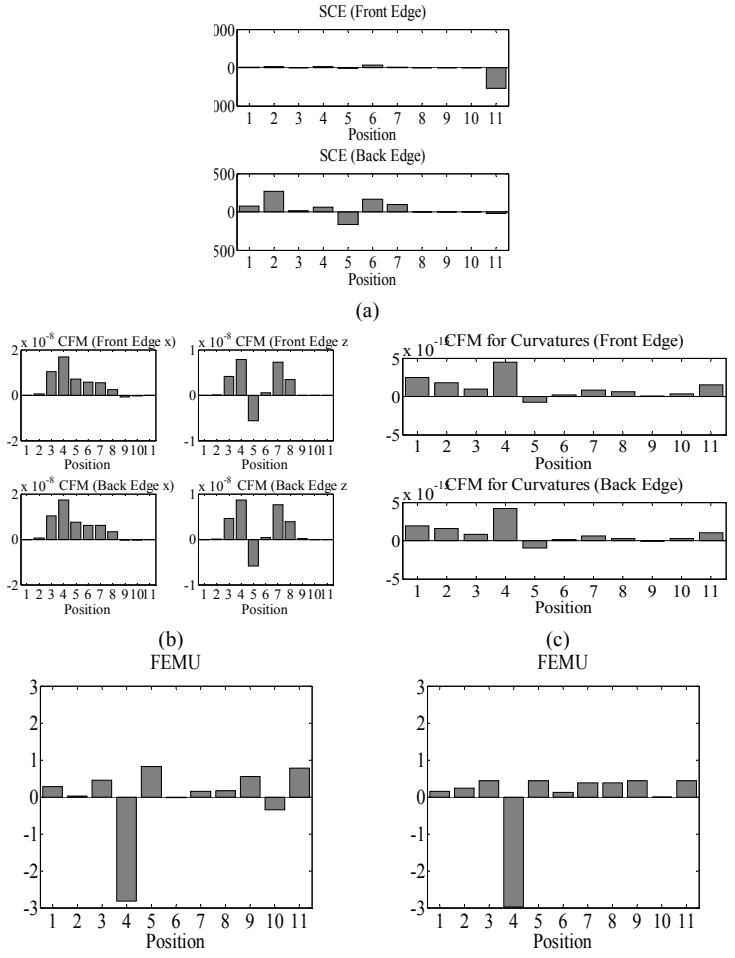


Figure A.28 – Model B, Damage Scenario II: (a) SCE; (b) CFM for modal displacements; (c) CFM for modal curvatures; (d) FEMU with unknown initial mechanical properties; and (e) FEMU with known initial mechanical properties

A.2.2.3 Damage Scenario III (30 mm Crack Depth)

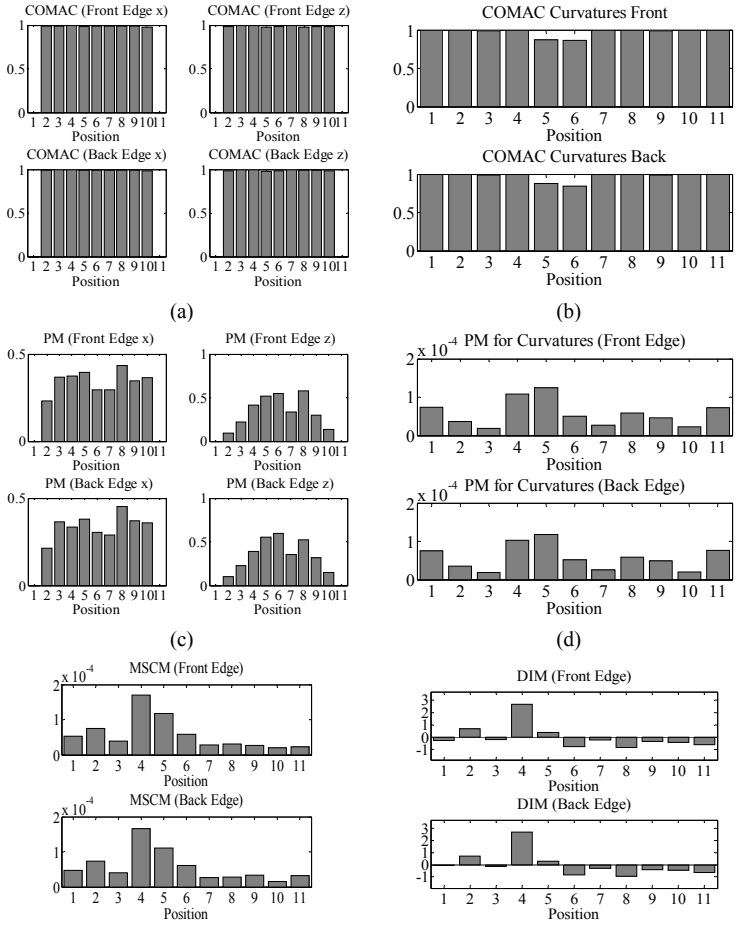


Figure A.29 – Model B, Damage Scenario III: (a) COMAC values for modal displacements; (b) COMAC values for modal curvatures; (c) PM for modal displacements; (d) PM for modal curvatures; (e) MSCM; and (f) DIM

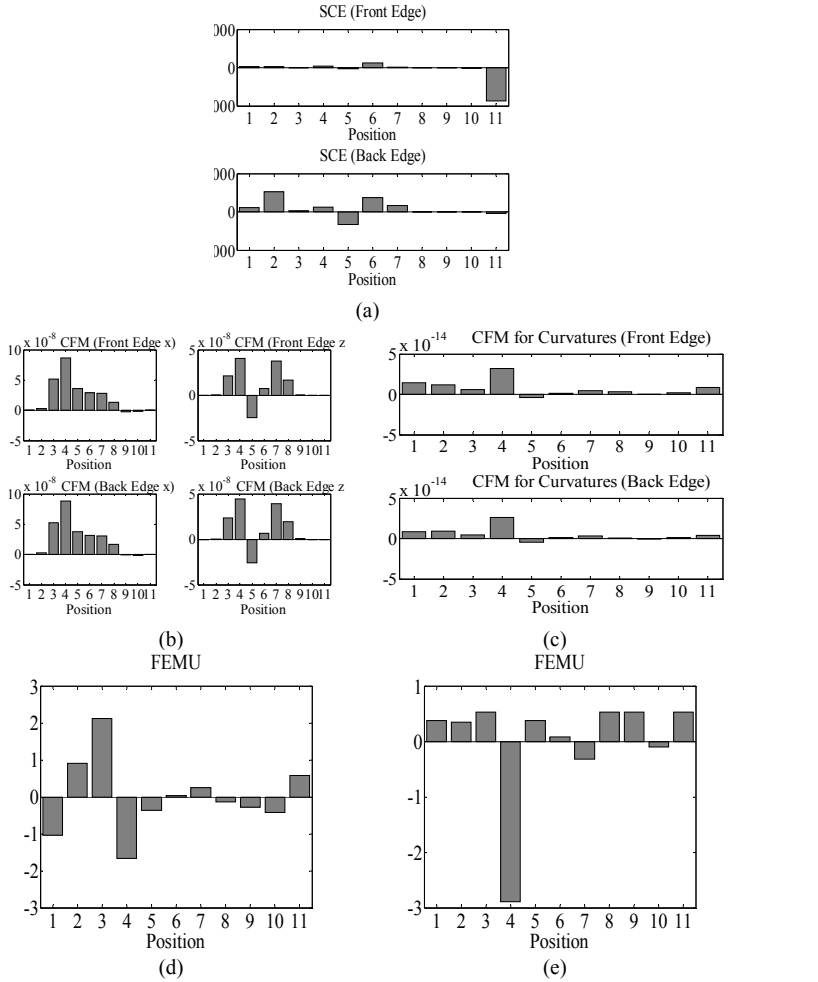


Figure A.30 – Model B, Damage Scenario III: (a) SCE; (b) CFM for modal displacements; (c) CFM for modal curvatures; (d) FEMU with unknown initial mechanical properties; and (e) FEMU with known initial mechanical properties

A.2.3 Model C – Crack at Position 4

A.2.3.1 Damage Scenario I (7.5 mm Crack Depth)

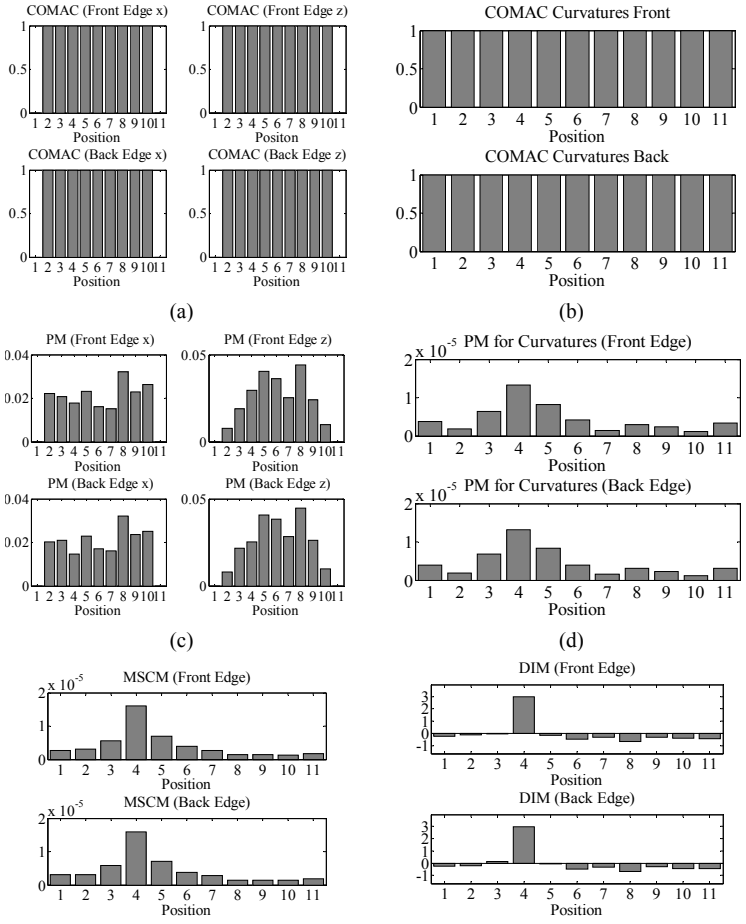


Figure A.31 – Model C, Damage Scenario I: (a) COMAC values for modal displacements; (b) COMAC values for modal curvatures; (c) PM for modal displacements; (d) PM for modal curvatures; (e) MSCM; and (f) DIM

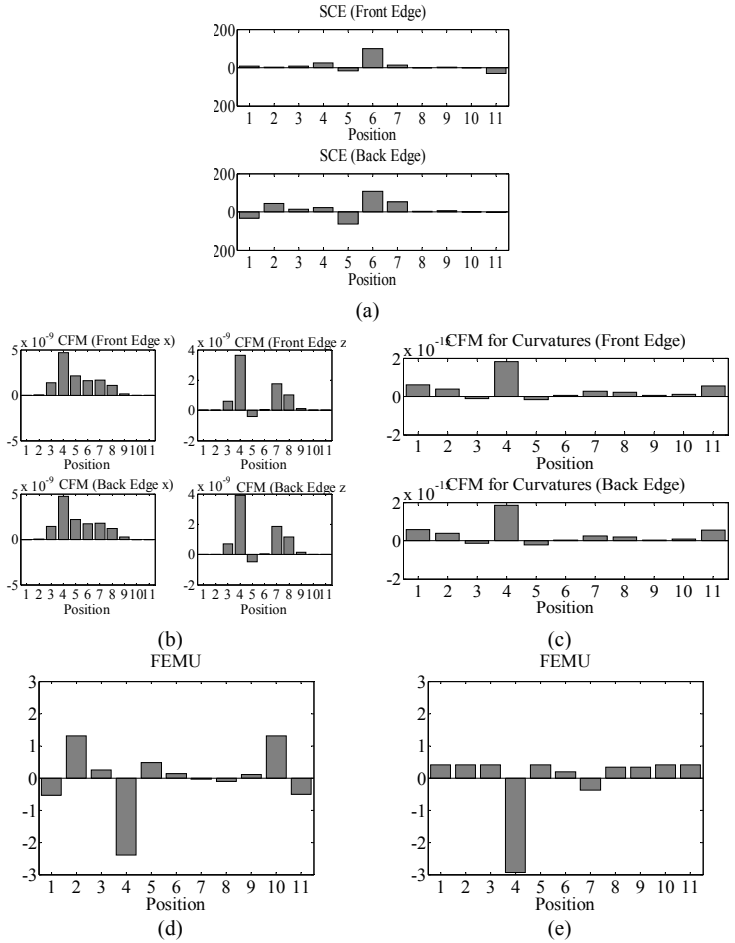


Figure A.32 – Model C, Damage Scenario I: (a) SCE; (b) CFM for modal displacements; (c) CFM for modal curvatures; (d) FEMU with unknown initial mechanical properties; and (e) FEMU with known initial mechanical properties

A.2.3.2 Damage Scenario II (15 mm Crack Depth)

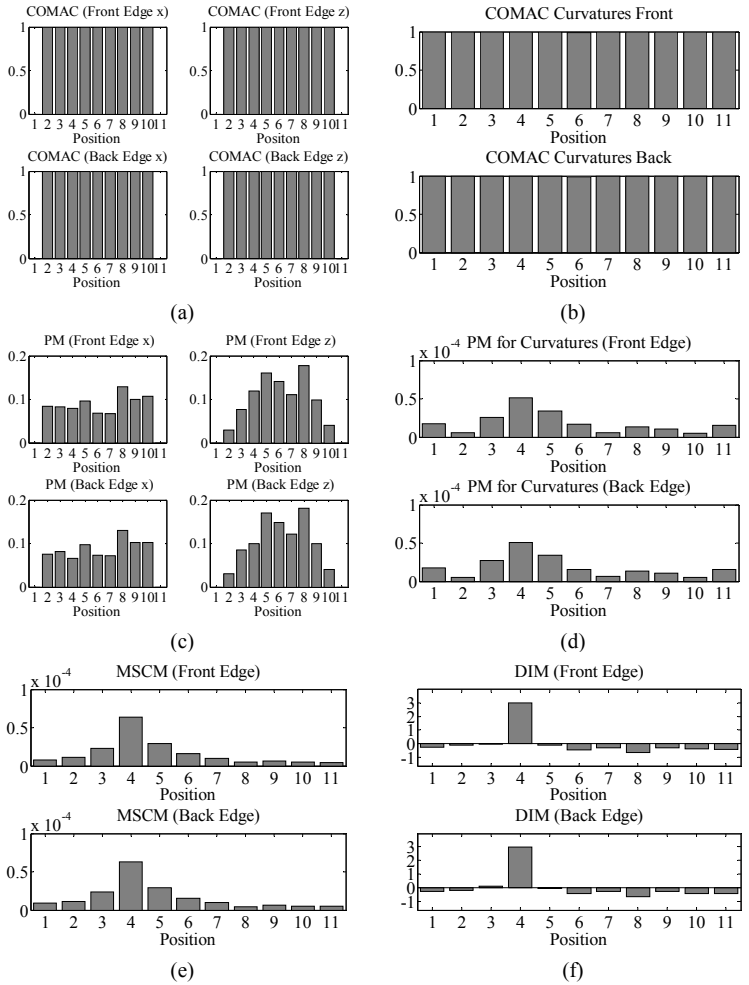


Figure A.33 – Model C, Damage Scenario II: (a) COMAC values for modal displacements; (b) COMAC values for modal curvatures; (c) PM for modal displacements; (d) PM for modal curvatures; (e) MSCM; and (f) DIM

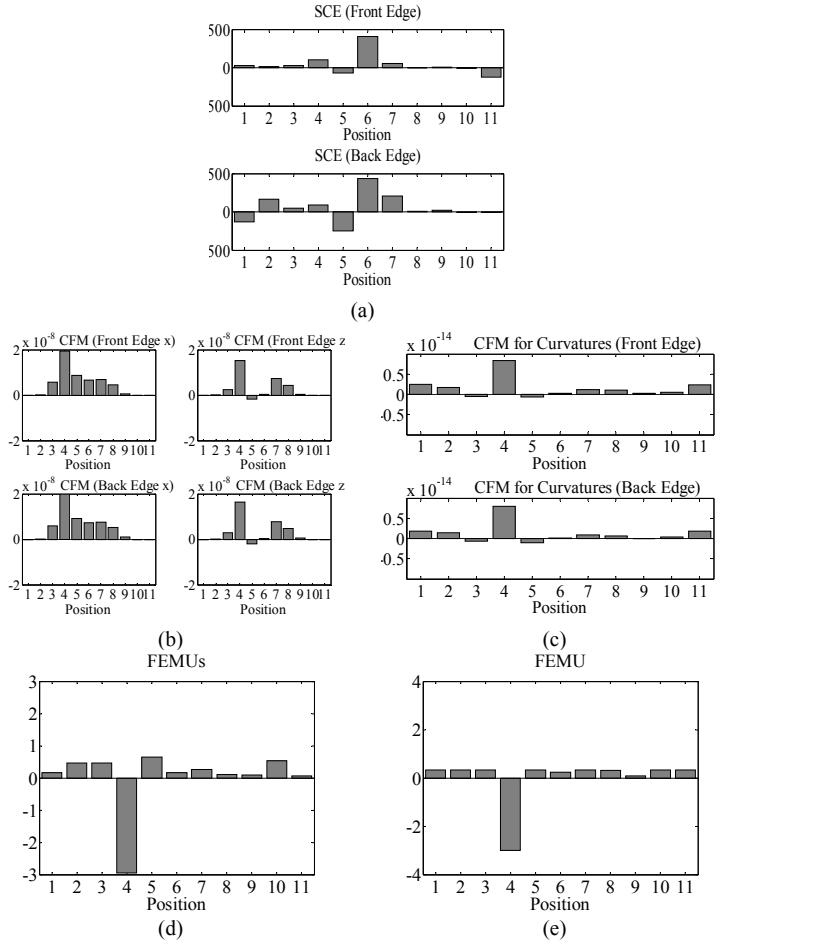


Figure A.34 – Model C, Damage Scenario II: (a) SCE; (b) CFM for modal displacements; (c) CFM for modal curvatures; (d) FEMU with unknown initial mechanical properties; and (e) FEMU with known initial mechanical properties

A.2.3.3 Damage Scenario III (30 mm Crack Depth)

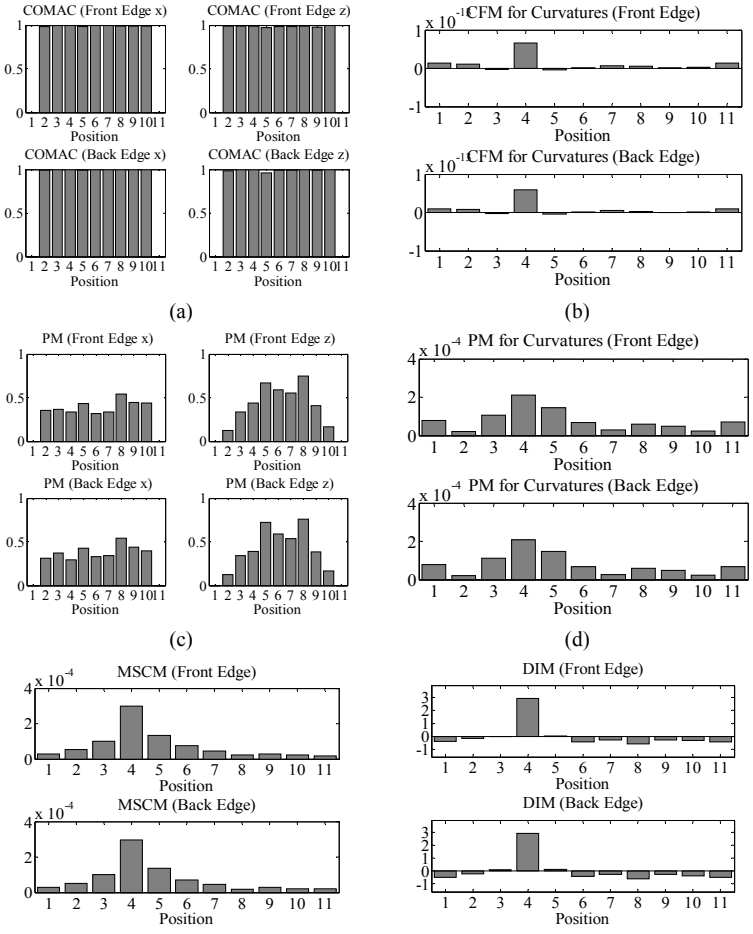


Figure A.35 – Model C, Damage Scenario III: (a) COMAC values for modal displacements; (b) COMAC values for modal curvatures; (c) PM for modal displacements; (d) PM for modal curvatures; (e) MSCM; and (f) DIM

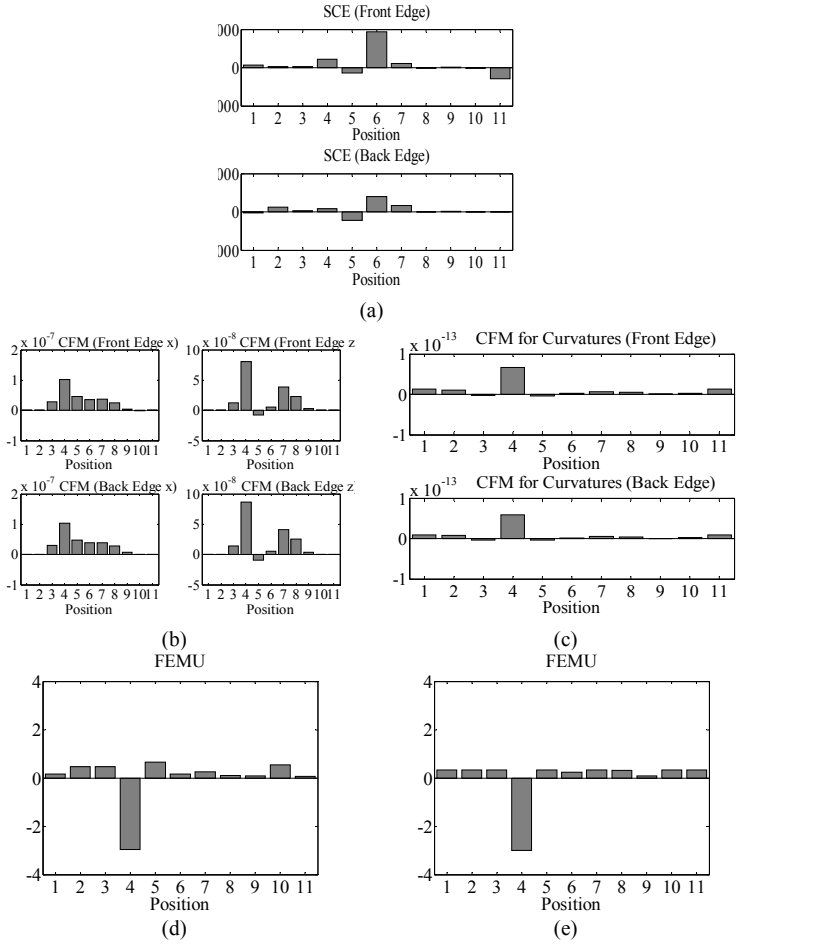


Figure A.36 – Model C, Damage Scenario III: (a) SCE; (b) CFM for modal displacements; (c) CFM for modal curvatures; (d) FEMU with unknown initial mechanical properties; and (e) FEMU with known initial mechanical properties

A.3 Numerical Crack Simulation for Model B – Crack between Positions 3 and 4 – with Noise

A.3.1 0.25% Noise for Frequencies and 1% Noise for Modal Displacements

A.3.1.1 Damage Scenario I (7.5 mm Crack Depth)

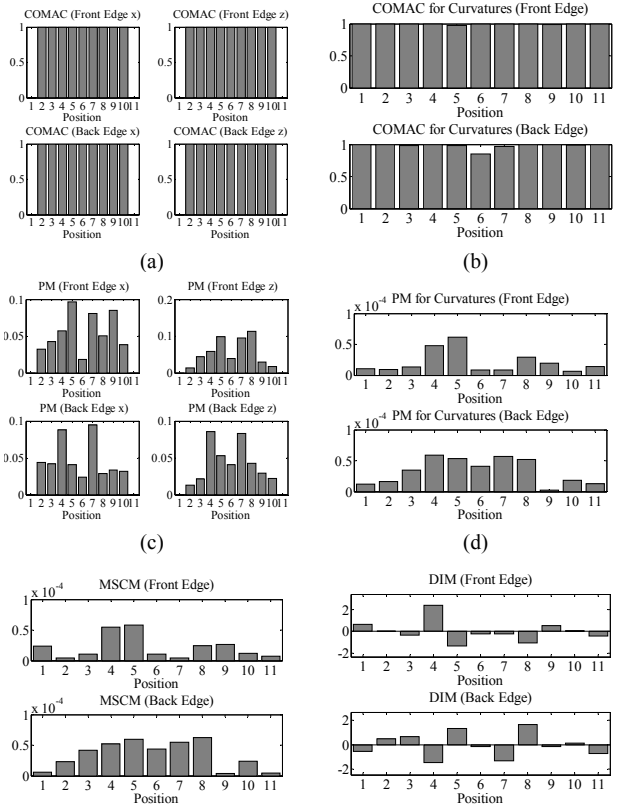


Figure A.37 – Model B, Damage Scenario I: (a) COMAC values for modal displacements; (b) COMAC values for modal curvatures; (c) PM for modal displacements; (d) PM for modal curvatures; (e) MSCM; and (f) DIM

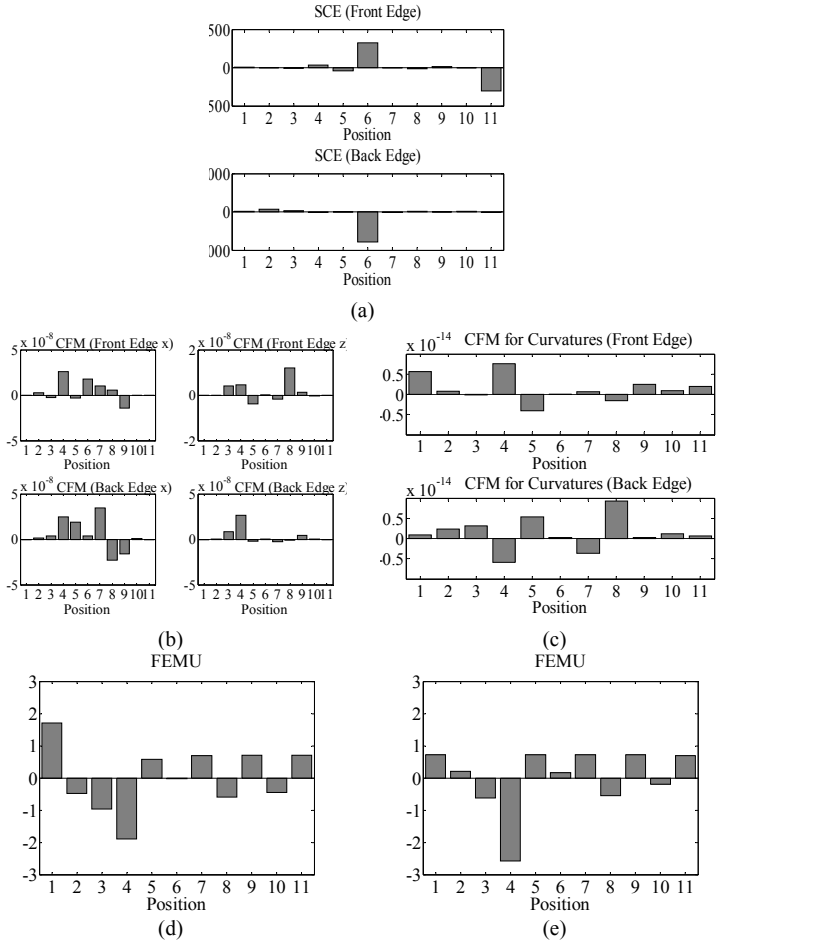


Figure A.38 – Model B, Damage Scenario I: (a) SCE; (b) CFM for modal displacements; (c) CFM for modal curvatures; (d) FEMU with unknown initial mechanical properties; and (e) FEMU with known initial mechanical properties

A.3.1.2 Damage Scenario II (15 mm Crack Depth)

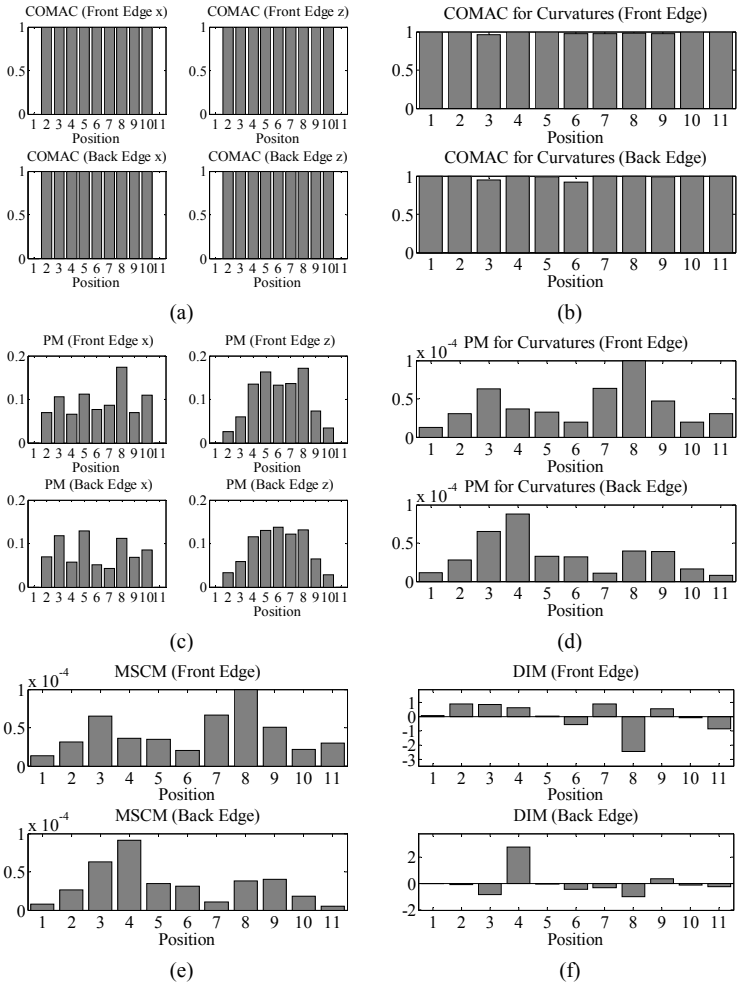


Figure A.39 – Model B, Damage Scenario II: (a) COMAC values for modal displacements; (b) COMAC values for modal curvatures; (c) PM for modal displacements; (d) PM for modal curvatures; (e) MSCM; and (f) DIM

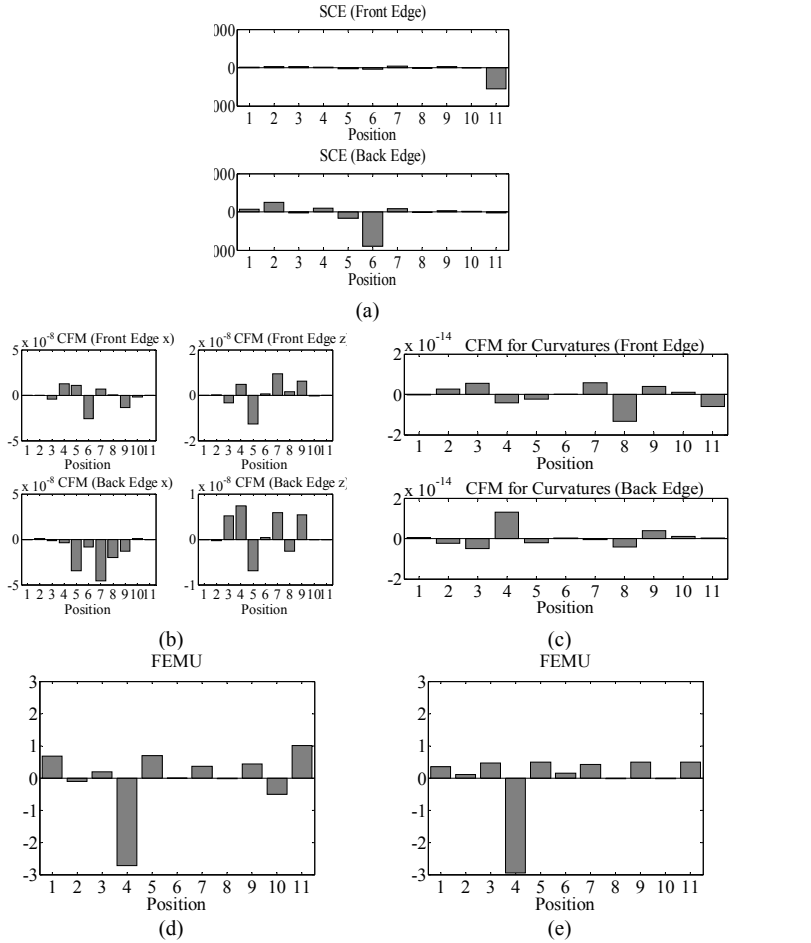


Figure A.40 – Model B, Damage Scenario II: (a) SCE; (b) CFM for modal displacements; (c) CFM for modal curvatures; (d) FEMU with unknown initial mechanical properties; and (e) FEMU with known initial mechanical properties

A.3.1.3 Damage Scenario III (30 mm Crack Depth)

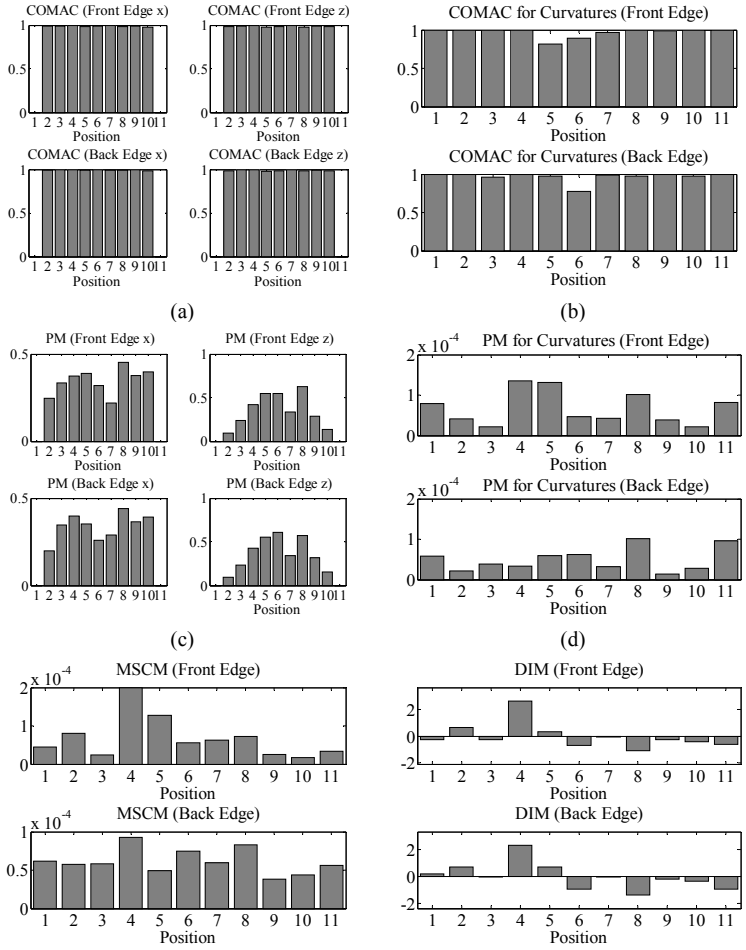


Figure A.41 – Model B, Damage Scenario III: (a) COMAC values for modal displacements; (b) COMAC values for modal curvatures; (c) PM for modal displacements; (d) PM for modal curvatures; (e) MSCM; and (f) DIM

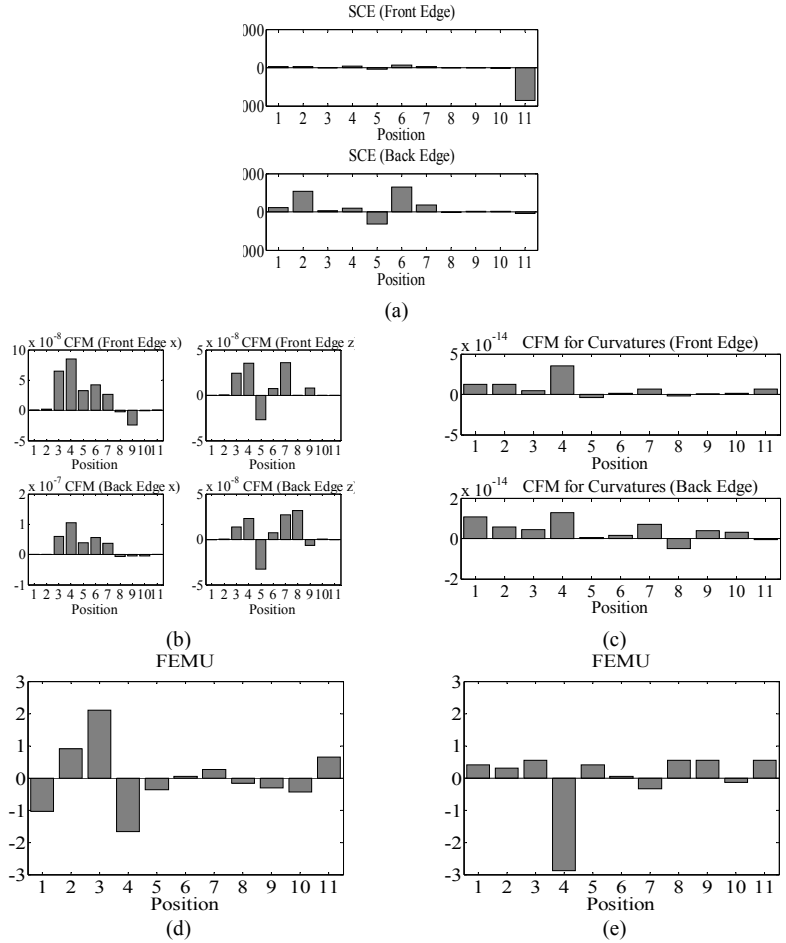


Figure A.42 – Model B, Damage Scenario III: (a) SCE; (b) CFM for modal displacements; (c) CFM for modal curvatures; (d) FEMU with unknown initial mechanical properties; and (e) FEMU with known initial mechanical properties

A.3.2 0.5% Noise for Frequencies and 2% Noise for Modal Displacements

A.3.2.1 Damage Scenario I (7.5 mm Crack Depth)

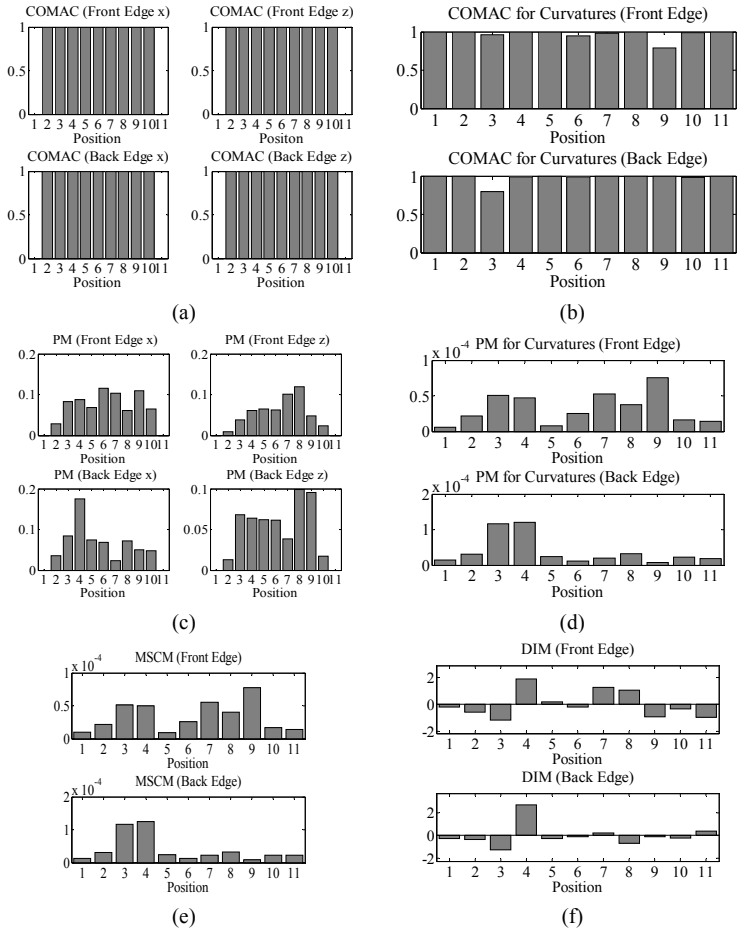


Figure A.43 – Model B, Damage Scenario I: (a) COMAC values for modal displacements; (b) COMAC values for modal curvatures; (c) PM for modal displacements; (d) PM for modal curvatures; (e) MSCM; and (f) DIM

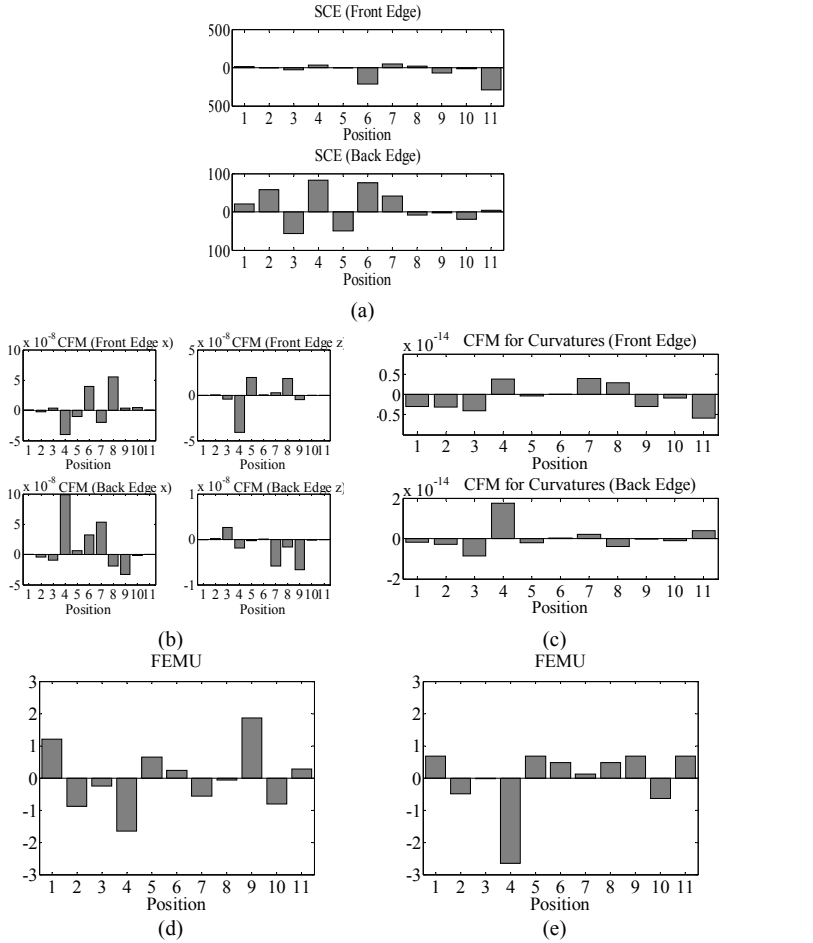


Figure A.44 – Model B, Damage Scenario I: (a) SCE; (b) CFM for modal displacements; (c) CFM for modal curvatures; (d) FEMU with unknown initial mechanical properties; and (e) FEMU with known initial mechanical properties

A.3.2.2 Damage Scenario II (15 mm Crack Depth)

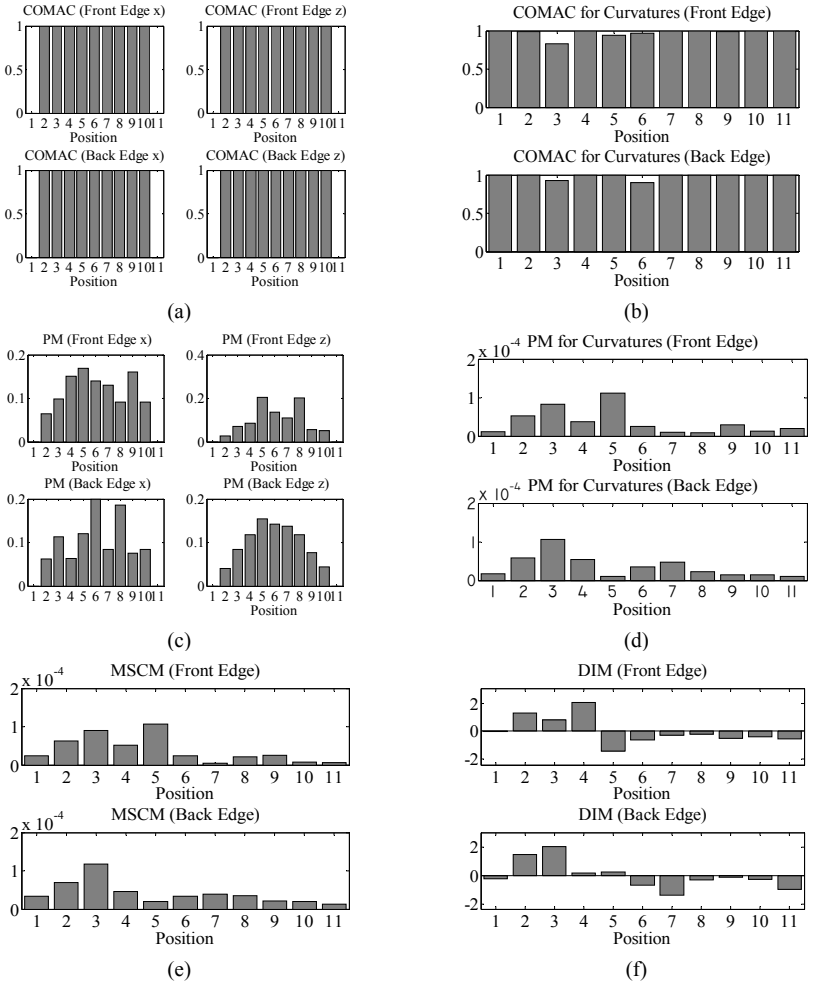


Figure A.45 – Model B, Damage Scenario II: (a) COMAC values for modal displacements; (b) COMAC values for modal curvatures; (c) PM for modal displacements; (d) PM for modal curvatures; (e) MSCM; and (f) DIM

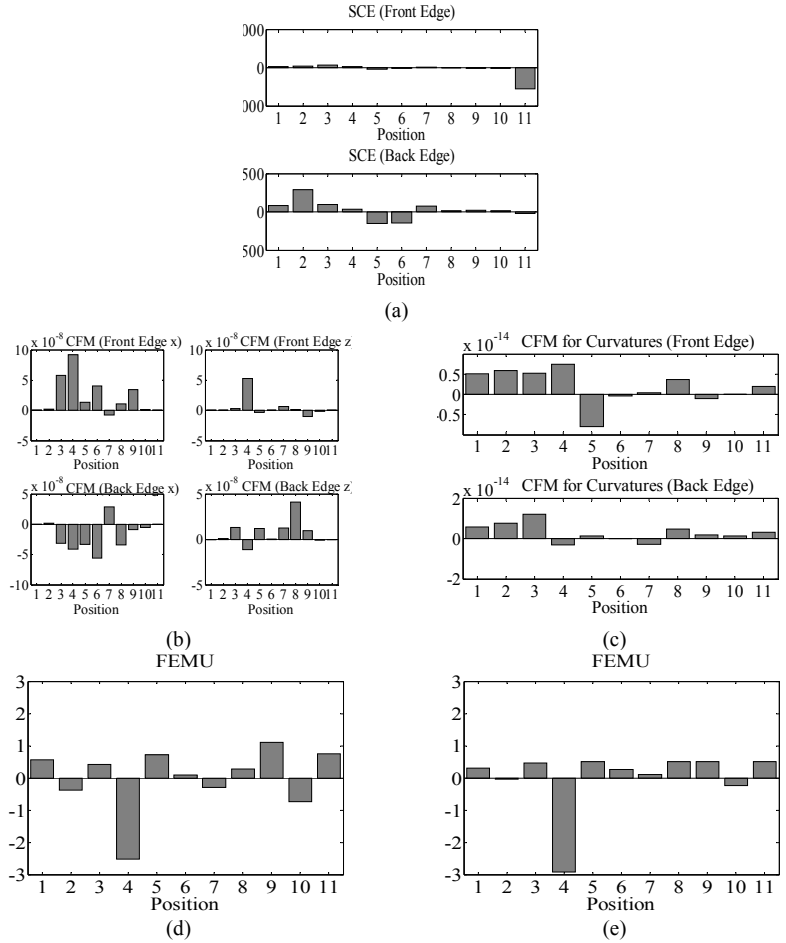


Figure A.46 – Model B, Damage Scenario II: (a) SCE; (b) CFM for modal displacements; (c) CFM for modal curvatures; (d) FEMU with unknown initial mechanical properties; and (e) FEMU with known initial mechanical properties

A.3.2.3 Damage Scenario III (30 mm Crack Depth)

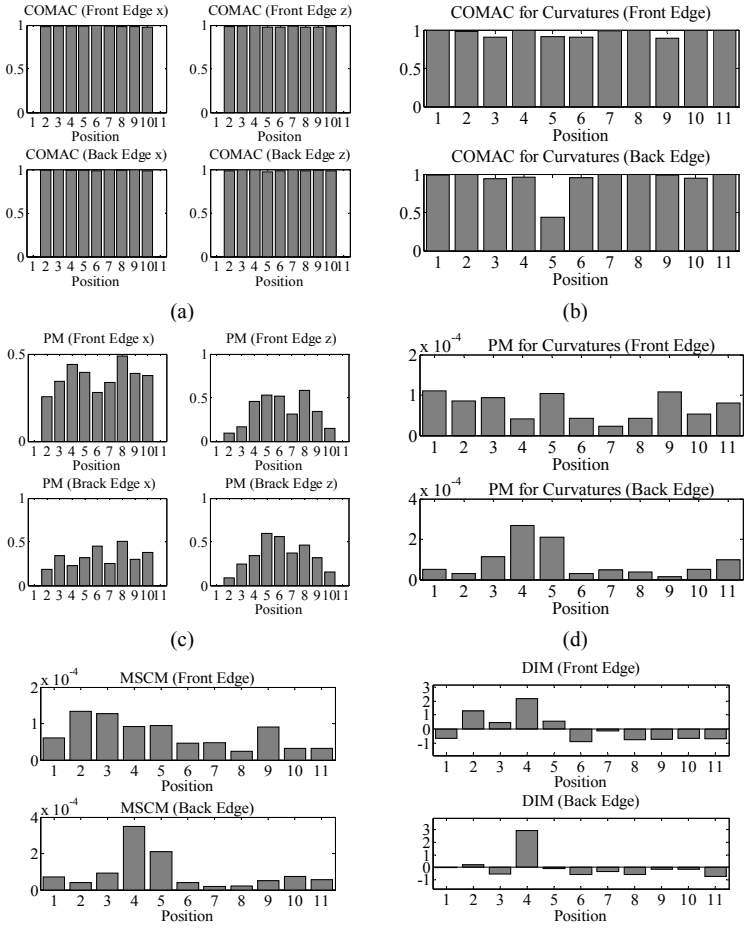


Figure A.47 – Model B, Damage Scenario III: (a) COMAC values for modal displacements; (b) COMAC values for modal curvatures; (c) PM for modal displacements; (d) PM for modal curvatures; (e) MSCM; and (f) DIM

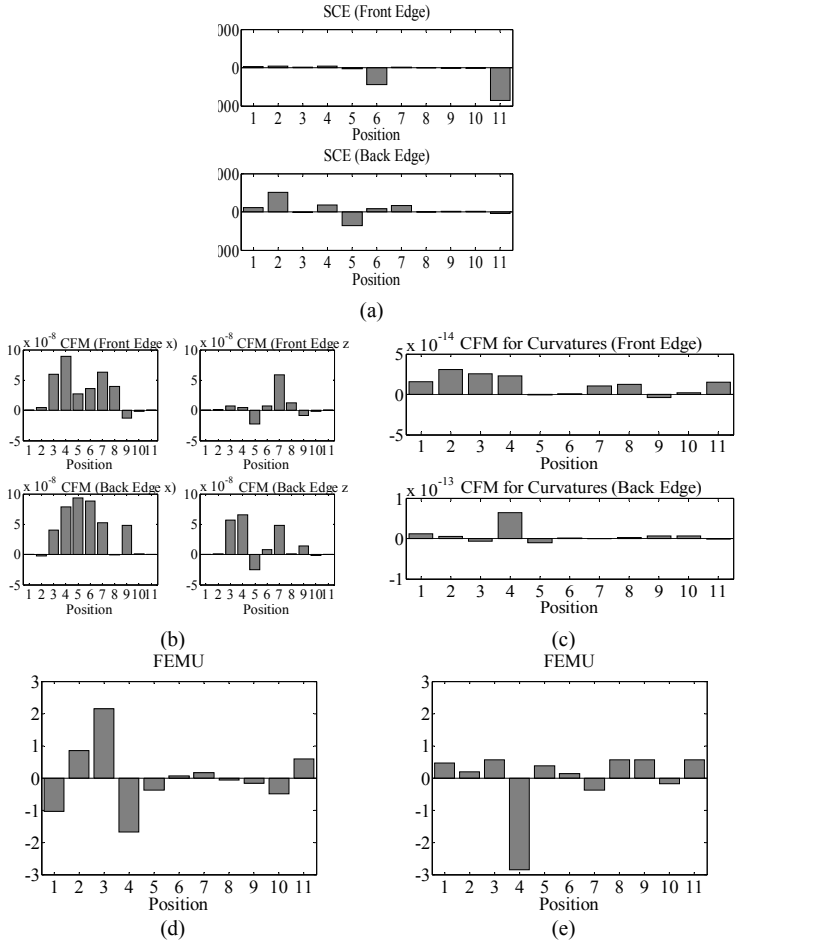


Figure A.48 – Model B, Damage Scenario III: (a) SCE; (b) CFM for modal displacements; (c) CFM for modal curvatures; (d) FEMU with unknown initial mechanical properties; and (e) FEMU with known initial mechanical properties

Annex B

Annex of Chapter 5

Index of Annex B

B.1 Non-Model Based Methods with Measured Curvatures for Random Impact Excitation.....B.4
B.1.1 Comparison with the Reference Scenario B.4
B.1.2 Relative Comparison B.12
B.1.3 Comparison with the Damage Scenario III B.19
B.2 Non-model Based Methods with Calculated Curvatures for Ambient Excitation.....B.23
B.2.1 Comparison with the Reference Scenario B.23
B.2.2 Relative Comparison B.31
B.2.3 Comparison with the Damage Scenario III B.38
B.3 Finite Element Model Updating Method B.42

B.1 Non-Model Based Methods with Measured Curvatures for Random Impact Excitation

B.1.1 Comparison with the Reference Scenario

B.1.1.1 Reference Scenario and Damage Scenario I

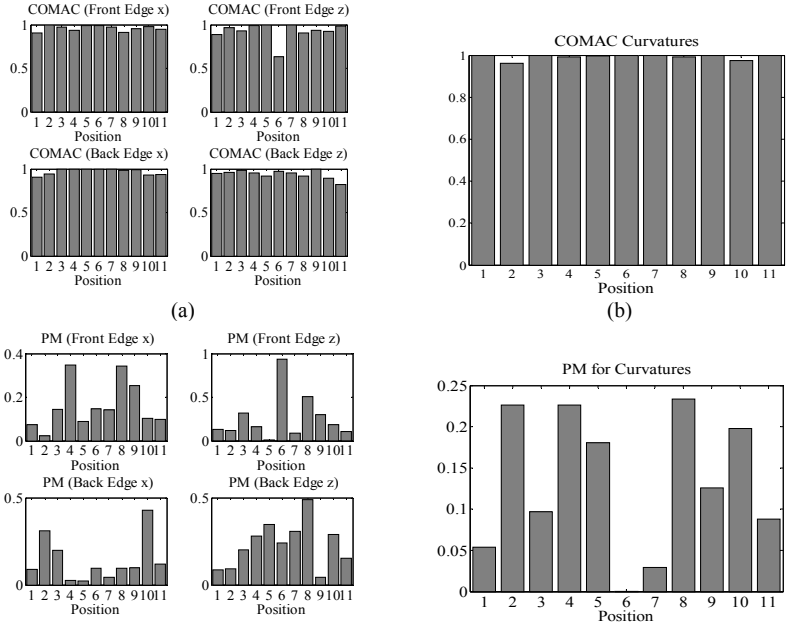


Figure B.1 – RS and DS_I: (a) COMAC values for modal displacements; (b) COMAC values for modal curvatures; (c) PM for modal displacements; and (d) PM for modal curvatures.

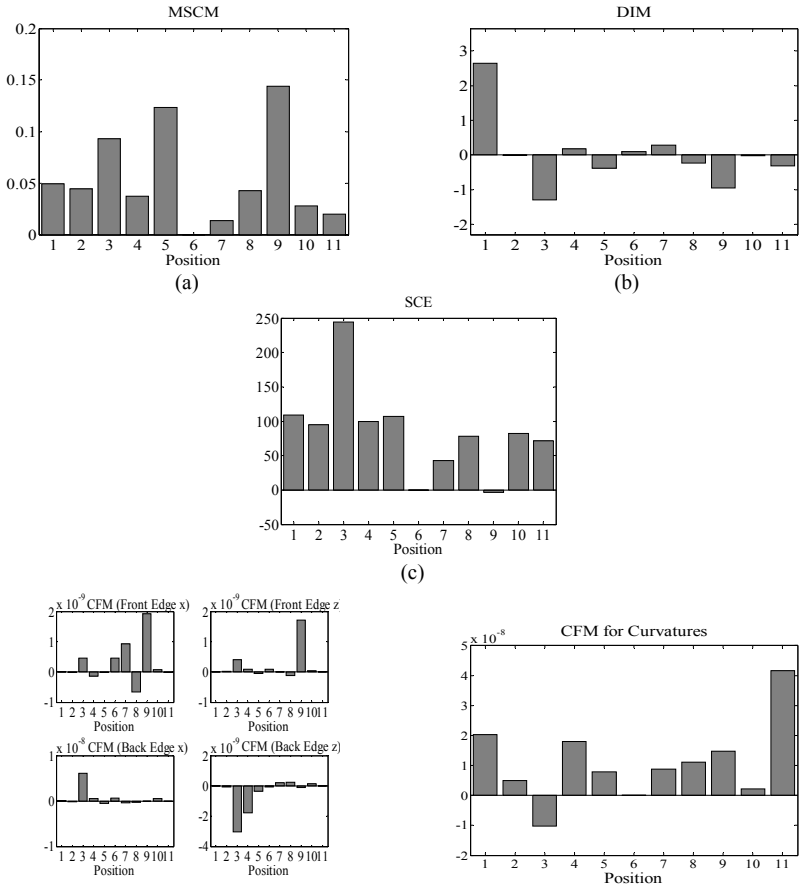


Figure B.2 – RS and DS_I: (a) MSCM; (b) DIM; (c) SCR; (d) CFM for modal displacements; and (e) CFM for modal curvatures.

B.1.1.2 Reference Scenario and Damage Scenario II

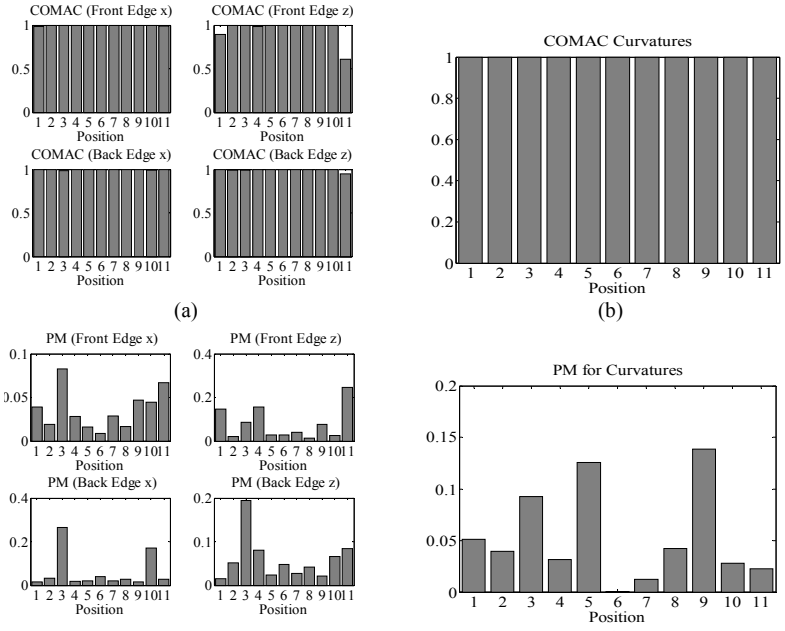


Figure B.3 – RS and DS_{II}: (a) COMAC values for modal displacements; (b) COMAC values for modal curvatures; (c) PM for modal displacements; and (d) PM for modal curvatures.

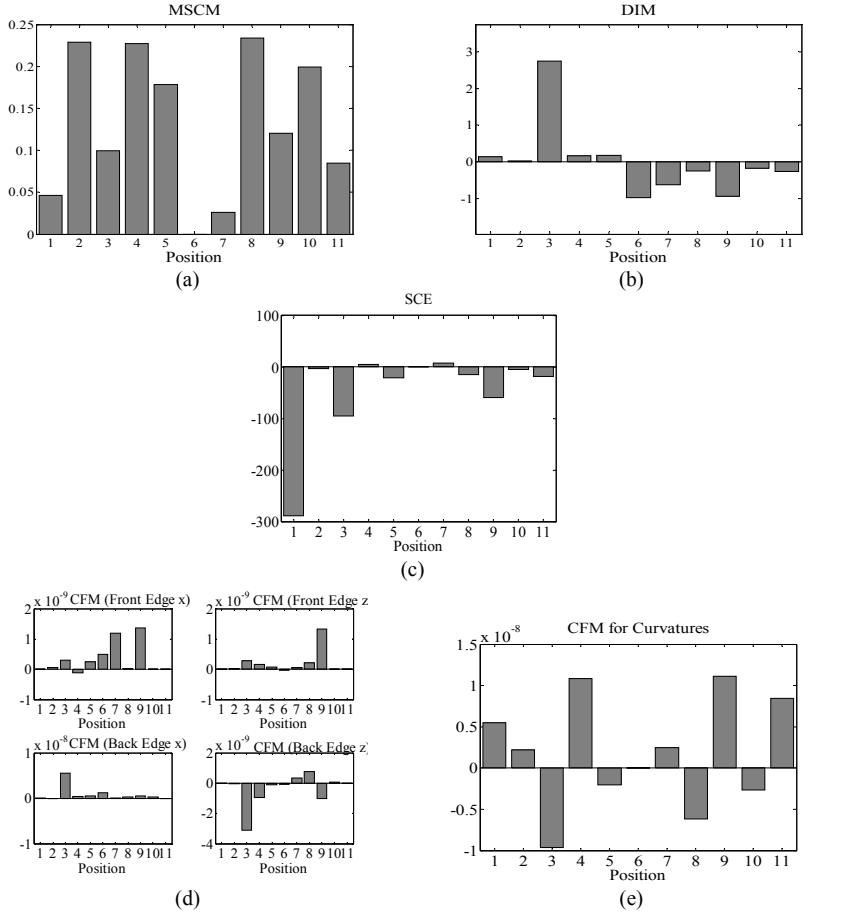


Figure B.4 – RS and DS_{II}: (a) MSCM; (b) DIM; (c) SCR; (d) CFM for modal displacements; and (e) CFM for modal curvatures.

B.1.1.3 Reference Scenario and Damage Scenario III

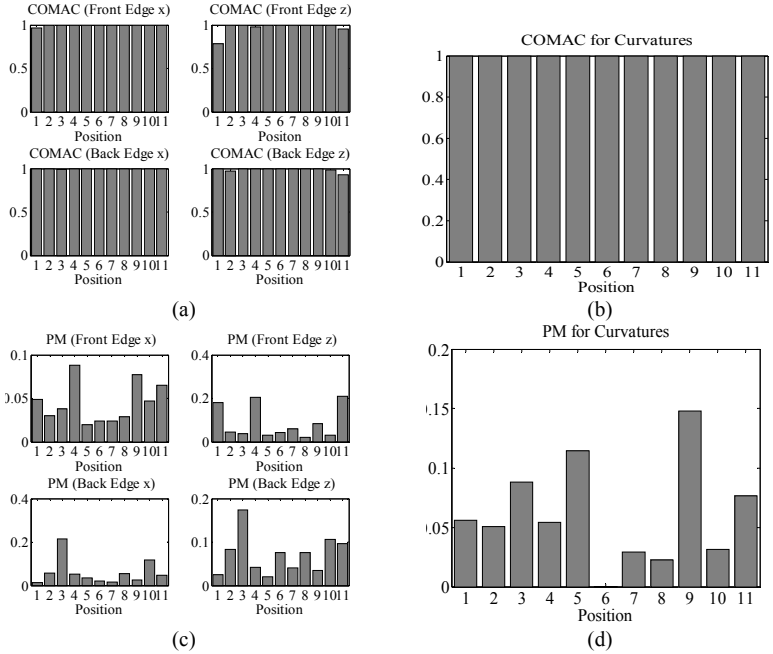


Figure B.5 – RS and DS_{III}: (a) COMAC values for modal displacements; (b) COMAC values for modal curvatures; (c) PM for modal displacements; and (d) PM for modal curvatures.

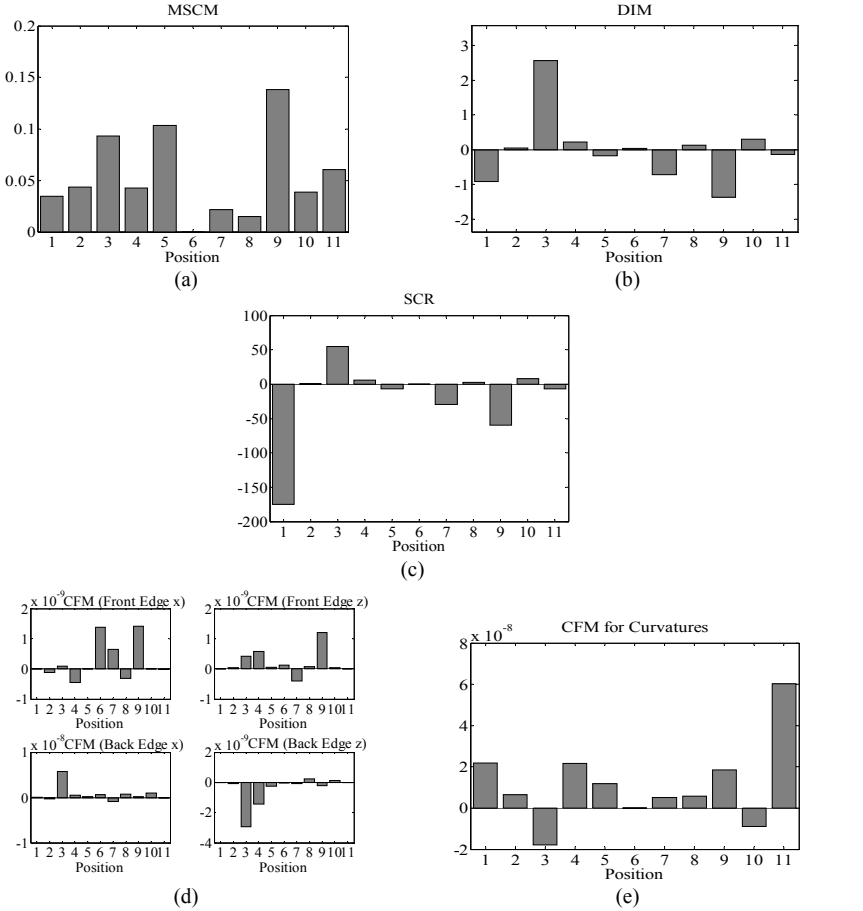


Figure B.6 – RS and DS_{III}: (a) MSCM; (b) DIM; (c) SCR; (d) CFM for modal displacements; and (e) CFM for modal curvatures.

B.1.1.4 Reference Scenario and Damage Scenario IV

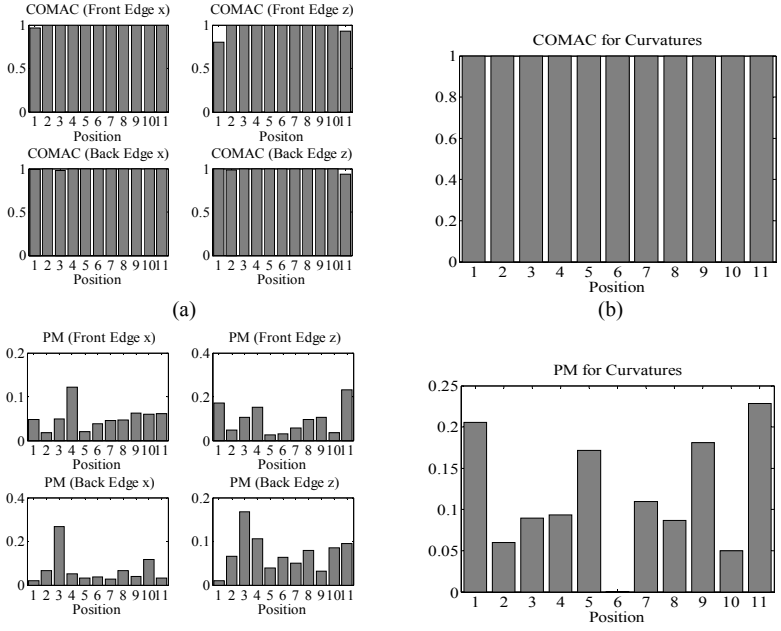


Figure B.7 – RS and DS_{IV}: (a) COMAC values for modal displacements; (b) COMAC values for modal curvatures; (c) PM for modal displacements; and (d) PM for modal curvatures.

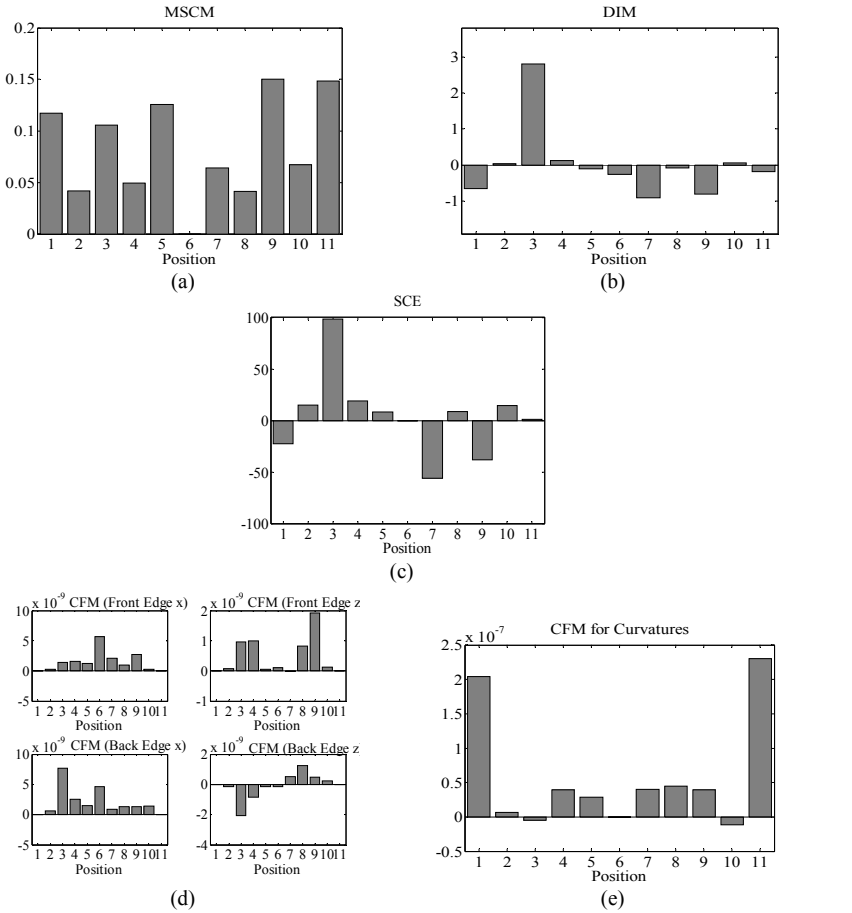


Figure B.8 – RS and DS_{IV}: (a) MSCM; (b) DIM; (c) SCR; (d) CFM for modal displacements; and (e) CFM for modal curvatures.

B.1.1.5 Reference Scenario and Damage Scenario V

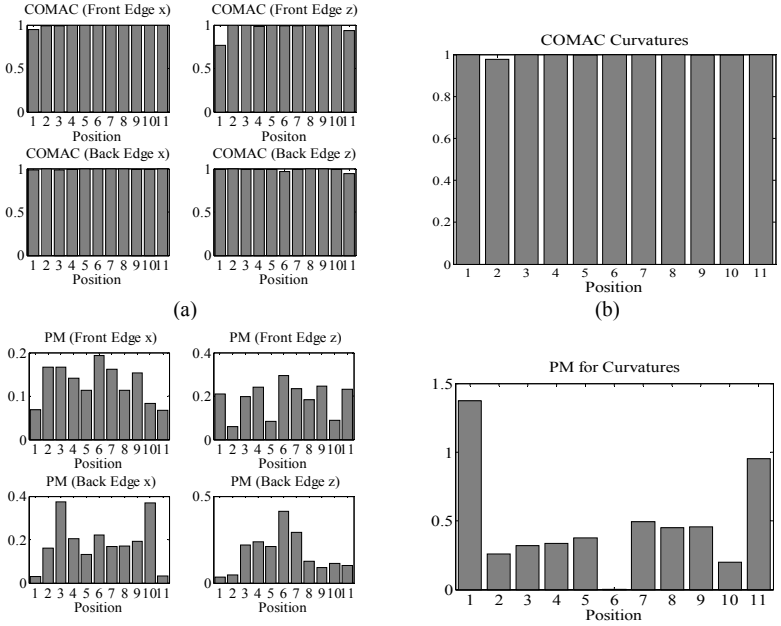


Figure B.9 – RS and DS_V: (a) COMAC values for modal displacements; (b) COMAC values for modal curvatures; (c) PM for modal displacements; and (d) PM for modal curvatures.

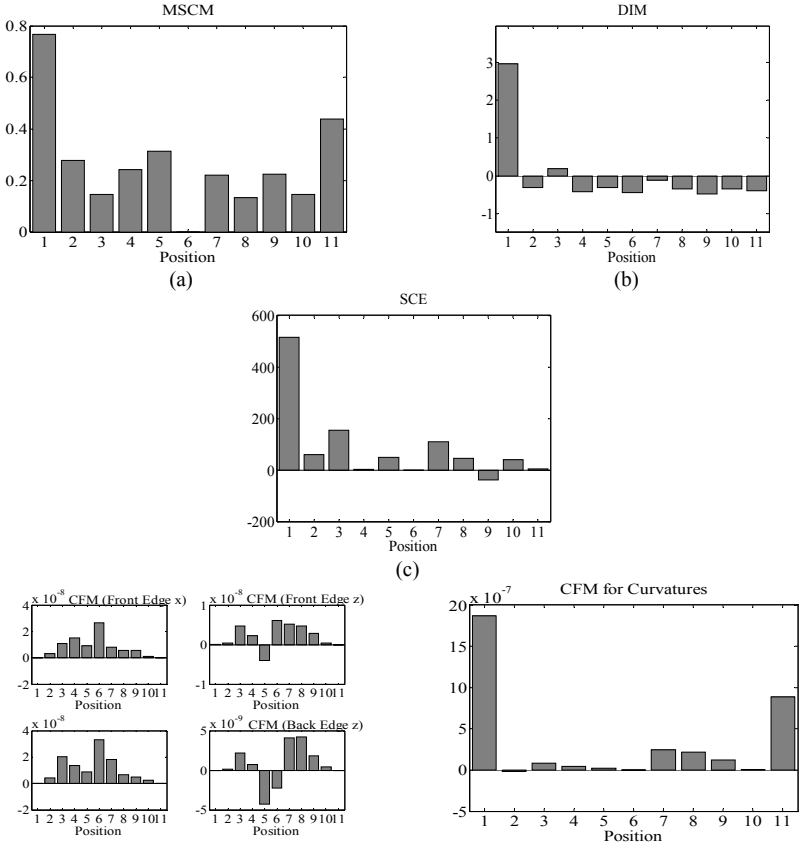
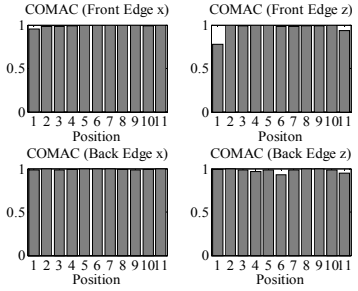
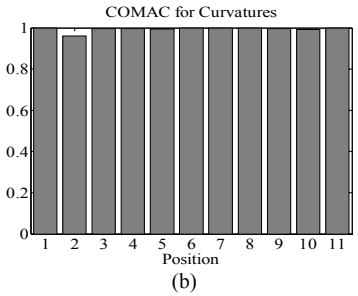
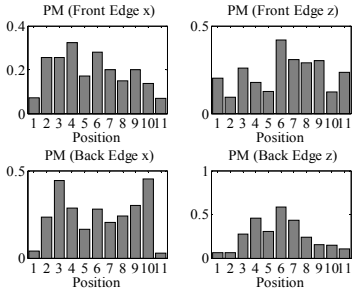


Figure B.10 – RS and DS_V: (a) MSCM; (b) DIM; (c) SCR; (d) CFM for modal displacements; and (e) CFM for modal curvatures.

B.1.1.6 Reference Scenario and Damage Scenario VI







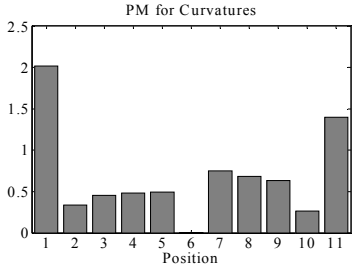
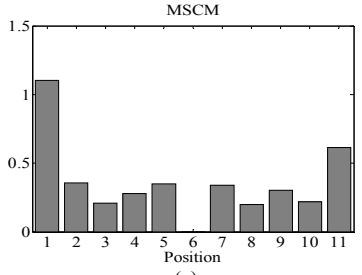
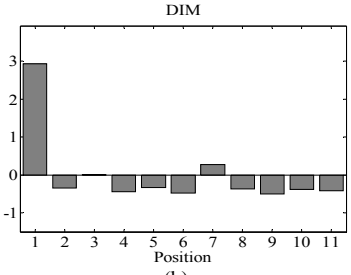
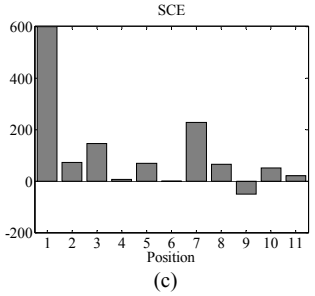
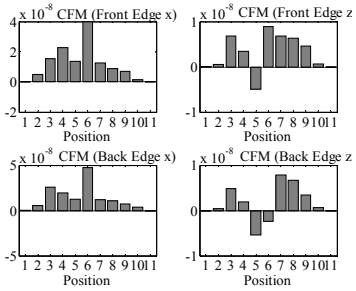


Figure B.11 – RS and DS_{VI}: (a) COMAC values for modal displacements; (b) COMAC values for modal curvatures; (c) PM for modal displacements; and (d) PM for modal curvatures.









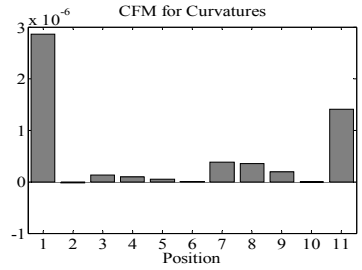


Figure B.12 – RS and DS_{VI}: (a) MSCM; (b) DIM; (c) SCR; (d) CFM for modal displacements; and (e) CFM for modal curvatures.

B.1.1.7 Reference Scenario and Damage Scenario VII

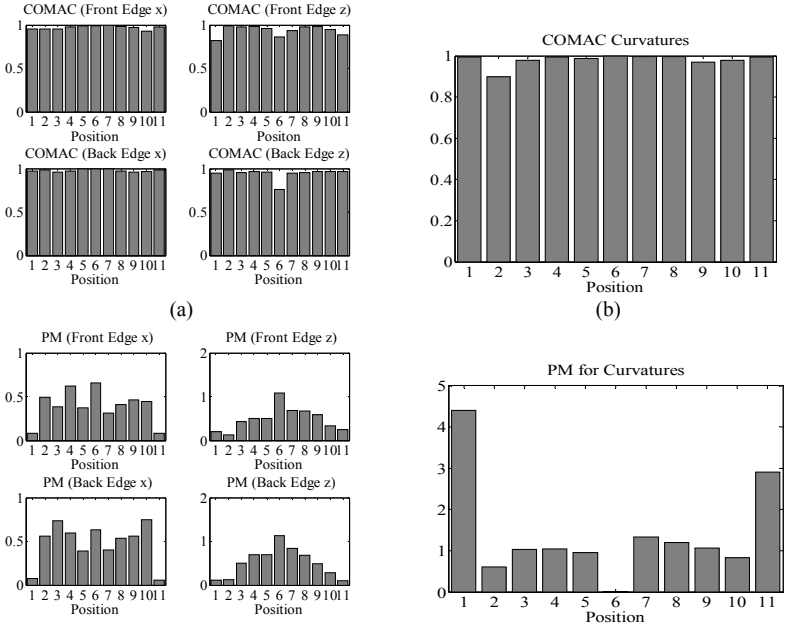


Figure B.13 – RS and DS_{VII}: (a) COMAC values for modal displacements; (b) COMAC values for modal curvatures; (c) PM for modal displacements; and (d) PM for modal curvatures.

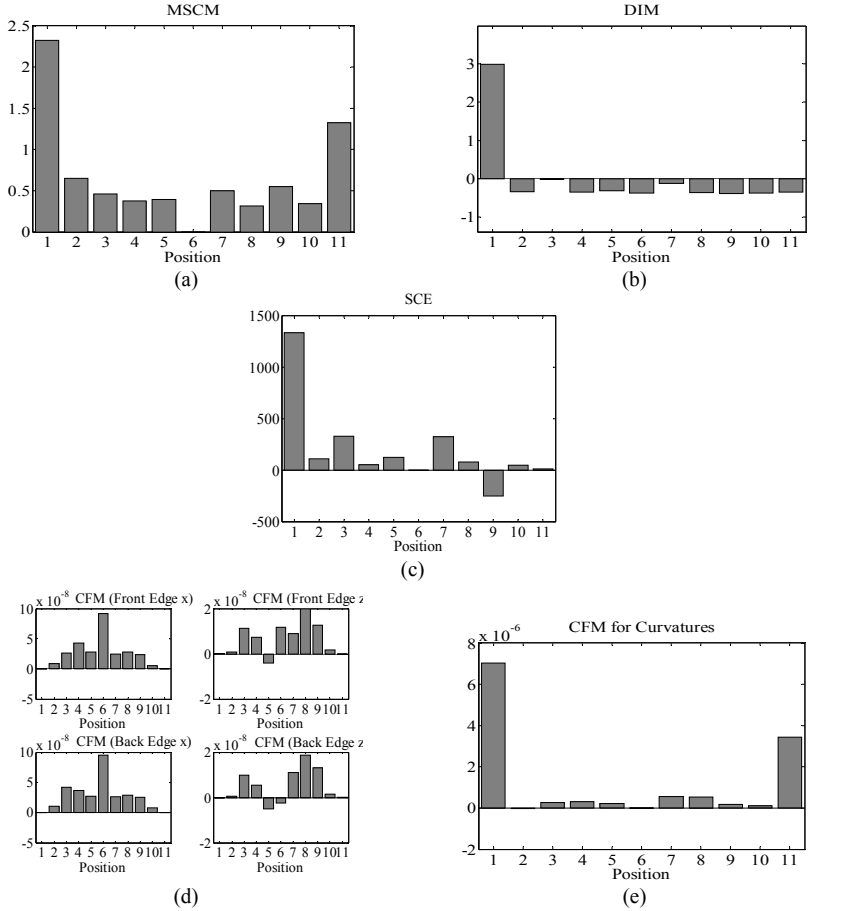


Figure B.14 – RS and DS_{VII}: (a) MSCM; (b) DIM; (c) SCR; (d) CFM for modal displacements; and (e) CFM for modal curvatures.

B.1.1.8 Reference Scenario and Damage Scenario VIII

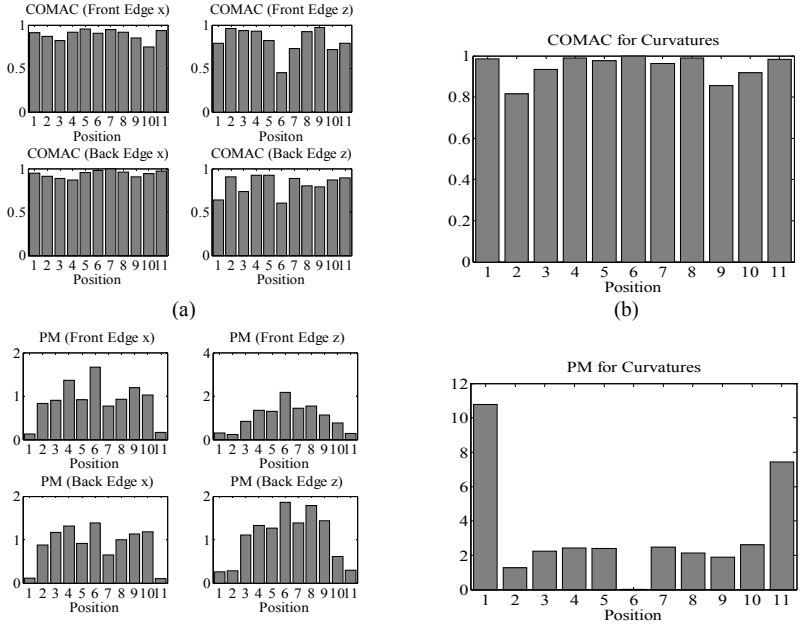


Figure B.15 – RS and DS_{VIII}: (a) COMAC values for modal displacements; (b) COMAC values for modal curvatures; (c) PM for modal displacements; and (d) PM for modal curvatures.

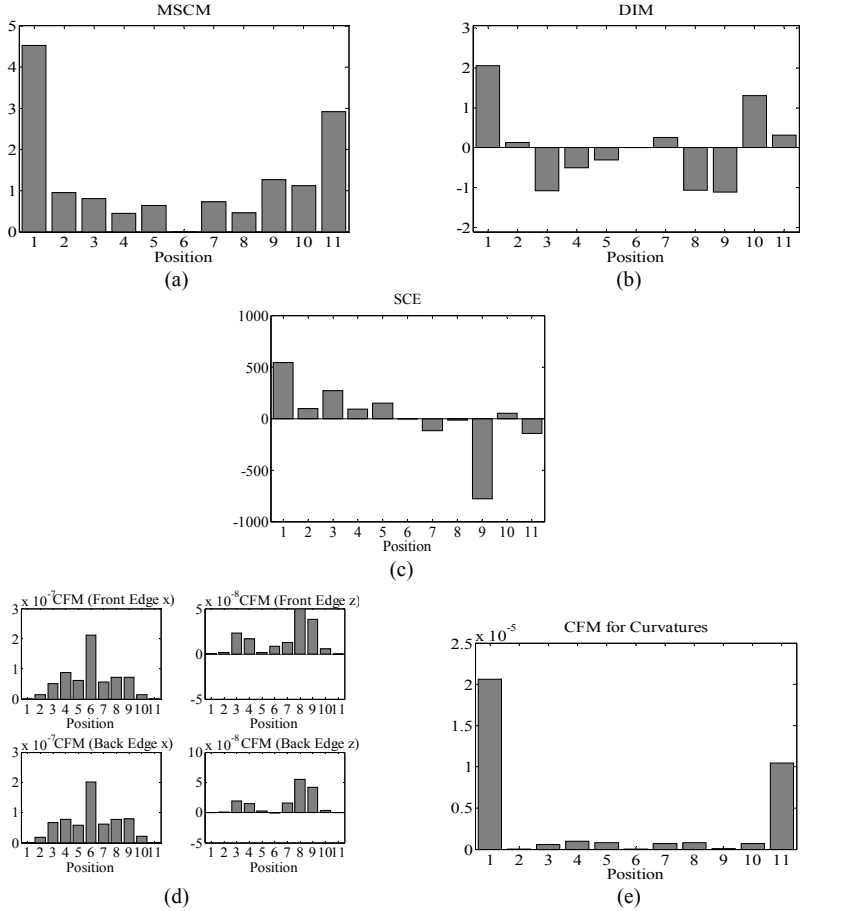


Figure B.16 – RS and DS_{VIII}: (a) MSCM; (b) DIM; (c) SCR; (d) CFM for modal displacements; and (e) CFM for modal curvatures.

B.1.2 Relative Comparison

B.1.2.1 Damage Scenario I and Damage Scenario II

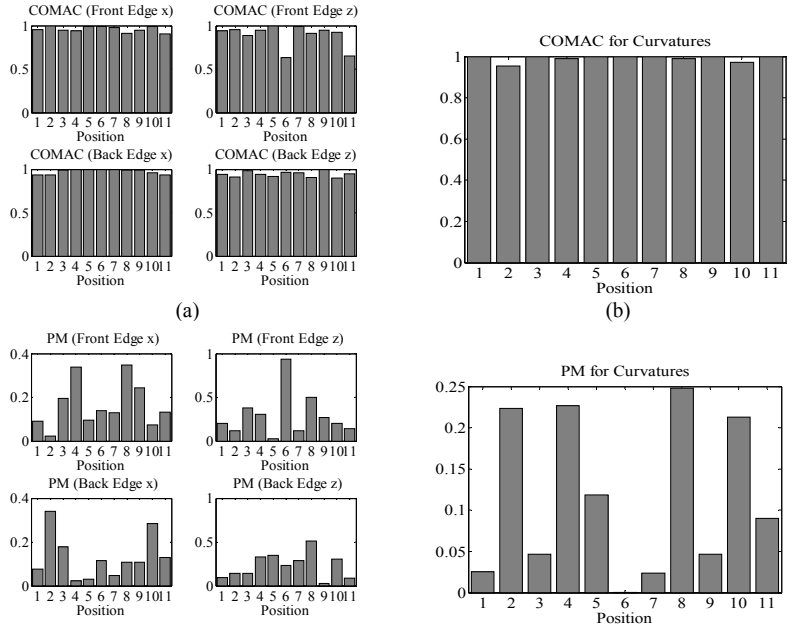


Figure B.17 – DS_I and DS_{II}: (a) COMAC values for modal displacements; (b) COMAC values for modal curvatures; (c) PM for modal displacements; and (d) PM for modal curvatures.

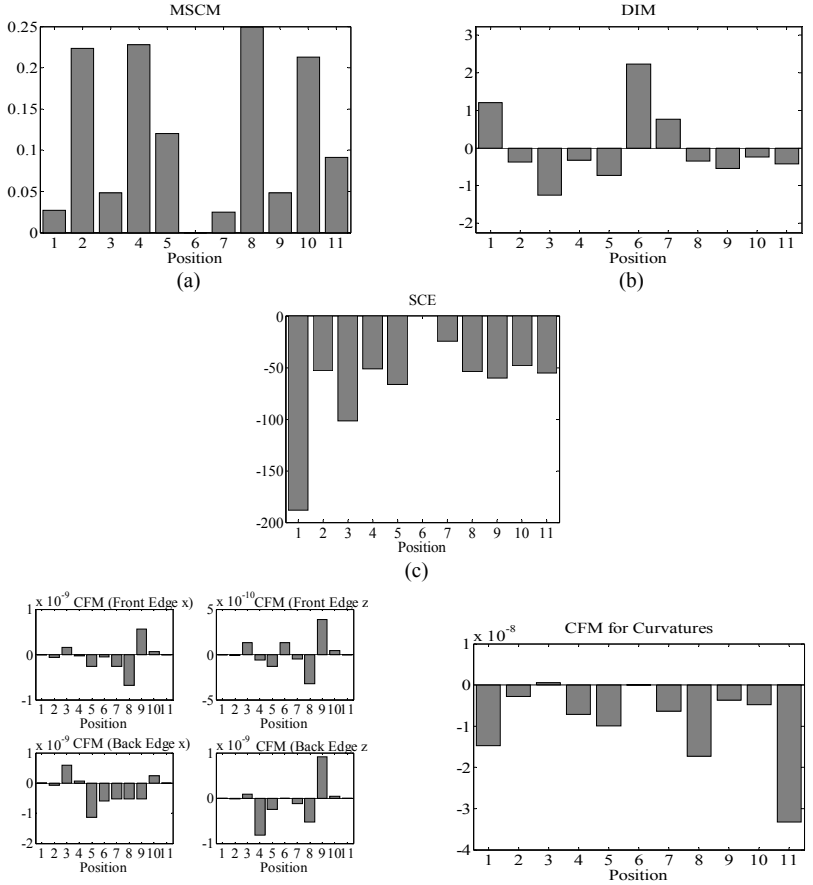


Figure B.18 – DS_I and DS_{II}: (a) MSCM; (b) DIM; (c) SCR; (d) CFM for modal displacements; and (e) CFM for modal curvatures.

B.1.2.2 Damage Scenario II and Damage Scenario III

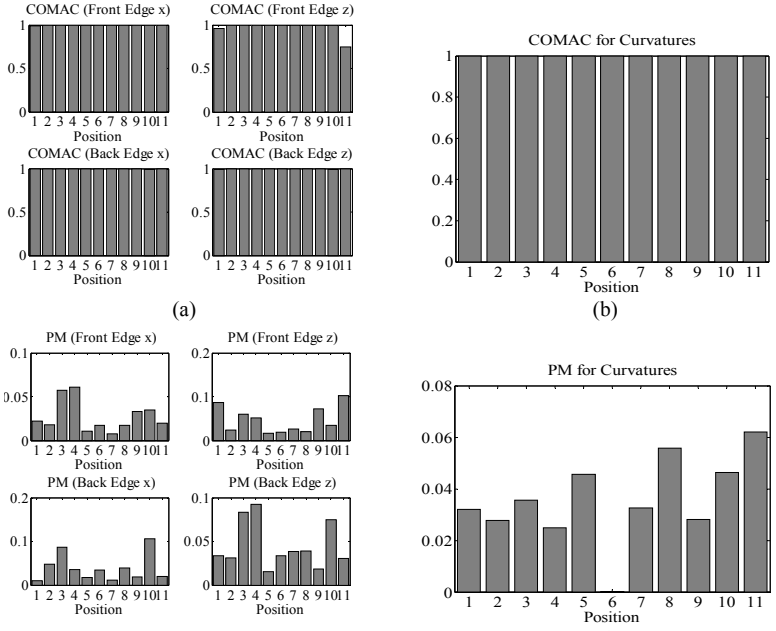


Figure B.19 – DS_{II} and DS_{III}: (a) COMAC values for modal displacements; (b) COMAC values for modal curvatures; (c) PM for modal displacements; and (d) PM for modal curvatures.

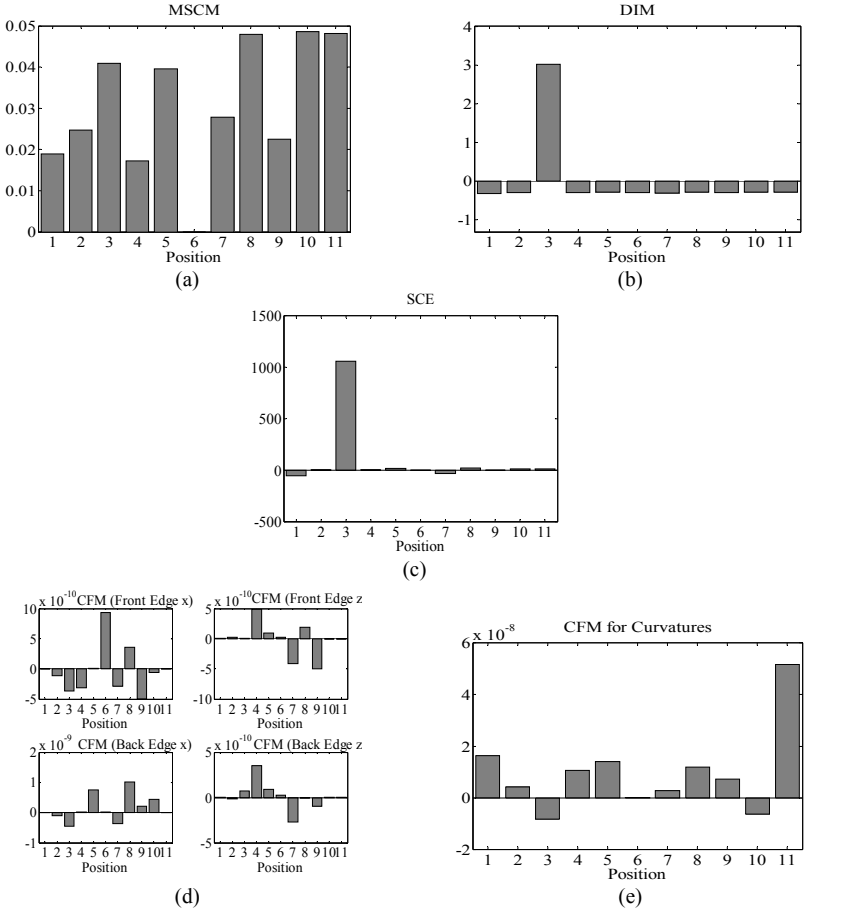


Figure B.20 – DS_{II} and DS_{III}: (a) MSCM; (b) DIM; (c) SCR; (d) CFM for modal displacements; and (e) CFM for modal curvatures.

B.1.2.3 Damage Scenario III and Damage Scenario IV

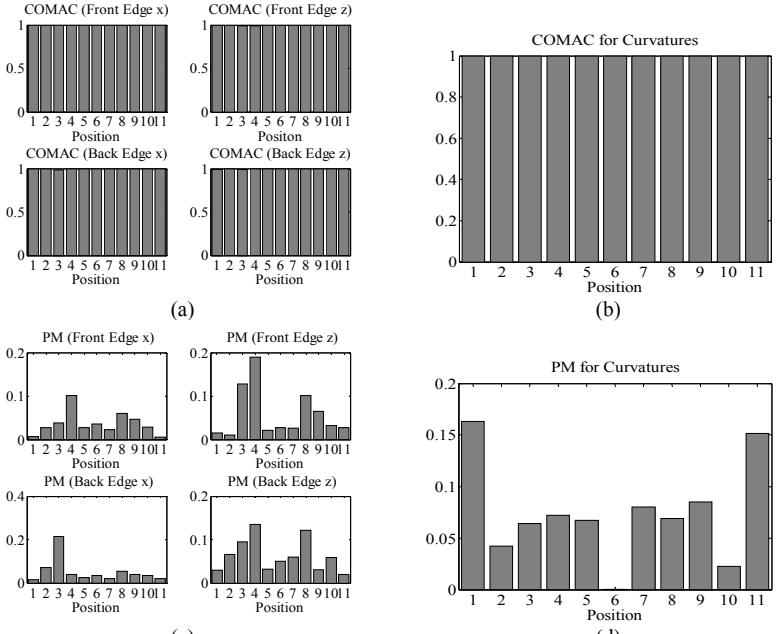


Figure B.21 – DS_{III} and DS_{IV}: (a) COMAC values for modal displacements; (b) COMAC values for modal curvatures; (c) PM for modal displacements; and (d) PM for modal curvatures.

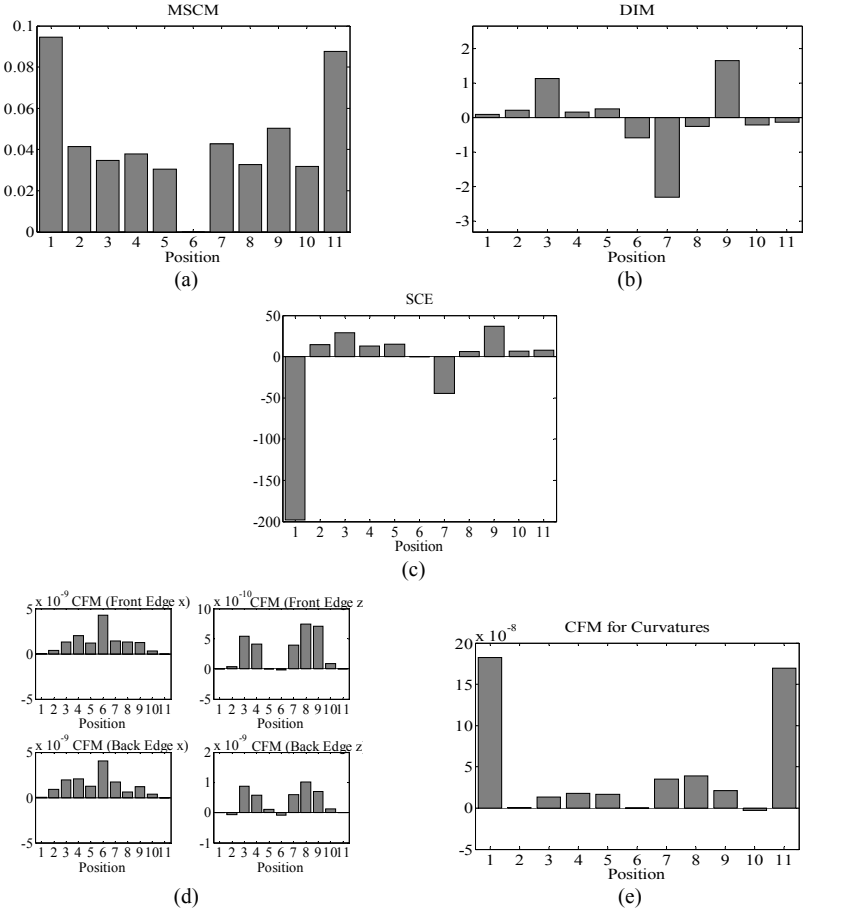


Figure B.22 – DS_{III} and DS_{IV}: (a) MSCM; (b) DIM; (c) SCR; (d) CFM for modal displacements; and (e) CFM for modal curvatures.

B.1.2.4 Damage Scenario IV and Damage Scenario V

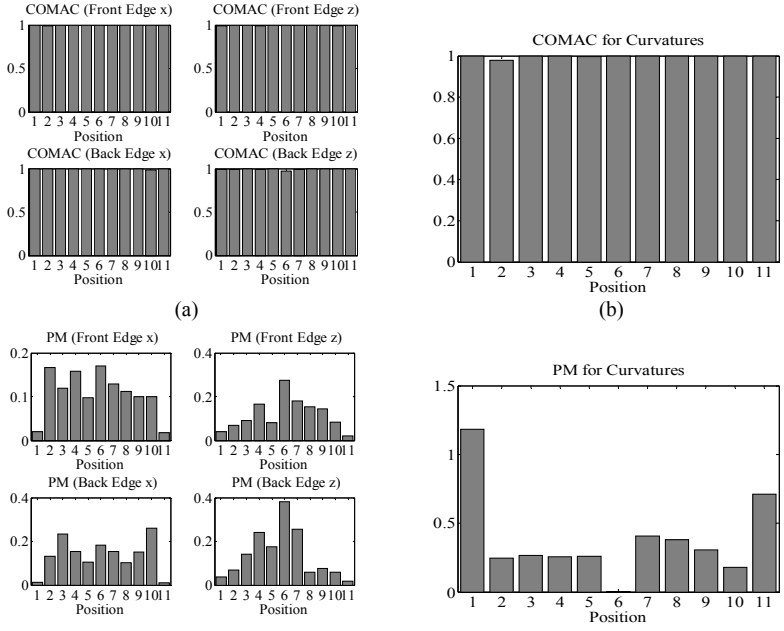


Figure B.23 – DS_{IV} and DS_{V}: (a) COMAC values for modal displacements; (b) COMAC values for modal curvatures; (c) PM for modal displacements; and (d) PM for modal curvatures.

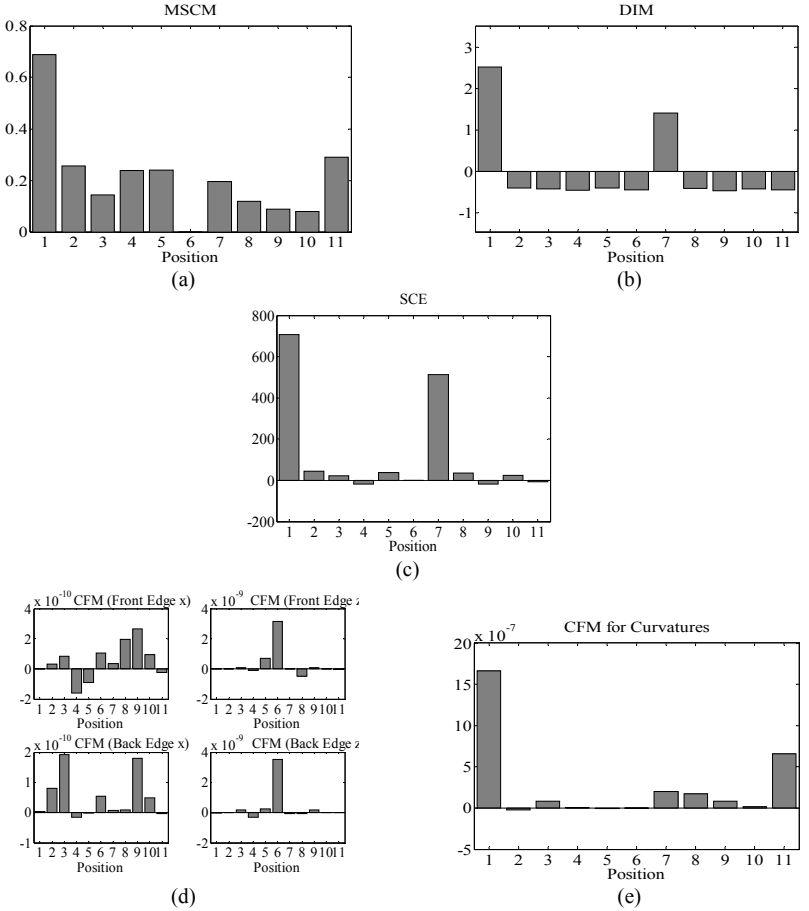


Figure B.24 – DS_{IV} and DS_{V}: (a) MSCM; (b) DIM; (c) SCR; (d) CFM for modal displacements; and (e) CFM for modal curvatures.

B.1.2.5 Damage Scenario V and Damage Scenario VI

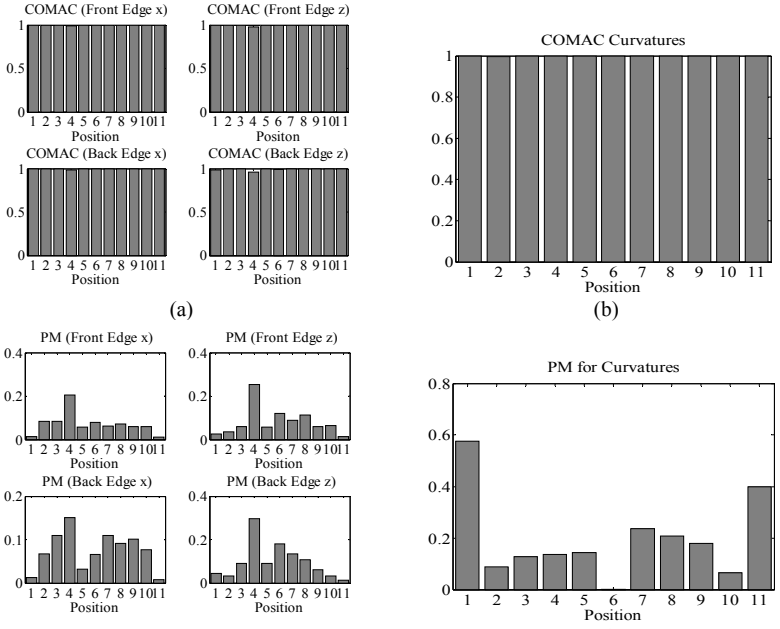


Figure B.25 – DS_V and DS_{VI}: (a) COMAC values for modal displacements; (b) COMAC values for modal curvatures; (c) PM for modal displacements; and (d) PM for modal curvatures.

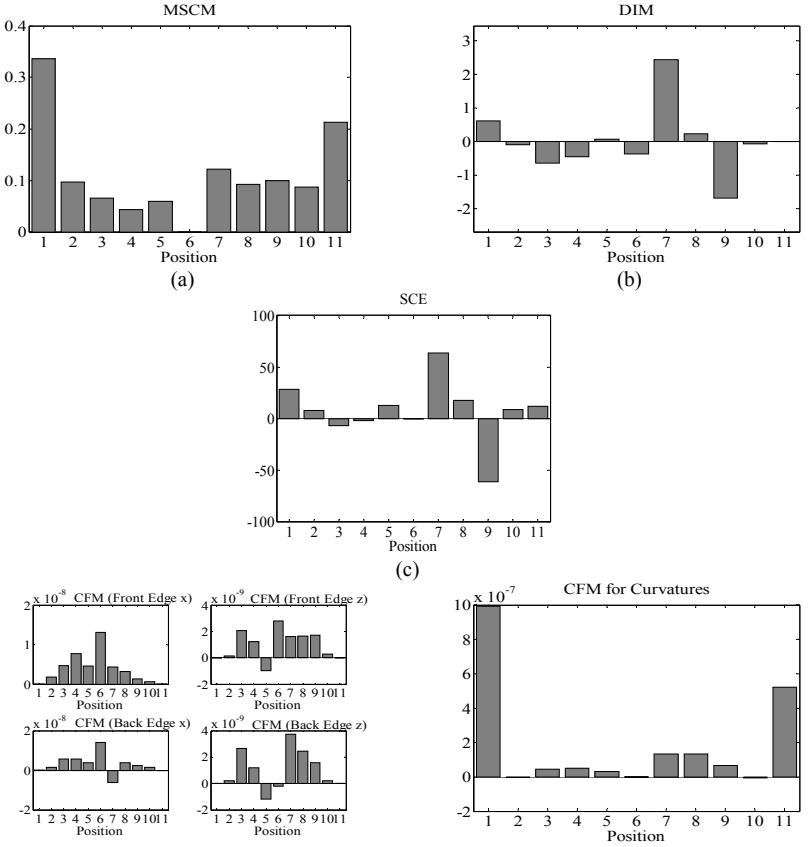


Figure B.26 – DS_V and DS_{VI}: (a) MSCM; (b) DIM; (c) SCR; (d) CFM for modal displacements; and (e) CFM for modal curvatures.

B.1.2.6 Damage Scenario VI and Damage Scenario VII

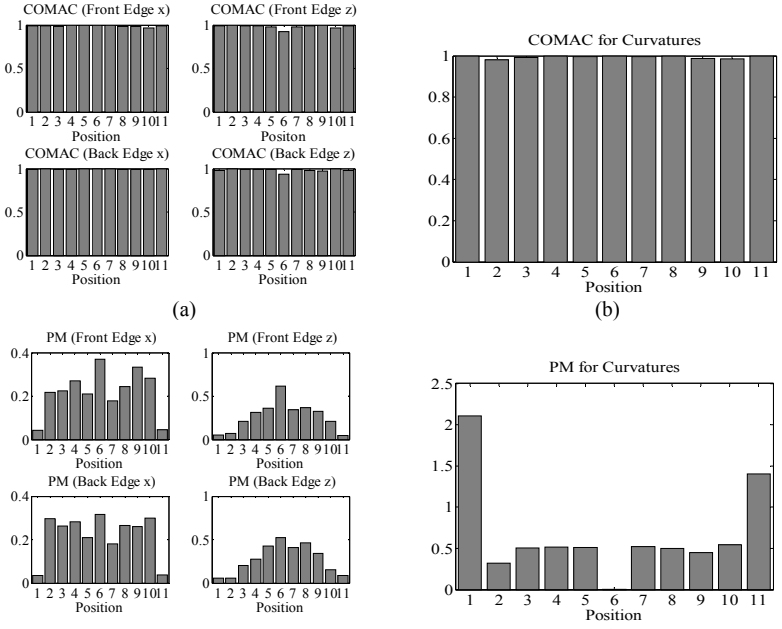


Figure B.27 – DS_{VI} and DS_{VII}: (a) COMAC values for modal displacements; (b) COMAC values for modal curvatures; (c) PM for modal displacements; and (d) PM for modal curvatures.

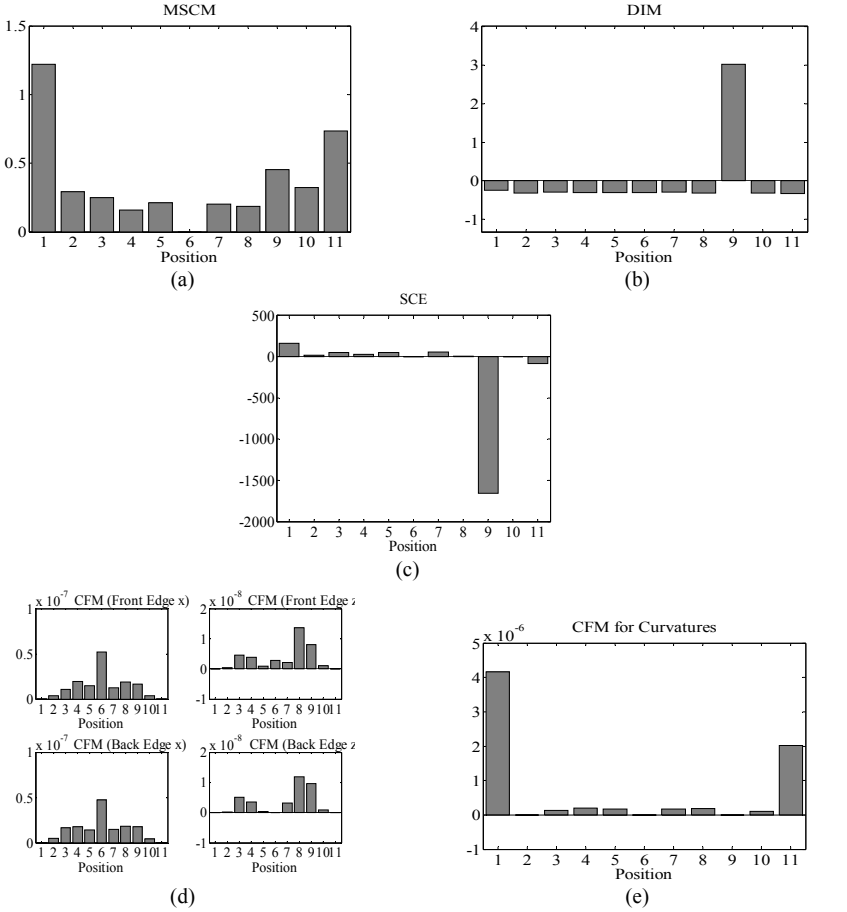


Figure B.28 – DS_{VI} and DS_{VII}: (a) MSCM; (b) DIM; (c) SCR; (d) CFM for modal displacements; and (e) CFM for modal curvatures.

B.1.2.7 Damage Scenario VII and Damage Scenario VIII

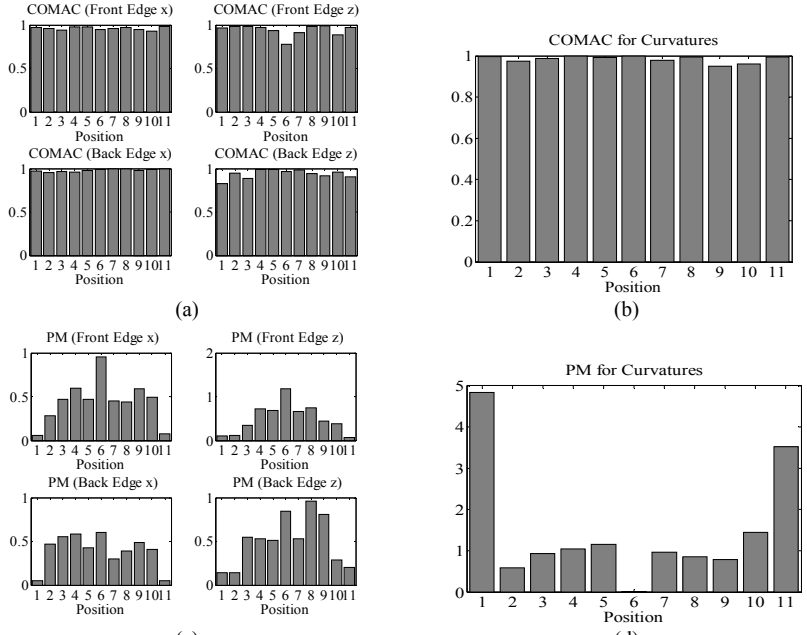


Figure B.29 – DS_{VII} and DS_{VIII}: (a) COMAC values for modal displacements; (b) COMAC values for modal curvatures; (c) PM for modal displacements; and (d) PM for modal curvatures.

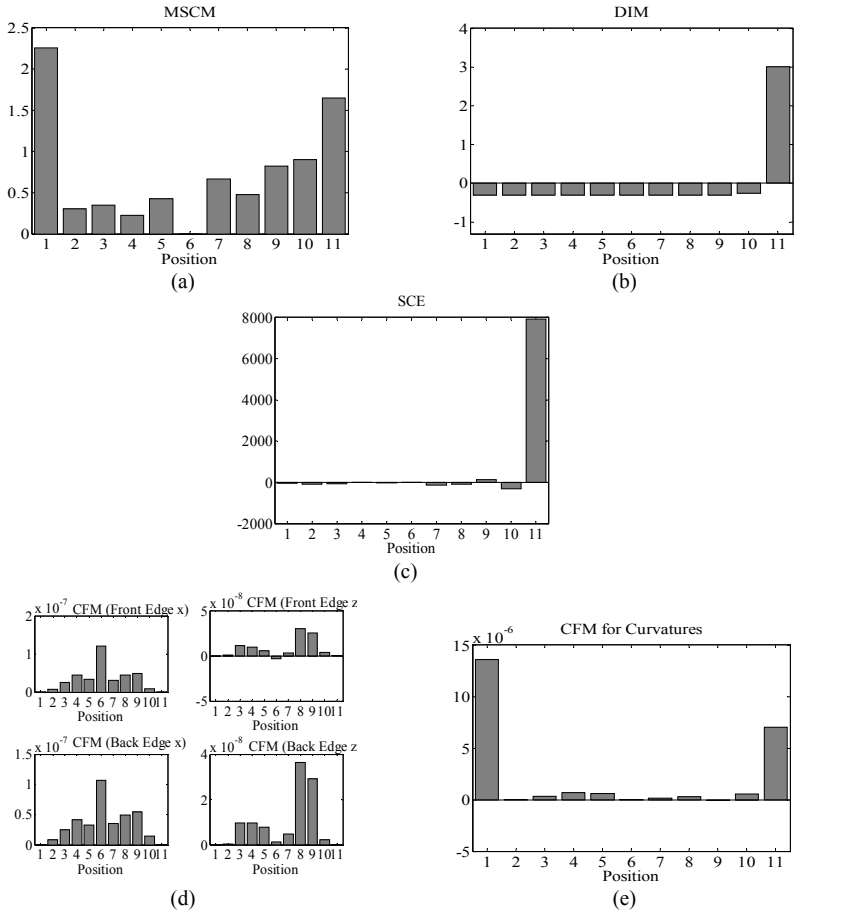


Figure B.30 – DS_{VII} and DS_{VIII}: (a) MSCM; (b) DIM; (c) SCR; (d) CFM for modal displacements; and (e) CFM for modal curvatures.

B.1.3 Comparison with the Damage Scenario III

B.1.3.1 Damage Scenario III and Damage Scenario V

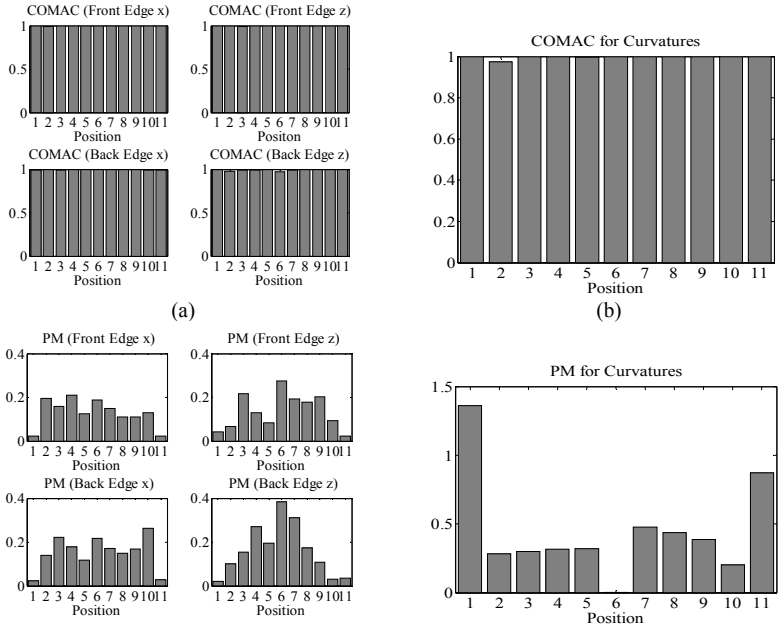


Figure B.31 – DS_{III} and DS_V: (a) COMAC values for modal displacements; (b) COMAC values for modal curvatures; (c) PM for modal displacements; and (d) PM for modal curvatures.

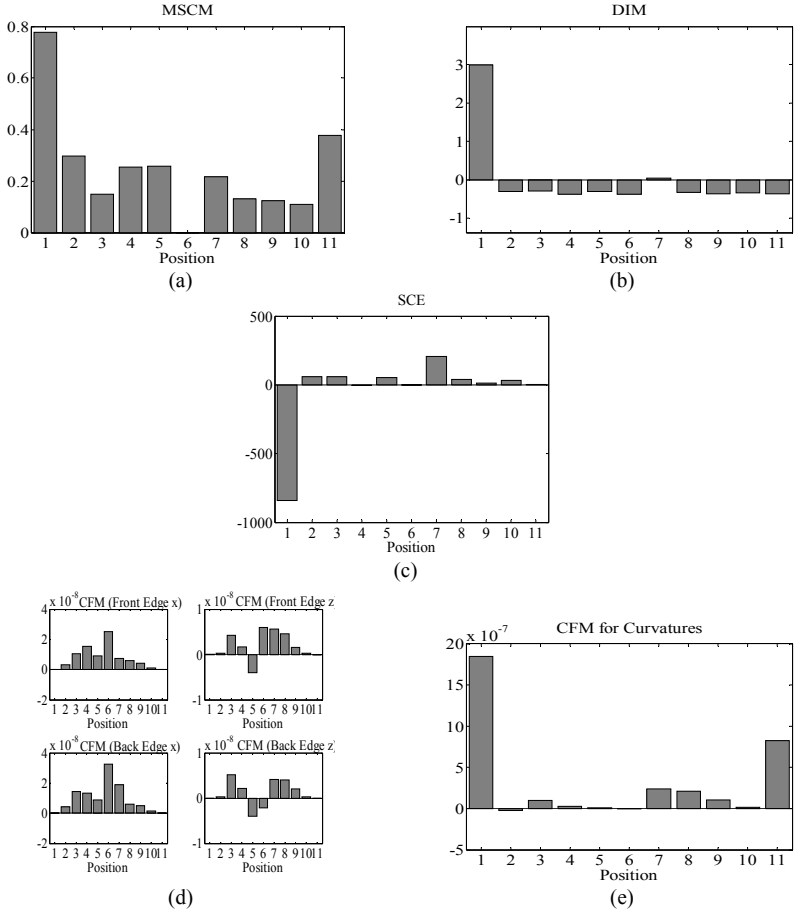


Figure B.32 – DS_{III} and DS_V: (a) MSCM; (b) DIM; (c) SCR; (d) CFM for modal displacements; and (e) CFM for modal curvatures.

B.1.3.2 Damage Scenario III and Damage Scenario VI

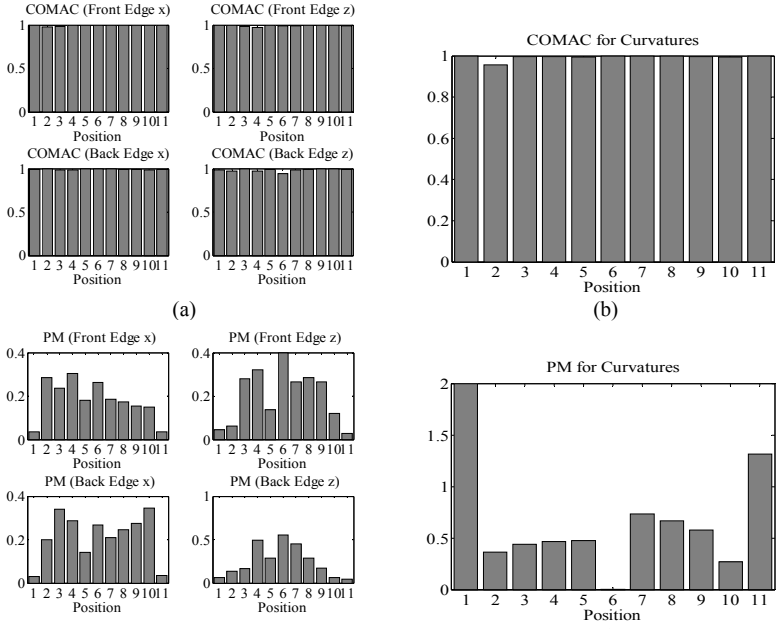


Figure B.33 – DS_{III} and DS_{VI}: (a) COMAC values for modal displacements; (b) COMAC values for modal curvatures; (c) PM for modal displacements; and (d) PM for modal curvatures.

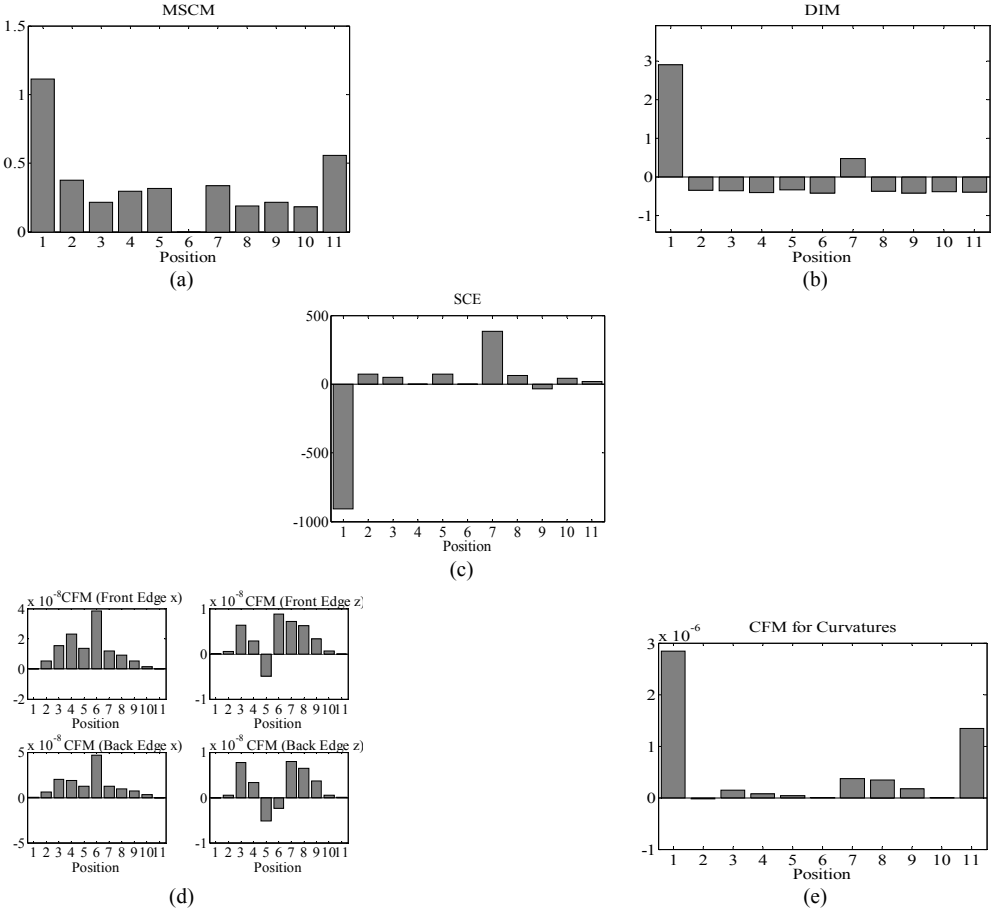


Figure B.34 – DS_{III} and DS_{VI}: (a) MSCM; (b) DIM; (c) SCR; (d) CFM for modal displacements; and (e) CFM for modal curvatures.

B.1.3.3 Damage Scenario III and Damage Scenario VII

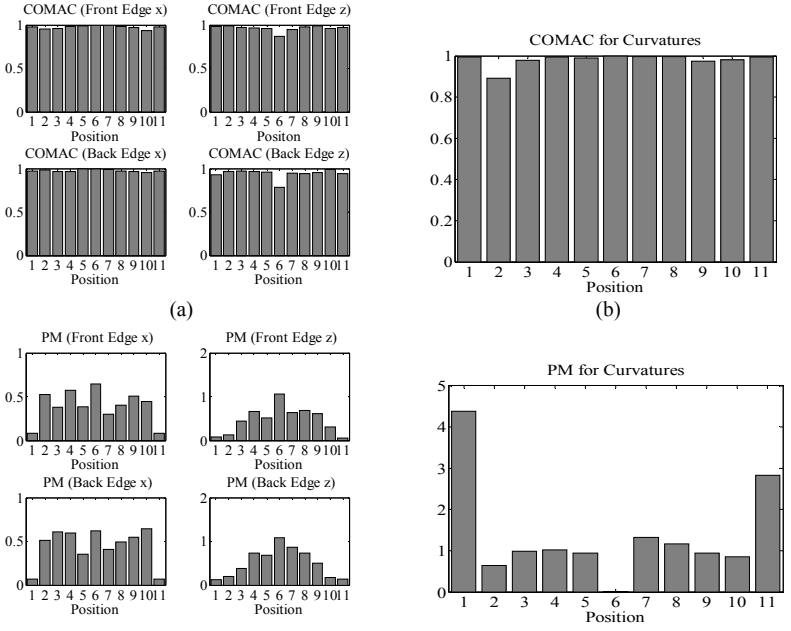


Figure B.35 – DS_{III} and DS_{VII}: (a) COMAC values for modal displacements; (b) COMAC values for modal curvatures; (c) PM for modal displacements; and (d) PM for modal curvatures.

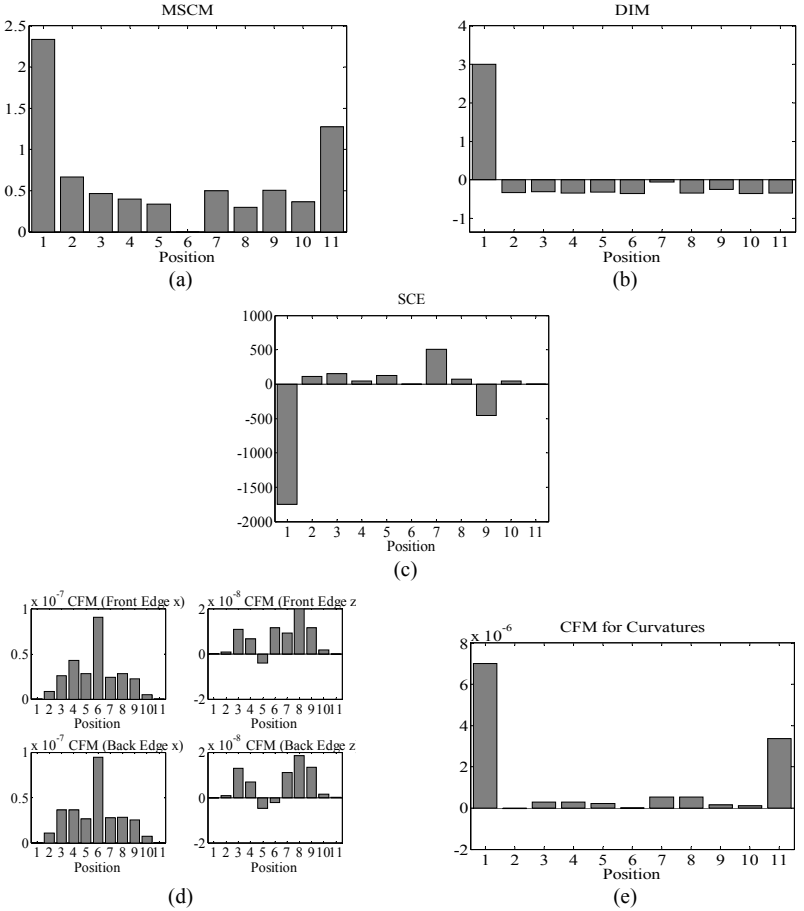


Figure B.36 – DS_{III} and DS_{VII}: (a) MSCM; (b) DIM; (c) SCR; (d) CFM for modal displacements; and (e) CFM for modal curvatures.

B.1.3.4 Damage Scenario III and Damage Scenario VIII

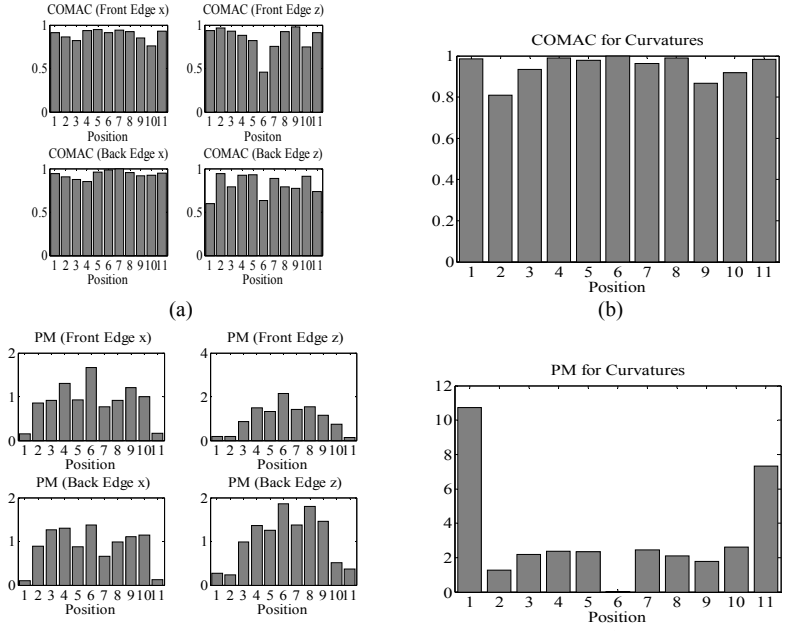


Figure B.37 – DS_{III} and DS_{VIII}: (a) COMAC values for modal displacements; (b) COMAC values for modal curvatures; (c) PM for modal displacements; and (d) PM for modal curvatures.

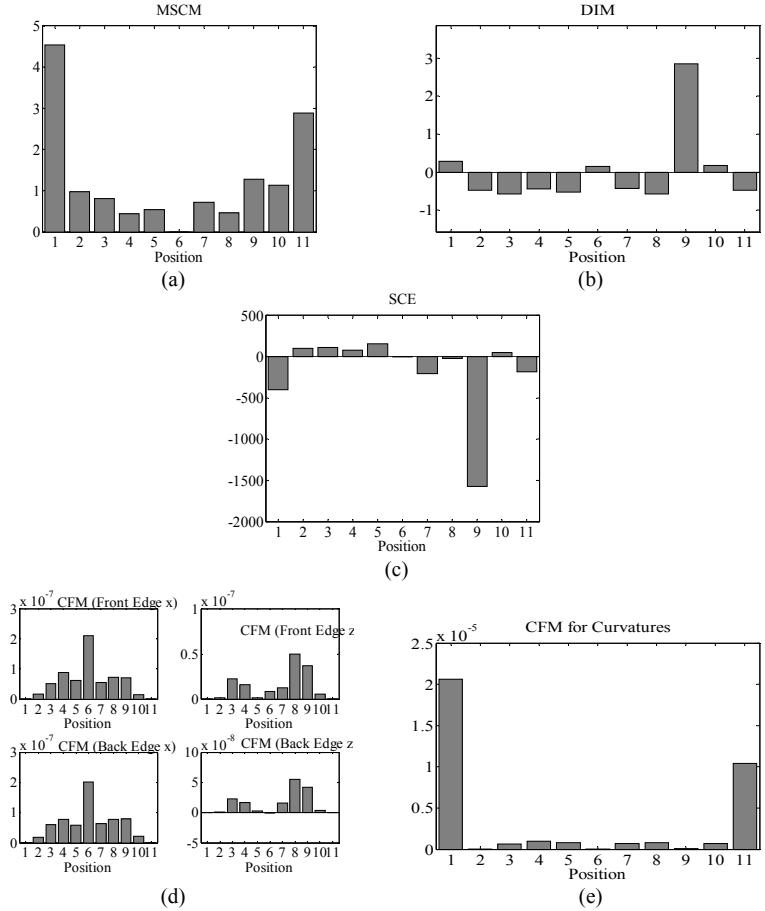


Figure B.38 – DS_{III} and DS_{VIII}: (a) MSCM; (b) DIM; (c) SCR; (d) CFM for modal displacements; and (e) CFM for modal curvatures.

B.2 Non-model Based Methods with Calculated Curvatures for Ambient Excitation

B.2.1 Comparison with the Reference Scenario

B.2.1.1 Reference Scenario and Damage Scenario I

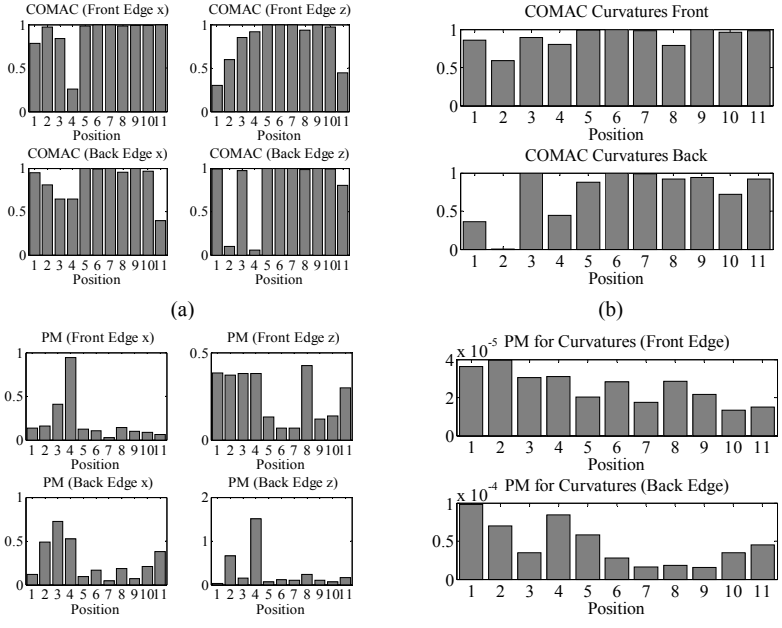


Figure B.39 – RS and DS_I: (a) COMAC values for modal displacements; (b) COMAC values for modal curvatures; (c) PM for modal displacements; and (d) PM for modal curvatures.

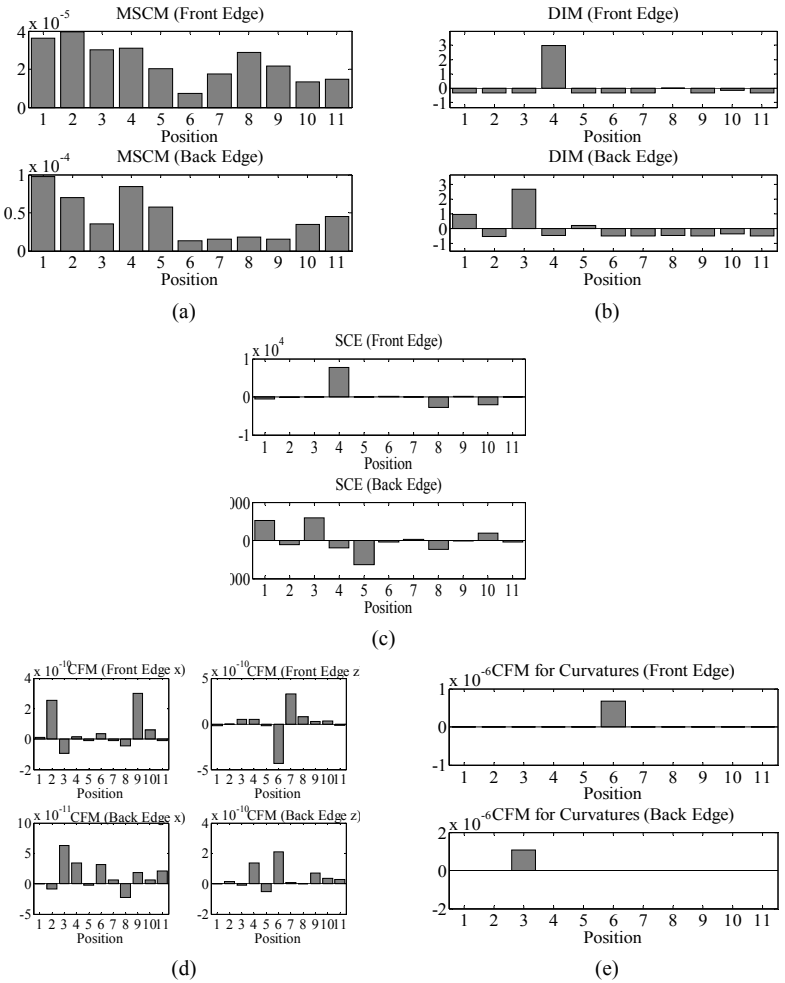


Figure B.40 – RS and DS_I: (a) MSCM; (b) DIM; (c) SCR; (d) CFM for modal displacements; and (e) CFM for modal curvatures.

B.2.1.2 Reference Scenario and Damage Scenario II

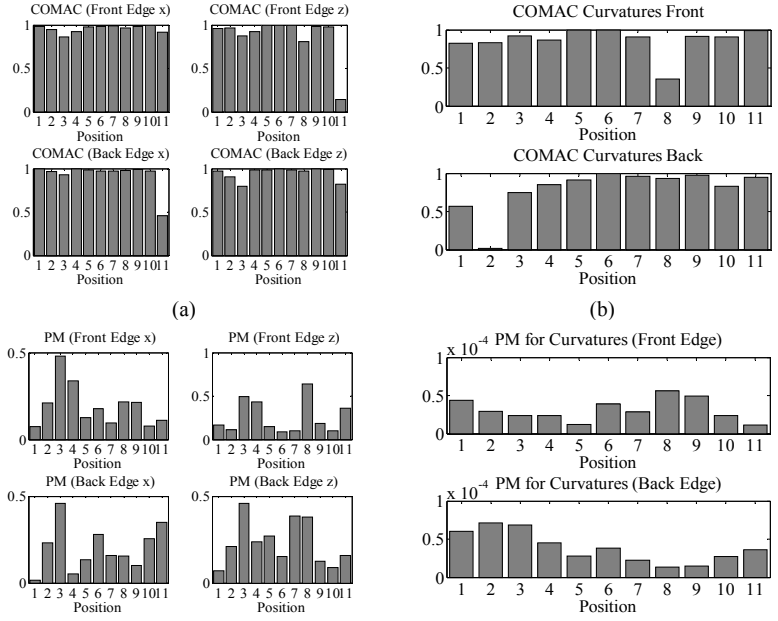


Figure B.41 – RS and DS_{II}: (a) COMAC values for modal displacements; (b) COMAC values for modal curvatures; (c) PM for modal displacements; and (d) PM for modal curvatures.

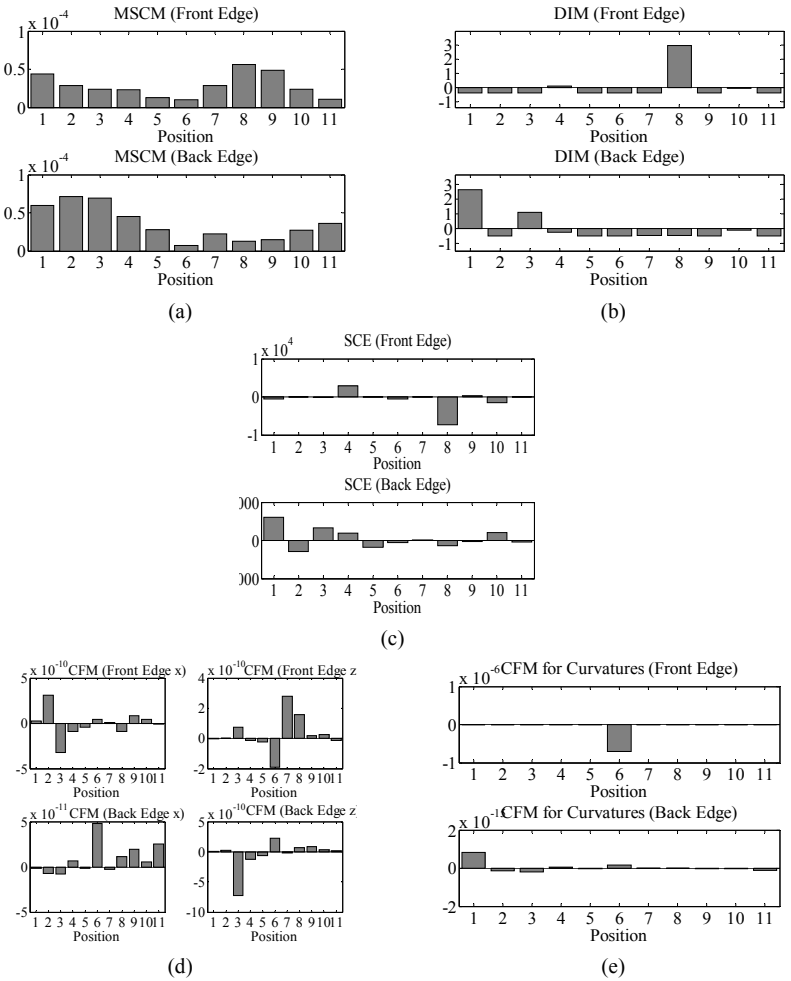


Figure B.42 – RS and DSII: (a) MSCM; (b) DIM; (c) SCR; (d) CFM for modal displacements; and (e) CFM for modal curvatures.

B.2.1.3 Reference Scenario and Damage Scenario III

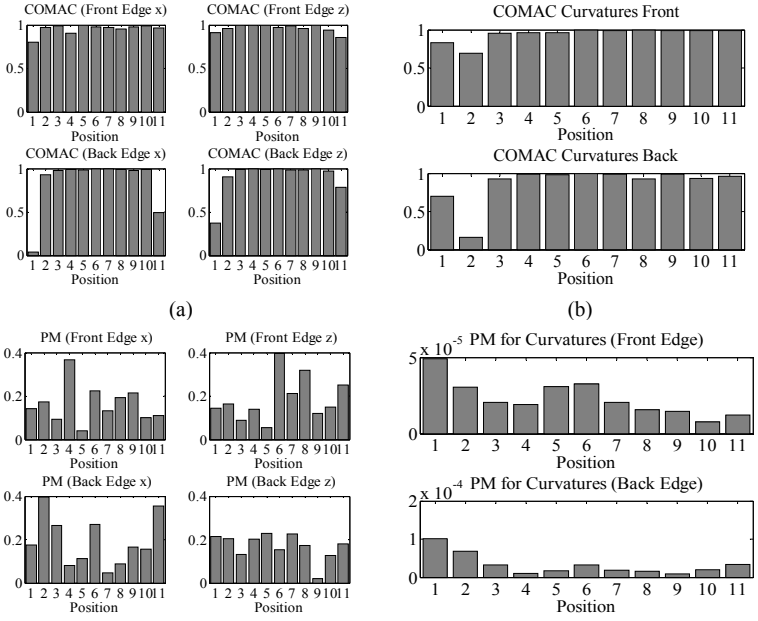


Figure B.43 – RS and DS_{III}: (a) COMAC values for modal displacements; (b) COMAC values for modal curvatures; (c) PM for modal displacements; and (d) PM for modal curvatures.

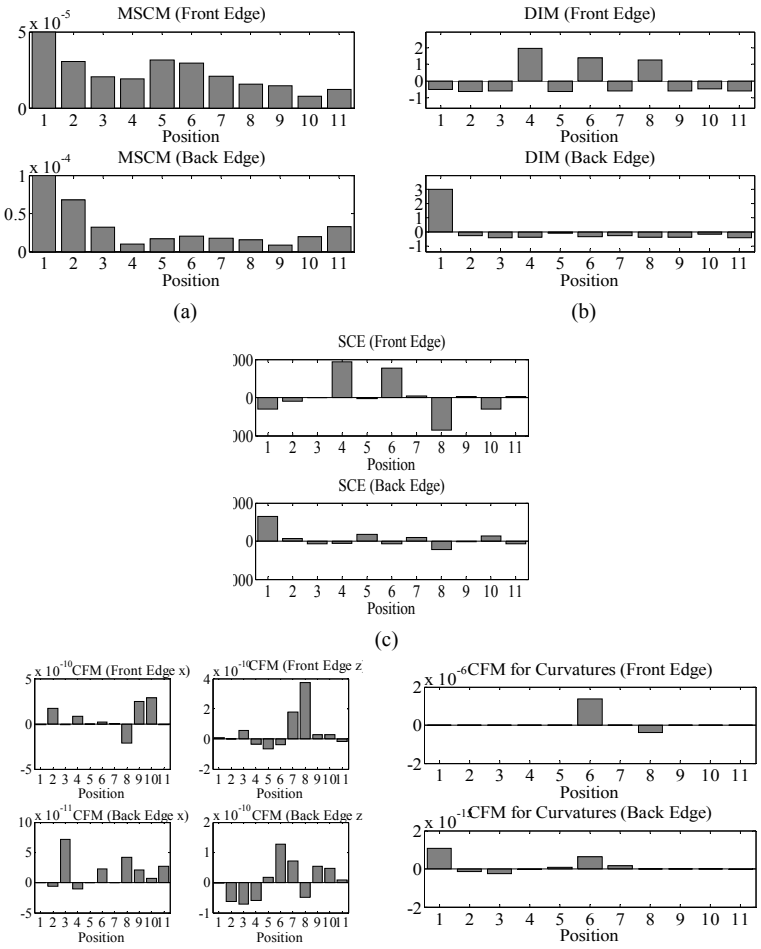


Figure B.44 – RS and DS_{III}: (a) MSCM; (b) DIM; (c) SCR; (d) CFM for modal displacements; and (e) CFM for modal curvatures.

B.2.1.4 Reference Scenario and Damage Scenario IV

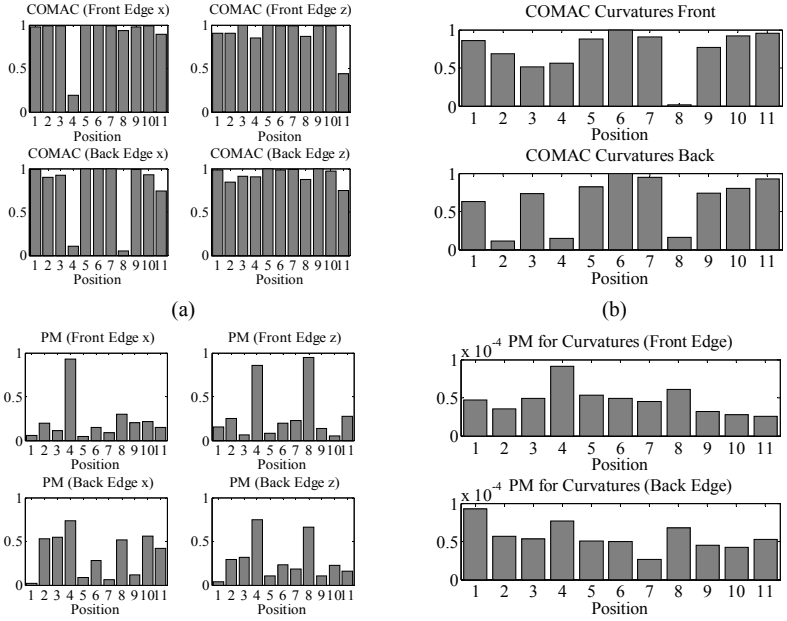


Figure B.45 – RS and DS_{IV}: (a) COMAC values for modal displacements; (b) COMAC values for modal curvatures; (c) PM for modal displacements; and (d) PM for modal curvatures.

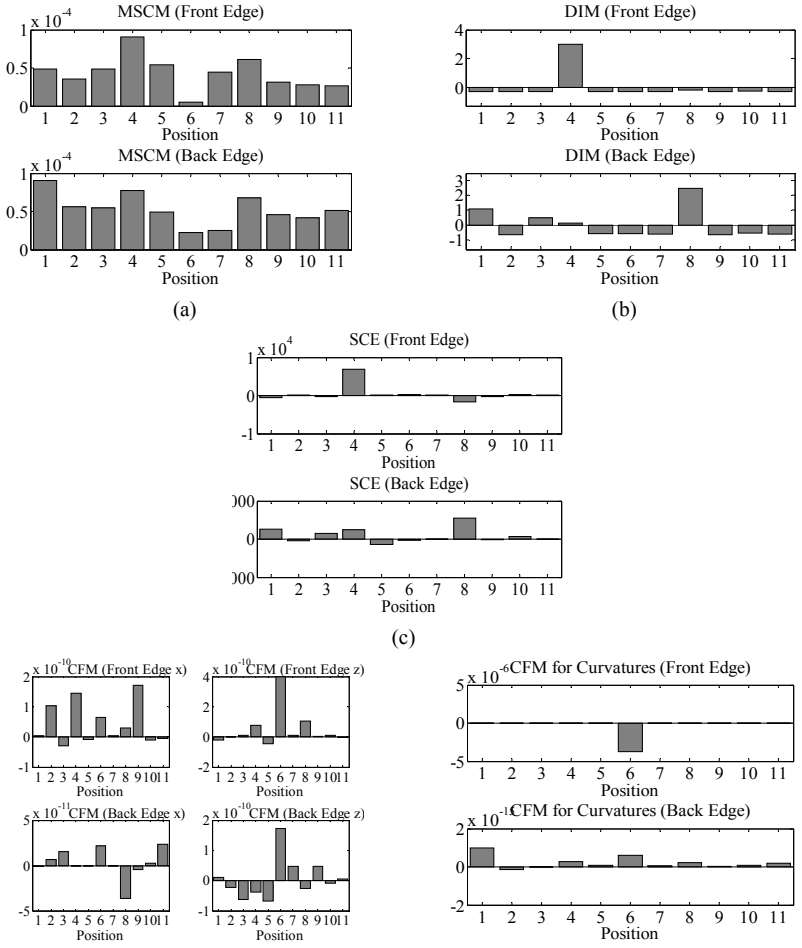


Figure B.46 – RS and DS_{IV}: (a) MSCM; (b) DIM; (c) SCR; (d) CFM for modal displacements; and (e) CFM for modal curvatures.

B.2.1.5 Reference Scenario and Damage Scenario V

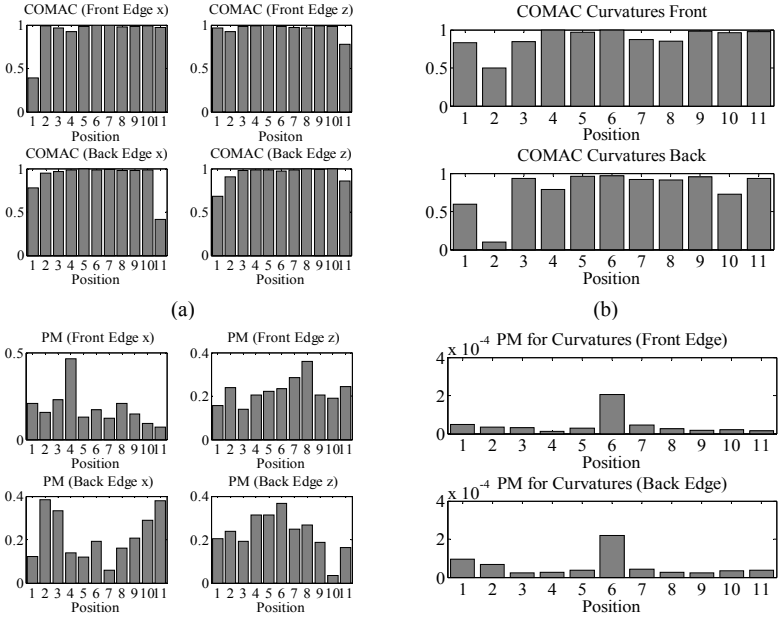


Figure B.47 – RS and DS_V: (a) COMAC values for modal displacements; (b) COMAC values for modal curvatures; (c) PM for modal displacements; and (d) PM for modal curvatures.

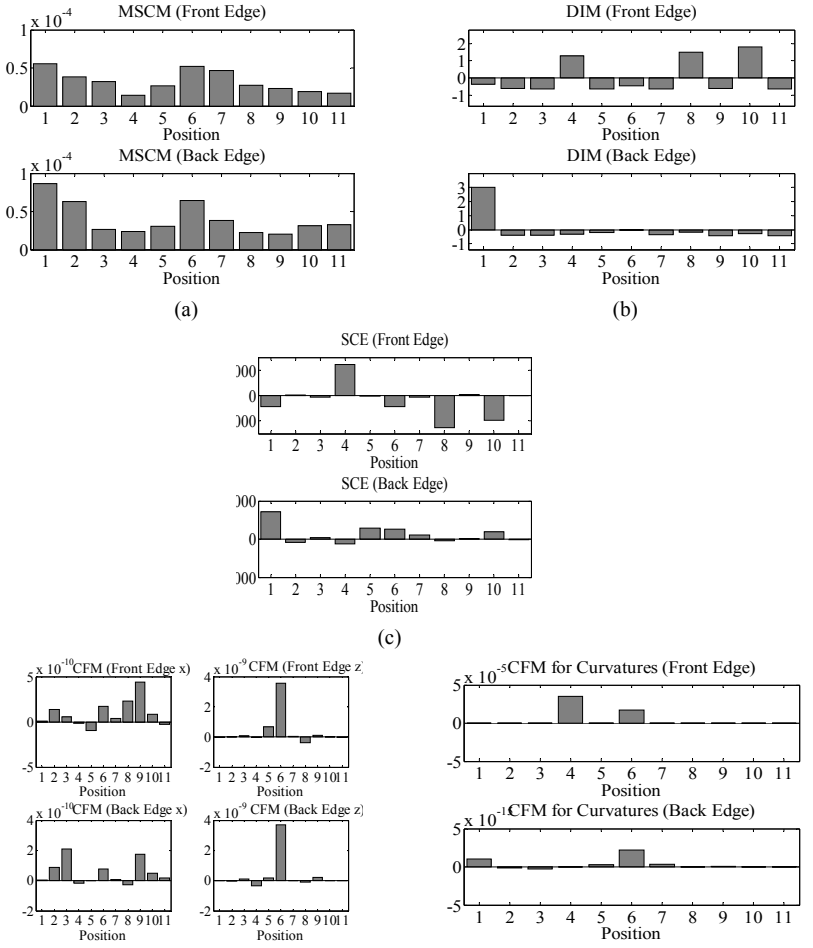


Figure B.48 – RS and DS_V: (a) MSCM; (b) DIM; (c) SCR; (d) CFM for modal displacements; and (e) CFM for modal curvatures.

B.2.1.6 Reference Scenario and Damage Scenario VI

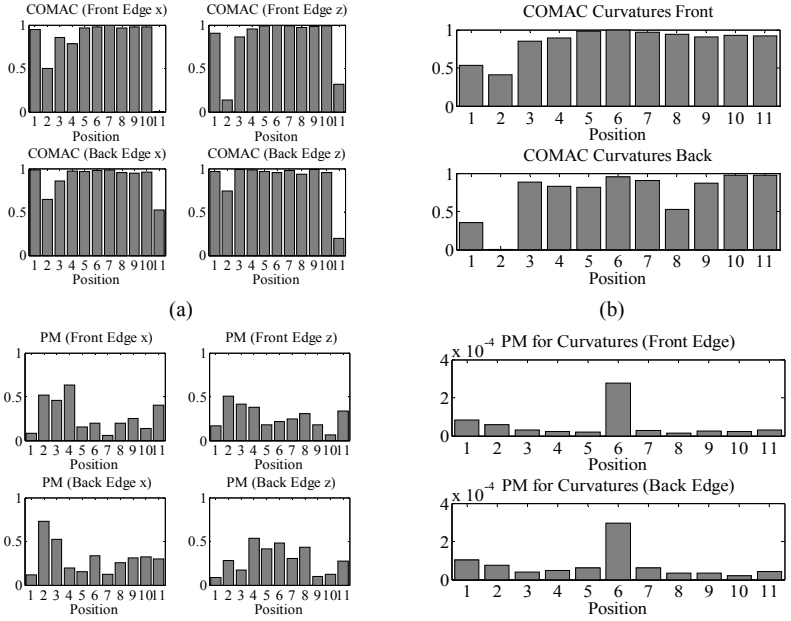


Figure B.49 – RS and DS_{VI}: (a) COMAC values for modal displacements; (b) COMAC values for modal curvatures; (c) PM for modal displacements; and (d) PM for modal curvatures.

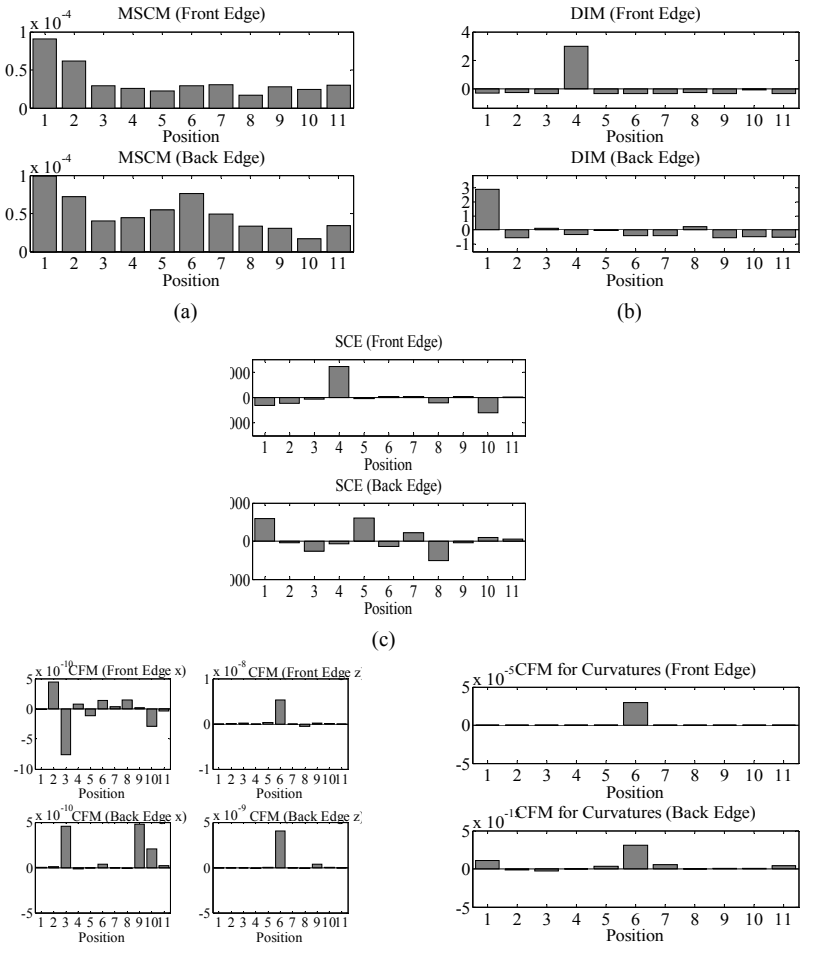


Figure B.50 – RS and DS_{VI}: (a) MSCM; (b) DIM; (c) SCR; (d) CFM for modal displacements; and (e) CFM for modal curvatures.

B.2.1.7 Reference Scenario and Damage Scenario VII

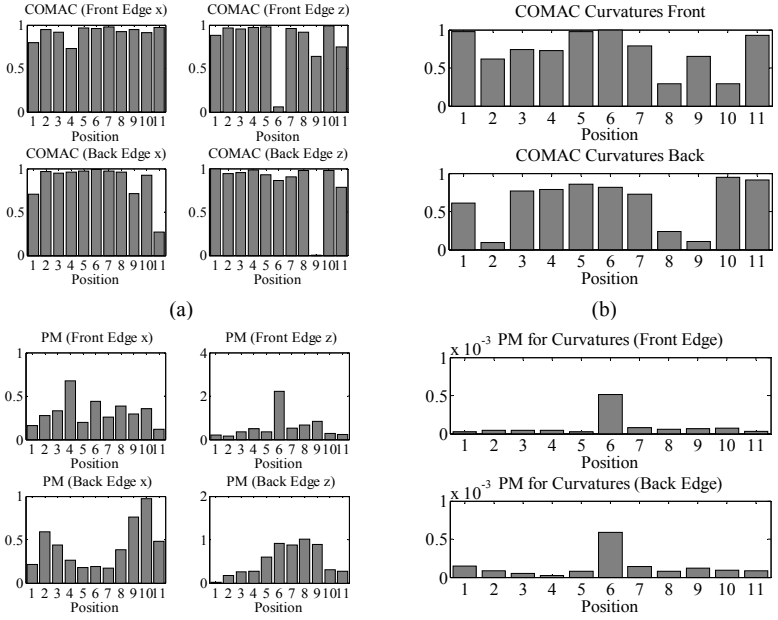


Figure B.51 – RS and DS_{VII}: (a) COMAC values for modal displacements; (b) COMAC values for modal curvatures; (c) PM for modal displacements; and (d) PM for modal curvatures.

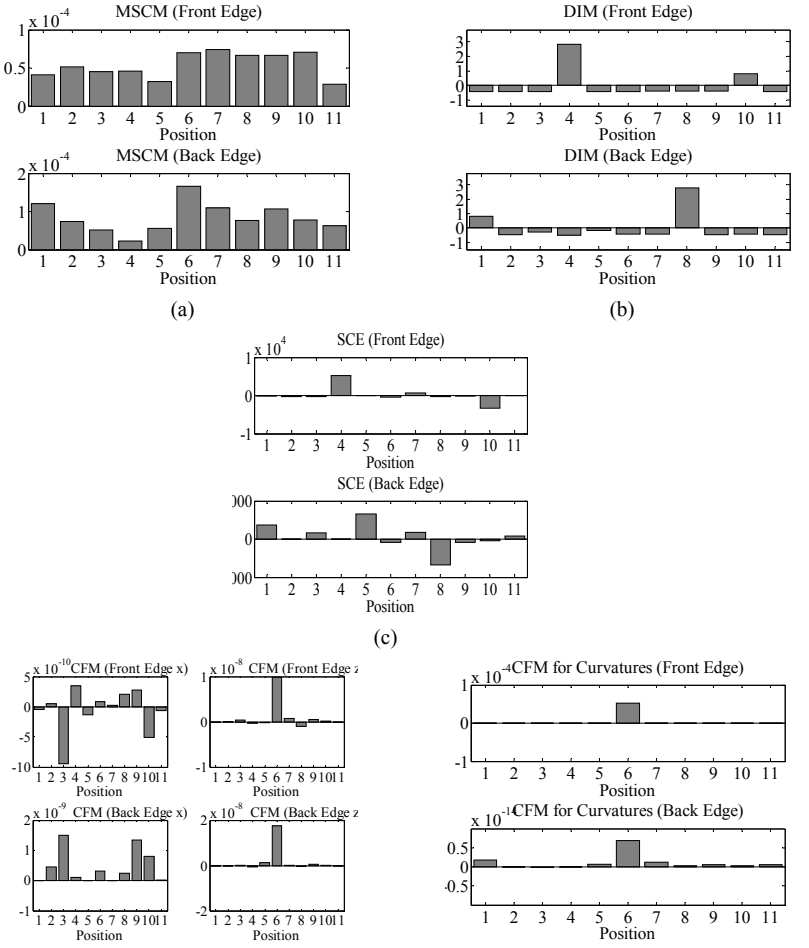


Figure B.52 – RS and DS_{VII}: (a) MSCM; (b) DIM; (c) SCR; (d) CFM for modal displacements; and (e) CFM for modal curvatures.

B.2.1.8 Reference Scenario and Damage Scenario VIII

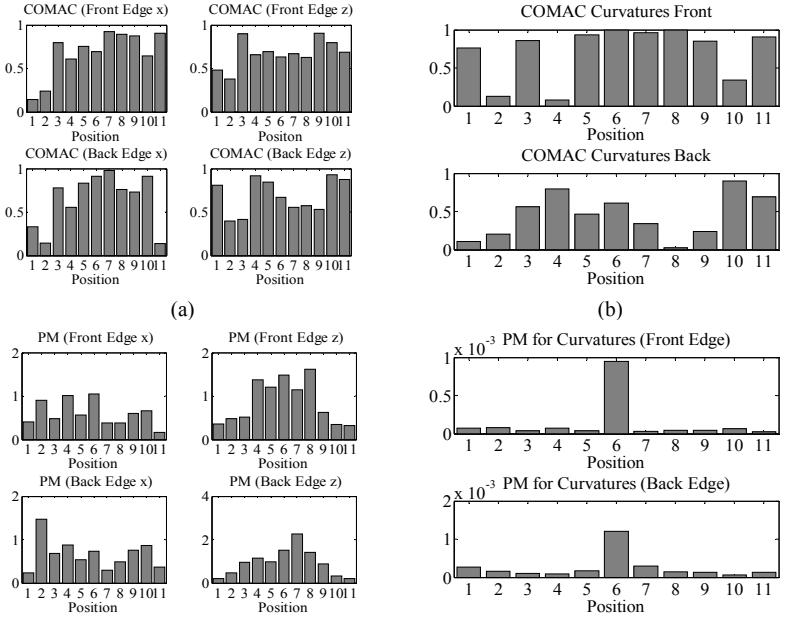


Figure B.53 – RS and DS_{VIII}: (a) COMAC values for modal displacements; (b) COMAC values for modal curvatures; (c) PM for modal displacements; and (d) PM for modal curvatures.

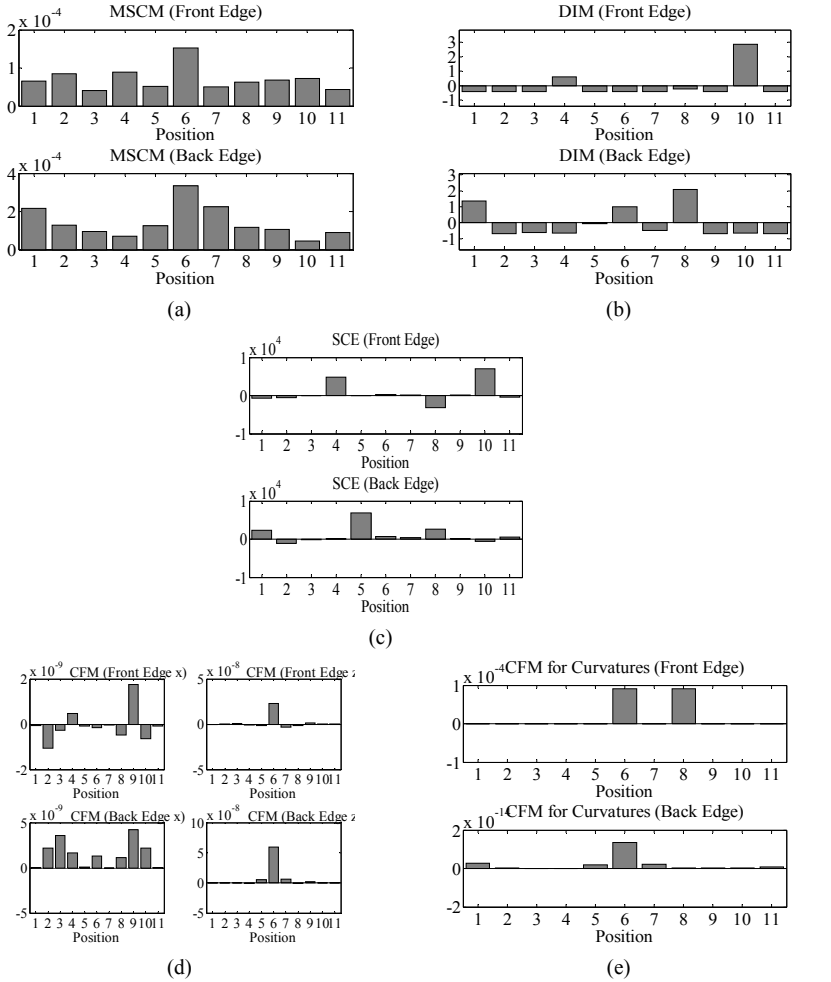


Figure B.54 – RS and DS_{VIII}: (a) MSCM; (b) DIM; (c) SCR; (d) CFM for modal displacements; and (e) CFM for modal curvatures.

B.2.2 Relative Comparison

B.2.2.1 Damage Scenario I and Damage Scenario II

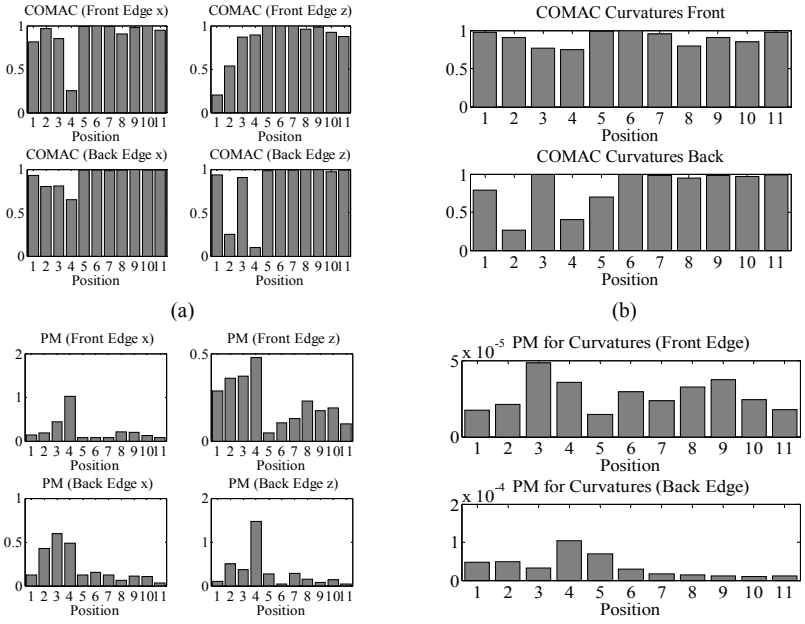


Figure B.55 – DS_I and DS_{II}: (a) COMAC values for modal displacements; (b) COMAC values for modal curvatures; (c) PM for modal displacements; and (d) PM for modal curvatures.

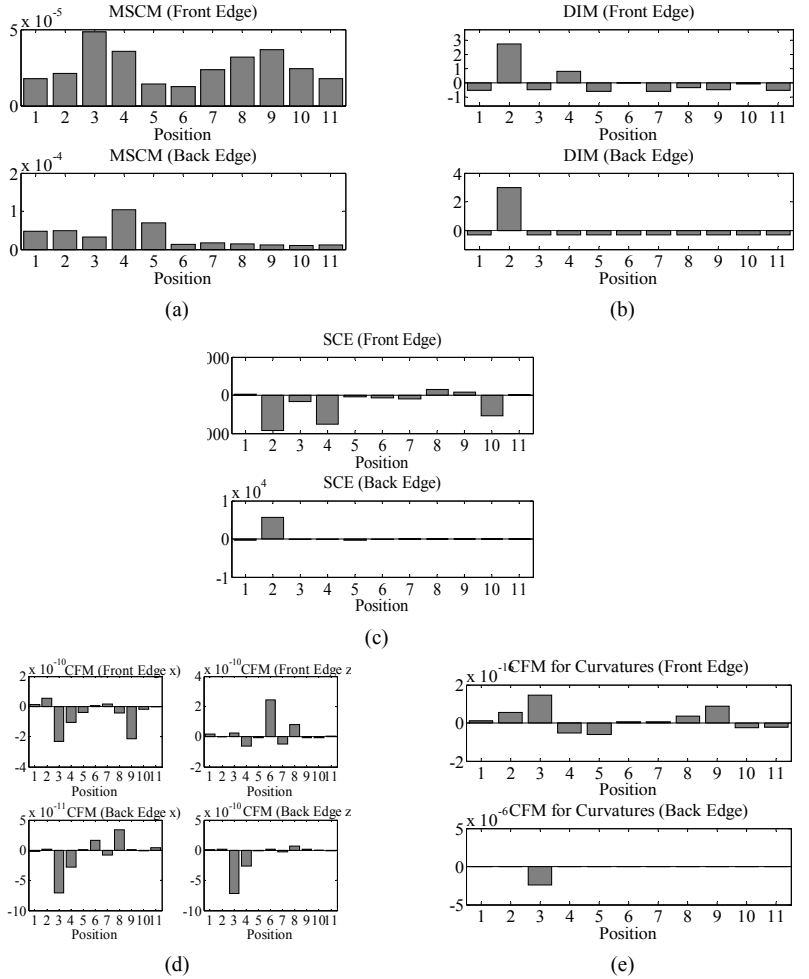


Figure B.56 – DS_I and DS_{II}: (a) MSCM; (b) DIM; (c) SCR; (d) CFM for modal displacements; and (e) CFM for modal curvatures.

B.2.2.2 Damage Scenario II and Damage Scenario III

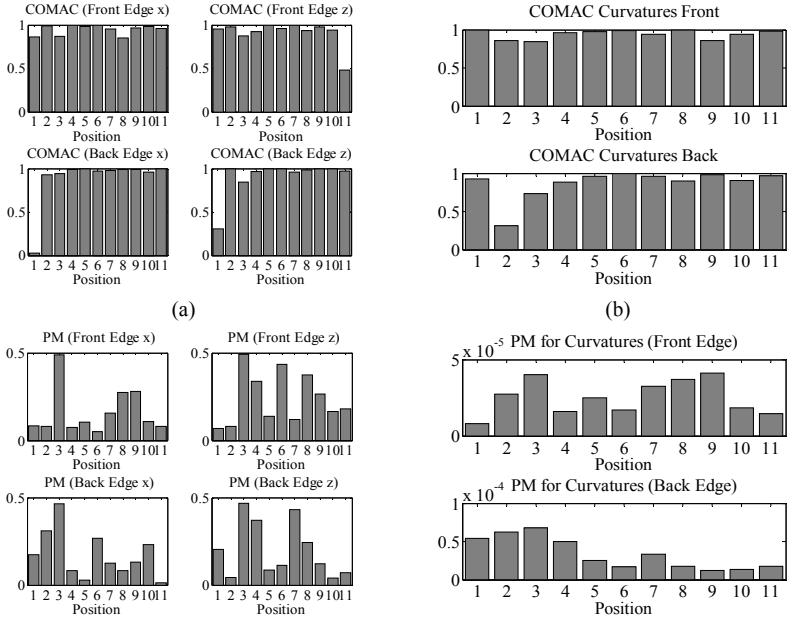


Figure B.57 – DS_{II} and DS_{III}: (a) COMAC values for modal displacements; (b) COMAC values for modal curvatures; (c) PM for modal displacements; and (d) PM for modal curvatures.

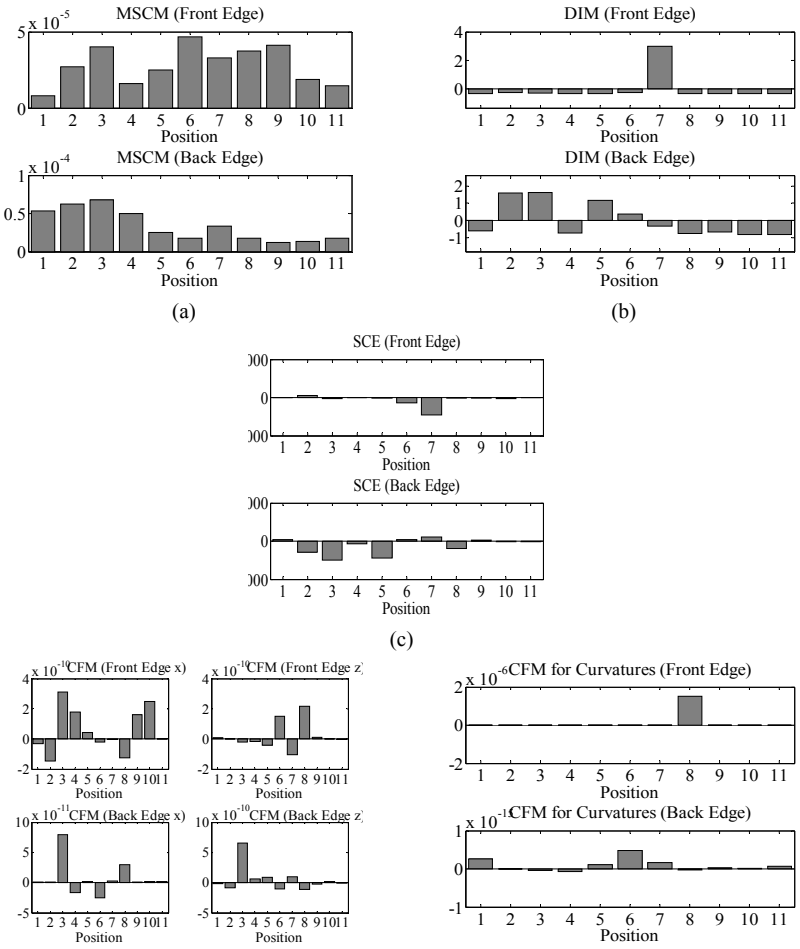


Figure B.58 – DS_{II} and DS_{III}: (a) MSCM; (b) DIM; (c) SCR; (d) CFM for modal displacements; and (e) CFM for modal curvatures.

B.2.2.3 Damage Scenario III and Damage Scenario IV

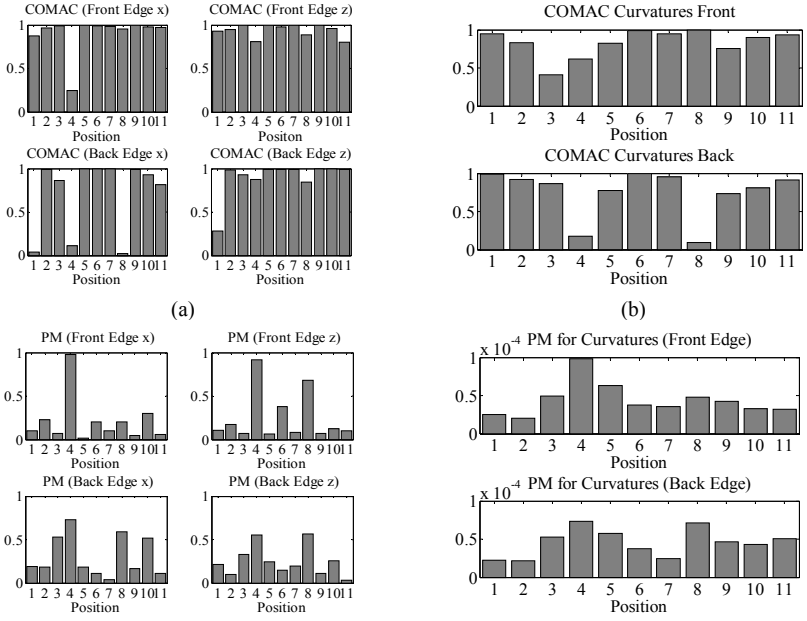


Figure B.59 – DS_{III} and DS_{IV}: (a) COMAC values for modal displacements; (b) COMAC values for modal curvatures; (c) PM for modal displacements; and (d) PM for modal curvatures.

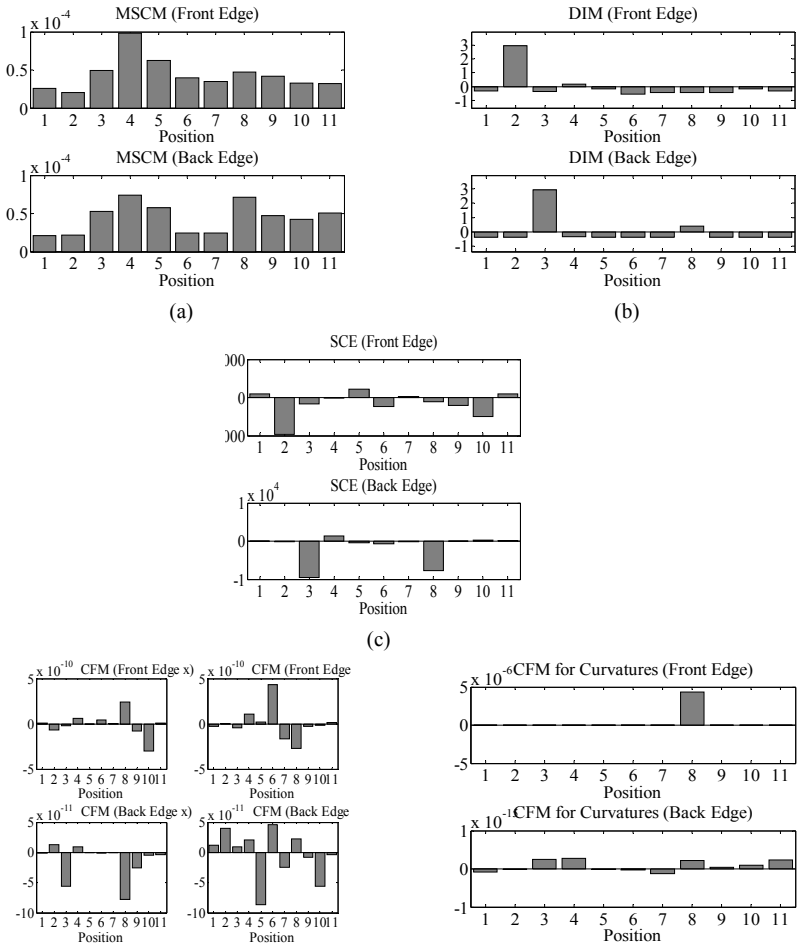


Figure B.60 – DS_{III} and DS_{IV}: (a) MSCM; (b) DIM; (c) SCR; (d) CFM for modal displacements; and (e) CFM for modal curvatures.

B.2.2.4 Damage Scenario IV and Damage Scenario V

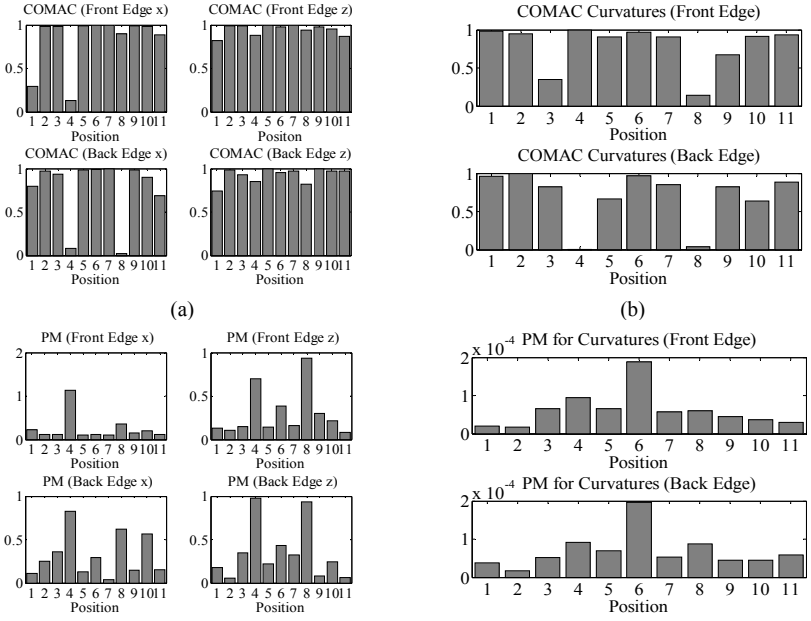


Figure B.61 – DS_{IV} and DS_V: (a) COMAC values for modal displacements; (b) COMAC values for modal curvatures; (c) PM for modal displacements; and (d) PM for modal curvatures.

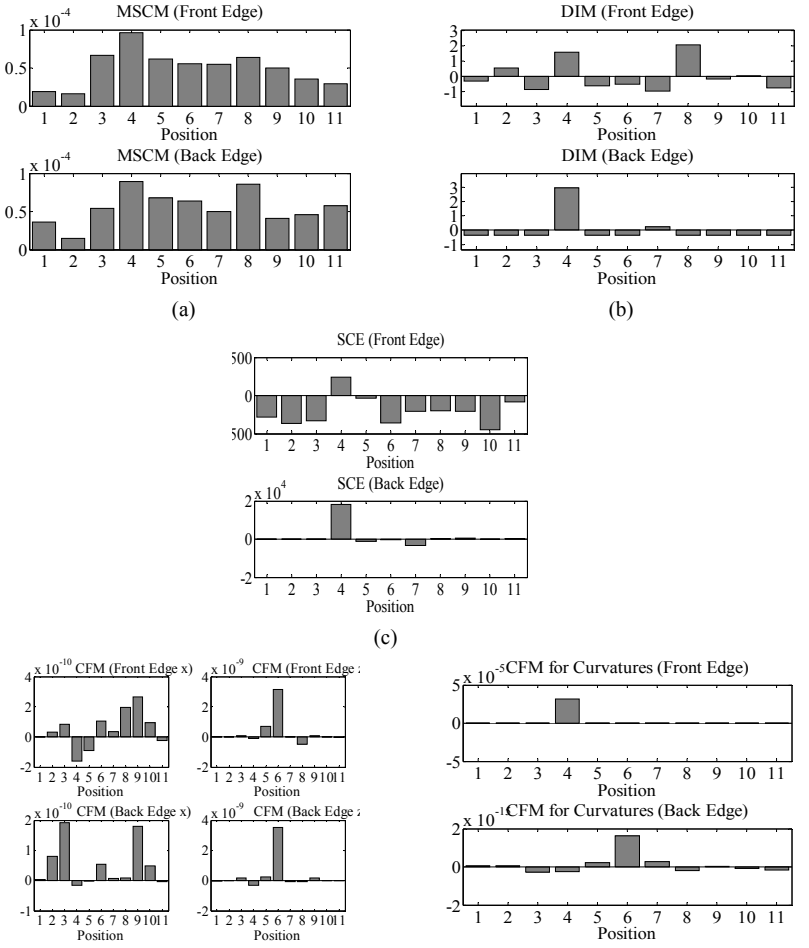


Figure B.62 – DS_{IV} and DS_V: (a) MSCM; (b) DIM; (c) SCR; (d) CFM for modal displacements; and (e) CFM for modal curvatures.

B.2.2.5 Damage Scenario V and Damage Scenario VI

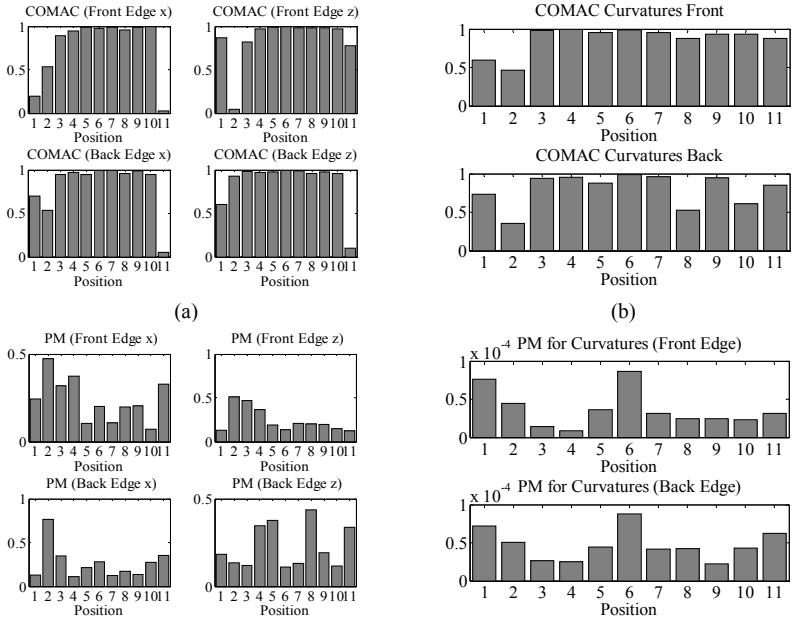


Figure B.63 – DS_V and DS_{VI}: (a) COMAC values for modal displacements; (b) COMAC values for modal curvatures; (c) PM for modal displacements; and (d) PM for modal curvatures.

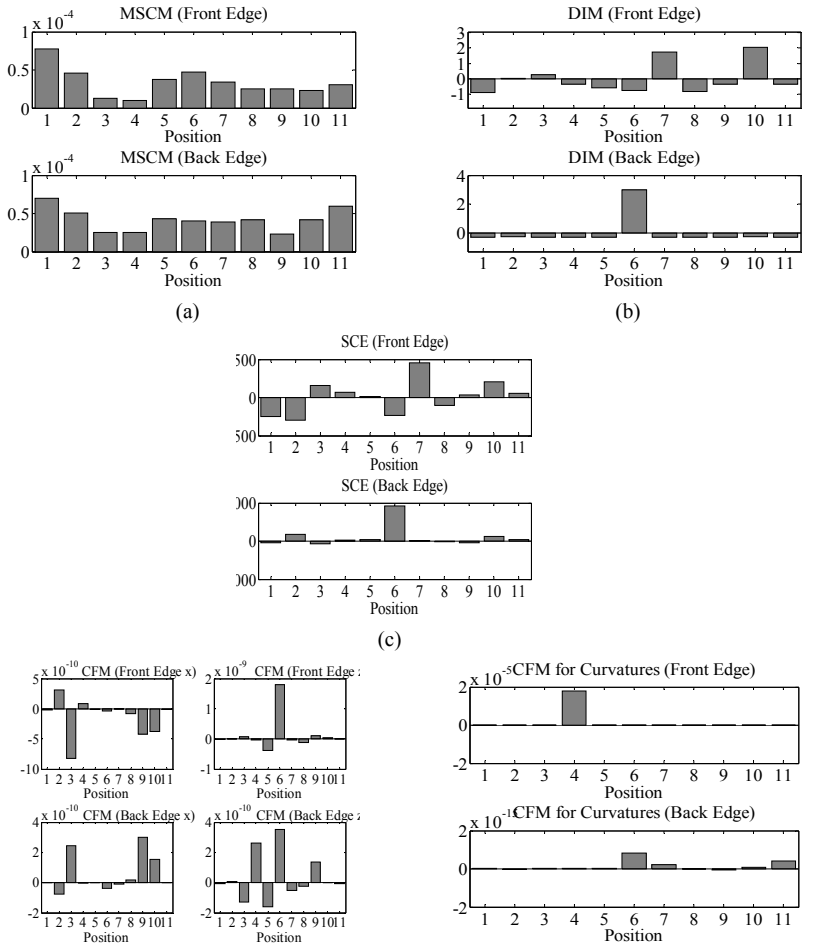


Figure B.64 – DS_V and DS_{VI}: (a) MSCM; (b) DIM; (c) SCR; (d) CFM for modal displacements; and (e) CFM for modal curvatures.

B.2.2.6 Damage Scenario VI and Damage Scenario VII

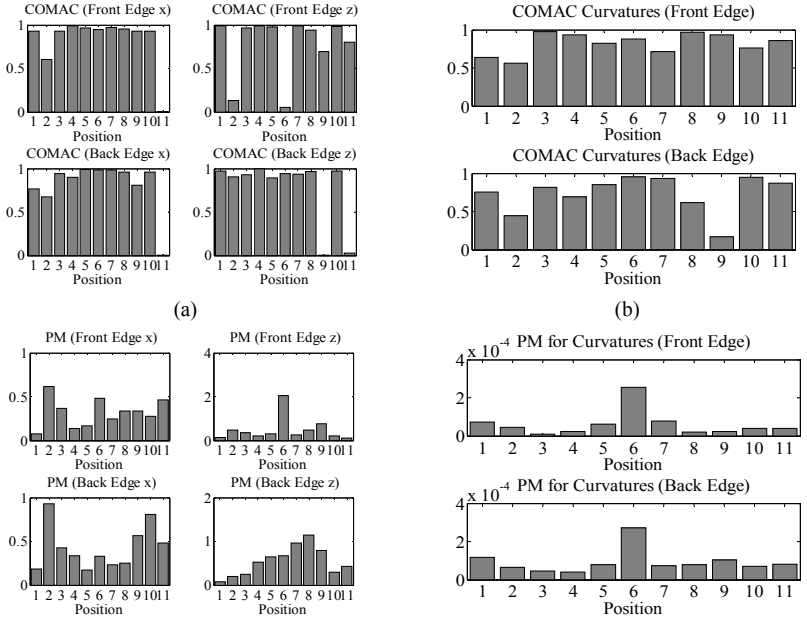


Figure B.65 – DS_{VI} and DS_{VII}: (a) COMAC values for modal displacements; (b) COMAC values for modal curvatures; (c) PM for modal displacements; and (d) PM for modal curvatures.

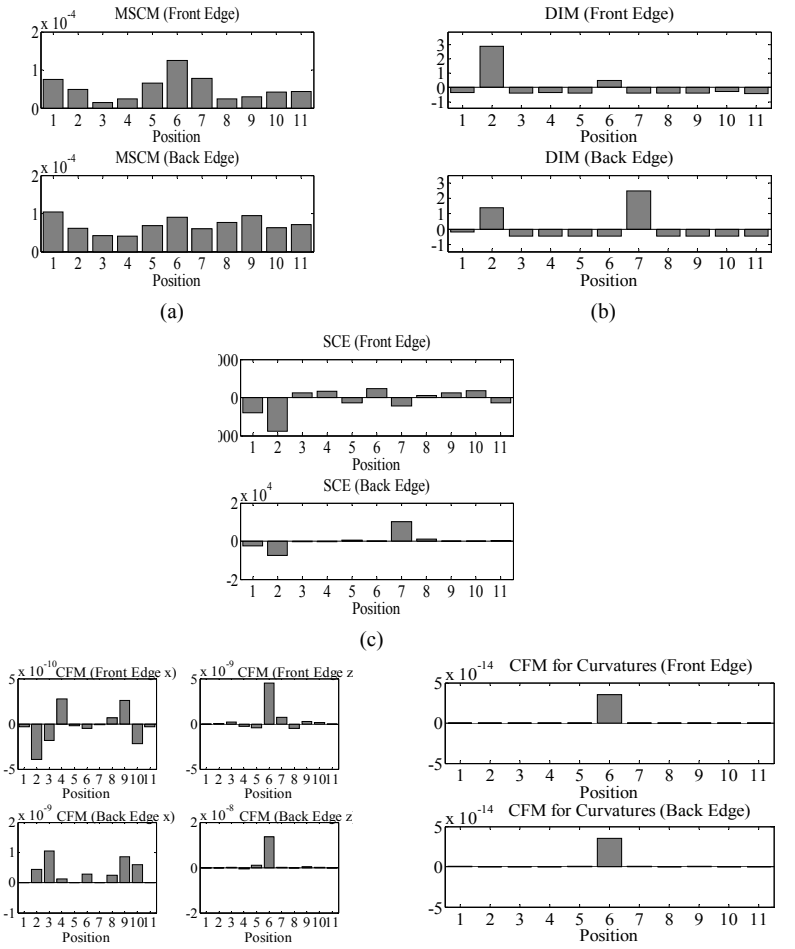


Figure B.66 – DS_{VI} and DS_{VII}: (a) MSCM; (b) DIM; (c) SCR; (d) CFM for modal displacements; and (e) CFM for modal curvatures.

B.2.2.7 Damage Scenario VII and Damage Scenario VIII

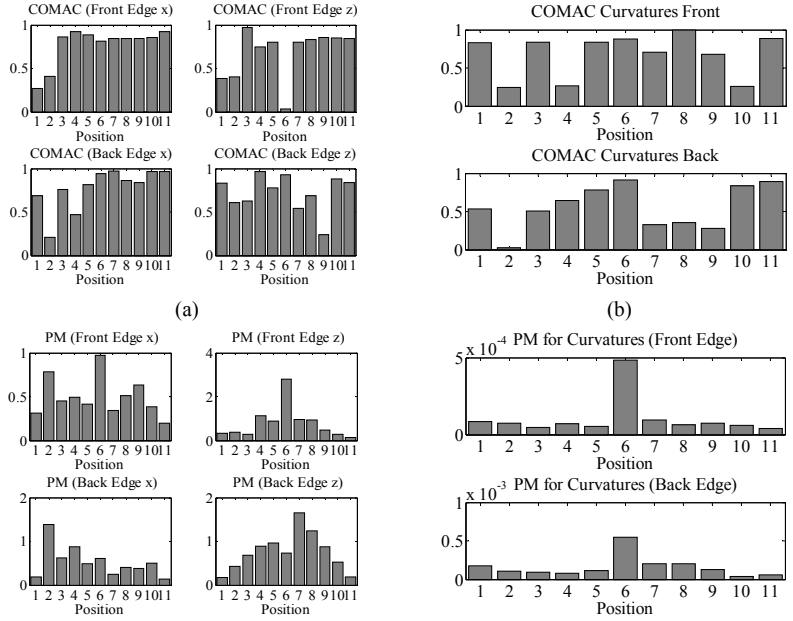


Figure B.67 – DS_{VII} and DS_{VIII}: (a) COMAC values for modal displacements; (b) COMAC values for modal curvatures; (c) PM for modal displacements; and (d) PM for modal curvatures.

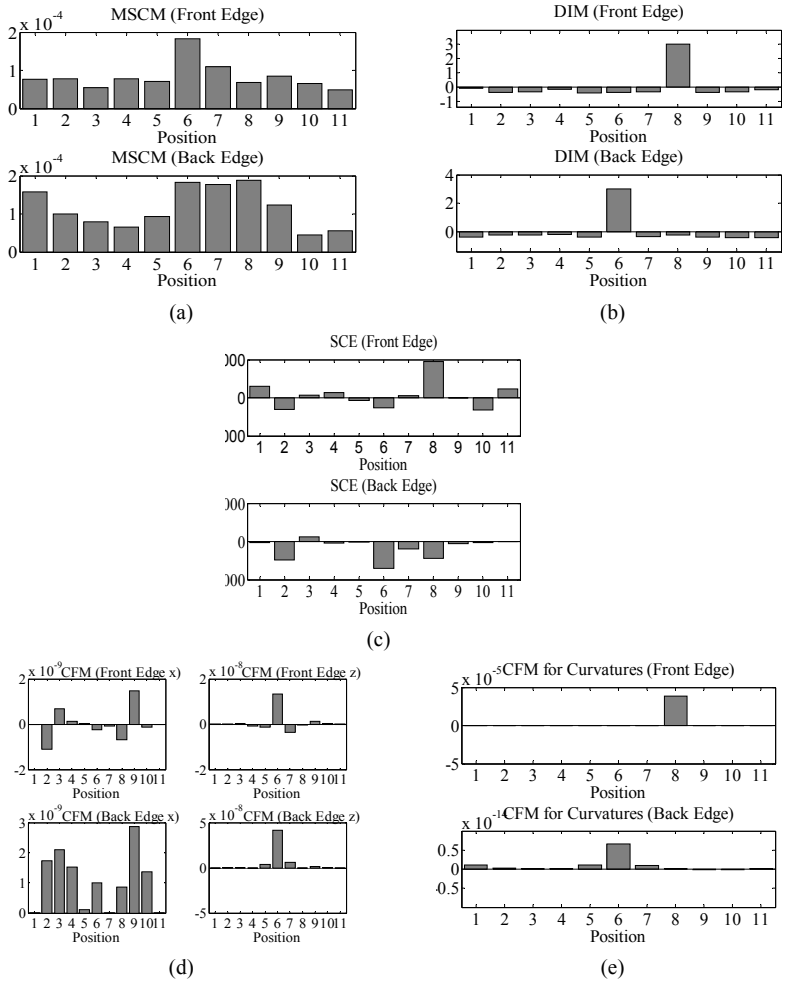


Figure B.68 – DS_{VII} and DS_{VIII}: (a) MSCM; (b) DIM; (c) SCR; (d) CFM for modal displacements; and (e) CFM for modal curvatures.

B.2.3 Comparison with the Damage Scenario III

B.2.3.1 Damage Scenario III and Damage Scenario V

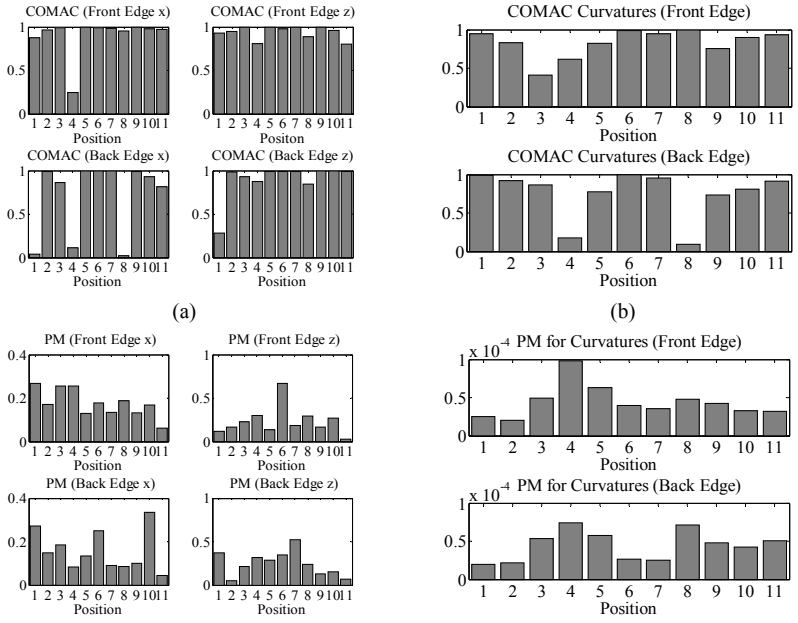


Figure B.69 – DS_{III} and DS_V: (a) COMAC values for modal displacements; (b) COMAC values for modal curvatures; (c) PM for modal displacements; and (d) PM for modal curvatures.

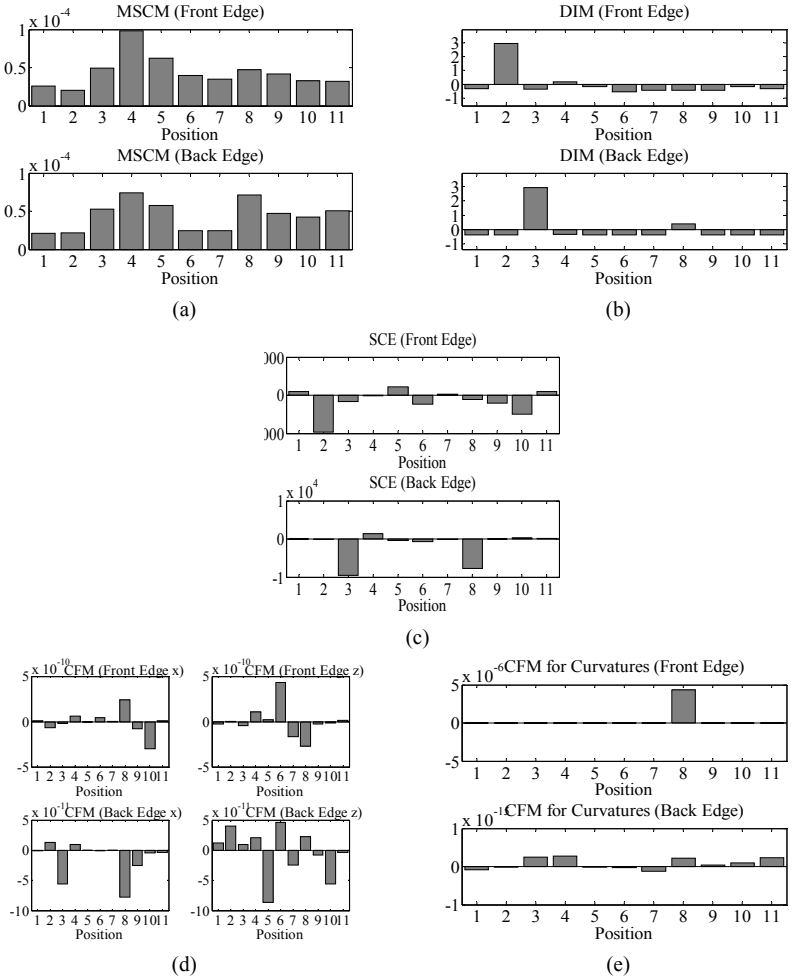


Figure B.70 – DS_{III} and DS_V: (a) MSCM; (b) DIM; (c) SCR; (d) CFM for modal displacements; and (e) CFM for modal curvatures.

B.2.3.2 Damage Scenario III and Damage Scenario VI

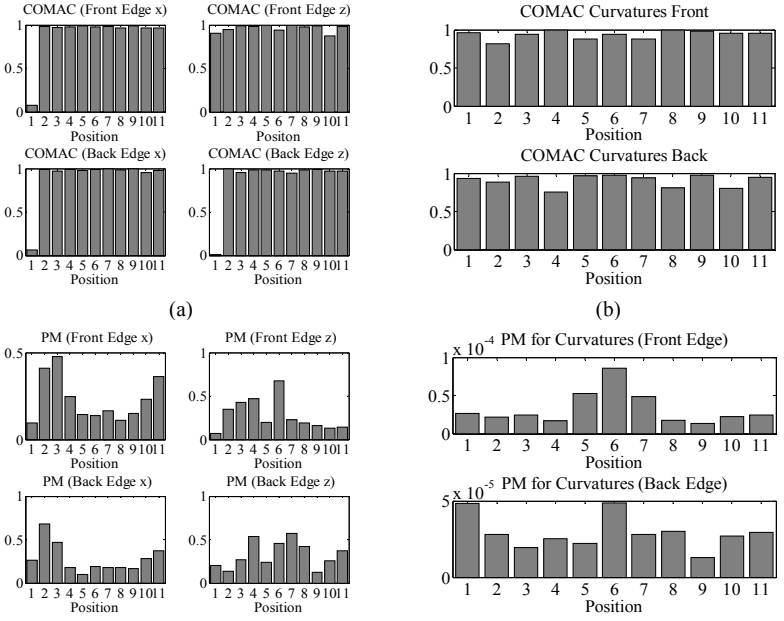


Figure B.71 – DS_{III} and DS_{VI}: (a) COMAC values for modal displacements; (b) COMAC values for modal curvatures; (c) PM for modal displacements; and (d) PM for modal curvatures.

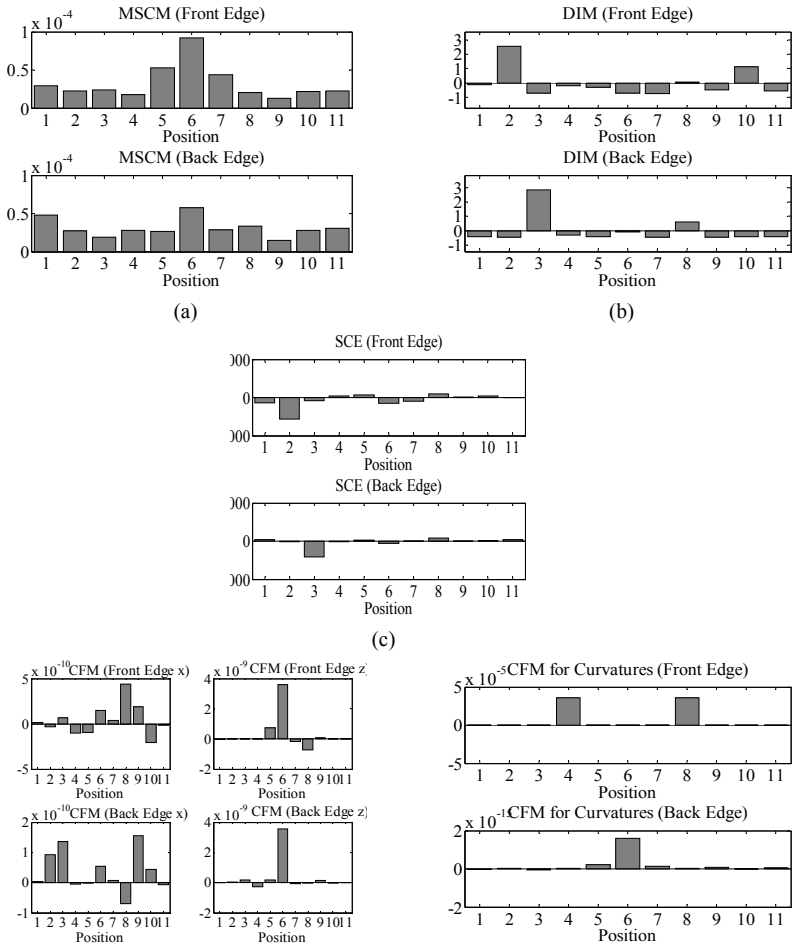


Figure B.72 – DS_{III} and DS_{VI}: (a) MSCM; (b) DIM; (c) SCR; (d) CFM for modal displacements; and (e) CFM for modal curvatures

B.2.3.3 Damage Scenario III and Damage Scenario VII

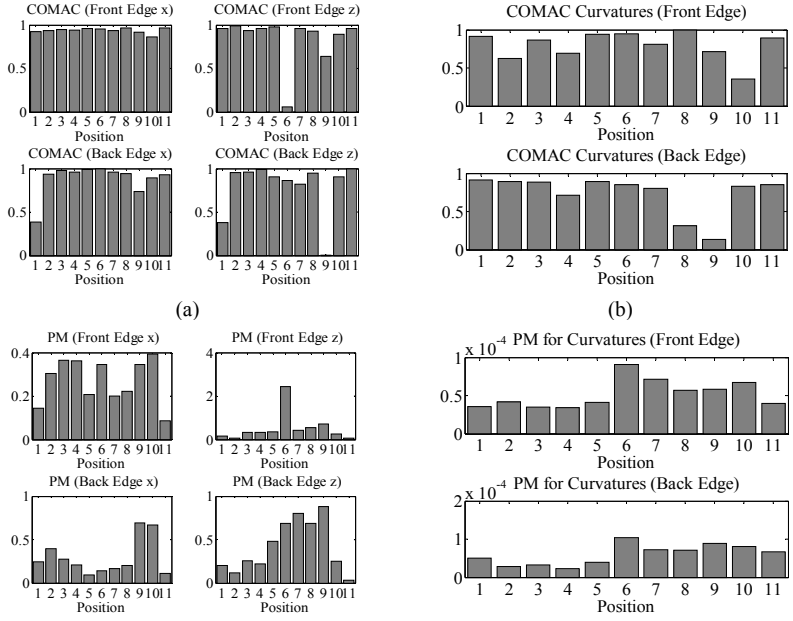


Figure B.73 – DS_{III} and DS_{VII}: (a) COMAC values for modal displacements; (b) COMAC values for modal curvatures; (c) PM for modal displacements; and (d) PM for modal curvatures.

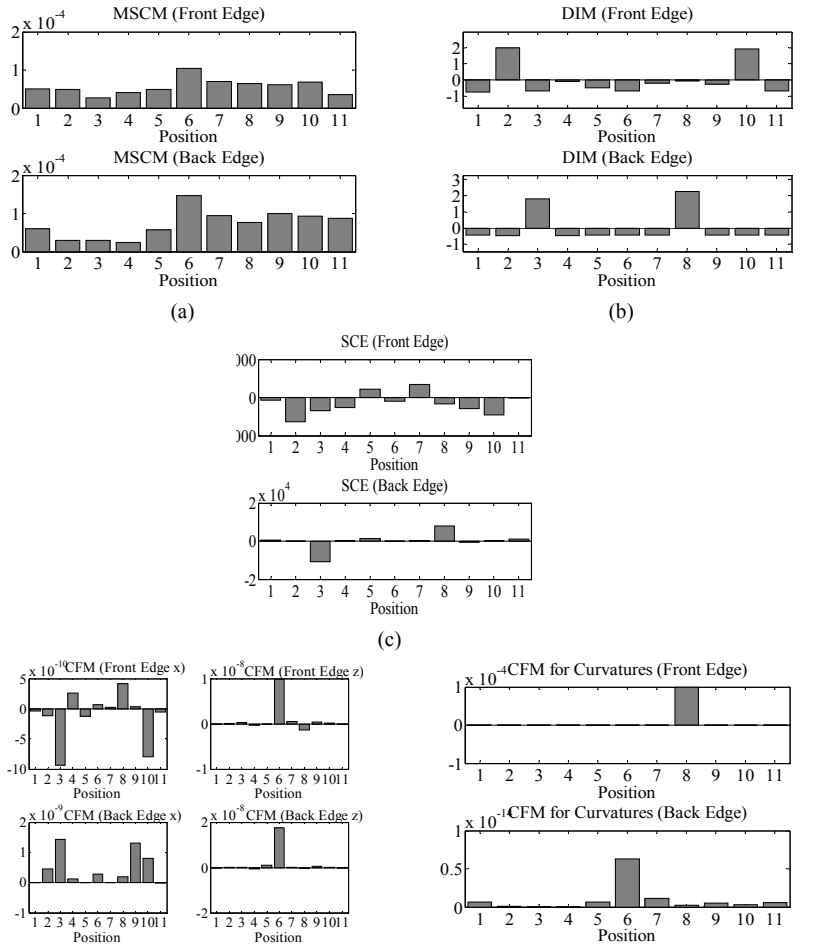


Figure B.74 – DS_{III} and DS_{VII}: (a) MSCM; (b) DIM; (c) SCR; (d) CFM for modal displacements; and (e) CFM for modal curvatures.

B.2.3.4 Damage Scenario III and Damage Scenario VIII

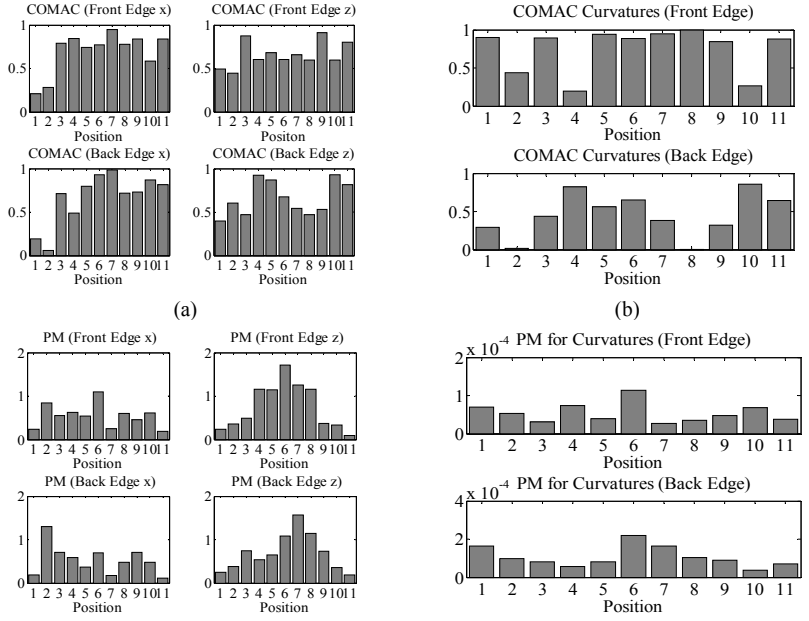


Figure B.75 – DS_{III} and DS_{VIII}: (a) COMAC values for modal displacements; (b) COMAC values for modal curvatures; (c) PM for modal displacements; and (d) PM for modal curvatures.

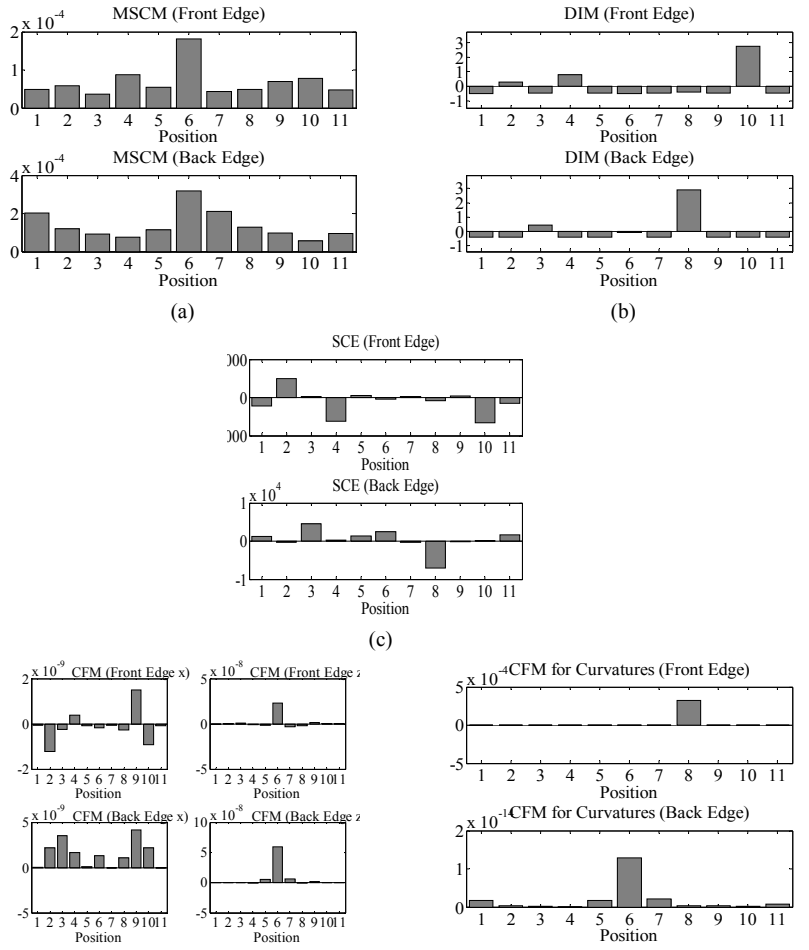


Figure B.76 – DS_{III} and DS_{VIII}: (a) MSCM; (b) DIM; (c) SCR; (d) CFM for modal displacements; and (e) CFM for modal curvatures.

B.3 Finite Element Model Updating Method

B.3.1.1 Damage Scenario IV

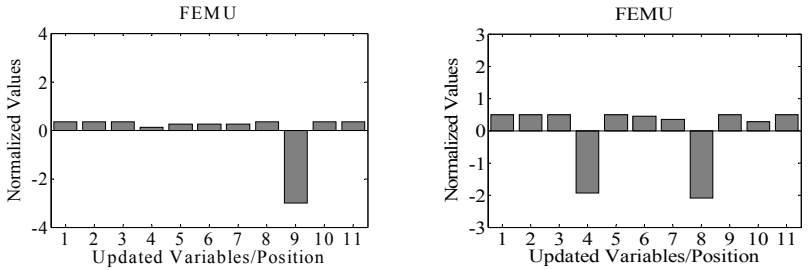


Figure B.77 – FEMU applied to DS_{IV}: (a) and (b) first and second global approach, respectively

B.3.1.2 Damage Scenario V

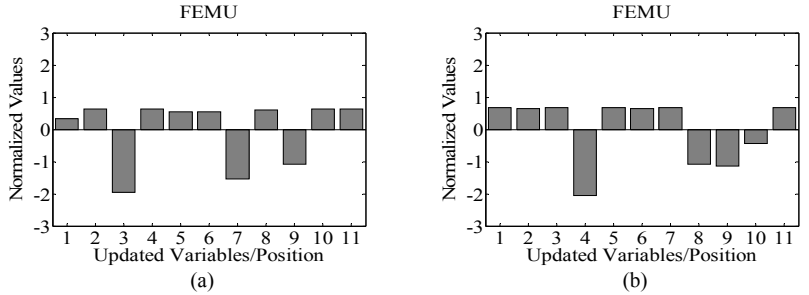


Figure B.78 – FEMU applied to DS_{V}: (a) and (b) first and second global approach, respectively

B.3.1.3 Damage Scenario VI

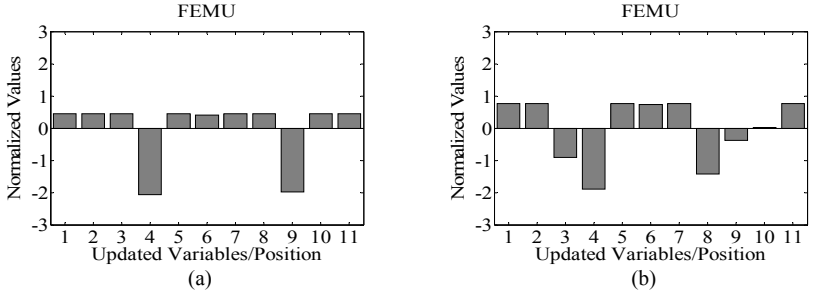


Figure B.79 – FEMU applied to DS_{VI}: (a) and (b) first and second global approach, respectively

B.3.1.4 Damage Scenario VII

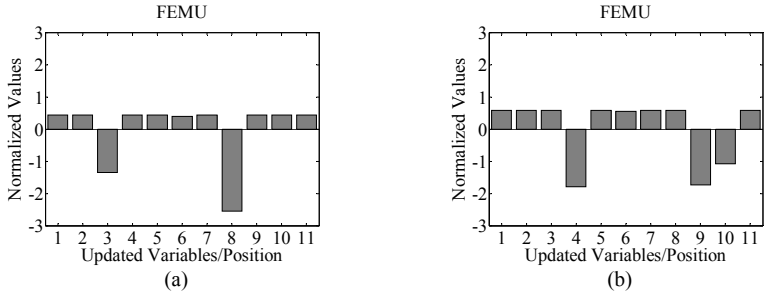


Figure B.80 – FEMU applied to DS_{VII}: (a) and (b) first and second global approach, respectively

B.3.1.5 Damage Scenario VIII

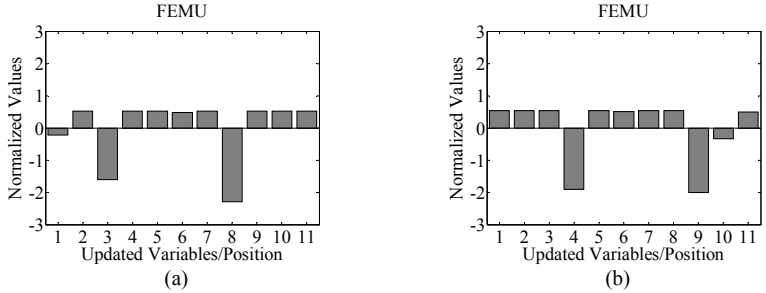


Figure B.81 – FEMU applied to DS_{VIII}: (a) and (b) first and second global approach, respectively

Annex C

Annex of Chapter 6

Index of Annex C

C.1 Non-Model Based Methods Applied to Series A C.3
C.1.1 Comparison with the Reference Scenario C.3
C.1.2 Relative Comparison C.8
C.2 Non-Model Based Methods Applied to Series B C.12
C.2.1 Comparison with the Reference Scenario C.12
C.2.2 Relative Comparison C.17
C.3 Non-Model Based Methods Applied to Series C C.21
C.3.1 Comparison with the Reference Scenario C.21
C.3.2 Relative Comparison C.25
C.4 Finite Element Model Updating Method Applied to Series A C.28
C.4.1 Damage Scenario II-A C.28
C.4.2 Damage Scenario III-A C.28
C.4.3 Damage Scenario IV-A C.28
C.4.4 Damage Scenario V-A C.28
C.5 Finite Element Model Updating Method Applied to Series B C.29
C.5.1 Damage Scenario III-B C.29
C.5.2 Damage Scenario IV-B C.29
C.5.3 Damage Scenario V-B C.29
C.6 Finite Element Model Updating Method Applied to Series C C.30
C.6.1 Damage Scenario II-C C.30
C.6.2 Damage Scenario III-C C.30
C.6.3 Damage Scenario IV-C C.30

C.1 Non-Model Based Methods Applied to Series A

C.1.1 Comparison with the Reference Scenario

C.1.1.1 Reference Scenario A and Damage Scenario I-A

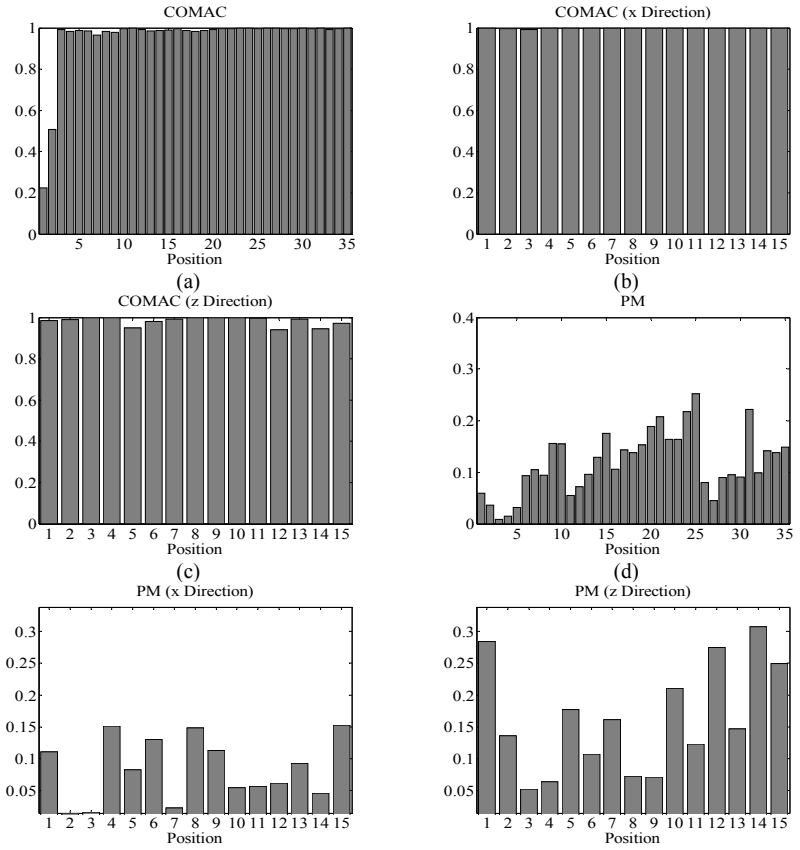


Figure C.1 – RS_A and $DS_{I\text{-}A}$: (a) COMAC values for modal displacements; (b) and (c) COMAC values for modal curvatures in the *x* and *z* direction, respectively; (d) PM for modal displacements; and (e) and (f) PM for modal curvatures in the *x* and *z* direction, respectively.

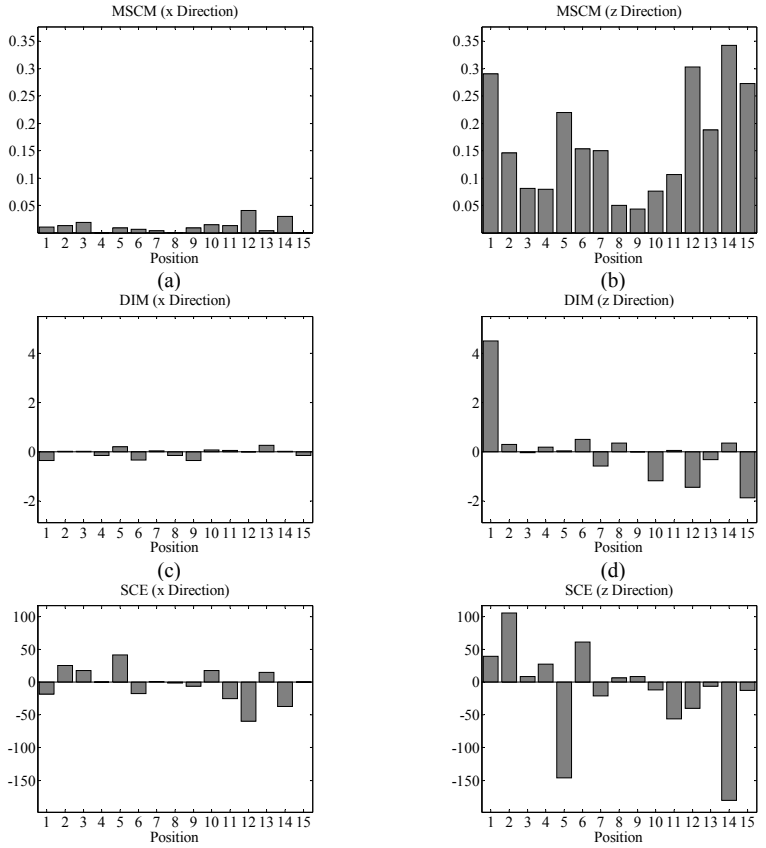


Figure C.2 – RS_A and $DS_{I\text{-}A}$: (a) and (b) MSCM for curvatures in the *x* and *z* direction, respectively; (c) and (d) DIM for curvatures in the *x* and *z* direction, respectively; and (e) and (f) SCE for curvatures in the *x* and *z* direction, respectively.

C.1.1.2 Reference Scenario A and Damage Scenario II-A

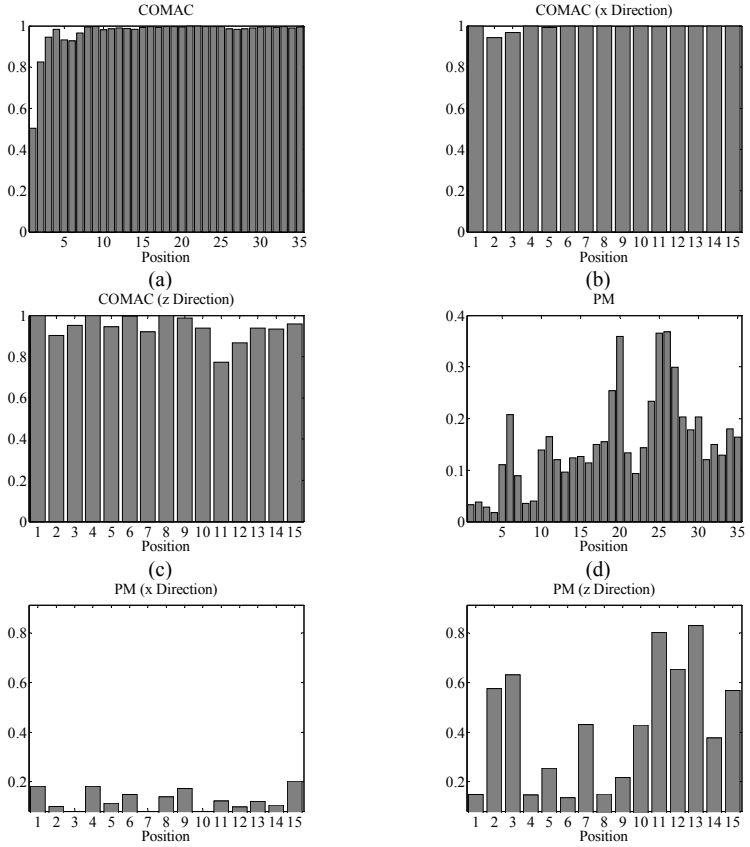


Figure C.3 – RS_A and $DS_{II\text{-}A}$: (a) COMAC values for modal displacements; (b) and (c) COMAC values for modal curvatures in the *x* and *z* direction, respectively; (d) PM for modal displacements; and (e) and (f) PM for modal curvatures in the *x* and *z* direction, respectively.

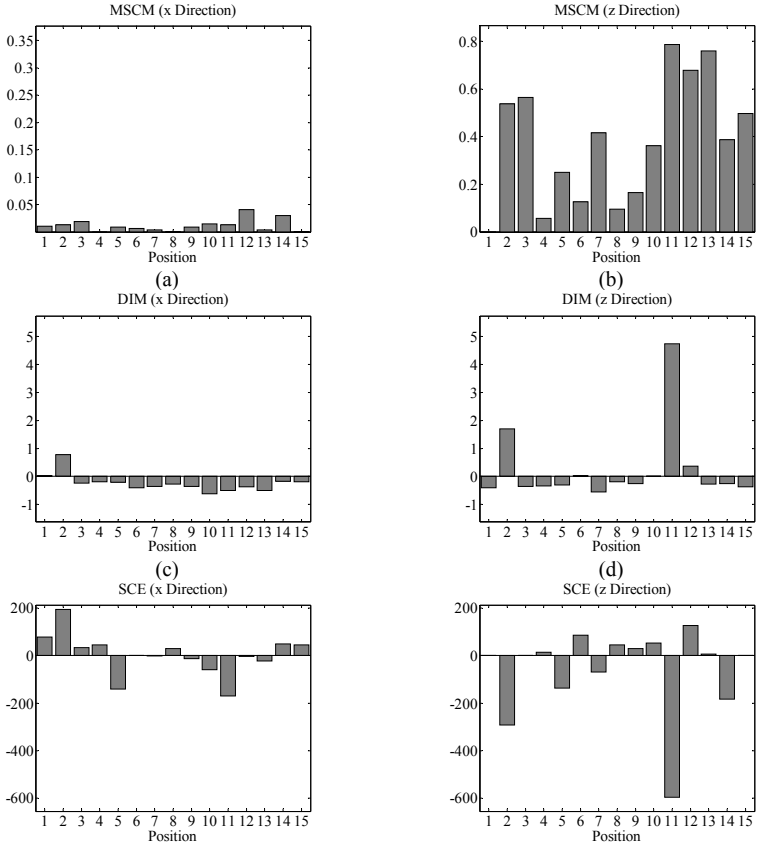


Figure C.4 – RS_A and $DS_{II\text{-}A}$: (a) and (b) MSCM for curvatures in the *x* and *z* direction, respectively; (c) and (d) DIM for curvatures in the *x* and *z* direction, respectively; and (e) and (f) SCE for curvatures in the *x* and *z* direction, respectively.

C.1.1.3 Reference Scenario A and Damage Scenario III-A

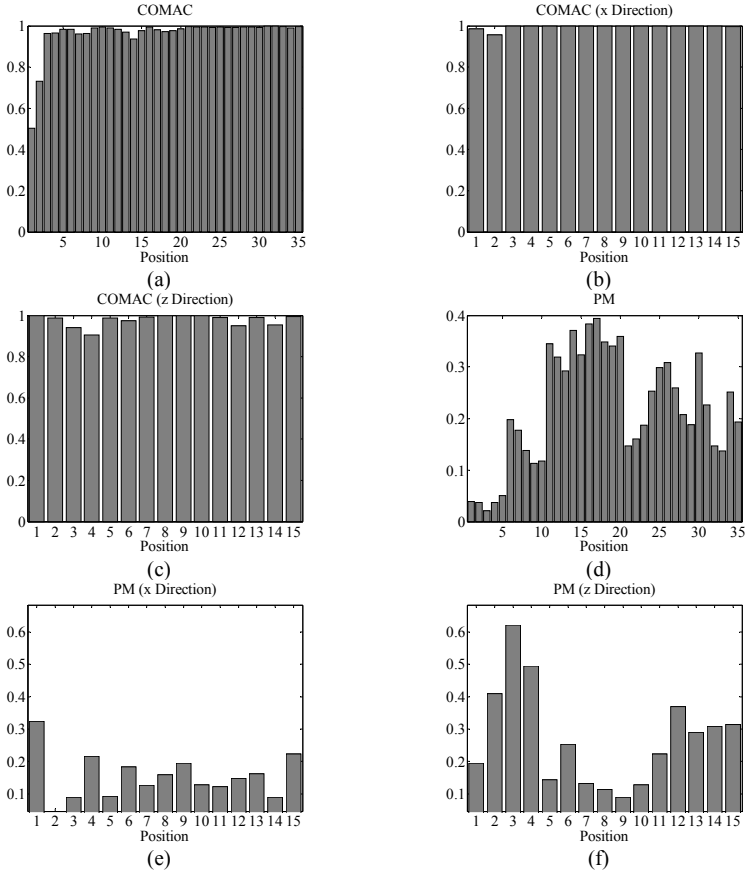


Figure C.5 – RS_A and $DS_{III\text{-}A}$: (a) COMAC values for modal displacements; (b) and (c) COMAC values for modal curvatures in the *x* and *z* direction, respectively; (d) PM for modal displacements; and (e) and (f) PM for modal curvatures in the *x* and *z* direction, respectively.

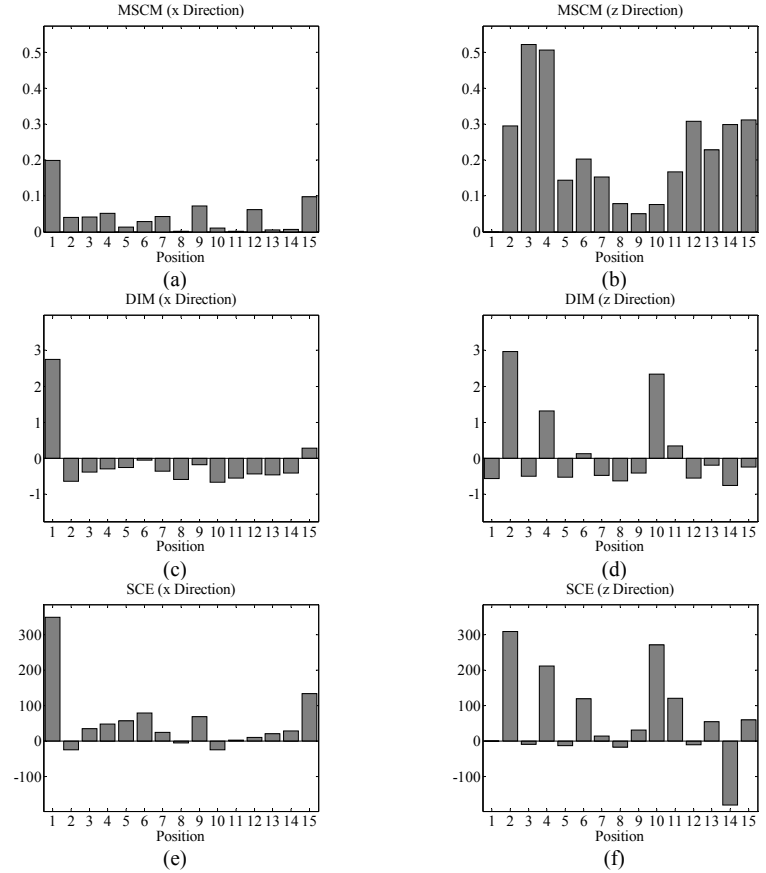


Figure C.6 – RS_A and $DS_{III\text{-}A}$: (a) and (b) MSCM for curvatures in the *x* and *z* direction, respectively; (c) and (d) DIM for curvatures in the *x* and *z* direction, respectively; and (e) and (f) SCE for curvatures in the *x* and *z* direction, respectively.

C.1.1.4 Reference Scenario A and Damage Scenario IV-A

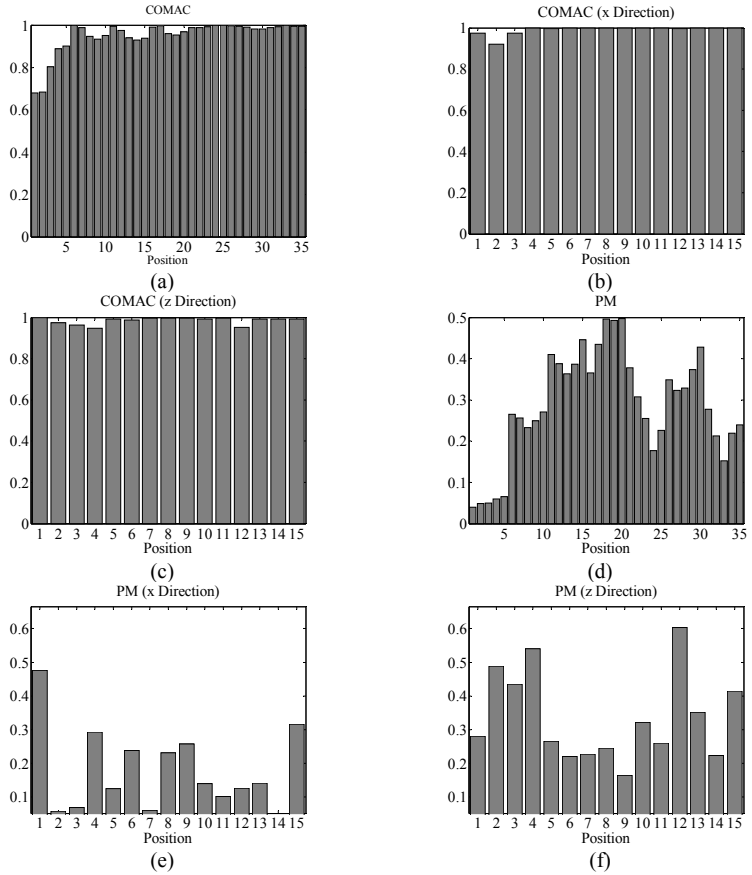


Figure C.7 – RS_A and $DS_{IV\text{-}A}$: (a) COMAC values for modal displacements; (b) and (c) COMAC values for modal curvatures in the *x* and *z* direction, respectively; (d) PM for modal displacements; and (e) and (f) PM for modal curvatures in the *x* and *z* direction, respectively.

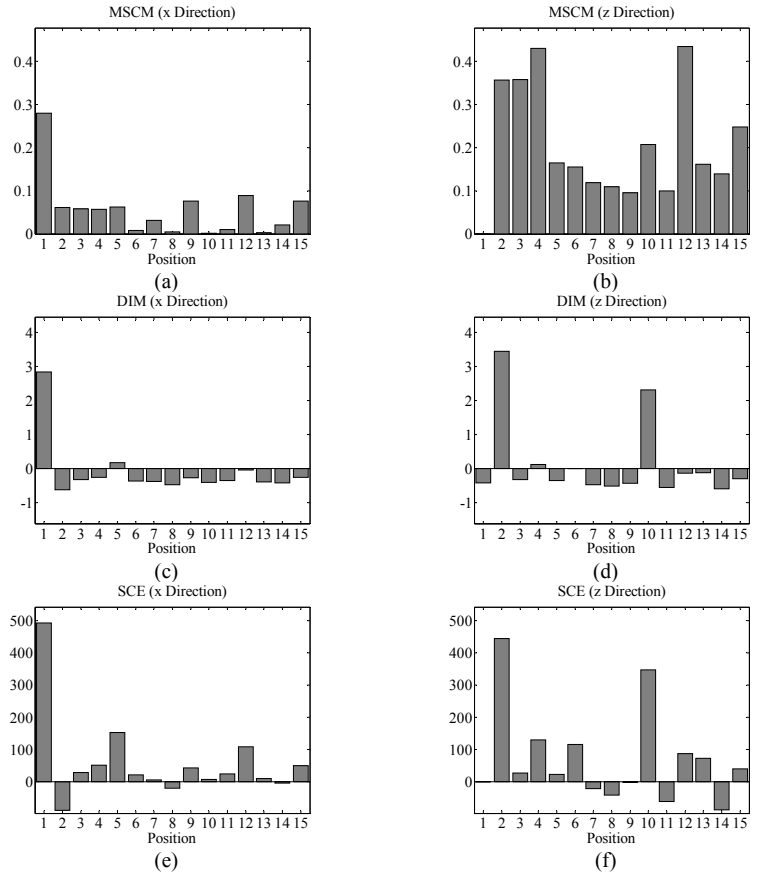


Figure C.8 – RS_A and $DS_{IV\text{-}A}$: (a) and (b) MSCM for curvatures in the *x* and *z* direction, respectively; (c) and (d) DIM for curvatures in the *x* and *z* direction, respectively; and (e) and (f) SCE for curvatures in the *x* and *z* direction, respectively.

C.1.1.5 Reference Scenario A and Damage Scenario V-A

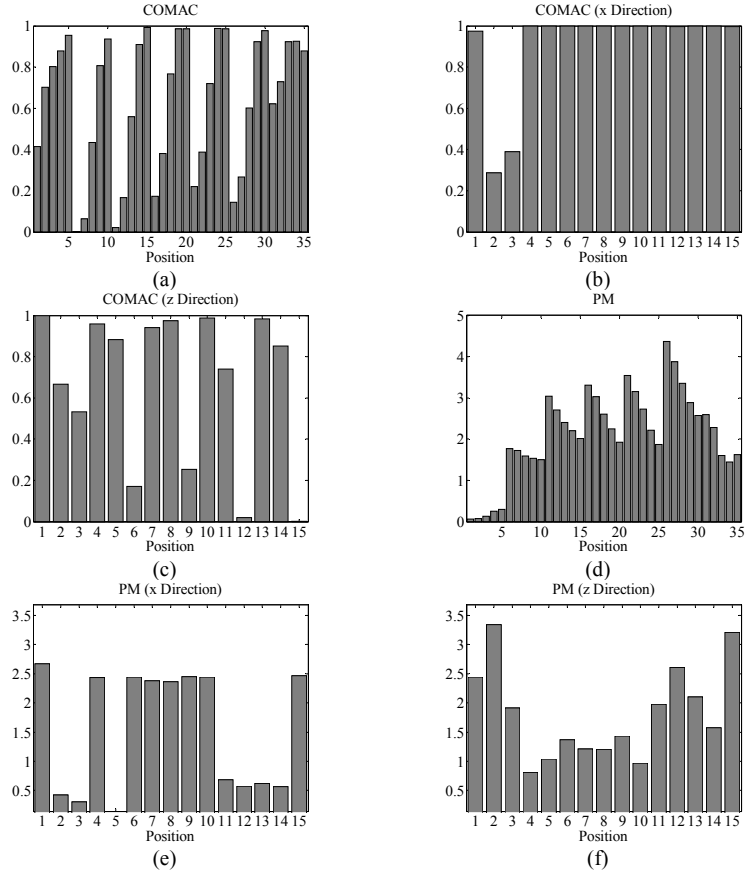


Figure C.9 – RS_A and $DS_{V\text{-}A}$: (a) COMAC values for modal displacements; (b) and (c) COMAC values for modal curvatures in the *x* and *z* direction, respectively; (d) PM for modal displacements; and (e) and (f) PM for modal curvatures in the *x* and *z* direction, respectively.

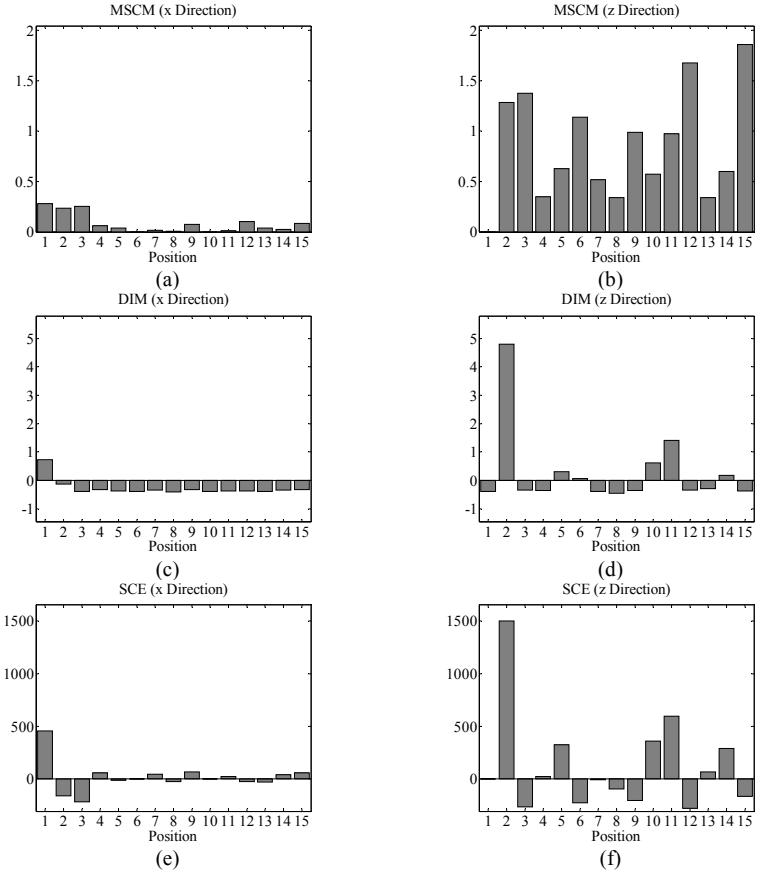


Figure C.10 – RS_A and $DS_{V\text{-}A}$: (a) and (b) MSCM for curvatures in the *x* and *z* direction, respectively; (c) and (d) DIM for curvatures in the *x* and *z* direction, respectively; and (e) and (f) SCE for curvatures in the *x* and *z* direction, respectively.

C.1.2 Relative Comparison

C.1.2.1 Damage Scenario I-A and Damage Scenario II-A

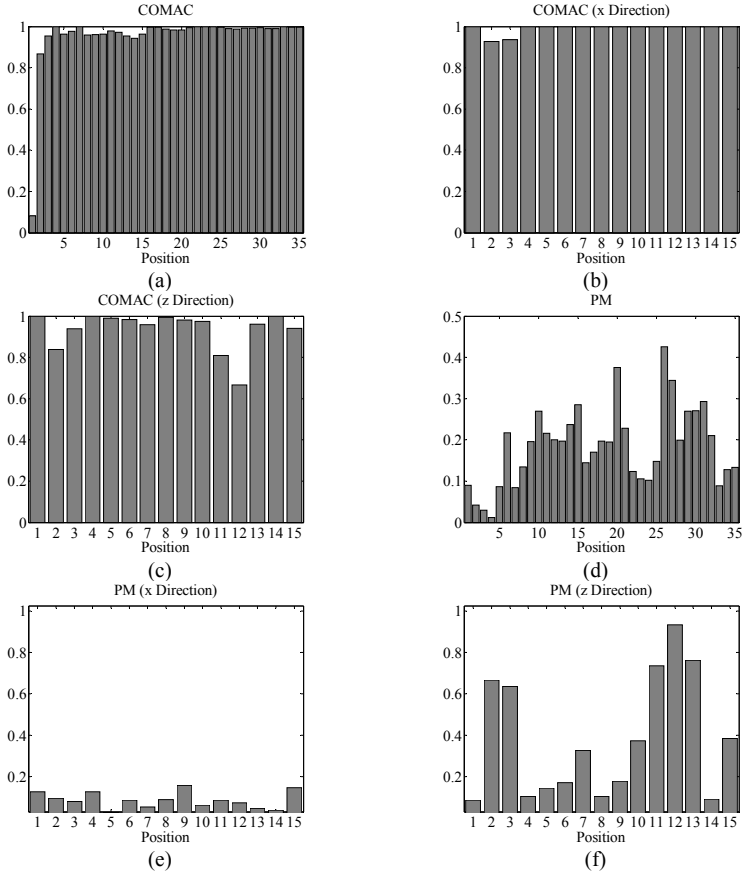


Figure C.11 – $DS_{I\text{-}A}$ and $DS_{II\text{-}A}$: (a) COMAC values for modal displacements; (b) and (c) COMAC values for modal curvatures in the *x* and *z* direction, respectively; (d) PM for modal displacements; and (e) and (f) PM for modal curvatures in the *x* and *z* direction, respectively.

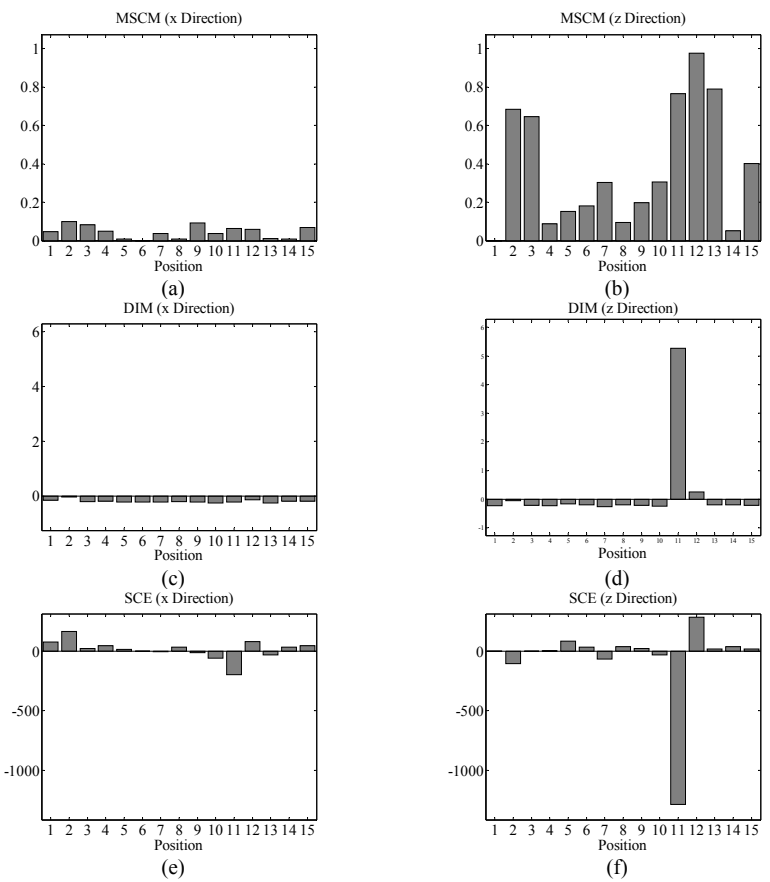


Figure C.12 – $DS_{I\text{-}A}$ and $DS_{II\text{-}A}$: (a) and (b) MSCM for curvatures in the *x* and *z* direction, respectively; (c) and (d) DIM for curvatures in the *x* and *z* direction, respectively; and (e) and (f) SCE for curvatures in the *x* and *z* direction, respectively.

C.1.2.2 Damage Scenario II-A and Damage Scenario III-A

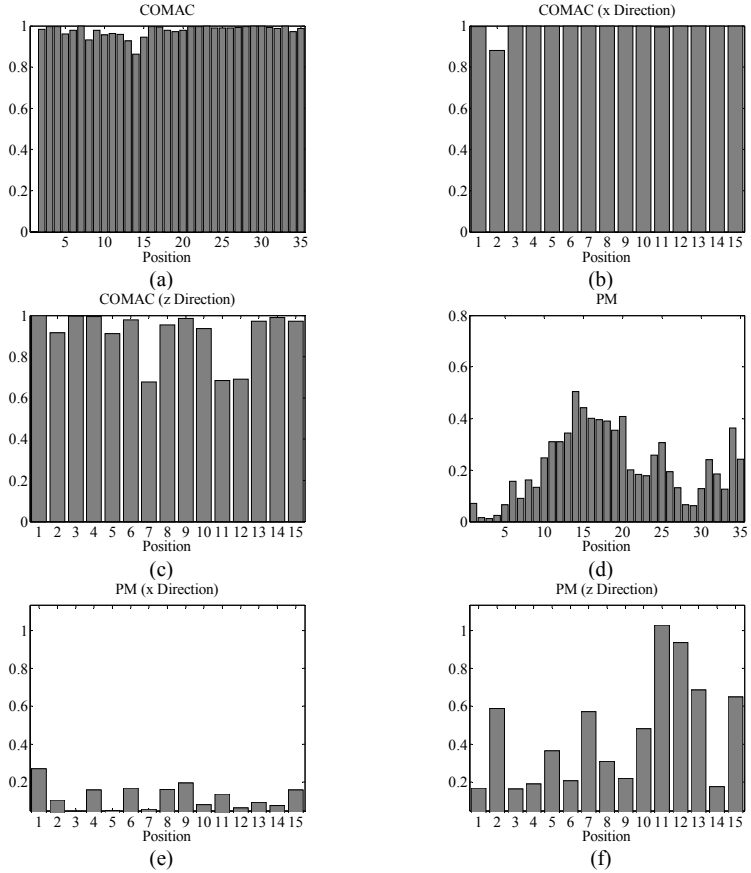


Figure C.13 – $DS_{II\text{-}A}$ and $DS_{III\text{-}A}$: (a) COMAC values for modal displacements; (b) and (c) COMAC values for modal curvatures in the *x* and *z* direction, respectively; (d) PM for modal displacements; and (e) and (f) PM for modal curvatures in the *x* and *z* direction, respectively.

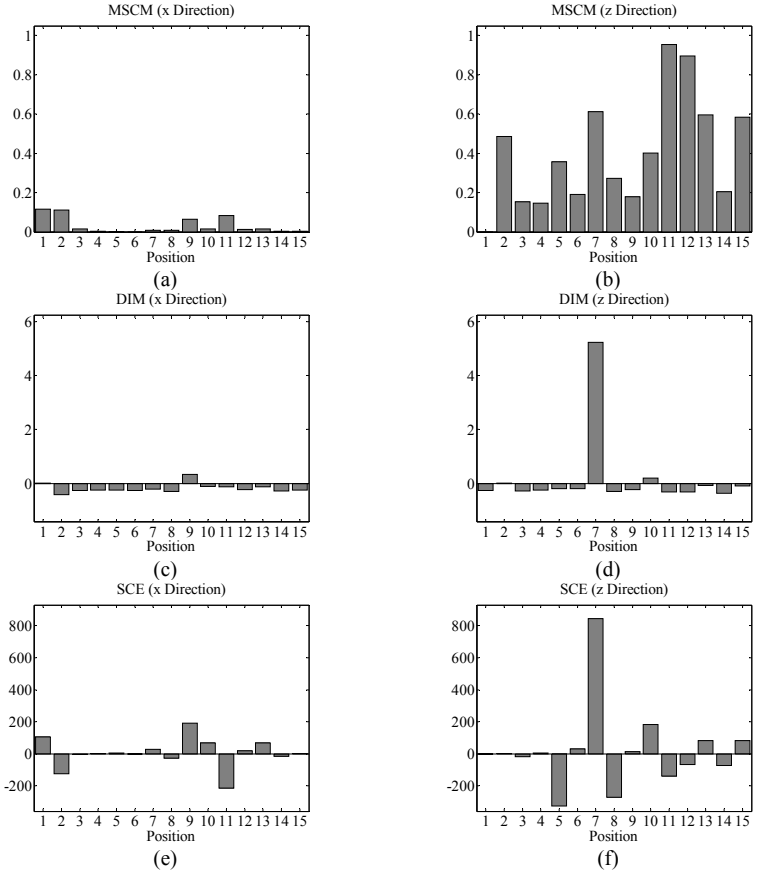


Figure C.14 – $DS_{II\text{-}A}$ and $DS_{III\text{-}A}$: (a) and (b) MSCM for curvatures in the *x* and *z* direction, respectively; (c) and (d) DIM for curvatures in the *x* and *z* direction, respectively; and (e) and (f) SCE for curvatures in the *x* and *z* direction, respectively.

C.1.2.3 Damage Scenario III-A and Damage Scenario IV-A

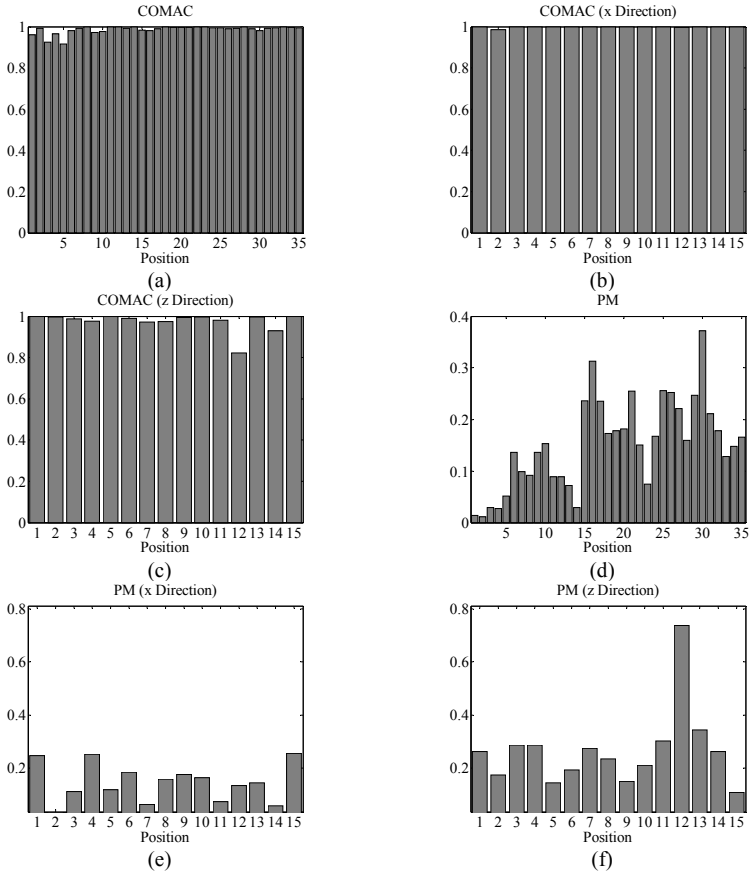


Figure C.15 – $DS_{III\text{-}A}$ and $DS_{IV\text{-}A}$: (a) COMAC values for modal displacements; (b) and (c) COMAC values for modal curvatures in the *x* and *z* direction, respectively; (d) PM for modal displacements; and (e) and (f) PM for modal curvatures in the *x* and *z* direction, respectively.

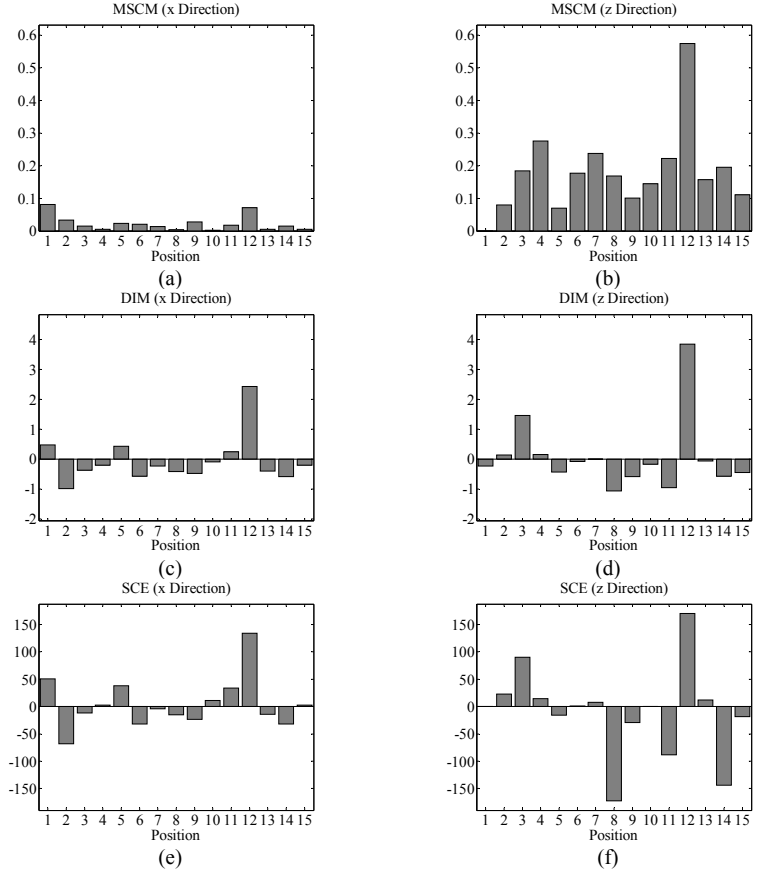


Figure C.16 – $DS_{III\text{-}A}$ and $DS_{IV\text{-}A}$: (a) and (b) MSCM for curvatures in the *x* and *z* direction, respectively; (c) and (d) DIM for curvatures in the *x* and *z* direction, respectively; and (e) and (f) SCE for curvatures in the *x* and *z* direction, respectively.

C.1.2.4 Damage Scenario IV-A and Damage Scenario V-A

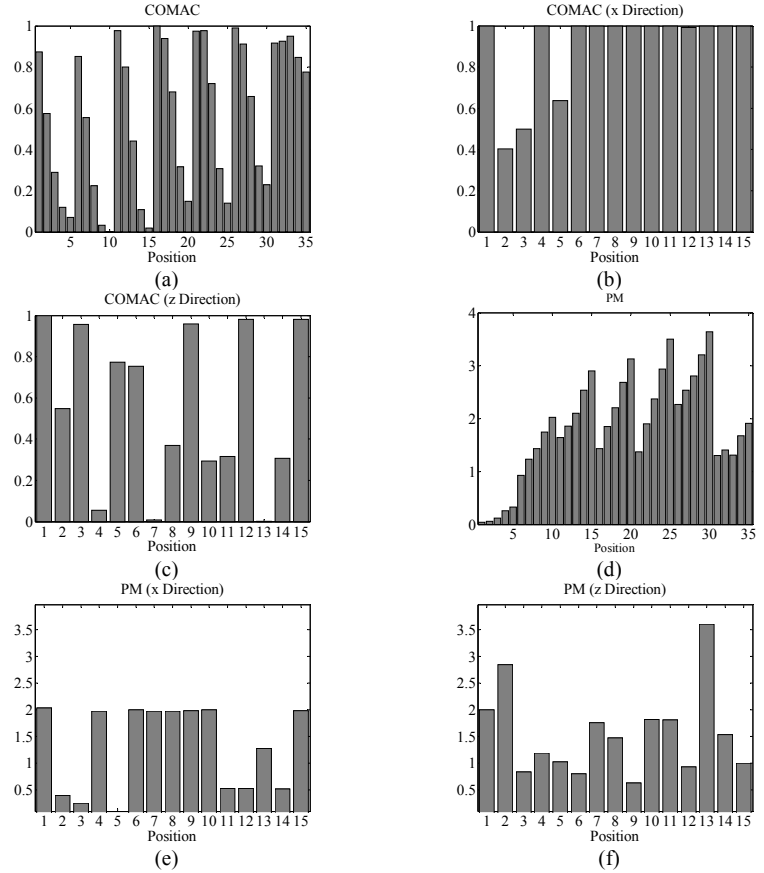


Figure C.17 – $DS_{IV\text{-}A}$ and $DS_{V\text{-}A}$: (a) COMAC values for modal displacements; (b) and (c) COMAC values for modal curvatures in the *x* and *z* direction, respectively; (d) PM for modal displacements; and (e) and (f) PM for modal curvatures in the *x* and *z* direction, respectively.

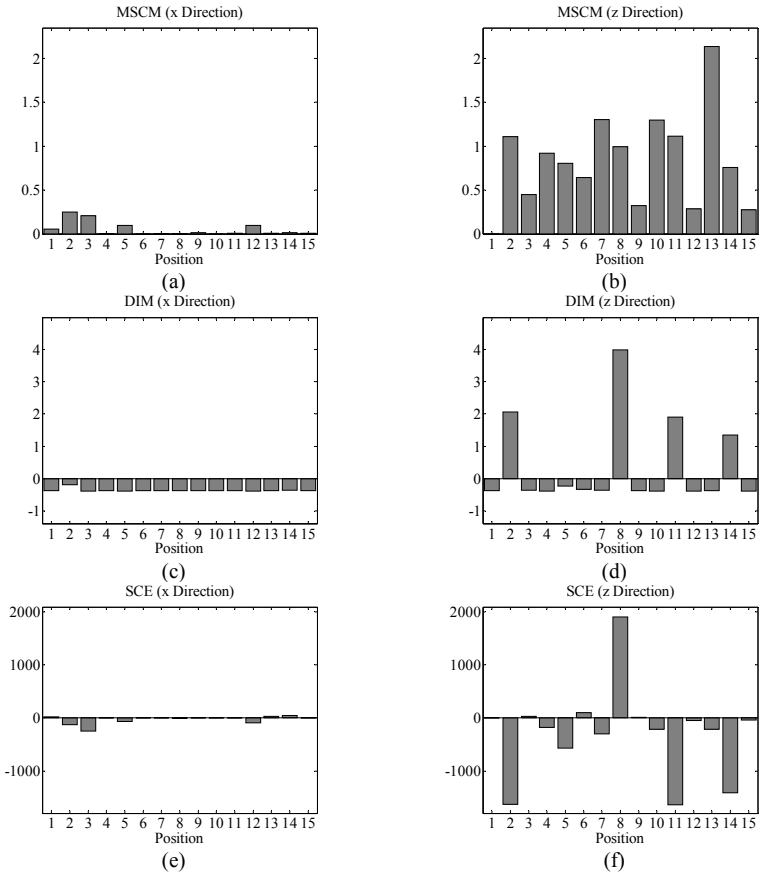


Figure C.18 – $DS_{IV\text{-}A}$ and $DS_{V\text{-}A}$: (a) and (b) MSCM for curvatures in the *x* and *z* direction, respectively; (c) and (d) DIM for curvatures in the *x* and *z* direction, respectively; and (e) and (f) SCE for curvatures in the *x* and *z* direction, respectively.

C.2 Non-Model Based Methods Applied to Series B

C.2.1 Comparison with the Reference Scenario

C.2.1.1 Reference Scenario B and Damage Scenario I-B

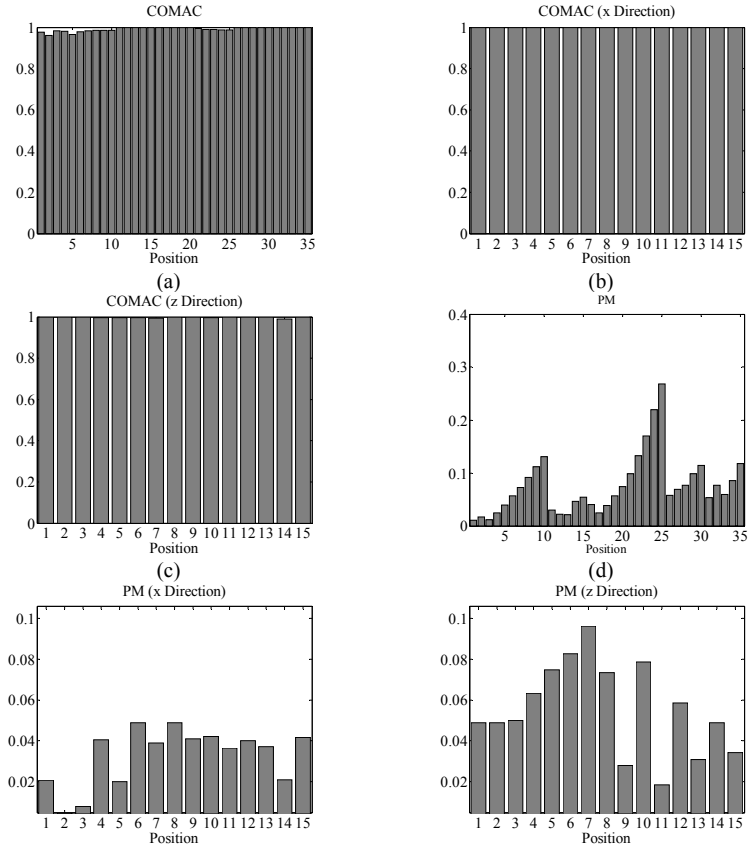


Figure C.19 – RS_B and $DS_{I\text{-}B}$: (a) COMAC values for modal displacements; (b) and (c) COMAC values for modal curvatures in the *x* and *z* direction, respectively; (d) PM for modal displacements; and (e) and (f) PM for modal curvatures in the *x* and *z* direction, respectively.

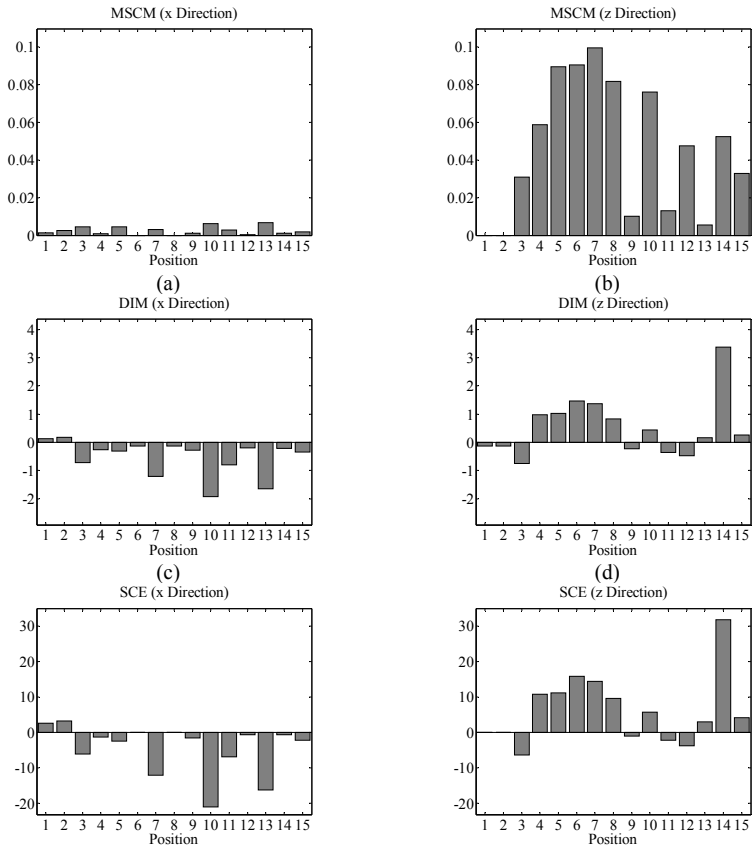


Figure C.20 – RS_B and $DS_{I\text{-}B}$: (a) and (b) MSCM for curvatures in the *x* and *z* direction, respectively; (c) and (d) DIM for curvatures in the *x* and *z* direction, respectively; and (e) and (f) SCE for curvatures in the *x* and *z* direction, respectively.

C.2.1.2 Reference Scenario B and Damage Scenario II-B

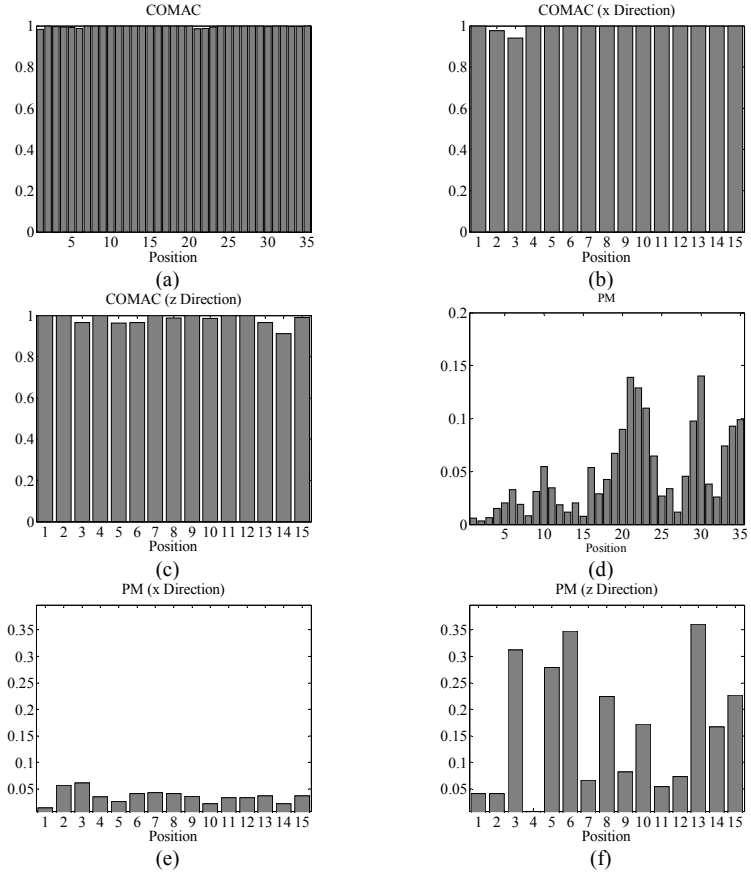


Figure C.21 – RS_B and DS_{II-B}: (a) COMAC values for modal displacements; (b) and (c) COMAC values for modal curvatures in the *x* and *z* direction, respectively; (d) PM for modal displacements; and (e) and (f) PM for modal curvatures in the *x* and *z* direction, respectively.

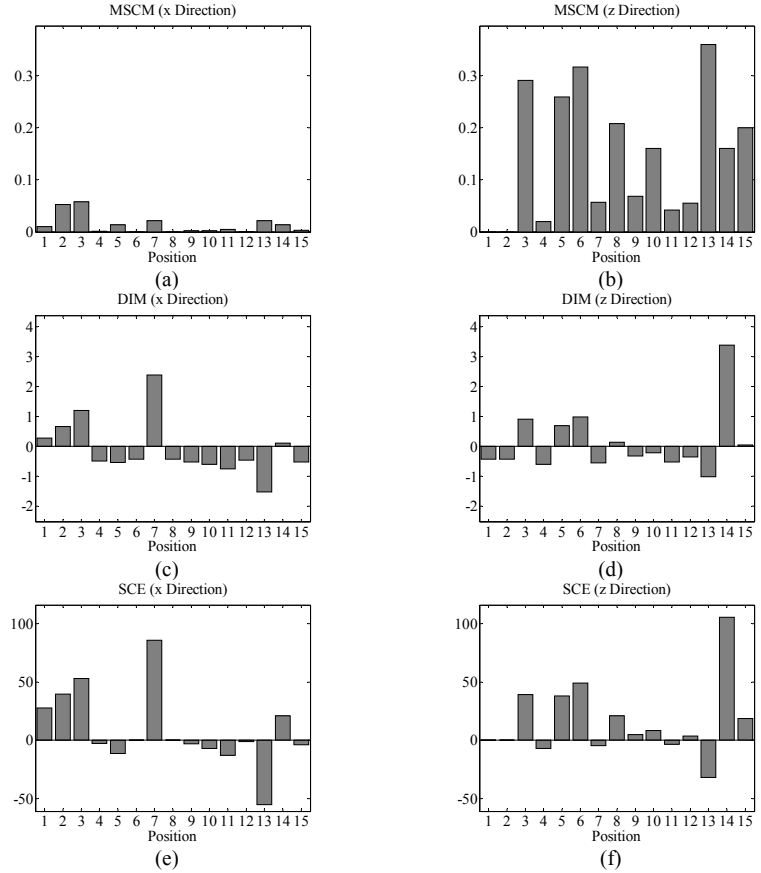


Figure C.22 – RS_A and DS_{II-A}: (a) and (b) MSCM for curvatures in the *x* and *z* direction, respectively; (c) and (d) DIM for curvatures in the *x* and *z* direction, respectively; and (e) and (f) SCE for curvatures in the *x* and *z* direction, respectively.

C.2.1.3 Reference Scenario B and Damage Scenario III-B

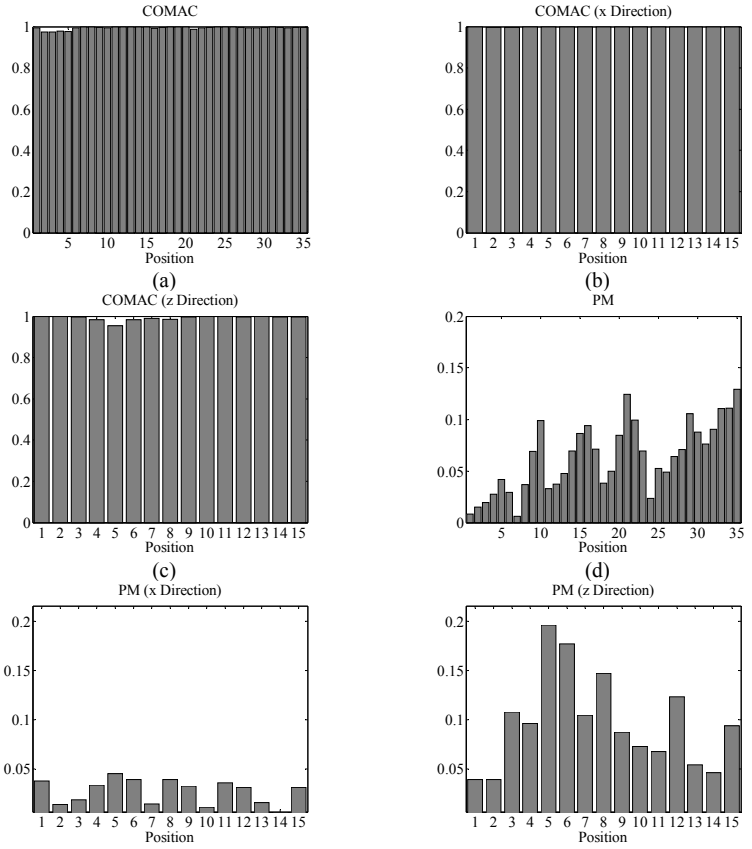


Figure C.23 – RS_B and $DS_{III\text{-}B}$: (a) COMAC values for modal displacements; (b) and (c) COMAC values for modal curvatures in the *x* and *z* direction, respectively; (d) PM for modal displacements; and (e) and (f) PM for modal curvatures in the *x* and *z* direction, respectively.

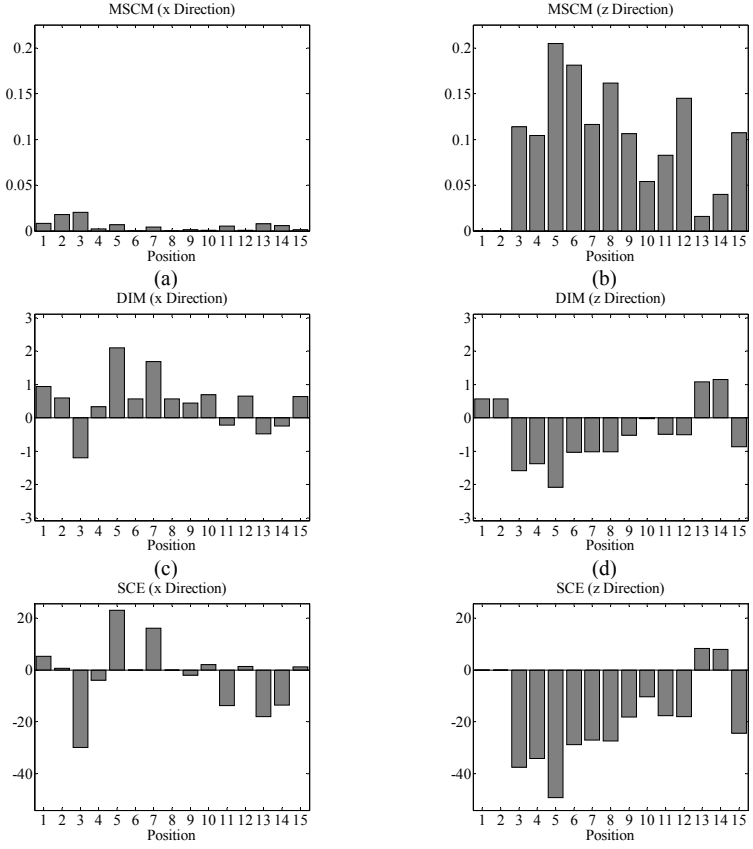


Figure C.24 – RS_B and $DS_{III\text{-}B}$: (a) and (b) MSCM for curvatures in the *x* and *z* direction, respectively; (c) and (d) DIM for curvatures in the *x* and *z* direction, respectively; and (e) and (f) SCE for curvatures in the *x* and *z* direction, respectively.

C.2.1.4 Reference Scenario B and Damage Scenario IV-B

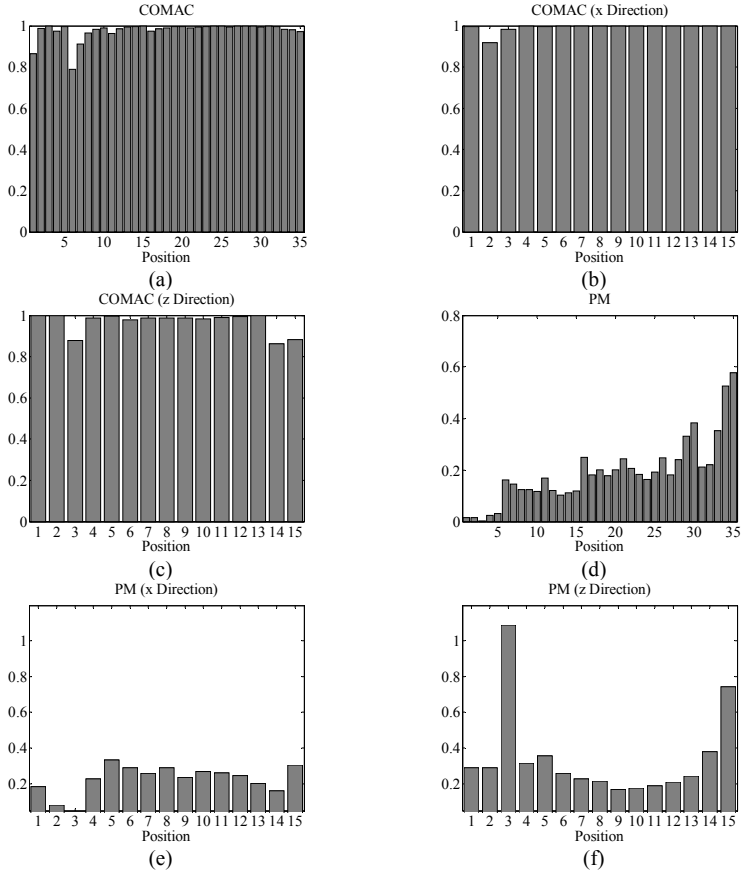


Figure C.25 – RS_B and $DS_{IV\text{-}B}$: (a) COMAC values for modal displacements; (b) and (c) COMAC values for modal curvatures in the *x* and *z* direction, respectively; (d) PM for modal displacements; and (e) and (f) PM for modal curvatures in the *x* and *z* direction, respectively.

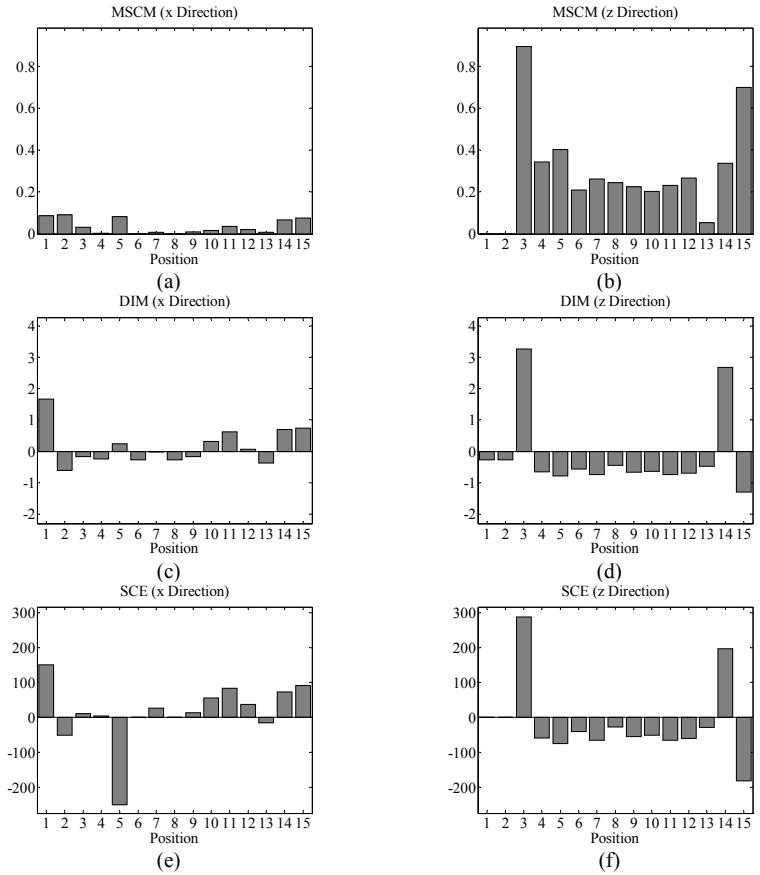


Figure C.26 – RS_B and $DS_{IV\text{-}B}$: (a) and (b) MSCM for curvatures in the *x* and *z* direction, respectively; (c) and (d) DIM for curvatures in the *x* and *z* direction, respectively; and (e) and (f) SCE for curvatures in the *x* and *z* direction, respectively.

C.2.1.5 Reference Scenario B and Damage Scenario V-B

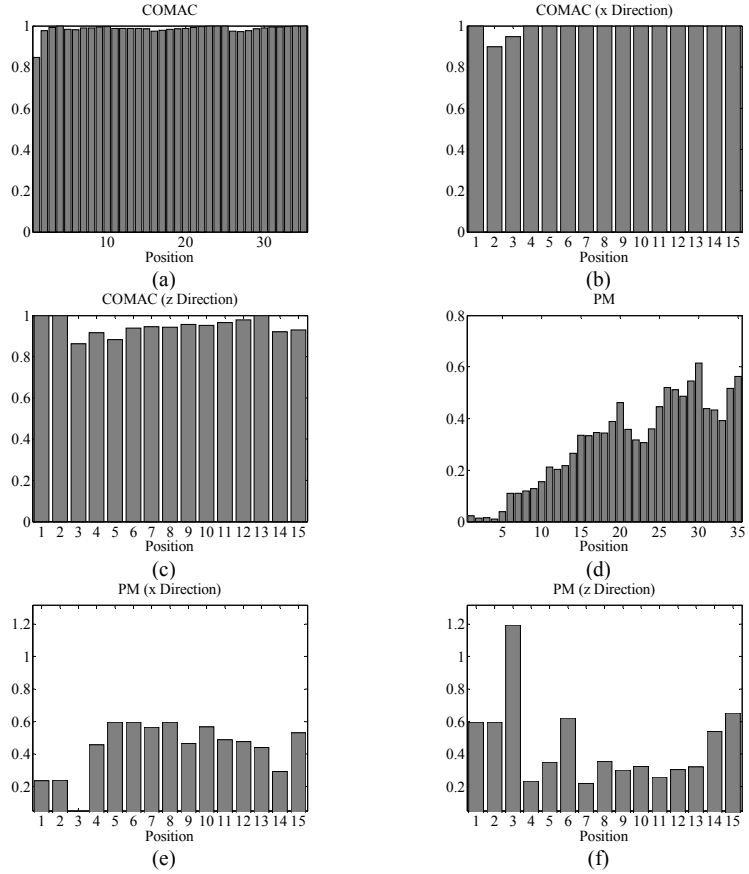


Figure C.27 – RS_B and $DS_{V\text{-}B}$: (a) COMAC values for modal displacements; (b) and (c) COMAC values for modal curvatures in the *x* and *z* direction, respectively; (d) PM for modal displacements; and (e) and (f) PM for modal curvatures in the *x* and *z* direction, respectively.

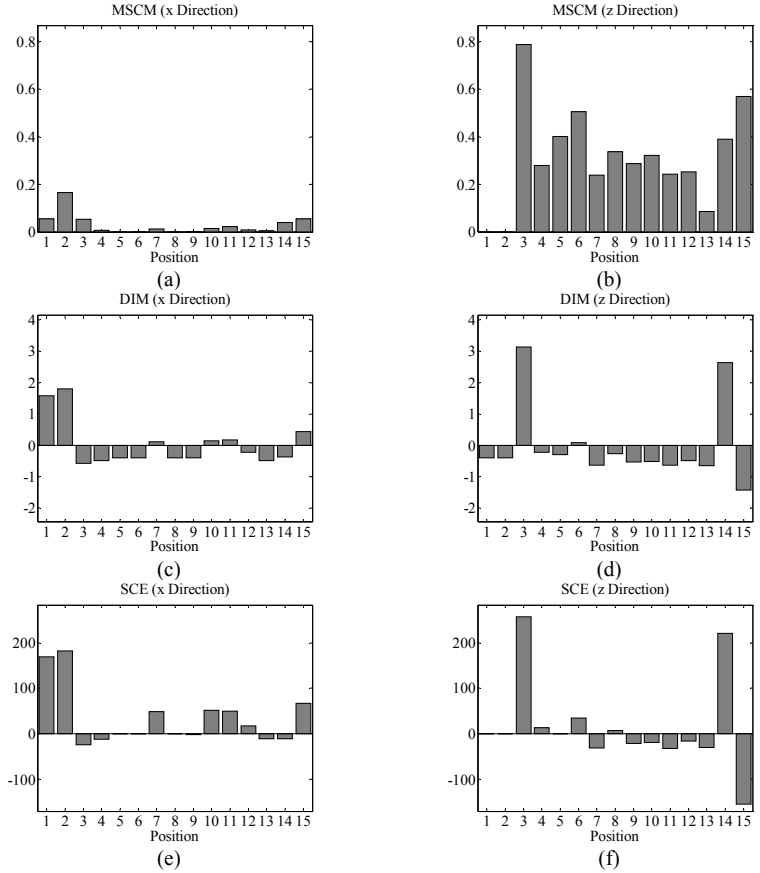


Figure C.28 – RS_B and $DS_{V\text{-}B}$: (a) and (b) MSCM for curvatures in the *x* and *z* direction, respectively; (c) and (d) DIM for curvatures in the *x* and *z* direction, respectively; and (e) and (f) SCE for curvatures in the *x* and *z* direction, respectively.

C.2.2 Relative Comparison

C.2.2.1 Damage Scenario I-B and Damage Scenario II-B

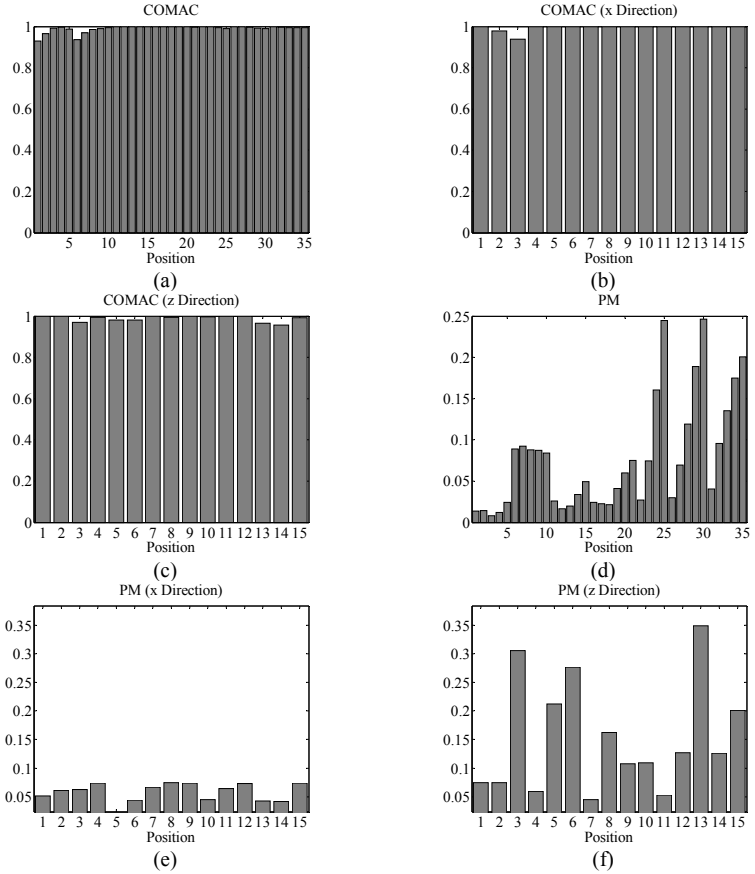


Figure C.29 – $DS_{I\text{-}B}$ and $DS_{II\text{-}B}$: (a) COMAC values for modal displacements; (b) and (c) COMAC values for modal curvatures in the *x* and *z* direction, respectively; (d) PM for modal displacements; and (e) and (f) PM for modal curvatures in the *x* and *z* direction, respectively.

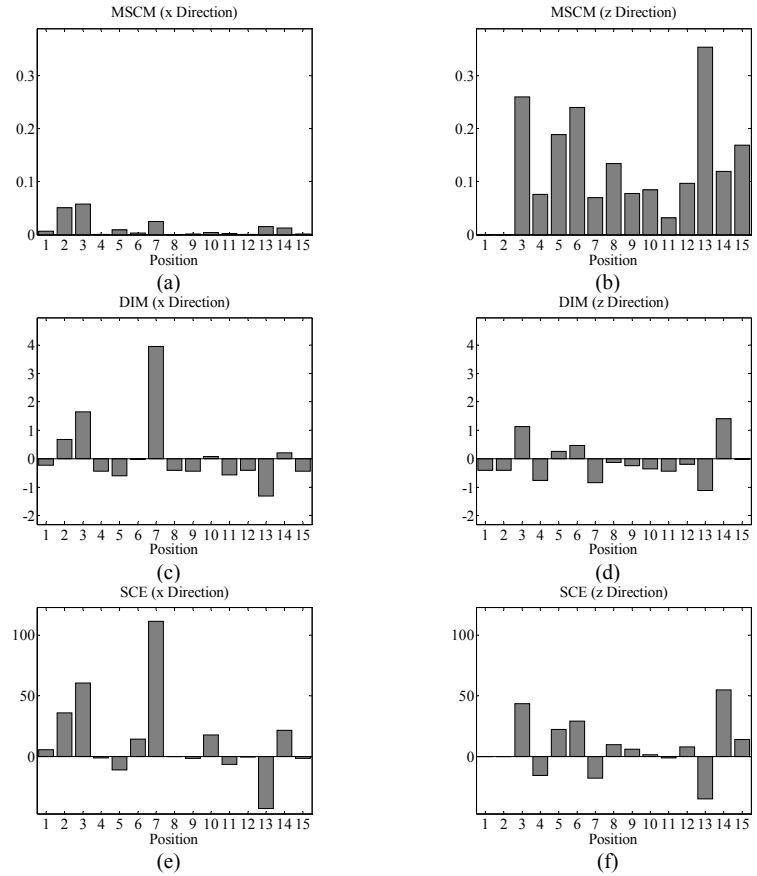


Figure C.30 – $DS_{I\text{-}B}$ and $DS_{II\text{-}B}$: (a) and (b) MSCM for curvatures in the *x* and *z* direction, respectively; (c) and (d) DIM for curvatures in the *x* and *z* direction, respectively; and (e) and (f) SCE for curvatures in the *x* and *z* direction, respectively.

C.2.2.2 Damage Scenario II-B and Damage Scenario III-B

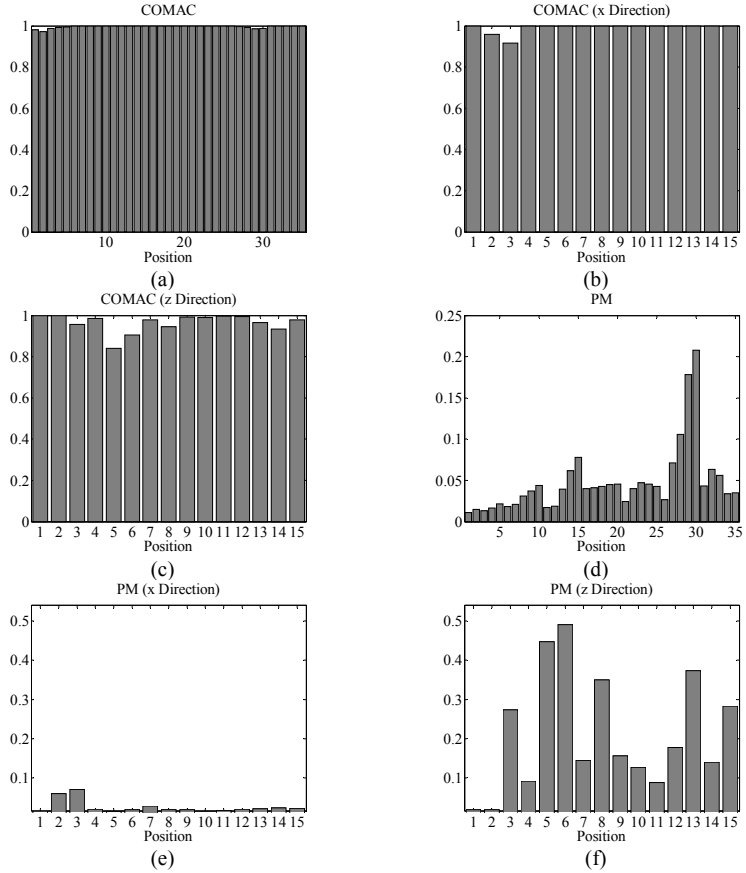


Figure C.31 – DS_{II-B} and DS_{III-B}: (a) COMAC values for modal displacements; (b) and (c) COMAC values for modal curvatures in the *x* and *z* direction, respectively; (d) PM for modal displacements; and (e) and (f) PM for modal curvatures in the *x* and *z* direction, respectively.

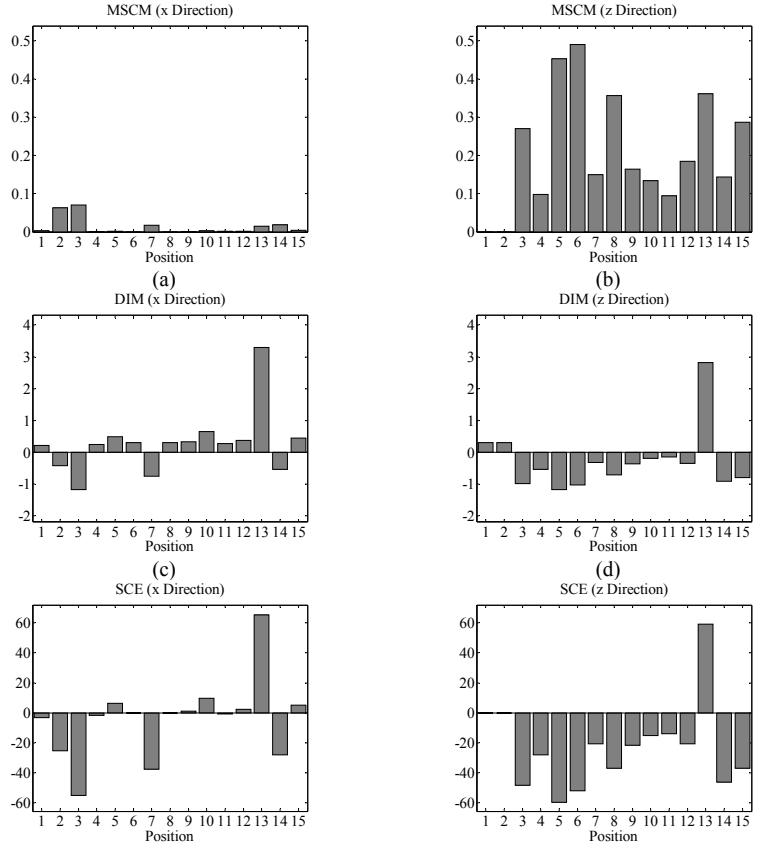


Figure C.32 – DS_{II-B} and DS_{III-B}: (a) and (b) MSCM for curvatures in the *x* and *z* direction, respectively; (c) and (d) DIM for curvatures in the *x* and *z* direction, respectively; and (e) and (f) SCE for curvatures in the *x* and *z* direction, respectively.

C.2.2.3 Damage Scenario III-B and Damage Scenario IV-B

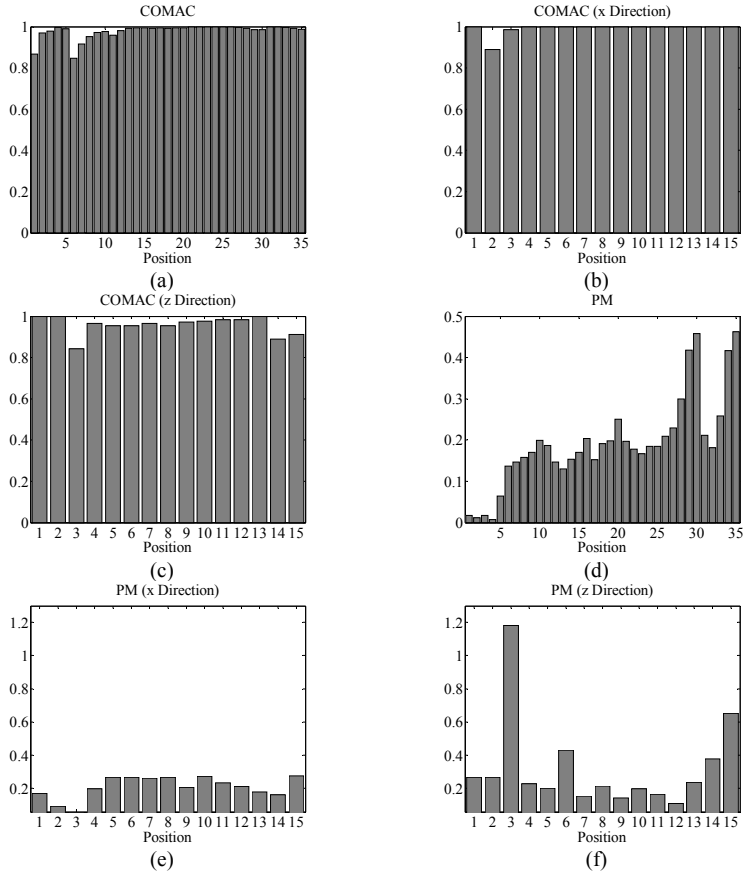


Figure C.33 – DS_{III-B} and DS_{IV-B}: (a) COMAC values for modal displacements; (b) and (c) COMAC values for modal curvatures in the *x* and *z* direction, respectively; (d) PM for modal displacements; and (e) and (f) PM for modal curvatures in the *x* and *z* direction, respectively.

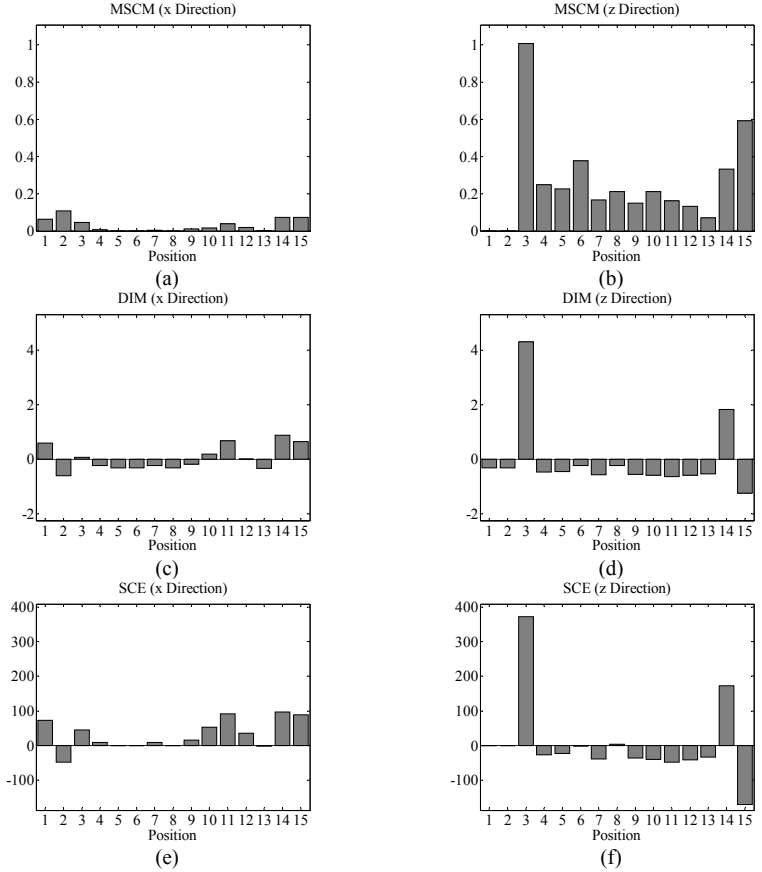


Figure C.34 – DS_{III-B} and DS_{IV-B}: (a) and (b) MSCM for curvatures in the *x* and *z* direction, respectively; (c) and (d) DIM for curvatures in the *x* and *z* direction, respectively; and (e) and (f) SCE for curvatures in the *x* and *z* direction, respectively.

C.2.2.4 Damage Scenario IV-B and Damage Scenario V-B

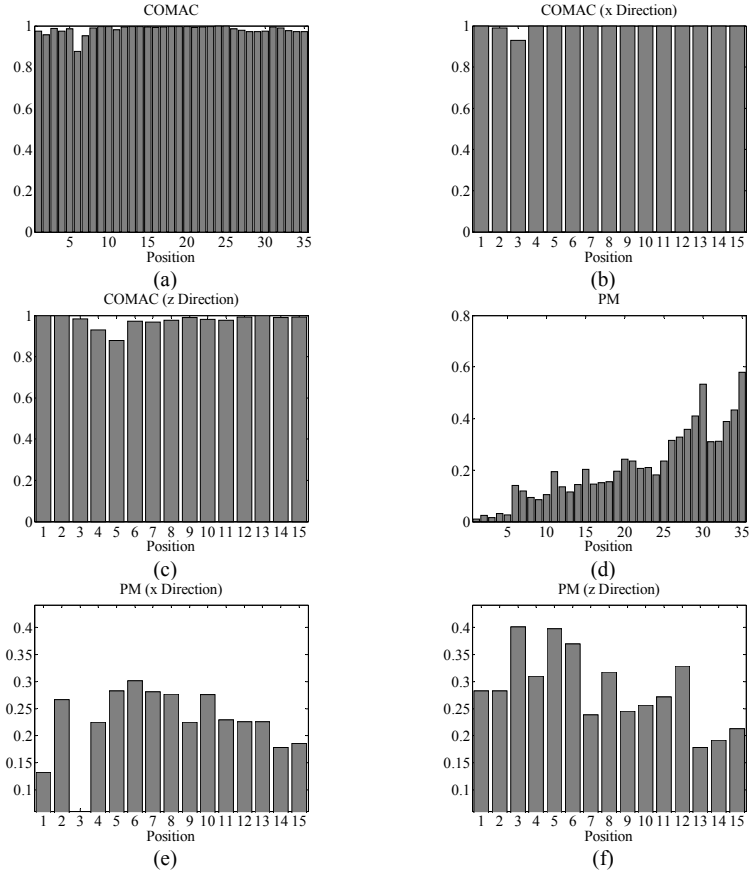


Figure C.35 – $DS_{IV\text{-}B}$ and $DS_{V\text{-}B}$: (a) COMAC values for modal displacements; (b) and (c) COMAC values for modal curvatures in the *x* and *z* direction, respectively; (d) PM for modal displacements; and (e) and (f) PM for modal curvatures in the *x* and *z* direction, respectively.

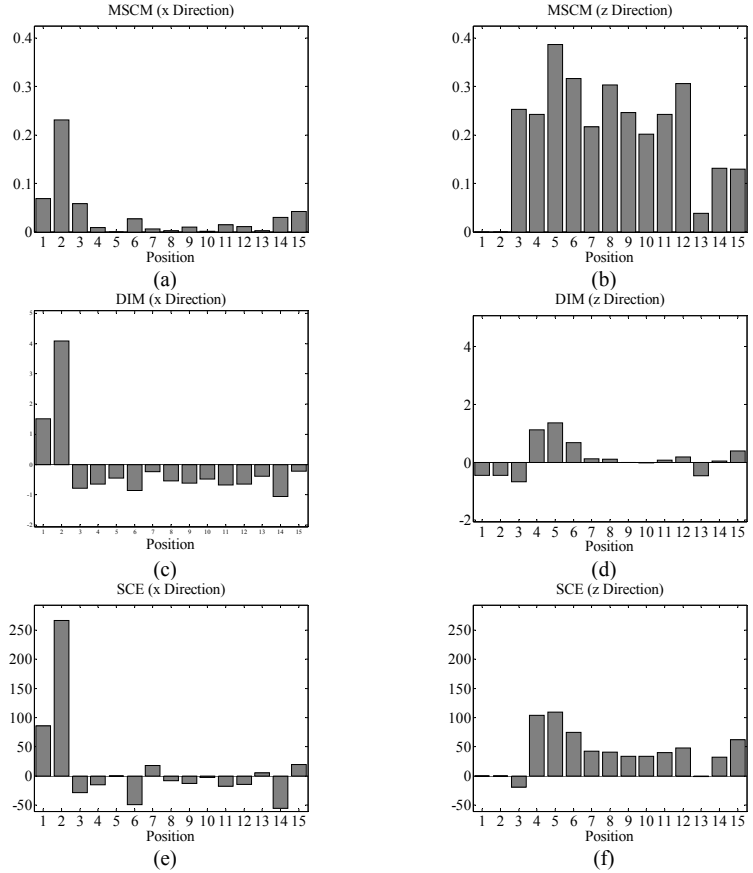


Figure C.36 – $DS_{IV\text{-}B}$ and $DS_{V\text{-}B}$: (a) and (b) MSCM for curvatures in the *x* and *z* direction, respectively; (c) and (d) DIM for curvatures in the *x* and *z* direction, respectively; and (e) and (f) SCE for curvatures in the *x* and *z* direction, respectively.

C.3 Non-Model Based Methods Applied to Series C

C.3.1 Comparison with the Reference Scenario

C.3.1.1 Reference Scenario C and Damage Scenario I-C

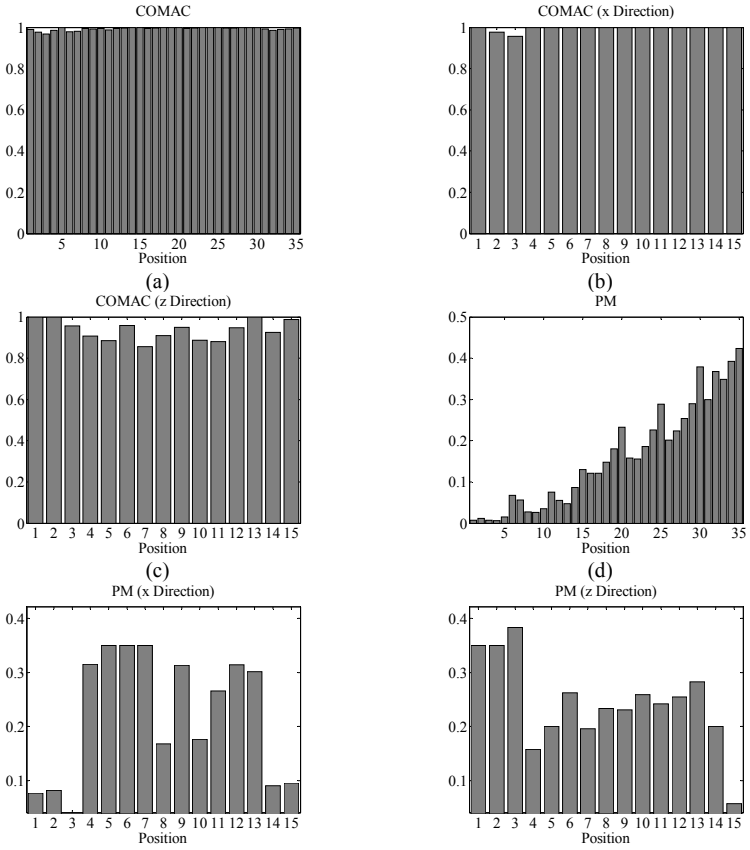


Figure C.37 – RS_C and $DS_{I\text{-}C}$: (a) COMAC values for modal displacements; (b) and (c) COMAC values for modal curvatures in the *x* and *z* direction, respectively; (d) PM for modal displacements; and (e) and (f) PM for modal curvatures in the *x* and *z* direction, respectively.

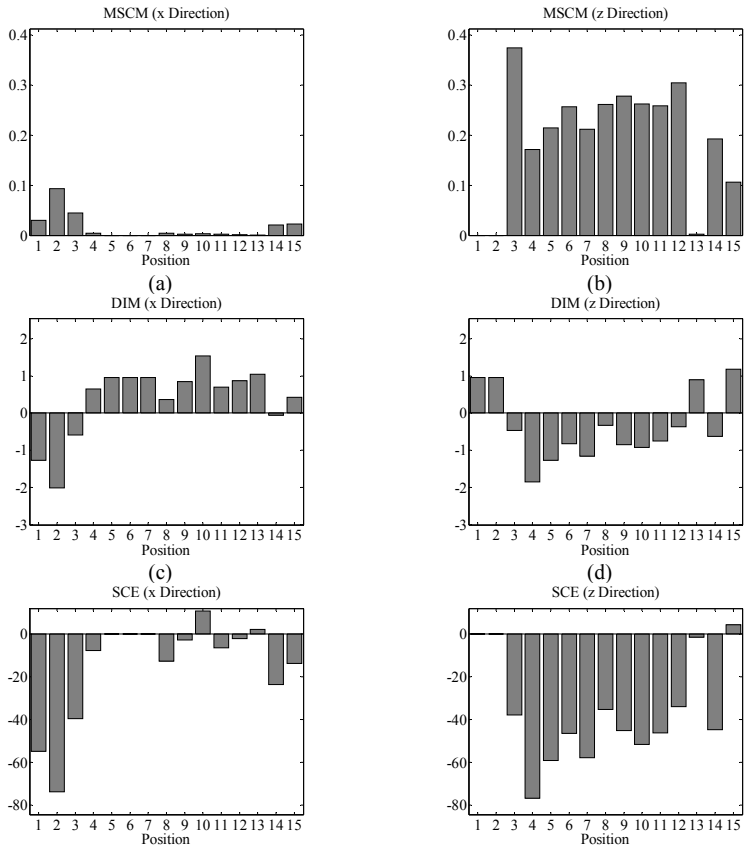


Figure C.38 – RS_C and $DS_{I\text{-}C}$: (a) and (b) MSCM for curvatures in the *x* and *z* direction, respectively; (c) and (d) DIM for curvatures in the *x* and *z* direction, respectively; and (e) and (f) SCE for curvatures in the *x* and *z* direction, respectively.

C.3.1.2 Reference Scenario C and Damage Scenario II-C

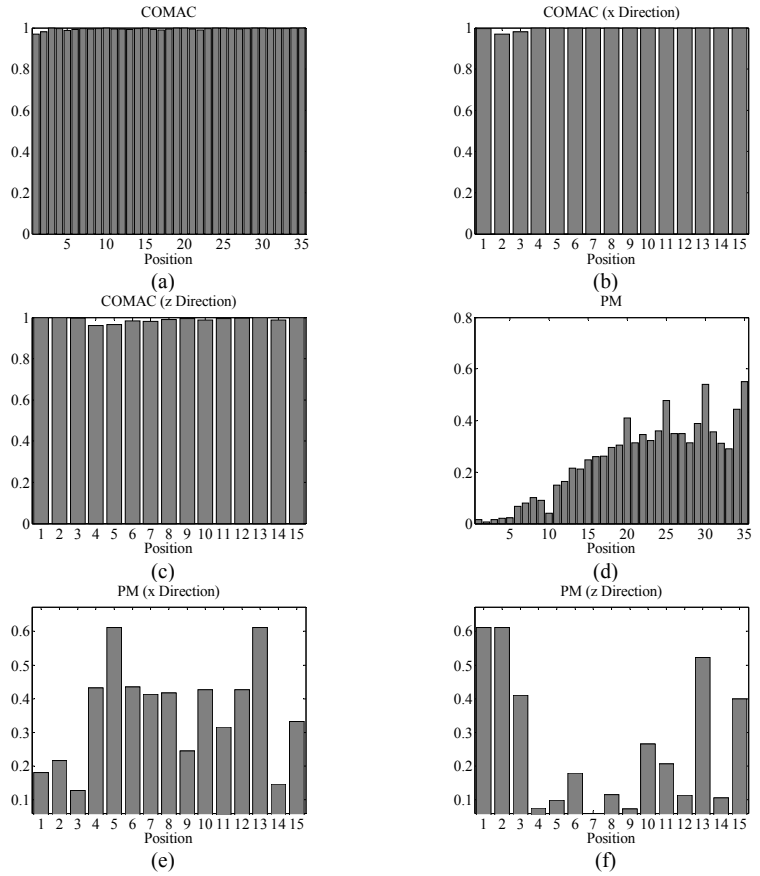


Figure C.39 – RS_C and DS_{II-C}: (a) COMAC values for modal displacements; (b) and (c) COMAC values for modal curvatures in the *x* and *z* direction, respectively; (d) PM for modal displacements; and (e) and (f) PM for modal curvatures in the *x* and *z* direction, respectively.

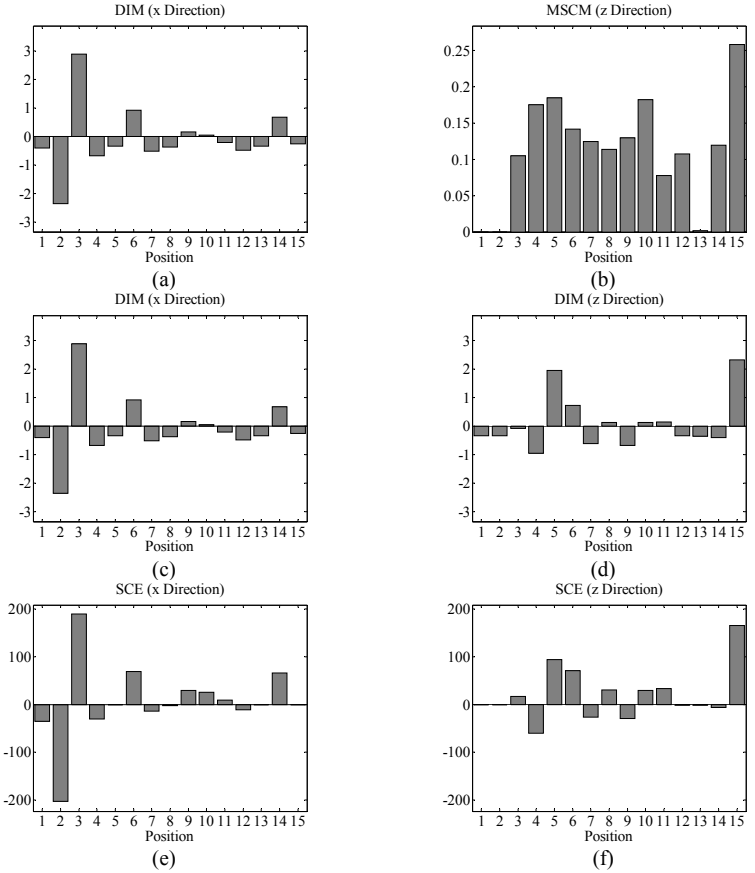


Figure C.40 – RS_C and DS_{II-C}: (a) and (b) MSCM for curvatures in the *x* and *z* direction, respectively; (c) and (d) DIM for curvatures in the *x* and *z* direction, respectively; and (e) and (f) SCE for curvatures in the *x* and *z* direction, respectively.

C.3.1.3 Reference Scenario C and Damage Scenario III-C

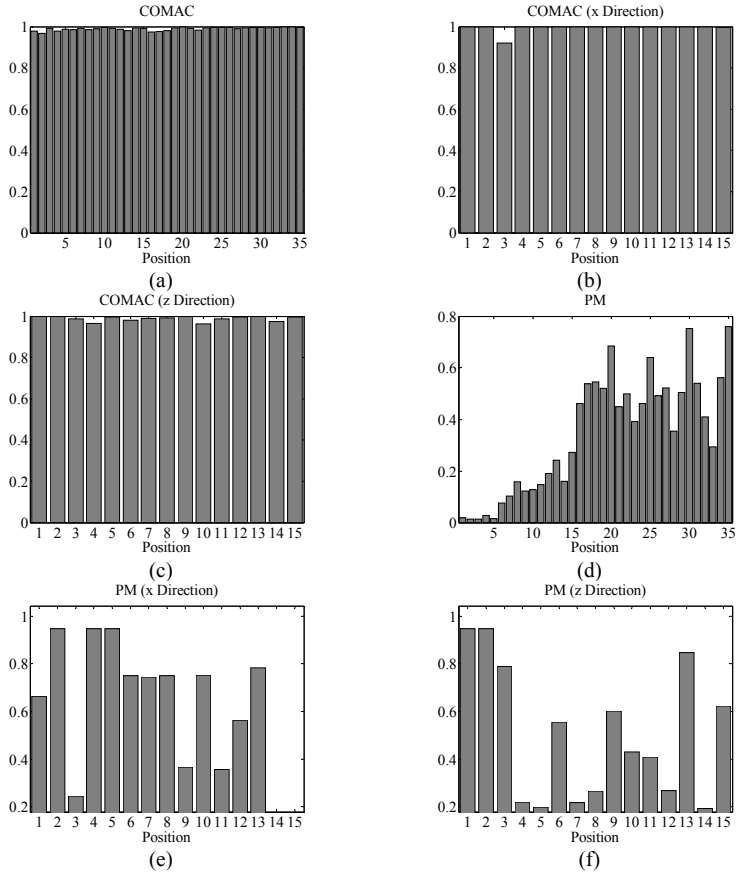


Figure C.41 – RS_C and $DS_{III\text{-}C}$: (a) COMAC values for modal displacements; (b) and (c) COMAC values for modal curvatures in the *x* and *z* direction, respectively; (d) PM for modal displacements; and (e) and (f) PM for modal curvatures in the *x* and *z* direction, respectively.

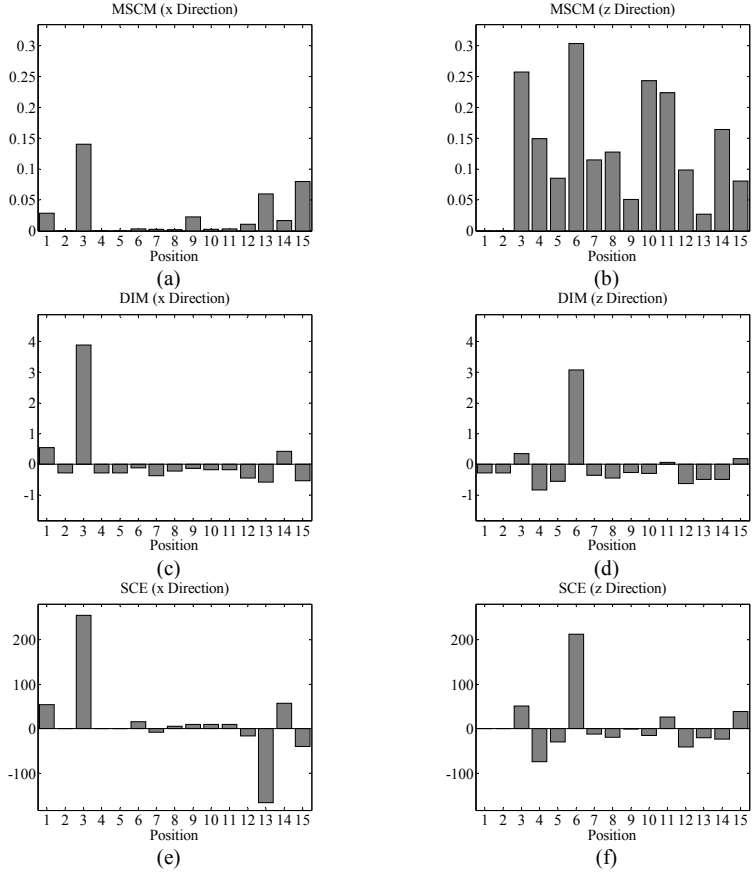


Figure C.42 – RS_C and $DS_{III\text{-}C}$: (a) and (b) MSCM for curvatures in the *x* and *z* direction, respectively; (c) and (d) DIM for curvatures in the *x* and *z* direction, respectively; and (e) and (f) SCE for curvatures in the *x* and *z* direction, respectively.

C.3.1.4 Reference Scenario C and Damage Scenario IV-C

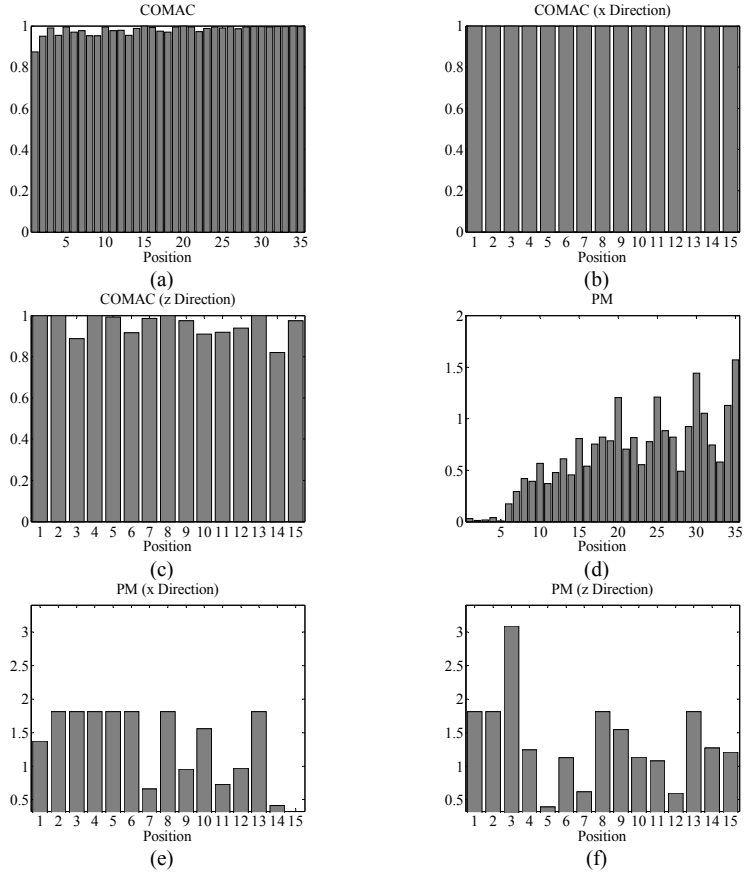


Figure C.43 – RS_C and $DS_{IV\text{-}C}$: (a) COMAC values for modal displacements; (b) and (c) COMAC values for modal curvatures in the *x* and *z* direction, respectively; (d) PM for modal displacements; and (e) and (f) PM for modal curvatures in the *x* and *z* direction, respectively.

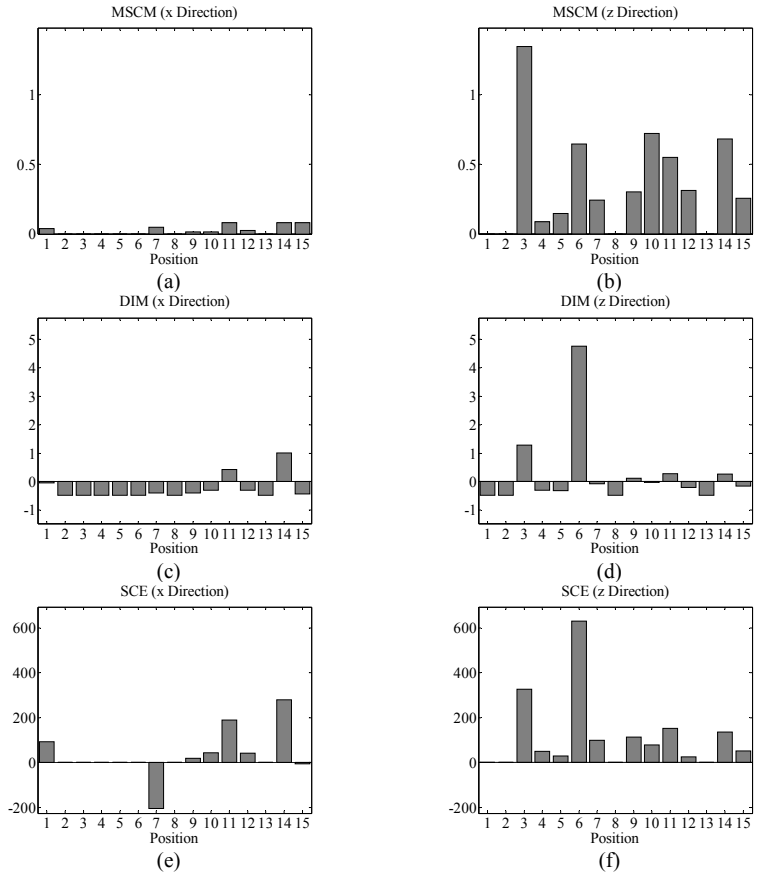


Figure C.44 – RS_C and $DS_{IV\text{-}C}$: (a) and (b) MSCM for curvatures in the *x* and *z* direction, respectively; (c) and (d) DIM for curvatures in the *x* and *z* direction, respectively; and (e) and (f) SCE for curvatures in the *x* and *z* direction, respectively.

C.3.2 Relative Comparison

C.3.2.1 Damage Scenario I-C and Damage Scenario II-C

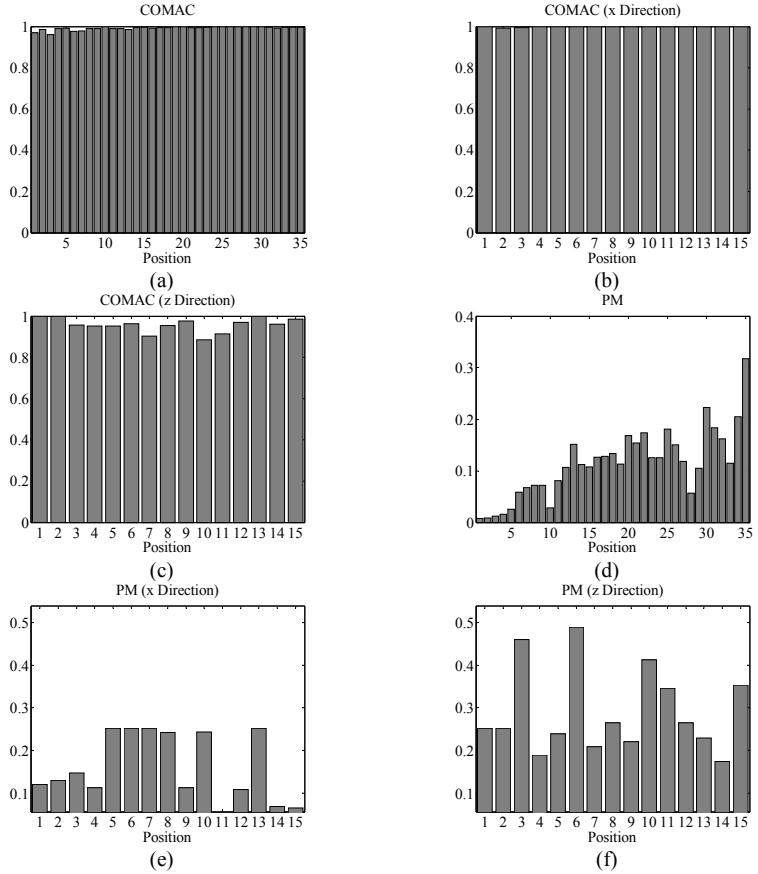


Figure C.45 – $DS_{I\text{-}C}$ and $DS_{II\text{-}C}$: (a) COMAC values for modal displacements; (b) and (c) COMAC values for modal curvatures in the *x* and *z* direction, respectively; (d) PM for modal displacements; and (e) and (f) PM for modal curvatures in the *x* and *z* direction, respectively.

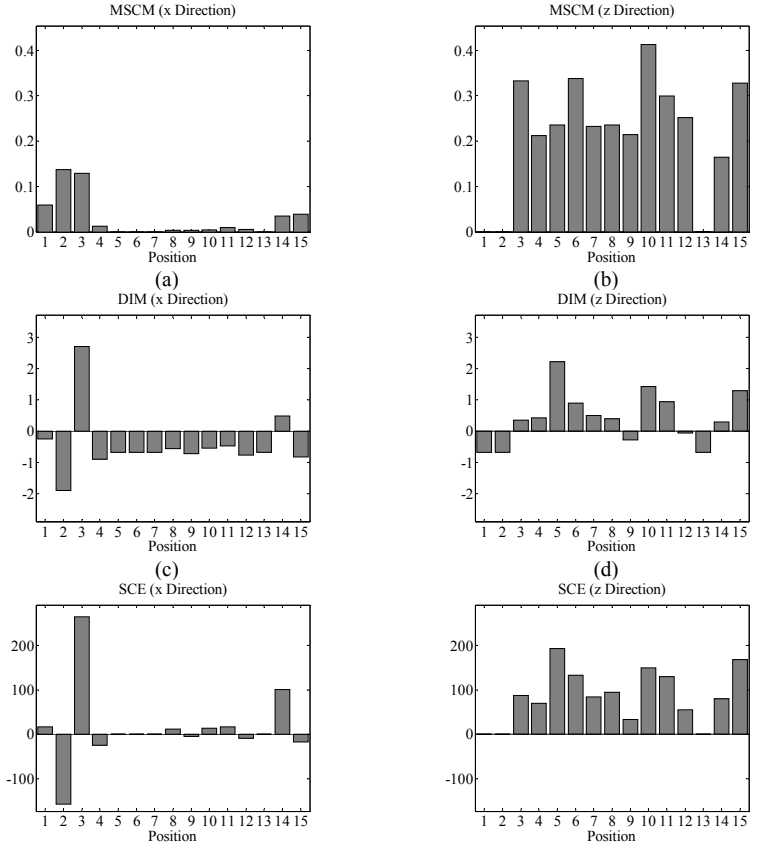


Figure C.46 – $DS_{I\text{-}C}$ and $DS_{II\text{-}C}$: (a) and (b) MSCM for curvatures in the *x* and *z* direction, respectively; (c) and (d) DIM for curvatures in the *x* and *z* direction, respectively; and (e) and (f) SCE for curvatures in the *x* and *z* direction, respectively.

C.3.2.2 Damage Scenario II-C and Damage Scenario III-C

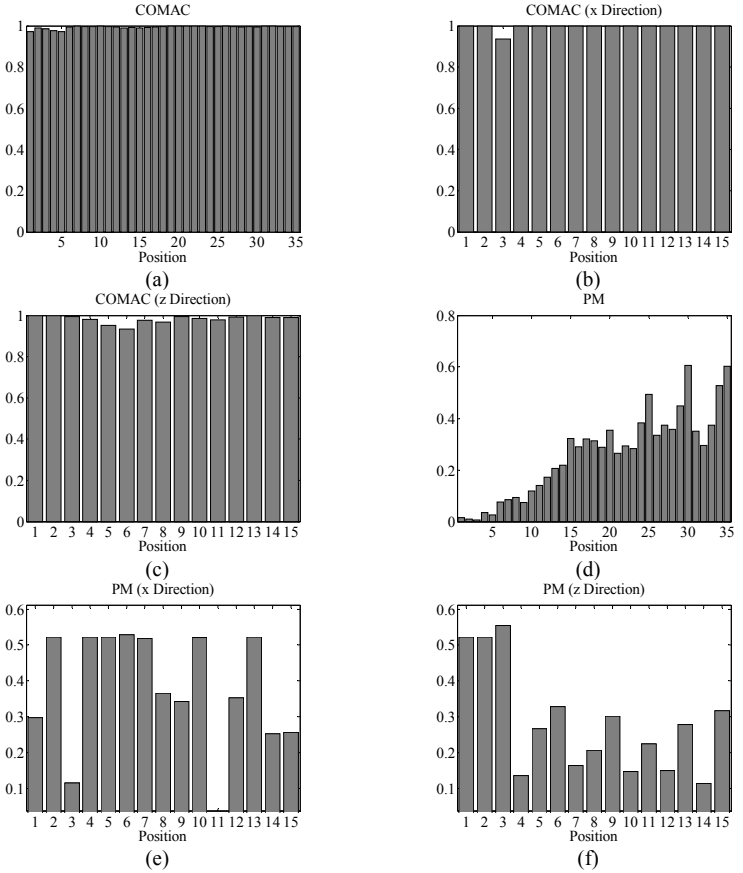


Figure C.47 – DS_{II-C} and DS_{III-C}: (a) COMAC values for modal displacements; (b) and (c) COMAC values for modal curvatures in the *x* and *z* direction, respectively; (d) PM for modal displacements; and (e) and (f) PM for modal curvatures in the *x* and *z* direction, respectively.

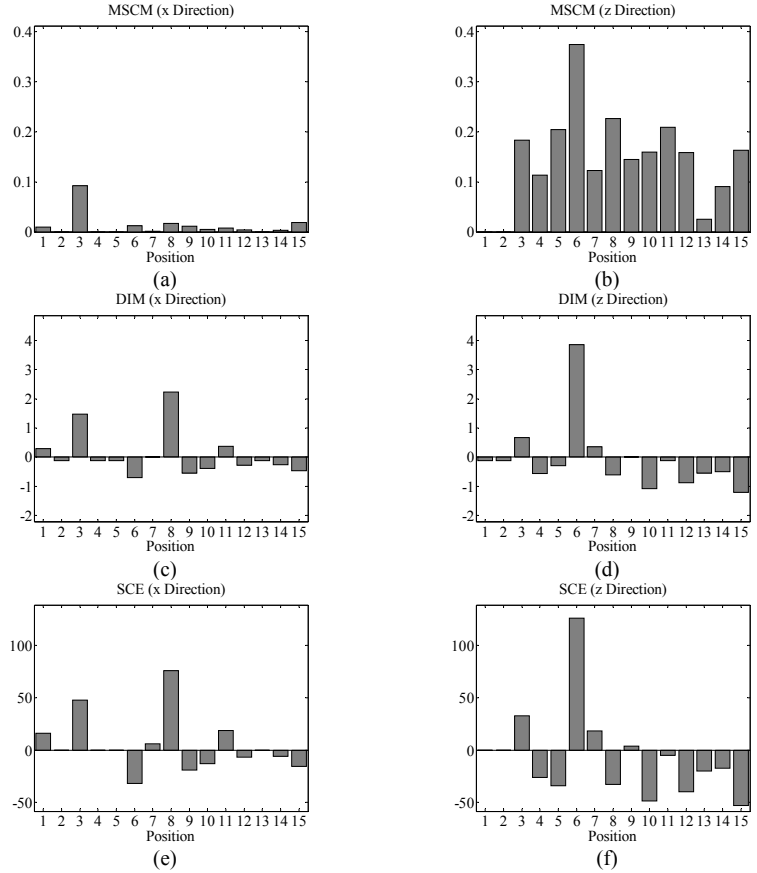


Figure C.48 – DS_{II-C} and DS_{III-C}: (a) and (b) MSCM for curvatures in the *x* and *z* direction, respectively; (c) and (d) DIM for curvatures in the *x* and *z* direction, respectively; and (e) and (f) SCE for curvatures in the *x* and *z* direction, respectively.

C.3.2.3 Damage Scenario III-C and Damage Scenario IV-C

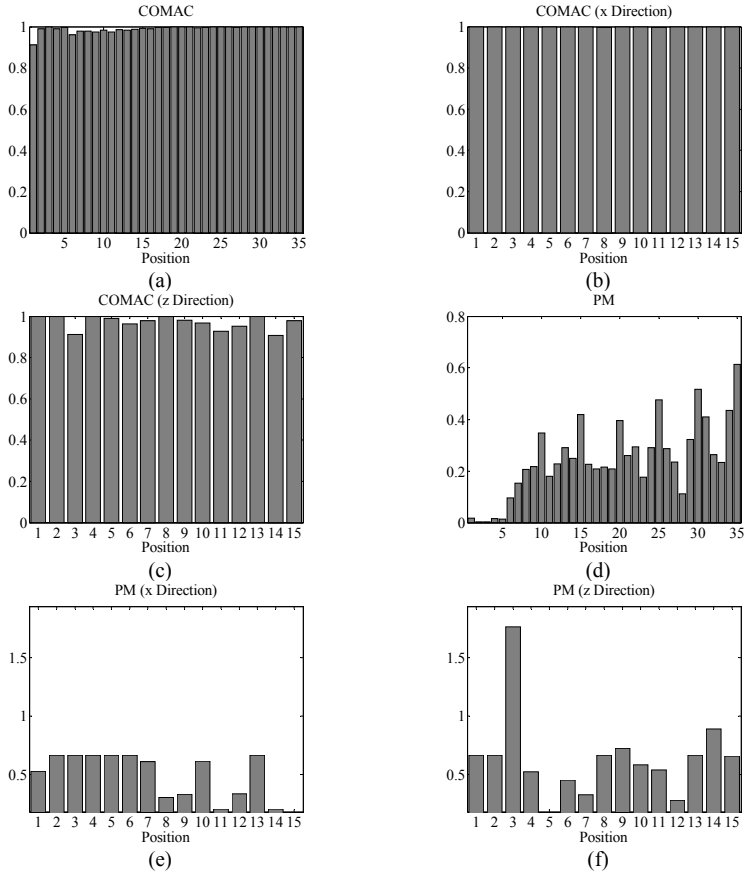


Figure C.49 – DS_{III-C} and DS_{IV-C}: (a) COMAC values for modal displacements; (b) and (c) COMAC values for modal curvatures in the *x* and *z* direction, respectively; (d) PM for modal displacements; and (e) and (f) PM for modal curvatures in the *x* and *z* direction, respectively.

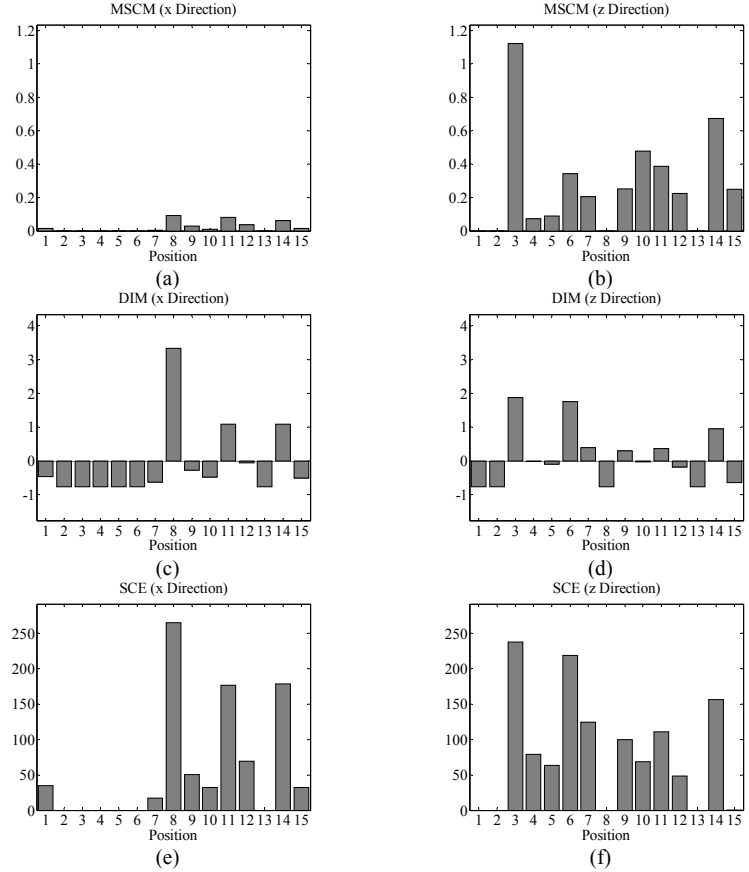
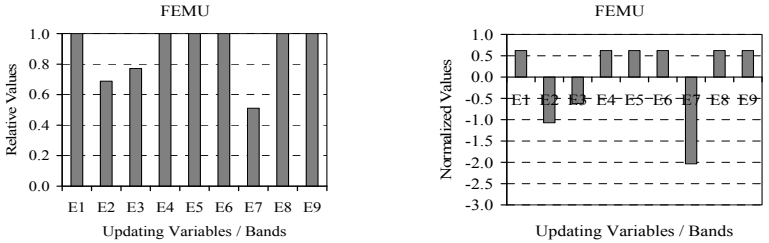


Figure C.50 – DS_{III-C} and DS_{IV-C}: (a) and (b) MSCM for curvatures in the *x* and *z* direction, respectively; (c) and (d) DIM for curvatures in the *x* and *z* direction, respectively; and (e) and (f) SCE for curvatures in the *x* and *z* direction, respectively.

C.4 Finite Element Model Updating Method Applied to Series A

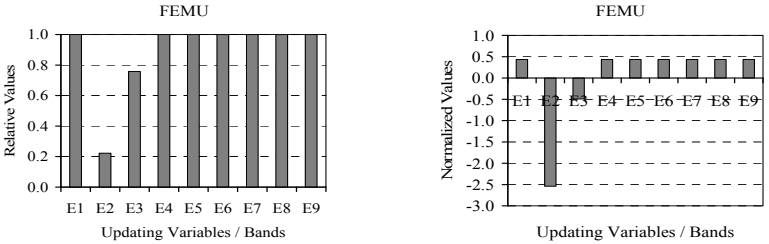
C.4.1 Damage Scenario II-A



(a) (b)

Figure B.51 – FEMU applied to $DS_{II\text{-}A}$: (a) relative values; and (b) normalized values

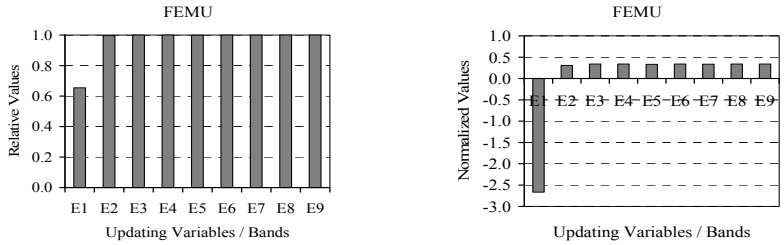
C.4.2 Damage Scenario III-A



(a) (b)

Figure B.52 – FEMU applied to $DS_{III\text{-}A}$: (a) relative values; and (b) normalized values

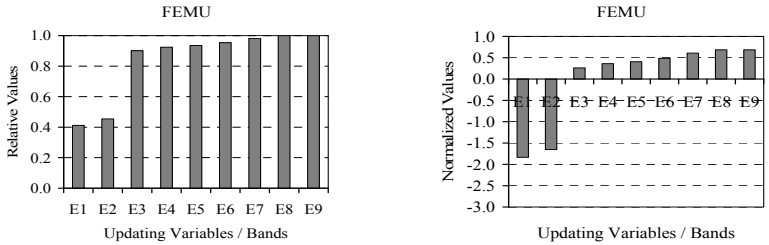
C.4.3 Damage Scenario IV-A



(a) (b)

Figure B.53 – FEMU applied to $DS_{IV\text{-}A}$: (a) relative values; and (b) normalized values

C.4.4 Damage Scenario V-A

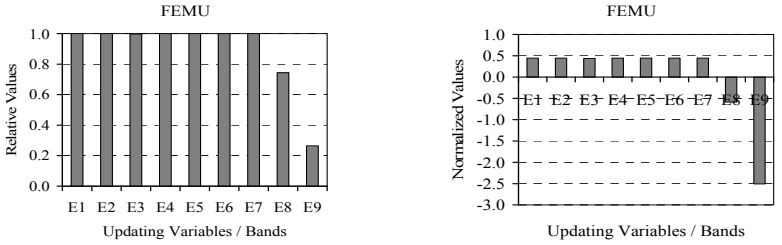


(a) (b)

Figure B.54 – FEMU applied to $DS_{V\text{-}A}$: (a) relative values; and (b) normalized values

C.5 Finite Element Model Updating Method Applied to Series B

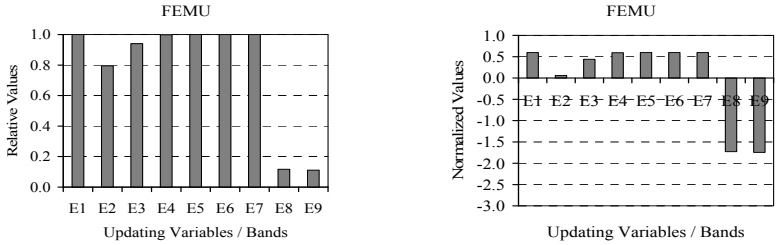
C.5.1 Damage Scenario III-B



(a) (b)

Figure B.55 – FEMU applied to DS_{III-B}: (a) relative values; and (b) normalized values

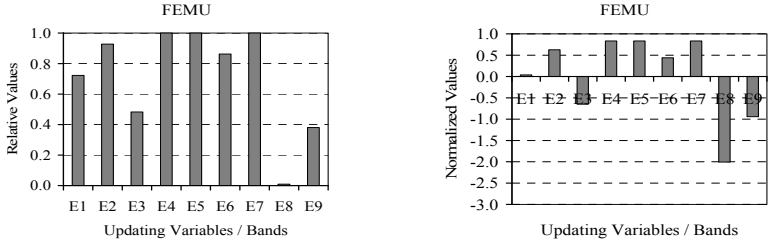
C.5.2 Damage Scenario IV-B



(a) (b)

Figure B.56 – FEMU applied to DS_{IV-B}: (a) relative values; and (b) normalized values

C.5.3 Damage Scenario V-B

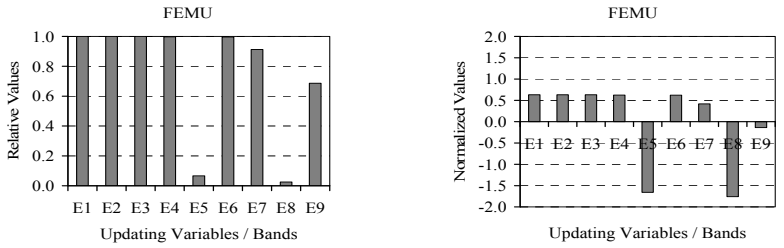


(a) (b)

Figure B.57 – FEMU applied to DS_{V-B}: (a) relative values; and (b) normalized values

C.6 Finite Element Model Updating Method Applied to Series C

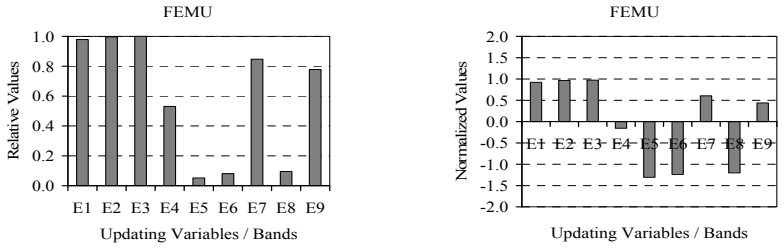
C.6.1 Damage Scenario II-C



(a) (b)

Figure B.58 – FEMU applied to $DS_{II\text{-}C}$: (a) relative values; and (b) normalized values

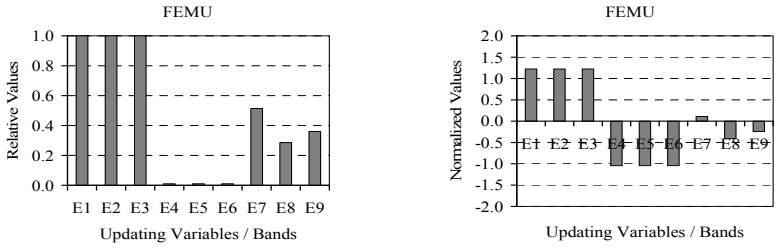
C.6.2 Damage Scenario III-C



(a) (b)

Figure B.59 – FEMU applied to $DS_{III\text{-}C}$: (a) relative values; and (b) normalized values

C.6.3 Damage Scenario IV-C



(a) (b)

Figure B.60 – FEMU applied to $DS_{IV\text{-}C}$: (a) relative values; and (b) normalized values

Annex D

Annex of Chapter 7

Index of Annex D

D.1 Case Study I: Mogadouro Clock Tower D.3
D.1.1 Environmental and Loading Effects on the First Frequency D.3
D.1.2 Environmental and Loading Effects on the First Damping D.7
D.1.3 Environmental and Loading Effects on the Second Frequency D.9
D.1.4 Environmental and Loading Effects on the Second Damping D.13
D.1.5 Environmental and Loading Effects on the Third Frequency D.15
D.1.6 Environmental and Loading Effects on the Third Damping D.19
D.1.7 Static and Dynamic Models D.21
D.2 Case Study II: Church of Monastery of Jerónimos D.22
D.2.1 Static and Dynamic Models for the Static Response D.22
D.2.2 Environmental and Loading Effects on the First Frequency D.22
D.2.3 Environmental and Loading Effects on the Second Frequency D.23
D.2.4 Environmental and Loading Effects on the Forth Frequency D.24
D.2.5 Static Models for the Dynamic Response D.25

D.1 Case Study I: Mogadouro Clock Tower

D.1.1 Environmental and Loading Effects on the First Frequency

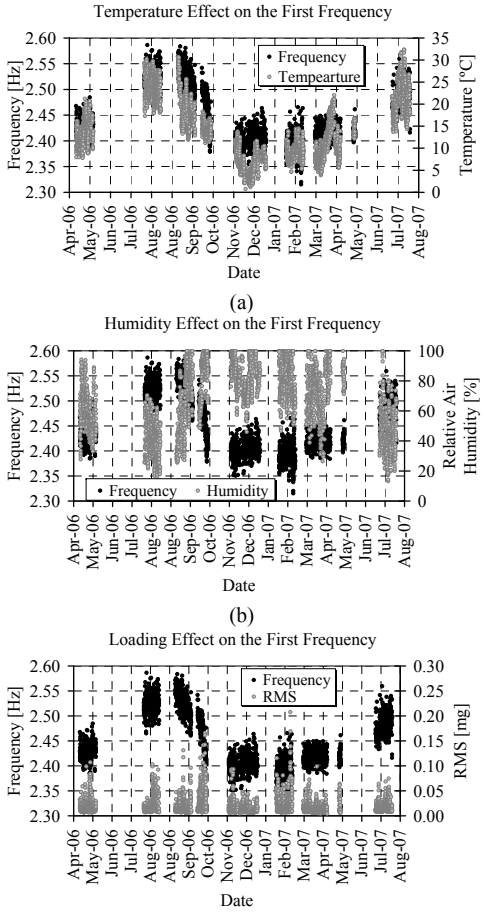


Figure D.1 – Environmental and loading effects on the first frequency: (a) temperature effect; (b) humidity effect; and (c) loading effect.

D.1.1.1 Frequency versus Temperature on each Series

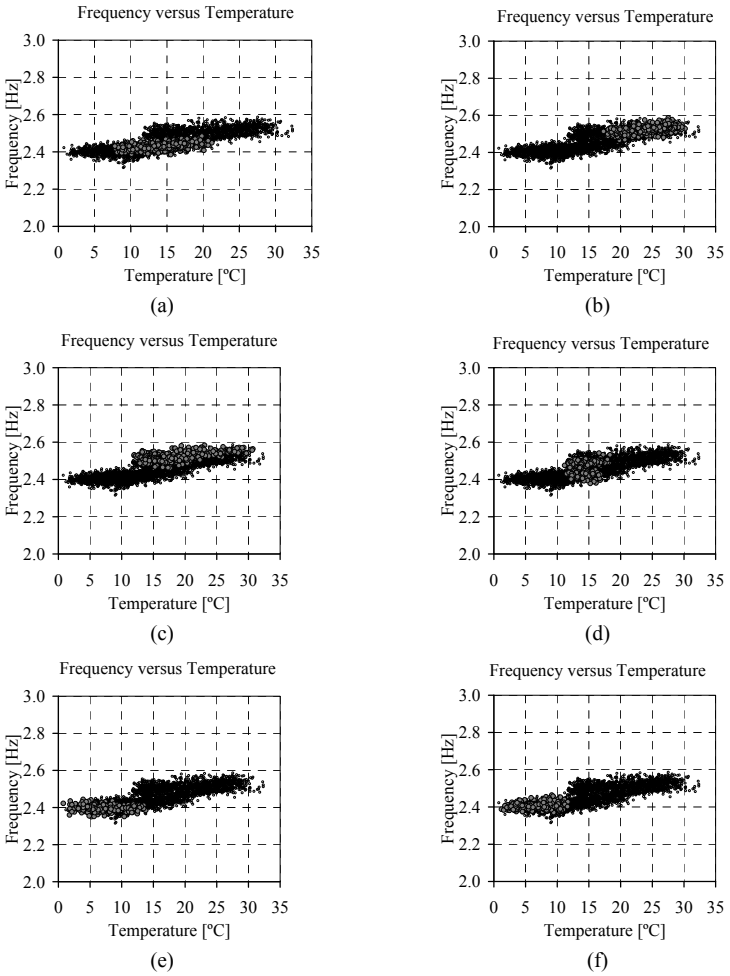


Figure D.2 – Frequency versus temperature: (a), (b), (c), (d), (e), and (f) for Series I, II, III, IV, V, and VI, respectively.

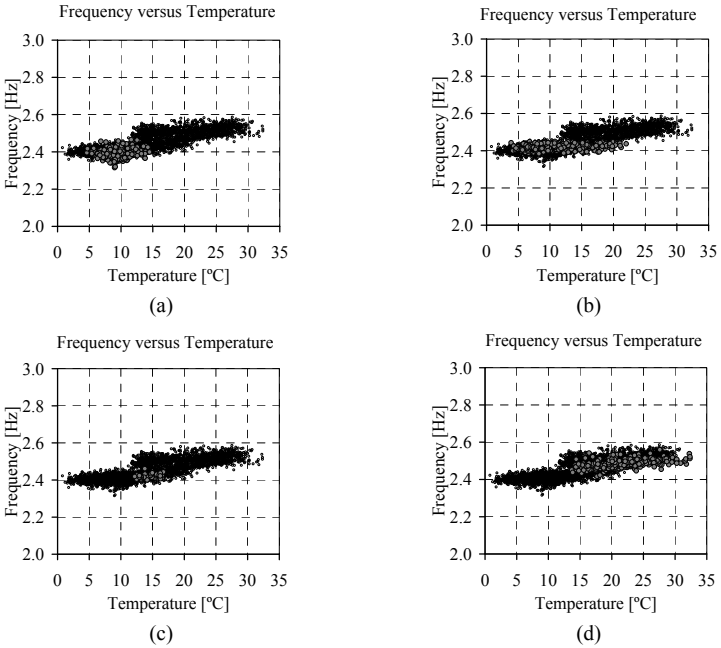


Figure D.3 – Frequency versus temperature: (a), (b), (c) and (d) for Series VII, VIII, IX and X.

D.1.1.2 Frequency versus Humidity on each Series

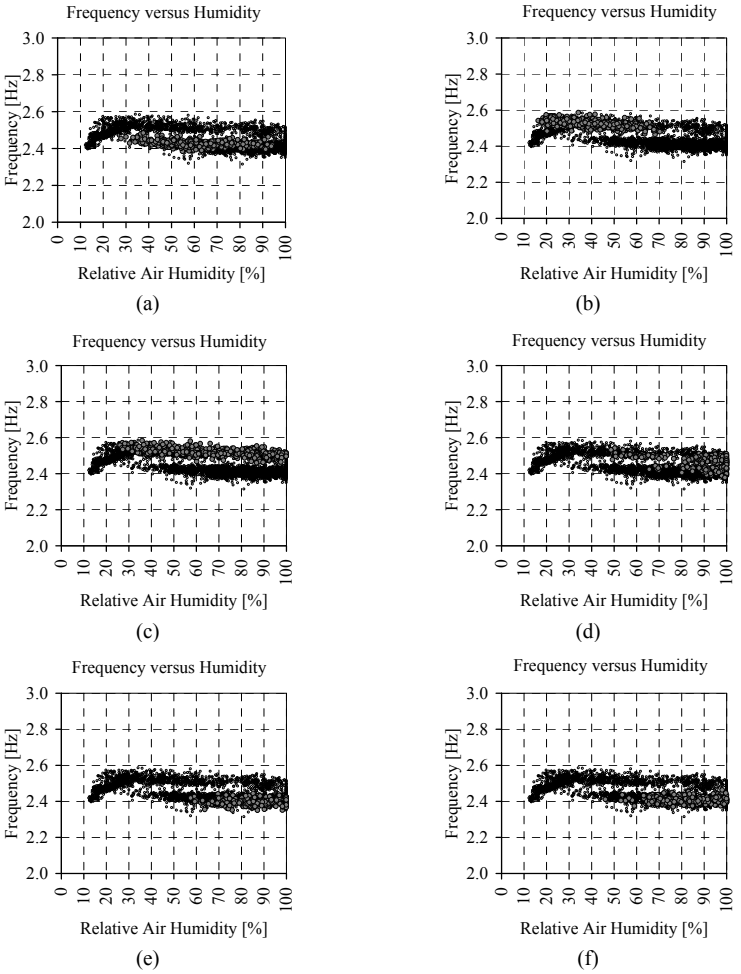


Figure D.4 – Frequency versus humidity: (a), (b), (c), (d), (e), and (f) for Series I, II, III, IV, V, and VI, respectively.

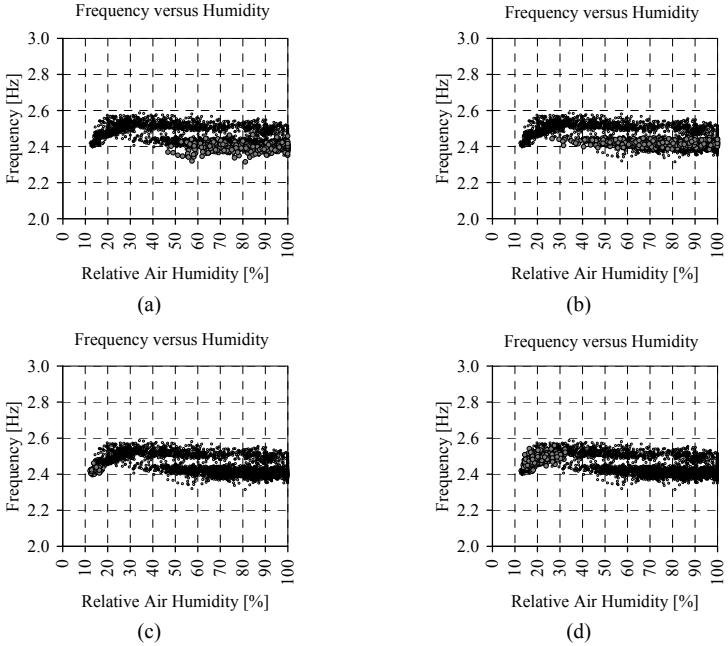


Figure D.5 – Frequency versus humidity: (a), (b), (c) and (d) for Series VII, VIII, IX and X.

D.1.1.3 Frequency versus RMS on each Series

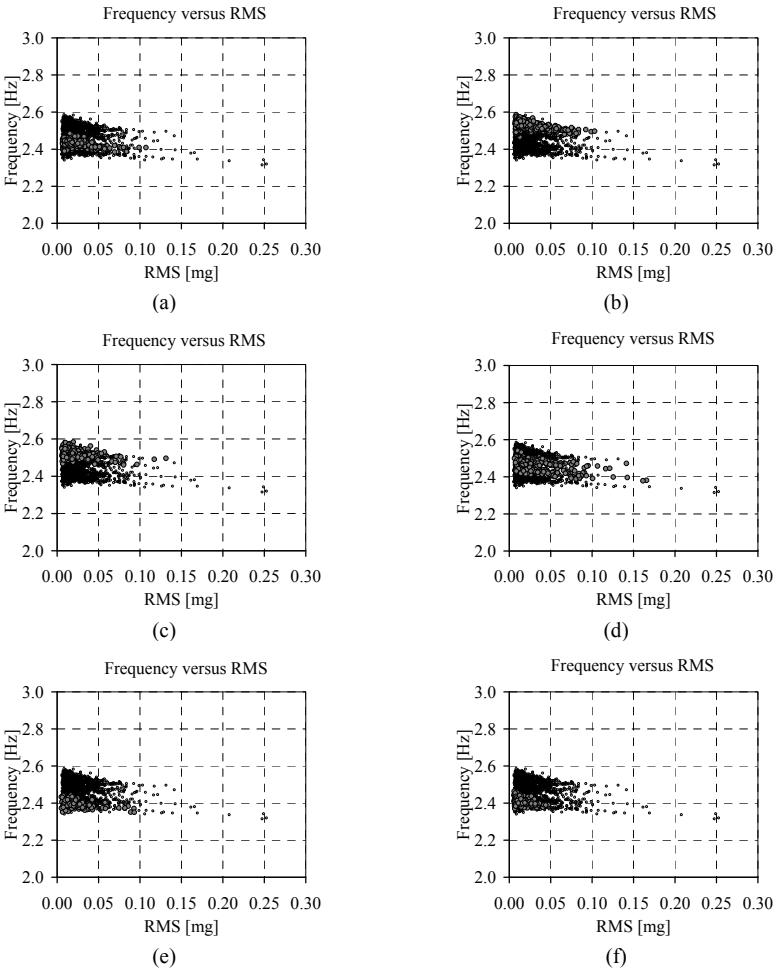


Figure D.6 – Frequency versus RMS: (a), (b), (c), (d), (e), and (f) for Series I, II, III, IV, V, and VI, respectively.

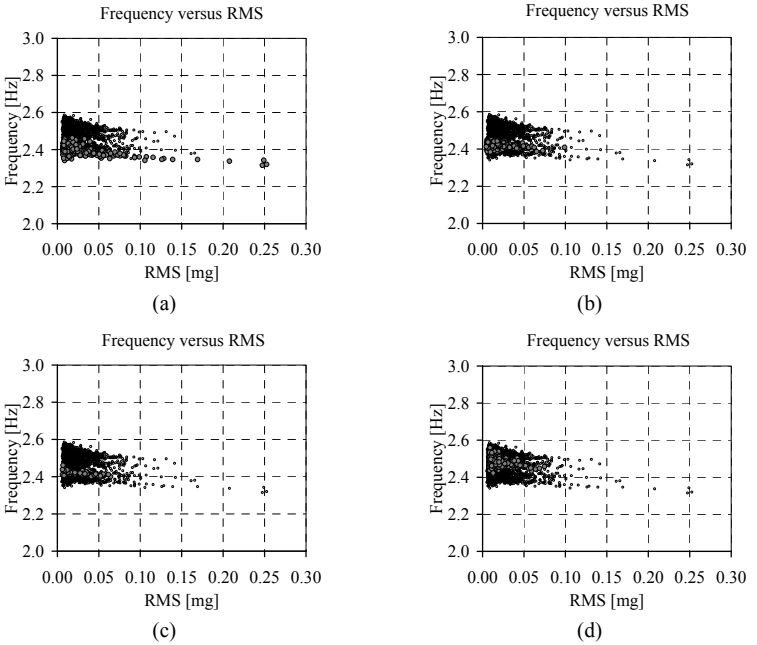


Figure D.7 – Frequency versus RMS: (a), (b), (c) and (d) for Series VII, VIII, IX and X.

D.1.2 Environmental and Loading Effects on the First Damping

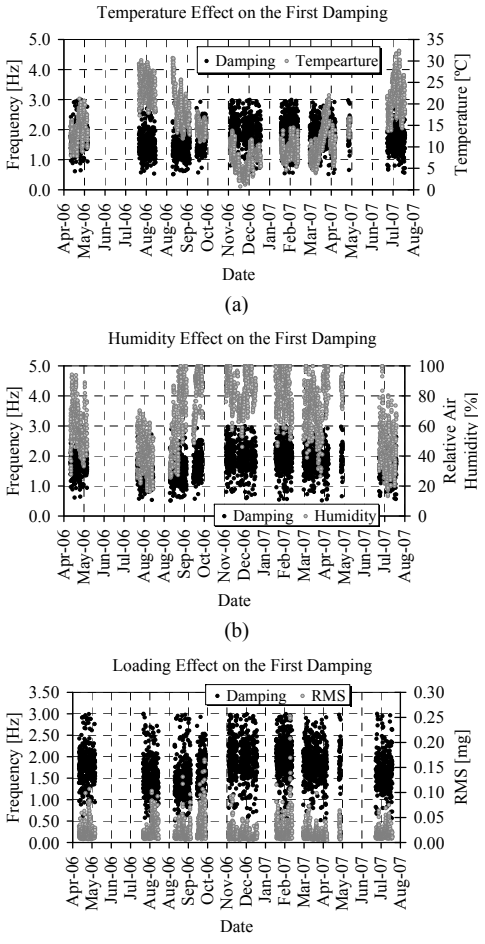


Figure D.8 – Environmental and loading effects on the first damping: (a) temperature effect; (b) humidity effect; and (c) loading effect.

D.1.2.1 Damping versus RMS on each Series

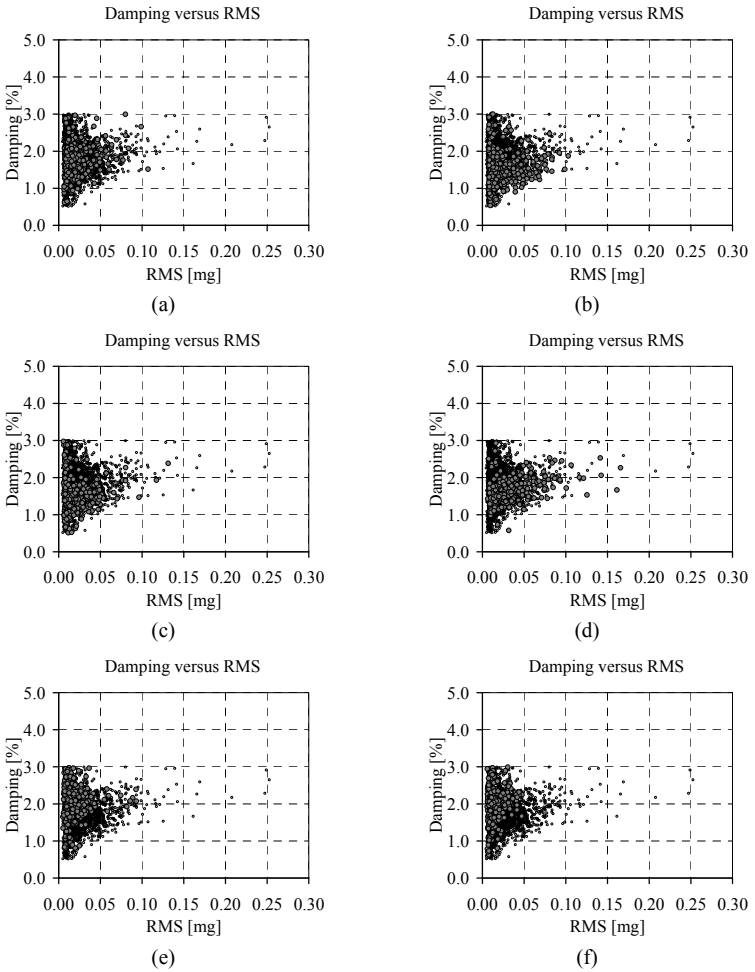


Figure D.9 – Damping versus RMS: (a), (b), (c), (d), (e), and (f) for Series I, II, III, IV, V, and VI, respectively.

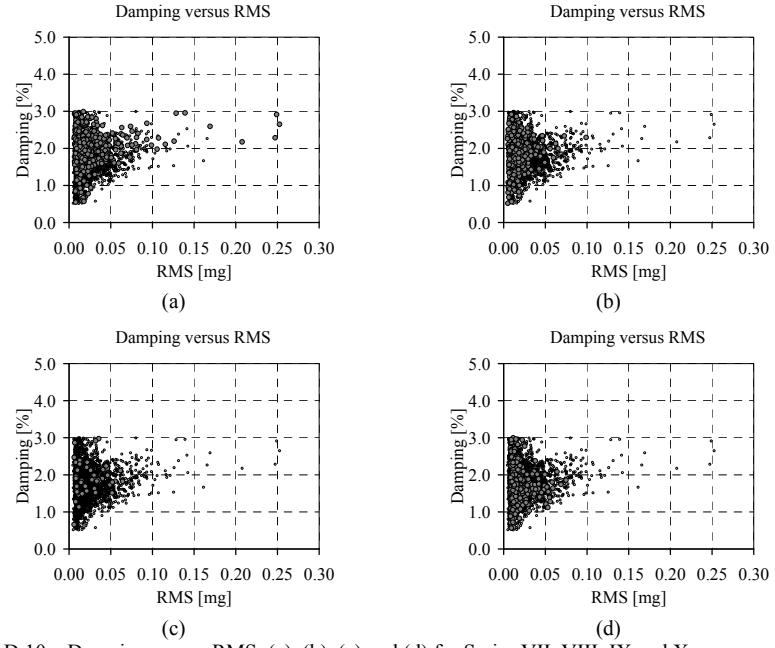


Figure D.10 – Damping versus RMS: (a), (b), (c) and (d) for Series VII, VIII, IX and X.

D.1.3 Environmental and Loading Effects on the Second Frequency

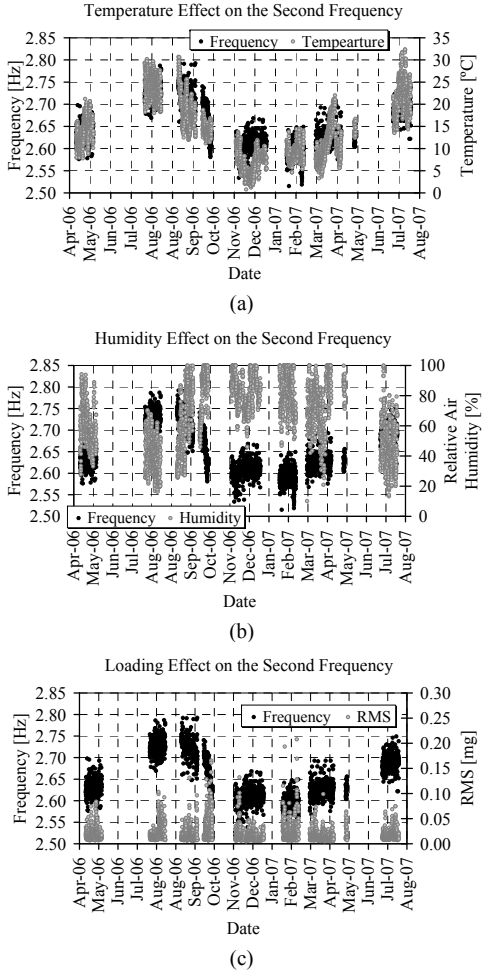


Figure D.11 – Environmental and loading effects on the first frequency: (a) temperature effect; (b) humidity effect; and (c) loading effect.

D.1.3.1 Frequency versus Temperature on each Series

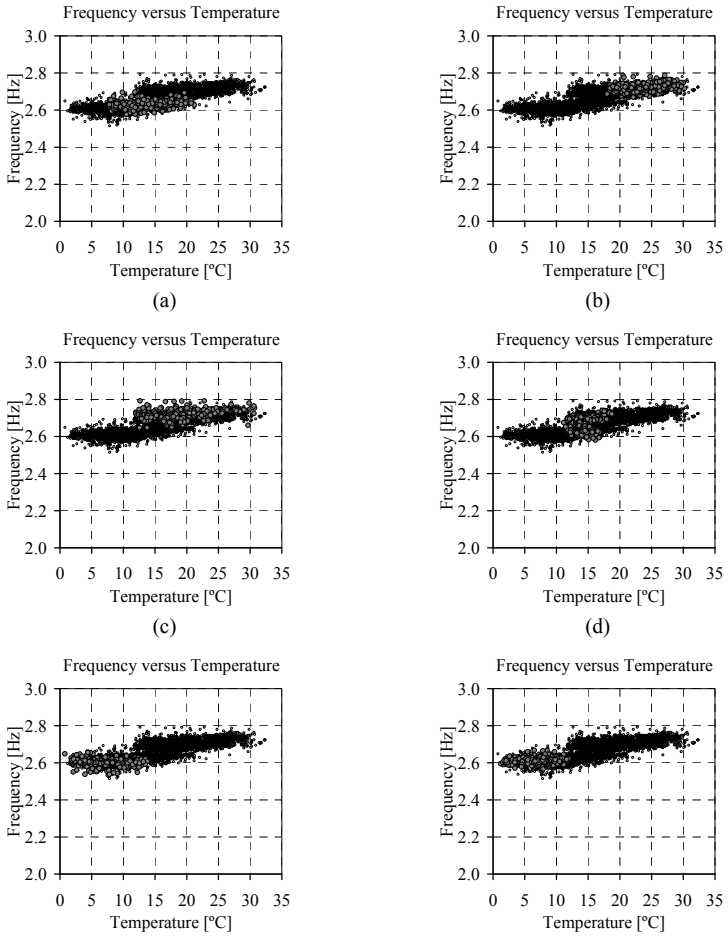


Figure D.12 – Frequency versus temperature: (a), (b), (c), (d), (e), and (f) for Series I, II, III, IV, V, and VI, respectively.

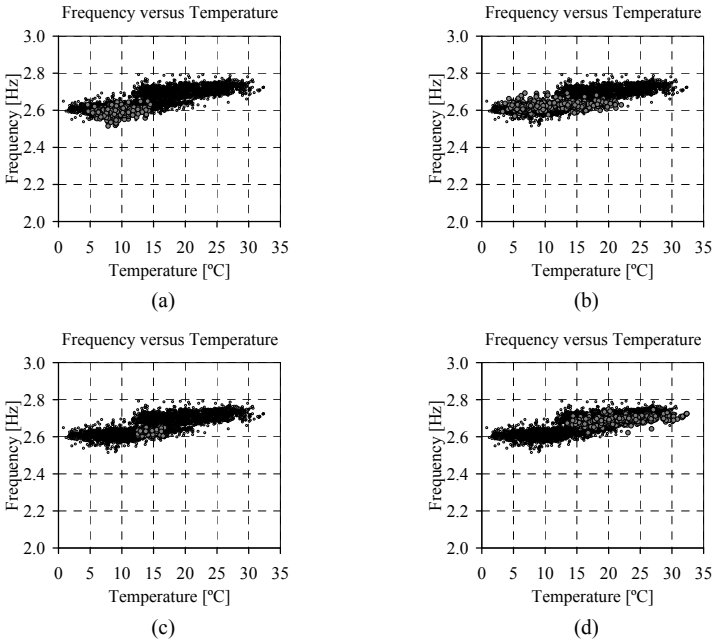


Figure D.13 – Frequency versus temperature: (a), (b), (c) and (d) for Series VII, VIII, IX and X.

D.1.3.2 Frequency versus Humidity on each Series

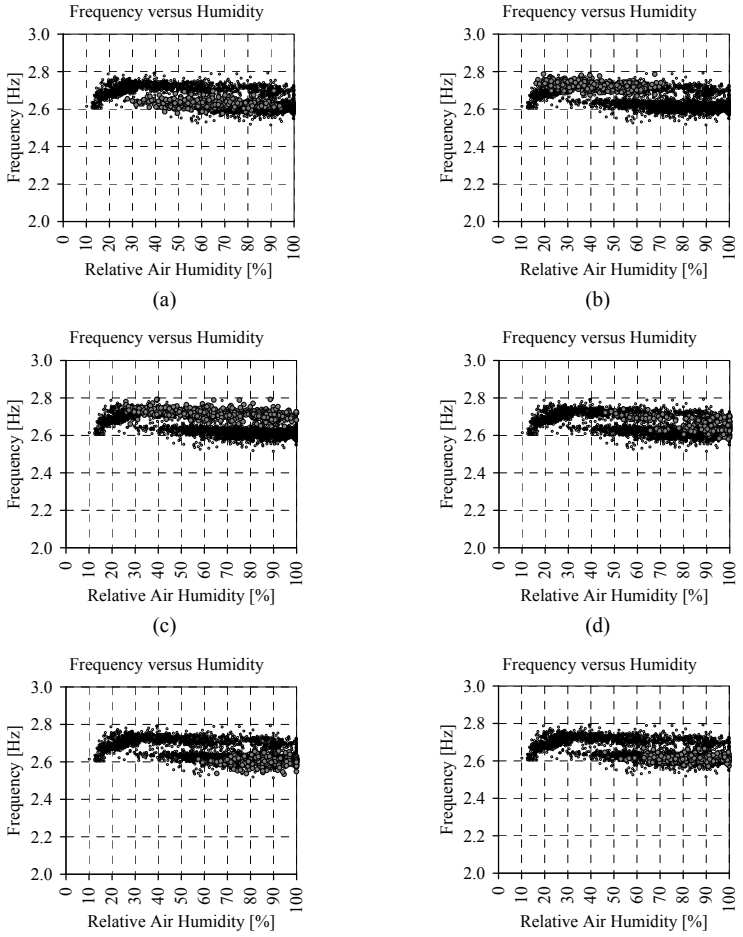


Figure D.14 – Frequency versus humidity: (a), (b), (c), (d), (e), and (f) for Series I, II, III, IV, V, and VI, respectively.

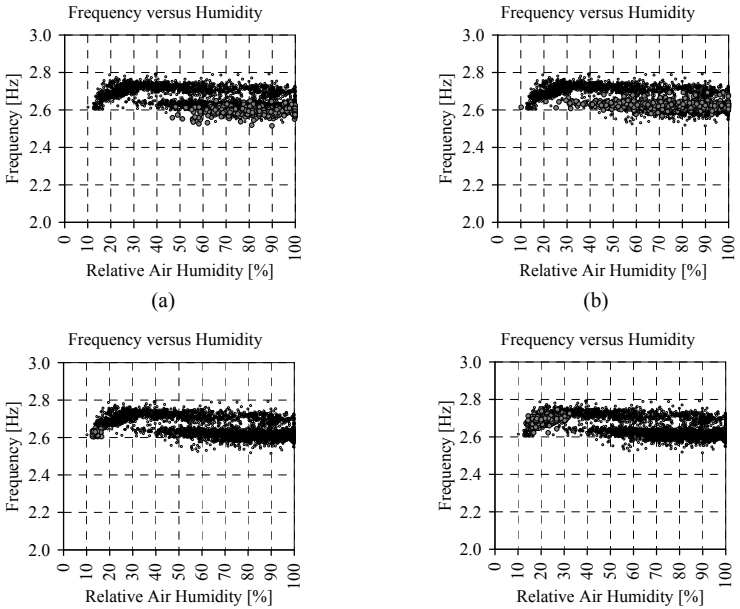


Figure D.15 – Frequency versus humidity: (a), (b), (c) and (d) for Series VII, VIII, IX and X.

D.1.3.3 Frequency versus RMS on each Series

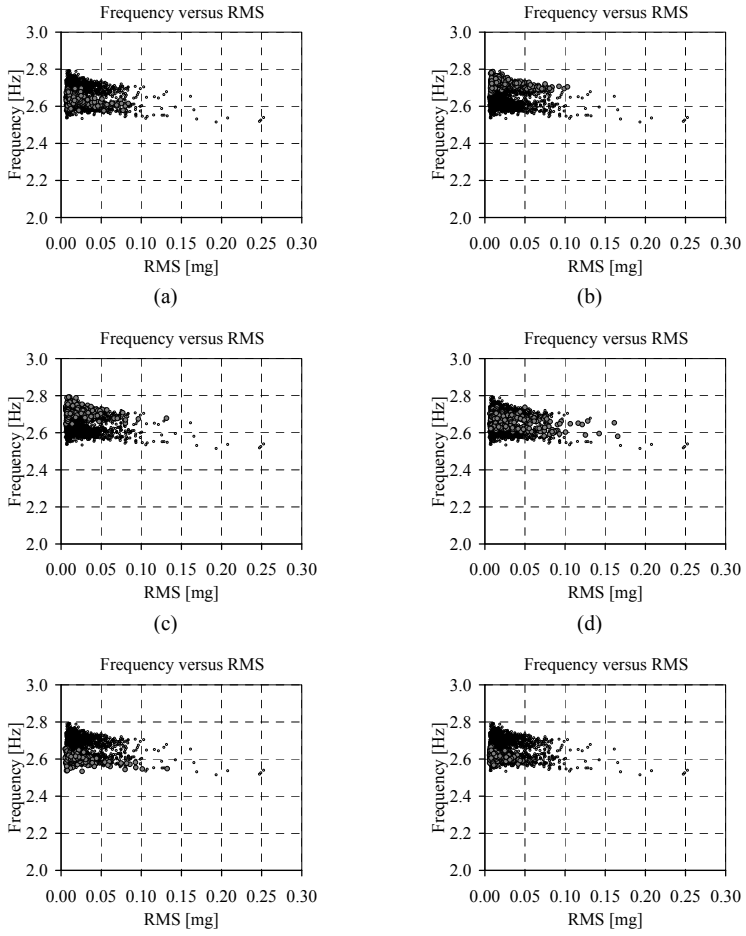


Figure D.16 – Frequency versus RMS: (a), (b), (c), (d), (e), and (f) for Series I, II, III, IV, V, and VI, respectively.

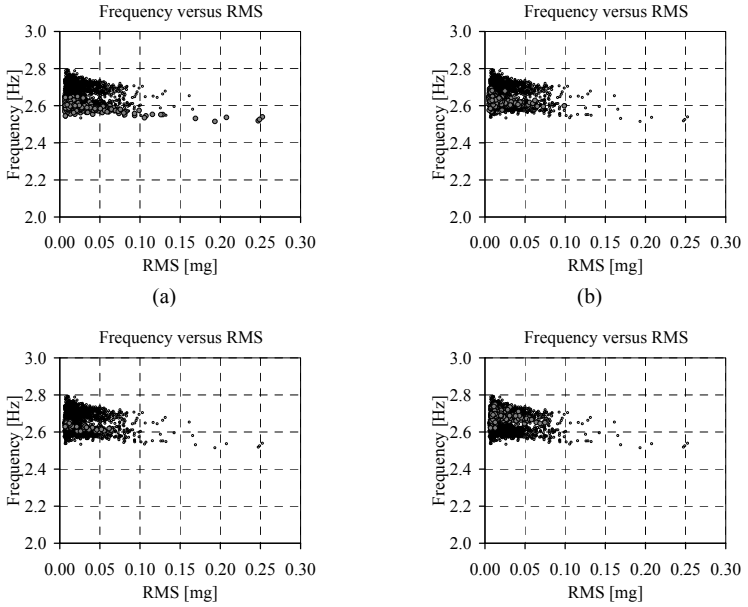


Figure D.17 – Frequency versus RMS: (a), (b), (c) and (d) for Series VII, VIII, IX and X.

D.1.4 Environmental and Loading Effects on the Second Damping

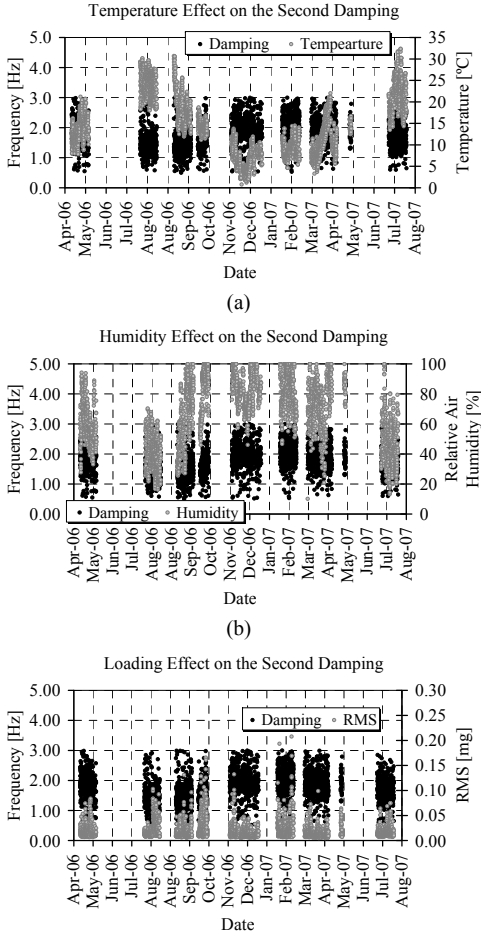


Figure D.18 – Environmental and loading effects on the first damping: (a) temperature effect; (b) humidity effect; and (c) loading effect.

D.1.4.1 Damping versus RMS on each Series

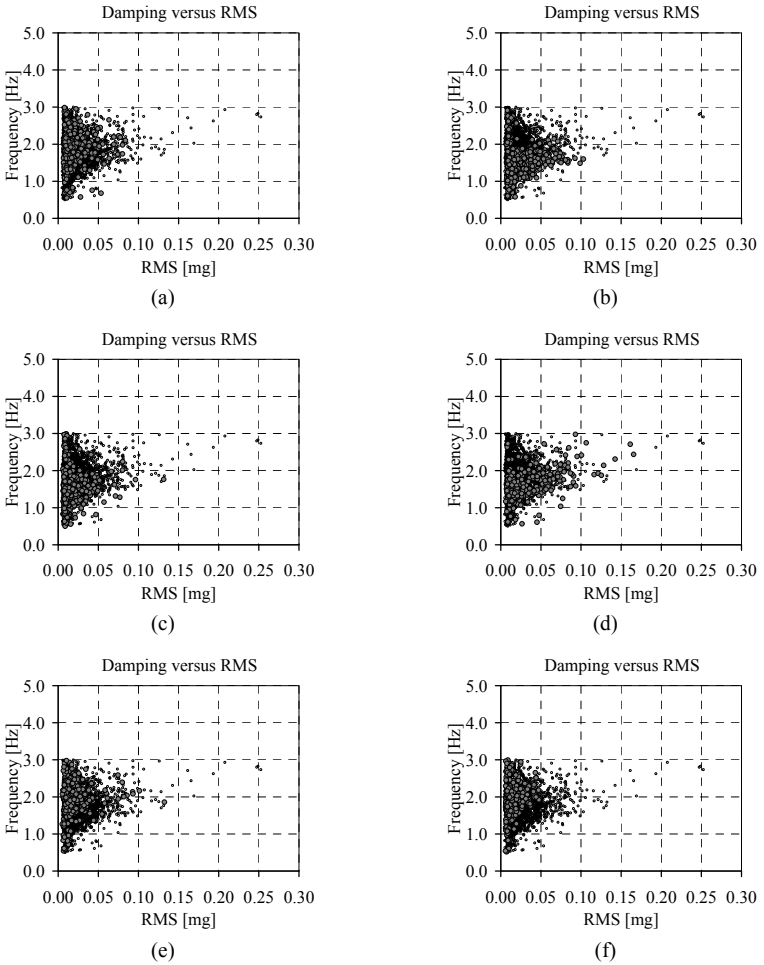


Figure D.19 – Damping versus RMS: (a), (b), (c), (d), (e), and (f) for Series I, II, III, IV, V, and VI, respectively.

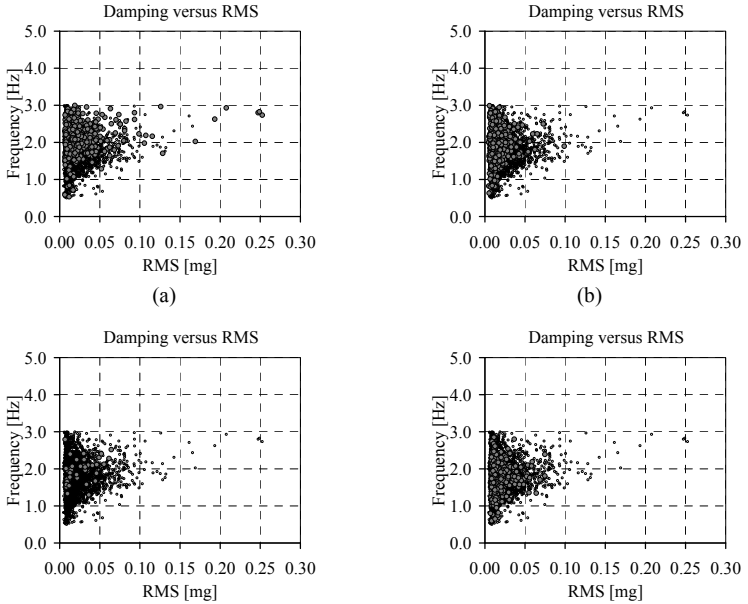
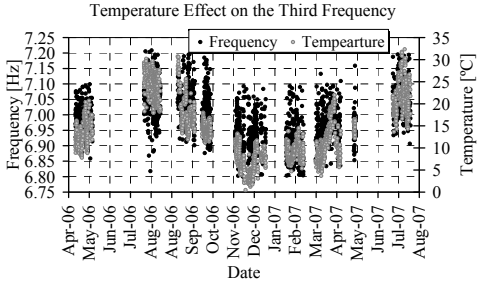
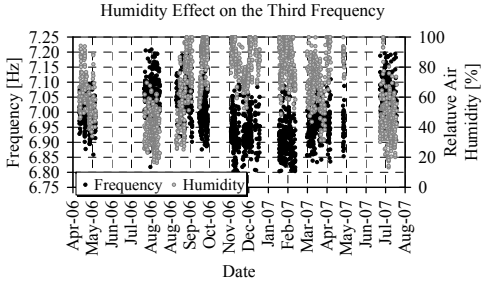


Figure D.20 – Damping versus RMS: (a), (b), (c) and (d) for Series VII, VIII, IX and X.

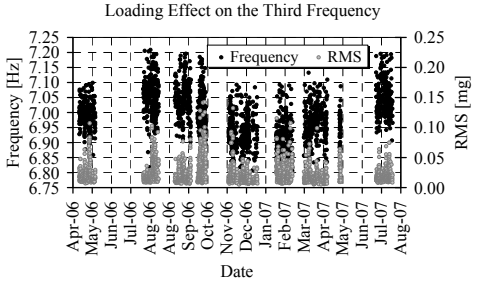
D.1.5 Environmental and Loading Effects on the Third Frequency



(a)



(b)



(c)

Figure D.21 – Environmental and loading effects on the first frequency: (a) temperature effect; (b) humidity effect; and (c) loading effect.

D.1.5.1 Frequency versus Temperature on each Series

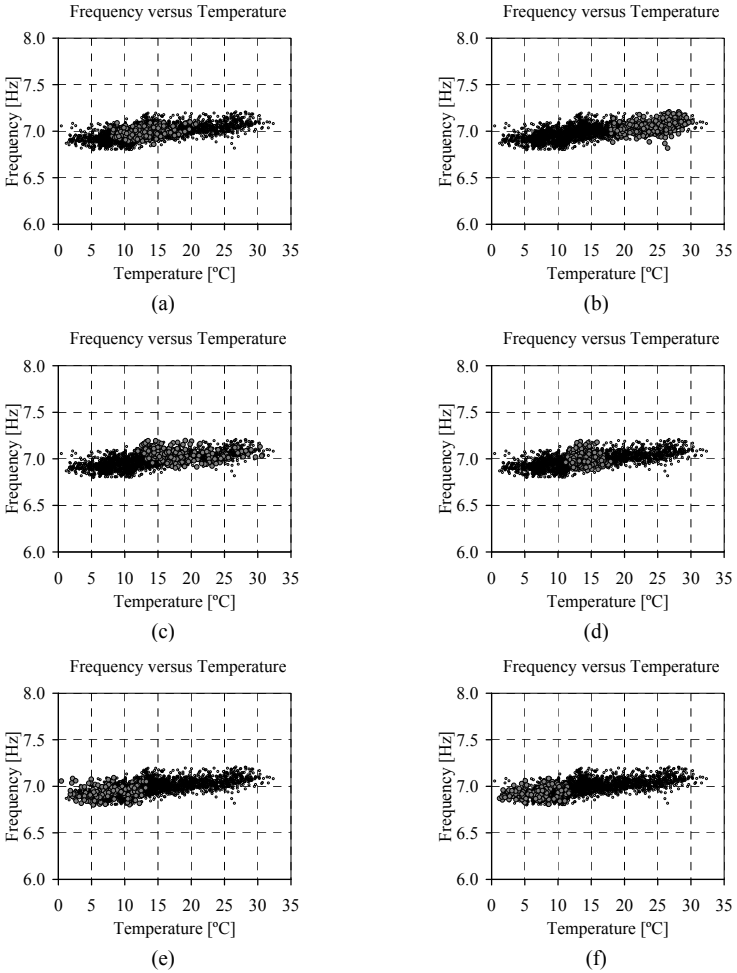


Figure D.22 – Frequency versus temperature: (a), (b), (c), (d), (e), and (f) for Series I, II, III, IV, V, and VI, respectively.

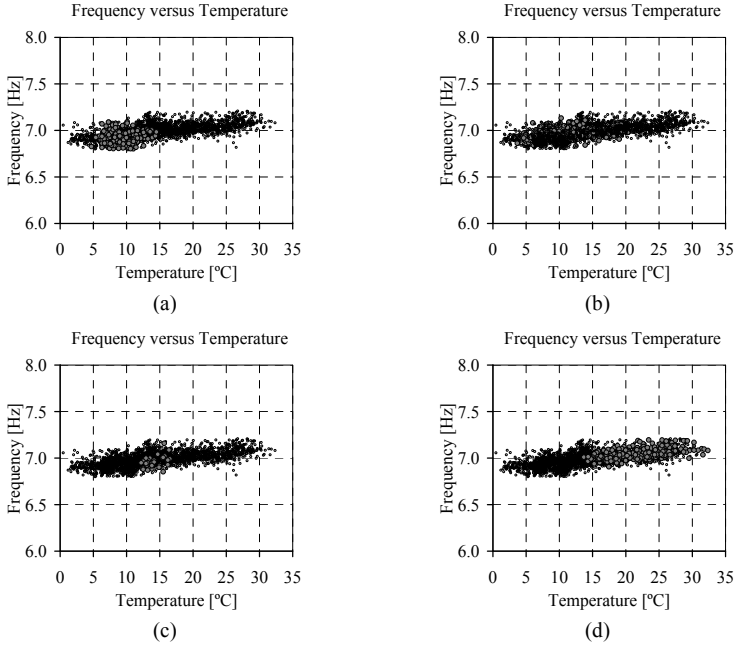


Figure D.23 – Frequency versus temperature: (a), (b), (c) and (d) for Series VII, VIII, IX and X.

D.1.5.2 Frequency versus Humidity on each Series

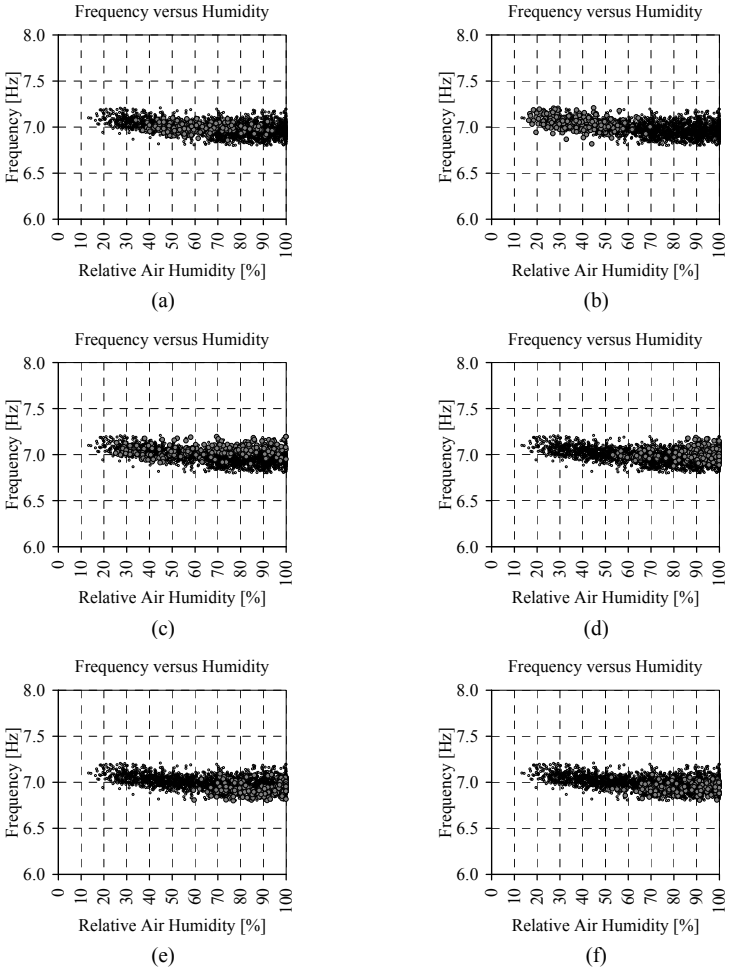


Figure D.24 – Frequency versus humidity: (a), (b), (c), (d), (e), and (f) for Series I, II, III, IV, V, and VI, respectively.

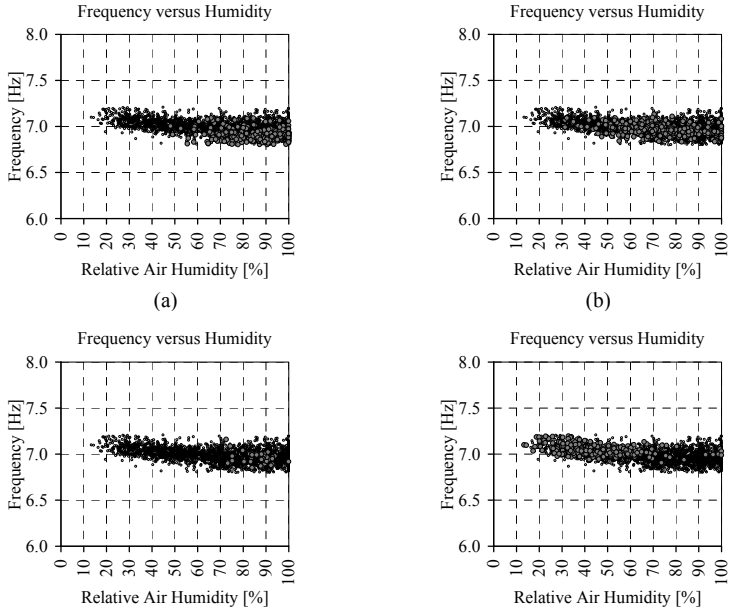


Figure D.25 – Frequency versus humidity: (a), (b), (c) and (d) for Series VII, VIII, IX and X.

D.1.5.3 Frequency versus RMS on each Series

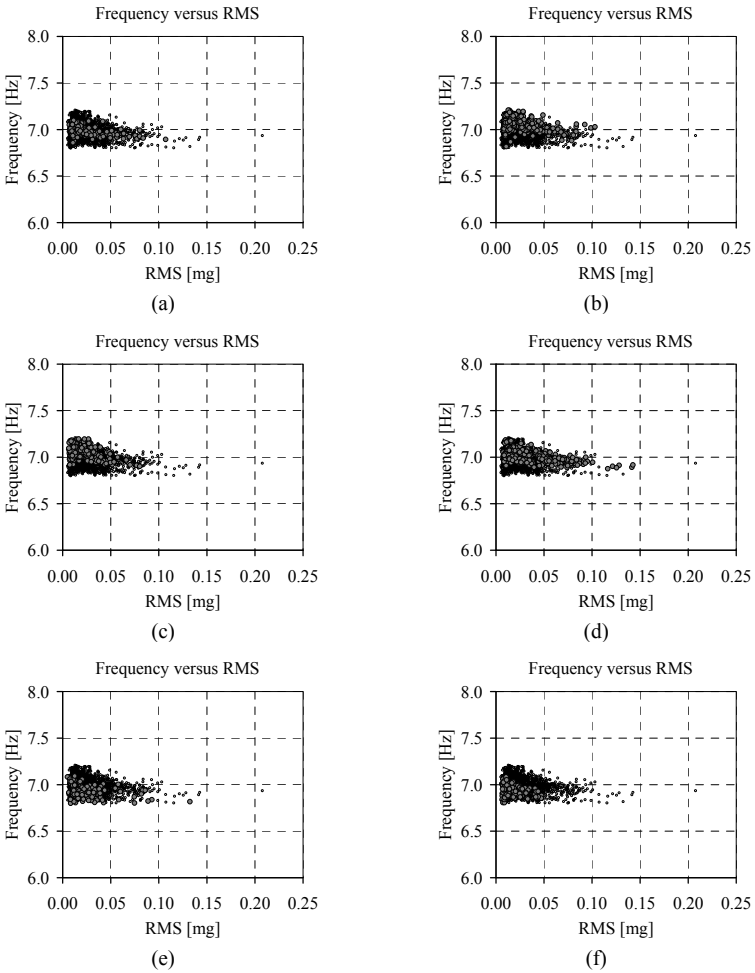


Figure D.26 – Frequency versus RMS: (a), (b), (c), (d), (e), and (f) for Series I, II, III, IV, V, and VI, respectively.

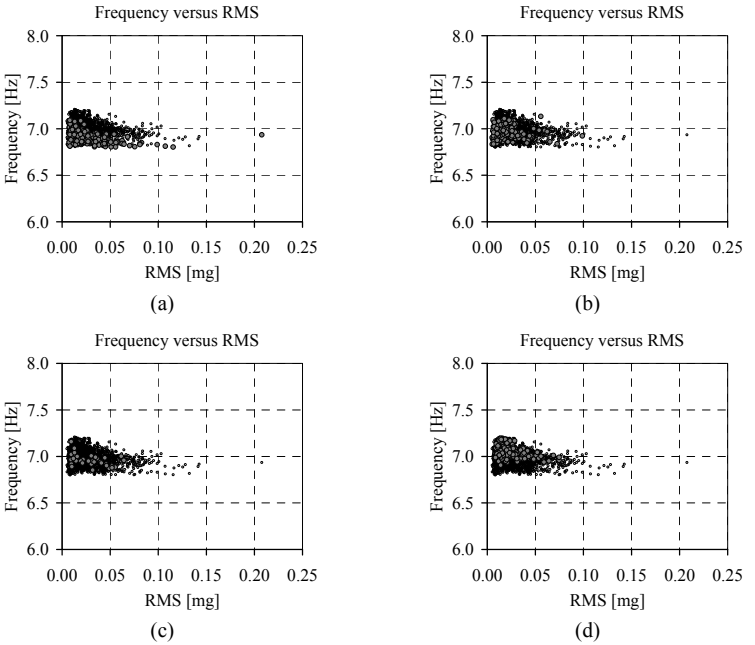


Figure D.27 – Frequency versus RMS: (a), (b), (c) and (d) for Series VII, VIII, IX and X.

D.1.6 Environmental and Loading Effects on the Third Damping

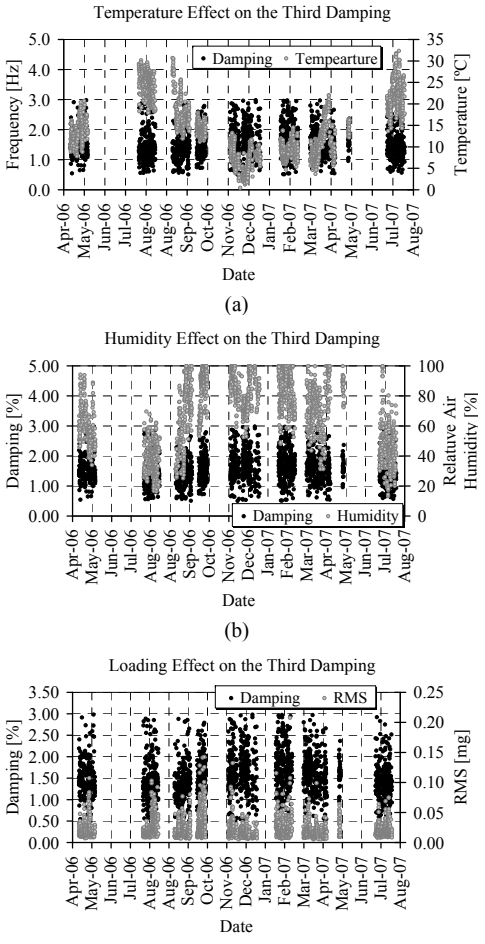


Figure D.28 – Environmental and loading effects on the first damping: (a) temperature effect; (b) humidity effect; and (c) loading effect.

D.1.6.1 Damping versus RMS on each Series

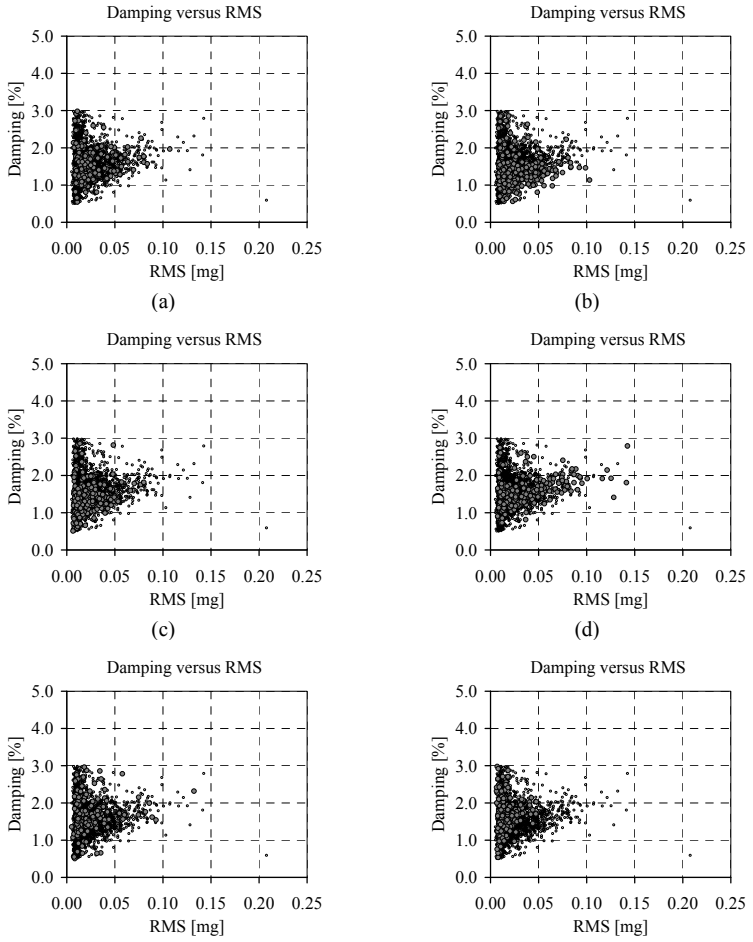


Figure D.29 – Damping versus RMS: (a), (b), (c), (d), (e), and (f) for Series I, II, III, IV, V, and VI, respectively.

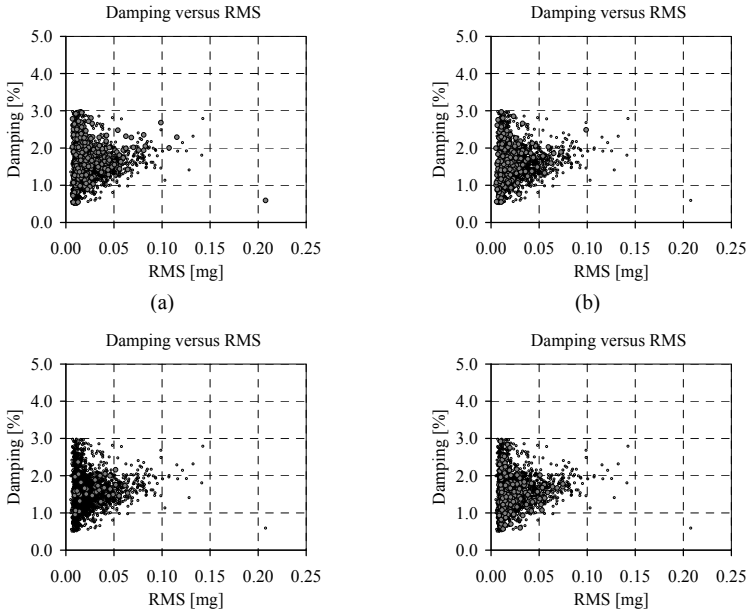


Figure D.30 – Damping versus RMS: (a), (b), (c) and (d) for Series VII, VIII, IX and X.

D.1.7 Static and Dynamic Models

Table D.1 – ARX model parameters and their standard deviations.

Mode	Model						
			a_0	a_1	a_2	a_3	a_4	a_5
		x	1	–0.471	–0.245	–0.231	–	–
		σ	–	0.032	0.035	0.031	–	–
			b_1^T	b_2^T	b_3^T	b_4^T	b_5^T	b_6^T
1	3 , 2 2 4 , 0 0 0	x	0.270 –0.035 –0.160	–0.231 0.020 0.055	– – 0.039	– – 0.044	–	–
		σ	0.031 0.025 0.009	0.032 0.025 0.012	– – 0.012	– – 0.010	–	–
			a_0	a_1	a_2	a_3	a_4	a_5
		x	1	–0.367	–0.219	–0.165	–0.177	–0.177
		σ	–	0.035	0.036	0.036	0.032	0.032
			b_1^T	b_2^T	b_3^T	b_4^T	b_5^T	b_6^T
2	4 , 1 2 4 , 0 0 0	x	0.055 –0.082 –0.147	– 0.069 0.021	– – 0.057	– – 0.033	–	–
		σ	0.018 0.025 0.012	– 0.024 0.013	– – 0.013	– – 0.012	–	–
			a_0	a_1	a_2	a_3	a_4	a_5
		x	1	–0.418	–0.158	–0.106	0.050	0.056
		σ	–	0.044	0.046	0.046	0.046	0.040
			b_1^T	b_2^T	b_3^T	b_4^T	b_5^T	b_6^T
3	5 , 2 3 5 , 0 0 0	x	0.282 –0.296 –0.276	0.096 –0.399 0.104	– –0.054 0.114	– – –0.013	– – –0.018	–
		σ	0.091 0.094 0.034	0.093 0.116 0.037	– 0.075 0.037	– – 0.037	– – 0.035	–

Table D.2 – Static Regression model parameters and their standard deviations.

Mode	Model		b_1		
1	0 , 1 1 1 , 0 0 0	x	0.809	0.010	–0.177
		σ	0.140	0.133	0.045
2	0 , 1 1 1 , 0 0 0	x	0.781	0.007	–0.196
		σ	0.151	0.145	0.040
3	0 , 1 1 1 , 0 0 0	x	0.555	0.112	–0.255
		σ	0.116	0.118	0.051

D.2 Case Study II: Church of Monastery of Jerónimos

D.2.1 Static and Dynamic Models for the Static Response

Table D.3 – ARX model parameters and their standard deviations.

Column	Model						
			a_0	a_1	a_2	a_3	a_4
C1	1 , 4 , 0	x	1	-0.988			
		σ	–				
			b_0	b_2	b_3	b_4	b_5
		x	1.600	-2.116	0.683	-0.1567	–
		σ	0.024	0.031	0.030	0.027	–
			a_0	a_1	a_2	a_3	a_4
C2	3 , 3 , 3	x	1	-0.737	-0.152	-0.049	–
		σ	–	0.011	0.013	0.011	–
			b_1	b_2	b_3	b	b_5
		x	–	–	1.006	-1.070	0.124
		σ	–	–	0.034	0.065	0.035

Table D.4 – Static Regression model parameters and their standard deviations.

Column	Model		b_1
C1	0 , 1 , 0	x	0.728
		σ	0.123
C2	0 , 1 , 0	x	0.942
		σ	0.055

D.2.2 Environmental and Loading Effects on the First Frequency

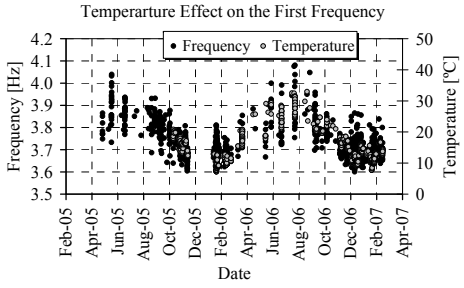


Figure D.31 – Environmental and loading effects on the first frequency: (a) temperature effect; (b) humidity effect; and (c) loading effect.

D.2.2.1 Frequency versus Temperature

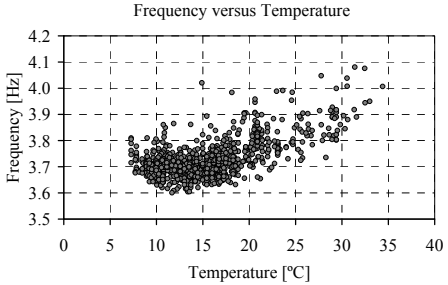


Figure D.32 – Frequency versus temperature.

D.2.2.2 Frequency versus RMS

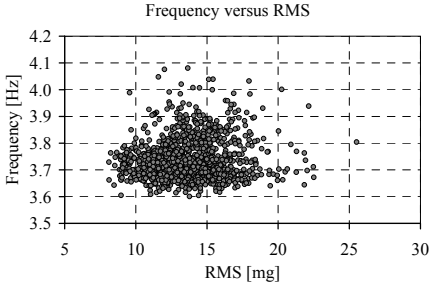


Figure D.33 – Frequency versus RMS.

D.2.3 Environmental and Loading Effects on the Second Frequency

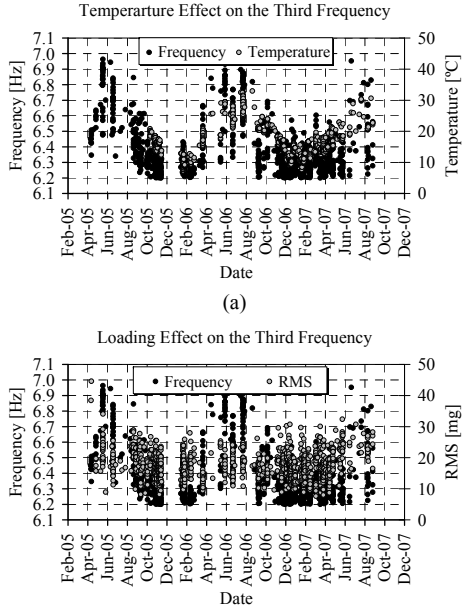


Figure D.34 – Environmental and loading effects on the first frequency: (a) temperature effect; (b) humidity effect; and (c) loading effect.

D.2.3.1 Frequency versus Temperature

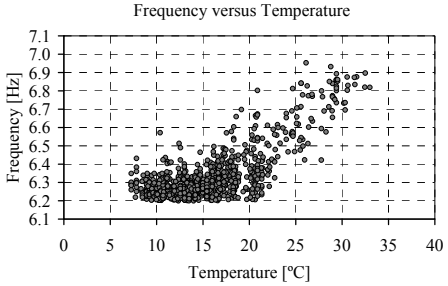


Figure D.35 – Frequency versus temperature.

D.2.3.2 Frequency versus RMS

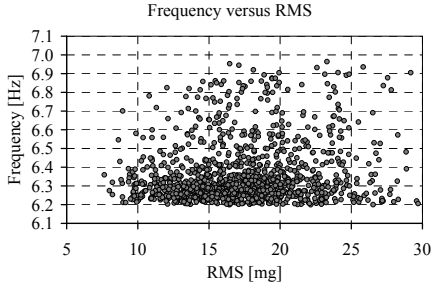


Figure D.36 – Frequency versus RMS.

D.2.4 Environmental and Loading Effects on the Forth Frequency

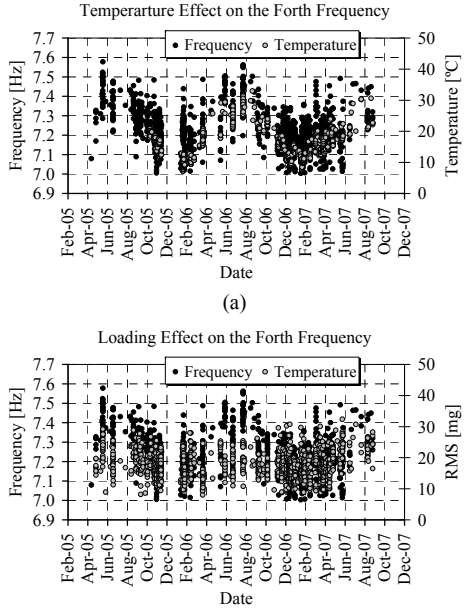


Figure D.37 – Environmental and loading effects on the first frequency: (a) temperature effect; (b) humidity effect; and (c) loading effect.

D.2.4.1 Frequency versus Temperature

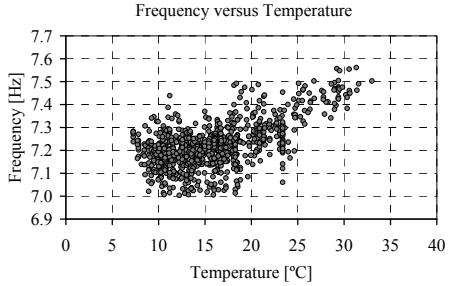


Figure D.38 – Frequency versus temperature.

D.2.4.2 Frequency versus RMS

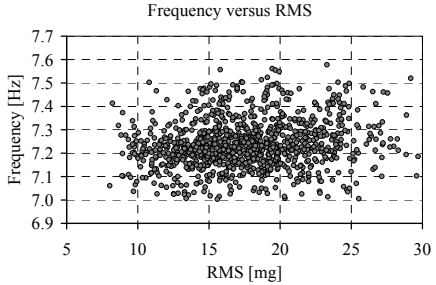


Figure D.39 – Frequency versus RMS.

D.2.5 Static Models for the Dynamic Response

Table D.5 – Static regression model parameters and their standard deviations.

Mode	Model	b_1 (T ≤ 17.5ºC)		b_1 (T > 17.5ºC)	
1	0 , 1 , 0	x	0.0215	x	0.6143
		σ	0.0729	σ	0.0913
2	0 , 1 , 0	x	0.2053	x	0.8100
		σ	0.0718	σ	0.0794
3	0 , 1 , 0	x	0.0553	x	0.6373
		σ	0.0604	σ	0.0874